UNIVERSIDAD AUTÓNOMA DE QUERÉTARO

CONIIN

LOOKING FOR SOLUTIONS WITH APPLIED ENGINEERING

FACULTAD DE INGENIERÍA

CONCYTEQ

CONIIN

LOOKING FOR SOLUTIONS WITH APPLIED ENGINEERING

CONACYT
Consejo Nacional de Ciencia y Tecnología

UNIVERSIDAD AUTÓNOMA DE QUERÉTARO

CONIIN

LOOKING FOR SOLUTIONS WITH APPLIED ENGINEERING

CONIIN: Looking for solutions with applied engineering, es una publicación anual de la Facultad de Ingeniería de la Universidad Autónoma de Querétaro, con arbitraje interno y externo (revista publicada desde el año 2016)
CONIIN: Looking for solutions with applied engineering, año1, No. 2, (2016), es una publicación anual publicada por la Universidad Autónoma de Querétaro, por medio de la Facultad de Ingeniería, con domicilio en el Edificio A de la Facultad de Ingeniería, Cerro de las Campanas S/N, Col. Las campanas, C.P. 76010.

Editores Responsables:
Karen Esquivel Escalante, Eduardo A.
Elizalde Peña y Carlos Guzmán Martínez.

Reserva de derechos al título exclusivo: en trámite
ISSN: en trámite

Certificado de Licitud y contenido otorgado por la Comisión calificadora de Publicaciones y Revistas Ilustradas de la Secretaría de Gobernación (en trámite).
Se distribuye actualmente mediante descarga electrónica.
Informes y correspondencia: Edificio A, Facultad de Ingeniería, Universidad Autónoma de Querétaro, Cerro de las Campanas s/n, Col. Las Campanas, C.P. 76010, Querétaro-México. Tel: +52 (442) 192 1200 ext. 6016 y 65401.

GENERAL INDEX

Mechanical and structural properties of a biomaterial compound with synthetic hydroxyapatite

José Rafael ALANIS GÓMEZ, Rodrigo Rafael VELÁZQUEZ CASTILLO[1], Eric Mauricio RIVERA MUÑOZ[2]

[1] Dirección de Investigación y Posgrado, Facultad de Ingeniería, Universidad Autónoma de Querétaro, Cerro de las Campanas S/N. Col. Niños Héroes, C.P. 76010, Santiago de Querétaro, Querétaro, México

[2] Centro de Física Aplicada y Tecnología Avanzada, Universidad Nacional Autónoma de México, A.P. 1-1010 Querétaro, Qro., C.P. 76000, México

Abstract— Biomaterials based on hydroxyapatite (HAp) are often studied due to the favorable answer presented as a substitute of bone tissue. However, the mechanical properties of this material have not been studied enough. In this work, we synthesized nanofibers of HAp through the microwave assisted hydrothermal method using $Ca(NO_3)_2$, $K_2(HPO_4)$ and KOH as precursors. The nanofibers presented a preferential crystalline orientation in the [300]. Structural studies were performed using X-Ray diffraction by powders, morphology and microstructure were analyzed by scanning electron microscopy and high resolution electron microscopy. Electron microscopy micrographs were processed in order to determine crystalline features of the HAp nanocrystals. Finally, the organic phase was added to the HAp and the compression tests were made to the composite, obtaining, as a result, a similar resistance to compression which has the trabecular bone.

Keywords— Hydroxyapatite, Mechanical properties, Modified Gel Casting Process

I. INTRODUCTION (HEADING 1)

It is well known that the HAp is a bioceramic that presents high biocompatibility as bone tissue replacement. HAp has been widely used as a bulk implant material in non-load bearing areas of the body [4]. Due to, the mechanical properties in the HAp composite materials present a low mechanical strength and brittle nature [6].

Different techniques have been tried to improve strength and fracture toughness of HAp such as making composites and using different morphologies of HAp as raw material of the composite like nanopowders [2], whiskers [12] or nanorods [7]. But, mechanical properties of the composite of HAp oriented fibers have not been studied deep enough.

One factor that must be considered is the porosity that plays an essential role in cell migration and adhesion, tissue formation, mechanical properties and nutrient diffusion, among others [8]. Also, a key component in tissue engineering for bone regeneration is the scaffold generation, which should be used as a template for cell interactions and the formation of bone-extracellular matrix through its pores and thereby provides structural support to the newly formed tissue [λ].

Moreover, other factor could enhance mechanical properties of HAp is decreasing the grain size of HAp [2]. With decreasing grain size, the fraction of the grain boundary phase is increased and thereby a greater amount of energy is absorbed during crack propagation through the grain boundaries of such fine grained microstructures (nanostructures) [11]. The decrease in the grain size from 1.5λ ȝm to 130 nm led to an increase in the fracture toughness from 0.85 MPa m1/2 to 1.3 MPa m1/2 [11].

The aim of this work is to obtain a biomaterial with a resistance and mechanical properties similar to those exhibited by the bone tissue. In this work, the samples were analyzed by XRD, SEM and TEM to verify the morphology and the size of the fibers of HAp, then, those fibers were molded by the modified gel casting process and then, compression tests were performed. The mechanical characterization results showed that the composite biomaterial possess a similar resistance under compression to that presented by the trabecular bone tissue.

II. METHODOLOGY

2.1 SYNTHESIS OF HAP

For the synthesis of HAp nanofibers through microwave assisted hydrothermal method, the reacting mixtures were prepared in two steps. Initially, one solution made of glutamic acid [$C_5H_\lambda NO_4 \cdot H_2O$] (J.T. Baker FW 147.13) and calcium nitrate [$Ca(NO_3)_2 \cdot 4H_2O$] (Sigma Ultra C4λ55) was prepared in deionized water. The two components were dissolved by mechanical agitation during 2 h at 60° C.

Subsequently, other solution of monobasic potassium phosphate [KH_2PO_4] (Mallinckrodt Chemicals FW 136.0λ) and potassium hydroxide [KOH] (SIGMA-ALDRICH 221473) was mixed in deionized water and stirred during 20 minutes. Then, both solutions were continued stirring for another 10 minutes [3].

Finally this reacting mixture was spilled inside Teflon vessels which were closed immediately and placed within a microwave oven (Synthos 3000 by Anton Paar). The power used in the oven was 1200 W. All synthesis reactions were carried out at 170° C and 70 kPa and the synthesis reaction´s time was 45 minutes.

2.2 Modified gel casting process

In order to obtain small porous ceramic pieces from the HAp nanofibers useful to obtaining of the biomaterial, modified gelcasting process was carried out. In this process, some chemical substances were used as solvent, dispersants or cross linking agent.

Ethanol was used as a solvent and the required amount of Polyvinyl butyral (PVB) (polymer) was added and then the solution was mixed by magnetic stirring. Furthermore, Polyethylene glycol (PEG) (dispersant) was melted and mixed with Polyacrylic acid (APA) (cross linking agent); then, both substances were incorporated to the mixture of Ethanol and PVB.

In the other hand, the HAp nanofibers were mixed with oxalic acid (microporous generator) and the necessary amount of Poly(methyl methacrylate (PMMA) spheres (macroporous generator). Finally, the initial mixture of ethanol, PVB, PEG and APA was added carefully to the HAp mixture to form a viscous paste which was molded and dried at room temperature. Once the paste got dry, it was removed from the molds and then sintered by a conventional oven at a temperature of 1100°C for 2 hours with a heating rate of 1°C/min.

Due to the fact that, the combination of polymers and hydroxyapatite to produce bone tissue substitutes is a natural strategy, gelatin was used to generate a composite material in this work. The ceramic scaffolds obtained from the modified gelcasting process absorbed different solutions of gelatin in water, 5.7, 6, 6.6 % weight by capillarity to generate organic-inorganic composite material.

2.3 X-Ray Diffraction (XRD)

In order to identify the crystalline phases contained in all amples, analyses by X-Ray diffraction by powder were performed using a D8 Advance diffractometer built by Bruker. The operation condition in the diffractometer were 35 kV and 15 mA, with a CuKα radiation wavelength of Ȝ= 1.5406 Å. The measurements were made from 10° through λ0° on a 2θ scale with a step size of 0.05°.

2.4 Scanning Electron Microscopy (SEM)

Observations of the morphology and microstructure of all materials were made using a scanning electron microscope Jeol JSM-63λ0 LV. The accelerating voltage used in the microscope was 20 kV and all the images were formed from secondary electrons. The sample was collected from the vessel by a pipette and separated from the solution. A small portion of the filtered solid was put on a sample holder and glued by a carbon painting and finally, the sample surfaces were coated with a thin gold film deposited by sputtering.

2.5 High Resolution Transmission Electron Microscopy (HRTEM)

Morphology and microstructure were observed through a JEOL JEM-2100F using 120 kV as accelerating voltage. Conventional bright field and high resolution images were recorded. Moreover, most of the images were analysed using the software Digital Micrograph® designed by Gatan in order to analyse the HAp Crystal structure of nanofibers. Sample preparation was dried and then a little amount of material was put on a carbon-film copper grid of 3 mm of diameter.

2.6 Mechanical Testing

All the composite biomaterial pieces obtained from the molding process were sanded up to obtain a cubic like shape with a size of 5x5x5 mm. Mechanical tests under compression were performed on all samples materials by means of a Zwick/Roell Tensile and Compression Testing Machine model Z005, at room temperature and using a deformation rate 1mm/min. Five samples of each different formulation were proved. The only variation in the formulation of the composite biomaterial was de containing of gelatin in the water solution. The average values of the ultimate strength were tabulated.

III. RESULTS AND DISCUSSION

The diffractograms recorded from most of the samples synthesized by the microwave assisted hydrothermal method are similar to that shown in the figure 1. The crystal phase identification was made by comparison using the International Centre for Diffraction Data (ICDD) powder diffraction file (PDF) bank, and the presence of the crystal phases 88-11λλ corresponding to HAp was identified.

In addition, the average crystallite size of the Hap nanocrystals were determined using the "EVA" software provided by Bruker, and a value of 64.15 nm was found. It is important to notice that the signals in the diffractogram are well defined and have low noise, indicating a highly crystallinity in the Hap samples [10].

The observation made by the scanning electron microscope showed the presence of Hap fibers with a clearly hexagonal cross section (Figure 2). It is necessary to remark that nanofibers were produced only, no nanoplates nor nanoparticles were observed as it was expected, and this found is desirable for the purposes of this study.

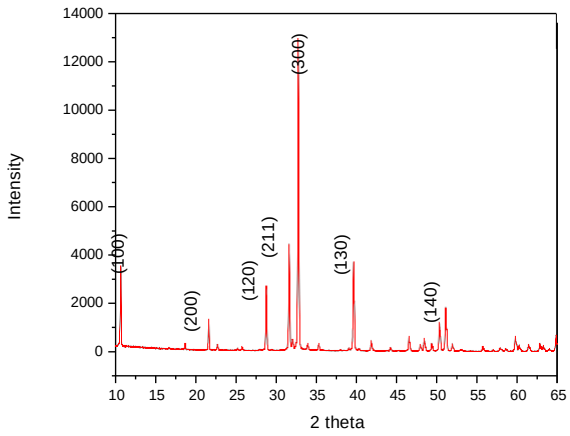

Figure 1. X-Ray diffractogram recorder from a HAp sample obtained by the microwave assisted hydrothermal method.

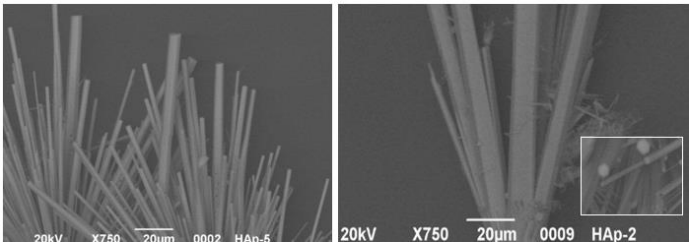

Figure 2. SEM micrographs of the synthetic HAp.

Using HRTEM, images of HAp nanofibers were recorded. In the figure 3 (left), it is possible to observe a line and dot pattern which was produced by the crystalline arrangement of HAp. This arrangement was analyzed by Digital Micrograph® software designed by Gatan, and the interplanar distances in the HAp crystal structure were determined. The distances between the lines from top to bottom was 0.81 nm which corresponds to the interplanar distance of (100) and the lines in the direction from left to right are spaced 0.35 nm, and this is related to (002) interplanar distance.

Then, a fast Fourier transform (FFT) was applied to the whole micrograph showed in the left side of figure 3, and the dot pattern produced is displayed in the right side of the same figure. The dot pattern is well defined, organized and possesses a symmetry two, which corresponds to the side planes (110) of the hexagonal crystal structure of HAP. The features of this dot pattern also confirm a high crystallinity in the HAp synthetized.

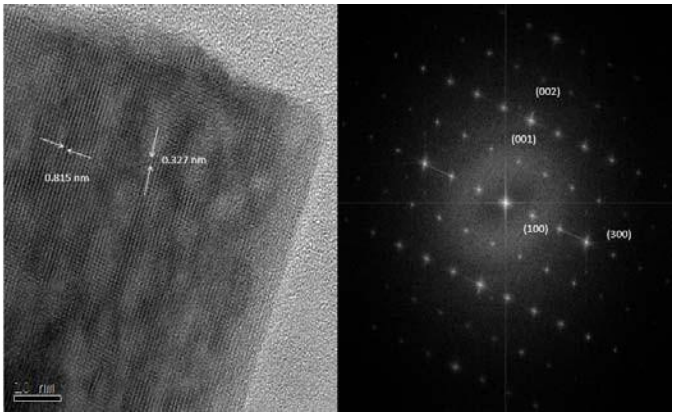

Figure 3. HRTEM micrograph of a nanofiber HAp showing its crystalline structure (left). In the right side, a FFT applied to that image produced the dot pattern presented.

The mechanical properties of a bone graft should be similar to those properties of bone-tissue receptors and thus adequately support load. These properties vary depending on the type of bone tissue. The maximum compressive strength effort is between 100 and 150 MPa for compact bone and between 2 and 12 MPa for trabecular bone [5].

In Figure 4, the different stages of the material´s respond against the applied load are shown. In the zone "A" of this plot, the cell material supports the applied stress suffering an elastic deformation; after that in the area B, the material begins plastic deformation. In the point C is the maximum effort that supports the material and it also is the beginning of the collapse of the cells within the cellular structure; in the region D, the cellular collapse is remarkable and a densification in the material takes place [1].

In Figure 5, typical stress-strain curves under compression for composite biomaterials with three different contents of gelatin were shown.

The ultimate strength had an increment associated to the increment of gelatin in the composite biomaterial, especially in the case of the biomaterial with 6.6 % by weight of gelatin. The ultimate strength values obtained were 4.17, 4.82 and 13.14 MPa for gelatin contents of 5.7, 6 and 6.6 % by weight respectively, these values are rather similar to those shown by the trabecular bone.

In order to obtain a deeper understanding of the mechanical properties of the composite materials synthesized in this work, a reference material was also mechanically characterized and theirs ultimate strength values were compared. The reference material was made in a similar way than the composite biomaterials obtained here; the only difference is the use of HAp powders (particles) instead of HAp nanofibers.

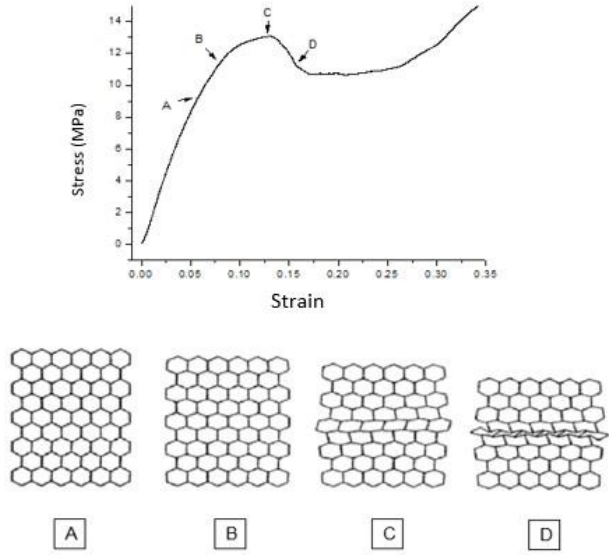

Figure 4.Schematic representation of the different stages of a celluar material respond against the applied load.

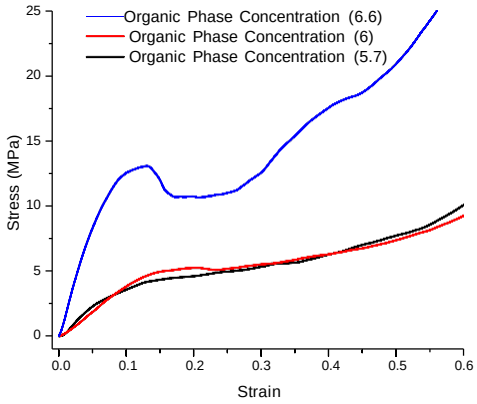

Figure 5. Stress-strain plots of the composites biomaterials with different content of gelatin.

Organic Phase Concentration	Ultimate Strength (MPa)
6.3	1.58
8	2.9
10.8	8.5
14.9	13.5
19.5	14

Organic Phase Concentration	Ultimate Strength (MPa)
5.7	4.17
6	4.82
6.6	13.14

Table 1- Comparative Ultimate Strength values for composite materials made of HAp particles (left) and HAp nanofibers (right).

In Table 1, the average ultimate strength values recorded for the composite materials made of HAp particles (left) are compared to those average values obtained for composites materials made of HAp nanofibers (right). These results show a significant increment in the ultimate strength for the biomaterials made of HAp nanofibers, the morphology, preferential crystalline orientation and dimensions of fibers could be relevant factors to improve the mechanical properties of the biomaterials. The biomaterial made of nanofibers is able to support 3 times more load than that supported for the composite material made of HAp particles; in addition, the composite material with fibers containing 6.6% by weight of gelatin had a similar ultimate strength value than that shown for a composite material made of HAp particles with 14.λ % by weight of gelatin. The interaction between organic phase and inorganic phase could be stronger for the biomaterials made of HAp nanofibers.

Finally, it is also significant how the ultimate strength increase with the increment of the concentration of organic phase present in the composite material, a synergic mechanical behavior between the inorganic and organic phases can be occurring, and as aconsequence, it is possible to emphasize that in those biomaterials made of fibers, these nanostructures improve significantly the mechanical properties of the composite.

IV. Conclusions

The application of the microwave assisted hydrothermal method combined with the use of the appropriate precursors can produce nanofibers with a preferential crystalline orientation in the [300], and the nanofiber can grow along the "c" direction. The synthesis method used in this work also proved to be a very efficient method saving time and energy.

The use of the obtained HAp nanofibers in the modified gel casting method to produce porous ceramic, and the posterior addition of the organic phases made of gelatin generated composite materials which presented a relevant synergic increment of the mechanical properties.

The maximum ultimate strength obtained in this work was 13.14 MPa at a low concentration of organic phase. This value is closely similar to that observed for the trabecular bone which is between 2 and 20 MPa. Possibly, and additional increment of the organic phase content in the composite material can produce a higher resistance under compression, and this way try to reach the mechanical resistance observed in the compact bone, but this supposition will be proved in further investigations.

The results obtained showed that the HAp nanofibers grown in direction "C" has a favorable effect on the mechanical

properties of the composite materials due to their morphology, preferential crystalline orientation and dimensions. The composite materials obtained here have similar characteristics than those present in the natural bone tissue, for this reason, these materials can be considered as bone tissue replacement.

ACKNOWLEDGMENT (Heading 5)

The authors would like to thanks the financial support of CONACyT Fondo Salud 2013-01-20132λ and the technical assistance of José Luis Cabrera Torres for the microscopy observations.

REFERENCES

[1] Ashby, M.F. and Hunkin. 2006. An introduction to microestructures, processing and design, D.R. de Engineering Materials 2. Great Britain, BH.

[2] Bose, S., Dasgupta, S., Tarafder, S. y Bandyopadhyay, A. 2010. Microwave- processed nanocrystalline hydroxyapatiteμ Simultaneous enhancement of mechanical and biological properties, Washington, USA, Acta Biomaterialia 6, 3782–37λ0.

[3] Cabrera, J.L., Velázquez, R. and Rivera, E.M. 2011. Synthesis of Hydroxyapatite Nanostructures Using Microwave Heating, Journal of Nanoscience and Nanotechnology. Qro., Mx., 11, 1 –7.

[4] Curran, D.J., Fleming, T.J., Towler, M.R. and Hampshire, S. 2011. Mechanical parameters of strontium doped hydroxyapatite sintered using micro- wave and conventional methods, Journal of the Mechanical Behavior of Biomedical Materials, 4 2063–2073.

[5] Fu, Q., Saiz, E., Rahaman, M.N. and Tomsia, A.P. 2011. Bioactive glass scaffolds for bone tissue engineeringμ state of the art and future perspectives, Review Materials Science and Engineering C, vol. 31, pp. 1245-1256.

[6] He, L., Standard, O.C., Huang, T.T.Y., Latella, B.A. and Swain, M.V. 2008. Mechanical behavior of porous hydroxyapatite, Acta Biomaterialia 4, 577–586.

[7] Sadat-Shojaia, M., Ataia, M. , Nodehia, A. and Khanlarb, L.N. 2010. Hydroxyapatite nanorods as novel fillers for improving the properties of dental adhesivesμ Synthesis and application, Dental Materials, vol. 26, pp. 471–482.

[8] Sobral, J.M., Caridade, S.G., Sousa, R.A., Mano, J.F. and Reis R.L. 2011. Three-dimensional plotted scaffolds with controlled pore size gradientsμ Effect of scaffold geometry on mechanical performance and cell seeding efficiency, Acta Biomateralia, vol. 7, pp. 100λ–1018.

[λ] Swain, S., Bhattacharyya, S. and Sarkar, D. 2011. Preparation of porous scaffold from hydroxyapatite powders. Materials science and enginnering C, nº 31, pp. 1240-1244.

[10] Triphathi, G. and Basu, B. 2011. A porous hydroxyapatite scaffold for bone tissue engineeringμ Physico-mechanical and biological evaluations, Ceramics International.

[11] Veljovića, D., Zaliteb, I., Palcevskisb, E., Smiciklasc, I., Petrovića, R. and Janaćkovića, D. 2010. Microwave sintering of fine grained HAP and HAP/TCP bioceramics, Ceramics International, vol. 36, pp. 5λ5–603.

[12] Zhang, H and Darvell, B.W. 2012. Mechanical properties of hydroxyapatite whisker-reinforced bis-GMA-based resin composites, Dental Materials, vol. 28, Issue 8, pp. 824–83.

[13] Alonso, S. 2013. Control de la macroporosidad de un material compuesto orgánico- inorgánico a base de hidroxiapatitaμ síntesis y caracterización. Tesis de Maestría, Querétaro, Qro.

Biomimetic nanoporous silica particles: Effects of surface on biocorona formation

Ing. Gerardo Paredes González, Dra. María de los Ángeles Cuán Hernández, Dr. Rufino Nava Mendoza
Directorate of Research and Graduate Studies, Faculty of Engineering
Autonomous University of Queretaro (UAQ)
Santiago de Queretaro, Queretaro, Mexico

Dra. Luz María López Marín
Nanotechnology Department, Center for Applied Physics and Advanced Technology
National Autonomous University of Mexico (UNAM), Campus Juriquilla
Santiago de Queretaro, Queretaro, Mexico

Abstract— **Design drug carriers using nanotechnology agents proves to be an alternative to drug release at specific locations. One of the most influential events on the recognition of nanoparticles in the body is the formation of a layer of proteins from biological fluids, also called biocorona. In this paper, the synthesis of silica nanoparticles was performed and the functionalization was proposed to confer lipid bilayers as specific surface characteristics like biomimetic particles upon contact with blood plasma. Additionally molecular modeling of a nanoparticle fragment and its interaction with the aspartic acid as a representative molecule was calculated to gain insight in the mechanism of the biocorona formation.**

Keywords— Nanotechnology, Nanomedicine, Drug delivery, Functionalization, Molecular simulation.

I. INTRODUCTION

The progress of medicine has caused a revolution in the way we treat disease. A drug taken orally loses much of its effectiveness to be metabolized in the liver or digested by the digestive system, causing only a very small percentage of the compound reaches the affected area and produce its effect (1) area, because of this and the possibility of reaching virtually any therapeutic target, the intravenous route of administration is widely used. However, the distribution of the drug throughout the body from this pathway results in low therapeutic efficacy. The pharmaceutical solution is to supply large amounts of the drug, resulting in high costs and side effects for patients (1).

Because of this problem in recent years has tried various disciplines to medicine and thus change the way we treat disease, among these disciplines is nanotechnology, which is a field of applied science devoted to the control and manipulation of materials at the level of atoms and molecules, corresponding to dimensions in the range 0.1 to 100 nanometers, although some authors include scales of several hundred nanometers to less micron. On this scale, the material displays different characteristics and applications traditionally known.

The application of nanotechnology to medicine has been called Nanomedicine, defined as the branch of nanotechnology that uses molecular tools, and knowledge of the human body, in order to preserve and improve health. The aim of this discipline is the bridge across these realms, biomolecular and physical, and take advantage of the unique capabilities of a kingdom for application in the other (2).

In turn, one of the branches of Nanomedicine is that dedicated to the use of nanoparticles for pharmaceutical purposes; its use provides a 'nano delivery "authentic. Drug delivery based Nanotechnology aims to guide the supply of drugs in the right place at the right time, with the optimal dose. The delivery system of nanodrug improves the bioavailability of each drug, reducing the negative side effects (3).

Great potential for this is the use of nanostructured materials, which have the advantage of having a size comparable to the cell, with biological macromolecules and cellular organelles such as (4) structures. Therefore they turn out to be suitable for functionalization with biomolecules, generating biomimetic materials that promote specific interactions and biocompatibility characteristics have shown (5). Therefore, the study and development of nanoparticles and, in particular, of biomimetic nanoparticles offers the opportunity to generate efficient vehicles treating diseases whose therapy is currently limited.

Nanotechnology has created new materials, one of which is interesting in this issue is the SBA-15. SBA-15 is a hexagonal mesoporous silica based on pores and with uniform distribution, and a pore diameter of between 5 and 15 nm. The wall thickness is approximately 3.1 nm 6.4. The large internal surface area is 400 to 900 m2 / g, which makes the SBA-15 a suitable material for various applications. (6)

SBA-15 is synthesized in a self-assembly process in acidic conditions using the triblock copolymer Pluronic 123 (EO20PO70EO20) as template and tetraethoxysilane (TEOS)

as silica source. After synthesis, the template can be removed by calcination. (7)

This paper aims to assess how the functionalization of the surface of mesoporous silica nanoparticles (SINP) to obtain a biomimetic envelope influences the adhesion of human blood serum proteins on the nanoparticles. Besides modeling a pore of IPNS and its interaction with some components of human albumin it is presented.

A. *Biocompatibility and evidence of use of silica particles*

Mesoporous silicate particles micro and nano systems are considered potential drug administration because their structures ordered pores, large areas and the ease with which they can be chemically modified (8).

Few studies have been reported cytotoxicity or biocompatibility, especially when administered in amounts necessary silicates to deliver drugs of low power.

After subcutaneous injection in rats silicate, the amount of residual material progressively decreased for three months with good biocompatibility in histology at all time points. By contrast, peritoneal and intra intra venous injections in mice resulted in the death or euthanasia. No toxicity was seen with subcutaneous injection of the same particles in mice. Microscopic analysis of lung tissue of mice indicates that death may be due to thrombosis. Although the local tissue reaction was mesoporous silicates benign, they caused severe systemic toxicity. This toxicity can be mitigated by modifying materials (9).

II ENVIRONMENT NANOPARTICLES WITHIN AN ORGANISM

B. *molecules within organisms*

In our bodies there is a huge number and variety of molecules. Proteins are some of these molecules, which correspond to biological polymers, or biopolymers synthesized inside the cell (10, 11).

Proteins are the most versatile molecules of living beings (12) and play crucial roles in virtually all biological processes.

Like all polymer, proteins are composed of large molar mass, molar weights ranging from thousands to hundreds of thousands of grams and are composed of many repeating units, and their physical properties are very different from the common small molecules (13).

The structural units of proteins are amino acids, which is a compound containing at least one amino group (-NH2) and a carboxyl group (-COOH), united in a linear sequence by a specific type of covalent bond, the peptide bond (Fig. 1).

The proteins of the human body consist of 20 different amino acids, characterized by having the amino group in alpha position of the acid group; in all the carbon α (alpha) is asymmetrical and is bonded to four different groups: the carboxyl group, amino group, a group R and a hydrogen atom (14).

By peptide bond amino acids form linear polymer chains, which vary by their structures in R (Fig. 1) groups.

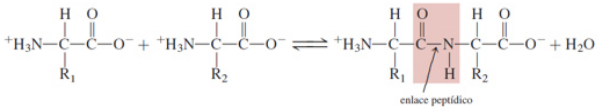

Fig. 1. Peptides are unions of amino acids through a peptide bond (marked red).

Primary, or linear sequence of a protein commonly contain 100 or more amino acid residues (10).

C. *Interactions between nanoparticles and biological fluids*

An important aspect to consider in the internalization of a particle within an organism is the existence of the innate immune system, which easily recognizes and destroys foreign material that enters the body's circulation. In the absence of camouflage, the nanoparticles interact with the blood proteins, thus increase the recognition and degradation by the mononuclear phagocyte system (MPS), which drastically reduces the lifetime of the nanoparticle (15).

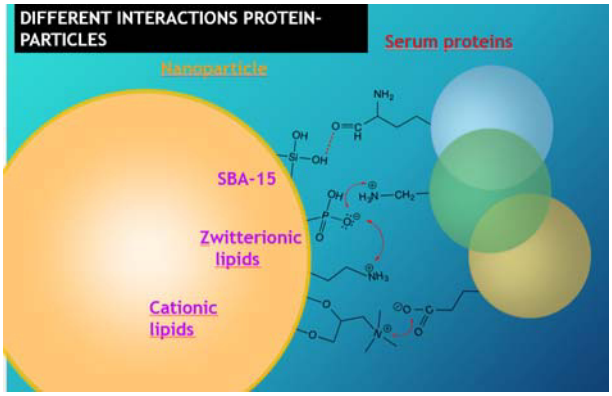

Fig. 2. Noncovalent interactions between a protein and functional groups of nanoparticles.

Another aspect of great importance to consider the interaction of a particle within the human body is its surface, as one of the events that influence this interaction is the adhesion of proteins present in the blood of the nanoparticles (Figure 3).

It is known that, depending on the surface characteristics, different types and amounts of protein could remain in a particle, forming a "crown protein" also called "biocorona" (16), where dynamic interactions are observed due to that biological environments are transient and not homogeneous. Such interactions may be key in modulating the biodistribution, elimination of immune responses and metabolism of nanomaterials (NM). In this context, it is proposed that the nature of the NM influence on nonspecific interactions with biological components, expected in the future to regulate such interactions as pharmaceutical interests (17).

For still unknown NM thoroughly the impact these can have on health, because their interaction with biological systems is very complex because of the large number of interactions with biomolecules and cells (Figure 2). To understand the relationship between the physical and chemical properties of NM and in vivo behavior, help in interpreting their biological behavior and so achieve selective delivery (18).

D. Selection of nanoparticles for this study

One attraction Nanomedicine systems is to use a recent materials development like the silica nanoparticles, which have a storage capacity of materials (or drugs); One advantage of these nanoparticles is to modify its surface properties easily and adapted to transport molecules of various nature.

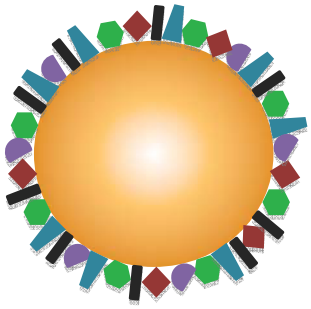

Fig. 3. Schematic representation of the crown of proteins, or crown, which is deposited on a nanoparticle in contact with biological fluids. Different proteins (represented as polygons of different color) are adhered by non-covalent bonds to the nanoparticles and can influence the evolution thereof in an organism. (50).

In this project the synthesis of nanoparticles with high biocompatibility proposed by functionalization of these with a lipid bilayer. Thus, the phospholipid bilayer membrane mimetizará a biological interacting with any other cells vesicle.

The use of lipids on silica surfaces has been shown for more than a decade in an attempt to emulate the coating biomimetically lipid cell membranes and improve biocompatibility of SiNPs (19). This lipid bilayer may have structural differences in their components, it may be formed of neutral lipids or lipid electrically charged.

Also the composition of lipids determines the molecules are more or less nonpolar or amphiphilic degree, and possesses the property of solubility (20).

In Figure 4 the arrangement is shown of amphiphilic lipids in an aqueous medium.

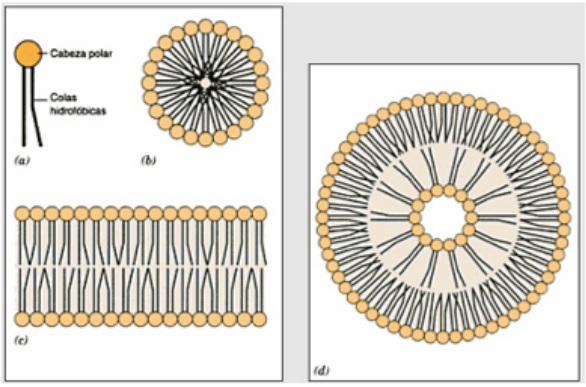

Fig. 4. Lipid in aqueous medium: a) amphipathic, b) a micelle cross section, c) cross-section of a lipid bilayer, d) cross-section of a liposome.

The use of lipids to functionalize the particles can be accomplished using liposomes which are composed of a lipid bilayer vesicles surrounding an internal aqueous compartment (Fig. 4) (21). The size of these nearly spherical lipid vesicles can range from a few nanometers to several micrometers. However, liposomes are applied to medical use range between 50 and 450 nm (22).

The mechanism and the extent of interaction of cells and liposomes are strongly influenced by the nature and density of the surface charge of the liposomes. Liposomes may include components that give them a positive or neutral charged overall negative charge. Neutral liposomes do not interact significantly with the cells, and this allows the drug release from liposomes in the extracellular space. An electrostatic surface charge could promote interaction of liposomes with cells (22).

II. TOOLS FOR ANALYSIS OF NANOPARTICLES

A. Structure and size

Technique of dynamic light scattering (DLS): with which the particle size distribution is obtained. A sample is irradiated with a laser beam light of wavelength λ0. Brownian motion of particles in suspension causes temporary fluctuations in the intensity of scattered light, Iθr (t), a measurement angle, θr.

The particles are in constant Brownian motion (constantly changing their positions). The scattered electric field (which depends on the position) is constantly changing, then the light intensity fluctuates in time.

Fluctuations in light intensity are inversely proportional to translational diffusion coefficient of the particles (with small particles moving faster than larger particles). Fluctuations are more frequently for smaller particles move quickly.

Currently, DLS allows the characterization of many colloidal systems in the approximate range of 1 nm to 5 microns, including latex (23).

B. *Functional Groups*

Raman spectroscopy: photonics technique is a high resolution (with wavenumber of 80-3500 cm-1) used for the study of the vibration modes, rotational and other low frequency in a system. It is based on impinging a beam of monochromatic light frequency Vo of the sample.

Most of the scattered light shows the same frequency as the incident light, but a very small fraction shows a change in frequency due to the interaction of light with matter.

The information can be obtained from a Raman spectrum is the frequency difference (energy) characteristic for each vibrational mode and this speaks of the links of the molecule (24).

III. PROTEIN ANALYSIS TOOLS

A. *Protein quantification*

The methods of protein quantification are based on colorimetric reactions. A common method is the Bradford assay, consisting in quantifying the binding of a dye, Coomassie Blue G-250, protein, comparing this binding with different amounts of a standard protein (Bovine Serum Albumin (BSA). the quantification is done by measuring the absorbance in a spectrophotometer and plotting the absorbance vs protein concentration, obtaining a calibration curve of the standard protein. this calibration curve can be interpolated protein concentration in a sample by measuring absorbance. the procedure is very fast and the time for trial is not limiting (25).

B. *Polyacrylamide gel electrophoresis (PAGE, for its acronym in English, polyacrilamide gel electrophoresis)*

The proteins have a net electrical charge if they are in a medium having a different pH of its isoelectric point and therefore have the property to move when subjected to an electric field. The migration speed is proportional to the ratio between the charges of the protein, its mass and shape. The higher charge per unit mass is faster migration.

An important advantage of polyacrylamide gels is that they are chemically inert, clear and stable in a wide range of pHs, temperature and ionic strength (26).

IV. METHODOLOGY

A. *Experimental Methodology*

a) Synthesis of nanoparticle

The mesoporous silica SBA-15 is synthesized by the sol-gel process and following the method proposed by Zhao et al procedure. (1998a) and Flodström and Alfredsson (2003), where a neutral surfactant used as structure directing, Pluronic P123.

The P123 is dissolved in a 4M hydrochloric acid solution (75 mL) and distilled water (112.5 mL) with constant stirring at 35 ° C. Once completely dissolved the P123, the Sol-Gel process begins by adding the precursor of silica, TEOS (11 mL). The reaction is performed for 24 hours at 35 ° C with constant stirring.

After this time the ripening process is effected by placing the gel obtained in a polypropylene container, stoppered and placed in muffle for 24 hours at 80 ° C (without shaking).

Upon completion allowed to cool and the solid was recovered by filtration. It is dried at room temperature and subsequently at 110 ° C for 18 hours at a heating rate of 2 ° C / min.

Finally calcined at 500 ° C for 4 hours at a heating speed of 1 ° C / min.

b) Blood Plasma

Blood sample (100 mL) of 12 healthy volunteer donors was obtained by 158vsp vacutainer tubes with heparin sodium as anticoagulant.

Fluids are passed centrifuge tubes 50 mL conical polypropylene had 17x120mm style).

The samples were centrifuged with a centrifugal Hermle Z230A, for 10 min at 1500rpm, filtered through 0.22 um membrane pore, and stored under sterile conditions.

The amount of protein in plasma was quantified by the Bradford method, and an amount of protein 29.8µg / .mu.l plasma was found.

c) Preparation of protein extraction solution

A solution of sodium dodecyl sulfate (catalog # 436143-100G) 2% with 100mM Dithiotheitol (catalog # D0632 Sigma

Aldrich, MW 15,425 gr7mol) (Philip ET AL 2015) was performed.

d) Incubation of nanoparticles in blood plasma.

Were centrifuged at 13000g plasma for 3 min. In a culture plate with 24 wells (Nunc Thermo) 500 .mu.l of a suspension of silica nanoparticles to 2 mg / ml in PBS per well they were deposited; immediately, the nanoparticles were exposed to plasma (500 ul of plasma centrifuge) for 24 h at 37 ° C. Incubations were prepared with PBS as controls. This procedure was performed under sterile conditions using autoclaved and handled in a biosafety cabinet material.

e) Analysis of the biocorona to nanoparticles

Following incubation with plasma, nanoparticles were recovered by centrifugation in an Eppendorf tube of 1.5 ml. The pellet was incubated with protein extraction solution to remove proteins incubation medium, the nanoparticles were washed three times with PBS, eliminating washed by centrifugation at 2500rpm for 5 minutes. Nanoparticles were stored suspended in 500 ul PBS at 4 ° C.

To remove proteins, the nanoparticles were centrifuged to remove PBS and incubated in 500 .mu.l of extraction solution protein in water bath at 70 ° C for 1 hour. Then, the supernatant proteins for further analysis recovered.

f) Quantification of proteins biocorona by bicinchoninic acid assay (BCA).

Extract proteins biocorona analyzed by the test of BCA, which is based on the quantitative reduction in alkaline Cu (II) to Cu (I) by the protein, and the coupled reaction of BCA becomes the Cu (I) complex having a purple an absorption maximum at 562 nm.

B. *Methodology Theoretical*

Using the software package Gaussian 09 (27) representative for the nanostructured material of the SBA-15, wherein the semiempirical method PM6 was used first model was constructed leaving free interacting molecule and neighboring her region model SBA-15. The solvent effect is taken into account by the continuous polarization model, taking water as solvent. Once the geometry of complex reoptimizó the model to a more accurate level of theory to account for electron correlation using the functional BLYP with the base 6-31-G (d).

V. RESULTS AND DISCUSSION

A. *Characterizations of the SBA-15*

Synthesis of mesoporous silica nanoparticles SBA-15 was made by the sol-gel method and proceeded to characterization by transmission electron microscopy (TEM) In this analysis can be seen the porosity of the particles. (Figure 6).

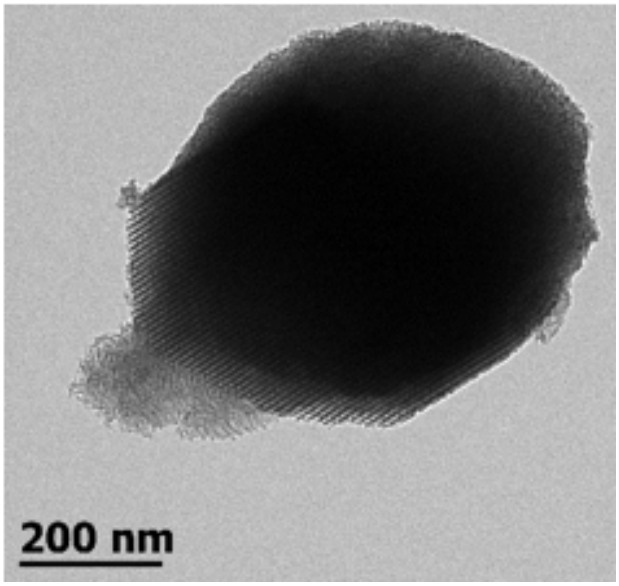

Fig. 5. Characterization of SBA-15 by TEM

A more detailed approach to the sample can be seen in Figure 6 in which the micrograph obtained with Scanning Electron Microscopy (SEM) is shown. In this micrograph you can best observe its morphology and porosity of the SBA-15, showing a hexagonal array with high porosity. As also can be appreciated the short particle size of about 400 nm wide.

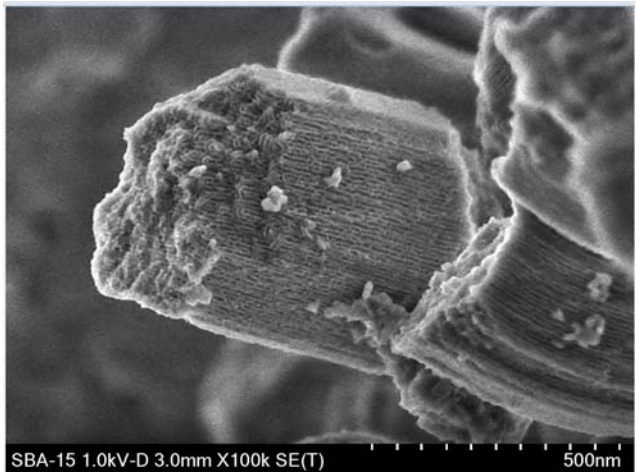

Fig. 6. Characterization of SBA-15 by SEM, approach

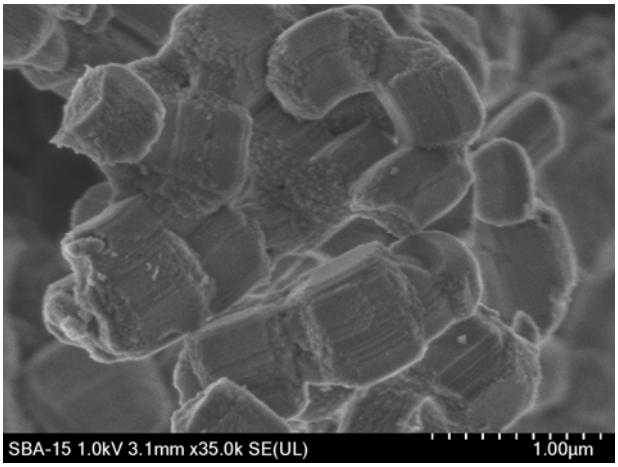

Fig. 7. Characterization of SBA-15 by SEM

The textural properties of the mesoporous silica material SBA-15 were determined by isothermal adsorption-desorption of N 2 at 77 K (Figure 8). The pore size distribution of the mesoporous silica material SBA-15 was calculated with the isotherm data dropout by B.J.H. method (Figure 9). The specific area of the sample was calculated according to the equation B.E.T. (Brunauer-Emmet-Teller). The total pore volume was estimated from the amount of nitrogen adsorbed at relative pressure of 0.98.

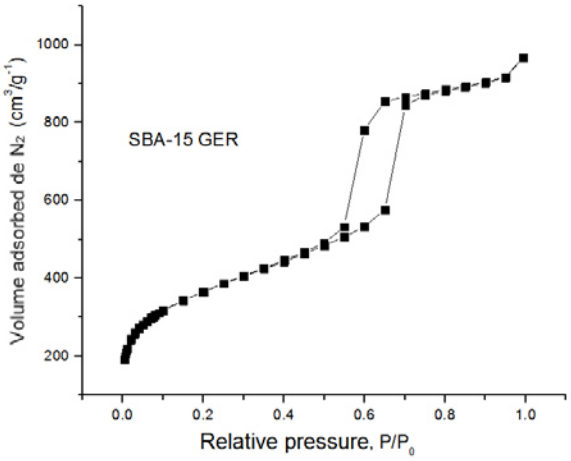

Fig. 8. Isotherm adsorption-desorption SBA-15

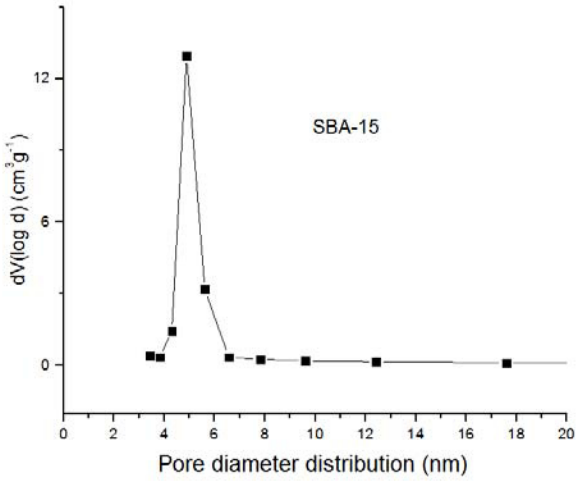

Fig. 9. Pore size distribution of SBA-15

From these analyzes it can be concluded that the textural properties of the synthesized SBA-15 are: surface area = 1267.162 m^2/g, pore volume = 1.269 cm^3/g and pore diameter = 4.881 nm.

B. Analysis of plasma protein

The plasma obtained was subjected to protein analysis by the method of Bradford (28), which consists of the colorimetric change of Coomassie blue protein contact. In Figure 10 a standard curve of bovine serum albumin colorimetric shown by the Bradford method. Colorimetric data interpolating plasma samples on this curve, it was found that the amount of protein was 35 microgram/µl plasma for men and for women 29.8 mg protein/µl plasma.

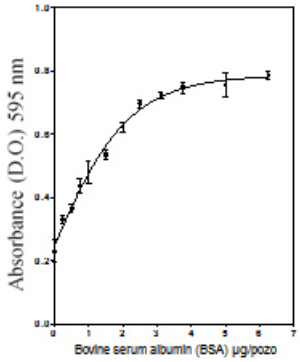

Fig. 10. Colorimetric reaction bovine serum albumin (BSA) with the Bradford reagent.

C. Analysis of SINP exposed to blood plasma

Adhering the IPNS proteins they were extracted with anionic detergent (dodecyl sodium sulfate) and a nonionic detergent (or dithiothreitol DTT). By the presence of these detergents, the Bradford method for protein quantitation could not be used, and the determination of proteins with Bicinchoninate (BCA) method was perfomed. According to preliminary analysis, the IPNS incubated with plasma containing a significant presence of adhered proteins (260mg / ml), while protein signal was detected in control samples, incubated with PBS. Currently conditions are standardized to analyze the protein profile of the biocorona by polyacrylamide gel electrophoresis.

D. Analysis of SBA-15 with biocorona

One of the methods used to demonstrate the presence of the nanoparticles was biocorona on thermogravimetric analysis. The sample analyzed by this technique was incubanda SBA-15 for 24 hours in human blood plasma.

In Figure 11, the graph of decomposition analysis shows the above, in which one can observe two distribution lines shown. The first line in red apare relates to SBA-15, which has been described as thermally stable than the REF protein. The second line, which is black, is referred to the protein that is known to be less thermally stable than the SBA-15, put another way, the graph shows the presence of an additional material to silica, which decreases percentage in function of temperature (black line). So we can conclude that the registration of two lines in the decomposition analysis indicates that there are two materials of different nature.

In Figure 12, the graph corresponds to the derivative of the curve of this gravimetric analysis generating differential thermal analysis (DTG) is shown, this analysis indicates accurately the temperature at which the material covering the SBA-15 It decomposes, which was 50.1 ° C. This result indicates that the material adhered to the SBA-15 does contain unstable molecules at temperatures of 50 ° C, consistent with a protein structure.

So far, analysis of the size and morphology of SINP exposed to plasma is pending, by dynamic light scattering (DLS, for its acronym in English dynamic light scattering) and transmission electron microscopy (TEM), and the presence of groups functional protein by FTIR spectroscopy.

Finally, the IPNS be prepared with modified through lipid bilayers surface, and the same tests to be carried biocorona analysis.

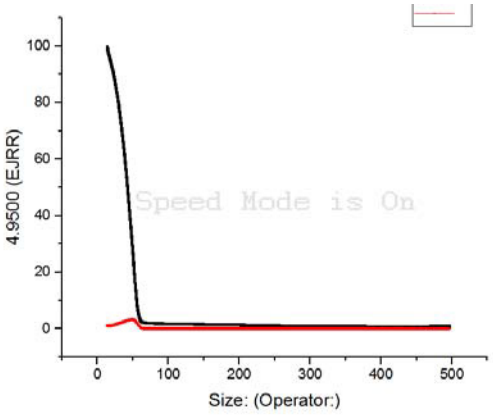

Fig. 11. TGD graph shows the SBA-15 incubated in plasma.

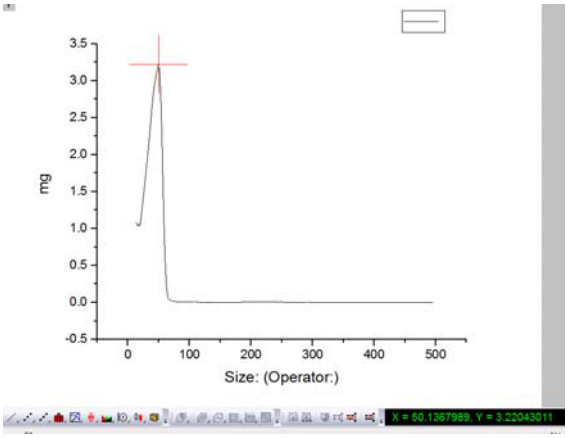

Fig. 12. DTG graph shows the SBA-15 incubated in plasma.

E. Simulation of interaction SINP - proteins.

The quantum mechanical study proposing a representative model for the mesoporous material, SINP is performed. In Figure 13, the structure is presented for a complete pore SINP, giving such a hex representation and as observed in the experimental micrographs. Since the size and number of atoms involved in a channel is very large, for the quantum model taken alone a representative section of pore IPNS-14If, as shown in Figure 14. The size simulated pore was 6 nm and is used for modeling the IPNS. The level of theory used to study quantum mechanical PM6 for optimizing the geometries and subsequently re optimizes the BLYP / 6-31G level (d). Once it built and optimized the representative model of the SBA-15, hereinafter IPNS-14If, we proceeded to give interacting molecule aspartic acid, in order to functionalize the IPNS-14If, it is placed in both the inside and outside the representative model of the pore. The study is done under vacuum and taking into account the effect of solvent. (water).

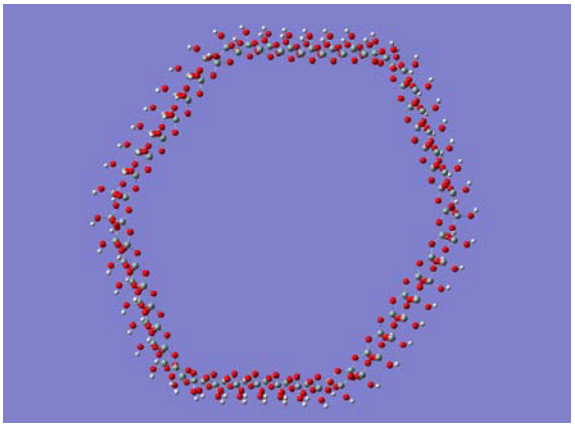

Fig. 13. Geometric representation of a semi channel SBA-15.

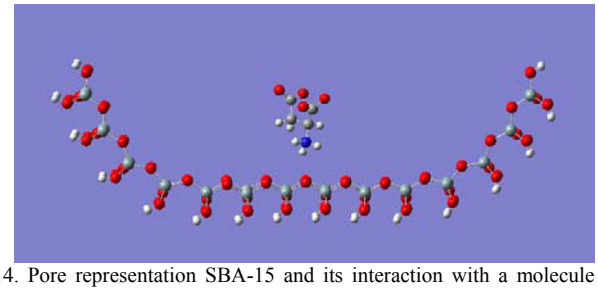

Fig. 14. Pore representation SBA-15 and its interaction with a molecule of aspartic acid.

The results show that the study is done under vacuum and taking into account the effect of solvent (water).

VI. CONCLUSIONS

In this paper the experimental characterization and simulation of the formation of the crown of proteins by exposing silica nanoparticles with human plasma were obtained.

The tests carried out show the strong interaction of silica nanoparticles unfunctionalized with human plasma proteins.

It is observed that the proteins are adhered to the SBA-15 particle by BCA method and 260mg / ml was quantified and verified with the DTG analysis. The quantum chemical results showed that the aspartic acid is linked to the surface model depending of the enviromental, i. e., if water is prensent in the medium or not. The preferential interaction is giving depending of the electronic structure of the molecule, when the solvent effect is taken into account the molecule interacts with the interior part of the pore, while in vacum conditions the molecule prefers interact outside of the pore.

VII. REFERENCES

[1] López Goerne T. M. Nanotecnología y nanomedicina. 1ª edición,, Cap. 1. Ediciones Arkhé, 2011, pp. 41-43. México D.F., México

[2] Wong I. Y., Bhatia S. N., Toner M. "Nanotechnology: emerging tools for biology and medicine". Genes Dev. Vol. 27(22), 2013, pp. 2397–2408.

[3] Banu A., Templeton A., Munshi A., Ramesh R. "Nanodrug Delivery Systems: A Promising Technology for Detection, Diagnosis, and Treatment of Cancer". PharmSciTech, vol. 15(3), 2014, pp. 709–721.

[4] Caballero R. (2013) Nanovectores híbridos para insertar material genético en células humanas. Tesis de Maestría, Posgrado en Ciencia e Ingeniería de Materiales, Universidad Nacional Autónoma de México.

[5] Balmert S. C., Little S. R. "Biomimetic Delivery with Micro- and Nanoparticles". Adv Mater. Vol. 24(28), 2013, pp. 3757–3778.

[6] Thielemann J. P.,Girgsdies F., Schlög R., Hess C. "Pore structure and surface area of silica SBA-15: influence of washing and scale-up". Beilstein J. Nanotechnol.,Vol. 2, 2011, pp. 110–118.

[7] Leofanti G., Padovan M., Tozzola G., Venturelli B. "Surface area and pore texture of catalysts". Catalysis Today Vol. 41, 1998, pp. 207-219

[8] Mateo D.; MORALES P.; AVALOS A., HAZA A. I. "Nanopartículas de oro: aplicaciones y citotoxicidad in vitro". Acta toxicol. argent. vol.21(2), 2013, pp. 102-109.

[9] Hudson S.P., Padera R.F., Langer R., Kohane D.S.. (2008). "Biocompatibility of mesoporous silicates. Biomaterials".Vol. 29, pp. 4045-4055.

[10] Chang Raymon. Química. 10a edición, Cap. 25. Editorial Mc Graw Hill, 2010, pp 1060-1073. México, DF, México

[11] López Marín, L. M., Lanéelle, M. A., Promé, D., Daffé, M., Lanélle, G., Promé, J. C. (1991) Glycopeptidolipids from Mycobacterium fortuitum: a variant in the structure of C-mycoside. Biochemistry Vol. 30 (43), pp. 10536-10542.

[12] Beas C., Ortuño D., Biología Molecular Fundamentos y Aplicaciones. 1a edición, Cap. 1. Editorial Mc Graw Hill, 2009, pp. 5-10. México D.F., México

[13] Peña Antonio, Arroyo Angel. Bioquímica. Cap 4. Editorial Limusa, 1985, pp 101-105. México, DF, México

[14] Luber Styler, Bioquímica. 6a edición., Cap 2. Editorial Reverté, 2007, pp. 25-34. Barcelona, España.

[15] Calixto G., Bernegossi J., Fonseca-Santos B., Chorilli M. "Nanotechnology-based drug delivery systems for treatment of oral cancer: a review". Int J Nanomedicine. Vol. 9, 2014, pp. 3719–3735.

[16] Pearson R., V. V. Juettner, Hong S. "Biomolecular corona on nanoparticles: a survey of recent literature and its implications in targeted drug delivery". Front Chem. Vol. 2, 2014, pp. 108.

[17] Wolfram J., Yang Y., Shen J., Mten A., Chen C., Shen H., Ferrari M, Zhao.J. Y. Wolfram. "The nano-plasma interface: Implications of the protein corona". Colloids and Surfaces B: Biointerfaces" vol.124, 2014, pp. 17-24.

[18] Guerrero S. (2013) "Implicancias Farmacéuticas de la Conjugación de Péptidos a Nanopartículas de Oro: efectos sobre la interacción con proteínas plasmáticas, la estabilidad, la toxicidad y la biodistribución" Tesis de Doctorado, Posgrado en Ciencias farmacéuticas, Universidad de Chile.

[19] Schwendene R. "Liposomes as vaccine delivery systems: a review of the recent advances". Ther Adv Vaccines. Vol. 2(6), 2014, pp. 159–182.

[20] Carmona-R. A. "Biomimetic nanoparticles: preparation, characterization and biomedical applications". Int J Nanomedicine. Vol. 5, 2010, pp. 249–259.

[21] P. Torchilin V. "Multifunctional, stimuli-sensitive nanoparticulate systems for drug delivery". Nat Rev Drug Discov. Vol. 13(11), 2014, pp. 813–827.

[22] Schuster B., Sleytr U. "Biomimetic interfaces based on S-layer proteins, lipid membranes and functional biomolecules". J R Soc Interface. Vol. 11(96), 2014, pp. 20140232.

[23] Bozzuto G., Molinari A. "Liposomes as nanomedical devices" Int J Nanomedicine. Vol. 10, 2015, pp. 975–999.

[24] Hornyak G., Moore J., Fundamentals of nanotechnology. Caps 12 y 13. Editorial CRC Press, 2009, pp 521-626. Broken Sound Parkway. U.S.

[25] Christopher K. M., Kensal E. V. H. Bioquímica. 3a edición, Cap. 5. Editorial Pearson Addison Wesley, 2002, pp 141- 146. Madrid, España

[26] McGrath, R. "Protein measurement by ninhydrin determination of amino acid released by alkaline hydrolysis". Anal. Biochem. Vol. 49 (1), 1972, pp. 95-102.

[27] Velasco A. (2012) Estudio teórico de los complejos de inclusión de β-ciclodextrina con dopamina y ácido ascórbico. Tesis de Maestría, Posgrado en Ciencia e Ingeniería de Materiales, Universidad Autónoma Metropolitana.

[28] Matsumura Y. "The drug discovery by nanomedicine and its clinical experience". Jpn J Clin Oncol. Vol. 44(6), 2014, pp.515-25

[29] López Marín, L. M., Lanéelle, M. A., Promé, D., Daffé, M., Lanélle, G., Promé, J. C. (1991) Glycopeptidolipids from Mycobacterium fortuitum: a variant in the structure of C-mycoside. Biochemistry Vol. 30 (43), pp. 10536-10542.

[30] Adler, A.F., Leong, K.W. "Emerging links between surface nanotechnology and endocytosis: impact on nonviral gene delivery". Nano Today, vol. 5, 2010, pp.553-569.

[31] Al-Halafi A. "Nanocarriers of nanotechnology in retinal diseases". Saudi J Ophthalmol. Vol. 28(4), 2014, pp. 304–309.

[32] Amoozgar Z., Yeo Y. "Recent advances in stealth coating of nanoparticle drug delivery systems". Wiley Interdiscip Rev Nanomed Nanobiotechnol. Vol. 4(2), 2012, pp. 219–233.

[33] Ansari A. A., Alhoshan M., Alsalhi S. M., Aldwayyan S. A. "Prospects of Nanotechnology in Clinical Immunodiagnostics". Sensors (Basel). Vol. 10(7), 2010, pp. 6535–6581.

Design of adaptation actions for road infrastructure faced with the effects of climate change

Márquez Zúñiga Hugo Fernando
Estudiante de la Maestría en Ingeniería de Vías Terrestres, Transporte y Logística
Facultad de Ingeniería, Universidad Autónoma de Querétaro
Querétaro, México
e-mail: ingfmarquez90@gmail.com

M. en C. Juan Fernando Mendoza Sánchez
Investigador especialista en Medio ambiente
Instituto Mexicano del Transporte
Querétaro, México
e-mail: mcmendozafernando@hotmail.com

***Abstract*— In recent years earth has suffered significant changes in average temperature, the records indicate that it has increased 0.8°C since 1880, causing a phenomenon known as global warming. This paper aims to present part of an investigation which analyzes the impacts of the climate change on the elements of the road infrastructure. The increased frequency and intensity of extreme weather events is a main issue for climate change adaptation. This paper considers the risks to existing transport infrastructure and the resulting considerations necessary in planning and designing of new infrastructure.**

Keywords*— *Climate change; road infrastructure; adaptation; impacts.

I. INTRODUCTION

Climate change is the set of large and rapid disruptions caused by rising of global temperature at the planet and it is the most important effect that global warming has generated on our planet. Climate change will affect transportation primarily through increases in several types of weather and climate extremes, such as very hot days; intense precipitation events; intense hurricanes; drought; and rising sea levels, coupled with storm surges and land subsidence. The impacts will vary by mode of transportation and region, but they will be widespread and costly in both human and economic terms and will require significant changes in the planning, design, construction, operation, and maintenance of transportation systems [1].

In Mexico the most used transport infrastructure is the road network due to its length of approximately 374,000 km of roads and the connectivity that this allow to reach to almost all the cities of the country, however most of them do not have resilient elements to resist the conditions presented by climate change.

Adaptation options in the sector can generally be divided into engineering options as subsurface conditions, material specifications, cross section and standard dimensions, drainage and erosion, and protective engineering structures, and non-engineering options as maintenance planning and early warning, alignment and master planning and land use planning, among others. Likewise, it is important to recognize that in a number of circumstances, a "do nothing" response to climate change—for example, allowing an infrastructure to deteriorate and be decommissioned instead of climate proofing the infrastructure—may be a preferred course of action.

Adaptation can be defined as the ability of a system to adjust to climate change to contain potential damages and take advantage of opportunities or be resilient to future consequences. Reference [2] defines resilience science as the simple premise that change is inevitable and that attempts to resist or control it in any strict sense are doomed to failure.

Adaptation should be linked to initiatives for disaster risk reduction and management. It is easier to introduce and consider climate impacts at the planning stage rather than after the system is complete [3].

Due to the effects of the climate change is very important to realize the analysis of the impact of the phenomenons produced by the global warming and the effects of these on the components of the road infrastructure to design resilient infrastructure.

According to studies by [4] and [5] the evaluation of the impacts of climate change on road infrastructure had focuses mainly on traffic accidents related to the weather, likewise, [6] argue that climate change poses a threat to the existing and future road infrastructure, including high costs of adaptation, maintenance and possible negative impacts on traffic and mention that the basis for considering climate change impacts on road infrastructure is well established , however , quantification of these results in monetary terms or in a time scale receive less attention. Even though, there are several tools to increase pavement management, prioritize investment and help build adaptive capacity in agencies or ministries of transport, as well as tools to monitor the effects of climate change. None of these is designed to link these changes to impacts on the built environment.

The complex and multifaceted impacts in the transport sector will require the prioritization of resources. Because of the uncertainties associated with the magnitude and duration of the effects of climate change, it is important to implement policies and plans that address both current and predicted vulnerabilities

II. IMPACTS OF THE CLIMATE CHANGE ON ROAD INFRASTRUCTURE

The project level is particularly critical for the consideration of climate change risks and for incorporating suitable adaptation measures. Infrastructure projects, which are critical for economic development, could be particularly sensitive owing to their long lifetimes during which many impacts of climate change may become progressively more and more significant. A project may also affect the vulnerability of natural and human systems to climate change and could therefore lead to maladaptation. For all these reasons, there has been considerable effort by development co-operation agencies and national governments to develop methodologies and tools to screen projects for climate change risks. These tools, however, have largely been stand-alone initiatives and their application within actual project settings remains quite limited [7].

The impact of climate change upon the road network and road pavement will indirectly affect the location of human settlements and associated activities. For example, the road network is not only essential for the interconnection and movement of goods amongst major urban and regional centres but also critical to stimulating and sustaining their industrial development and economy. At an urban scale, it sustains the lifeline' of communities by enabling the supply of food, water and other critical services. The road network also plays an important role during extreme events or disasters by providing evacuation routes and communication channels between communities. Therefore, it is important that the planning and delivery of the road network should consider the potential impact of climate change.

Climate change impacts on the road network demand a re-think about how roads are designed, constructed and maintained, particularly due to potential effects on road pavement. For example, changes in average rainfall, temperature and evaporation patterns can alter the moisture balances in the pavement foundation. Further, the rise in the water table due to rising sea level can lead to the reduction of the structural strength of the pavement. Additionally, a rise in air temperature can accelerate the ageing of road surfacing bitumen layers. Consequently, climate change is likely to have impacts on the pavement performance and influence the rate of pavement deterioration. Nevertheless, given that the lifetime of some transportation infrastructure such as road pavement is relatively short (e.g. 10-20 years), there is considerable scope for the sector to adapt to climate change impacts as they emerge [8].

A. *Changes in precipitation*

Decreased precipitation, has the potential to result in increased ground movement, changes in the watertable and associated increases in the salinity of soils. The combination of these changes has the potential to accelerate the degradation of materials, structures, reinforcement and foundations, reduce the life expectancy of the transport infrastructure, increase maintenance costs and may eventually contribute to structural failure when stressed by extreme climate events. Significant flood damage to road, rail, bridge and tunnel infrastructure may result from the increased frequency and intensity of extreme rainfall events. The magnitude and frequency of floods also plays an important role in the design and planning of transport infrastructure. The short term impacts of precipitation changes relate to pavement and drainage design, foundation conditions, the approach used to estimate the design flood and the development of targeted maintenance schemes. Longer term impacts may require changes in culvert design and the design and materials specifications of road subgrade [9].

Changing precipitation intensity may affect the drainage performance of the bridge deck or approaches in such a way that traffic safety is impacted, and different design standards or related factors of safety may be needed to account for such changes during the design process.

B. *Changes in temperature*

Reference [10] asseverate that global climate change is projected to bring warmer temperatures and changes in the seasonality of precipitation. These changes are projected to lead to increased extreme high temperatures and decreased the extreme low temperatures, wetter conditions in winter, spring, and fall, and drier summers.

Temperature extremes increase the expansion stress and movement experienced on steel bridges and rail tracks, and also cause the expansion of concrete joints, protective cladding, coatings and sealants on bridges. Higher temperatures combined with increased solar radiation may reduce the life of asphalt road surfaces through an increase in the embrittlement of the surface chip. Embrittlement causes surface cracks to form such that water can infiltrate the road surface resulting in potholes and rapid loss of surface condition. Increased maintenance would be necessary to manage this phenomenon. High temperatures also result in the softening of asphalt and may lead to traffic related rutting. Pavements can also buckle under extreme temperatures. Temperature extremes and the general warming of the climate may also limit the undertaking of maintenance and construction activities due to heat stress conditions for workers. The increased number of hot days is expected to have minimal impact on pavement or structural design in the short term (30 to 40 years); however, a significant change would be required long term (40 to 100 years) in pavement and structural design, the substitution of materials, and a higher level of maintenance service 10].

Research should be undertaken to identify climate related thresholds that may lead to a significant increase in infrastructure deterioration; for example, temperature thresholds for pavement degradation will signal appropriate decision points to implement higher standards for new projects or reassessment of vulnerable infrastructure. The creation of thresholds allows for efficient allocation of resources given the wide range of possible climate scenarios [11].

TABLE I. IMPACTS OF CLIMATE CHANGE ON ROAD INFRASTRUCTURE.

Climatic event		Impact to Infrastructure	Vulnerable infrastructure	Possible adaptation measures
Temperature	Increased extreme maximum temperature	- Premature deterioration of infrastructure; - Damage to paved roads from rutting, buckling, and raveling; - Bridges stressed by thermal expansion and movement;	Pavements; bridges and slopes.	Use of rigid pavements, materials treatments to reduce heat absorption. Corrosion protection on bridges. Planting vegetation to reduce heat exposure of the roads. Build infrastructure such as parks, to reduce exposure.
	High thermal gradients	-Contraction and expansion of pavements	Pavements	Using special asphalts, PG grade.
Precipitation	Greater seasonal precipitation variation	-Increases the risk of landslides, slope failures, and run-off caused floods; - Increased soil moisture levels may lead to loss of structural foundation integrity of roads, bridges, and tunnels;	Slopes; embankments; pavements and drainage culverts.	Flood estimation, designing with higher return periods.
	Increased intense precipitation and storm events	- Greatly increased risk of fluvial erosion embankment deterioration; - Increased rate of bridge scour or aggregation; - Greater likelihood of exceeding culvert capacity; - Signs and bridges stressed by increased wind;.	Embankments; pavements, bridges, signs and drainage culverts.	Drainage design with increased hydraulic capacity, including adjustments in size, shape and slope.

Source: Elaboration from [11] and [12].

III. DEVELOPMENT

According to the inventory system of effects of disasters (DesInventar) of the OSSO Corporation in Colombia, phenomena such as sliding, hurricane, flood, rain, tide, heatwave, drought, mainly, from 1970 to 2013 were recorded around of 9950 events across the country, causing damage to different sectors. This type of environmental phenomena has increased the vulnerability of transport infrastructure, producing in it impacts such as flooding of the road, landslides and slopes and embankments, damaged bridges and drainage work , flaws in the paving and other structures, as road accidents.

So increasing adaptation actions on the road infrastructure, has become today an absolute necessity when it refers to the geometric design of the roads and its components.

A. The database

The use of a database to obtain information about the effects caused by various natural phenomena will be critical in carrying out this research, whence we will make use of the virtual platform "DesInventar" which is a conceptual and methodological tool of public access that has information from losses, damages or effects caused by emergencies or disasters, providing information of disasters from a local spatial scale, providing reliable tools for the analysis of weather events and their effects on roads.

This database comes to mid 90's due to the need for systematic information on the occurrence of daily disasters of small and medium impact in Latin America and the Andean sub region.

Since 1994 began the building of a common conceptual and methodological framework by groups of researchers, academics and institutional actors, grouped in the Network for Social Studies on Disaster Prevention in Latin America, who conceived an acquisition system, query and display of information on disasters of small, medium and large impacts, based on existing data, newspaper sources and reports from institutions in nine countries in Latin America [13].

B. Cause and effect diagrams

According [14] the cause and effect diagram is a diagram in which the relationship between an event and its origin or causes factors is presented. It is the graphic representation of each and every one of the possible causes of an event and can be represented by this diagram any kind of problem.

Once you have made this diagram it represents orderly and completely all possible causes that influence in a problem and provides the basis for start searching for the real causes, namely, the real analysis cause - effect.

This analysis is the process of defining precisely the effect to be studied, and through the representation of the situation by building diagram allows an analysis of the causes that influence the effect studied.

This tool will build for each weather event, the effect that it will have on infrastructure, identifying the impact of climate change and its direct adaptation measure.

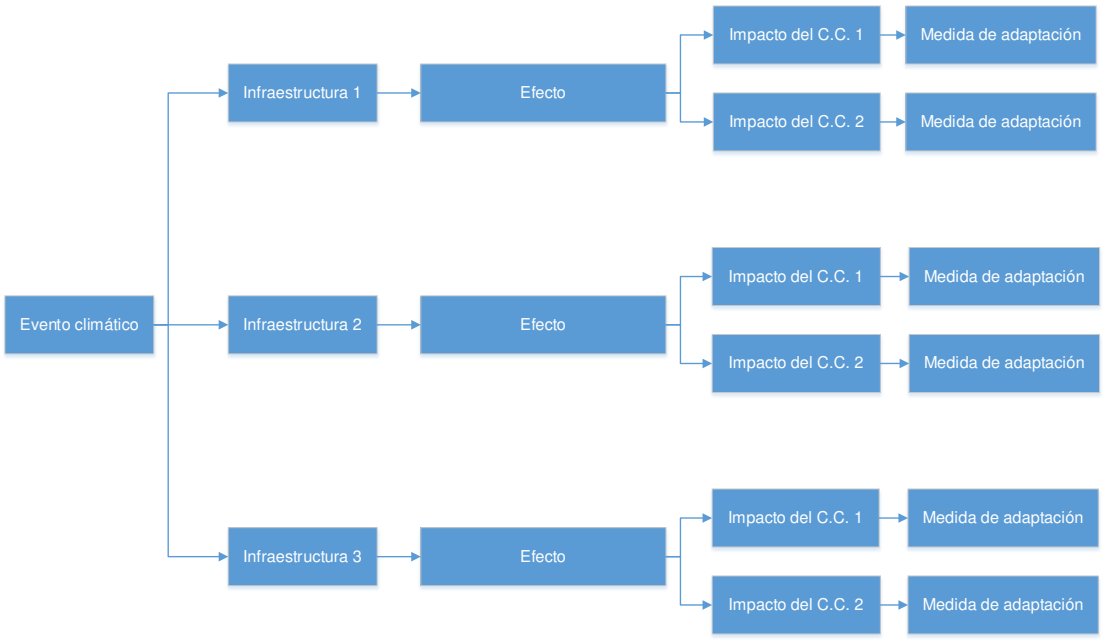

Figure 1. - Diagram Cause and Effect

C. *Interrelationships diagrams*

Reference [15] mention that a diagram of interrelationships allows to extract overriding ideas and develop logical relationships between categories.

It is an instrument used to explore and identify relationships of the existing causes between different elements, being specially focused for cases that aim to identify complex relationships of cause and effect. Its use is appropriate for the resolution of complex cases with lots of relationships or a large number of causes.

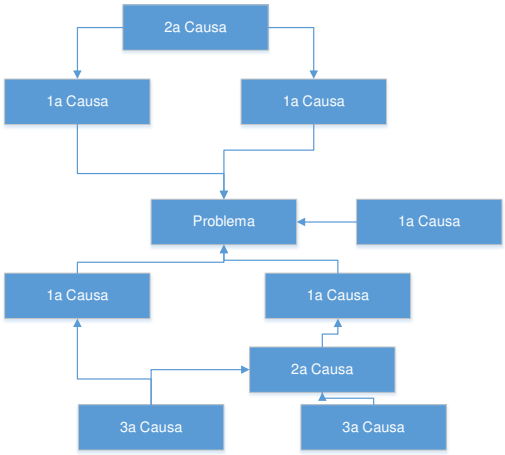

Figure 2. – Interrelationships diagram

D. *Delphi method*

The Delphi method is a structured communication method, originally developed as a systematic, interactive forecasting method which relies on a panel of experts [16].

The specialists answer questionnaires in a serie of rounds. After each round, a organizer [17] provides an anonymous summary of the experts' forecasts from the previous round as well as the reasons they provided for their verdicts. Thus, experts are encouraged to revise their earlier answers in light of the replies of other members of their panel. It is believed that during this process the range of the answers will decrease and the group will converge towards the "correct" answer. Finally, the process is stopped after a predefined stop criterion and the mean scores of the final rounds determine the results [18].

Delphi is based on the principle that or decisions from a controlled group of individuals are more accurate than those from unstructured groups.

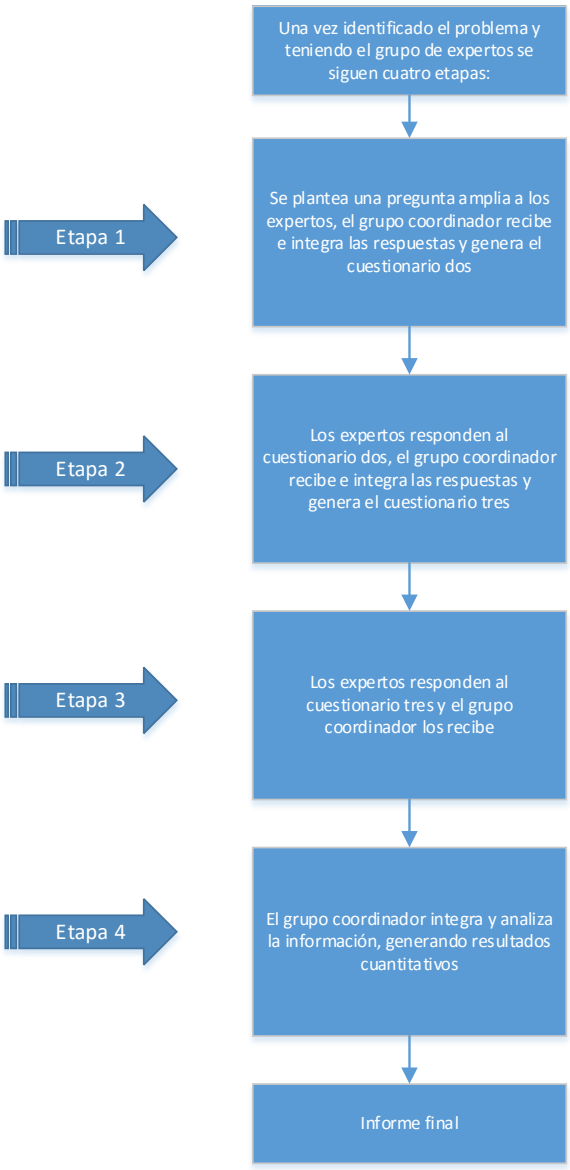

Figure 3. – Basic stages of the Delphi method.

IV. EXPECTED RESULTS

With the final results of this research we hope to obtain enough information by which we can prepare a document for the adaptation of road infrastructure to climate change , it will enable decision makers to have a basis for incorporating resilient infrastructure on roads in the country.

ACKNOWLEDGMENT

This research was supported by the Instituto Mexicano del Transporte. I thank to M. in C. Juan Fernando Mendoza Sánchez who provided insight and expertise that greatly assisted the research. We would also like to show our gratitude to the Universidad Autónoma de Querétaro for sharing their pearls of wisdom with us during the course of this research.

REFERENCES

[1] Transportation Research Board, Potential Impacts of Climate Change on U.S. Transportation, Special Report 298, National Research Council, United States, 2008.

[2] Rees, William E. "Foundation Concepts." The Post Carbon Reader Series. Santa Rosa, CA: Post Carbon Institute, 2010.

[3] Regmi, Madan B.; Hanaoka, Shinya, A survey on impacts of climate change on road transport infrastructure and adaptation strategies in Asia, Environmental Economics and Policy Studies, 13, 21-41, 2011.

[4] Hambly, Derrick; Andrey, Jean; Mills, Brian y Fletcher, Chris. Projected implications of climate change for road safety in Greater Vancouver, Canada. Climatic Change, 116 (3-4), 613-629, 2013.

[5] Andersson, Anna K. y Chapman, Lee, The impact of climate change on winter road maintenance and traffic accidents in West Midlands, Accident Analysis & Prevention, 43 (1), 284-289,2011.

[6] Schweikert, Amy; Chinowsky, Paul; Espinet, Xavier y Tarbert, Michael, Climate Change and Infrastructure Impacts: Comparing the Impact on Roads in ten Countries through 2100, Humanitarian Technology: Science, Systems and Global Impact 2014, *HumTech2014*, Vol. 78, pp. 306 – 316, 2014.

[7] Agrawala S., A. Matus Kramer, G. Prudent-Richard and M. Sainsbury, "Incorporating climate change impacts and adaptation in Environmental Impact Assessments: Opportunities and Challenges", OECD Environmental Working Paper No. 24, OECD Publishing, © OECD. doi: 10.1787/5km959r3jcmw-e, 2010

[8] Serrao-Neumann, Silvia; Low Choy, Darryl; Cobus Van Staden, Rudi; Crick, Florence; Sahin, Oz; Chai, Gary; Guan, Hong, Climate Change Impacts on Road Infrastructure Systems and Services in South East Queensland: Implications for Infrastructure Planning and Management, State of Australian Cities Conference 2011 Proceedings, (12 pp.), 2011.

[9] Taylor, Michael AP; Philp, Michelle, Adapting to climate change – implications for transport infrastructure, transport systems and travel behavior, Road and Transport Research, 19 (4), pp. 69-82, 2010.

[10] Hamlet, Alan F., Impacts of Climate Variability and Climate Change on Transportation Systems and Infrastructure in the Pacific Northwest, Available in: http://cses.washington.edu/db/pdf/hamlettransportation743.pdf, (2011).

[11] Vermont Agency of Transportation (VTrans) (2012), "Adapting Vermont's Transportation Infrastructure to the Future Impacts of Climate Change: VTrans Climate Change Adaptation White Paper." VTrans Policy, Planning & Intermodal Development Division. Available in < http://vtransplanning.vermont.gov/sites/aot_policy/files/documents/planning/Climate%20Change%20Adaptation%20White%20Paper.pdf>

[12] Hanaoka, Shinya, Assesment on impacts of climate change on road transport, Department of international development engineering Tokio institute of technology, Ookayana, Tokio, (pp. 13), 2009.

[13] DesInventar [on line]. Cali-Valle-Colombia,. Sistema de inventario de efectos de desastres. Available in: <http://www.desinventar.org/es/>

[14] Galgano, Alberto, Los siete instrumentos de la calidad total, Ediciones Díaz de Santos, (pp. 320), 1995.

[15] Miranda González, Francisco Javier; Chamorro Mera, Antonio; Rubio Lacoba, Sergio, Introducción a la gestión de la calidad, Delta Publicaciones, (258 páginas), 2007.

[16] Dalkey, Norman; Helmer, Olaf. "An Experimental Application of the Delphi Method to the use of experts". Management Science 9 (3): 458–467. doi:10.1287/mnsc.9.3.458, 1963.

[17] Milbrey W. McLaughlin, The Rand Change Agent Study Revisited: Macro Perspectives and micro Realities, Stanford, CA: Stanford University, 1990.

[18] Rowe and Wright: The Delphi technique as a forecasting tool: issues and analysis. International Journal of Forecasting, Volume 15, Issue 4, October 1999.

Characteristics of mobility of people with disabilities in conurbation of Querétaro, México

Jesús Reyes Alaniz[1], Ovidio González Gómez[2]

[1]*Estudiante de la Maestría en Ingeniería de Vías Terrestres, Transporte y Logística,* [2]*Profesor – Investigador, División de Estudios de Posgrado*
[1,2]*Facultad de Ingeniería, Universidad Autónoma de Querétaro*
Querétaro, México
[1]e-mail: jesusreyesalaniz1@hotmail.com
[2]e-mail: ovidio@uaq.mx

***Abstract*— Around the world there is a lot of people with disabilities, of which mobility problems have been little seen. Public transport has been a physical barrier to the mobility of persons with disabilities, since its inception in the suburbs of Queretaro, where as in Latin America the displacements of the population rely on mostly public transportation since it is the most cheapest to move within a metropolis. For the specific case of the suburbs of Queretaro, the law of existing mobility is a dead letter since being ignored as in addition to the number of people with physical limitations and it is unknown to meet their transport problems. This article aims to make a comparison of movements and characteristics for two groups of people with disabilities: motor and visual since together they represent more than 80% of the disabled.**

Research conducted the comparison of the general population and persons with disabilities: study levels, means of transport and movements per day.

In addition to the above is a comparison between the two groups of people with disabilities to learn their form of transportation, description of travel: number, cost, length and time.

It is observed as there is an exclusion of persons with disabilities in social activities and the poor infrastructure of the public transportation for people with disabilities.

Keywords: disability, mobility, public transport

I. INTRODUCTION

The International Labour Organization, (ILO) [1] mentions that one tenth of the world's population are people with disabilities. Research around the world about the mobility of individuals with a physical limitation reveal the importance of the inclusion to the public transportation system for people who suffer from some type of physical deficiency[2], which coincides with what was expressed with [3] who also described the existence of physical barriers that hinder further correct mobility for those who bear some kind of physical restraint and lack of specialized transportation for their travel. [4]also agrees with the above mentioned.

Since the beginning of passenger transport initially in the young city of Querétaro [5]. Due to the imposition of physical barriers and poor condition of the infrastructure in the area of suburbs in Queretaro has not existed accessibility for those with a limited physical condition [6], in addition to existing narrow between poverty and disability tie, if they do not have access to public transport, disabled people use other more expensive means of transportation and even limit your mobility, according to [7].

Improve access to means of transport and mobility contributes in reducing poverty and participation of individuals with physical limitations in socio-economic activities [2], public transport is important in the search for jobs [8]. Besides [9] described the difficulty faced by those who suffer from disabilities in search of transport.

As part of a wider investigation, are presented in this document a description of the distribution area of displacement of those with disabilities within the suburbs of Queretaro. The study has two types of motor disability and blindness, who, based on [10] represent 84% of disabled people of the State of Querétaro.

II. MOBILITY AND ITS IMPORTANCE

The right to mobility, law of mobility for the transport of the State of Querétaro [11], becomes a dead letter for people with physical limitations by the inaccessibility to public transportation. As mentioned it [12], "persons with disabilities have fewer opportunities and quality of life also faced to more challenges during their displacement and the use of public transport", which is in line with social and occupational segregation of persons with disabilities which mentions [13].

Mobility is affected by the following aspects according to [7] for: income, age, gender, means of transport, culture and disability.

Forms of displacement

In Latin America a lot of its mobility depends basically collective and public transport and automotive (fundamentally buses), since they are countries where most of the population is the only form of transport. This is even more critical for the unemployed population, devoid of resources, the disabled and the vulnerable groups for which, due to lack of resources, mobility becomes negligible [14].

Mobility of people with disabilities

This research will define the term disability according to the World Health Organization as: a lack or limitation (because of a deficiency) of the ability to carry out an activity in the range that is considered normal for the human being [15].

According to the International Labour Organization [1], a tenth of the people around the world suffer from some kind of physical limitation, i.e. around $ 650 million, of which 450 million are in productive age, i.e. which can perform some kind of work.

For the State of Queretaro, according to [10] the number of persons with disabilities in the State sector is approximately 80,000 although it is not known with accuracy since it lacks control over them.

Throughout history and depending on the society in which they live, people with disabilities have been treated in different ways (sometimes with respect and all the services available, but in other cases without having the same fate). In the aspect of mobility, initially there was concern about providing service to people with disabilities (of any type), "the rights of the elderly and pregnant women, were only" was until 1963 that the rights of vulnerable groups were listening at the first International Congress for the removal of architectural barriers and in 1975 with the Declaration of the Organization of the United Nations on the law of the disabled today internationally named disabled that make clear the creation of environments more accessible.

The concern of the mobility of persons suffering from physical limitations began in the Decade of the 70s and 80s in countries that began a legislation in this regard: Sweden, United States and United Kingdom [16]. Unfortunately efforts to combating and overcoming discrimination depend on legislation, legal barriers and transport systems which vary in each country [17]

According to [18] three phenomena affect the inclusion of persons with disabilities to public transportation:

I. High rates of service

II. Informal or poor offer of public transport (quality and availability of the service).

III. Under the access to the vehicle for mainly economic reasons and because design does not in general facilitates its correct use.

III. METHODOLOGY

There isn´t a precise and clear definition at national or international level which mentions what is an indicator, however [19] points out that the indicators are "tools to clarify and define, way more precise objectives and impacts, they are measures of change or designed to provide a standard for assess, estimate or demonstrate the progress".

Meanwhile another concept on indicators are those that play an important role in public policies of a city or nation systems, since they help the perception of complex problems and provide quantitative information that is helpful for making public decisions, such as [20] says it. With the intention of clarifying later in the investigation of which this effort is a part, characterized the mobility of disabled persons, with the understanding that this complex description will yield clues to the construction of an indicator.
The Querétaro metropolitan area includes three municipalities: Marques, Corregidora and Santiago de Querétaro.

The study area population grew at rates accelerated in recent years [10], as shown in Figure 1. Having such growth, similarly have grown their problems such as increases in distance and time of travel, road congestion caused by the motorization and the unit to perform movements in vehicles.

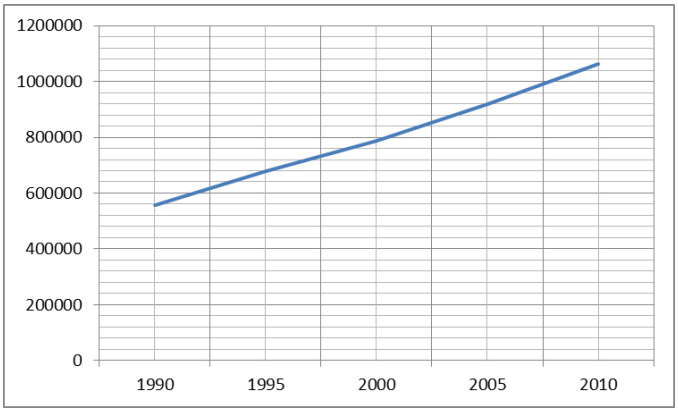

Figure 1. Population growth of the suburbs of Queretaro. Source: Own elaboration based on [1].

To obtain data on the mobility of persons with disabilities was conducted to survey source - target with which according to [21], obtained the information on the number of trips, generators and attractors, the quality of the service and unmet demands. Simple random sampling technique was used to the determination of the sample on the basis data provided by the Municipal Institute for the prevention of discrimination (INMUPRED), i.e., of a small database with which this Institute has.

It is important to note that there isn´t a census which detail exactly the number of people with disabilities, the type of this and its location, so it had problem to find people with disabilities because the survey unlike other studies, is for a sub group of the society which is hardly identified. Thanks to the INMUPRED could be more easily to people with a disability, either this drive type or blindness.

Provided data base was adjusted to the suburbs, i.e. was a cleansing of data which included people outside the area and within the same State of Queretaro and belonging to the State of Guanajuato; in this way it ended with a total of 779 persons belonging to the above described area, therefore proceeded to determine the size of the sample.

The field work was carried out with three interviewers, of which two graduate students from the Autonomous University of Queretaro and an external person, the household survey was applied to persons who suffer disabilities asking about movements that made the previous day (only working days, i.e. from Monday to Friday).

For the size of the sample was carried out the following, as proposed by [22]:

$$n= (N*Z2*P*(1-P))/ ((E2*(N-1)+Z2*P*(1-P)) \quad (1)$$

Where:
n = Sample size
N = Total population
Z = Value corresponding to the Gauss distribution
P = Expected prevalence of the parameter to be evaluated in case of unknown is taken (p =0.5)
E = Error of estimation

As well as noted above is unknown the exact number of people with disabilities within the metropolitan area, so it was taken:
N= 779
P= 0.5
Z = 1.96, describing a reliability of 95%
E= 0.05

By the result of the expression described above resulting in a total of n = 258 surveys, which were conducted in the metropolitan area of Querétaro beginning on September 29th 2015 and ending on November 11th 2015.

It should be noted that there are support groups as: schools, rehabilitation centers, and sports centers where a significant number of people with disabilities, concentrates such as Querétaro 2000 Sports Park, where people with any physical problems come together for different sports as: swimming, basketball, among others, and in these meeting points no surveys were conducted since no cared skew the study and keep the essence of the household survey.

IV. Results and Discussion

Throughout the data collection, detected situations not foreseen in the format of the survey and that they deserve to be described.

Due to high gasoline prices, General taxi owners modified the units through the adaptation of the trunks inside LP gas tanks for greater utility in the service, therefore denies service to people with motor disabilities who use wheelchairs due to the insufficient space in the trunk or by the lack of culture and sensitivity of some operators of taxis than to observe that it is of a person with disabilities they serve not stop pointing them.

There are taxis specialized so unfortunately presented adverse situations that further hinder the mobility of persons with disabilities as the high fees for its use (double the conventional taxis), that is detected that they are only present in the Mexican Institute of the Social insurance, in addition to the above if the service is required should program a day in advance and sometimes if the colonies are far from where they are they are simply the service is not provided.

Those who use public transport face problems as the negation of the operators of the service. Note Although it is not subject to this investigation, which drivers must meet a maximum time that by breaking it are punished, they argue that they have time to wait for people with disabilities as well as not having proper training for the treatment and service to people with disabilities.

People with visual disabilities suffered by the fact of not having hearing tools that provide help to identify lines of public transport at the time of Ascend and bus stops for its descent, so sometimes the operators or persons who use this means of transport for lack of education or sensitivity do not help blind people to identify their destination.

It was observed during the work that large number of people with disabilities are mobilized in own, family car or even there is support from neighbors or acquaintances, or via taxis that although the majority of people with disabilities are not high-income must travel hereby due to not having adequate accessibility to public transport and do not own a car himself or family.

The breakdown by gender for the State of Querétaro is of 49.61% men and 50.39% women. A distribution was obtained by very similar gender survey 48.5% and 51.5% respectively, which suggests that the survey collects faithfully this characteristic of the population as a whole.

The age of respondents does not reflect the distribution of the population in general, because the managed database considers a large number of older people, i.e. existed a shortage of people in early ages in the database that were available, such distribution can be seen in the population pyramids listed in Figure 2.

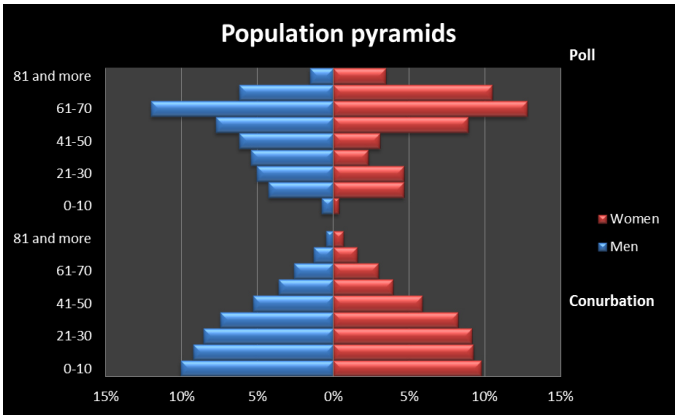

Figure 2. Population pyramids of the suburbs and the one used in the survey.

Civil status[a]

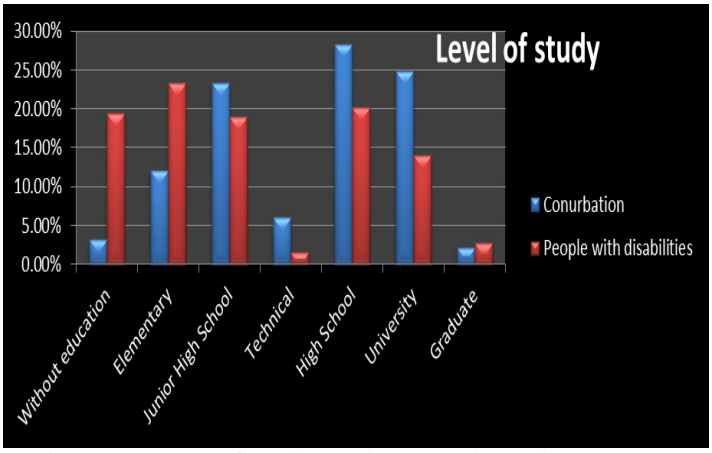

Figure 3. Degree of studies *of the general population and people with disabilities in the suburbs of Queretaro.*

You can assert that there are many people with disabilities are excluded from the right to study (Figure 3), therefore there are substantial percentages of illiteracy, 10% people with disability and 35% for the visually impaired.

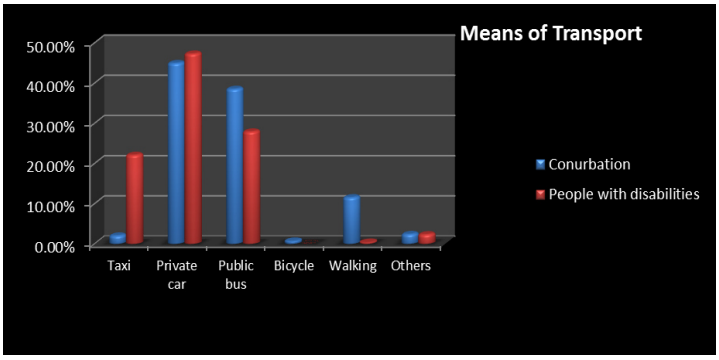

Figure 4. Comparison of means of transport used

[a] The civil status of the respondents was: Singles a third part and singles two thirds parts

Figure 4 shows the great dependence mobility motorized by persons with disabilities for a considerable percentage their main way of travel is by private vehicle.

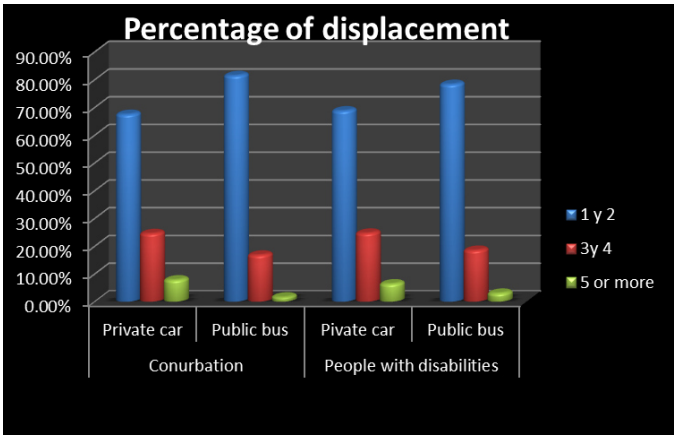

Figure 5. Comparison of the percentages of displacement.

Figure 5, expresses that just like the general population, people with disabilities are mostly only two displacements, round trip

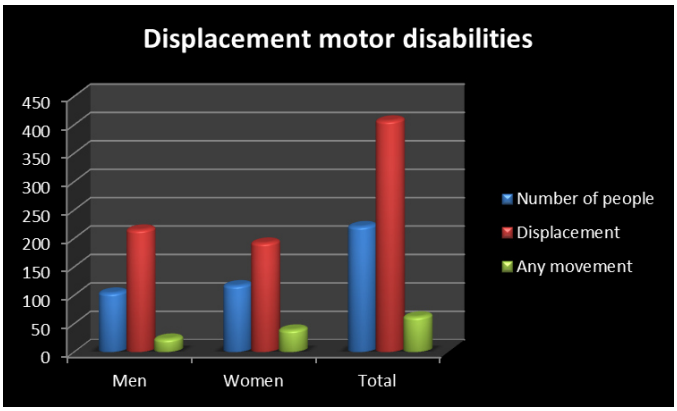

Figure 6. Displacement by gender for the motor disability

In Figure 6, it says that men suffering from disability do slightly greater amount of displacement that women who suffer from this same type of disability.

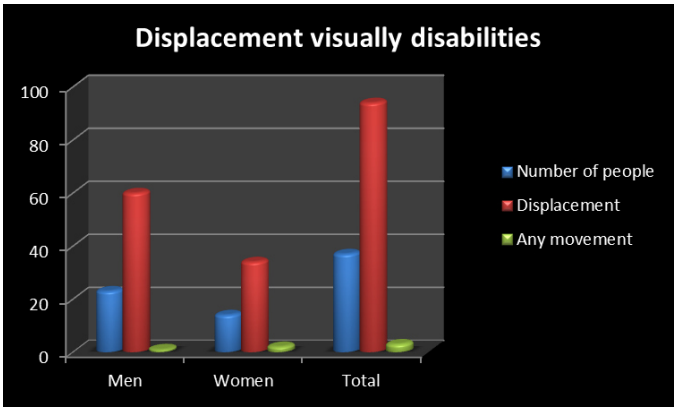

Figure 7. Displacement by gender for the visually disability.

Figure7 indicates that visually impaired men do more displacement than women with the same disability.

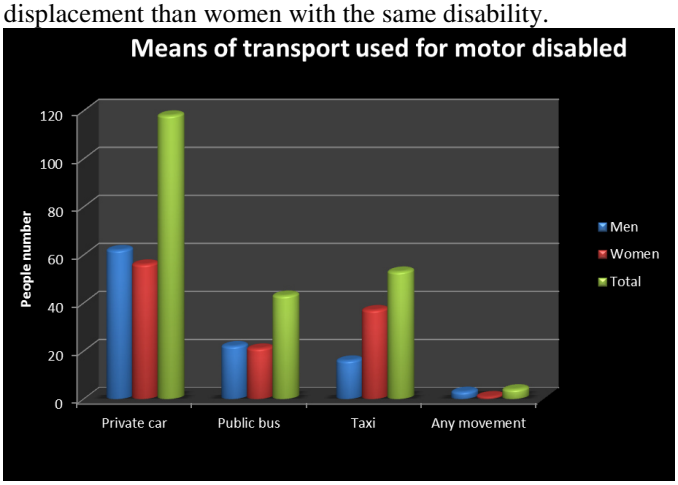

Figure 8. Means of transport used for motor disabled.

Persons with disability use mainly private car and taxi compared with public bus.

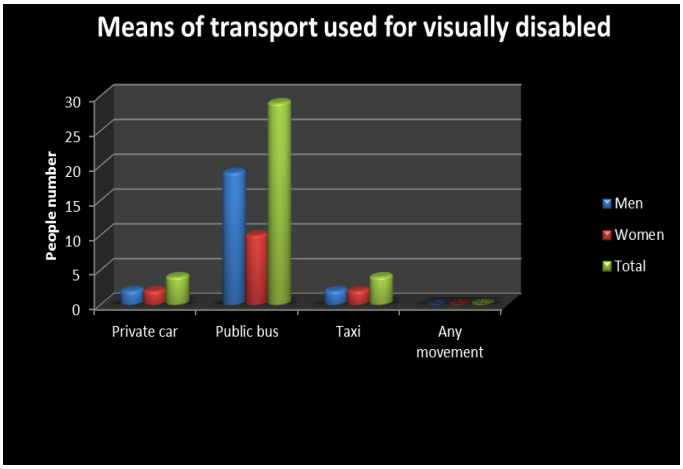

Figure 9. Means of transport used by visually impaired

People with visually disabled used mainly the public bus compared with others means of transportation.

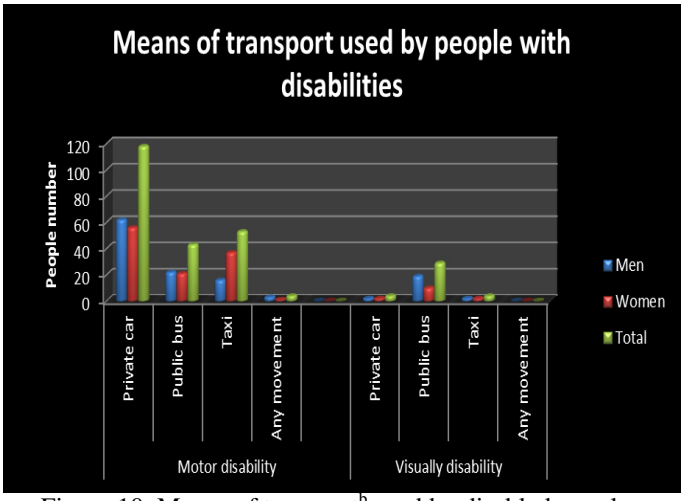

Figure 10. Means of transport[b] used by disabled people.

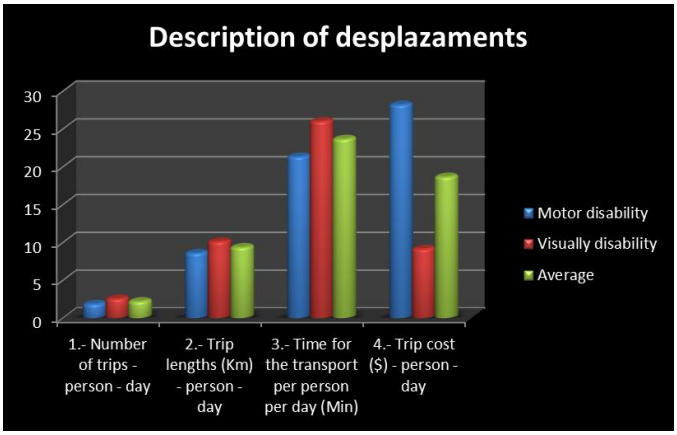

Figure 11. Average of movements made by the disabled.

Movement of persons with disabilities are few, expensive and very slow.

V. Conclusions

It is notorious that the people with disabilities in the study area are excluded from social activities such as health, employment, education among others.

It is the deficiency of public transport and the public towards persons with disabilities infrastructure already shows that there is with the correct accessibility so that this group of people to enjoy a proper mobility.

Within the Group of disabled people in the study, people with motor disabilities move less than the visually impaired also the travel cost is higher.

[b] Nearly half of respondents said not having made travel to lack of accessibility to public transport in addition to about 90% believe that the lack of accessibility to public transport the limits of social activities such as health, education and employment.

It is clear that persons with disability have greater reliance on mobility in private car while the visually impaired greater amount of travel by public bus.

VI. Acknowledgment

Thanks to the following people and dependencies

National Council for Science and Technology (CONACYT) for the scholarship

Autonomous University of Queretaro

Ovidio González Gómez for his unconditional support

God, family and friends.

VII. References

[1] Internacional Labour Organization, ILO (2011). Global economic crisis opens new spaces for discrimination at work. Recovered at: [<http://www.oit.org.pe/index.php?option=com_content&view=article&id=2451:crisis-economica-mundial-abre-nuevos-espacios-para-la-discriminacion-en-el-trabajo&catid=117:ultimas-noticias&Itemid=1305 > consulted on November 5th, 2015].

[2] Wang Wei, Mehndiratta Shomik Raj and Shen Dianzhong (2012).Inclusive Mobility in China, in Transportation Research Board 91st Annual Meeting (No. 12 – 2560).

[3] Samer Gerd, Unbehaun Wiebke, Milloning Alexandra, Mandl Bettina, Dangschat Jens and Mayr René (2012). Identification of Mobility Impaired Persons and Analysis of Their Travel Behaviour as well as their needs, in Transportation Research Board´s 91st Annual Meeting, Washington, D.C.

[4] Santiago Nora, Bajrami Bukurije, Kaziu Afrona and Gordon Cameron (2012). Accessibility for disabled persons in New York rail transit: a comparison for rail road stops in urban and suburban areas.

[5] González Gómez Carmen Imelda and González Gómez Ovidio (1990). The transport in Querétaro in the nineteenth century, Querétaro, México. Mexican Institute of Transportation and Goverment of the State of Querétaro.

[6] Queretano Natural Resource Center, CQRN (2009). Diagnosis and proposed solutions for problem of transportation system in rural regions center of the State of Querétaro, CONCYTEQ, México.

[7] Alcántara Vasconcelos Eduardo (2010). Analysis of urban mobility. Space, environment and equity, editorial CAF, Colombia.

[8] Lubin Andrea and Deka Devajyoti (2012). The Role of Public Transportation as a Job Access Mode: Lessons from a Survey of Persons with Disabilities in New Jersey, Transportation Research Board 92nd Annual Meeting, Washington, D.C.

[9] Lei Ting, Chen Yali and Goulias Konstadinos (2012). Opportunity Based Dynamic Transit Accessibility in Southern California: Measurement, Findings and Comparison with Automobiles Accessibility. Transportation Research Record: Journal of the Transportation Research Board.

[10] National Institute and Statistics and Geography, INEGI (2010). Popultation, distribution by age and sex. Recovered at: [<http://www3.inegi.org.mx/sistemas/sisept/Default.aspx?t=mdemo03&s=est&c=17500> consulted on June 30th, 2015].

[11] LVIII Legislature of the State of Querétaro. Recovered at: [<http://www.legislaturaqueretaro.gob.mx/repositorios/46.pdf> consulted on September 30th, 2015].

[12] Khalifeh Soltani, Seyed Hassan, Sham Mashita, Awang Mohamad and Yaman Rostam (2012). Accessibility for Disabled in Public Transportation Terminal, Procedia Social and behavioral Sciences, no35, 89-96.

[13] Maroto Michelle and Pettinicchio David (2014). Disability, structural inequality and work: The influence of occupational segregation on earnings for people with different disabilities, Research in Social Stratification and Mobility, no38, 76-92.

[14] Hernández Diego (2012). Assets and structures of mobility opportunities: a proposed analytical study of accessibility by public transport, the well-being and equity, EURE, vol. 38, num. 15, p. 117 – 135.

[15] Egea García Carlos and Sarabia Sánchez Alicia (2001). Clasification of World Health Organization of disability. Royal Trust Bulletin Disability. Num. 50, 15-30.

[16] Nelson John, Wright Steve, Masson Brian, Ambrosino Giorgio and NaniopoulosAristotelis (2010). Recent developments in flexible transport services.Research in Transportation Economics.Vol. 29, No. 1.

[17]Neven An, Braekers Kris, DeclercqKatrien, Wets Geert, Janssens Davy and Bellemans Tom (2015). Assessing the impact of different policy decisions on the resource requirements of a Demand Responsive Transport system for persons with disabilities.TransportPolicy. Vol. 44

[18] Figueroa Oscar (2005). Urban transport and globalization: Policies and effects on Latin America. EURE. Vol. 31, Un.m. 94, p. 41 – 53.

[19] Mondragón Pérez Angélica Rocío (2002). What are the indicators? Magazine of Information and Analysis, INEGI. Num. 19, México, p. 52-53.

[20] Escobar Luis (2006). Synthetic indicators of environmental quality: a general model for large urban áreas. EURE Magazine, Vol. 32, Num. 96, Chile, p. 73 – 98.

[21]Molinero Molinero Ángel and Sánchez Arellano Luis Ignacio (2003). Public Transport: Planning, design, operation and management. México. Quinta del Agua

[22] Devore, Jay L. (2008) Probability and statistics for engineering and Sciences. Editorial Cengage Learning, México, p. 720.

Bioreactor start-up for biogas production from mezcal vinasses

López-Velarde S., M.
Hensel, O.
Faculty of Organic Agricultural Sciences
Kassel University, Nordbahnhofstr. 1a
37213 Witzenhausen, Germany
mlopezvelarde@uni-kassel.de
agrartechnik@uni-kassel.de

Rodriguez Morales, J.A.
Ventura Ramos, E. J.
Faculty of Engineering
Autonomous University of Queretaro, Cerro de las Campanas s/n 76000 Queretaro, Qro. Mexico
josealberto970@hotmail.com
eventura@uaq.mx

***Abstract*—Vinasses are a very harmful residue of the mezcal production, their discharge into soil and water can cause negative environmental impacts, if not prior treatment takes place. Anaerobic digestion (AD) has shown to be the best economical and technological method to treat this residue, thus biogas can be generated as by-product of this process. Nevertheless, an acclimatization process of the sludge and substrate in the bioreactor is very important to enhance the efficiency of the methane production. In this work, the first step of the acclimatization process of the anaerobic digestion of mezcal vinasses was carried out in two 15-days periods. Sludge and vinasses were mixed in a ratio 7:3, after 15 days 30% of the total volume was replaced with new vinasses. Biogas was quantified and qualified. Biogas production reached 230 l · kg $VS_{vinasses}^{-1}$ and methane production 40 l · kg $VS_{vinasses}^{-1}$. The acclimatization step should be optimized in order to increase the efficiency of the methane yield and COD removal.**

Keywords—vinasses; anaerobic digestion; chemical oxygen demand; acclimatization

I. INTRODUCTION

Yearly, about eight million liters mezcal are produced in Mexico, from which 90 million liters vinasses remain as residue of the distillation step. These wastes are very aggressive to the environment due to the high organic matter content, high temperature and low pH. If untreated vinasses are discharged, the ecosystem could be seriously affected e.g. causing eutrophication in water bodies and soil or crop contamination [1]. Table 1 shows the composition of tequila vinasses reported by Reference [2]. Due to the similar production processes, tequila and mezcal vinasses are comparable.

TABLE I. COMPOSITION OF TEQUILA VINASSES [2]

Parameter	
pH @ 25°C	3.35
Temperature (°C)	50.4
Biochemical Oxygen Demand BOD (g · l^{-1})	13-24
Chemical Oxygen Demand COD (g · l^{-1})	28-50
Sediment solids (ml · l^{-1})	333
Total suspended solids TSS (g · l^{-1})	12
Volatile suspended solids VSS (g · l^{-1})	9.8
Acetic acid (g · l^{-1})	2.5 – 3.4
Total nitrogen (g · l^{-1})	0.243
Total phosphorus (g · l^{-1})	0.021
Fats and oils (g · l^{-1})	0.018-0.031

Several methods for vinasses treatment have been researched and used in recent years. The most suited method is the AD (anaerobic digestion) for biohydrogen or biogas production [2] [3] [4] [5] [6]. The AD has found practical applications in industrialized countries through biogas plants for the production of heat and electricity or for the production of biomethane as biofuel or as network supply. Nevertheless, the efficiency of the biogas production depends on the operational parameters of the biogas plant and the substrate characteristics such as pH, alkalinity, temperature, organic matter content or toxic compounds concentrations [7].

Through the metabolic pathway of the biodegradation of most of the vinasses compounds, such as fructose and glucose [4], the required compounds for the generation of biogas and biomethane are produced. That is why vinasses are a very suitable substrate for the production of bioenergy. Also, due to the increased amount of vinasses produced from the tequila and mezcal industry, AD suggests to be a very competitive method regarding technical and economical advantages over aerobic processes [3].

However, the use of a stable and acclimated inoculum adapted to the substrate to be fermented, is a clue step for the enhancement of the methane potential. Reference [2] reported an acclimatization period of 5 months using sludge and vinasses in the proportion 7:3. Every two weeks, 30% of fermented substrate was taken from the bioreactor and replaced with new vinasses.

In this work, a 30-days start-up of an 8-liter bioreactor operated with vinasses was carried out under anaerobic conditions. Biogas production was daily measured and characterized. The objective of this work was to start the

acclimatization process of a bioreactor in order to stress the microbial population as less as possible.

II. MATERIAL AND METHODS

A. *Bioreactor configuration*

The bioreactor was made of PVC and had a volumetric capacity of 8 l. For pH adjustment the bioreactor had an inlet at the top for the addition of sodium hydroxide (NaOH). Also at the top a tedlar bag was connected for biogas storage. The reactor had a tap at the bottom and a twist-off lid at the top to replace a certain volume of the substrate with new substrate. A magnetic stirrer was placed inside the bioreactor so that the bioreactor could be daily stirred.

B. *Inoculum and substrat*

Sludge from the wastewater treatment plant of the university was used as inoculum. As substrate, vinasses were collected from the mezcal factory Laguna Seca located in the Mexican state San Luis Potosi. The characteristics of the sludge and vinasses are listed on table 2.

TABLE II. PARAMETERS OF SLUDGE AND VINASSES

Parameter	***Sludge***	***Vinasses***
pH @27°C	8.24	4.77
Chemical Oxygen Demand COD (mg · l $^{-1}$)	5700	59000
Total solids TS (g · ml $^{-1}$)	0.0053	0.049
Volatile solids VS (g · ml $^{-1}$)	0.0034	0.035

C. *Bioreactor start-up*

The reactor acclimatization consisted of filling 90% of the total reactor volume with sludge and vinasses at the proportion 7:3. Every day the amount of produced biogas and the content of methane, carbon dioxide and hydrogen sulfide were measured. Before every measurement was carried out, the bioreactor was stirred with the magnetic stirrer for 15 minutes, according to the norm VDI-4630 [8] for the fermentation of organic materials for biogas production. Every 15 days 30% of the total volume was replaced with new vinasses. The reactor was kept at anaerobic conditions at 39°C. This first step of the experiment was carried out for 30 days. The pH value of the reactor was daily measured and adjusted with NaOH to pH 7, if necessary.

D. *Measurements*

The biogas quality (content of methane, carbon dioxide and hydrogen sulfide) was measured with a gas analyzer Multitec 540 from the German company SEWERIN GmbH. Biogas quantity was measured according to tedlar bags marks. The Chemical Oxygen Demand (COD) was measured according to the norm DIN 38414-9 [9]. FOS/TAC was measured according to Reference [10] to analyze the biochemical state of the fermentation sludge. The initials FOS/TAC come from the German language and stand for the quotient of the volatile organic acids (Flüchtigen Organischen Säuren) and the total inorganic carbonate or alkaline buffer capacity (Total Alkalischen Carbonaten). In other words, the FOS/TAC value measures the quotient of the acid concentration and the buffer capacity of the bioreactor. If the fermentation substrate contains many organic acids, the methanogenic bacteria will be inhibited, especially if the pH value sinks.

III. RESULTS AND DISCUSSION

A. *Biogas and methane production*

Fig. 1 shows the cumulative biogas and methane production of mezcal vinasses over a time period of 30 days. Biogas production reached a biogas yield of 230 l · kg$_{VS\ vinasses}^{-1}$ and a methane yield of 90 l · kg $_{VS\ vinasses}^{-1}$. The biogas production began the second day of the start-up process and the methane production began on the fifth day. Biogas production occurs in four steps (hydrolysis, acidogenesis, acetogenesis and methanogenesis) where different bacteria groups in the inoculum need different reproduction rates to degrade the substrate polymers to generate acetic acid, hydrogen and carbon dioxide for the methane production [11]. The reproduction rate of the methanogenic bacteria is the most slowly of all the groups. Methanosarcina needs up to 360 hours for reproduction and the methanococcus 240 hours. In comparison, the hydrolytic and acidogenic bacteria need 24 – 36 hours and the acetogenic bacteria 40 – 132 hours for reproduction [12]. For this reason, the methanogenesis is the slowest step to methane production. This is reflected on the experiment, where the methane generation started after 5 days.

The biogas rate in terms of liters biogas produced daily, varied up to 2.75 l · d^{-1} in the 30 days acclimatization period. Reference [2] reported by the start-up of a 40 l bioreactor operated with vinasses, that the biogas production increased from 0.1 up to 2 l · d^{-1} in 30 days. Reference [14] reported the production of 0 to 6 l · d^{-1} biogas by a 30 day start-up period of a bioreactor using biofilms for a better biogas performance.

Fig. 1: Biogas and methane production from vinasses

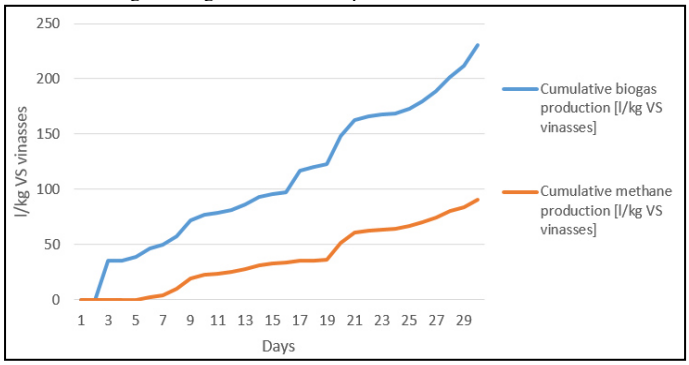

At the end of the 30 days, the methane content of biogas was only 40%. This is a very low rate if we consider that most

of the substrates reach up to 70% methane content [11]. Reference [2] achieved a methane content of 60% during the start-up period of 50 days using a lower COD content on the mixture wastewater vinasses. Reference [14] reported an increase on the methane production from 60 to 70% during the start-up period of 28 days of a 2.8 l bioreactor using vinasses. In this case, biofilms in the bioreactor were used for biogas and methane production enhancement.

B. COD removal

The COD of the vinasses-sluge mixture was at the beginning of the experiment 17375 mg · l^{-1}, after 15 days the COD diminished up to 16460 mg · l^{-1}. Only 5% of the COD was removed during the first feeding digestion. At the beginning of the second reactor feeding COD was 26810 mg·l^{1}. After 15 days COD diminished up to 17720 mg · l^{-1}, which means 34% of COD was removed during the second bioreactor feeding. These results suggest that the efficiency of COD removal was higher when the reactor was better acclimated and when more COD was available for consumption. Due to the high substrate availability, there is an increase in microorganism consumption of organic matter [13]. Similar results were obtained by Reference [2] operating a biroeactor with vinasses with a lower COD content. During the start-up period the COD remotion increased from 3% to 85% in 50 days. By day 30 the COD remotion was around 70%. Reference [14] reported a COD removal of 80% during the 28 days start-up period of a 2.8 l bioreactor using biofilms.

C. FOS/TAC

The FOS/TAC value describes the condition of the bacteria in regards to acidification. If the FOS/TAC value is more than 0.4, the substrate supply must be throttled. A low FOS/TAC value (0.2) indicates that more substrate needs to be fed in the bioreactor to increase the efficiency of the biogas production [10]. In these experiments, the FOS/TAC values were 1.7 at the beginning of the first feeding and 1.6 at the end. At the beginning of the second feeding FOS/TAC value was 2.4 and decreased up to 1.4 after 15 days. The falling FOS/TAC value at the second feeding suggests that more substrate was used on the biodegradation pathway of the vinasses and that the total inorganic carbon decreased after the degradation and thus the buffer capacity. The bacteria in sludge have the capacity to work with a higher vinasses content to enhance the efficiency of the biogas production.

IV. CONCLUSIONS

Due to their composition, especially the fructose and glucose content, vinasses are a very promising substrate for the biogas production. Biogas can be used directly to generate electricity and heat, or can be purified to biomethane as biofuel or as network supply. Acclimatization of the vinasses on the bioreactor is a very important step in order to stress the microbial population as less as possible. Acclimatization can be done increasing stepwise the amount of vinasses added to the sludge. In this work, results are reported regarding the first month of acclimatization, where 30% of vinasses were mixed with 70% sludge from a wastewater plant. Biogas production reached 230 l · kg $_{VS\ vinasses}^{-1}$ with 40% methane content. The highest achieved COD removal was about 34%.

Results regarding COD removal and CH_4 production can be improved using biofilms inside the reactor and lowering the COD content in fermented substrate. These conditions will be tested first in batch experiments, before a continuous or semi-continuous operation takes place.

ACKNOWLEDGMENT

We would like to thank the laboratory GRUTAR of the Faculty of Engineering of the Autonomous University of Queretaro, as well as the University of Kassel for the completion of these experiments.

REFERENCES

[1] V. Robles-González, J. Galíndez-Mayer, N. Rinderknecht-Seijas and H. M. Poggi-Varaldo, „Treatment of mezcal vinasses: A review," *Journal of Biotechnology 157,* p. 524–546, 2012.

[2] H. O. Méndez-Acosta, R. Snell-Castro, V. Alcaraz-González, V. González-Alvarez and C. Pelayo-Ortiz, „Anaerobic treatment of Tequila vinasses in a CSTR-type digester," *Biodegradation 21,* p. 357–363, 2010.

[3] A. López-López, G. Davila-Vazquez, E. León-Becerril, E. Villegas-García and J. Gallardo-Valdez, „Tequila vinasses: generation and full scale tratment process," *Reviews in Environmental Science and Biotechnology 9,* p. 109–116, 2010.

[4] F. M. Espinoza-Escalante, et al., „Multiple response optimization analysis for pretreatments of Tequila's stillages for VFAs and hydrogen production," *Bioresource Technology 99,* p. 5822–5829, 2008.

[5] A. Jimenez, R. Borja, A. Martín and F. Raposo, „Kinetic analysis of the anaerobic digestion of untreated vinasses and vinasses previously treated with Penicillium decumbens," *Journal of Environmental Management 80,* pp. 303-310, 2006.

[6] E. L. Barrera, H. Spanjers, O. Romero, E. Rosa and J. Dewulf, „Characterization of the sulfate reduction process in the anaerobic digestion of a very high strength and sulfate rich vinasse," *Chemical Engineering Journal 248,* pp. 383-393, 2014.

[7] F. M. Espinoza-Escalante, et al., „Anaerobic digestion of the vinasses from the fermentation of Agave tequilana Weber to tequila: The effect of pH, temperature and hydraulic retention time on the production of hydrogen and methane," *Biomass and Bioenergy 33,* Nr. 33, pp. 14-20, 2009.

[8] German engineers association - Verein Deutsche Ingenieure VDI-4630, „Fermentation of organic materials," VDI, Germany, 2006.

[9] German Institute for standardization - Deutsches Institut für Normung DIN 38414-9, „German standard methods for the examination of water, waste water and sludge; sludge and sediments (group S); determination of the chemical oxygen demand (COD) (S 9)," Germany, 1986.

[10] Fermenter Doktor Verwaltung GmbH "Instructions for determining the FOS/TAC value by titration" - „Anleitung zur Ermittlung des FOS/TAC mittels Titration," Germany, 2008.

[11] Fachagentur Nachwachsende Rohstoffe e.V., „Handout, biogas production and use“ - „Handreichung, Biogasgewinnung und -nutzung“ Germany, 2006.

[12] KWS, “Biogas, basics of fermentation biology” - „Biogas, Grundlagen der Gaerbiologie“ KWS Mais GmbH, Germany, 2012.

[13] V. Oliveira , M. Simoes, L. Melo and A. Pinto, „Overview on the developments of microbial fuel cells,“ *Biochemical Engineering Journal 73,* pp. 53-64, 2013.

[14] J. Jauregui-Jauregui, H. Mendez-Acosta, V. Gonzalez-Alvarez, R. Snell-Castro, V. Alcaraz-Gonzalez und J. Godon, „Anaerobic treatment of tequila vinasses under seasonal operating conditions: Start-up, normal operation and restart-up after a long stop and starvation period,“ *Bioresource Technology ,* pp. 33-40, 2014.

Application of heuristic techniques based on micro-genetic algorithms for detection and classification of harmonic content in electrical signals

Martínez-Luna S. K.[#1], Jaen-Cuellar A. Y.[#2], Osornio-Ríos R. A.[#3]
[#1, 2, 3] Facultad de Ingeniería, Campus San Juan del Río, Universidad Autónoma de Querétaro
Av. Río Moctezuma 249, C.P. 76808, San Juan del Río, Querétaro, México
[1] smartinez31@alumnos.uaq.mx
[2] ayjaen@hspdigital.org
[3] raosornio@hspdigital.org

Abstract*— There are many optimization methods that are known as heuristic techniques, which perform a search in a design space to find the optimal solution to a specific problem. Unlike conventional techniques based on gradients, the heuristic methods do not require the application of advanced mathematics to provide an optimum result, because they are based on procedures that mimic the natural behavior. Currently, the optimization methods have been implemented in different applications, and they are focused on certain behaviors and biological characteristics such as the case of the genetic algorithms. This paper develops a micro-genetic algorithm-based method, which applies the micro-population concept instead of using hundreds of members as the standard genetic algorithm. The proposed methodology is focused on detecting and classifying the harmonic content as a disturbance in an electric network. This phenomenon occurs due to the drastic increase of different kind of loads, such as electrical and electronic equipment; causing possible damage to the devices connected to the network. For that reason, in this work the developed methodology employs an heuristic technique such as the Genetic Algorithms for detection and classification of harmonics, the proposed approach is valued through experimental tests over synthetic signals, and experimental tests over real signals from an IEEE data base and from a physical test bench.

Keywords*— power quality; genetic algorithms; classification of electrical disturbances, micro-genetic algorithms.

I. INTRODUCTION

The electrical energy consumption has been increased due to the drastic increment of electrical equipment with non-lineal characteristics [1]. These devices are the cause of disturbances that affect areas such as the public sector and industries. Based on the IEEE 519-1995 standard, these electrical disturbances consider any type of deviation from their nominal value of the input ac power signal. Therefore, the concept of power quality has had impact in recent years, these disturbances are the cause of electrical equipment degradation, deterioration, distortion, and poor performance when they are connected to the electrical grid being a problem of great interest [2].

For this reason the monitoring of electric variables is a necessity in the electrical research field. Monitoring, diagnosis, detection and classification in the power quality field has taken great importance in industrial sectors and scientific researches in order to find a solution to these problems [3]. There are several classical techniques dedicated to the detection of power disturbances in the electrical signals, such as the Fourier transform, the Wavelet transform, and Hilbert transform, among many others. Sometimes, classical techniques provide insufficient information and they are limited because their implementation is over signals in the steady state [4]. In consequence, there is a large number of developed works that treats this topic; they use modern methodologies or combinations between them, which are applied in two stages; the first for detection and the second for classification. Emphasizing the necessity to develop a system with the capability of detecting and classifying electric power disturbances, some relevant works are presented in the following lines. Related to the monitoring field, the work presented by [3] describes an acquisition system for current and voltage signal from a CNC machine, where power disturbances are analyzed by using the Fourier transform, Wavelet transform, parametric methods and combinations between them. On the other hand, the three phases of an engine are analyzed through their voltage and current signals in [5], showing the reliability and profitability that an FPGA offers in the monitoring of electrical signals. Also, the research proposed by [6] develops a methodology for detection of disturbances using the Wavelet transform with an extension of genetic algorithms, emphasizing that it can be a tool for future research on the classification of disturbances. In accordance with the field of detection, the work presented by [7] uses the Chirp-Z transform to obtain a spectrum of high frequencies and to detect signals with white noise harmonics, noise and harmonic to mention some. In researches about classification, there are works which used the S-transform to classify perturbations using an adjustment of the Gaussian window with the genetic algorithms as in [8]. Otherwise, in work presented by [2], they developed a methodology to classify disturbances, using a neural network, an adaptive linear neural

network and indices of THD (Total Harmonic Distortion). Moreover, the detection and classification of some disturbances are presented by [9], where the SSD technique (Sparse Signal Decomposition) was used with a matrix OHD (Overcomplete Hybrid Dictionaries). In the meantime, in [10] the Gabor transform composed of a probabilistic neural network model is used, in this method features extracted from the matrix of output of Gabor as a vector of input to the neural network classifier, developing in the software PSCAD/EMTDC. In conclusion, there are methods that perform the detection of disturbances, and other techniques which are in charge of the classification task. These techniques are often combined to obtain a better detection and classification of the disturbances.

In this work an optimization technique, such as the genetic algorithms, is proposed as a novel methodology for detection and classification in a single stage. These algorithms do not need the differential calculus or complex math techniques in their functionality, it only requires the value of an objective function to get an excellent solution. However, a variant of the standard genetic algorithms, better known as the micro-genetic algorithms (MGA) were used, this is because they use a smaller amount of processed data than the standard genetic algorithms, highlighting, that only the detection and classification of harmonic content in electrical signals were carried out. The experimental tests were performed over synthetic signals and experimental tests over real signals from an IEEE data base and from a physical test bench in a software implementation.

II. THEORETICAL BACKGROUND

A. *Power Quality*

In a globalized world of constant competition, major quality and better products are required. The electricity sector is not immune to this requirement. The consumption of electric energy is very important for the production in the industry, and it is subject to the requirements of reliability, stability, quality, control, etc [10]. Moreover, the development of technology is moving up rapidly, since the advancement of electronics, electrical devices and appliances are being more sophisticated every day, influencing the electrical network to be more complicated, resulting in affecting the power quality [11].

For this reason, the term of power quality has been a boom in recent decades. The concept "power quality" has different meanings from different sources. It is used as a synonym for "reliability of supply", "quality of service", "quality of tension" and "quality of consumption" [12]. However, the term power quality refers to a wide variety of electromagnetic phenomena that characterize the voltage and current at a given time and at a given location on the power system according to the European Standard EN 50160.

B. *Electrical Disturbance*

Electricity has become an indispensable mean to carry out a large number of activities. Some electrical equipment has several characteristics which can be critical for its successful operation. This occurs more frequently in modern equipment. Although electricity, when produced in power plants is highly controlled, a considerable disturbance generation occurs in the customer supply terminals. These disturbances are caused by the nature and characteristics of operation of electrical and electronic equipment, as well as the same supply system. Since the characteristic perturbations can cause degradation of the electrical equipment performance, these phenomena are often referred to as electromagnetic interference. Either the design of this equipment or its operation mode, or both, can have the effect of injection of disturbances (such as interharmonic or harmonic distortion, fluctuations of voltage, etc.) in electrical networks.

Accordingly, the characteristics of tension are under the influence of various parts:

- end users
- manufacturers of equipment and systems
- designers of plants and facilities[13]

The harmonics are the disturbance to be worked on in this paper, for this reason, only these will be explained. The harmonics are sinusoidal or current tensions that have frequencies that are integer multiples of the frequency at which the supply system is designed to work (called the fundamental frequency, usually 50 or 60 Hz). These periodically distorted waveforms can be decomposed in the sum of the fundamental frequency and the sum of harmonics [12]. Equipment based on power electronics is an important factor in the generation of harmonics in power system. These devices and loads can usually be modeled as sources of current which inject harmonic in the electrical system. These cause non-linear drops voltage through the system impedance. Harmonic distortion is a growing concern for many clients and the system of global energy due to the increasing use of power electronics equipment. The levels of harmonic distortion can be characterized by the total spectrum of harmonics with magnitudes and angles of phase of each individual harmonic component [14]. Some instruments used for measurements of harmonics express their output with reference to the fundamental component of the tension, especially those which indicate the factor THD [13]. Harmonic currents are the result of the normal operation of nonlinear devices in the power system. Although the distortion of current levels can be characterized by a THD, this can often be misleading in accordance with IEEE 519-1995 [14].

C. *Genetic Algorithms*

There are many optimization methods known as heuristics techniques, which perform a search in a space of design to find the optimal result of a specific problem. Unlike conventional techniques based on gradients, the heuristic methods do not require to apply advanced mathematics to provide an optimum result, because they are based on procedures that mimic the behavior of nature. [15]. These methods are focused on certain behaviors and characteristics of biological, molecular, neural systems, etc. Some of these are: neural networks, ant colony, particle swarm, genetic algorithms, among others. In particular, this work is about genetic algorithms.

The Genetic Algorithms or Standard genetic algorithms (SGA) are optimization algorithms inspired by natural selection and natural genetics. The method is generally capable of being applied to an extremely broad range of problem. They are used in problems in which specific values are required and the conditions of the problem are complex. The Genetic Algorithms are applied when pervious knowledge about a specific problem is unknown, in such a way that parameterized models or functions are impossible to define [16]. Also, they are applied to problems whose characteristics such as a wide design space, multi-objective, non-linearity, etc., make it impossible for classical methodologies to find an acceptable solution. The SGA find the specific value of a variable or variables in a design space, that is the range of values in which the variable or variables could be found [8].

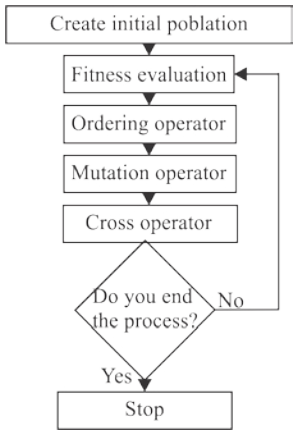

Figure 1 Flow diagram of SGA process

The process of the algorithm is shown in Figure 1, showing the process that the algorithm follows. As a first step, the SGA are initialized with a supposed random population, the population uses many individuals, and it is a big population. The typical algorithm uses three operators: selection or reproduction operator, crossover operator and mutation operator, these lead the population to converge on the global optimal solution [17]. Reproduction operator is also known as selection operator that selects the best individuals of the population. The crossover operator creates new individuals and exchange information between them. Finally, the operator of mutation, which creates new individuals provides diversity to the population [18]. So, a cycle of reproduction, crossover, mutation and the evaluation of the objective function is known as a generation. When a generation comes to an end, the final population is now the initial population and it is evaluated again by the objective function and the three operators. The process continuous through several generations until it satisfies the criterion of this convergence (number of generations) and the process is completed [19]. To make it clear, the objective function is used to provide a measurement of what role the individuals have played in the problem domain. In the case of a minimization problem, the fittest individuals will have the lowest numerical value and would be the best. [20].

D. Micro Genetic Algorithms

A micro genetic algorithm differs from the SGA because of the number of employed individuals, as it only works with a small population, and the number of iterations is less. Three or four individuals are considered as a small population [21].

The population size is the key in the micro-genetic algorithm performance. In this way, computational resources are saved in comparison with the SGA, since SGA has a large number of individuals and they have to be analyzed at each stage of the operators, taking more time and resources to be computed, while with few individuals the computational load decreases.

The process for the operators is not the same as that for the SGA. They are applied in a different way because MGAs have only four individuals. If applied as in SGAs, information could be lost, thus leading to wrong results.

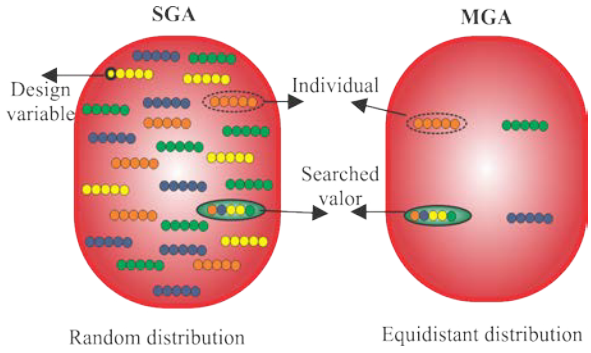

Figure 2 Comparison between SGA and MGA

Figure 2 shows that a SGA distributes the individuals randomly across its range of possible solution. Similarly, a MGA has four individuals equidistantly distributed in the area of possible solutions.

III. METHODOLOGY

This work presents an analysis methodology for three types of signals which are synthetic signals, signals from the IEEE data base and signals obtained from a real test bench. In addition, this methodology is developed in MATLAB software. The section A presents the mathematic model that characterizes the signal with harmonic content and the section B describes the proposed methodology.

A. Mathematical model of harmonics

The mathematical model that characterizes the harmonics content in a signal is the function in which the individuals of the micro-genetic algorithm within the proposed approach will be evaluated. That means, these individuals represent the variables to be found or the variables with the expected solution. Thereby, the mathematical model that characterizes a pure electrical sine wave is presented in (1)

$$v(t) = A \sin(2\pi fo\, t + \varphi) \quad (1)$$

Where, A is the voltage amplitude; *fo*, is the voltage fundamental frequency; and φ, is signal phase; finally, *v(t)* is the instantaneous voltage of the signal in a specific time.

The mathematical model for the harmonics consists of the sum of the fundamental wave with the sum of the third, fifth, seventh and the ninth harmonic for this particular work. Equation (2) represents the general form of a sinusoidal wave with harmonic content. Where $w= 2\pi fo$.

$$v(t)=v_0(t)+\Sigma\, v_k \sin(wk\, t + \varphi) \quad (2)$$

Where, v_o is the fundamental signal; v_k is the amplitude of each harmonic and *wk* is the *n-th* harmonic.

The algorithm will make the optimization of the parameters that are related to the harmonic amplitudes as stated in (3), which represents the model used in this paper.

$$v(t)=A \sin(w\, t) + A_3 \sin(3w\, t) + A_5 \sin(5w\, t) + A_7 \sin(7w\, t) + A_9 \sin(9w\, t) \quad (3)$$

Therefore, with this methodology, it is expected to obtain the harmonic amplitudes every half cycle during the optimization process. In this sense, if the proposed approach obtains the harmonic amplitudes with values different from zero, then this implies that a disturbance was found but mainly a harmonic disturbance.

B. Methodology description

Once the signal with harmonic content is loaded in the MATLAB software, the signal goes to a file text; then, it is necessary to find each of the zero cross values of this signal. Subsequently, two filters are applied, a band-pass filter and a band-stop filter. The band-pass filter let the fundamental waves pass and the band-stop filter analyzes the sum of harmonics or the remaining signal. Then, the phase of filtered signal is detected, this step is important because it is a characteristic parameter in the equation. After that, the MGA is applied.

The first step of the algorithm is the initialization of the parameters. The parameters proposed are shown in Table 1. Then each individual is evaluated in the objective function. The objective functions used were the Integral Squared Error (ISE), (4), and the Integral Absolute Error (IAE), (5). Then the error values are obtained from the filtered signal and the approximated signal by the evaluation of the objective functions. While the error is minus the approximation is better.

$$\mathrm{IAE} = \int \| e(t) \| dt \quad (4)$$

$$\mathrm{ISE} = \int \| (e(t))^2 \| dt \quad (5)$$

After the evaluation of the objective function, the four individuals are ordered from best to worst, first the best individual with the lower error, then the second best, continuing with the third best and finally the worst individual, this is called ranked selection of the optimization process.

TABLE 1 PARAMETERS USED IN MICRO GENETIC ALGORITMH

Parameters	***Quantity***
Number of generations	100
Number of individuals	4
Mutation probability	0.2
Range of solutions	[0 2]
Objetive function	IAE, ISE
Variable to optimize	A

Subsequently, the crossover operator is applied, the first individual will not change because it is the best value and if altered, the solution could be lost and the optimum value could be inaccurate, that means the valuable genetic information could be lost. The crossover operator is applied to the best and the second best individuals, then, it is applied to the best and the third best individuals. Consequently, the worst individual changes completely, taking a random value. The crossover takes both values, first and second individual values for example, and obtains the mean between them, so, this new value, provided by the mean, is the new value of the individual.

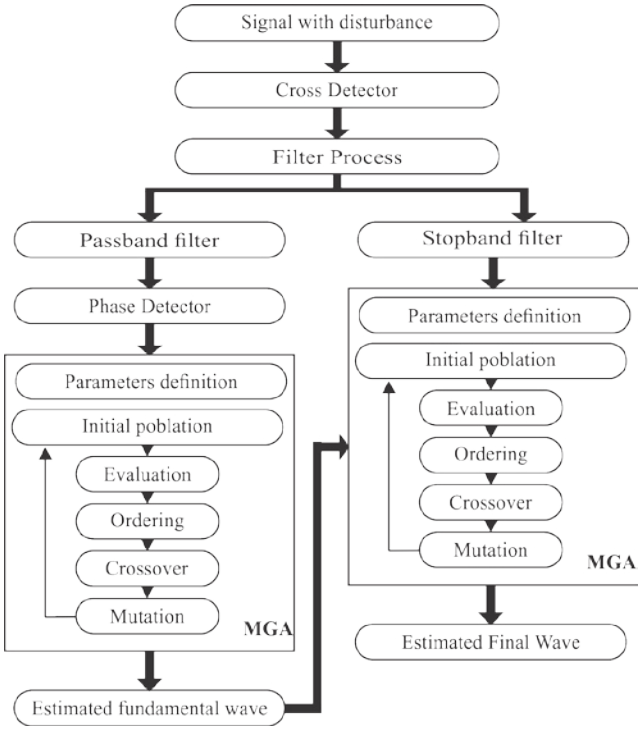

Figure 3 Block diagram of the proposed methodology

Afterwards, the mutation operator is applied according to the numerical values of certain parameters, these values are: a random value and a proposed mutation of probability value. This operator is not applied to the first individual. These values

are compared, if the random value is greater than the mutation probability, the individual remains the same; if not, the mutation operator is applied to the individual. When the operator mutation is applied, the individual changes completely being substituted by other random value.

The MGA process is done every generation or cycle, adopting the final population as the initial population for the next generation to be evaluated. The process finishes when the number of generations is completed.

Besides, the former process is applied to the filtered signal to find the fundamental wave. In the next step, the sum of harmonics is analyzed, taking as reference the filtered signal by the band-stop filter. This signal filtered by the band-stop needs the previous analysis applied to the fundamental wave and then the MGA process is applied to obtain the amplitude of each of the terms of every harmonic. The previous described methodology is represented in the Figure 3.

IV. RESULTS Y DISCUSSION

The results are shown in the following figures. . The experimental tests were done with synthetic signals, real signals from an IEEE data base and from a physical test bench. A single explanation is provided for the results in section A, since the procedure is the same for all the sections below.

A. Results with synthetic signal

These signals were simulated in the same software employing the equations before being explained with a frequency of 60 Hz, as in the power line. The Figure 4 shows the signal with harmonics. The first step of the methodology was to filter the input signal. Figure 5 a) shows the fundamental waveform filtered by the band-pass filter and the Figure 5 b) shows the remaining signal filtered by the band-stop filter. Subsequently, the phase of the fundamental wave is detected as shown in the Figure 6, and then the micro genetic algorithm-based approach is applied.

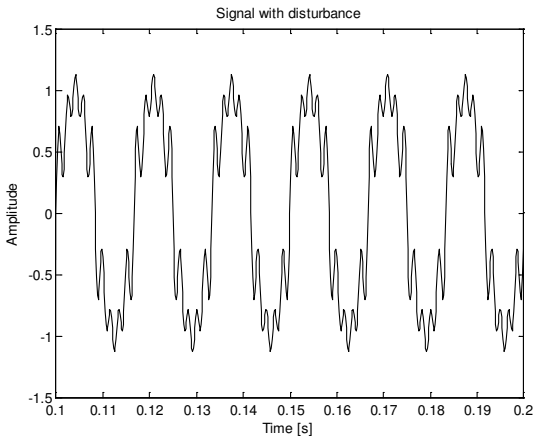

Figure 4 Synthetic harmonic signal

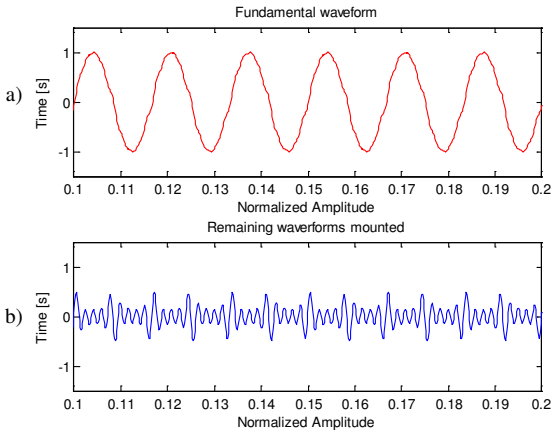

Figure 5 a) Bandpass filtered signal, b) Bandstop filtered signal

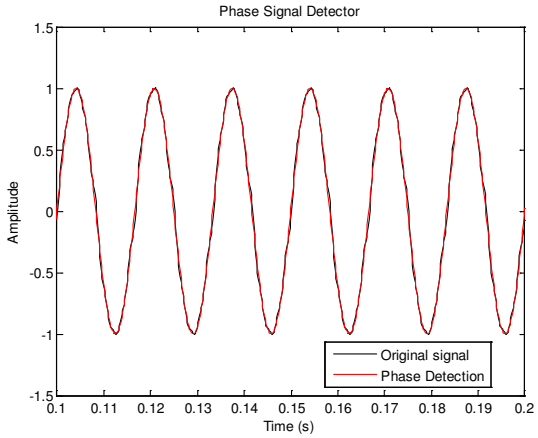

Figure 6 Phase detection

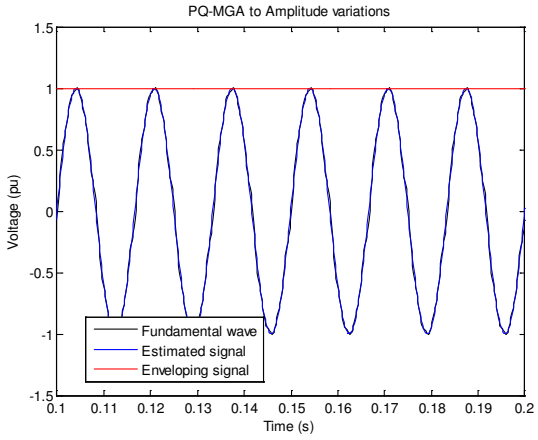

Figure 7 Fundamental wave compared to estimated signal with MGA

The result of the fundamental wave is compared to the signal obtained by the MGA, as shown in the Figure 7. The error between the fundamental waveform against the resulting signal obtained by the MGA is shown in the Figure 8. Once the fundamental wave is obtained through MGA as the principal

part of the mathematical model of the harmonics, the MGA are applied again to obtain the remaining signal.

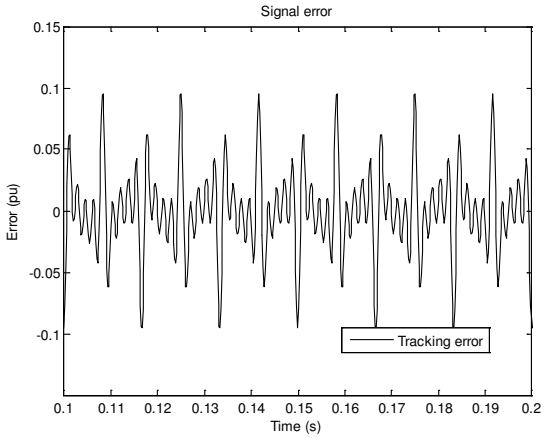

Figure 8 Error between fundamental wave and estimated signal with MGA

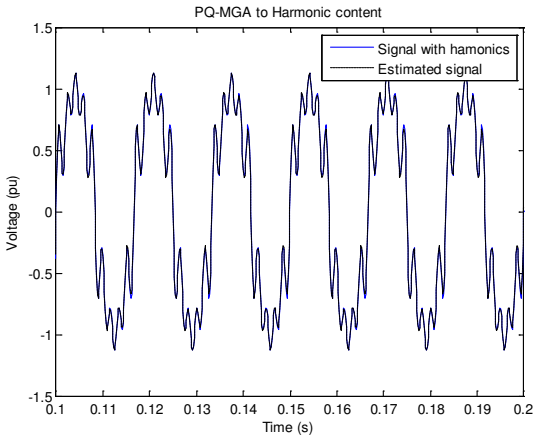

Figure 9 Estimated signal with MGA

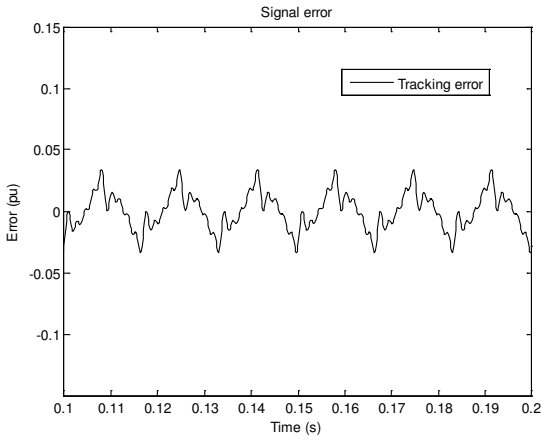

Figure 10 Error final signal

Finally, the results obtained from detection and classification through the MGA-based approach is presented in Figure 9. The coincidence between the signal with disturbance and signal approximated by methodology is considerably high. Figure 10 shows the error between them.

B. Results over real signals from an IEEE data base

The experimental tests were performed taking data from the IEEE data base, work group (P1159.3). These data were used due the prestige of this institution and its security. The nominal voltage is of 400 Vrms. Figure 11 shows the signal from an IEEE data base. Figure 12 a) shows the fundamental wave band-pass filtered and the Figure 12 b), shows the remaining signal band-stop filtered. Subsequently, the detection of the phase is shown in the Figure 13.

The result of the detection and classification of a harmonic through MGA-based approach is presented in Figure 14. The error between the fundamental waveform against the resulting signal obtained by the methodology is shown in the Figure 15.

Finally, the result of the detection and classification of a harmonic through MAG approach is presented in Figure 16. Figure 17 shows the final error.

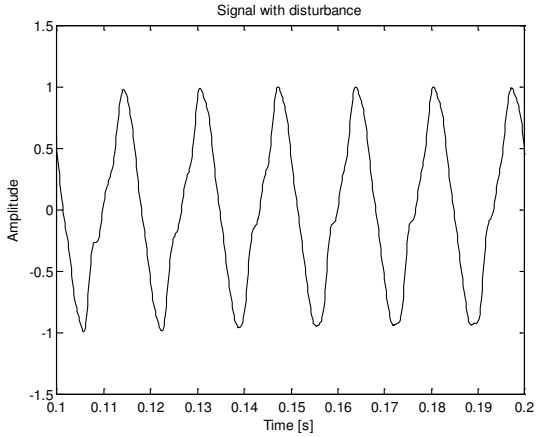

Figure 11 Signal from an IEEE data base

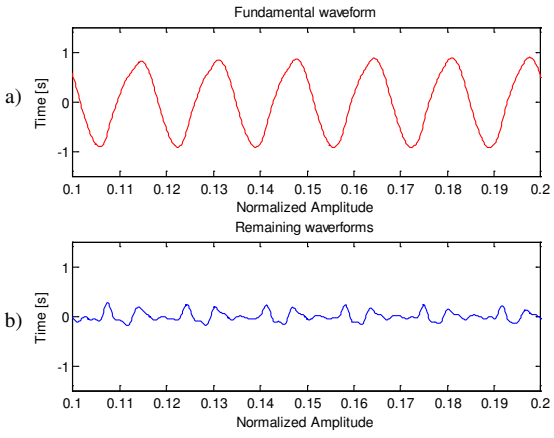

Figure 12 a) Bandpass filtered signal, b) Bandstop filtered signa

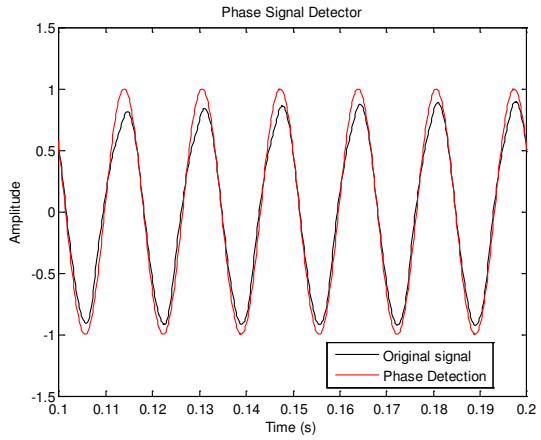

Figure 13 Phase detection

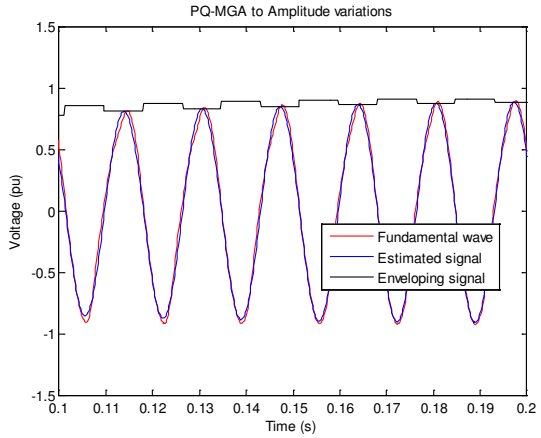

Figure 14 Fundamental wave compared to estimated signal with MGA

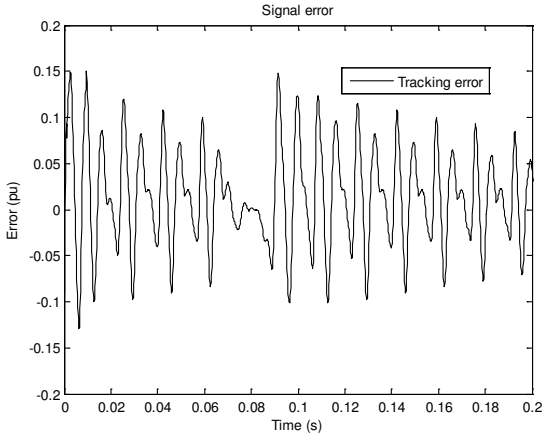

Figure 15 Error between fundamental wave and estimated signal with MGA

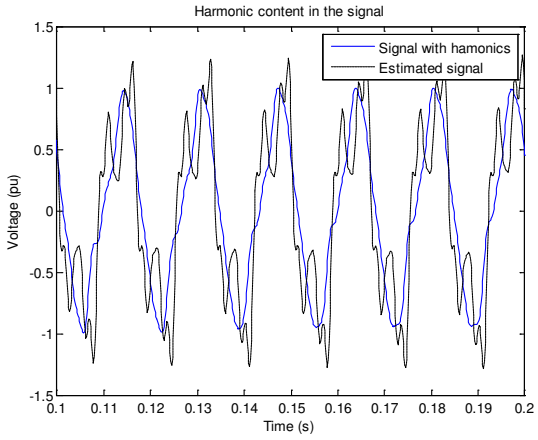

Figure 16 Estimated signal with MGA

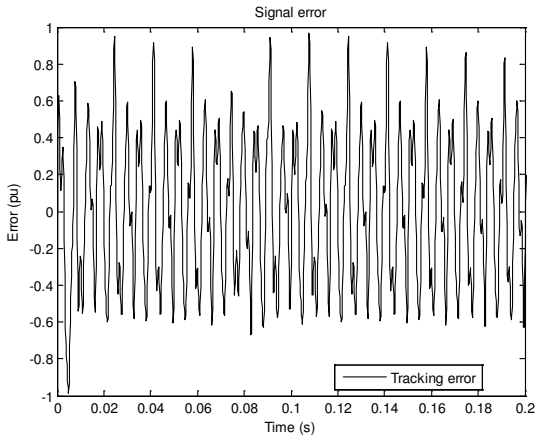

Figure 17 Error final signal

C. Results of signals of physical test bench

These signals are of an experimental test obtained from an implemented test bench.

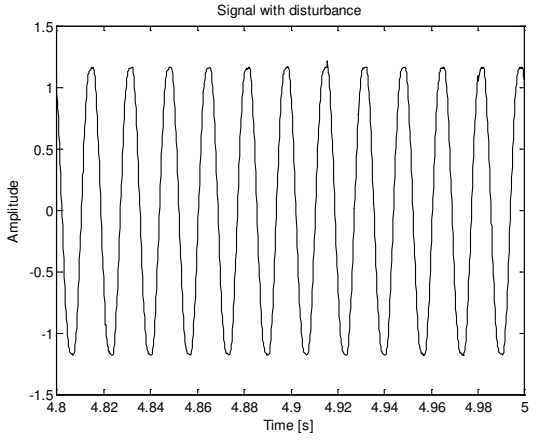

Figure 18 Signal of physical test bench

The test bench consists of an analog power system integrated by amplifiers, a high power transformer, and other electric elements to inject the power disturbances; the nominal voltage used was 127 Vrms. These disturbances were generated digitally in a proprietary synthesis board through a digital-to-analog converter. For each experiment, only one phase of the power system was considered. Figure 18 shows the signal from an IEEE data base. In Figure 19 a) shows the fundamental wave by band-pass filter and in the Figure 19 b), shows the remaining signal by band-stop filter. Subsequently, the detection of the phase is in Figure 20.

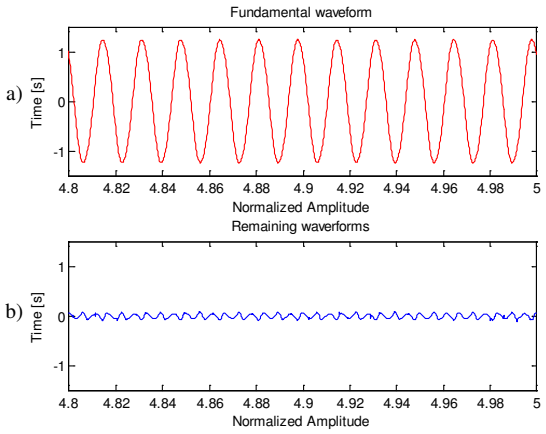

Figure 19 a) Bandpass filtered signal, b) Bandstop filtered signal

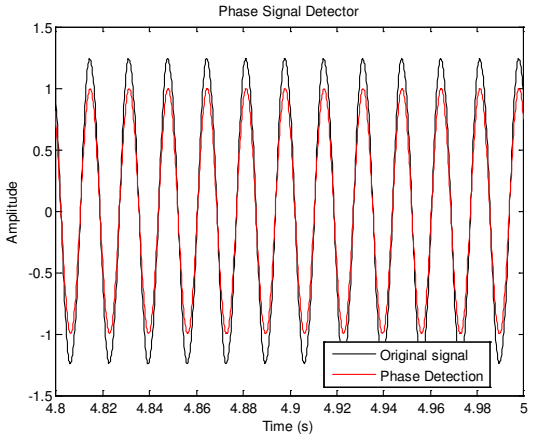

Figure 20 Phase detection

The result of the fundamental wave compared to the signal obtained by the MGA, is shown in Figure 21. The error between the fundamental waveform against the resulting signal of the MGA is seen in Figure 22. Finally, the result of the detection and classification of a harmonic through MAG is presented in Figure 23. Figure 24 shows the final error.

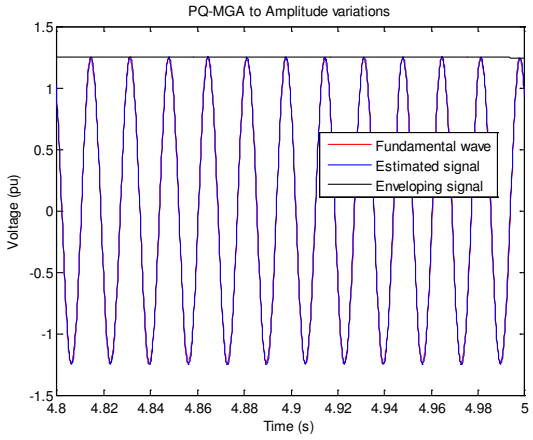

Figure 21 Fundamental wave compared to estimated signal with MGA

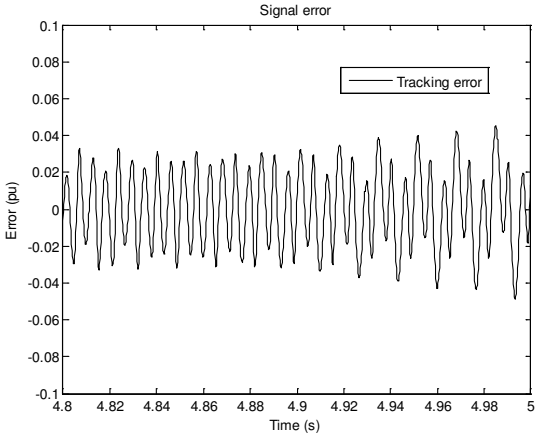

Figure 22 Error between fundamental wave and estimated signal with MGA

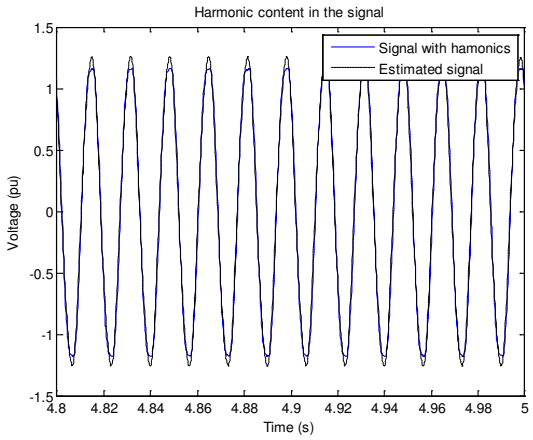

Figure 23 Estimated signal with MGA

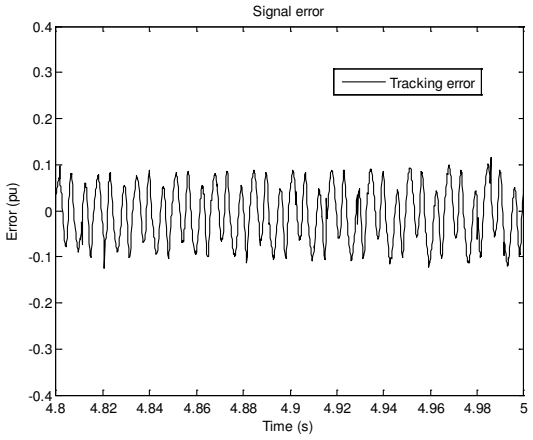

Figure 24 Error final signal

TABLE 2 RESULTS OF OBJECTIVE FUNCTION

Signal	***Individual 1***	***Individual 2***	***Individual 3***	***Individual 4***
	IAE			
Synthetic	31.9943	37.134	75.99	33.1662
IEEE	13.8693	16.2379	40.0431	15.7126
Real	33.4307	49.1578	258.725	35.365
	ISE			
Synthetic	25.075	222.6847	9.45E+05	29.2564
IEEE	10.0201	31.9076	3.17E+03	12.5034
Real	35.9918	110.0565	1.84E+06	42.6476

It could be observed that the methodology used in this paper makes a fine approach to the real signal. In the case of the synthetic signal, the approximation produces less than 0.5% of error. Nevertheless, the variation obtained from the IEEE waveforms tests is far greater than that of the tests executed with synthetic waveforms. This methodology also offers a fine approximation done with a signal obtained in a real test bench, with less than 10 % error.

Finally, Table 2 shows the mean values of the different objective functions used. The best approach was obtained with ISE function. Although the values obtained with both functions were very close, it is important to get small value variations, as this offers a better final result.

V. CONCLUSIONS

In conclusion, the heuristic methods are a suitable technique capable of solving many problems in engineering as shown by the results obtained from the proposed methodology. In the developed work, the proposed methodology with the micro-genetic algorithms for detection and classification in a single stage verifies the versatility of the technique. Furthermore, another important aspect of the proposed methodology is that the micro-genetic algorithms can work with problems in which the non-linearity is present, as with waveforms present in the real world. In addition, introducing a MGA to this approach leads to save computational resources by reducing the amount of individuals. Other advantage about this methodology is the application of the heuristic methods; they do not require the application of advanced mathematics, differential calculus or gradients to provide an optimal result as the conventional techniques. Moreover, the proposed methodology works in each cycle of the signal with disturbance and is able to find a different amplitude or alteration in the fundamental waveform, thus detecting the harmonic content. In the meantime, the proposed methodology is capable of detecting and classifying the different harmonic content in only one stage, offering an alternative solution for the detection and classification of disturbances in the field of power quality.

ACKNOWLEDGMENT

This work was partially supported by CONACyT scholarship 666290/575895 and by projects SEP-CONACyT 222453-2013 and PROMEP 103.5/14/710401.

REFERENCES

[1] C. Gutiérrez Torres, “Sistema de generación y monitoreo de disturbios eléctricos,” UAQ, 2014.

[2] M. Valtierra-Rodriguez, R. D. J. Romero-Troncoso, R. A. Osornio-rios, and A. Garcia-perez, “Detection and Classification of Single and Combined Power Quality Disturbances Using Neural Networks,” vol. 61, no. 5, pp. 2473–2482, 2014.

[3] D. Granados Lieberman, “Análisis en maquinaria CNC ante variaciones de bajo voltaje y sus efectos en la calidad de la energía,” 2013.

[4] D. Granados-Lieberman; R.J. Romero-Troncoso; R.A. Osornio-Rios; A. Garcia-Perez; E. Cabal-Yepez, “Techniques and methodologies for power quality analysis and disturbances classification in power systems : a review,” no. July 2010, pp. 519–529, 2011.

[5] R. J. Romero-Troncoso, E. Cabal-Yepez, A. Garcia-Perez, R. A. Osornio-Rios, R. Alvarez-Salas, and D. Granados-Lieberman, “Reconfigurable instrument for power quality monitoring in 3-phase power systems,” *SDEMPED 2011 - 8th IEEE Symp. Diagnostics Electr. Mach. Power Electron. Drives*, pp. 186–191, 2011.

[6] M. Wang and Y. Tseng, “A novel analytic method of power quality using extension genetic algorithm and wavelet transform,” *Expert Syst. Appl.*, vol. 38, no. 10, pp. 12491–12496, 2011.

[7] D. Granados-lieberman, R. J. Romero-troncoso, E. Cabal-yepez, R. A. Osornio-rios, and L. A. Franco-gasca, “A Real-Time Smart Sensor for High-Resolution Frequency Estimation in Power Systems,” pp. 7412–7429, 2009.

[8] P. Sánchez, F. G. Montoya, F. Manzano-agugliaro, and C. Gil, “Genetic algorithm for S-transform optimisation in the analysis and classification of electrical signal perturbations,” vol. 40, pp. 6766–6777, 2013.

[9] M. S. Manikandan, S. R. Samantaray, and S. Member, “Detection and Classification of Power Quality Disturbances Using Sparse Signal Decomposition on Hybrid Dictionaries,” vol. 64, no. 1, pp. 27–38, 2015.

[10] G. M. Robledo Leal, “Calidad de la Energía Eléctrica : Camino a la Normalización,” p. 1, 2008.

[11] S. Chattopadhyay, M. Madhuchhanda, and S. Sengupta, *Electric Power Quality.pdf*. Springer, 2011.

[12] R. C. Dugan, M. F. McGranaghan, S. Santoso, and H. W. Beaty, *Electrical Power Systems Quality.pdf*, Third. McGrawHill, 2012.

[13] Eurelectric, “Application guide to the European Standard EN 50160 on ‘ voltage characteristics of electricity supplied by public distribution systems ,’” no. July, 1995.

[14] D. Committee, *IEEE Std 1159™-2009, IEEE Recommended Practice for Monitoring Electric Power Quality*, vol. 2009, no. June. 2009.
[15] S. K. Martínez Luna, "Módulo embebido para el procesamiento de micro algoritmos genéticos," UAQ, 2015.
[16] C. Wan, Z. Zhu, and W. Zhong, "Genetic algorithms for designing energy-efficient optical transport networks with mixed regenerator placement." IEEE International Conference on Communications (ICC), 3015–3019. doi: 10.1109/ICC.2012.6363777, 2012.
[17] D. A. Coley, "An Introduction to Genetic Algorithms for Scientists and Engineers.pdf." World Scientific, 1999.
[18] E. K. P. Chong and S. H. Zak, *An Introduction to Optimization*, Second. Wiley, 2001.
[19] S. S. Rao, *Engineering Optimization*, vol. 56, no. 772801201. 2009.
[20] A. J. A. Nazir, Gautham, R. Surajan, and L. S. Binu, "A simplified Genetic Algorithm for online tuning of PID controller in LabView," *2009 World Congr. Nat. Biol. Inspired Comput. (Nabic 2009)*, pp. 1515–1518, 2009.
[21] C. A. Coello Coello and G. Toscano Pulido, "A Micro-Genetic Algorithm for Multiobjetive Optimization," 2001.

Field drilling alternative to reduce soil expansion

Guillermo Enrique Meza Tapia[#1], T. Lopez-Lara [#2], Jaime Horta-Rangel[#3], Juan Bosco Hernandez-Zaragoza[#4]

[#1] *Estudiante de Maestria, División de Estudios de Posgrado de Ingeniería, Universidad Autonóma de Querétaro*
Cerro de las Campanas SN, CP 76010, Santiago de Querétaro, Querétaro, México

[1] *e-mail: guillermo_meza7@hotmail.com*

[#2] *Profesora-Investigadora, División de Estudios de Posgrado de Ingeniería, Universidad Autonóma de Querétaro*
Cerro de las Campanas SN, CP 76010, Santiago de Querétaro, Querétaro, México

[2] *e-mail: lolte@uaq.mx*

[#3, 4] *Profesor-Investigador, División de Estudios de Posgrado de Ingeniería, Universidad Autonóma de Querétaro*
Cerro de las Campanas SN, CP 76010, Santiago de Querétaro, Querétaro, México

[3] *e-mail: horta@uaq.mx,* [4] *bosco@uaq.mx*

***Abstract*—Expansive soils are very problematic to civil engineering because they experience changes of volume due to variation in their moisture. Those soils can produce damage to light structures and heavy economics looses. For many years, extensive research has been carried out on the usability of some conventional additives to improve the quality and/or stability of fine grained soils. This paper presents a recompilation of methods or techniques for stabilization of an expansive soil consisting in reducing its swelling capacity using polymer, lime, cement, fly ash, plaster, sodium chloride etc. It presents progress on the experimental program for the abatement technique of the expansive soil. The physical and mechanical properties of soils are affected by the freeze-thaw cycles in cold regions. Many geotechnical applications such as embankments, unpaved roads, railroads and buried structures may be vulnerable in expansive soils. In order to improve the engineering behavior of these soils, several techniques are available in geotechnical engineering practice such as mechanical stabilization, chemical stabilization, or a combination of many methods to create an improved soil material that possesses the desired engineering properties. Environmental conditions as wetting-drying cycles cause variation in the moisture content of soil, resulting in cyclic swelling and shrinkage. Soil in nature undergoes volume change in several ways; swelling or collapsing due to an increase in water content, rebound due to release of load, settlement due to load application and shrinkage due to water loss.**

Keywords— Expansive clays; Stabilization; Polymer; Lime; Cement; Swelling- shrinkage potential, fly ash, wet-dry cycle soil, inverted hollow structures.

I. INTRODUCTION

Expansive soils are those which experience great changes in volume when their water content varies, these types of soils are widely distributed throughout the world (Huang and Wu 2007; Sabtan 2005)**.** Volume changes in this type of soil are a major cause of natural disaster, since they cause extensive damage to the structures and infrastructure on top of them (Assadi and Shahaboddin, 2009; Avsar et al., 2009; Chen and Lin 2009; Ferber et al., 2009).

The swelling is related to three factors: geology, mechanical engineering soil and environmental conditions. Volumetric changes of these soils produce extensive damage to structures and infrastructure on top of them (Seco, 2010).

Grain sizes less than 2 microns are classified as clay mineral. The main clay minerals are silicates aluminia; sometimes it is replaced by iron, sodium, magnesium, lithium. Clay minerals are divided according to their structure into three groups: montmorillonite, kaolinite and illite (Avsar et al., 2009). The montmorillonite has the property of swelling upon contact with water. The swelling is due to the cation exchange capacity possessed by the mineral to absorb water molecules.

There are some methods to stabilize swelling clays such as:

- Stabilization by mechanical methods, compaction is best known.
- Stabilization drainage.
- Stabilization by electrical means, where the electroosmosis is best known.
- Stabilization use of heat and ignition.
- Stabilization by chemical means, usually accomplished by specific agents such as cement, lime, asphalt (López-Lara et al, 2010).

Durability is the property of a geotechnical material that reflects its performance under freeze-thaw and wetting-drying cycles. Freeze-thaw test should be conducted in areas that are subject to freezing conditions, such as cold regions, while wetting-drying cycles should be conducted in all geographic areas (Zhang and Tao, 2006).

In general, there are several scholars who have examined the utilization of waste and recycled materials as a stabilizing agent to enhance the strength of weak soil (Ahmed et al., 2010; Attom and Al-Sharif, 1998; Arora and Aydilek, 2005; Jha and Gill, 2006; Kamei et al., 2007; Khattab et al., 2008; Khouri and Zaman, 2007; Maslehuddin et al., 2008; Miller and Azad, 2008).

II. LITERATURE REVIEW

II-A POLYMER STABILIZATION

In recent years, construction has been used so-called geosynthetic products manufactured using polymers that are geotextiles and geomembranes products which have four main functions: separation, to avoid or minimize mixing of materials of different particle size; filtration and drainage, to prevent the migration of soil particles allowing the free flow of water and gases; reinforcement to withstand stresses, stabilize the soil mass and protect geomembranes; and sealing, to form a barrier that prevents the passage of fluid and soil particles. The use of the polymers is to form a water-resistant structure; some synthetic resins such as aniline system of organic nature increase the mechanical strength of the soil improving cohesion (López-Lara et al., 2010). Polymers can be reinforced with different fillers to improve the surface textures. The most common nano-sized fillers were carbon nano-tubes, nano-sized particles and intercalated layers. Because nano-particles have significant surface sizes quantum effects, their incorporation into a polymer matrix improve several material properties. In general, the microstructures of clay/polymer nanocomposites are classified according to the level of intercalation and exfoliation of polymer chains into the clay galleries (Hussain et al., 2006; Kiliarisand and Papaspyrides, 2010).

II-B CEMENT STABILIZATION

The chemical stabilization of expansive soils using lime and cement has been tested years ago (Abduljauwad, 1991) Stabilized with cement is similar to using lime and produces similar results. Through links between calcium cement hydration products silicate and aluminate with soil particles (Al-Rawas, 2005). Cement binds the particles together causing soil reinforcement and thus reduces swelling parameters (Nalbantoglu and Gucbilmez, 2001). Similarly the use of cement for stabilizing soils reduces the liquid limit, plasticity index and increases the shrinkage limit and shear (Al-Rawas, 2005).

II-C LIME STABILIZATION

The lime additive reacts with the soil particles, and decreases the swelling potential while increasing the strength and durability o the soil (Du et al., 1999; Guney et al., 2007).

A number of waste materials have been used in the stabilization of soils in order to reduce both environment problems and the requirement for traditional additives such as lime and cement. Rice husk ash (RHA) is an agriculture residue that is one of these waste materials obtained from the outer covering of rice grains during milling process. RHA includes a huge amount of silica with high specific surface that is very suitable for activating the reaction of soil and lime (Choobbasti et al., 2010)**.** Some researchers showed that the RHA was a promising pozzolanic material to improve lime or cement-stabilized soils (Balasubramaniam et al., 1999; Basha et al., 2005; Muntobar, 2002). Muntobar (2004) shows that the addition of 6% lime in combination with RHA principally has a significant effect in reducing swell and swelling pressure (ps) of the clayey soil. Alhassan, (2008) started that the unconfined compressive strength (UCS) of the specimens increased with the addition of lime-RHA in clayey soil. Lime improves the engineering properties of clay.

Lime is used in engineering works such as road construction, walls, foundations and slabs. If lime is added to the clay soils in the presence of water, a series of reactions occur resulting in the improvement of the properties of soils. Such reactions contain cation exchange, flocculation, carbonation and pozzolanic reaction (Al-Rawas, 2005). This involves strong attractive forces between the layers and a stack of a great number of layers (Al-Mukhtar et al., 2012). Such reactions change the texture of the clay providing coarser particles decrease in plasticity and increase in soil resistance. The cation exchange is carried out between the cations of the surfaces of the particles of clay and lime. The effect of this exchange causes those clay particles approaches to each other.

Flocculation is essential for altering the engineering properties of clay soils treated with lime (Al-Rawas, 2005). The adhesion of clay particles in flocs occurs and results in a floor with improved engineering properties as denser structure, low plasticity, greater permeability and low swelling (Avsar et al., 2009).

In cold regions the most important factor determining the engineering behavior of fine-grained expansive soil is freeze-thaw (F-T) cycles. Fine grained soils influenced by F-T cycles show changes in volume, strength and compressibility, densification, unfrozen water content, bearing capacity and microstructure (Mohmann-Porebska, 2006).

The lime column technique consists of holes in the ground filled with lime. Lime columns are constructed in situ by mixing quicklime with the natural soils using a giant egg-beater auger. To construct a column the auger is drilled into the soil to the required depth, the direction of rotation is reserved, and the auger is slowly withdrawn. As the auger is withdrawn, powdered quicklime is pneumatically pumped into the soil. Tenoz et al., (2006) the stabilization process provided by the lime columns is controlled mainly by the lime migration. For an efficient stabilization, calcium and hydroxyl ions should migrate through the clay, because hydroxyl ions cause highly alkalinic conditions in clay soil. Highly alkalinic conditions give rise to the slow solution of alumino-silicates which are then precipitated as hydrated cimentitious reaction products (Diamond and Kinter, 1966).

II-D LIME AND CEMENT MIXTURE STABILIZATION

Improving fine-grained soils and its stabilization is a technique used in road construction. The process makes compact soft soils reducing its plasticity and therefore improves their ability to support mainly Lime (quicklime, slaked lime and lime milk) are the most used products (Khemissa and Mahamedi, 2014). Some treatment studies affirm the action of cement and lime in its plasticity and swelling characteristics (Abdelkrim and Mohamed, 2013;

Afés and Didier, 2000; Bahara et al., 2004; Bell, 1996; Nalbantoglu, 2006; Stavridakis, 2006; Tenoz et al., 2006).

However, mix treatment allows:

- To more decrease the plasticity index, clay becomes no expansive and better compactable.
- To increase the soaked and unsoaked CBR values, allowing this fact of increasing the bearing pressure of clay and reduction of its expansibility.
- To increase the shear strength of clay, therefore of its bearing capacity (Khemissa and Mahamedi, 2014).

However, the best performances are obtained for a mixed treatment corresponding to 8% cement and 4% lime contents (Khemissa and Mahamedi, 2014).

II- E PLASTER STABILIZATION

Soil stabilization with plaster is not very common in practice and information about their behavior is very limited, although over time there have been some studies with this additive.

Bell (1996) Reported on the effect of stabilizing dispersive plaster floor (erodible) especially in the construction of dams and earthen walls, and reported that the cast in the form of finely divided powder can be used as a stabilizing material due to its relatively reasonable cost and water solubility.

comparative study of different additives for stabilization in concluding that the plaster although considered to be ineffective as a soil stabilizer is possible to use this effectively, provided it has been in proper hydration and best gypsum content was 4-6 % (López-Lara et al., 1999).

Yilmaz and Civelekoglu (2009) conduct tests with different contents of bentonite compacting plaster adding to its optimum water content. After a curing period, changes in plasticity parameters percent swell and resistance were evaluated concluded that the cast may also be a good stabilizer for expansive clay soils to be diminished this. Although clays can also be stabilized with lime, gypsum cost is about 2-3 times less expensive than lime. In addition, waste gypsum-based products in the industry can also be used in stabilizing clay soils.

II- F FLY ASH STABIILIZATION

The use of fly ash produced by coal combustion as an expanding agent to stabilize the soil is very productive for improving mechanical properties of this (Ferreira et al., 2003). Fly ash improving favorably reduces the swelling power and swelling clays prevent swelling under small pressures foundations (Nalbantoglu, 2004). Fly ash is widely used in the construction industry since it is a pozzolan, which is a silica material and aluminosilicates silica possess little or no cementitious value, but in the presence of water chemically react with calcium hydroxide at temperatures ordinary to form compounds possessing cementitious properties.

Nalbantoglu (2004) reported clays studies with fly ash in Cyprus improved efficiency on these to improve the texture and plasticity of the soil by reducing the size of clay particles, and expansive plastic potential index due to the cation exchange capacity (CEC).

II- H SODIUM CHLORIDE STABILIZATION

Salt is a natural stabilizer, which is approximately 98% sodium chloride (NaCl) and 2% clay and silt, whose fundamental being hygroscopic property, is to absorb moisture from the air and surrounding materials to evaporation reducing point and improve soil cohesion.

Garnica (2002) says that the coagulating power that has produced less mechanical effort to bring the desired densification, this occurred because the ion exchange between sodium and fine mineral components of cementitious materials causes a reaction. There are some published papers presenting stress-strain behavior of soils stabilized with sodium chloride. Various authors have studied the effect of sodium chloride on the mechanical properties of soils, mainly in the physical properties with contradictory points regarding the change in the volumetric weight of a clay with the addition of the salt, because some researchers say a small increase, others have found no such thing; but it does seem to be a common agreement is that the addition of salt makes optimum moisture is decreased (Garnica, 2002).

Analyzing studies evidenced that not all soils respond adequately to the addition of sodium chloride way to improve their physical and mechanical properties.

II-G SLABS ON EXPANSIVE SOILS

A- STRUCTURAL FLOOR SLABS

The best method to prevent floor movement is to construct a structural slab supported on each side by grade beams and provide a void beneath the slab to prevent contact between the soil and the slab.

The most convenient construction method is to provide a crawl space beneath the slab. This can be readily provided in major structures such as schools and office buildings. The crawl space provides access for inspection, can be ventilated, and can also as a convenient area for utility pipes and conduits (Huan Chen F., 1975).

B- RAISED FLOOR SYSTEM

The raised floor system is constructed by placing Verticel J-void (waved cardboard boxes) upon a level subgrade. The spaces between the boxes contain reinforcing and form-supporting ribs and cardboard boxes in a monolithic concrete placement. A typical plan and cross-section is shown on figure 1 (Huan Chen F., 1975).

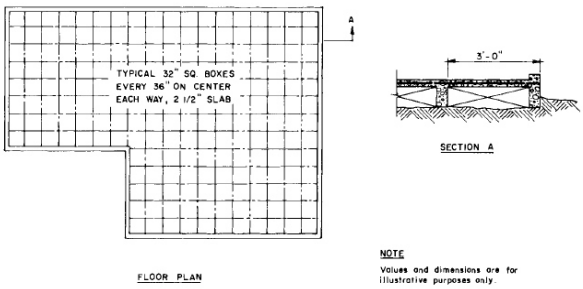

Fig. 1. Raised concrete floor system (Huan Chen F., 1975).

C- HONEYCOMB SYSTEM

The development of the honeycomb system was based upon the assumption that comparatively slight movements of some clays reduce or relieve swelling pressure. The foundation consist of longitudinally split sonotubes that are placed with the opening toward the soil as shown in figure 2, the bottom 2 inches of the space between sonotubes being filled with sand. The sonotube forms stand up well during placing of the concrete but disintegrate after being wetted. After the tube disintegrates, the sand runs out from under the joints.

It was theorized that as the clays swells, it could expand into these openings and reduce the swelling pressure. The system has been tried in a few limit cases in Denver area with doubtful success (Huan Chen F., 1975).

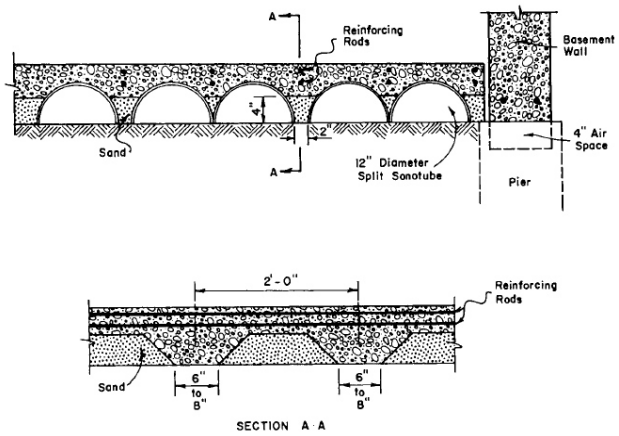

Fig.2. Typical honeycomb form system (Huan Chen F., 1975).

At the Universidad Autonóma de Querétaro in 2014 an experimentation was realized in laboratory using test tubes of remolded soils placing a varied quantify drills and realizing on expansive tests.

Based on the same principle has been used as an alternative solution to the problem of expansion of soils using hollow structures inverted to be kept in good condition despite the expansion, in structures that can be supported directly on the ground controlling the expansion direction (Behzad, 2012). This technique is described by Bowles (1996), and is to enable the floor expand into cavities built into the foundation in order to reduce movement to a tolerable amount. There are different solutions that work under this principle; the principal is the foundation by ribbed slab (López-Lara et al., 2014).

The principle used for the analysis of ribbed slabs in which the expansion is controlled soil where knowing the volume change soil working expansion is possible for this to act in a convenient manner and not harmful to the structure. This was achieved by drilling the soil mass whose dimensions are calculated in volume dimension requiring be absorbed (López-Lara et al., 2014).

Soil was taken with the following characteristics:

- SUCS Rating = high plasticity clay, CH
- Specific gravity relative, Ss = 2.55
- Volumetric weight, γm = 1.62 g / cm3
- Expansion under load, 27.50%
- Properties index (Table 1)

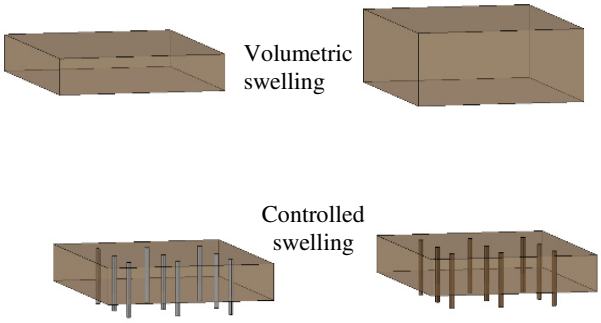

Fig.2. Comparing between ground natural expansion and expansion using the proposed method (López-Lara et al., 2014).

Table I. Rate of natural soil properties (López-Lara et al., 2014).

Physical characteristic of the soil	
Characteristics	Values
Color	Dark brown
Depth (m)	1.20
Natural water content (%)	41.79
Liquid limit (%)	86.00
Plastic limit (%)	32.53
Plastic index (%)	53.47
Linear contraction (%)	21.15
Contraction limit (%)	15.93
Volumetric weigth (gr/cm3)	1.58
Specific gravity	2.62
Passing No. 200 sieve (%)	98.62

Based on the results it was found that 5% to reduce expansion of the land, the volume percentage is necessary to remove 1.40% (López-Lara et al., 2014).

III EXPERIMENTAL PROGRAM

III-A SITE SELECTION AND MATERIAL

The soil used for this study was obtained from Jurica, Querétaro, México. Previous ground investigations carried out at the site indicated the presence of expansive soil. We obtained a disturbed sample by excavating in the field. The expansive soil was encountered at a depth of about 1.20 m below the ground surface. The disturbed soil was excavated and transported by dump truck to the Autonomous University of Querétaro for preparation and testing. Based on the Casagrande plasticity chart, the soil was classified as high plasticity clay (CH) shown in Fig 3. The soil showed a high plasticity index 37.40% (Table I) (López-Lara et al., 2014). Generally, if you get a higher plasticity index and activity of a soil, the higher will bethe swelling potential (Al-Rawas, 2005).

Fig. 3. Sampling site and dump truck.

III-B STABILIZATION TECHNIQUE

At the Autonomous University of Querétaro the soil was excavated to replace the expansive soil; the dimension area was 2 m x 2 m and 1.40 m of depth. They were placed in the ground 8 tubes PVC C80 with 10 cm of diameter and a length of 1.20 m. The tubes were perforated in totally with a diameter of 5 cm shown in Figs 4 and 5.

Fig.4. Tubes PVC C80

Fig. 5. Site exvacated at the Autonomous University of Querétaro

An impervious surface and a layer of 20 cm of gravel were placed before the expansive soil was compacted with a vibrator compactor layered 20 cm show in Fig. 6. Four hoses were placed to the bottom of the excavation to saturate the ground shown in Fig. 7, after the same is loaded with 2 tons / m2 with sand bags.

Fig. 6. Impervious surface, 8 inches of gravel and a hose.

Fig. 7. Compaction of the expansive soil with the vibrator compactor.

After loading the ground, the expansive soil was saturated for 2 months, and we to took measurements of level every day for a couple of months to see if there was a volumetric expansion on the ground and know how much the swelling potential of the expansive soil was reduced.

IV RESULTS AND DISCUSSION

Expansive problems occure all around the world, causing damage to all types of structures, producing electrical and

economic losses. Some authors use mechanical methods to separate, such as compaction electroosmosis, or the use of chemical additives, cementitious products like lime, cement and gypsum. While not all chemicals react as agents or additives, in practice it is more common to use the cement or lime or a mixture of 8% of cement and 3% or 4% lime (López-Lara et al., 2014). This technique was tested in the laboratory with very great results, therefore it was concluded that this technique reduced extracting volume of 5.40% and 6.60% from the initial swelling of the unchanged soil, meaning that given the unchanged natural vertical swelling soil of 12.70%, this technique would be reducing it to 74% (López-Lara et al., 2014).

Table II. Parameters obtained to calculate the load capacity according to Skempton (Bimbela-Osuna, 2014).

Cohesión (tn/m^2)	Ángulo de fricción	γ_m Material	qc (tn/m^2)	Diámetro (cm)	Volumen extraído (%)
3.39	Compresión inconfinada	1.62	18.7206		Suelo remoldeado sin perforaciones
2.75	15°	1.62	15.431	0.3	Suelo con **1.6%** de volumen extraído
2.45	15°	1.62	13.889	0.37	Suelo con **2.2%** de volumen extraído
2.45	13°	1.62	13.889	0.52	Suelo con **4.4%** de volumen extraído
2.3	14°	1.62	13.118	0.617	Suelo con **5.4%** de volumen extraído
2.2	14°	1.62	12.604	0.632	Suelo con **6.6%** de volumen extraído
1.5	17°	1.62	9.006	0.925	Suelo con **13.8%** de volumen extraído

As shown in Table II we observe the loading capacity of the soil in a remoulded state, we also obtained loading values with a retired volume of 1.60%, 2.20%, 4.40%, 5.40%, 6.60% and 13.80%, these percentages were taken because of the results of a considerable expansion decrease. The tests were conducted in a natural water content.

By observing the results for the loading capacity, it is considered that is feasible, considering the living place weight of 4 ton/m2 for an average house of two levels.

V REFERENCES

[1] Abdelkrim M., Mohamed K., "Cement Stabilization of Compacted Expansive Clay," *TOJSAT,* vol. 3, no. 1, pp. 33-38, 2013.

[2] Abduljauwad, S. N., "Characteristics and chemical treatment of expansive clay in Al-Qatif, Saudi Arabia," *Elsevier,* vol. 31, no. 2, pp. 143-158, 1991.

[3] Afès M., Didier G. , "Stabilisation des sols gonflants: cas d'une argile en provenance de Mila (Algérie)," *Bulletin of Engineering Geology and the Environment,* vol. 59, no. 1, pp. 75-83, 2000.

[4] Ahmed A., Ugai K., Kanei T., "Application of gypsum waste plasterboard and waste plastic trays to the performance of sandy soil.," *Ground improvement and geosynthetics, geotechnical special publication, ASCE,* vol. 207, pp. 165-173, 2010.

[5] Alhassan M., "Permeability of lateritic soil treated with lime and rice husk ash," *Assumption university journal of technology* , vol. 12, no. 2, pp. 115-120, 2008.

[6] Al-Mukhtar M., Khattabc S., Alcovera J.F., "Microstructure and geotechnical properties of lime-treated expansive clayey soil," *Elsevier,* Vols. 139-140, pp. 17-27, 2012.

[7] Al-Rawas A. A., "Effect of lime, cement and Sarooj (artificial pozzolan) on the swelling potencial of an expansive soil from Oman," *Elsevier,* vol. 40, no. 5, pp. 681-687, 2005.

[8] Assadi and Shahaboddin , "A micro-mechanical approach to swelling behavior of unsaturated expansive clays under controlled drainage conditions," *Applied clay science,* vol. 45, no. 1-2, pp. 8-19, 2009

[9] Attom M.F., Al-Sharif M.M., "Soil stabilization with burned olive waste," *Applied clay science,* vol. 13, no. 3, pp. 219-230, 1998.

[10] Arora S., Aydilek A.H., "Class F fly ash-amended soils as highway base materials," *Journal materials in civil engineering, ASCE,* vol. 17, no. 6, pp. 640-649, 2005.

[11] Avsar E., Ulusay R., Sonmez H., "Assessments of swelling anisotropy of Ankara clay," *Elsevier,* vol. 105, no. 1-2, pp. 24-31, 2009.

[12] Basha E.A., Hashim R., Mahmud H.B., Muntobar A.S, "Stabilization of clay and residual soil using cement-rice husk ash mixtures," *Construction and building materials* , vol. 5, no. 1, pp. 448-453, 2005.

[13] Bell, F. G., "Lime stabilization of clay minerals and soils," *Elsevier,* vol. 42, no. 4, pp. 223-237, 1996.

[14] Bahara, R. Benazzouga M., Kenaib S. , "Performance of compacted cement stabilized," *Elsevier,* vol. 26, no. 7, pp. 811-820, 2004.

[15] Balasubramaniam A.S., Lin D.F., Acharya S.S.S., Kamruzzaman A.H.N., Uddin K., Bergadi D.T., "Behavior of soft Bankik clay treated with additives. Proceeding the 11th asian regional conference on soil mechanics and geotechnical engineering, Seoul," vol. 1, pp. 11-14, 1999.

[16] Behzad K., "Foundations on Expansive Soils: A Review," *Research Journal of Applied Sciences, Engineering and Technology,* vol. 4, no. 18, pp. 3231-3237, 2012.

[17] Bowles J. E., Foundations Analysis and Design, Mc Graw Hill, 1996.

[18] Chen L., Lin D.F., , "Stabilization treatment of soft subgrade soil by sewage sludge and cement," *Journal of hazardous materials,* vol. 162, no. 1, pp. 321-327, 2009.

[19] Choobbasti A.J., Ghodrat H., Vandathrad M.J., Firouzian S., Barari A., Torabi M., Bagherian A., "Influence of using rice husk ash in soil stabilization method with

lime," *Frontiers of earth science in china,* vol. 4, no. 4, pp. 471-480, 2010

[20] Diamond S., Kinter E. B., "Adsorption of calcium hydroxide by montmorillonite and kaolinite," *Elsevier,* vol. 22, no. 3, pp. 240-249, 1966.

[21] Du y. J., Li S.L., Hayashi S., "Swelling-shrinkage properties and soil improvement of compacted expansive soil, Ning-Liang highway, China," *Engineering Geology,* vol. 53, pp. 351-358, 1999.

[22] Ferber V., Auriol J.C., Cui Y.J. Magnan J.P., "On the swelling potential of compacted high plasticity clays," *Engineering geology,* vol. 104, no. 3-4, pp. 200-210, 2009.

[23] Ferreira C., Ribeiroc A., Ottosena L., "Possible applications for municipal solid waste fly ash," *Elsevier,* vol. 96, no. 2-3, pp. 201-216, 2003..

[24] Garnica A. P. , "Estabilización de suelos con cloruro de sodio para uso en las vías terrestres," in *Secretaría de Comunicaciones y Transporte*, México, 2002.

[25] Guney Y., Sary d., Ceti M., Tuncan M., "Impact of cycling wetting-drying on swelling behavior of lime-stabilized soil," *Journal of building and environment,* vol. 42, no. 2, pp. 681-688, 2007.

[26] Huang R. and Wu L., "Stability of unsaturated expansive soil sope," *Earth science frontiers,* vol. 14, no. 6, pp. 129-137, 2007

[27] Jha J. N., Gill K.S., "Effect of rice husk ash on lime stabilization," *Journal of institution of engineers (india),* vol. 87, pp. 33-39, 2006.

[28] .Hussain F., Hojjati H., Okamoto M., Gorga R.E., "Reviwe article: polymer matrix nanocomposites, processing, manufacturing and application: an overview," *Journal of composite materials,* vol. 40, no. 17, pp. 1511-1565, 2006.

[29] Kamei T., Kato T., Shuku T., "Effective use for bassenite as soil improvement materials-recycling of waste plasterboard," *Geotechnical soecity electronic journal,* vol. 2, no. 3 (japanese), pp. 245-254, 2007.

[30] Khattab S.A.A., Al-Juari K.A.K., Al-kiki I.M.A., "Strength, durability and hydraulic properties of clay soil stabilized with lime and instrustial waste lime," *Al-Rafidain engineering ,* vol. 16, no. 1, pp. 102-116, 2008.

[31] Khemissa M., Mahamedi A., "Cement and lime mixture stabilization of an expansive," *Elsevier,* no. 95, pp. 104-110, 2014.

[32] Khoury N.N., Zaman M.M., "Durability of stabilized base courses subjected to wet-dry cycles," *International journal of pavement engineering ,* vol. 8, no. 4, pp. 265-276, 2007.

[33] Kiliarisand P., Papaspyrides C.D., "Polymer/layered silicate (clay) nanocomposites: an overview of flame redundancy," *Prog. Polym Science,* vol. 35, pp. 902-958, 2010.

[34] Ling D.F., Lin K.L., Hung M.J., Luo M.L., "Sludge ash/hydrated lime on the geotechnical properties of soft soil," *Journal of hazardous materials,* vol. 145, pp. 58-64, 2007.

[35] López-Lara T., Zepeda-Garrido J.A., Castario V.M., "A Comparative Study of the Effectiveness of," *EJGE,* 1999.

[36] López-Lara T., Hernández-Zaragoza J. B., Horta-Rangel J., Coronado-Márquez A., "Polímeros para la estabilización volumétrica de arcillas expansivas," *Revista Iberoamerica de Polímeros,* vol. 11, no. 3, pp. 159-168, 2010.

[37] López-Lara T., Hernández-Zaragoza J. B., Horta-Rangel J., Rodriguez-Morales N. P., Bimbela-Osuna C. A., "Analysis of inverted hollow structures placed on expansive soils," *Sociedad Mexicana de Ingeniería Géotecnica,* pp. 1-7, 2014.

[38] Maslehuddin N., Al-Amoudi O.S.B., Shameen M., Rehman M.K., Ibrahum M., "Usage of cement kiln dust in cement products- research rewiew and preliminary investigations," *Constructions and building materials,* vol. 22, pp. 2369-2375, 2008.

[39] Miller G.A., Azad S., "Influence of soil type on stabilization with cement kiln dust," *Construction and building materials,* vol. 14, pp. 89-97, 2008.

[40] Mohmann-Porebska M., "Microfabric effect in frozen clays in relatation to geotechnical parameters.," *Applied clay science,* vol. 21, pp. 77-87, 2006.

[41] Muntobar A.S., "Utilization of uncontrolled burn of rice husk ash in soil improvement," *Civil engineering dimension ,* vol. 5, no. 1, pp. 100-105, 2002.

[42] Muntobar A.S., "Uses of RHA enhanced lime-stabilized clay soil," *International conference of geotechnical engineering. University of Sharjah, United Arab Emirate,* 2004.

[43] Nalbantoglu Z., Gucbilmez E., "Improvement of calcareous expansive soils in semi-arid environments," *Elsevier,* vol. 47, no. 4, pp. 453-463, 2001.

[44] Nalbantoğlu Z., "Effectiveness of Class C fly ash as an expansive soil stabilizer," *Elsevier,* vol. 18, no. 6, pp. 377-381, 2004.

[45] Nalbantoglu Z., "Lime stabilization of expansive clay," in *Expansive soils: recent advances in characterization and treatment*, Taylor & Francis/Balkema, 2006, pp. 341-348.

[46] Sabtan A., "Geotechinical properties of expansive clay shale in Tabuk, Saudi Arabia.," *Journal of asian earth sciences ,* vol. 25, no. 5, pp. 747-757, 2005.

[47] Seco A., Ramírez F., Miqueleiz L., García B., "Stabilization of expansive soils for use in construction," *Elsevier,* no. 51, pp. 348-352, 2010..

[48] Stavridakis, "Stabilization of problematic soils using

cement and lime," in *Expansive soils: recent advances in characterization and treatment*, Taylor & Francis Group, 2006, pp. 385-397

[49] Tenoz M. C., Gokceoglu C., Ulusay R., "Stabilization of expansive ankara clay with lime," in *Expansive Soils: Recent Advances in Characterization and Treatment*, Taylor & Francis Group, 2006, pp. 317-339.

[50] Yilmaz I., Civelekoglu B., "Gypsum: An additive for stabilization of swelling clay soils," *Elsevier,* vol. 44, no. 1-2, pp. 166-172, 2009.

[51] Zhang Z., Tao H., "Stability calcium sulfate course in a wet environment technical report no. FHWA/LA-06/419," 2006.

Development of a new material with physical, chemical and electrical prospects for improving Connection Systems grounding in buildings

E. Segura Carranza*, M. Trejo Perea,

J. L. Reyes Araiza and J. G. Rios Moreno

Division of Research and Graduate Studies.Faculty of Engineering.

Universidad Autónoma de Querétaro, México.

*elian.segura@gmail.com

G. Ronquillo Lomelí

Center for Engineering and Industrial Development

Querétaro, México

Abstract- This paper aims at improving the development of any system ground (SPT) by developing a new bio-friendly materials (MPS) with low resistivity to the passage of an electric current high or low magnitude to replace or improve soil around the electrode in a system ground).

The new material is a combination (mixture) of different materials with low electrical resistivity, having as base material bentonite.

The purpose of this substitution or soil improvement is to improve the dissipation of a current in the ground in case of high magnitude discharge (lightning) or low volume (a short circuit), this in order to protect both the building wiring and equipment installed in the buildingbut mainly users such construction.

KEYWORDS: Material Soil Enhancer (MPS) Grounding System (PTS), Sodium Bentonite, soil resistance.

1. INTRODUCTION

A power system in a building is usually protected by lightning strikes with lightning conductors that are provided with a low resistance connection to the ground, to allow large currents can be downloaded to the general mass of earth, which provides some resistance current flow.

Three phase power systems are connected to ground by connecting one or more points selected neutral grounding system buried. Such lands are designated as land system. In electrical installations, all conductive metal parts are interconnected and grounded to protect people against electric shock. . (Essam Al-Ammar, 2010).

Ideally, the grounding system must be designed to "zero impedance" to provide effective performance of fault currents and to avoid the potential increase in and around the substation. In practice, however, could not be reached "zero impedance". In order to obtain an adequate system performance grounding, the grounding system must be designed with low impedance earth, and the optimal design of grounding systems can be achieved by considering two properties main electrode geometry parameters-earth / configuration and soil.

2. BACKGROUND

a) System Grounding

A grounding system is a safety mechanism that is part of the electrical installations and that is to lead any deviation from the current to the ground, preventing the user from contact with electricity.

This means that some plants sector is connected through a conductor to earth so that in case of an unforeseen current shunt or failure isolates, people do not electrocute on contact with the devices connected to it.

Also called grounding or earthing, the grounding system involves the use of a piece of metal that is buried in the soil and can even reconnect to the metal parts of a structure. Through an insulated wire, this piece of metal is connected to the electrical system and through the sockets, the devices connected to electricity. The grounding also contemplates the use of a differential switch that is responsible for opening the electrical connection to register a current through the ground.

What we call grounding is a mechanism that has buried metal parts (called spears, pikes or electrodes) and drivers of different classes that link the various parts of the facility. Fig. 1 illustrates all components of a grounding system.

Arresters, for example, operate with a grounding system, driving the discharge to an area of low resistance.

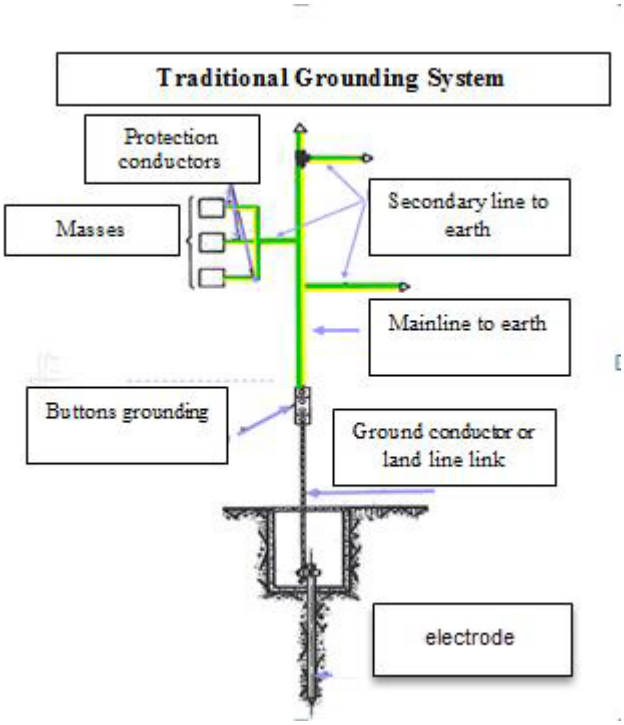

Fig. 1. Traditional Grounding System

a) Earthenhancing material

Invented in 1992, the ground reinforcing material (GIM) is a high-quality conductive material that solves the toughest grounding problems. The GIM has low resistance, non-corrosive, is composed of coal dust, material that improves the efficiency of Grounding System, especially in areas where the conductivity is very poor.

GIM improves grounding regardless of soil conditions. It is ideal for use in areas of poor conductivity such as rocky ground, mountain tops and sandy soil material. GIM is also the answer in situations where they can not be buried ground rods, or where the limitations of the soil surface hinder proper grounding by conventional methods. The conclusion is one. GEM is the best material to reduce the resistance to ground and keep it down permanently. No other material provides a high conductivity so over the lifetime of the grounding system

In order to maximize the benefits of filling, IMT in use must have the following characteristics:

- Must be compactable both GIM as soil.
- Naturally inert.
- Having low and stable resistivity.
- Able to maintain resistance grounding with low minimum fluctuation for a long period of time.
- Are filtered over time.
- Economically viable.

b) Methods to reduce the resistance (impedance) of land

There are two ways to reduce ground resistance; ie, permanent and temporary. Many materials have been used for this purpose. Include bentonite, steel furnace slag, the accumulation of groundwater through deep wells, and a variety of other methods and techniques (R. Zeng, 2002). Have been reported kilo-ohm-meters on the rocks to a few ohm-meter in clays. Data describing the change in resistivity for different soil types are the grain size, temperature, moisture and salt content. (N. MohamadNor, 2006). However, these data are representative of soils under low magnitude currents, low frequency, and are not necessarily valid in large Quick pulse magnitude.

c) Bentonite

Clay is known for its low soil resistivity compared with sand and rock. Using a coaxial cylindrical test cell, and PortelaVisacro (1987) reported that for the same percentage of soil water content and for a given applied voltage low frequency magnitude, the resistivity of wet clay was found to ten times smaller than sand with the same moisture content.

Bentonite applying enhancement material as electrical ground (GIM) has been investigated. Bentonite is a type of clay that has a high propensity to absorb and retain water, and swells. This property makes it desirable for applications in improving the system grounding, and that could result in the reduction and minimize the fluctuation of the earth resistance over a long period of time. However, these properties depend on the type of bentonite. Commercially, there are two types of bentonite available; namely sodium bentonite and calcium bentonite.

3. METHODOLOGY

The project will consist primarily in making the characterization of materials used in three stages, to choose optimal for our purposes.

a) Physical characterization

Relations between weights and volumes of soil

The relationship between weight and volume of a soil sample, are very important for the comprehensive management of the mechanical properties of soils and complete mastery of meaning and physical sense. It is imperative to express affordably data and conclusions of soil mechanics.

In soil mechanics weight of the different phases (liquid, gaseous solid) with corresponding volumes, through the concept of specific gravity, ie the ratio between the weight of the substance and its volume is related.

$$\gamma_m = \frac{W_m}{V_m} = \frac{W_s + W_w}{V_m} \quad (1)$$

$$\gamma_s = \frac{W_s}{V_s} \quad (2)$$

γ_m = Specific weight of the soil mass
V_m = Total volume of the soil sample
V_s = Volume of the solid phase from the soil sample
V_v = Empty volume of soil sample
W_m = Total weight of the soil sample
W_s = Weight of the solid phase from the soil sample

The specific gravity is defined as the relationship between the specific gravity of a substance and the specific gravity of water at 4 ° C, distilled and subjected to an atmosphere pressure.
Units in appropriate systems, its value is identical to the specific module, corresponding weight, as seen from the above. The following specificrelative weights differ.

$$s_m = \frac{\gamma_m}{\gamma_0} = \frac{W_m}{V_m * \gamma_0} \quad (3)$$

$$s_m = \frac{\gamma_s}{\gamma_0} = \frac{W_s}{V_s * \gamma_0} \quad (4)$$

s_m= Specific gravity of the soil mass
s_s= Specific gravity relative to the solid phase
γ_0 =Specific weight of distilled water.

Is called void ratio, porosity index cavity or the ratio between the voids volume and a solid ground:

$$e = \frac{V_v}{V_s} \quad (5)$$

Soil porosity is the ratio of the volume of voids and the volume of its mass. Itisexpressed as a percentage:

$$n(\%) = \frac{V_v}{V_m} * 100 \quad (6)$$

$n(\%)$= Soil porosity
V_v = Empty volume of soil sample
V_m = Total volume of the soil sample

The degree of saturation of a soil is the ratio of the volume of water and the volume of voids. Usuallyexpressed as a percentage:

$$G_w(\%) = \frac{V_w}{V_v} * 100 \quad (7)$$

G_w= Degree of saturation of the soil
V_W = Water volume of the soil sample
V_v = Empty volume of soil sample

Is known as water or moisture content of a soil, the ratio of the weight of water contained in it and the weight of the solid phase.Usually expressed as a percentage:

$$w(\%) = \frac{W_w}{W_s} * 100 \quad (8)$$

W_s = Weight of the solid phase from the soil sample
W_w= Weight of the liquid phase of the soil sample
w= Water or moisture content of the soil sample.

b) Chemical characterization

The X-ray crystallography is an experimental technique for the study and analysis of materials, based on the phenomenon of diffraction of the X-rays by solid state crystalline.

The X-rays are diffracted by electrons surrounding the atoms to be your wave length the same order of magnitude as the atomic radius. The beam of X-rays emerging after this interaction contains information on the position and type of atoms found in his way. Crystals, thanks to its periodic structure, elastically scattered X-ray beams in certain directions and amplified constructive interference, Creating a pattern of diffraction. Several types of special detectors to observe and measure the intensity and position of the diffracted X-rays, and subsequent analysis by mathematical means allows a representation on the atomic scale of atoms and molecules of the material studied.

c) Electrical characterization

The soil resistivity is an electro-physical property that depends on soil type, moisture content, the amount of salt in the soil and temperature. Increasing the moisture content or temperature increase reduces its resistivity, while a small amount of dissolved salts can easily reduce the value of the resistivity. (IEEE, 2000).

Measurement of earth resistance of a single pylon or other construction usually requires the overhead wire earth to be disengaged or separation of the grounding system of the building. Otherwise, you may get a false reading of the resistance of the ground electrode and can occur because of the parallel connection of the other pylons connected by a cable above ground.

Therefore the resistance RE grounding the tower is determined as a parallel circuit:

$$R_E = \frac{1}{\frac{1}{R_1}+\frac{1}{R_2}+\frac{1}{R_3}+\frac{1}{R_4}} \quad (9)$$

Where

RE = total equivalent resistance grounding system (Ω).
Ri = Resistance of each state or spades system grounding (Ω).

Since the resistance value RE, soil resistivity calculated according to equation:

$$\rho_E = 2 * \pi * a * R_E \quad (10)$$

ρ_E = Average value of soil resistivity (Ω).
RE = total equivalent resistance grounding system (Ω).
a = distance between stakes (m).

The measuring method according to Wenner determines the soil resistivity down to a depth of approx. the distance "a" between two ground stakes. By increasing "a", deeper strata can be measured and monitored for homogeneity. By changing "a" several times, a profile can be measured from which a suitable earth electrode can be determined.

According to the depth to be measured "a" is selected between 2 m and 30 m.

In the calculations of impedance grounding usually only the resistance value is determined. In much of the literature related to this topic analysis thus addressed, so that in most of the published work appears only the resistance value. To know the value of the capacity of the ground is part of the equation of resistance grounding (eg a vertical electrode) and thus becomes (Angel C. Valcárcel, 2003):

$$C = \frac{\rho}{4 * \pi * R_E} * \mathcal{E} \quad (11)$$

Where:

C = capacity of the medium.
Ɛ = absolute electrical resistivity of the medium in which it propagates.
RE = total equivalent resistance grounding system (Ω).

As any wave propagating in a medium is known as done with a speed equal to:

$$v = \frac{1}{\sqrt{L * C}} \quad (12)$$

Where:

L = inductance of the propagating medium.
C = capacity of the medium.
V = velocity of wave propagation.

And it can also be expressed by:

$$v = \frac{1}{\sqrt{\mathcal{E} * \mu}} \quad (13)$$

Where:

μ = absolute magnetic permeability of the medium.
Ɛ = absolute electrical resistivity of the medium in which it propagates.
V = velocity of wave propagation.

Equating the above equations, we obtain:

$$L = \frac{\mathcal{E} * \mu}{C} \quad (14)$$

Where:

Ɛ = absolute electrical resistivity of the medium in which it propagates.
L = inductance of the propagating medium.
C = capacity of the medium.

With these data connection impedance grounding system is given by an equivalent circuit, through a model of a median line.

Theoretically, the ground resistance of any land or electrode system, R, can be calculated using the general formula of resistance:

$$R = \rho\left(\frac{L}{A}\right) \quad (15)$$

Where:
ρ → soil resistivity (ohm-meter)
L → Length of path conductor (meters)
A → cross-section of the route (square meters)

It is essential to measure the resistivity of the ground as part of the design process. The resistivity can vary widely in different media terrain. In general, the total resistance having an earthing installation consists of the sum of the following parts:
The resistance of the conductor (land line and trunk with the electrode) that connects the ground electrode system must be grounded,
The contact resistance between the electrode surface and the ground,
The resistivity of the soil in which the electrode is buried.

4. RESULTS

Chemical tests

One commercial GIM was chemically studied, in order to know what was it anatomic composition. In the table 1 are showed the elements finned.

The micrographs and quantitative elemental analysis were obtained through the SEM-EDX (Scanning Electron Microscopy-Energy Dispersive X-ray spectroscopy), detecting largely carbon and less sodium magnesium and aluminum, so these elements have a great affinity by water retention.

TABLE I PROPORTIONS OF MATERIAL IN COMERCIAL GIM

El	AN	C norm.
C	6	59.58
O	8	28.7
Na	11	1.34
Mg	12	0.64
Al	13	2.31
Si	14	5.19
S	16	0.2
CL	17	1.16
K	19	0.12
Ca	20	0.16
Fe	26	0.59
	Total	**100**

Physical tests

Soil finned in situ

In the excavation it was finned several soils with different resistivity, caused by the composition of each soil.

When excavation is performed felt the floor consisted of several layers, a characterization was performed a priori, based on previous experience.

Figure 2. Wells were used for field testing and soil stratification.

In the figure 2 are sowed all the stratum of soil finned in situ and in the figure 3 the resistivity measured of the soil.

Figure 3. Colocation of Fluke device for measuring the resistivity of the natural ground and subsequent measurement of such resistivity.

Volumetric weight

Specific weight of bentonite 676.7 kg / m3

Specific weight of magnesium sulfate 2660 kg / m3

Specific weight sodium sulfate 2664 kg / m3

Based on the results of the physical characterization of each material, two mixtures were prepared with different sulfating percentage of salts such sum of percentages would not exceed 15% relative to the total mass of the bentonite, to avoid corrosion and also avoid associating negative ion pairs which reduces the capacity to conduct electricity in a material.

TABLE II PROPORTIONS OF MATERIAL USED IN THE PROPOSAL MIXTURE 1

Mix 1 according to the mass of bentonite	
Proportion material according to the weight of bentonite	
MgSO4	5%
Na2SO4	7%
H2O	3.5

Mix 2 according to the mass of bentonite	
Proportion material according to the weight of bentonite	
MgSO4	5%
Na2SO4	10%
H2O	3.5

TABLE III PROPORTIONS OF MATERIAL USED IN THE PROPOSAL MIXTURE 2

For both mixtures absorption analysis finding that exceeded 100% in each took place. In fact for the two mixes a result of 104.69% was obtained, ie weight absorbed water than its own weight, this due to the anisotropy properties of bentonite and sodium sulfate.

Electrical tests

Soil analysis was performed and it was determined that the soil of the place was a silty clay and it had a resistance of 130.2 Ω * m.
Mixtures of sodium bentonite a GIM Material, you mixture 1 and commercial mixture 2 were placed in the same amount each of them and in this way to compare the results.

In table number 3, are showed average resistivity results of bentonite, mixture 1 and mixture 2 and it respective percentage comparable with the resistivity of the soil finned in situ.

TABLE IV PERCENTAGE REDUCTION IN RESISTIVITY WITH RESPECT TO THE NATURAL SOIL

	Average values (Ω * m)		
Natural soil (Ω*m)	Bentonite	Mixtures 1	Mixtures 2
130.2	12.71	10.19	9.01
	Percentage compared to natural soil (%)		
	9.78	7.84	7.00

Figure 4, illustrates the results obtained in all the test made in situ (bentonite, commercial GIM, mixture 1 and mixture 2). Is easy to see that two mixture have almost the same resistivity about all the measured. Also it can be see it, that the mixture number two has the better results and the resistivity falls until 7 % (9.01 Ω*m) comparable with the resistivity of the soil finned in situ (130.2 Ω*m).

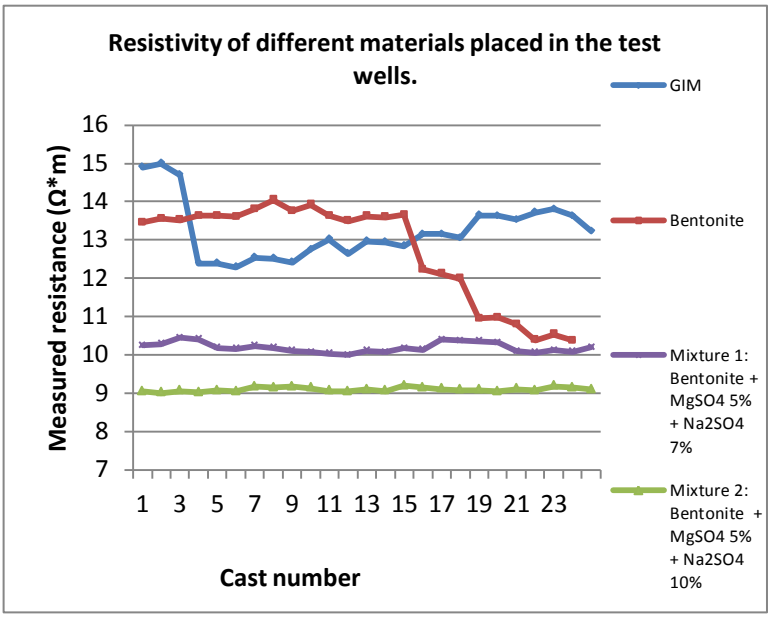

Figure 4. Comparison of resistivity of different materials placed in the test wells.

5. CONCLUSIONS

The difference between the mixture 1 and mixture 2 proposals is just over one ohm average, ie is achieved by increasing the sodium sulphate at 3% according to the weight of bentonite. However one cannot adhere more to the mixture because the dissolved salts should be less than 15% to avoid corrosion of the electrode and the formation of ion pairs.
Similarly, the difference in resistivity of the mixtures without salts with bentonite is about 3 ohm. This means you can see a relationship than 1 ohm per 3% of sodium sulfate dissolved in the mixture. Because sulfate is the best of disolved salts due to their chemical and electrical properties.

the relationship with bentonite is obtained, namely that for our soil was reduced by 90% the resistivity of the natural ground with a contact area: 1.013 m2 (sonotubo 30 cm diameter) plus 1% extra for every 3 % of dissolved salts in the bentonite according to weight up to a limit of 10% in the sodium sulfate. That is, it is reduced depending on the contact area that has the GIM.
If you want to standardize the results for soil types that were found at the site, you can use the following procedure and apply the following formulas to mix 2.

Area covered by the samples in the evidence presented in sit

$$A = (D * \pi) + \frac{D^2 * \pi}{4} \quad (16)$$

$$\%\ \text{Reduction gradient}\ (\%GR) = \frac{\rho E}{R} * 100 \quad (17)$$

$$\text{Required amount of M2}\ (CM2) = \frac{\%GR}{\%Rm2} \quad (18)$$

Where:
$\rho_E \rightarrow$ Resistivity objective of the earth (ohm-meter)
R → Soil resistivity measured with Tellurometer (square meters)
A → Ground contact area with the material placed (square meters)
D → sonotubo diameter (m)

TABLE V AMOUNTS OF MATERIAL REQUIRED FOR ANY SOIL

Amount of bentonite Required (Bent)	1
Amount of sodium sulfate (kg)	(Bent)*0.10

Amount of magnesium sulfate (kg)	(Bent)*0.05

This means any type of soil could be replaced by our GIM (mixture 2) and resistivity could obtain needed or equal to or less than current regulations. All this depending on the contact area of our GIM with surrounding soil, assuming our GIM is homogeneous and the electrical energy dispersed in all directions in the same way.

Acknowledgements

Support We thank my thesis advisor, CONACYT and the Government of the State of Querétaro, offered through the QRO-2012-C01-193364 Call FOMIX Project 2012-01: Strengthening Laboratory through the Master of Science Faculty of Engineering of the University of Queretaro.

REFERENCES

REFERENCES

[1] Akihiro Ametani. 2012. Impedance Characteristics of grounding electrodes on earth surface. Electric Power Systems Research, vol. 85, (2012), pp. 38-43.

[2] Camilo A. Acosta-Urrego. 2013. Identification of technical losses in low voltage earthing systems. Dyna, no. 181, pp. 40-50. Colombia, October, 2013.

[3] Daniel S. Gazzana. 2014. A study of human safety Against lightning Considering the grounding system and the evaluation of the Associated parameters. Electric Power Systems Research, vol. 113, (2014), pp. 88-94.

[4] Essam Al-Ammar. 2010. Development of Low Resistivity materials for grounding resistance reduction. 2010 IEEE International Energy Conference.

[5] F. P. Dawalibi. 1986. Electromagnetic fields generated by overhead and buried conductors short, part 2 - ground conductor. IEEE Transaction on Power Delivery, vol. 1, pp. 112-119.

[6] Hirotaka Shimizu. 2012. Grounding resistance of grounding electrode plate using charcoal made of woody material. 2012 International Conference on Lightning Protection (ICLP).

[7] Badillo Juárez and Rico Rodriguez. 2005. Soil Mechanics I: Fundamentals of Soil Mechanics. Mexico, Limusa.

Time-Frequency Algorithms to Estimate the Modal Parameters of Civil Structures using Ambient Vibrations

Carlos Andres Perez-Ramirez[1], Juan Pablo Amezquita-Sanchez [1*], Martin Valtierra-Rodriguez [1], David Camarena-Martinez [2], Aurelio Dominguez-Gonzalez[1], Jhonatan Perez-Galeana[1], Jorge Armando Escalante-Valdivia[1], Francisco Javier Vázquez-Arvizu[1], Elian Segura-Carranza[1]

[1]*Facultad de Ingeniería, Campus San Juan del Rio, Universidad Autónoma de Querétaro, Rio Moctezuma 249, Col. San Cayetano, 76807 San Juan del Rio, Querétaro, México*

[2] *División de Ingenierías, Campus Irapuato-Salamanca, Universidad de Guanajuato, Carr. Salamanca-Valle de Santiago km 3.5+1.8, Comunidad de Palo Blanco, 36700 Salamanca, Guanajuato, México.*

*****Corresponding author: jamezquita@uaq.mx

***Abstract*—The accurate estimation of modal parameters such as natural frequencies and damping ratios is an important concern since their values allow the condition assessment of the structure, vibration control, as well as to build or update a proper model of the structure. Unfortunately, an accurate estimation of these values represents a challenge since the acquired measurements of structures are noise-contaminated; therefore, signal processing techniques should be able to process the signal without affecting the natural frequencies and damping ratios estimation. In this article, different time-frequency algorithms (fast Fourier transform-FFT, random decrement technique-RDT, half power bandwidth-HPB and logarithmic decrement-LD), to estimate the natural frequencies and damping ratios of a civil structure using ambient vibrations are presented. This study allows observing which algorithm can estimate the modal parameters of a civil structure with accuracy. To validate the accuracy of the proposed algorithms, they are applied to the estimated responses of a benchmark 4-story 2 × 2 bay 3D steel frame structure subjected to broadband ambient inputs (Gaussian noise) applied in the x and y-directions. The results are also compared with those obtained by a finite element-based model.**

Keywords—FFT, RDT, HPB, LD, Natural frequencies estimation, Damping ratios estimation, Civil structures.

I. INTRODUCTION

The modal parameters such as natural frequencies and damping ratios are important values of the civil structures since they allow observing the behavior assessment during an earthquake and designing a suitable structure capable of having a better adaptation to the motion caused by external forces. Further, their calculation can be used to implement a structural health monitoring (SHM) scheme in an online way [1].

To perform the modal parameter identification (MPI) of civil structures, artificial and natural excitations have been used. The artificial excitations are characterized by requiring mechanical systems such as shakers, and drop weights, among others [2-3]; but, these types of excitations require an ease access to the structure and its temporary closing during the monitoring of the structure [4]. Further, the artificial excitation for large structures presents some problems. For example, if the excitation is small, the structure will not be excited correctly making that the measured dynamic signals contain only noise; in contrast, if the excitation is too big, the structure can suffer damages [5]. For these reasons, recently a significant part of modal parameters identifications research has focused on ambient vibrations such as wind, traffic, and earthquakes. The ambient vibrations present the advantages of being low-cost and not interrupting the structure normal operation because no excitation equipment and traffic interruption are required. Further, it allows implementing a real-time condition assessment [6-8]. However, the modal parameter identification using ambient vibrations represents a challenge, since measured data is non-stationary and it is embedded in high-level noise.

In this article, different algorithms, FFT, RDT, HPB, and LD, are investigated to estimate the natural frequencies and damping ratios of a civil structure using ambient vibrations. To validate the usefulness of the classical algorithms, they are applied to estimate responses of a benchmark 4-story 2 × 2 bay 3D steel frame structure subjected to ambient vibrations [9]. The results are compared with those obtained by a finite element-based model.

II. THEORETICAL BACKGROUND

This section presents the theoretical background of the proposed techniques for MPI of civil structures.

A. FFT analysis

FFT is an optimized algorithm for performing the discrete Fourier transform (DFT), which is used to obtain the frequency content of a time series signal [10]. It is considered an efficient technique for analyzing stationary signals. DFT is defined by Eq. (1), where $x(n)$ is the discrete time series signal, N is the sampling period, n and k are the discrete time

This work was supported in part by the National Council on Science and Technology (CONACYT). Mexico, under Scholarships: 289377.

and frequency indexes, respectively, and the transformation kernel W_N^{nk} is given by Eq. (2).

$$X(k) = \sum_{n+0}^{N-1} x(n) W_N^{nk} \quad for\, 0 \le k \le N \text{ and } 0 \le \mathrm{n} \le N \quad (1)$$

$$W_N^{nk} = \cos\left(\frac{2nk\pi}{N}\right) + j\sin\left(\frac{2nk\pi}{N}\right) \quad (2)$$

B. RDT analysis

Proposed by Cole [11], RDT is a time domain method, which uses the environmental excitation responses to obtain the free response from the raw response measurements. The algorithm considers that the random response of any mechanical structure is composed by a random part and a deterministic part. Averaging enough selected responses with a common initial condition *a*, the random part is removed, allowing its utilization as a filter. Hence, the result is the deterministic part associated to the free-decay response [12].

RDT vector is obtained as follows:

$$\delta(\tau) = \frac{1}{N}\sum_{i=1}^{N} y\left(\tau + \tau_i\right)\Big|_{y(t)=a} \quad (3)$$

where *y(t)* is a measurement from the response signal *x(t)* at the time instant t_i, which satisfies the triggering condition *a*; *N* is the number of the triggering points obtained, and τ is the time variable. The used trigger condition is the level crossing condition, *a*, expressed mathematically as follows [13]:

$$a = \sqrt{2}\sigma_x \quad (4)$$

where σ_x is the measurement standard deviation. 1024 points after each sample are recommend because it allows generating a suitable free-decay response [14].

C. HPB analysis

The half-power bandwidth method is used to calculate the damping ratio of each natural frequency obtained by FFT analysis [15]. The damping ratio, ξ, is estimated as follows:

$$\xi = \frac{\omega_2 - \omega_1}{2\omega_n} \quad (5)$$

where ω_n represents the natural frequency, ω_1 and ω_2 are the frequencies corresponding to the two half-power points, (Fig. 1). A small damping means that the structural system cannot dissipate the vibration easily, in contrast, a high damping value means that the structural system can dissipate the vibration quickly.

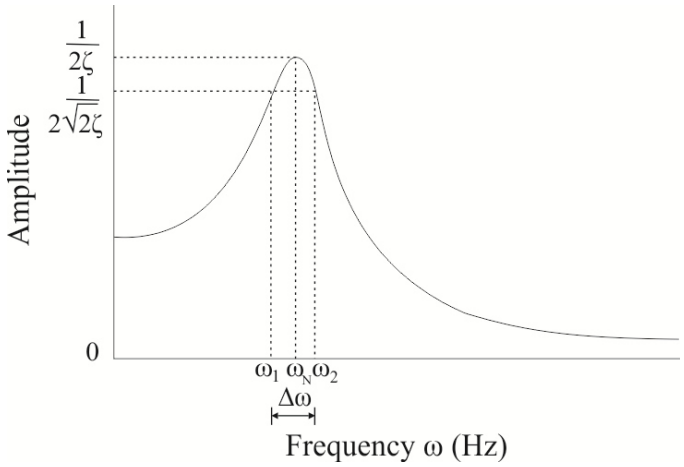

Fig. 1. Damping ratio estimation using HPB analysis.

D. LD analysis

LD method is a time domain technique, which exploits the exponential decay property of the free response of a damped system to obtain damping ratio information [16]. It is estimated by comparing the amplitude of a time signal in different periods as follows:

$$\xi = \frac{1}{2\pi(n-1)} \ln \frac{A_1}{A_n}$$

where *A* is the amplitude value of time series signal in different periods and *n* is the period selected as shown in Fig. 2.

It is important to mention that the free vibration must be mono-component, which means that the analyzed signal contains only one frequency; therefore, a pre-processing or filtered of signal is necessary.

III. Numerical Validation of the Algorithms Efficacy

A. Simulated data

In order to demonstrate the effectiveness of the proposed algorithms for identification of natural frequencies (FFT and RDT-FFT) and damping ratios (FFT-HPB, RDT-FFT-HPB and LD) of a civil structure, a MATLAB-based FEA code provided by the IASC-ASCE SHM Task Group, where a 4-story 2 × 2 bay 3D steel frame structure, has been used [17]. The structure was subjected to broadband ambient inputs applied in the x and y-directions (Fig. 3). Vibration signals were acquired by

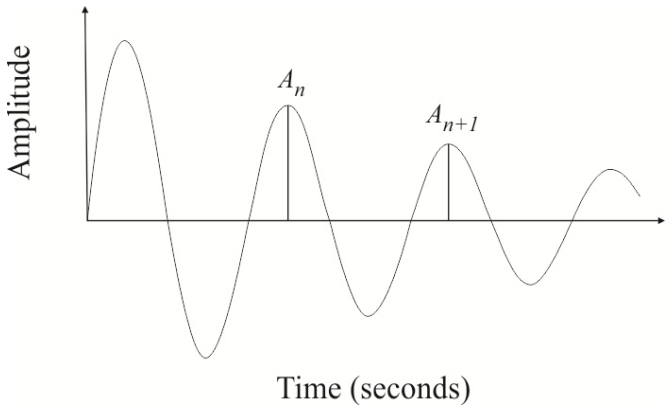

Fig. 2. Damping ratio estimation using LD analysis.

sixteen sensors placed on the building exterior at all four stories in the two horizontal directions (x- and y-direction) as shown in Fig. 3. Using a sampling frequency of 1,000 Hz, 40,000 samples were obtained during a time window of 40 s. A 1% modal damping was assigned to each mode. The vibration response data of sensor 15 in the x-direction and sensor 16 in the y-direction are used to test the proposed algorithms. Fig. 4 shows the acquired vibration in x- and y- directions by the sensors 15 and 16, respectively.

B. Results

Once acquired the signals, firstly, they are analyzed by FFT and RDT combined with FFT, respectively, as shown in Fig. 5 and 6, in order to estimate the natural frequencies of the structure. From these figures, the RDT combined with FFT (Fig 6) allows observing and estimating the natural frequencies of structure with accuracy, since a maximum error of 1.6% is obtained, which is considered as accurate because the identified natural frequencies are within 2% of the theoretical ones [18], summarized in Table I, demonstrating that the RDT helps to lessen the noise contained in the signal; on the other hand, the natural frequencies calculated by FFT (Fig. 5) present similar results that RDT-FFT (see Table I), however they are embedded in noise, which limit and difficult their correct estimation.

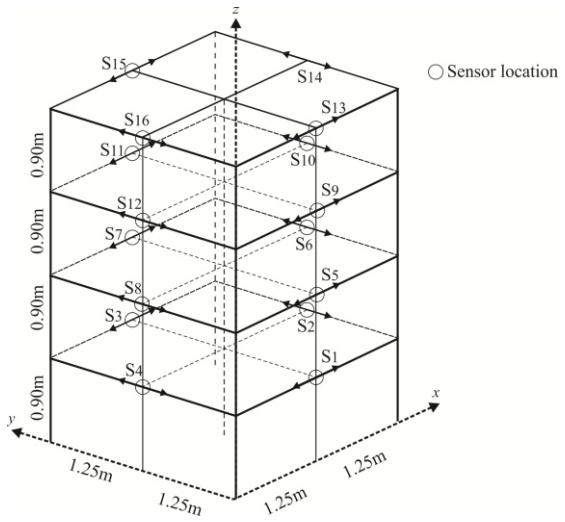

Fig. 3. 4-story benchmark structure and locations of the 16 measurement sensors.

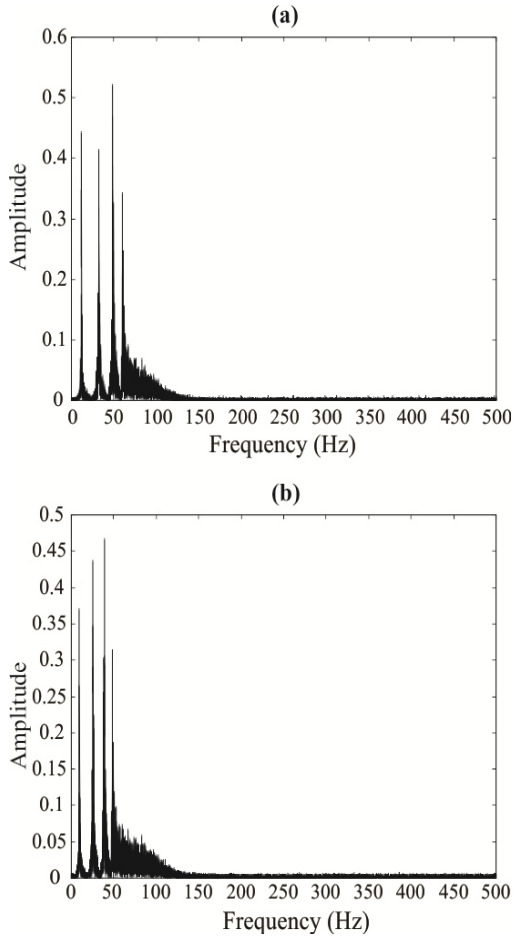

Fig. 5.FFT of the measured data in sensors (a) 15 and (b) 16.

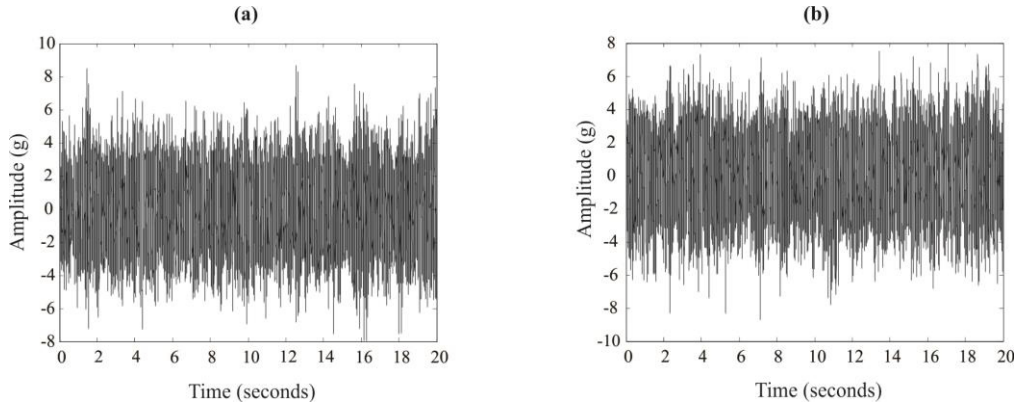

Fig. 4. Acquired vibration in (a) x-direction and (b) y-direction by the sensors 15 and 16, respectively.

TABLE I
Identified natural frequencies and damping ratios of the benchmark structure using simulated data.

Mode	FEA		FFT-HPB (error %)		RDT-FFT-HPB (error %)		RDT-DF-LD (error %)
	Frequency (Hz) - direction	Damping ratio (%)	Frequency (Hz)	Damping ratio (%)	Frequency (Hz)	Damping ratio (%)	Damping ratio (%)
1	9.410—y	1.0	9.43 (0.2)	0.17 (83)	9.566 (1.6)	0.60 (40.0)	0.87 (13)
2	11.79—x	1.0	11.83 (0.3)	0.08 (92)	11.72 (0.5)	1.57 (57.85)	0.90 (10)
3	25.54—y	1.0	25.41 (0.5)	0.10 (90)	25.39 (0.5)	0.78 (21.22)	0.88 (12)
4	32.01—x	1.0	32.0 (0.7)	0.03 (97)	32.23 (0.6)	0.51 (48.41)	0.89 (11)
5	38.66—y	1.0	38.67 (0.1)	0.02 (98)	39.06 (1.0)	0.66 (33.89)	0.81 (19)
6	48.01—y	1.0	48.2 (0.4)	0.03 (97)	47.85 (0.3)	0.44 (56.11)	0.88 (12)
7	48.44—x	1.0	48.45 (0.1)	0.02 (98)	48.10 (0.7)	0.49 (51.14)	0.91 (09)
8	60.15—y	1.0	59.97 (0.3)	0.01 (99)	60.55 (0.6)	0.43 (56.23)	0.91 (09)

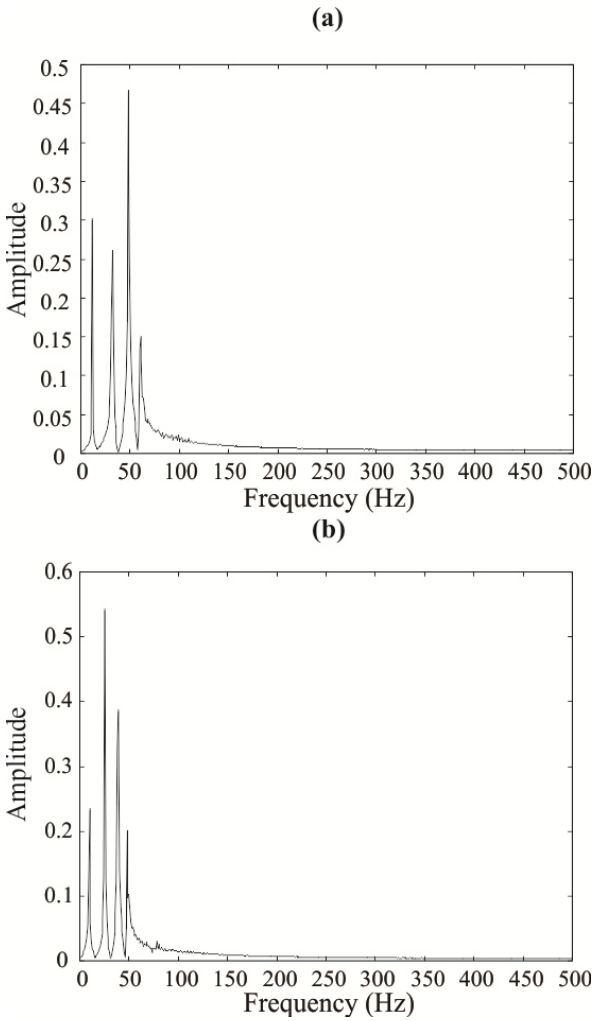

Fig. 6. RDT-FFT of the measured data in sensors (a) 15 and (b) 16.

Once estimated the natural frequencies of the structures, the next step is to estimate the damping ratios of civil structure. To perform this task, three algorithms are tested (FFT-HPB, RDT-FFT-HPB and RDT-Digital Filter (DF)-LD). In the last algorithm, a Butterworth filter of order 4 is used to separate the natural frequencies in time series signals which are mono-components in order to be compatible with the LD method. Fig. 7 shows the estimated mono-components using the RDT and FD, where is possible to observe the eight modes of structure, 4 in x-direction and 4 in y-direction, respectively.

According to damping ratios estimated by three different algorithms, the RDT-FD-LD presents the best results, since a maximum error of 19% in the mode 5 is estimated. Therefore, the results are considered accurate because the identified modal damping ratios are within 20% of the theoretical ones [18], summarized in Table I. In summary, these results show clearly that RDT-DF-LD is immune to noise and can accurately identify the modal damping ratios; however, other alternatives should be explored in order to improve the obtained results.

IV. CONCLUSIONS

This article presents a comparative of different algorithms to estimate the natural frequencies and damping ratios of civil structures using ambient vibrations. The accurate estimation of modal parameters is an important concern since their values allow the condition assessment of the structure, vibration control, as well as to build or update a proper model of the structure.

In order to validate the accuracy of the proposed algorithms, they are applied to the estimated responses of a benchmark 4-story 2 × 2 bay 3D steel frame structure subjected to broadband ambient inputs (Gaussian noise) applied in the x and y-directions. The benchmark problem demonstrates that RDT-FFT and RDT-DF-LD methodology are effective in estimating the modal parameters using ambient vibrations. The estimated natural frequencies and damping ratios values are similar to the estimated by the FEA-based model. The maximum errors for frequency and damping ratio identification are 1.6% and 19%, respectively.

REFERENCES

[1] C. A. Perez-Ramirez, J. P. Amezquita-Sanchez, H. Adeli, M. Valtierra-Rodriguez, D. Camarena-Martinez, and R. J. Romero-Troncoso, "New methodology for modal parameters identification of smart civil structures using ambient vibrations and synchrosqueezed wavelet transform," *Eng. Appl. Artif. Intell.,* vol. 48, pp. 1-12, Feb. 2016.

[2] C. S. Huang, S. L. Hung, C. I. Lin, and W. C. Su, "A wavelet-based approach to identifying structural modal parameters from seismic response and free vibration data," *Compt.-Aided Civil Infrastruct. Eng.*, vol. 20, no. 6, pp. 408-423, Aug. 2005.

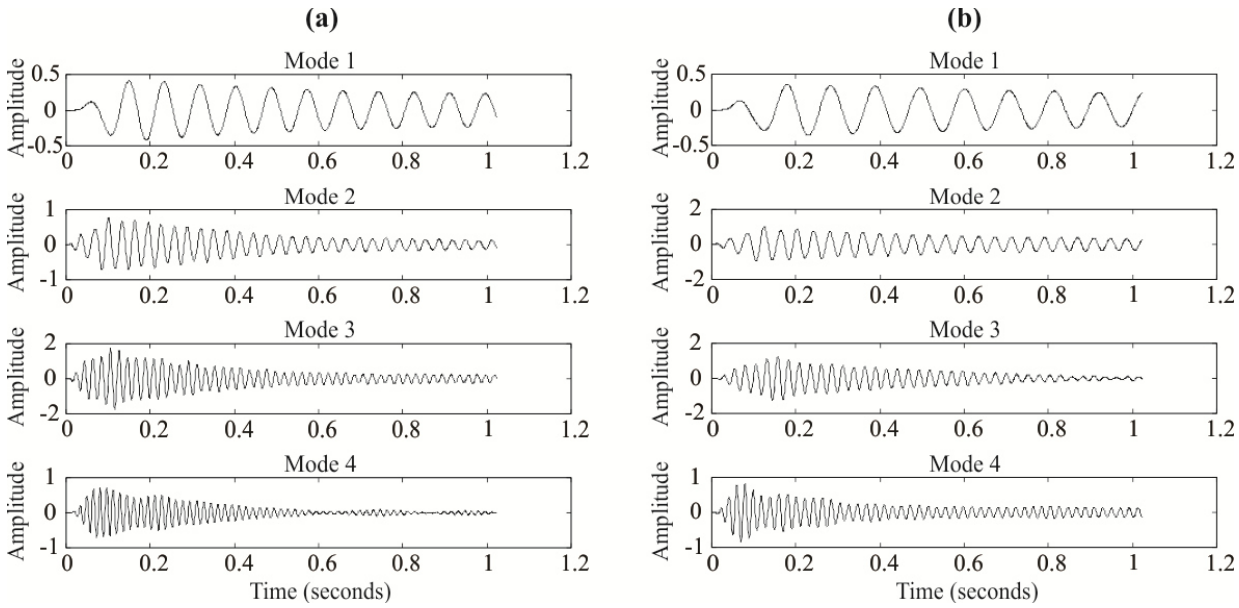

Fig. 7. Estimated individual modes in (a) x- and (b) y-direction of the 4-story benchmark structure.

[3] B. Peeters, J. Maeck, and G. De Roeck, "Vibration-based damage detection in civil engineering: excitation sources and temperature effects," *Smart Mater. Struct.*, vol. 10, no. 3, pp. 518-527, Jun. 2001.

[4] J. P. Amezquita-Sanchez, A. Garcia-Perez, R. J. Romero-Troncoso, R. A. Osornio-Rios and G. Herrera-Ruiz, "High-resolution spectral-analysis for identifying the natural modes of a truss-type structure by means of vibrations," *J. Vib. Control*, vol. 19, no. 16, pp. 2347–2356, Nov. 2013.

[5] X. H. He, X. Hua, Z. Chen, and F. Huang, "EMD-based random decrement technique for modal parameter identification of an existing railway bridge," *Eng. Struct.*, vol. 33, no. 4, pp. 1348–1356, Apr. 2011.

[6] J. N. Yang, Y. Lei, and N. Huang, "Identification of natural frequencies and damping of in situ tall buildings using ambient wind vibration data," *J. Eng. Mech.*, vol. 130, no. 5, pp. 570–577, May 2004.

[7] W. Shi, J. Shan, and X. Lu, "Modal identification of Shanghai World Financial Center both from free and ambient vibration response," *Eng. Struct.,* vol. 36, pp. 14–26, Mar. 2012.

[8] D. Camarena-Martinez, J. P. Amezquita-Sanchez, M. Valtierra-Rodriguez, R. J. Romero-Troncoso, R. A. Osornio-Rios, and A. Garcia-Perez, "EEMD-MUSIC-Based analysis for natural frequencies identification of structures using artificial and natural excitations," *Scientific World J.*, pp. 1-12. Article ID: 587671, 2014

[9] E. A. Johnson, H. F. Lam, L. S. Katafygiotis, and J. L. Beck, "Phase I IASC-ASCE structural health monitoring benchmark problem using simulated data," *J. Eng. Mech.*, vol. 130 no. 1, pp. 3-15, Jan. 2004.

[10] J. P. Amezquita-Sanchez, R. A. Osornio-Rios, R. J. Romero-Troncoso, and A. Dominguez-Gonzalez, "Hardware-software system for simulating and analyzing earthquakes applied to civil structures," *Nat. Hazards Earth Sys. Sci.*, vol. 12, no. 1, pp. 61-73, Jan. 2012.

[11] H. A. Cole, "On-the-line analysis of random vibrations", in *Proc. AIAA/ASME Ninth Struct., Struct. Dyn. Materials Conf.*, Palm Springs, CA, April 1-3, 1968, AIAA.

[12] J. He and Z.-F. Fu, "Modal Analysis", Boston, MA: *Butterworth-Heinemann*, 2001.

[13] J. Rodrigues, & R. Brincker, "Application of the Random Decrement Technique in Operational Modal Analysis", in *Proc. 1st Int. Operational Modal Ana. Conf.*, Copenhagen, Denmark, April 26-27, 2005, pp. 191-200.

[14] S. R. Ibrahim, "Efficient Random Decrement Computation for Identification of Ambient Responses", in *Proc. 2001 Int. Modal Ana. Conf.*, Orlando, FL, USA, February 5-9, 2001, pp. 1–6.

[15] A. K. Chopra, "Dynamics of Structures," *Pearson-Prentice Hall*: New Jersey, 2007; pp. 80–89.

[16] Y. Liao, and V. Wells, "Modal parameter identification using the log decrement method and band-pass filters," *J. Sound Vib.*, vol. 330, no. 21, pp. 5014-5023, Oct. 2010.

[17] S. J. Dyke, D. Bernal, J. L. Beck, and C. Ventura, "An experimental benchmark problem in structural health monitoring," in *Proc. 3rd Int. Workshop Struct. Health Monitoring*, Stanford, Calif, USA, 2001.

[18] W. C. Su, C. S. Huang, C. H. Chen, C. Y. Liu, H. C. Huang, and Q. T. Le, "Identifying the modal parameters of a structure from ambient vibration data via the stationary wavelet packet," *Compt.-Aided Civil Infrastruct. Eng.,* vol. 29, no. 10, pp. 738–757, Nov. 2014.

Transient thermal analysis for a cell of adiabatic calorimeter

González Durán J. Eli, Sanchez Rodríguez Álvaro
Departamento de Ingeniería Mecánica
Instituto Tecnológico de Celaya
Celaya, Guanajuato, México
eli.gonzalez@iqcelaya.itc.mx
alvaro.sanchez@itcelaya.edu.mx

Lira Cortés Leonel
División de Termometría Área Metrología Eléctrica
Centro Nacional de Metrología
El Marqués, Querétaro, México
llira@cenam.mx

***Abstract*—The present work shows the mathematical formulation of transient heat conduction for a cell of adiabatic calorimeter, which is considered the best technique for measuring heat capacity. For development of the cell was established and solved the mathematical model in transient way, which approximates the physical phenomenon under which the cell operates. To validate or analysis performance among use a numerical method for complex geometries. Were compares the results of solve the transient heat transfer in a cylinder under boundary and initial conditions by means of analytical solution and numerical analysis through element finite method by commercial software. The analysis from the temperature distribution, allow to obtain design criteria, that are generated by changing parameters like dimension, temperature and working fluids to measure the heat capacity. Is showed the mathematical solution with its initial and boundary conditions as well the comparison with numerical solution for a cylindrical cell with a maximum error from 0.070 % in temperature value among the theoretical and numerical analysis for a temperature difference of 1 °C.**

Keywords—Adiabatic calorimetry; adiabatic calorimeter; heat capacity; element finite method.

I. INTRODUCTION

For engineering design, where exist heat exchange as refrigerators or the car engine in the research or development of new substances as refrigerants or working fluids. It is essential to known the amount of energy as heat it takes to raise the temperature of a substance by one degree (heat capacity), as accurately as possible for the efficient use and development of the fluids involved in the exchange of heat. The most reliable way to obtain the value of heat capacity is adiabatic calorimetry technique [1]. And some researchers have developed their own devises which working under this principle as Tan et al. [1], Lang [2], Kobashi [3], Sorai [4], Matsuo [5], Inaba [6] and Magee [7], with different configurations for the geometry of the cell (piece of calorimeter containing the fluid to measure heat capacity) a key element in this type of apparatus. In the laboratory of thermophysical properties of Centro Nacional de Metrología (CENAM), it is developing an adiabatic calorimeter for measuring the heat capacity of fluids at room conditions. One of the most important elements of the adiabatic calorimeter is the cell, which containing the fluid to determine the value of heat capacity and it has some other elements such as sensors, heaters inlets and outlets for the fluid. According to the technique, the cell is surrounded by a shield called adiabatic, and its functions is to stay at the same temperature of the cell to avoid heat transfer between both. Both elements are located within a cryostat which is responsible for generating and environment with constant temperature. For a thermal design criteria with respect to the cell, is necessary to analyze the temperature distribution in cell, in ideal case should be constant or equal in any point, but in a real case the temperature gradients are present. Therefore the design criteria will be obtained from the theoretical and numerical analysis necessary considering the smaller temperature gradients, resulting from change of parameters such as size or geometry. Knowing the temperature distribution within the cell, additional information is also obtained, as the location of temperature sensor and the inlets and outlets of fluid. Therefore the following formulations were made: theoretical and numerical (by finite element method) for a cylindrical cell and only numerical for spherical cell. In the present work shows comparison among the results of the analytical and numerical solution for a cylindrical cell and the results of numerically evaluate a spherical cell are also included. To compare and evaluate the temperature distribution between the cylindrical and spherical cell and change the effect to vary its dimensions.

II. THEORETICAL ANALYSIS

A. Mathematical formulation

For theoretical analysis equation of heat conduction is set in a cylindrical coordinate system because the proposal cell presents this geometry.

The differential equation of heat conduction in the cylindrical coordinate system is:

$$\frac{\partial^2 T}{\partial r^2}+\frac{1}{r}\frac{\partial T}{\partial r}+\frac{1}{r^2}\frac{\partial^2 T}{\partial \phi^2}+\frac{\partial^2 T}{\partial z^2}=\frac{1}{\alpha}\frac{\partial T}{\partial t} \qquad (1)$$

where

$$\alpha = \frac{k}{\rho c_p}$$

Where α is the thermal diffusivity, k is the thermal conductivity, ρ is density and c_p is the heat capacity of the material to be analyzed. Now it considers that the cell is a solid of radius b, height c, and its boundaries are temperature constant T_c. Initially the entire system is at temperature T_0, where there is not heat generation inside the cell like Fig. 1 shows together with the coordinate system. Under these conditions and because there is azimuthal symmetry, T is independent of ϕ thus the equation to solve is:

$$\frac{\partial^2 T}{\partial r^2} + \frac{1}{r}\frac{\partial T}{\partial r} + \frac{\partial^2 T}{\partial z^2} = \frac{1}{\alpha}\frac{\partial T}{\partial t} \tag{2}$$

Whit the initial condition at $t=0$ with $T=T_0$ at $0 \leq r \geq b$; $0 \leq z \geq c$ and $t>0$. And boundary condition $T=T_c$, at $r=0$, $r=b$, $z=0$ and $z=c$. It assumes that the variables can be separated $T(r,z,t)=R(r)Z(z)\Gamma(t)$ then substituting in (2) simplifying and dividing by ZRΓ we have

$$\frac{1}{R}\left(\frac{d^2 R}{dr^2} + \frac{1}{r}\frac{dR}{dr}\right) + \frac{1}{Z}\frac{d^2 Z}{dz^2} = \frac{1}{\alpha\Gamma}\frac{d\Gamma}{dt} \tag{3}$$

Thus in (3) the left side are spatial coordinates and time coordinate the right side.

1) Solving the temporal part
The differential equation is equal to a constant

$$\frac{1}{\alpha\Gamma}\frac{d\Gamma}{dt} = -\lambda^2 \tag{4}$$

it uses the method of separation of variables

$$\frac{1}{\alpha\Gamma} d\Gamma = -\lambda^2 dt \tag{5}$$

both sides of the equation are integrated

$$\int \frac{1}{\alpha\Gamma} d\Gamma = \int -\lambda^2 dt \tag{6}$$

after integration, we have

$$\frac{1}{\alpha}\ln\Gamma = -\lambda^2 t \tag{7}$$

we separate α, namely thermal diffusivity

$$\ln\Gamma = -\alpha\lambda^2 t \tag{8}$$

both sides are multiplied by the exponential

$$e(\ln\Gamma) = e(-\alpha\lambda^2 t) \tag{9}$$

finally we have the temporary solution

$$\Gamma = e^{-\alpha\lambda^2 t} \tag{10}$$

2) Solving the spatial part 1
For the axe z we have

$$\frac{1}{Z}\frac{d^2 Z}{dz^2} = -\eta^2 \tag{11}$$

$$\frac{d^2 Z}{dz^2} + Z\eta^2 = 0 \tag{12}$$

and de solution to (12) is the way

$$Z = A\cos z\eta + B\sin z\eta \tag{13}$$

where $A=(A+B)$ and $B=(iA+iB)$

3) Solving the spatial part 2
For the axe r we have

$$\frac{1}{R}\left(\frac{d^2 R}{dr^2} + \frac{1}{r}\frac{dR}{dr}\right) = -\lambda^2 + \eta^2 = -\beta^2 \tag{14}$$

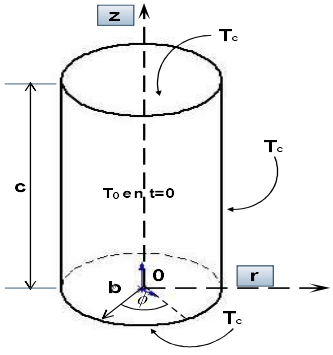

Fig.1. Cylinder of radius and height specified under certain initial and boundary conditions in the cylindrical coordinate system.

and (14) is a differential equation from Bessel of order ν and is written as:

$$\frac{1}{R_\nu}\left(\frac{d^2R_\nu}{dr^2}+\frac{1}{r}\frac{dR_\nu}{dr}\right)=-\beta^2 \tag{15}$$

rearranging

$$\frac{d^2R_\nu}{dr^2}+\frac{1}{r}\frac{dR_\nu}{dr}+\beta^2R_\nu=0 \tag{16}$$

the solution to (16) are the Bessel functions of order ν, which are

$$R_\nu(\beta r)=\{J_\nu(\beta r),Y_\nu(\beta r)\} \tag{17}$$

The solution is the superposition of all solutions therefore the solution to (3) is:

$$T(r,z,t)=\sum_{m=1}^{\infty}\sum_{p=1}^{\infty}R_\nu(\beta_m r)Z(\eta_p,z)\Gamma(t) \tag{18}$$

where $R_\nu(\beta_m r)$ and $Z(\eta_p,z)$ are the eigenfunctions, solutions of the equations separated; β_m and η_p are the respective eigenvalues.

B. Applying boundary conditions to find the eigenvalues

To find the value of β, we make a change of variable and define $T^*=T-T_c$ the from

$$R_\nu(\beta r)=AJ_\nu(\beta r)+BY_\nu(\beta r) \tag{19}$$

and the boundary condition at $r=0$

$$r=0\rightarrow T=T_c\Rightarrow T^*+T_c=T_c\rightarrow T^*=0$$

substituting into (19), and since at $r=0$, $R_\nu(\beta_r)$ is finite we have

$$BY_\nu(\beta r)=0\Rightarrow B=0$$

from boundary condition at r=0

$$AJ_\nu(\beta b)=0 \tag{20}$$

because A can not be 0, the values of β are the positive roots of

$$J_\nu(\beta_m b)=0 \tag{21}$$

since the problem includes the origin, $Y_\nu(\beta_r)$ implies that $\nu=0$, is divergent.

To find η, from equation

$$Z=A\cos z\eta+B\sin z\eta \tag{22}$$

and from boundary condition at $Z(z=0)=T^*=0$ implies that $A=0$. And from the boundary condition at $Z(z=c)=T^*=0$

$$0=B\sin(c)\eta \tag{23}$$

because of (24) B can not be 0, the values of η are

$$\eta_p=\frac{p\pi}{c} \tag{24}$$

The solution of the equation is

$$T^*(r,z,t)=\sum_{m=1}^{\infty}\sum_{p=1}^{\infty}C_mJ_0(\beta_m r)\sin(\eta_p z)e^{-\alpha\beta^2t} \tag{25}$$

Applying the initial condition to (25), we have

$$\begin{aligned}&T^*(r,z,t=0)=\\&T_0-T_c=\sum_{m=1}^{\infty}\sum_{p=1}^{\infty}C_mJ_0(\beta_m r)\sin(\eta_p z)\end{aligned} \tag{26}$$

To find the constant C_m. we have

$$\begin{aligned}&C_m=\frac{1}{N(\beta_m)N(\eta_p)}=\\&\int_0^b\int_0^c rJ_0(\beta_m r')\sin(\eta_p z')dr'dz'\end{aligned} \tag{27}$$

now to find the norms, to $N(\beta_m)$

$$N(\beta_m)=\int_0^b rJ_0^2(\beta_m r) \tag{28}$$

from Özisik [8], we have

$$N(\beta_m)=\frac{b^2}{2}\left[J_\nu'^2(\beta_m b)+\left(1-\frac{\nu}{\beta_m^2 b^2}\right)J_\nu^2(\beta_m b)\right] \quad (29)$$

with ν=0

$$N(\beta_m)=\frac{b^2}{2}\left[J_0'^2(\beta_m b)+\left(1-\frac{0}{\beta_m^2 b^2}\right)J_0^2(\beta_m b)\right] \quad (30)$$

and we have

$$N(\beta_m)=\frac{b^2}{2}\left[J_0'^2(\beta_m b)\right] \quad (31)$$

now to find $N(\eta_p)$

$$N(\eta_p)=\int_0^c \sin\eta_p z(\sin\eta_p z)dz \quad (32)$$

$$N(\eta_p)=\int_0^c \sin^2\eta_p z dz \quad (33)$$

$$N(\eta_p)=\int_0^c \frac{1}{2}-\frac{1}{2}\cos 2\eta_p z dz \quad (34)$$

evaluating in our dimension, *c*

$$N(\eta_p)=\frac{z}{2}-\frac{1}{4}\sin 2\eta_p z\Big|_0^c \quad (35)$$

finally we have

$$N(\eta_p)=\frac{c}{2} \quad (36)$$

substituting in (18) we have:

$$T^*(r,z,t)=\sum_{m=1}^{\infty}\sum_{p=1}^{\infty}\frac{1}{N(\beta_m)N(\eta_p)}J_0(\beta_m r)\cdot \cdot\sin(\eta_p z)e^{-\alpha\beta^2 t}\int_0^b\int_0^c rJ_0(\beta_m r')\sin(\eta_p z')dr'dz' \quad (37)$$

Solving the integral on the right side of (37)

$$(T_0-T_c)\int_0^b\int_0^c r'J_0(\beta_m r')\sin(\eta_p z')dr'dz' \quad (38)$$

$$(T_0-T_c)\int_0^b\int_0^c r'J_0(\beta_m r')dr'-\frac{1}{\eta_p}\cos\eta_p z'\Big|_{z'=0}^{z'=c} \quad (39)$$

simplifying and evaluating in (39)

$$(T_0-T_c)\left[\frac{b}{\beta_m}J_1(\beta_m b)\right]\left[-\frac{c}{p\pi}(-1)^p+\frac{c}{p\pi}\right] \quad (40)$$

Finally the solution according to the initial and boundary conditions posed is:

$$T(r,z,t)=\sum_{m=1}^{\infty}\sum_{p=1}^{\infty}\frac{J_0(\beta_m r)\sin\left(\frac{p\pi}{c}z\right)e^{-\alpha\left[\beta_m^2+\left(\frac{p\pi}{c}\right)^2\right]t}}{\frac{b^2}{2}\left[J_0'^2(\beta_m b)\right]\frac{c}{2}}(T_0-T_c)\left[\frac{b}{\beta_m}J_1(\beta_m b)\right]\left[-\frac{c}{p\pi}(-1)^p+\frac{c}{p\pi}\right]+T_c \quad (41)$$

Equation (41) was programmed in MATLAB®, and all that is provided are: initial temperature T_0, the temperature at the border T_c; the thermal diffusivity value according on the material to be assigned to the cylinder; the radius, the height *c* and the number of divisions required in the discretization; the initial and final time as well as the time steps, to obtain the temperature in coordinates *r,z* and any time *t*. The solution described, convergence is achieves with 65 values for *p* and for *m* were taken 200. The finite element method is used by a commercial software to compare the results obtained from the analytical solution.

III. Numerical Solution

A. *Model to compare the analytical solution*

For the numerical solution, is used a commercial code that uses the finite element method to approximate the solution of heat conduction (2) show above.

The model uses in commercial software is two-dimensional, axisymmetric, which allows for the condition of azimuthal symmetry established for the analytical problem. The type of element that was used is a plane 77, which is a 8-node element for thermal analysis, which accepts axisimmetry conditions and transient or steady-state analysis. To calculate the numerical solution was selected a cylinder whose properties: thermal conductivity, heat capacity and density are from the water [9]. The dimension of the cylinder are: radius 24.5 mm and height 74.24 mm. The Fig. 2 shows the mesh used in the model. The boundary conditions are a constant temperature of $T_c = 25$ °C. The condition T_0 en $t = 0$, was established of $T_0 = 23$ °C. The study was solved for a time of 6000 seconds.

IV. Analysis Results

Comparison between analytical solution and the numerical solution is shown in the analysis of results. Fig. 3 shows the evolution of temperature according to the boundary conditions mentioned, which are: $T_0 = 23$ °C at t = 0 and constant temperature $T_c = 25$ °C for 6000 seconds. The point analyzed exactly was the centroid of the cylinder, according to the coordinates shown in Fig. 1, the location of centroid is $r = 0$ and $z = 3.712$ *cm*. The curve shown in Fig. 3, has a maximum error percentage of 0.065 % between the analytical and numerical solution with a temperature increase of 2 °C.

In this section are shown the results to 4 different size of cylinder and the sphere. Where is compared the analytical solution (with legend CYLINDRICAL) against the solutions obtained by the finite element method for the cylinder (MEF CYLYNDRICAL) and for the sphere (MEF SPHERICAL). At the point where the temperature gradients is larger and is located at the centroid of the sphere and the cylinder. To reduce solution time and the amount of data the value of thermal diffusivity was taken as the unit.

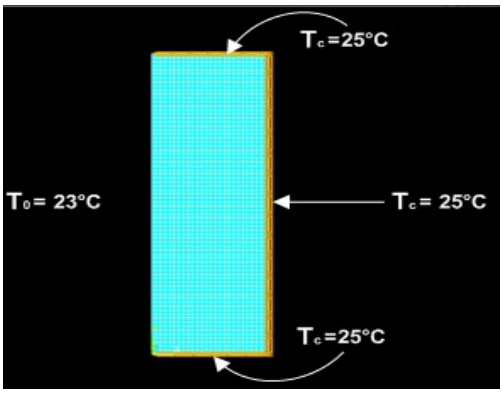

Fig. 2. Mesh for the numerical model.

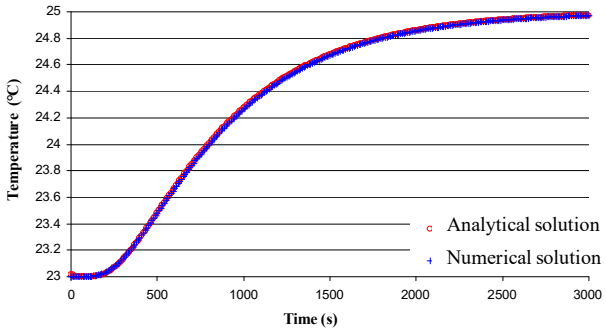

Fig.3. Comparison among analytical and numerical solution at centrod of cylinder, located at radius of 0.0 cm and height of 3.71 cm.

Figures 4 to 8, shown comparison of solutions obtained in temperature over time with initial condition $T_0 = 30$ °C and with boundary condition of $T_c = 29$ °C. For different dimensions of the cylinder and a sphere of radius 2.5 cm. As can be seen the dimensions of the cylinder which smaller temperature gradient has the 1.5 of radius and 9.9 cm of height. And this is because in a time of 1.5 seconds all the cylinder reaches a uniform temperature. Against to the other configurations, which take longer time, almost twice.

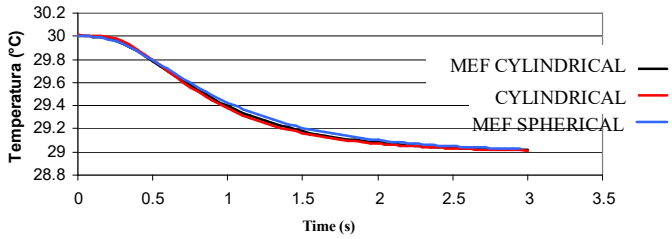

Fig.4. Comparison among analytical and numerical solution for a cylinder with radius 2.2 cm and hegiht 4.5 cm, against sphere of 2.5 cm radius.

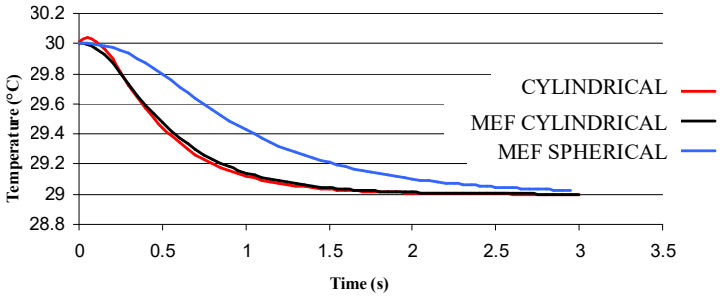

Fig.5. Comparison among analytical and numerical solution for a cylinder with radius 1.5 cm and hegiht 9.9 cm, against sphere of 2.5 cm radius.

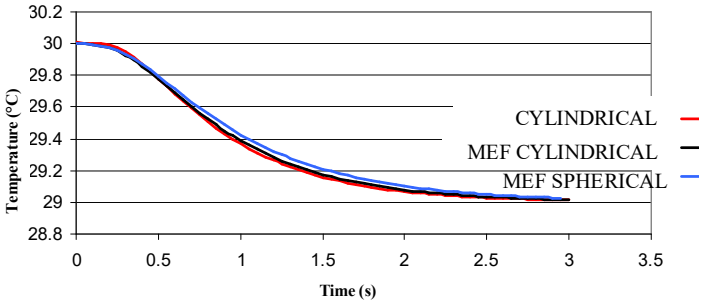

Fig.6. Comparison among analytical and numerical solution for a cylinder with radius 2.5 cm and hegiht 3.5 cm, against sphere of 2.5 cm radius.

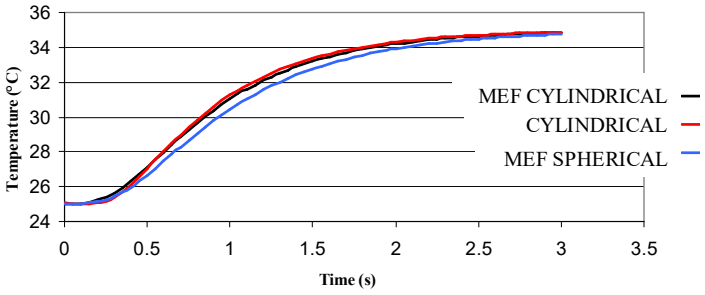

Fig.8. Comparison among analytical and numerical solution, for initial condition of 25 °C and boundary condition of T_c = 35 °C. For a cylinder with radius 2.2 cm and hegiht 4.5 cm, against sphere of 2.5 cm radius.

For the next case, the Fig. 8 shows comparison among analytical and numerical solution for a initial condition of T_0 = *25* °C and boundary condition of T_c = *35* °C. And is included the result numerical for a sphere of radius 2.5 cm. The error obtained about 0.86 % for this case among analytical and numerical solution was the highest. And it is probably by the big difference in temperature, 10 °C, in contrast to the 1 °C difference in the another cases.

V. Conclusions

The maximum error obtained in this work among the analytical result and numerical method was around 0.86 % for an increase of 10 °C and 0.075 % for an increase of 1 °C. These results show that exist a good agreement by the finite element method.

From the results shown, the cylinder of 1.5 cm radius and height 9.9 cm reached in a time of 1.5 s a uniform temperature throughout all, half time with respect to other dimensions evaluated. And is seems a good option to development of the cell, however, is needed evaluate another parameters such as temperature sensor location, cell´s material, inlets and outlets for fluid to the cell.

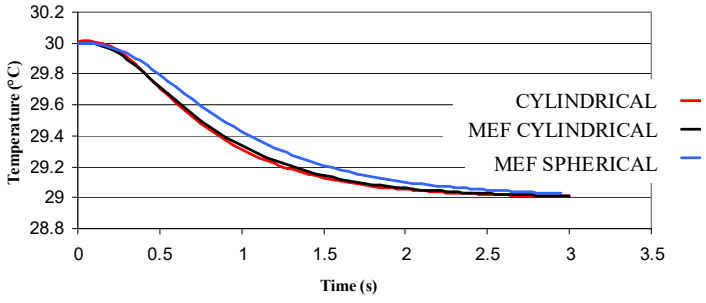

Fig.7. Comparison among analytical and numerical solution for a cylinder with radius 2.5 cm and hegiht 3.5 cm, against sphere of 2.5 cm radius.

It was shown that the cylinder has best performance than sphere, because the gradients temperature are smaller and reaches steady state in less time.

The error among analytical and numerical results increase with increasing temperature and decreases as the steady state is reached.

Numerical analysis provides a tool to change parameters as dimensions, geometric shapes and initial and boundary conditions to analyze the behaviour of a mathematical and/or physical model in less time.

However the mathematical and numerical models provide only approximations to the physical phenomenon, so it is important to validate the results and the best way is through a prototype and characterize it.

References

[1] Tan Z. C., Q. Shi, B. P. Liu and H. T. Zhang, “A fully Automated Adiabatic Calorimeter for Heat Capacity measurement between 80 and 400 K”. Journal of Thermal Analysis and Calorimetry, vol. 92 (2008) pp. 367-374.

[2] Lang B. E., J. Boerio-Goates and B. F. Woodfield, “Design and construction of an adiabatic calorimeter for samples of less than 1 cm3 in the temperature range T = 15 K to T = 350 K ,” Journal of Chemical Thermodynamics., vol. 38, pp. 1655, 2006.

[3] Kobashi K., T. Kyomen and M. Oguni, "Construction of an adiabatic calorimeter in the temperature range between 13 and 505 K, and thermodynamic studi of 1-chloroadamantane," J. Phys. Chem. Solids, vol.59, pp.667-677, 1998.

[4] Sorai M., K. Kaji and Y. Kaneko," An automaten adiabatic calorimeter for the temperature range 13K to 530 K the heat capacities of benzoic acid from 15 K to 305 K and of synthetic sapphire from 60 K to 505 K," Journal of Chemical Thermodynamics., vol. 24, pp. 167-180, 1992.

[5] Inaba A., An adiabatic calorimeter for use at intermediate and higher temperatures the heat capacity of synthetic saphire (α-Al2O3) from 70 to 700 K, Journal of Chemical Thermodynamics., vol. 15, pp. 1137, 1983.

[6] Matsuo T. and H. Suga, "Adiabatic microcalorimeters for heat capacity measurement at low temperature" Thermochimica Acta, vol.88 pp. 149-158, 1985.

[7] Magee W. Joseph, Deal J. Renee, Blanco C. John, “High-Temperature Adiabatic Calorimeter for Constant-Volume Heat Capacity

Measurements of Compressed Gases and Liquids" Journal of Research of the National Insitute of Standards and Technology. vol. 103, pp. 63, 1998.

[8] Özisik Necati M, Heat Conduction, 2nd ed,. John Wiley & Sons Inc.. 1992, pp. 99,672.

[9] Incropera P Frank., DeWitt P. David, Fundamentals of Heat and Mass Transfer, 4th ed., John Wiley & Sons Inc . 1996, pp. 846.

Susceptibility of asphalt concrete mixtures to temperature changes on tensile strength

*MAURICIO CENTENO SILVA
Student of Master's Vías Terrestres, Transporte y Logística
Facultad de Ingeniería, Universidad Autónoma de Querétaro
Santiago de Querétaro, Querétaro, México.
e-mail: ingcenteno.21@gmail.com

MARÍA DE LA LUZ PÉREZ REA
Professor and Researcher, División de Estudios de Posgrado
Facultad de Ingeniería, Universidad Autónoma de Querétaro
Santiago de Querétaro, Querétaro, México.
e-mail: perea@uaq.mx

Abstract— ***In this paper the performance of mixes mostly used in flexible pavements in Mexico for binders asphalt concrete is analyzed. Five different temperature values, that is 10, 20, 30, 40 and 50 °C control samples were used in the preparation. Performance test based on indirect tensile strength in different temperature conditions mixtures were evaluated. The test results indicate that resistance of the specimens directly decreased with increasing temperature, with indirect tensile strength index that can be used to measure the moisture susceptibility of the test samples was determined the laboratory job to provide a closer result to what was it present in the field.***

Keywords— ***Permanent deformation, Temperature, Indirect tensile strength.***

I. INTRODUCTION

Since the early years of this century up to date has been given the job of understanding how they work mechanically pavements and thus provide better performance to users, plus they are durable to perform its functions, the roads are the main means of communication and transportation between people and movement of goods within the country, and most are covered by a surface layer of asphalt.

The behavior of this mixture depends on the materials used and thermal environmental conditions to which they are exposed, which are reflected in the pavement performance.

The temperature of the pavement and traffic loads are two variables that have a significant role in the development of permanent deformations in the pavement. The effects of the bearing surface more important when subjected to high temperatures, while fatigue damage are more pronounced at intermediate temperatures and low [1].

The permanent deformations are one of the types of failures that occur in asphalt pavements when it is exposed either separately or in combination at high temperatures, low speeds and heavy traffic load [4].

Asphalt mixtures have nonlinear or viscous behavior, depending on the linear behavior of temperature change and the time of application of the load thereon [5].

Morca [6] found that at low temperatures the elastic behavior is essentially linear and begins to behave as a nonlinear elastic material, the viscous behavior appearing as the temperature continues to rise, which causes the mixture to flow and move easily. Hence, in winter, when temperatures are low, there is no plastic deformation, because the mixture behaves elastically, while in autumn and spring, when there regularly intermediate temperatures, the mixture has much of its elastic behavior and plastic deformations are minimal. In summer, at high temperatures, the cohesion of the mixture decreases and deformations caused by traffic increases; rutting occurs due to the viscous component of the mixture and give rise to permanent and unrecoverable deformations.

This study shows the behavior of the asphalt mix in relation to indirect tensile strength, ASTM D6931 [1], for five different temperatures (10, 20, 30, 40 and 50 ° C) with the purpose of analyze its performance under different temperature levels which may be exposed to ambient temperature. In addition to this an index of resistance to indirect tensile strength that can be used to measure the susceptibility of the temperature of the asphalt mixes in the testing of samples in the laboratory was determined, and the result may vary according to temperature testing and temperature at which they will actually be exposed on the site.

II. MATERIALS AND TESTING METHOD

The objective proposed in this paper is to analyze the correlation of temperature directly involved in the permanent deformations such as viscous that are irreversible. That is why the implementation of the indirect tension test was conducted to evaluate the performance of the mixture to temperature changes.

Tension indirect tests were performed on specimens of asphalt mixture; according to ASTM D6926 [2] and tested according to ASTM D6931 [3]; the specimen is tested at constant deformation of 50.8 mm / min in order to indirectly calculate the tensile strength and where most opposition to cohesion failure presents asphalt with mineral aggregate, all carried out different temperatures at the time of test.

A. *Materials*

A type of aggregates were used, determining properties specified by SCT normative for a nominal size ¾". Test results are shown in Table 1. According to specifications, it is quite clear that aggregates do success such standards, in spite of the fact that these aggregates are employed in the mostly places in the region for asphaltic mixtures production.

TABLE I. AGGREGATE GRADUATION

SIEVE	SAMPLE	NORM
		N-CMT-4-04-08
2"		
1 1/2"		
1 "	100	100
3/4 "	94	90 - 100
1/2 "	88	72 - 90
3/8 "	73	60 - 76
1/4 "	56	44 - 57
No. 4	45	37 - 48
No. 10	27	20 - 29
No. 20	19	12 - 19
No. 40	13	8 - 14
No. 60	10	6 - 11
No. 100	7	4 - 8
No. 200	4	2 - 5

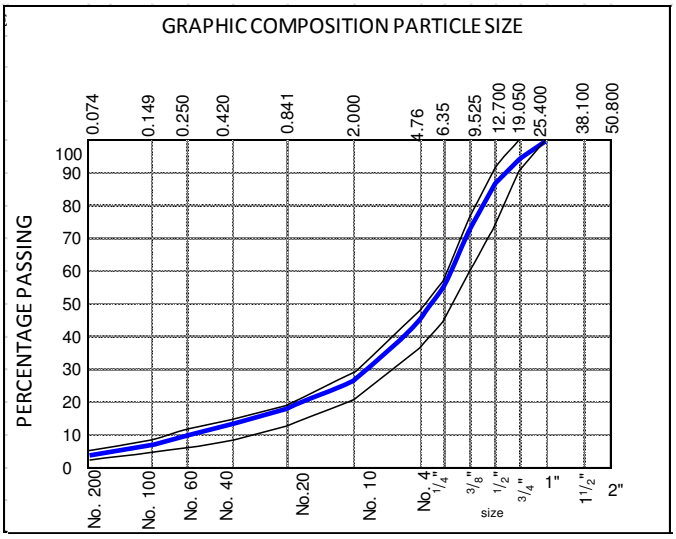

Fig. 1. Curve of aggregate graduation

B. *Asphaltic Mixture*

The design of this mixture was done from Marshall Method. Based on this methodology, the optimum content of asphalt cement is obtained, a conventional asphalt was used (AC-20) to test specimens for five percentages of asphalt (4.5, 5.0, 5.5, 6.0 and 6.5%), molded 75 was used beats by face as specified in the International standard (MMP M • 4 • 05 • 035).

Results for the optimum content of asphalt cement related to volumetric weight, the percentage of voids (% VTM), the percentage of mineral aggregate (% VAM), Marshall stability and flow were obtained. Table 2 summarizes these data.

TABLE II. SUMMARY OF VALUES FOR THE OPTIMUM CONTENT

DATUM FOR ASPHALTIC CEMENT CONTENT						
OPTIMUM	*% C.A.*	*VOL W. kg/m³*	*VOIDS %*	*V.A.M. %*	*STABILITY kg*	*FLOW mm*
	5.95	**2405**	**3.00**	**15.70**	**950**	**3.30**

C. *Indirect Tensile Strength Test*

As mentioned earlier the Indirect Tensile Strength (ITS) of asphalts mixtures is conducted by loading a cylindrical specimen across its vertical diametral plane at 50mm/min deformation rate and 25 ºC test temperature. The peak load at failure is recorded and used to calculate the ITS of the specimen.

The value of ITS is used to evaluate the relative quality of bituminous mixtures in conjunction with laboratory mix design testing and for estimating the potential for rutting or cracking. The results can also be used to determine the potential for field pavement moisture damage when results are obtained on both unconditioned and conditioned samples [1].

$$ITS=2P/2\pi HD \quad (1)$$

Where:

ITS = Indirect tensile strength of specimens

P = applied load to fail specimens

H = thickness of the specimens

D = diameter of the specimens

π = 3,14159

III. RESULTS AND DISCUTION

Once done the characterization of asphalt, Marshall specimens were performed to estimate tensile strength test by indirect tension under specified in the aforementioned standard. The results correspond to specimens subjected to stress under various temperature values in order to see how it directly affects behavior of the mixture. The different temperature values with which they worked were established according to the temperatures recorded for the area of the municipality of Queretaro, therefore the temperature range in which the pavement surface varies is 10-50 ° C, so the assay of samples of asphalt were performed at 10, 20, 30, 40, 50 ° C At temperatures ranging binders in the study area. In Table 3 the results of the indirect tension for different values of temperature were recorded.

Table 3 Summary Indirect Tension test for specimen Marshall

TEST TUBE			THICKNESS cm	WEIGHT g	U.W. Kg./m³	LOAD Kg.	INDIRECT TENSION MPa
SAMPLE num.:	TEMP ºC	PILL num.					
1	10	1	6.60	1202.20	2274	1635.00	1.53
		2	6.70	1190.00	2217	1960.00	1.81
PROM			**6.65**	**1196**	**2245**	**1797.50**	**1.67**
2	20	3	6.40	1208.00	2367	960.00	0.93
		4	6.40	1201.70	2350	900.00	0.87
PROM			**6.40**	**1205**	**2358**	**930.00**	**0.90**
3	30	5	6.20	1151.10	2384	425.00	0.42
		6	6.30	1204.00	2382	500.00	0.49
PROM			**6.25**	**1178**	**2383**	**462.50**	**0.46**
4	40	7	6.50	1212.70	2410	238.00	0.23
		8	6.50	1210.00	2398	220.00	0.21
PROM			**6.50**	**1211**	**2404**	**229.00**	**0.22**
5	50	9	6.30	1201.00	2380	112.00	0.11
		10	6.10	1090.00	2410	130.00	0.13
PROM			**6.20**	**1146**	**2395**	**121.00**	**0.12**

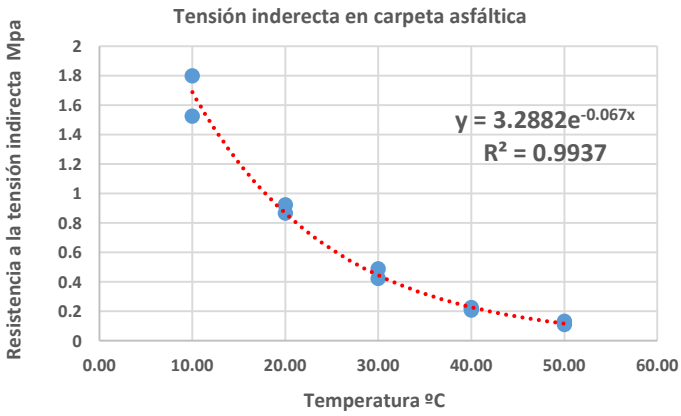

Fig. 2. Results of ITS and tendency curve (red line).

Figure 2 presents the results of ITS graphically. We can see that the mixture asphalt presented the indirect tensile strength decreased considerably above 25°C, the reference temperature in the test. Also show that the temperature has a no linear behavior influence on this parameter, such as is illustrated the curve that best fits is the exponential function with, $R^2 = 0.9937$. As seen in Table 3, the results of the tests show that the indirect tension is susceptible to the asphalt to changes in temperature, where high temperatures is more vulnerable to failure.

If the value of the indirect tensile strength at the temperature specified in the standard 25 °C in the equation obtained is calculated, has a value of 0.6159 MPa, therefore, for the most critical 50 °C condition all assay it was obtained a ITS value of 0.1153 MPa, estimating a relationship between these values we get the following: 0.1153 / 0.6159 = 0.18, as can be seen there is a reduction of 18% of a laboratory test result regarding what is present in the field.

IV. CONCLUSIONS

The indirect tensile strength is an important parameter to analyze the behavior of asphalt mixtures, in spite of this in Mexico is not regulated this procedure, however in some national specifications apply this parameter to determine the quality of the mixture, taking tests by ASTM where the test is performed at 25 ° C under load at a strain rate of 50 mm / min (Press Marshall). According to the observed one you can say that at this temperature the state of stress in the asphalt mixture sample to calculate the tensile strength differs with the requirements under which it will be in its lifetime. With all this we must better utilize data ITS test. Finally what was done in this study was reached the following conclusions:

- It's important to determine the temperature gradients in which it will be exposed the asphalt mix in the field, for the purpose of make a better design with better materials that respond better under these effects.

- It was observed that the behavior of the mixture through the different temperature decreases exponentially its tensile strength.

- According to the estimate of the relationship between ITS calculated for the standard temperature of 25 ° C and would be presented in the field concluded that there is a reduction of 18%, which should be considered in the design of the asphalt mix and calculation permanent deformations.

Based on all this, one can conclude that the information obtained thus far for changes in temperature asphalt mixtures should be analyzed for future search as nonlinear behavior with the effect of viscosity submitted by the asphalt directly involved in the behavior of the mixture itself.

ACKNOWLEDGMENT

Authors express their gratitude to the Mexican National Council for Science and Technology (CONACYT) for financing this work research, and I would also like tanks to Pavement Laboratory of Universidad Autonoma de Queretaro for supporting me with my equipment to perform tests in this investigation.

REFERENCES

[1] Kim Y., Allen D. H., y Little D. N. (2007). Computational constitutive model for predicting nonlinear viscoelastic damage and fracture failure of asphalt concrete mixtures. *International Jurnal Geomechanics*; 7, pp: 102–110.

[2] ASTM D6926: (2010) Standard Practice for Preparation of Bituminous Specimens Using Marshall Apparatus.

[3] ASTM D6931 – 07 (2007) Standard test method for indirect tensile (IDT) strength of bituminous mixtures. American Society for Testing and Materials.

[4] Guzmán, J. E., Rodríguez J. C., (2004). Análisis comparativo de resultados de ensayos de módulos resilientes y deformaciones permanentes de mezclas asfálticas compactadas con martillo Marshall y con compactador giratorio, Bogotá, Colombia.

[5] Delgadillo R, Cho DW, Bahia HU (2006) Nonlinearity of repeated creep and recovery binder test and the relationship with mixture permanent deformation. Transp Res Rec J Transp Res Board, No. 1962. TRB, National Research Council, Washington, pp. 3–11.

[6] Morca F. (2011). Deformaciones Permanentes en mezclas asfálticas. Efecto de la rcología de los asfaltos, la temperatura y las condiciones de carga. PhD. Thesis, Universidad de La Plata, La Plata, Argentina.

Green roofs to generate thermal comfort inside school buildings

Ing. Guadalupe Ramos Silva
Student of Masters in Sciences (Construction)
Engineering Faculty, Autonomous University of Queretaro
Querétaro, Qro.
inggrs88@gmail.com

Dr. Jose Gabriel Rios Moreno; Dr Mario Trejo Perea; Dr. Eusebio Jr. Ventura Ramos; Dr Jose Luis Reyes Araiza
Teacher- Researcher, Engineering Faculty
Engineering Faculty, Autonomous University of Queretaro
Queretaro, Qro.
araiza@uaq.mx; mtp@uaq.mx;
riosg@uaq.mx;eventura@uaq.mx

Abstract— The green edification is the practice of create models too much friendly with the environment through the efficient use of resources and materials used in construction, the buildings must provide a comfortable and healthy ambient to the occupants able to carry out their activities, if the environmental factors in the buildings are in the comfort limits, the yield of the students will be better and the work of the teachers will be of better quality, so is important generate a space with the adequate conditions of temperature, humidity and air movement, that is to say, could reach to the thermal comfort inside of the classrooms. This article shows a comparative studio of a traditional classroom and different classrooms appointed with intensives and extensives green roofs with thickness of 25, 15 and 10 cm which they were developed and characterized by a substratum which was composed with a mixture of pumice sand, clay and organic material, for this study a plant species of the region was used and is known as Aptenia cordifolia, and irrigation that was used is with recycled water. The results show us that in one of the hottest month in Querétaro, the intensives green roofs came down the temperature in 3°C so it is concluded that the technologies of the green roofs are a viable alternative to achieve comfortable and healthy spaces.

Keywords—green roofs, sustainability, thermal comfort.

I. INTRODUCTION

The green edification is the practice of create models too much friendly with the environment through the efficient use of resources used in the construction, the introduction of plants and landscapes to the surface of roofs could be considerate as a technique that reduce the temperature of the building to 20°C, in addition reduce the consume of electric energy between 25 and 80% in air conditioner [1]. The green roofs, also called "eco roofs", "living roofs" or "garden roofs", are basically roofs with plants in the final layer [2], this roofs are generally constructed to improve the energetic efficiency in the buildings, but is important to know that exist many benefits, in the topsoil the photosynthesis process occur while the soil layer permit the absorption of precipitation, frequently, the result is an improvement in the water quality that runoff of the roof [3]. The green roofs are generally classified like extensives and intensives, although some authors include semiintensives [4,5]. Table 1 show us the classification and the principal characteristics of the intensives and extensives green roofs

TABLE I. GREEN ROOFS CLASIFICATION

Principal Characteristics	Extensive	Intensive
Thickness of the crop	Less than 150 mm	Greater than 150 mm
Weight	60 -150 kg/cm²	Greater than 150 kg/cm ²
Irrigation	Could be not necessary	Need of irrigation and drainage systems
Construction	Moderately easy	Complex technique
Cost	Low	High
Plant diversity	Luw (moss and grass)	High (bush, grass and trees)
Maintenance	Simple	Complex

The principal function of the Green roofs is to avoid the solar radiation that is transmitted inside the building as heat. The Green roofs are capable of reflect and absorb about 27 and 60% of solar radiation respectively through the photosynthesis and transmit the rest (13%) to the crop [6]. The green roofs forbid essentially the solar heat penetration for the cutlery components of the construction [7, 8 9, 10]. Reference [11] denote that the green roofs improve the thermal yield of a building through the shading, isolation and the thermal mass. Reference [12], states that the solar absorption is the key property of a green roof. Depending of the thickness of the green roof, they will fail to generate lower profits or losses of heat, and often has better thermal performance. Increased 10 cm thick substrate increases the thermal resistance of the roof of the building [13], however, the presence and amount of water largely influences on the thermal properties of the green roof, in fact provides a wet roof additional evapotranspiration which prevents the flow of

heat in the building and acts as a passive cooler for removing heat inside the building [14, 15, 16, 17] match the type of vegetation is crucial to thermal performance.

The majority of the school buildings in Querétaro doesn't have the thermal isolation efficiency, without the protection of the vegetation, such roofs with bad isolation, absorb and transmit a considerable quantity of heat for the underlying interior spaces. The aim of this paper is a comparative study of traditional classroom lectures and classrooms equipped with technology green roofs, characterized by intensive and extensive substrates, to assess the operating ranges of temperature and humidity generated inside thermal comfort.

II. STUDY AREA AND METHODS

A. *Study area*

The study was carried out in the building of the School of Engineering of the Autonomous University of Queretaro (Fig 1). Santiago de Queretaro, is characterized by a dry and semi-dry climate, the temperature is high in summer and cold noticeable in winter, the maximum temperature on average does not exceed 35 ° C and the temperature in cold average is 5 a – 1°C , the period of rainfall is comprised of May to October , the average rainfall is 600-700 mm.

Figure 1. Classrooms of the studied building, south view.

The building structure has four classrooms, a meeting room, a control room and a pottery. Four classrooms have an area of 48m², the meeting room an area of 56 m², the pottery as well as the control room 16 m². The building has a concrete slab with a thickness of 12 cm, the concrete of the slab has a resistance of 300 kg / cm², the side walls are made with bricks, and the four classrooms counts with two large windows at the sides of 2.00 X 4.00 m, the walls dividing the classrooms are concrete blocks coated with mortar. For this comparative study all four classrooms are considered only reference being structurally identical (Fig 2).

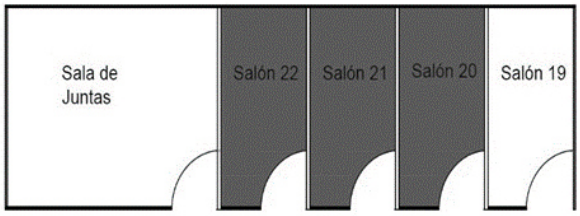

B. *Characterization of the substrate*

Based on the review of the literature, materials that have had a better impact to improve conditions of thermal comfort inside, are compound mixtures, an ideal substrate, it must be light, have a good anchorage for the plants, the supply of nutrients, be stable and have good capacity retention of water [2]. It is therefore important to consider these characteristics for a proper development of a green roof.

The materials used for the characterization of the substrate in the green roof are 60 % clay with organic matter and 40 % pumice sand, this combination provides the characteristics of the clays as are the concentration of nutrients and retention water due to its particle size and structure ; pumice sand as organic matter , provides larger particles that allow plant roots to develop and move freely in order to obtain the nutrients and allow the substrate to obtain the nutrients and the substrate allows air flow . These materials are obtained locally and used in its original form in the experiments.

For the development of this research is needed to characterize the materials to be known about its possible behavior and irrigation variation based on this. The data required for characterization of the substrate include humidity, bulk density, true density, permeability which are defined as follows:

- Relative Humidity.

$$w = (W / Ws) * 100\ (\%) \qquad (1)$$

Where w, is the moisture content expressed in %, Ww is the weight of water existing in the soil mass, Ws is the weight of the solid particles.

- Apparent Density.

$$Da = Pss / Vt \qquad (2)$$

Where *Da* is the density of soil in g / cm3, *Pss* is weight in grams of dry soil and *Vt* is the total volume of the sample in cm^3.

- Permeability

$$Q = k * I * A \qquad (3)$$

Which *k* is the amount of water drained through the sample per unit time in m^3 /h , *I* is the permeability coefficient in

cm/ h , *A* is the piezometric gradient available in m/m is the cross section through which filtered the water sign m^2.

These materials are obtained locally and used in its original form in the experiments (Fig. 3).

Figure 3. Materiales colocated in the place of study.

The characteristics of the substrate materials and the mixture of them are shown in Table II. Tests were performed in the laboratory of the same Faculty of Engineering, were conducted different tests like density tests, humidity tests, permeability tests and a sieve analysis, to see the properties of these materials.

TABLE II. CHARACTERIZATION OF MATERIALS AND SUBSTRATE.

Parameters	Substrate (mixture)	Pumice sand	Clay with organic matter
Humidity (%)	36.45	38.94	49.75
Density ($kg/cm^{3)}$	1.63	1.05	1.10
Permeability (cm/s)	7.5 x 10 -4	8.7 x 10 -3	9.6 x 10 -5

C. Selection and characteristics of the vegetation

Studies claimed that the use of various types of plantations could be useful to maximize the effectiveness of green roofs [18, 19]; however, selecting the type of vegetation must be established by the climatic conditions [20, 21].

It is essential when choosing vegetation to consider it, suits own climatic zone of where they will install the system, because as you might meet in outdoor, it is essential that the species tolerate the weather it is also vital that require little maintenance in terms of watering and pruning. The type of vegetation species will depend on where the building is located, as well as its orientation and exposure ceilings (shade, full sun).

Figure 2. Plain View of the building.

Was chosen for this study a vegetation of the region called Aptenia cordifolia, widely known as dew or frost, due to its favourable properties both economic and sustainable, in addition to its reproduction is easy at any time of the year, since just cut any branching and plant it so the cutting becomes, coupled with that watering you need is very weak and requires zero maintenance.

They are succulent plants, which has the features of developing stems or thick, fleshy leaves to store the water, this succulent or thickening is a phenomenon of adaptation that occurs in ecosystems where the rain is very scarce, very irregular, or where the ground has little capacity to store water (Fig. 4).

Figure 4. Picture of Aptenia cordifolia.

III. METHODOLOGY

A. Instalation of the substrates.

For the comparative study of the classroom are considered: a traditional roof, an extensive green roof and two intensive green roofs; (19, 20, 21 and 22 respectively) all located in the H building area Postgraduate School of Engineering (Fig 1). The roof of the building gave a clean and covered with a layer of waterproofing Protexa, followed by a layer of geomembrane which is a laminate film of 1.2 mm which serves as a protective cushion between the substrate layer and the concrete (Fig . 5) .

Figure 5. Picture of geomembrane colocation.

Following to that an irrigation system is placed with a 1/2" PVC pipe, in the center of each roof is placed a sprinkler,

which cover the total area to be irrigated , the irrigation system is connected to a treated water tank. Subsequently placed 10 cm thick substrate in classroom 20 , 15cm in classroom 21 and 25 cm in classroom 22 (Fig 6).

Figure 6. Colocation of the substrate.

Finally, at the top, a layer of vegetation was colocated, Aptenia cordifolia, (Fig. 7).

Figure 7. Colocation of the irrigation system, substrate and vegetation.

B. Thermal comfort

Thermal comfort is the condition of the mind which expresses satisfaction with the thermal environment [22]. When conditions of temperature, humidity and air movement are favorable to the activity that is done, the building must provide to their occupants this comfortable and healthy environment to work, if the weather environmental factors in the halls are within the limits of comfort, the yield of the students and teachers will be better and the work will be of higher quality. Reference [22], we make a comfort area is acceptable as long as the temperature remains between 22.5 ° C to 28.5ºc and maintain a humidity content of 30% to 80%.

To measure the variables of temperature and humidity inside the building, was placed a data logger Hobo U23 Pro v2 per classroom, which are sensors for humidity and temperature inside the building, which is adapted to a coupler and then of the Optic USB Base-T-4 station to download data recorded by the data logger and this in turn connects to the computer through a USB cable, Figure 8. The external variables are like outside temperature, outdoor humidity, air velocity, wind direction and solar radiation are measured by the weather station placed in the building to study.

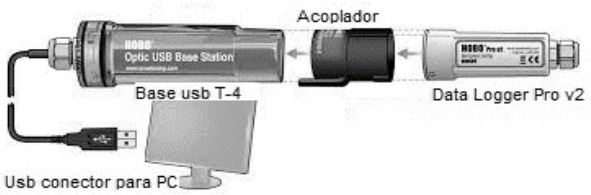

Figure 8. Scheme sensor and the Reading process variables inside the building.

IV. RESULTS

Green roofs are new technologies, implemented for the reduction of the temperature and humidity inside the educational spaces, i.e. to generate internal thermal comfort, reducing to 5 ºc temperature inside the school and College classrooms.

A conventional roof maintains temperatures ranging from 23.4 ° C and 29.9 ° C, in comparison of teches them extensive Greens that maintains maximum temperatures up to 29.1 ° C, in contrast to the intensive green roofs coming to record maximum temperatures of 28.6 ° C, whereas the temperature of thermal comfort standard ASRHAE stays in a range of 22.5 ° C at 28.5 ° C intensive green roofs is maintained in the designated rang.

This study explores the influence of green roofs on thermal comfort, the comparative study of traditional roof and intensive and extensive green roofs are made . It was taken as reference a whole year January 2015 to December 2015. Table III shows variations in temperature per month in the classrooms which you own green roof technologies as well as the traditional roof, the maximum values per month were considered.

TABLE III. MAXIMUM TEMPERATURE VARIATIONS IN GREEN ROOF AND TRADITIONAL ROOF.

Variations of máximum temperaturas.				
Month	Classroom 19	Classroom 20	Classroom 21	Classroom 22
January	23.486	23.236	22.944	22.393
February	25.176	24.985	24.508	25.137
March	26.868	26.178	25.137	25.793
April	29.899	29.19	28.122	29.19
May	28.186	27.995	27.949	27.604
June	29.899	28.574	27.161	27.382
July	28.841	28.45	27.554	26.989

August	29.715	29.19	28.617	29.414
September	29.617	28.866	27.949	29.54
October	28.196	27.21	25.89	27.014
November	26.061	24.436	24.026	24.629
December	24.557	23.857	23.136	24.436

Thrown data mark us that the maximum temperatures throughout the year for the traditional roof , as well as technologies of green roofs were as follows , Classroom 19 traditional roof as temperature inside the classroom was in the month of June and registration value of 29.899ºC, classroom 21 with extensive green roof substrate with a thickness of 10 cm , the highest temperature ever recorded was in the month of August and was 29.19ºC in classroom 21 with intensive green roof thickness of 15 cm also recorded its highest temperature in the month of August and was 28,617°C, and finally in the classroom 22 with intensive green roof with the greatest thickness of 25cms, register its maximum temperature in September and this was 29.54ºC . Figure 9 show us as our comfort zone that marks the reference [22], which is bounded by the frame.

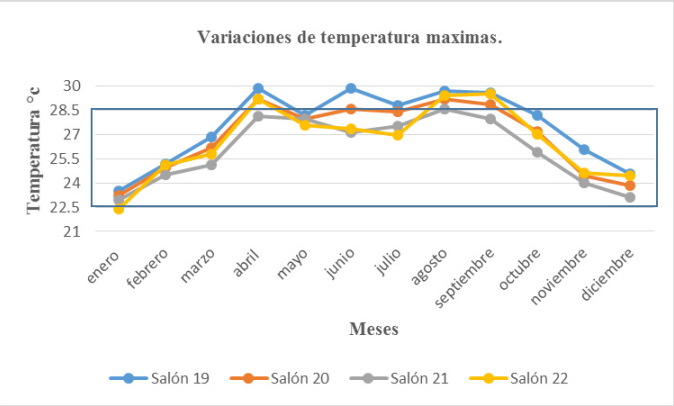

Figure 9. Variations of the máximum temperatures in green roofs about the confort zone.

Table IV show us the variations of humudity for each month, in the classrooms that count with green roofs due to the classroom with a traditional roof, máximum values per month are considerated.

TABLE IV. MAXIMUM HUMIDITY VARIATIONS IN GREEN ROOF AND TRADITIONAL ROOF.

Variations of máximum humidities				
Month	Salón 19	Salón 20	Salón 21	Salón 22
January	63.876	44.012	59.04	44.612
February	71.235	62.602	69.739	60.078
March	78.053	75.384	80.857	65.855
April	68.653	66.901	62.602	65.171
May	66.435	63.721	65.736	66.173
June	79.876	77.589	71.147	72.959
July	85.763	82.367	71.42	72.37
August	69.867	66.594	67.81	66.901
September	76.8	70.864	74.8	72.85
October	76.211	73.184	74.04	73.766
November	76.828	74.988	75.384	69.899
December	73.603	63.897	63.22	73.985

Thrown data we mark the maximum moisture throughout the year, for the living room which features 19 traditional roof, the maximum was recorded in the month of June, classroom 20 with extensive green roof substrate thickness 10 cm, it was in the month of July in room 21 which has an intensive green roof with thickness of 15 cm, the maximum record was in March, finally in the classroom 22 which also has intensive green roof with the greatest thickness of 25 cm was in the month of December. Figure 10 show us our comfort zone that marks the reference [22], which is delimited by the black box.

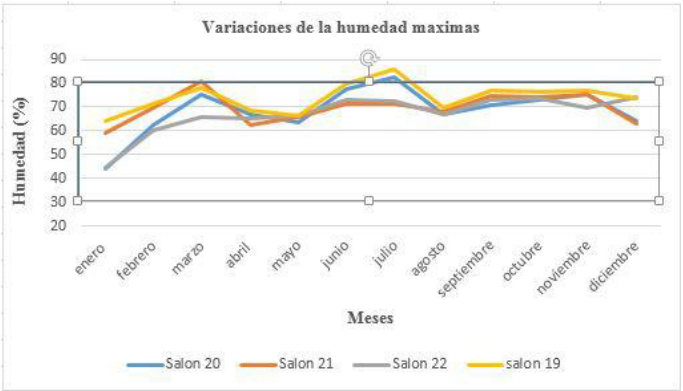

Figure 10. Variations of the máximum humidities in green roofs about the confort zone.

V. CONCLUSIONS

In the comparative study of a classroom with traditional roof and different classrooms with intensive green roofs (15, 20 cm) and extensive roof (10cm), he came to the conclusion that the roofs with green technologies help reduce the

temperature inside the buildings. Intensive green roofs maintain the required constant temperature and according to the reference [22], and two types of intensive green roofs which were placed on 15 cm thickness is more feasible than 25 cm, as a thinner kept the temperature required by the standard, coupled with this, the weight transmitted to the building would be smaller and the cost would decrease as a thinner lower volume of material and less water for irrigation.

THANKS

The authors wish to thank to Consejo Nacional de Ciencia y Tecnología (CONACyT) and Autonomous University of Queretaro for their support, with which was posible to carry out this research.

REFERENCES

[1] Cidell J., Beata A. Spatial variation among green building certification categories: Does place matter?, Landscape and Urban Planning 91 (2009) 142-151.

[2] Dunnett N., Kingsbury N. Planting green goofs and living walls. Portland, OR: Timber Press, Inc. (2004).

[3] Bates, A.J., Sadler, J.P., Mackay, R., 2013. Vegetation development over four years on two green roofs in the UK. Urban For. Urban Green. 12, 98e108.

[4] Yang J, Yu Q, Gong P. Quantifying air pollution removal by green roofs in Chicago. Atmos Environ 2008; 42(31):7266–73..

[5] Liu K, Minor J. Performance evaluation of an extensive green roof. In: Third annual greening rooftops for sustainable communities conference, Awards and Trade Show. Washington, DC; 4–6 May 2005.

[6] Weng Q, Lu D, Schubring J. Estimation of land surface temperature-vegetation abundance relationship for urban heat island studies. Remote Sens Environ 2004; 89(4):467–83.

[7] Castleton HF, Stovin V, Beck SBM, Davison JB. Green roofs; building energy savings and the potential for retrofit. Energy Build 2010; 42:1582–91.

[8] Morau D, Rakotondramiarana H, Andriamamonjy Al. Modelo sencillo para el encuesta teórica del comportamiento térmico techo verde. J Technol Innovat Renovar Energía 2012; 1 (2): 92-102.

[9] Jaffal I, Ouldboukhitine S, Belarbi R. A comprehensive study of the im-pact of green roofs on building energy performance. Renew Energy 2012; 43:157–64.

[10] Chen CF. Evaluación y desarrollo de estrategias de funcionamiento de los techos verdes en Taiwán: una revisión. Ecol Esp 2013; 52: 51-8.

[11] Liu KY, Bask ran BA. NRCC-46412: thermal performance of green roofs through field evaluation. Ottawa, Ontario: National Research Council Canada; 2003 [p. 1–10].

[12] Saiz S, Kennedy C, Bass B, Pressnail K. Comparative life cycle assess-ment of standard and green roofs. Environ Sci Technol 2006; 40:4312–6.

[13] Wong NH, Cheong DKW, Yan H, So J, Ong CL, Sea A. The effects of rooftop garden on energy consumption of a commercial building in Singapore. Energy Build 2003; 35:353–64.

[14] Emilsson T. Vegetation development on extensive vegetated green roofs: influence of substrate composition, establishment method and species mix Ecol Eng 2008; 33(3–4):265–77.

[15] Nagase A, Dunnett N. Establishment of an annual meadow on extensive green roofs in the UK. Landscape Urban Plan 2013; 112:50–62.

[16] Theodosiou T. Green roofs in buildings: thermal and environmental behaviour. Adv Build Energy Res 2009; 3:271–88.

[17] Lundholm J, Maclvor JS, MacDougall Z, Ranalli M. Plant species and functional group combinations affect green roof ecosystem functions. PLoS ONE 2010; 3:9677.

[18] Wolf D, Lundholm JT. Water uptake in green roof microcosms: effects of plant species and water availability. Ecol Eng 2008; 33:179–86.

[19] Nagase A, Dunnett N. Establishment of an annual meadow on extensive green roofs in the UK. Landscape Urban Plan 2013; 112:50–62.

[20] Getter KL, Rowe DB. The role of extensive green roofs in sustainable development. Hort Science 2006; 41(5):1276–85.

[21] Blanusa T, Vaz Monteiro MM, Fantozzi F, Vysini E, Li Y, Cameron RWF. Alternatives to Sedum on green roofs: Can broad leaf perennial plants offer better 'cooling service'? Build Environ 2013; 59:99106.

[22] ASHRAE, ASHRAE Standard 55: Thermal environmental conditions for human occupancy, American Society of Heating, Refrigerating and Air-Conditioning Engineers, Inc. 2004.

Haptic Interface: Study of PD and PD with Gravity Compensation Controllers to Trayectory Tracking

J. M. Hernández-Paredes
Mechatronics engineering / Robotics Laboratory
Instituto Tecnológico Superior de Huichapan
Huichapan, México
jmhernandez@iteshu.edu.mx

B. Muñoz-Barron and L.F Serna-Hernández
Mechatronics engineering / Robotics Laboratory
Instituto Tecnológico Superior de Huichapan
Huichapan, México

***Abstract*— A haptic interface is an electromechanical device that allows a human operator to interact with a digital computer, this mechanism returns a force on the grade user interaction.**

In this article obtaining mathematical models that define the haptic interface is presented, as are the direct kinematic model of position and the inverse kinematic model position, then compare two laws that are implement in C++, one is proportional - derivative control and second one proportional-derivative with gravity compensation, these two controllers are validated in experiments lasting 20 seconds and follow a trajectory shaped four polar rose petals, as results are obtained errors of up to +/- 1 mm and a series of figures that show a desired position versus proportional-derivative control and proportional-derivative with gravity compensation, show the articular error and Cartesian error and torque on robot's joint.

Keywords*— Control; Error; Kinematics; Gravity, Haptics; Model; Robotics.

I. INTRODUCTION

The haptic devices are means that enable interaction between a human operator/user and a digital computer that have made significant progress in recent years. Are abundant contributions of virtual reality, ranging from applications in entertainment to more complex applications such tasks minimally invasive surgery using robotic manipulators, in which a human operator interacts with an environment of virtual viewing across electromechanical devices, entering signals representative of actual movements to change the position and orientation of objects that constitute the virtual world and in some cases, receive in response a signal as a result of the modification that was performed [1-3].

The device six degrees of freedom PHANToM Omni company Geomagic is a mechanism that was developed with the objective to cover needs in the area of the haptic interfaces, their first three joints implement DC motors that allow a force feedback to end user and three joints that do not implement motors and only serve to guide the robot in Cartesian space [4].

Omi PHANToM haptic interface is used in a variety of areas, however the principal is in rehabilitation and medical operations [5-7]. In the area of research and development (R & D) are control works robots, teleoperation using the Omni device [8-10]. In 2012 at the annual conference SICE held in Japan, Sansanayuth and company published an article "Teleoperation with Inverse Dynamics Control for PHANToM Omni Haptic Device" where a controller for teleoperation two Omni interfaces in master slave configuration presents, as desired track a reference trajectory proposed a circular [9]. In 2014 Michael Mortimer in Australia introduced an amendment to Omni device for surgical simulations, this paper shows the direct and inverse kinematic models corresponding to such modification [11]. In 2015 it was presented at International Conference on Automation, Robotics and Applications a job where the robot is parameterized by the Data Driven Modeling method for obtaining the dynamic model of the interface [12].

II. KINEMATIC MODEL OF HAPTIC DEVICE

In this paper we proposed obtain the forward kinematic model of position (FKMP) and inverse kinematic model of position (IKMP) this models are obtained across the geometrical and mathematical analysis of the device. This models serves to implement the control laws in robotics devices.

A. Forward Kinematic Model of Position

A haptic interface is considered as a manipulator robot, therefore this can be treated as a kinematic chain that is formed of rigid links connected together with joints of the rotational and/or prismatic type [13].

For that a robot manipulator can perform a specific task, change for firstly the position and and orientation of the end effector must be selected (end of the robot), i.e. its position or configuration in connection with its base. This is essential to solving problems of positioning in robotics. In the analysis of position, it is a relationship between the Cartesian coordinates

and a reference system, that is, the position of a point of the end effector and its orientation angles of the joints [14].

The forward kinematic model of position allows to know the Cartesian position of end effector across of the angular position of each joint, thus the problems is reduced to find a homogeneous transformation matrix H that related the position and orientation the robot (end effector) with the fixed reference system that is situated in the base of this [13].

By the method of Denavit-Hartenberg is obtained homogeneous transformation matrix that handles both translation and rotation of a coordinate system with each other, parameters Denavit-Hartenberg (DH) are introduced and the matrix is derived corresponding homogeneous transformation, thereby known each of the positions of the end effector [13-14]. You can get an H matrix for each joint and this may have the following form:

$$ {}^{i-1}A_i = \begin{bmatrix} \cos(\theta_i) & -\cos(\alpha_i)\sin(\theta_i) & \sin(\alpha_i)\sin(\theta_i) & a_i\cos(\theta_i) \\ \sin(\theta_i) & \cos(\alpha_i)\cos(\theta_i) & -\sin(\alpha_i)\cos(\theta_i) & a_i\sin(\theta_i) \\ 0 & \sin(\alpha_i) & \cos(\alpha_i) & d_i \\ 0 & 0 & 0 & 1 \end{bmatrix} \quad (1) $$

where θ_i, α_i, a_i and d_i are the parameters of each joint. Equation (1) the submatrix with dimensions 3x3 indicates rotation suffering the joint being analyzed, and the vector 3x1 solves the problem of the position, then, if each joint parameters are obtained, and transformations will homogeneous that are multiply rotation and position of the end effector of the manipulator, equation (2) [13].

$$ T = {}^0A_1^1A_2 \ldots {}^{n-1}A_n \quad (2) $$

The initial conditions of the PHANToM OMNI haptic interface that allows to obtain the DH parameters shown in Fig. 1.

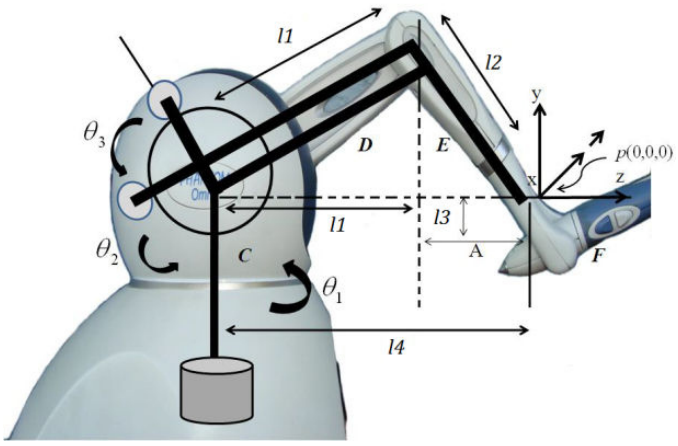

Fig. 1. Initial conditions of the PHANToM OMNI [15].

Therefore to obtain parameters DH has the transformation is 0 to 3 wherein the rotation of the second joint is excluded.

$$ {}^0T_3 = \begin{bmatrix} \mathrm{c}\theta_1 & 0 & s\theta_1 & 0 \\ 0 & 1 & 0 & 0 \\ -s\theta_1 & 0 & c\theta_1 & 0 \\ 0 & 0 & 0 & 1 \end{bmatrix} \quad (3) $$

where: $\mathrm{s}\theta_x$ is equal to $\sin\theta_x$ and $\mathrm{c}\theta_x$ is equal to $\cos\theta_x$ and x is the articulation one to three.

Now the transmutation matrix of two to three where include the second rotation of the device.

$$ {}^2T_3 = \begin{bmatrix} 1 & 0 & 0 & 0 \\ 0 & c\theta_3 & s\theta_3 & l_2s\theta_2 \\ 0 & -s\theta_3 & c\theta_3 & l_2c\theta_2 \\ 0 & 0 & 0 & 1 \end{bmatrix} \quad (4) $$

The homogeneous matrix of three to four is:

$$ {}^3T_4 = \begin{bmatrix} 1 & 0 & 0 & 0 \\ 0 & 1 & 0 & -l2 \\ 0 & 0 & 1 & 0 \\ 0 & 0 & 0 & 1 \end{bmatrix} \quad (5) $$

Multiplying the matrices (3), (4) and (5) the homogeneous matrix of rotation and position of the end effector is obtained ${}^0T_4 = {}^0T_3{}^2T_3{}^3T_4$.

$$ {}^0T_4 = \begin{bmatrix} c\theta_1 & -s\theta_1s\theta_3 & c\theta_3s\theta_1 & -\mathrm{s}\theta_1(l_1c\theta_2 + l_2s\theta_3) \\ 0 & c\theta_3 & s\theta_3 & l_1s\theta_2 - l_2c\theta_3 \\ -s\theta_1 & -c\theta_1s\theta_3 & c\theta_1c\theta_3 & c\theta_1(l_1c\theta_2 + l_2s\theta_3) \\ 0 & 0 & 0 & 1 \end{bmatrix} \quad (6) $$

Of the matrix (6) the position vector of the end effector is obtained, however according to Fig. 1 must make a correction coordinate Y and Z, as the forward model position only provides to the end of the length l2 and effector established to the point where the wrist support, therefore the coordinates of the end effector are as:

$$ \begin{aligned} x &= -\mathrm{s}\theta_1(l_1c\theta_2 + l_2s\theta_3) \\ y &= l_3 + l_1s\theta_2 - l_2c\theta_3 \\ z &= c\theta_1(l_1c\theta_2 + l_2s\theta_3) - \mathrm{l}_4 \end{aligned} \quad (7) $$

where:

$$ l_1 = l_2 = 0.133m $$

A=0.03486m

$l_4 = l_1 + \mathrm{A}$

$l_3 = 0.02328\mathrm{m}$

B. Inverse Kinematics Model of Position

The goal of inverse kinematic problem is to find the values that should take the coordinates robot joints $q = [q_1, q_2, \ldots, q_n]^T$ to its end position and orient according to a specific spatial location. As can be addressed direct kinematic problem in a systematic manner from using arrays of homogeneous transformation, and independently from the configuration of the robot, not the case with the inverse kinematic problem, and the procedure for obtaining equations strongly dependent on the configuration of the robot.

When trying to solve the problem of inverse kinematics is desired to find the locked solution. That is, to find an explicit mathematical relationship of the form [13]:

$$q_k = f_k(\mathrm{x}, \mathrm{y}, \mathrm{z}, \sigma, \beta, \gamma) \qquad \mathrm{k} = 1, 2, \ldots, \mathrm{n(GDL)} \tag{8}$$

Through the application of geometric methods you can usually find the values of the first joint variables, which are those achieved position the robot. To do trigonometric and geometric relationships on elements of the robot are used. It is often used to solving triangles formed by the elements and joints of the robot.

Through the analysis of Fig. 2 and 3 it can be determined the equations to solve θ1, θ2 and θ3 joints.

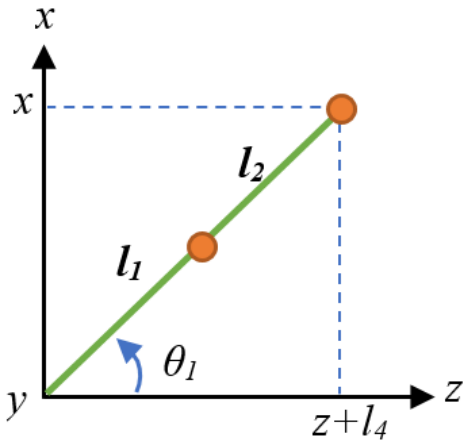

Fig. 2. Superior view of the PHANToM Omni.

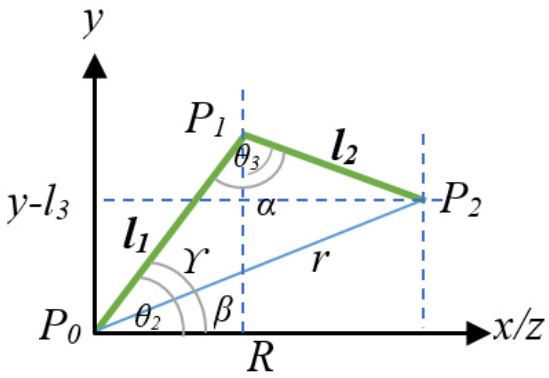

Fig. 3. Lateral view of PHAToM Omni.

$$\begin{aligned} \theta_1 &= -arctan(x, z + l_4) \\ \theta_2 &= \gamma + \beta \\ \theta_3 &= \theta_2 + \alpha - \frac{\pi}{2} \end{aligned} \tag{9}$$

where:

$$\beta = atan2(y - l_3, R)$$

$$\gamma = \cos^{-1} \frac{l_1^2 + r^2 - l_2^2}{2 l_1 r}$$

$$r = \sqrt{x^2 + (z + l_4)^2 + (y - l_3)^2}$$

$$R = \sqrt{x^2 + (z + l_4)^2}$$

$$\alpha = \cos^{-1} \frac{l_1^2 + r^2 - l_2^2}{2 l_1 l_2}$$

Equations (7) and (9) solve the haptic interface in the geometric aspect without taking the forces acting on the device.

C. Dynamics Model

The motion control problem of robot manipulators can be formulated as follows: consider the dynamic equation of a robot *n* degrees of freedom:

$$\tau = \boldsymbol{M(q)\ddot{q} + C(q,\dot{q})\dot{q} + G(q)} \tag{10}$$

where: $\boldsymbol{M(q)}$ is a symmetric matrix positive defined of *nxn* and is called inertial matrix, $\boldsymbol{C(q,\dot{q})}$ is a vector of dimension *nx1* called vector of centrifugal and Coriolis forces, $\boldsymbol{G(q)}$ it is a vector of *nx1* of external forces or gravitational pairs.

The gravity matrix is defined as:

$$G(\mathrm{q}) = [\mathrm{g}_x, \mathrm{g}_y, \mathrm{g}_z]^{\mathrm{T}}$$

$$\mathrm{g}_x = 0$$

$$\mathrm{g}_y = \mathrm{k1}\cos(\theta_2) + \mathrm{k2}(\theta_2 - \pi/2)$$

$$\mathrm{g}_z = \mathrm{k2}\sin(\theta_3)$$

where:

$$\mathrm{k1} = 164.158 \times 10^{-3}$$

$$\mathrm{k2} = 94.050 \times 10^{-3}$$

$$\mathrm{k3} = 117.294 \times 10^{-3}$$

Note that g_x is zero because the gravity doesn´t affect in this coordinate.

III. Trajectory Tracking Control

Given a set of dimensional vectors q_d, $\dot{q}_d$ y $\ddot{q}_d$ referred to as positions, velocities and accelerations desired joints, is to determine a vector function τ, so that the positions q that are associated with the joint coordinates of the robot follow accurately at q_d, i.e., the goal path tracking is to determine τ, such that:

$$\lim_{t\to\infty} \tilde{q}(\mathrm{t}) = 0$$

where:

$$\tilde{q}(t) = q_d(t) - q(t)$$

A. PD Control

The algorithm control Proportional-Derivative (PD) is the schematic of control simpler and more popular that it can be use in manipulators robots. In 1981, Takegaki and Arimoto demonstrated that the equation (11) in close loop of robot´s dynamic model and the PD control has a global stable equilibrium [16].

$$\tau = K_p\tilde{q} - K_v\dot{q} \tag{11}$$

where: K_p and K_v are positive matrix gains of *nxn* dimensions.

In Fig. 4 are show the blocks diagram of the proportional derivative control.

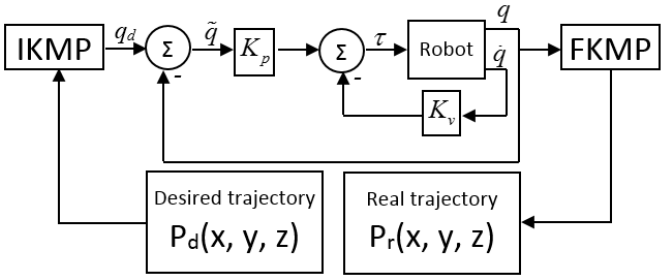

Fig. 4. PD control diagram.

B. PD with Gravity Compensation Control

PD control does not guarantee compliance control target position for manipulators whose dynamic models contain the term gravitational pairs ***G(q)***.

Contrast to the PD control, which does not require any knowledge about the structure of the robot model, the PD + G controller makes explicit use of partial knowledge model of the robot. However it is important to note that for a given robot pairs gravitational vector can be obtained relatively easily, since for this purpose sufficient to calculate the potential energy.

The position control problem can be formulated as follows:

$$\lim_{t\to\infty} \tilde{q}(t) = \lim_{t\to\infty} (q - q_d) \to 0$$

$$\lim_{t\to\infty} \tilde{q}(t) = \lim_{t\to\infty} (\dot{q} - \dot{q}_d) \to 0$$

The proportional derivative with compensation gravity control is defined in (12) and the Fig. 5 show de block diagram for the PD+G controller.

$$\tau = K_p\tilde{q} - K_v\dot{q} + g(\mathrm{q}) \tag{12}$$

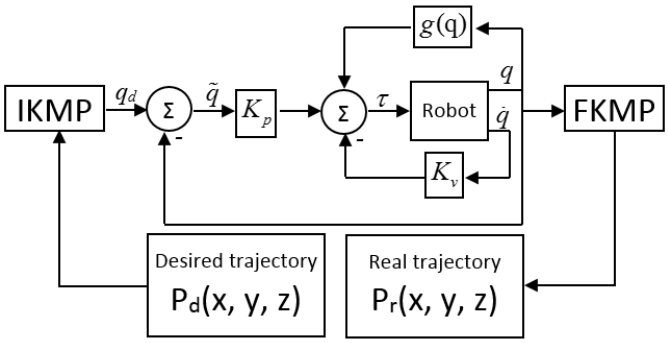

Fig. 5. PD+G control diagram.

IV. Experiments & Results

To implement the two control laws was used the SDK Open Haptics that allows communicate with the PHANToM Omni device and return articular position and articular velocity variables. So, the desired trajectory proposed was a polar rose defined by (13).

$$\begin{aligned} x_d &= x_c + \alpha + r\cos(\gamma)\sin(\beta\gamma) \\ \mathrm{y}_d &= 0 \\ z_d &= -z_c + \alpha + r\sin(\gamma)\sin(\beta\gamma) \end{aligned} \tag{13}$$

where:

ts=8

$\omega=2\pi$

f=(2ts)$^{-1}$

$\gamma=\omega$*f*(t-1)

$x_c=y_c=\alpha=0$

r=0.02

$\beta=2$

The time of each test was of 20 seconds and in two experiment the initial position of device was the same. In the Fig.6 is show in the 3D Cartesian the desired (blue line), PD (red line) and PD+G (green line) trajectory.

In Fig. 7 show the X_d, X_{PD} and X_{PD+G}, where are appreciate that response of controllers in X is similar because the gravity doesn´t affect in this robot's position.

In Fig. 8 show the Y_d, Y_{PD} and Y_{PD+G}, where are appreciate that response of PD+G controller is better than PD to tracking desired trajectory, this is because the gravity affect this robot´s position and the same effect pass with the Z position (see Fig. 9). In Fig. 10 show the error on this position note that error in two cases is close to cero.

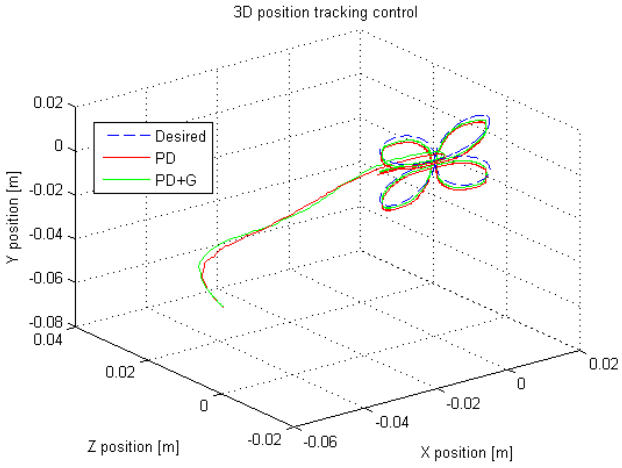

Fig. 6. Desired (blue line), PD (red line) and PD+G (green line) trajectory in 3D Cartesian Position.

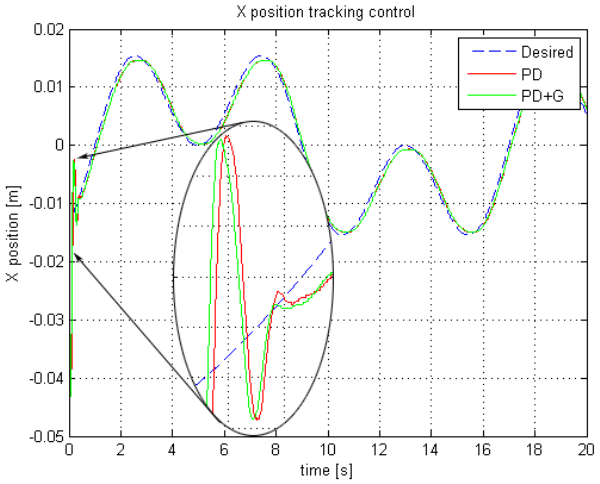

Fig. 7. Tracking x position, note that the controllers response is similar because gravity doesn´t affect it.

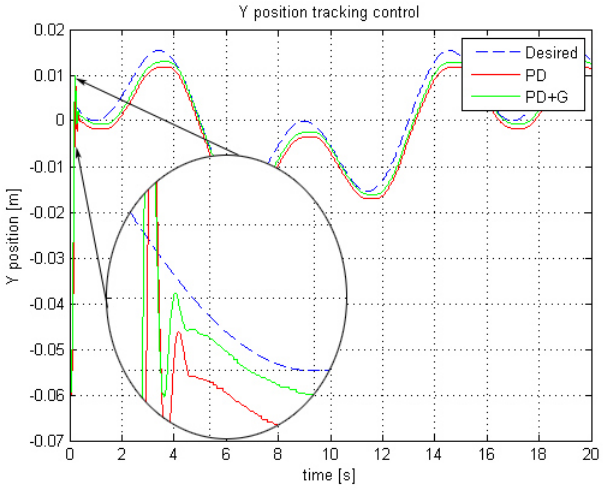

Fig. 8. Tracking *y* position, note that the PD+G controller response is better than PD response.

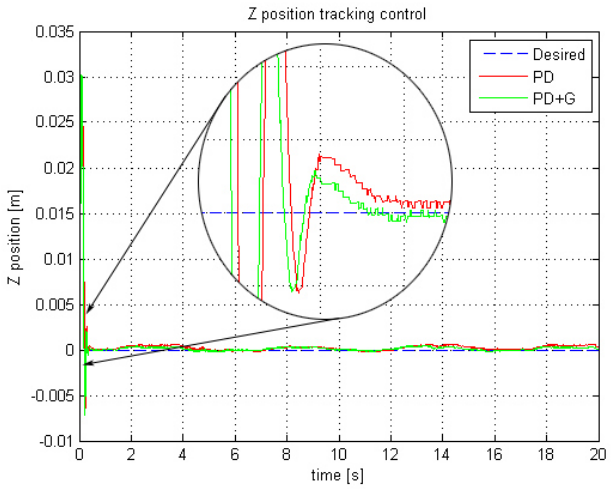

Fig. 9. Tracking *z* position, note that the PD+G controller response is better than PD response.

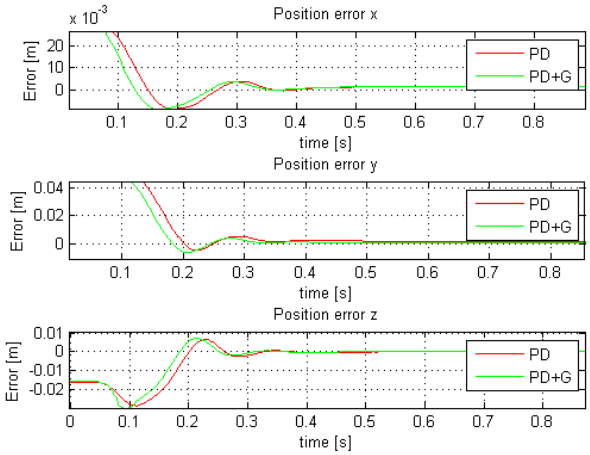

Fig. 10. Error of x, y and z positon.

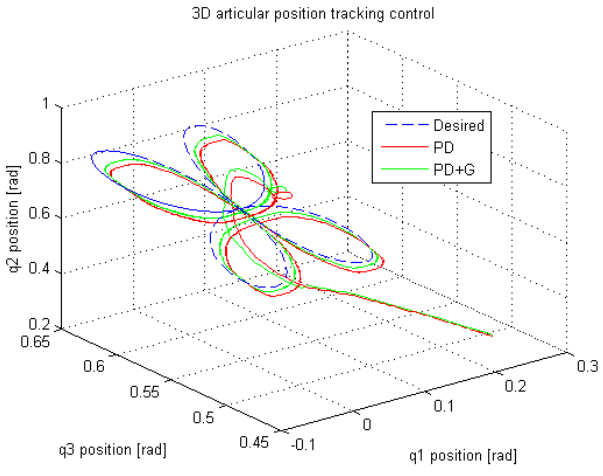

Fig. 11. Desired (blue line), PD (red line) and PD+G (green line) trajectory in 3D articular position.

In Fig. 11 show the 3D perspective in articular space, in this figure are appreciate that booth controllers follow the reference with small error in one extreme on the articular desired position. In Fig. 12 are presented the independently q_1, q_2 and q_3, note that the joints go forward in 0.35s, 0.45s and 0.55s respect the reference. The Fig. 13 present the torque apply in the robot's actuators.

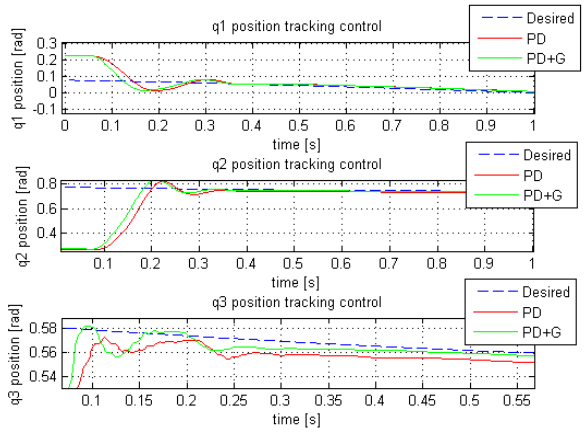

Fig. 12. Articular position q1, q2 and q3 response to PD and PD+G controllers.

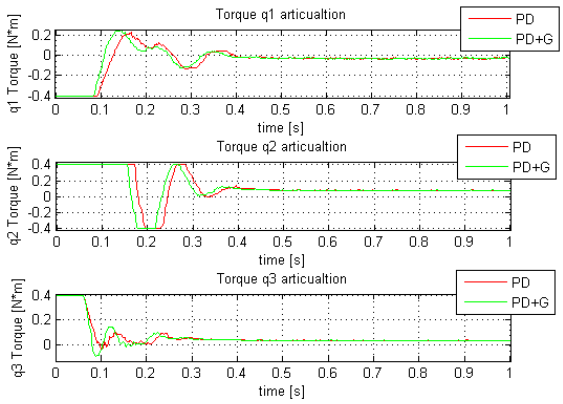

Fig. 13. Torque apply in the three joints of robot.

From the data obtained in the experiments can calculate the root mean square error (RMSE) (14) and the error rate of the Cartesian plane with respect to workspace PHANToM Omni, in TABLE 1 shows the results of this analysis.

$$ECM = \sqrt{\frac{\sum_{i=1}^{n}(v_i - \overline{v}_i)^2}{n}} \qquad (14)$$

TABLE I. MEAN SQUARE ERROR AND ERROR RATE IN XYZ

	Workspace	*RMSE (mts) PD*	*%Error*	*RMSE (mts) PD+G*	*%Error*
X	160 mm	2.4509e-3	1.5318	2.3234e-3	1.4521
Y	120 mm	6.01192e-3	5.0099	5.2720e-3	4.3933
Z	70 mm	2.05217e-3	2.9316	1.94630e-3	2.7804

V. CONCLUSIONS

The direct and inverse kinematic models of position were obtained, were implemented in C ++ two laws of PD control and PD + G where it is concluded that PD + G controller is better than the PD since this is taken into account the gravity vector which is the robot itself, however both controllers always has a steady-state error, this error can be reduced to zero if an integrative action to PD + G is implemented.

REFERENCES

[1] Díaz López Fabián Alfonso, Domínguez Ramírez Omar Arturo, Ramos Velasco L. E. & Parra Vega Vicente, *Identificación y control wavenet para sistemas MIMO: Aplicación en una interfaz háptica*, Asociación de México de Control Automático (AMCA), Cd. del Carmen, Campeche, México, del 17 al 19 de Octubre de 2012.

[2] Domínguez-Ramírez O. A. *Diseño e Integración de una Interfaz Háptica Activa Real*- lista. CINVESTAV, Sección de Mecatrónica, PhD Tesis, México, 2005.

[3] Domínguez-Ramírez O. A. and V. Parra-Vega. *Active haptic exploration of deformable* objects. Chapter 17 in DAAAM International Scientific Book, pages 191–204, 2006.

[4] Sensable-Technologies. *PHANToM Omni, 3D Touch Components, Hardware and Technical Manual*. Sensable Technologies, Inc., Woburn, MA, 1998.

[5] A. P. Aldana-Suáres y S. P. Yañez-Mantilla, Adaptación de Pinzas de Laparoscopia a Dispositivos Hápticos Phantom Omni y Desarrollo de Software de Evaluación, Tesis de Ingeniería, Universidad Militar Nueva Granada, 2013.

[6] M. L. Pinto-Salamanca, Análisis E Implementación de Una Interfaz Háptica en Entornos Virtuales, Tesis de Maestría, Universidad Nacional De Colombia, 2009.

[7] Éllen S. Corrêa, Paulo R. Trenhago, Thiago E. A. Oliveira, Jauvane C. de Oliveira, Performance Evaluation of an xSight 3120 HMD and Usability Analysis of the Phantom Omni in a Thoracocentesis Simulation, SBC Journal on 3D Interactive Systems, volume 4, number 2, 2013.

[8] Jarillo Silva A. Domínguez-Ramírez O. A and V. Parra-Vega. *Haptic Training Method Using a Nonlinear Joint Control*, volume 2. International Journal of Scientific and Engineering Research, April 2011.

[9] Thitipong Sansanayuth, Itthisek Nilkhamhang and Kanokvate Tungpimolrat. Teleoperation with Inverse Dynamics Control for PHANToM Omni Haptic Device, SICE Annual Conference, Japan, 2012.

[10] Gang Song, Shuxiang Guo and Qiang Wang, A Tele-operation system based on haptic feedback, International Conference on Information Acquisition, Weihai, Shandong, China, August 20 - 23, 2006.

[11] Michael Mortimer, Ben Horan, Alex Stojcevski, 4 Degree-Of-Freedom Haptic Device for Surgical Simulation, World Automation Congress, 3-7 Aug. 2014.

[12] B.J.E. Milne, H.P.G.J. Beelen, R.W.H. Merks, S. Weiland, X.Q. Chen, C.E. Hann and R.J. Parker, Verification of Sinusoidal Steady State system identification of a Phantom Omni haptic device using Data Driven modeling, International Conference on Automation, Robotics and Applications, Feb 17-19, 2015.

[13] A. Barrientos, L.F. Peñín, C. Balaguer, R. Aracil, *Fundamentos de robótica*, McGraw Hill, 1997.

[14] Saha S.K. *Introducción a la Robótica*, Mc Graw Hill, 1era. Edición, 2010.

[15] A.J.Silva, O.A.D.Ramirez, V.P.Vega, J.P.O.Oliver, "PHANToM Omni Haptic Device: Kinematic and Manipulability", Electronics, Robotics and Automotive Mechanics Conference, CERMA, pp.193-198, 2009.

[16] F. Reyes-Cortés, Matlab Aplicado a Robótica y Mecatrónica, Alfaomega, ISBN 978-607-707-357-4, 2012.

Vibration analysis of a tapered bearing by using time-frecuency methods

Carlos Elí Martínez Pérez
Dirección de Investigación y Posgrado, Facultad de Ingeniería
Universidad Autónoma de Querétaro
Santiago de Querétaro, México
Cerro de las campanas S/N. Col. Niños Héroes, C.P. 76010

Juan Carlos Jáuregui Correa
Dirección de Investigación y Posgrado, Facultad de Ingeniería
Universidad Autónoma de Querétaro
Santiago de Querétaro, México
Cerro de las campanas S/N. Col. Niños Héroes, C.P. 76010

***Abstract*— This paper presents a comparative study of performance of time-frequency methods to detect failures in bearings elements. The vibration signal issued by a bearing can contain spectral components which are related with the bearing geometry. In this work we show the experimentation using a tapering bearing which have a unknown failure level, also we compare two time-frequency techniques as be Short Time Fourier Transform (STFT) and Wavelet Transform (WT).**

Keywords—vibration analysis; Fourier Transform, Wavelet Transform; bearing failure.

I. Introduction

The bearings are found extensively at industrial aplications (turbines, compressors, motors, etc.) and are fundamental elements of rotative machines [1]. A defect into a bearing, at less that be detected in time, could produce a bad behavior into a machine and will can trigger a catastrophic failure.

Today the most of modern industries use into their predictive maintenance program the monitoring and vibration analysis to determine which are the machine healthy state, particularly their elements like bearings, gear, supports and of this way to prevent failures. The bearings act like a noise source and vibration due to the compliance variation as the presence of defects in they.

A lot of research work has been publised in the last two decades, on the detection and diagnosis of bearing defects by vibration and acoustic methods. Some of these works have also been reviewed by researchers. Several techniques have been aplied to measure the vibration response from detective bearings; i.e., vibration measurements in time and frequency domains [2].

The traditional methods of maintenance applied to bearings are based in its replacement over intervals of time of fixed operation. This methods, although are very popular, are not totally reliable due that are based in an expected time of operation of bearing.

Therefore this work are centred in monitoring of bearing using time-frequency analysis of signal. With the Fourier Transform (FT) we can obtain the frequency components of a signal but the problem is that we don't know in which time occurs the failure. With the time-frequency analysis we can see the non-linear behavior of signal which results as a failure into the bearing, also we can see the moment in which failure occurs.

Examples of these physical variables are acceleration, vibration, acoustic emission, cutting forces and driver current which can be measured through a great variety of sensors. The measured signals are processed in different ways in order to find features thar can provide important information of the process. Traditional monitoring methods use Fast Fourier Transform (FFT) as a signal processing method. Although FFT methods are theoretically constrained to linear stationary processes, acceptable results have been obtained in practice for a great variety of manufacturing processes [3].

Although traditional FFT analysis can provide an aceptable detection of the principal spectral components involved in an unstable chatter phenomenon, novel approaches derived from nonlinear methods has been

explored to gain further insights in the nature an complexity of this kind of signals. Examples of these methods are wavelet transform and Hilbert-Huang transform (HHT) [4], which can provide temporal information of the dominant spectral components involved in the process as well as of potential nonlinearities that can lead to unstable dynamics.

II. Problem definition and theory

Failure alarm for a rolling element bearing is often base don the detection of the onset of localized defects [5]. Once localized defect emerges in the inner or outer race of the bearing, an impact occurs every time the rolling element crosses the defected área of the bearing race. The bearing failure is once of bigger common problems into a rotative machine. Aproximately, 50% of electric motor failures, the more popular actuator, are failures into a bearings [6]. This failures can make severals economic losses asociates to non planed interruptions into a interprise.

A. *Rolling bearing*

This mechanical elements, same that elements, allow join rotative axis with stacionaries structures, as is shown in the figure 1.

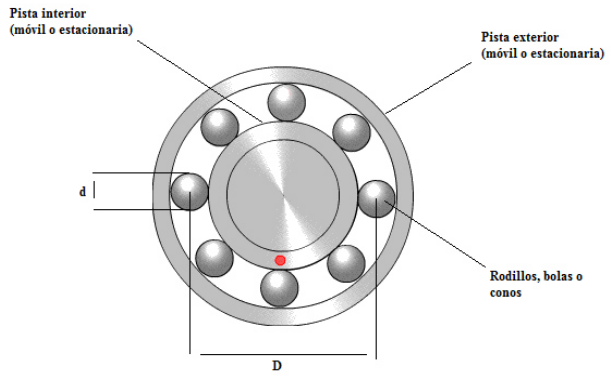

Fig 1. Principal bearing elements.

In general, a bearing consist of a inner ring with a solid race and a out ring with a race, whose surface is hardened, staying in two series of roller or balls. The windows that present the bearing are its low friction coeffiecients, allow aligns the axis accurately, they have a big resistent to momentary oveloads, its lubrication is easy and can be able axial and transverse loads.

B. *Localized defects*

This measurement and others are deliberate, using specifications that anticipate your paper as one part of the entire proceedings, and not as an independent document. Please do not revise any of the current designations. Are in general make by fissures, bite and wear. The bite is the most commoun of all, it is caused when a fissure due a fatigue, which is originated inside surface and it's propagated to the surface until a metal piece it appears superficially producing a defect [7].

C. *Distributed defects*

This kind of defects can be: surface roughness and non equals rolling elements. The distributed defects can be caused for mistakes in its manufacture, a bad instalation o due to the wear. Vibrations generated by manufacture defects have resulted be more low in the mostly than due to produce defects for wear.

Varying the contact forces between the rolling elements and the races causing an increase in vibration level. Since it is difficult to discern when the vibration is caused by localized defects or distributed, it is recommended to analyze both the frequency and the amplitude of the spectral components related to vibration.

D. *Bearing fundamental frequencies*

The frequencies that rolling element bearings generate when roller pass over a surface anomaly on either the roller or the raceway are called fundamental frequencies. These frequencies are a function of the bearing geometry (that is, pitch diameter and roller diameter) and the relative speed between the two reaceways.

The load capacity of a bearing depends of the resistence to compression and wear that the roller elements presents. This capacity is asociated to a life useful period, which is a function of his operation velocity. Of this way, every element of bearing produce a vibration that is asociated with its rotation velocity, distinguishing four frequencies in its operation; the ball pass frequency (BPF), fundamental train frequency (FTF), ball pass frequency inner race (BPFI) and ball pass frequency outer race (BPFO). When the bearing geometry is known, the fundamental fault frequencies can be calculated [8].

The FTF is calculated using the equation 1.

$$FTF = \left(1/2\right)\left(1 - r^2\right)x \qquad (1)$$

As the roller ball touches two races in each revolution, a defect is manifest in 2FTF. The BPF is calculate using the equation 2.

$$BPF = \left(1/2\right)(1-r)x \quad (2)$$

A defect of outer race is manifest over a rotation frequency of balls, and that can be calculated with the equation 3.

$$BPFO = \left(n/2\right)(1-r)x \quad (3)$$

If the defect is located on inner race, this manifest its vibration to the rotation frequency of balls, it can be calculated with the equation 4.

$$BPFI = \left(n/2\right)(1+r)x \quad (4)$$

Where

$$r = \left(d/D\right)\cos\alpha \quad (5)$$

x= rotation frequency

D= pitch diameter of bearing

d= ball diameter

α= contact angle among balls and races

Is a common use the the next empirical equations to determine the rotational frequency of balls compared to the races, when haven't the dimensions of bearing use the equations 6 and 7.

$$BPFO = 0.4nx \quad (6)$$

$$BPFI = 0.6nx \quad (7)$$

The bearings set a time of life to de mecahanical equipment, especially when they opérate with high velocities and high loads. Generally, the first vibration problems are presented on bearings. This elements, which are that have a failure first, because are more weak.

The bearings affect the behavior of axis in rotation, due that the roller elements are elastic elements which can present little difference in its operation, so that they don't present a good dynamic response.

The kinds of failures that occur in bearings are the wear on ball surface, superficial fatigue and the grated due the contact between the cage and the race [9].

E. High-frequency Natural Bearing Resonance Indicators (HFNBRI)

Fundamental bearing frequencies and their harmonics are generally observed in the velocity spectrum. In addition to those frequencies, there are high-frequency natural bearing resonances between 3 and 50 kHz. Testing was performed involving the vibratory response of a rolling element bearing, which was monted on a high-speed spindle. The first stage of testing involved two-channel impact testing to identify the bearing's natural frequencies. The second stage comprised running the spindle through a broad sweep of operating speeds. As expected, rotational speed of the spindle excited the natural frequencies noted in the first stage. Also of note was indication that early bearing wear caused by impacting from wear, and friction caused by lubrication problems, excited the same natural frequecies [10].

Realizing the benefit of HFNBRIs, many companies have developed their own proprietary measurements for detection of sonic and/or ultrasonic frequencies that produced a value (magnitude) which was a summation of the energy in the frequency band of interest. The measurements of HFNBRI include: spike energy; shock pulse at resonant frequecy of 32 KHz (measured in dBsv); high frequency (>5 kHz) detection band (measued as peak g); high frequency (1 to 20 kHz) and (measured in *g* RMS); general purpose ultrasonics in the frequency range of 20 to 50 kHz (measured in dB); spectral emitted energy between 250 and 350 kHz (measured in dB); and acoustic emission measurements in the frequency ange of 20 kHz to 1 MHz (measured in dB).

F. Discrete Frequency Indicators

Bearing frequencies less than 10 kHz may present in predective maintenance (PdM) route data (veloity spectrum). Typically, route data is collected with a high pass filter of 2 Hz, a los pass filter of 1 or 2 kHz, and standard sampling (to prevent aliasing). Such data collection techniques will pick up bearing wear later in their deterioration cycle, but not in ther initial progression.

Alternate signal processing techniques are needed in order to observe bearing frequencies early in their wear cicly. Discrete frequency indicator use a high pass filter of at least 500 Hz with a high rate of sampling and high-frequency low pass filters to obtain a short time durations of schock measurements. Many of these measurements utilize full wave retification of the time waveform, then process an FFT for analysis. This will help give a root cause as to waht the initial bearing problem may be [11].

Similar to HFNBRI, the same companies and others developed additional propietary measurements which provide dicrete frequency indicators (that is, spectral data) for detection of sonic and/or ultrasonic frequencies,

including: spike energy; shock pulse; spectral emitted energy; cepstral analysis (measured in g dB); and bearing demodulation (measured in g).

If using a sonic HFNBRI and discrete frequency indicator, special care should be taken with magnetically mounted accelerometers for route based PdM programs, as their frequency response ranges will be limited due to the change in stiffness (K) and added mass (M).

G. Four stages of bearign wear

The most common configuration for rotating machinery is horizontally mounted (that is, axis of rotation perpendicular to gravity) with a rotating inner race. Given such a configuration, certain factors lead to a higher or lower probability for wear of the various bearing components.

The ourter raceway has the highest probability for wear and is usually the first discrete bearing frequency detected. The outer race is stationary with a stationary load zone. Transmission of high frequencies generated by lubrication and/or wear is very high for outer race frequencies. The load zone is relatively small with respect to the pitch diameter. The progession of wear allows for trending.

The inner raceway experiences wear at a faster rate than the outer raceway. The fundamental bearing frequency for an inner race is greater than that of an outer race, meaning that for one revolution of the shaft, more damage producing events will occur for an inner race fault. The main reason why inner race problems are detected less frequently than outer race problems is because transmission of high frequencies generated by lubrication and/or wear is attenuated greatly through multiple transition and lubrication boundaries. The por transmission of vibratory energy results in more severe wear by the time a problem is detected. Therefore, trending is limited for inner raceway wear [12].

The rolling elements and cage are typically the last components to fail though roller spin frequencies, and are often observed in non-ball bearing configurations.

The indications associated with the four stages of bearing wear are general and may not be all-inclusive for each bearing wear event. The stages are provided as follows as a point of reference used in the evaluation of bearing severity for an estimate of wear in lieu of disassembly and inspection.

Stage 1: HFNBRIs is excited with possible fault frequencies (harmonics) in the second bearing band. Since BPFO is easily detectable, a discrete frequency indicator should be used to identify the fault problem progression.

When bearings are in stage 1 of deterioration, the typcal recommendation is to continue to monitor for deterioration at the normal monitoring interval. The risk assesment for risk indicator (ARI) is typically less than two.

Stage 2: When bearing wear progresses to stage 2, the damage to the raceways and7or rollers grows from having microscopic size to being visible to the naked eye. Stage 2 wear will also be accompanied by rising quenatity and amplitude of fault frequency (BPFO) may apper in the first bearing band. Also, harmonics of the fundamental inner race fault frequency (BPFI) may be seen in the second bearing band. The discrete frequency indicator should have increasing amplitudes, and multiple bearing fault frequencies should be present. Harmonics of bearing fault frequencies may be present in a velocity spectrum. Side banding around fault frequencies may occur in the second bearing band if modulation of time-waveform is present.

When bearing are in stage 2 of deterioration, the typical recommendation is to continue with scheduled repairs at the next normal preventative maintenance interval. The risk assessment for catastrophic failure is moderate (ARI is typically two to three).

Stage 3: When bearing wear progresses to stage 3, the damage to the raceways and/or rollers grows substantially in all dimensions, as well as in in multiple locations. Stage 3 wear will result in even higher levels of HFNBRI amplitude. Outer rece fault frequency and harmonics will propagate to both first and second bearing band with side banding. Inner race fault frequency harmonics will now be present distinctly in the second bearing band with side bands. Possible ball spin frequencies (BSF) may appear in the first bearing band. The discrete frequency indicator should have increasing amplitudes along with multiple falt frequencies, and harmonics of bearing fault frequencies should be easily identified in a velocity spectrum.

When bearings are in stage 3 of deterioation, the typical recommendation is to schedule repair in the next 30 to 45 days. The risk assessment for catastrophic failure is high (ARI is typically three to five).

Stage 4: At stage 4, the change in bearing geometry with increased wear produces a drop in HFNBRI

amplitude. Random vibration will increase, generating a raised broad noise floor thath may mask low amplitude bearing fault frequencies. Looseness will appear at one, two and three times revolutions per minute (RPM). At this time, the overall spectral (velocity) levels will exceed alarm. If the discrete frequency indicator shows the presence of cage frecuency (FTF), the bearings is very near the end of life. HFNBRI may dramatically increase and the amplitude of vibration at turning speed may become excessive due to out specification clearances.

When bearing are in stage 4 of deterioration, the typical recommendation is to schedule immediate repairs. The risk assessment for catastrophic failure is very high (ARI is typically equal to or greater than five).

III. Analys of vibration signal

Several techniques have been aplied to measure and analyze of vibration signals from bearings with some failure. This techniques are not independent, many times are used to complement each other.

Signal analysis is one of the most important methods used for condition monitoring and fault diagnostics, whose aim is to find a simple and effective transform to the original signals. Therefore, the important information contained in the signals can be shown; and then, the dominant features of signals cab be extracted for fault diagnostics. The FFT is one of the most widely used and well-establised methods [13]. Unfortunately, the FFT-based methods are not suitable for non-stationary signals. However, various kinds of factors, such as a the change of the environment and the faults from de machine itself, often make the output signals of the running machine contain non-stationary components.

A. Frequency domain analysis

The frequency domain or spectral analysis of vibration signal may be is the more used method to detection of failures in bearing. The FFT has been used to obtain the spectrum of narrow band more easily and efficiently [14].

The Fourier Transform (FT) express a periodic function as a sum of complex exponentials how we can see in equiation 8.

$$F(k)=\frac{1}{\sqrt{2\pi}}\int_{-\infty}^{\infty} f(x)e^{-ikx}dx \qquad (8)$$

Where k is a continuous real variable.

The function can be reconstructed from Fourier components, through the Fourier Inverse Transform (equation 9).

$$f(x)=\frac{1}{\sqrt{2\pi}}\int_{-\infty}^{\infty} F(k)e^{ikx}dk \qquad (9)$$

Where *f(x)* is the signal in time domain.

The FT is widely used in the signal analysis and signal processing with satisfactory results when the signals are periodics and relugar, but isn't occurs the same to signal analysis whose spectrum change over time (non-stationary signals).

The FT detects the presence of a certain frequency but doesn't give it an information about the evolution over time of spectral features of signal. Several temporal aspects of signal, such the beginning and end of finite signal and the instant of emergence singularity of transitory signal, cannot be appropriately utilized to Fourier analysis.

B. Time-Frequency analysis

Define abbreviations and acronyms the first time they are used in the text, even after they have been defined in the abstract. Abbreviations such as IEEE, SI, MKS, CGS, sc, dc, and rms do not have to be defined. Do not use abbreviations in the title or heads unless they are unavoidable [15].

The methods based in frequency domain analysis are not suitable to non-stationary signal analysis and they are unable to disclose information inherent of non-stationary signal. However, many factors, as the change of environment and the own failures of machine, often do that out signals of machine have non-stationary compounds. Usually, this non-stationary compounds contain important information about the health machine, therefore, is very important to analyze the non-stationary signals [16].

Short Time Fourier Transform

The first method fo producing a Time Frequency Map is the Short Time Fourier Transform (STFT). It is derivated from the Wigner probability distribution. Wigner, in 1932, constructed his function over the phase space in queantum mechanics. One of the problems of their approach was suggested. This approach cuts the signal into slices, followed by performing a Fourier transform of each slice. In this way, the signa lis separate by time intervals (slices) and frequency components are calculated piecewise. This segmentation produces a non

periodic function, which creates discontinuities at the boundaries; thus, the Fourier transform crates large coefficients at high frequencies. To avoid these effects, the windowing concept is introduced. Instead of a rectangular segmentation, a smooth window-function is employed to segment the original signal. The window function is almost one at the origin and zero at the edges. Common window functions are identified with names such as: Hamming, Hanning, Barlett or Kiser [17]. If the window function is infinitely differentiable, the localized Fourier coefficients will show a polynommical decay.

The STFT is one of the first original analysis techniques that are able to process the transient part of a signal. What it does, is the transformation of a single dimensión vector into a two dimensión vector. The method defines a sliding window *w(t)* centered at time τ. With this function, the STFT processes localized frequency analysis. In this way, the analysis identifies time variations on the frequency response.

If we store the signal content, in a vector *y(t),* the STFT is computed as (equation 9):

$$S(\tau, f) = \int w(t-\tau)\, y(t) e^{-j2\pi ft}\, dt \qquad (9)$$

Where τ is related to the size of the window function.

The resolution of the signal decomposition depends directly on the window function. Plotting S as a function of t and f wil produce a time-frequency map.

The time-frequency map is also identified as "spectrogram". With it, we can see how the frequency content of a signal changes over time. A simple explanation of a map construction is: we cut the signal into blocks and compute the spectrum of each block; the blocks can overlap in order to avoid artificial peaks, as explained before.

Wavelet transform

Wavelets have been applied in diferent fields; they have proven to be a powerful tool for signal analysis and data processing. Although, it is the best transform for many vibration problems, its practical application hasn't been very popular. Most of the comercial analysis systems are based on the FFT, and only specialized literature describe the way wavelets can analyze transient and nonlinear vibration problems [18].

The big difference between the Wavelet Transform (WT) and the STFT is that wavelets can introduce a window function with variable size; thus, instead of a and b be a constant values, they can vary depending on the frequency component. Thus, for window with the same wavelet function. The result is a constant relative-bandwidth analysis which allows us the identification of transient and non-linear responses that varies with time. The advantage of the Wavelet Transform is that it descomposes the signal into a set of functions at different scales and shifted along the time variable.

In the mathematical terms, a wavelet is a function with zero average:

$$\int_{-\infty}^{\infty} \psi(t)\, dt = 0 \qquad (10)$$

This is the basic condition for determining the wavelet function, which is dilated by a scale parameter s, and translated by τ.

$$\psi_{\tau,s}(t) = \frac{1}{\sqrt{s}} \psi\left(\frac{t-\tau}{s}\right) \qquad (11)$$

Once the wavelet function satisfies this condition. The WT is computed in a similar way as the STFT. The WT transform of a signal *y(t)*, at the scale s and position τ, is computed by correlating y with a wavelet function ψ.

$$\psi(\tau, s) = \int y(t) \psi^*_{\tau,s}(t)\, dt = \frac{1}{2\pi} \int \hat{y}(f) \hat{\psi}\, df \qquad (12)$$

Where $\psi^*_{\tau,s}(t)$ is the complex conjugate wavelet function.

Several wavelet functions have been applied to vibration analysis, one of the most powerful is the Morlet wavelet function (equation 13).

$$\psi\left(\frac{t-\tau}{s}\right) = e^{\left(\frac{j2\pi f_0 (t-\tau)}{s}\right)} e^{\left(\frac{-\alpha(t-\tau)^2}{s^2\beta^2}\right)} \qquad (13)$$

Where f_0, α, and β are constant.

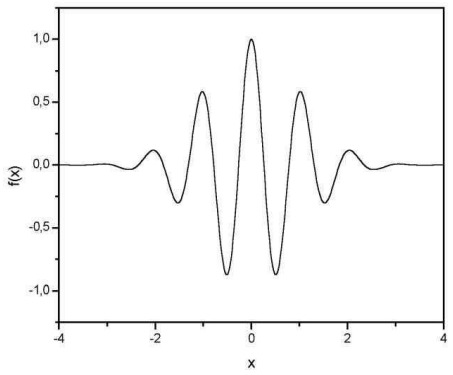

Fig 2. Morlet function.

The operation is a procedure that looks for similarities between the wavelet function ψ and the vibration signal. In other words, the wavelet function is a reference, or template, and the procedure consist on the identification of which sections of the signal matches the template. This matching is stored into a set of vectors defined as the wavelet coefficients. The figure 2, shows a schematic representation of the wavelet coefficient identification [19].

Another way of understanding this procedure is through filtering the original signal with two filters: a low-pass and high-pass filters, namely *H(z)* and *G(z)* (figure 2).

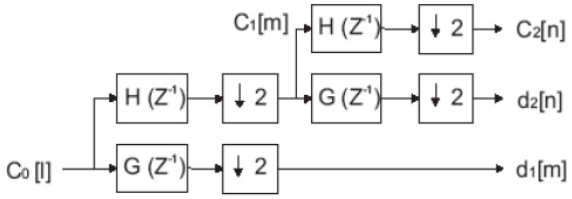

Fig 3. Detail levels DWT.

Where

$$G(z)=(-1)^n H(1-n) \tag{14}$$

These two filters are constructed from the original wavelet function ψ and a scale function ϕ determinated from:

$$\begin{cases}\phi(t)=\sqrt{2}\sum H(n)\phi(2t-n)\\ \psi(t)=\sqrt{2}\sum G(n)\phi(2t-n)\end{cases} \tag{15}$$

The coefficients of the decomposition are known as the wavelet coefficients and are calculated as:

$$c_{j,n}=\sum_m H(2n-m)c_{m,j-1} \tag{16}$$

$$d_{j,n}=\sum_m G(2n-m)c_{m,j-1} \tag{17}$$

Coefficients $c_{j,n}$ represent the low frequency components of the original signal, and $d_{j,n}$ the high frequency components. The low frequency and high frequency coefficients are calculated at j level by convolving the low frequency coefficients at level *j-1*.

The signal is filtered with the low-pass filter H and high-pass filter G. The high-pass coefficients are stored at vector $d_{1,m}$. At level 2, the resulting low-pass filter signal is filtered again, and the resulting high-pass coefficients are stored at vector $d_{2,n}$. The procedure is repeated for an aceptable level of decomposition [20].

The wavelet function determines the ability to identify transient and nonlinear components. There is a match between the "shape" of the nonlinear and transient components with the wavelet function that is originally selected. Thus, it is fundamental to select the most appropriate wavelet function for the type of nonlinear phenomenon under study. The most commonly use wavelet functions are: Haar, Daubechies, Symlet, Coiflet and Meyer.

The goal of the a Discrete Wavelet Transform (DWT) is to decompose any arbitrary signal *y(t)* in a discrete form it will be *y(n)* into an infinite sum of wavelet functions with different scales *s*, and different shift time τ.

IV. Experimental setup

Testing over a bearing were carried out on a tapered bearing model x32306, which is join trhough an shaft to an AC servomotor type SGMGV-44A3A6C (Figure 4), to provide the rotative move.

Fig 4. Motor SGMGV-44A3A6C model.

A dual axis Analog Devices ADXL321 +/-18g, 100 mV/g, 0.5 hz, 2.5 kHz accelerometer were used, which were measured the radial and axial vibrations from bearign (Figure 5).

Fig 5. Radial and axial accelerometers.

Both signals were anti-alias filtered and sampled (15,000 samples/s) with a National Instruments NI-USB 6366 16 bits 2 MS/S data acquisition card connected to a 2.16 GHz Inter Celeron Accer CPU N2840 laptop computer (see Figure 6).

Fig 6. NI USB 6366 and Acer computer.

Experiments were carried out at different ranges of velocity, beginning from a low speed until 3000 RPM, which is the maximum speed. To acquisition of signals, a code was implemented using LabVIEW 2012, basically was programed a code with which we acquired the signals and saving into a .lvm file.

The testing bank consist in a gear box, which has an entry gear that transmit move to an ouput gear, each gear have a tapered bearing, which are shown in figure 7.

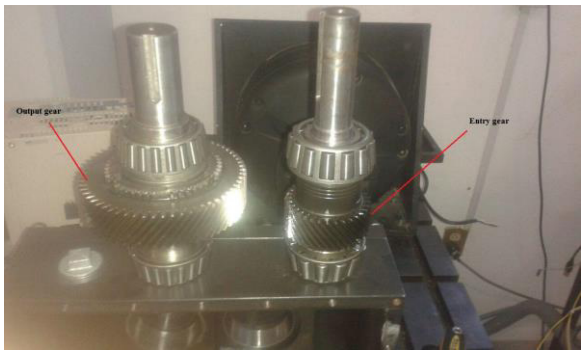

Fig 7. Entry gear and output gear.

The testing bank consist in a gear box, which has an entry gear that transmit move to an ouput gear, each gear have a tapered bearing, which are shown in figure 7.

After that we get the signal and saved into a file, we analized the signal in frequency domain to see the signal spectrum using MATLAB 2014 and then we analized the signal in time-frequency domain using Autosignal 1.7. For the frequency domain we used the FFT and for the time-frequency domain the STFT and the Continuous Wavelet Transform (CWT).

V. Results and discussion

Three experimental test were selected to illustrate the performance of the different purpose methods, is important to mention that the test were did on a bearing which we don't know the fault level, but before long the same test will be conducted on a healthy bearing and in damaged bearing.

A. Test 1

This experiment was chosen because we wanted to see the axial and radial vibration produce by the bearing when the speed is low, the speed which this was used is 250 RPM. The axial and radial measurements are shown in figure 8, this figure shows the difference of amplitude between both signals.

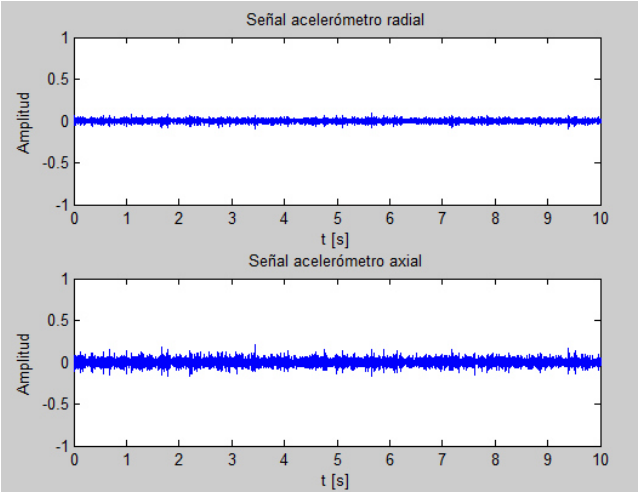

Fig 8. Axial and radial vibration with 250 RPM.

In this test we could see that the axial acceleration is bigger than the radial acceleration but only using the FFT we would obtain information to determinate or not the bearing state.

The figures 9 and 10 shown the spectrum of every singnal, for this analysis, was used MATLAB in where a code was written. The FFT is very used to see the frequential compounds of a signal, this kind of analysis allow us determinate the fundamental frequencies in a bearing but in this document just will help us to compare the differents methdos for signal process. The problem to use the FFT analysis is that we can see the fundamental frequencies of a signal but we don't know when a non-linear behavior presents in a signal, this non-linearities can be represent a failure into a bearing.

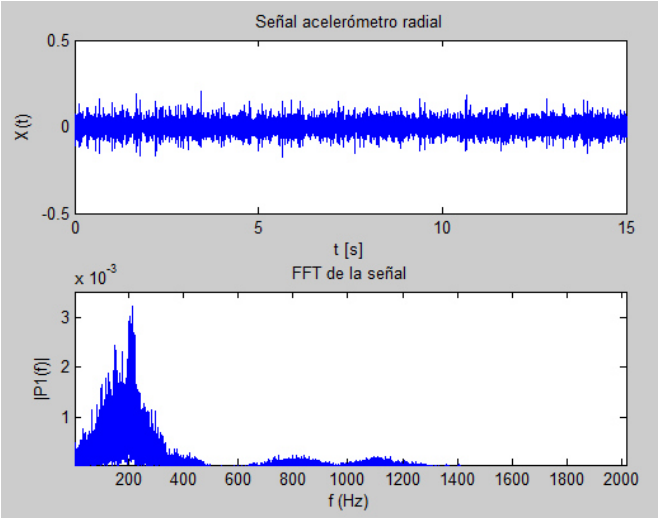

Fig 9. FFT of radial vibration signal.

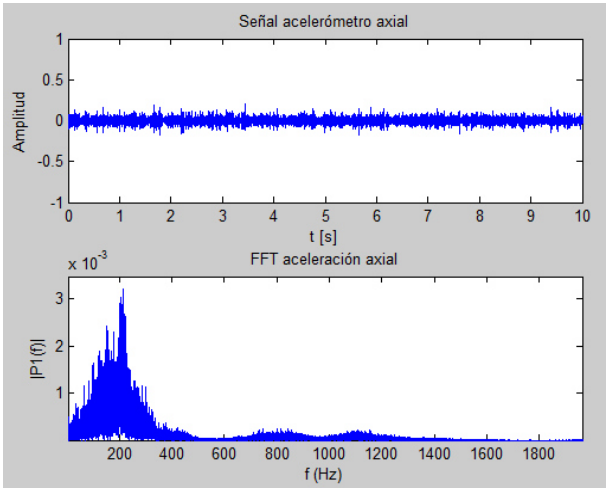

Fig 10. FFT of axial vibration signal.

For the time-frequency analysis two methos were done, the STFT analysis and the CWT analysis. First the STFT was implemented using a Hamming window with a size of 1024 samples that be transform (see figure 11).

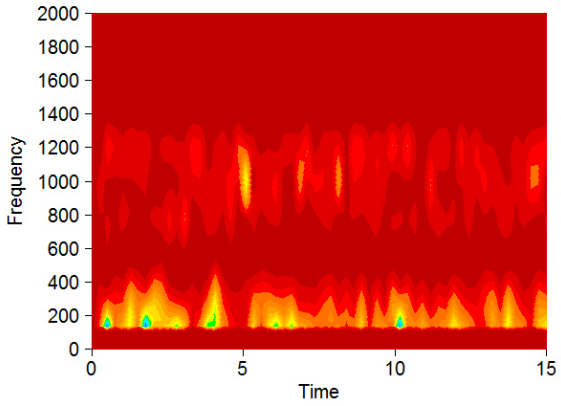

Fig 11. STFT of radial vibration with 250 RPM.

This kind of analysis allow us to see the different frequencies of signal but we don't know when this frequencies occur.

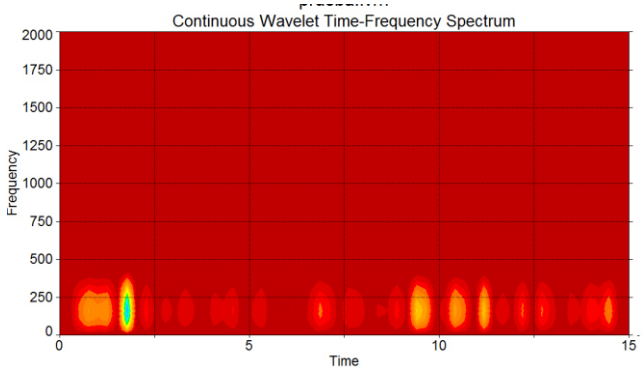

Fig 12. CWT of radial vibration with 250 RPM.

Therefore this time-frequency method is very useful to observe all phenomena that happen into a signal, with this information we can determine if the bearing has any failure.

B. Test 2

For second test the radial and axial acceleration of bearing was obtained, for this test, the rotation speed of motor was 1250 RPM, we observe the behavior of both signal. In figure 13 the axial and radial acceleration can be observed.

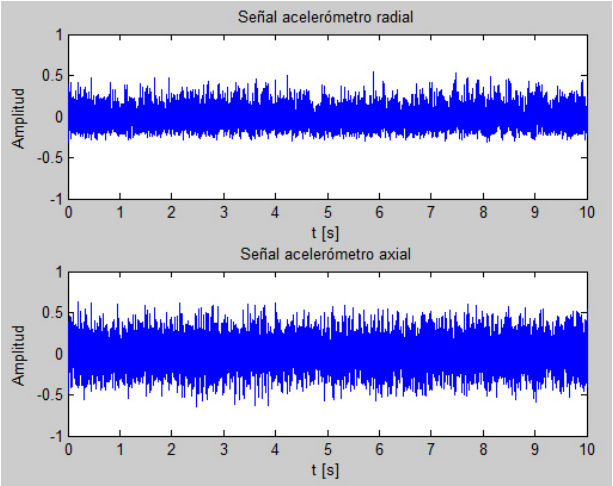

Fig 13. Radial and axial vibration with 1250 RPM.

The signal spectrum of both signals was obtain to see how with a increase of rotation speed the frequencies of signal have change (see Figures 14 and 15).

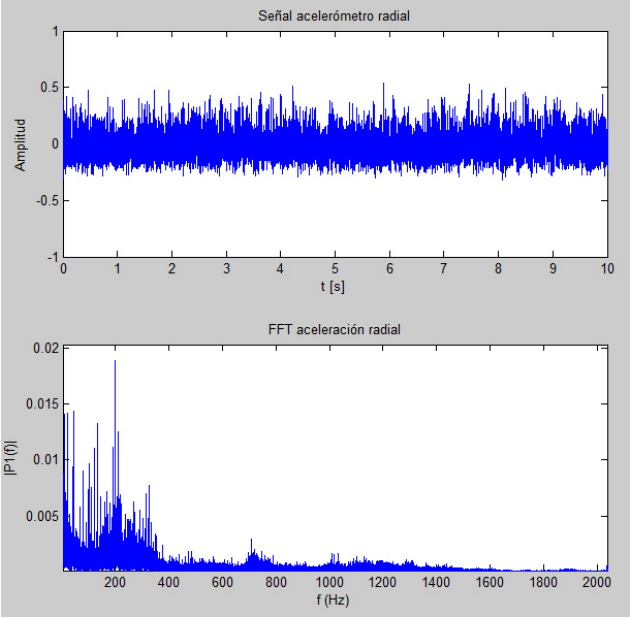

Fig 14. FFT of radial vibration signal with 1250 RPM.

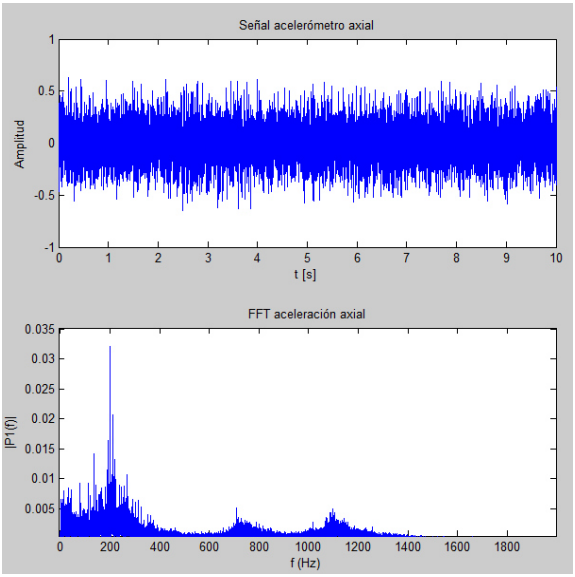

Fig 15. FFT of axial vibration signal with 1250 RPM.

With the spectral analysis we can determine if with the increase of speed, the frequencies of bearing changed too. Unfortunately, we only can see the fundamental frequencies but not when there was a changed, for this reason we use the STFT and CWT to observe this changes. In figure 16 shown the SFTF of radial acceleration.

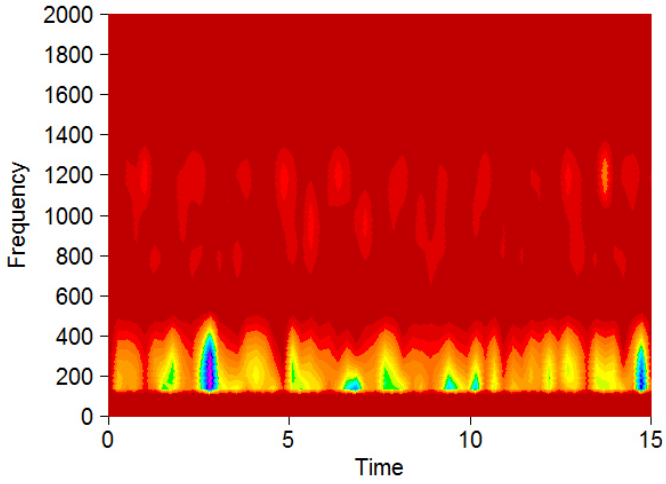

Fig 16. STFT of radial vibration with 1250 RPM.

In this figure, we can see that the signal frequency is nearly to 200 Hz, also can observe how in second three approximately we have a big amount of energy of the signal, this could be a signal of the bearing have a failure, but as we said, the fault level is unknown yet, in next

tests, we will similar test with a healthy bearing and with a damaged bearing to ensure the bearing state.

The STFT have the problem of resolution, we have choose if want time resolution or frequency resolution. The CWT fix this problem and in figure 17 shown this kind of analysis.

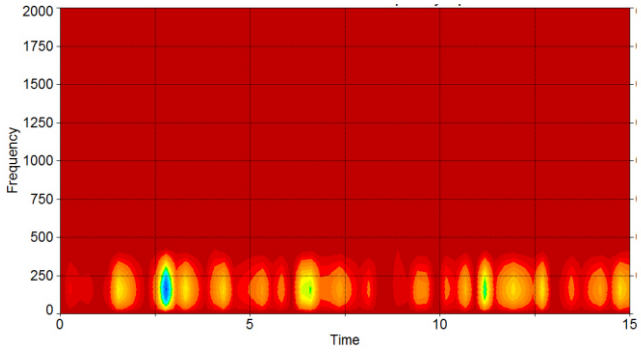

Fig 17. CWT of radial vibration with 1250 RPM.

With the CWT we have a best time-frequency resolution and we can see that in the second three occur a release of energy.

C. Test 3

For third test the radial and axial acceleration of bearing was obtained, for this test, the rotation speed of motor was 2500 RPM, first we supposed that the fundamental frequencies of bearing would have a change or better said, new frequencies appear using a spectral analysis. The results are shown in figures 18 and 19 using a FFT of both signals.

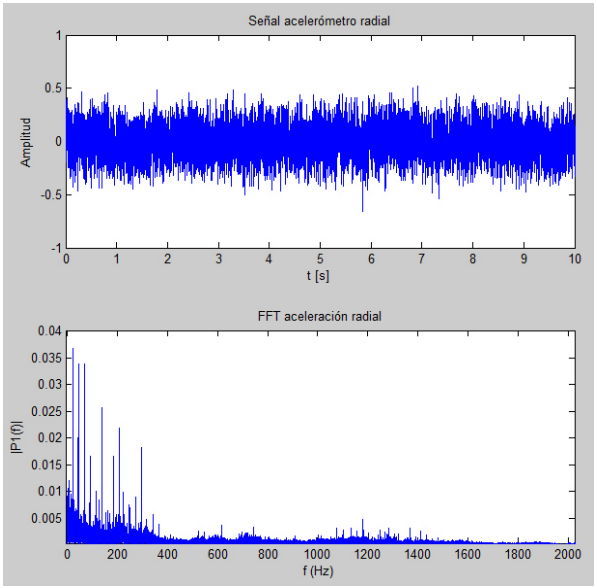

Fig 18. FFT of radial vibration signal with 2500 RPM.

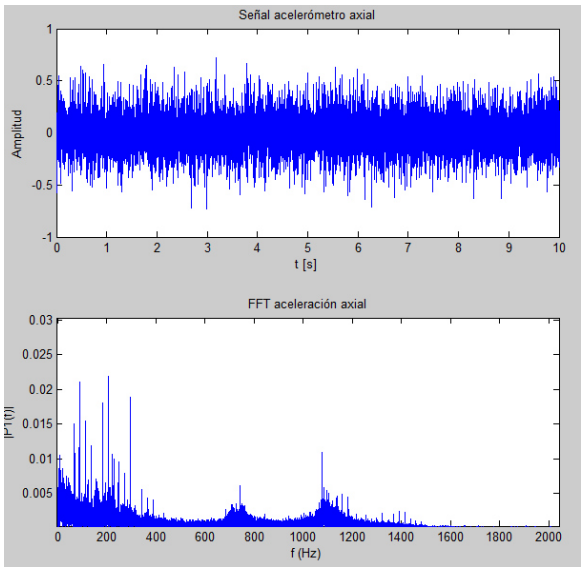

Fig 19. FFT of axial vibration signal with 2500 RPM.

Both radial as axial acceleration, new frequencies appear due to the speed increase. In figure 20 shown the signal analysis using the STFT.

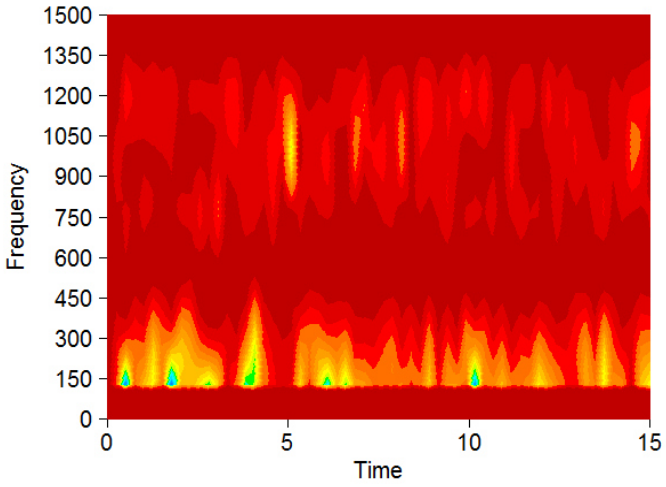

Fig 20. STFT of radial vibration with 2500 RPM.

This test show us that with more rotation speed, the STFT of signal change and the increase of energy in second three disappear and look like the analysis with a low speed. When we use a healthy and damaged bearing, we will can observe the difference of this kind of analysis and determine when can say that a bearing have a failure or the fault level is low. In figure 21 the CWT is shown.

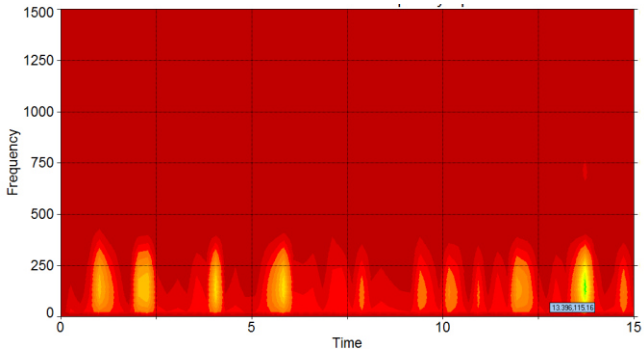

Fig 21. CWT of radial vibration with 2500 RPM.

With this analysis, we can observe the change of frequencies of signal through the time, this figure don't shown a significant change of energy in signal as occur when the speed was 1250 RPM.

VI. Conclusions

In this paper experimental signals were obtained from tapered bearing analysis to identify non-linearities through of time-frequencies methods. The FFT is useful when we want to known what frequencies are involved into the signal but don´t tell us when this frequencies occur, for this reason the time-frequency techniques are more useful to find the frequencies that can show us the moment in where happened this energy release. As were said, the unknowing of state of bearing don´t let us give a better point of view. The STFT is a good tool to analize a signal but have the disadvantage of the selection of a good window size, if the size of windowing function is width, the frequency resolution is good and if the size is narrow, the time resolution is good but we lose frecuencial information. With CWT analysis we can obtain a good results, the morlet function is a good wavelet function because its features are same like the vibrations signal. In a future more analysis will be done to have a better conclusión about this techniques and determine which is the better.

Acknowledgment

Special acknowledgment to CONACYT (Consejo Nacional de Ciencia y Tecnología), for the economic and technical support, also to the Engineering Faculty of Universidad Autónoma de Querétaro, México.

References

[1] N. Tandon and a Choudhury, "A review of vibration and acoustic measurement methods for the detection of defects in rolling element bearings," *Tribol. Int.*, vol. 32, no. 8, pp. 469–480, 1999.

[2] N. Hiremath and D. M. Reddy, "Bearing fault detection using acoustic emission signals analyzed by empirical mode decomposition," pp. 22–25, 2014.

[3] D. P??rez-Canales, J. ??lvarez-Ram??rez, J. C. J??uregui-Correa, L. Vela-Mart??nez, and G. Herrera-Ruiz, "Identification of dynamic instabilities in machining process using the approximate entropy method," *Int. J. Mach. Tools Manuf.*, vol. 51, no. 6, pp. 556–564, 2011.

[4] Y. Yang, X. J. Dong, Z. K. Peng, W. M. Zhang, and G. Meng, "Vibration signal analysis using parameterized time–frequency method for features extraction of varying-speed rotary machinery," *J. Sound Vib.*, vol. 335, pp. 350–366, 2015.

[5] J. Ma and J. C. Li, "Detection of localised defects in rolling element bearings via composite hypothesis test," *Mech. Syst. Signal Process.*, vol. 9, no. 1, pp. 63–75, 1995.

[6] A. Prudhom, J. Antonino-Daviu, H. Razik, and V. Climente-Alarcon, "Time-frequency vibration analysis for the detection of motor damages caused by bearing currents," *Mech. Syst. Signal Process.*, pp. 1–16, 2015.

[7] P. N. Saavedra, "La Medicion Y Analisis De Las Vibraciones Como Tecnica De Inspeccion De Equipos Y Componentes , Aplicaciones ,."

[8] E. Estupiñan and P. Saavedra, "Tecnicas De Diagnostico Para El Analisis De Vibraciones De Rodamientos," 2011.

[9] E. a. Estupiñan and P. N. Saavedra, "Analisis De Vibraciones Aplicado a Las Maquinas Rotatorias De Baja Velocidad," 2008.

[10] A. Moazen Ahmadi, D. Petersen, and C. Howard, "A nonlinear dynamic vibration model of defective bearings – The importance of modelling the finite size of rolling elements," *Mech. Syst. Signal Process.*, vol. 52–53, pp. 309–326, 2015.

[11] T. G. Q. S. Quiroga J. E., "Estudio de fallas incipientes en rodamientos usando la técnica de la envolvente y cepstrum.," *Ingeniare. Rev. Chil. Ing.*, vol. 20, no. 3, pp. 350–359, 2012.

[12] H. Sandoval, C. a. Pedraza Ramirez, and J. E. Quiroga Mendez, "Acoustic emission-based early fault detection in tapered roller bearings.," *Rev. Ing. e ...*, vol. 33, no. 3, pp. 5–10, 2013.

[13] M. Zhao, X. Jin, Z. Zhang, and B. Li, "Fault diagnosis of rolling element bearings via discriminative subspace learning: Visualization and classification," *Expert Syst. Appl.*, vol. 41, no. 7, pp. 3391–3401, 2014.

[14] S. M. A. Al-Obaidi, M. S. Leong, R. I. R. Hamzah, and a. M. Abdelrhman, "A Review of Acoustic Emission Technique for Machinery Condition Monitoring: Defects Detection &

Diagnostic," *Appl. Mech. Mater.*, vol. 229–231, pp. 1476–1480, 2012.

[15] J. Chen, Z. Li, J. Pan, G. Chen, Y. Zi, J. Yuan, B. Chen, and Z. He, "Wavelet transform based on inner product in fault diagnosis of rotating machinery: A review," *Mech. Syst. Signal Process.*, pp. 1–35, 2015.

[16] B. Eftekharnejad, M. R. Carrasco, B. Charnley, and D. Mba, "The application of spectral kurtosis on Acoustic Emission and vibrations from a defective bearing," *Mech. Syst. Signal Process.*, vol. 25, no. 1, pp. 266–284, 2011.

[17] K. Gurumoorthy and A. Ghosh, "Failure investigation of a taper roller bearing: A case study," *Case Stud. Eng. Fail. Anal.*, vol. 1, no. 2, pp. 110–114, 2013.

[18] J. Luis, F. Chacon, V. Kappatos, W. Balachandran, and T. Gan, "A novel approach for incipient defect detection in rolling bearings using acoustic emission technique," *Appl. Acoust.*, vol. 89, pp. 88–100, 2015.

[19] O. Rioul and M. Vetterli, "Wavelets and Signal Processing," *IEEE Signal Processing Magazine*, vol. 8, no. 4. pp. 14–38, 1991.

[20] G. Ghodrati Amiri and a. Asadi, "Comparison of different methods of wavelet and wavelet packet transform in processing ground motion records," *Int. J. Civ. Eng.*, vol. 7, no. 4, pp. 248–257, 2009.

Influence of drought in the accumulation of nutraceuticals in (*Capsicum annuum*) var. Revolution

Vargas-Hernández, Marcela., Torres-Pacheco, Irineo., Feregrino-Perez, Ana A., Jiménez-García, Sandra N., García-Mier, Lina., Macias-Bobadilla, Israel., Guevara-González, Ramón G.

Facultad de Ingeniería, Campus Amazcala.
Universidad Autónoma de Querétaro.
Querétaro, México.
marcela.vhz@gmail.com

Abstract— *Capsicum annuum* is the most widely cultivated species of peppers worldwide. It is an important source of secondary metabolites which have a wide variety of biological activities such as antioxidant, antimutagenic, antimicrobial, and antifungal, among others. The production of these compounds can be enhanced by applying Metabolite Modifying Factors (MMFs). The aim of this study was to evaluate whether the application of a physical MMFs in pepper plants increases the amount and antioxidant properties of nutraceuticals. To which, we implemented a pepper production system under the effect of 50% drought as MMF. Methanolic extracts were obtained to identify nutraceuticals compounds. Antioxidant capacity was measured by spectrophotometric techniques DPPH and ABTS. This experiment showed a significative increase of the level of phenolic compounds under the influence of drought treatment. Also an increase of flavonoids and tannins is observed but is non-significant (α>0.05). Finally, drought treatment showed higher antioxidant activity for the method of ABTS with 96.04 ±2.06 % of inhibition but non-significant difference (α>0.05) was observed.

Keywords— MMFs, nutraceuticals, pepper, antioxidant.

I. INTRODUCTION

Chili pepper (*Capsicum annuum* L.) is one of the most important cultivars arround the world. México is the second largest pepper producer [1]. The origin of domesticated chili pepper, is Mexico [2], where the phenotypic diversity of pepper cultivars include pungent and non-pungent species. It is an important source of secondary metabolites having a function as nutraceuticals due to its wide variety of biological activities such as antioxidant, antimutagenic, antimicrobial, and antifungal, among others. Studies indicated that diverse secondary metabolites are synthetized by plants when recognize several enviromental factors, defined as Metabolite Modifying Factors (MMFs), which are divided into biotic or abiotic [3]. Within the abiotic MMFs include the temperature, pH, UV radiation and drought. Studies evaluated the influence of drought stress in pungent pepper cultivars reported an increase in secondary metabolites including the capsaicinoid content [4, 5]. On the other hand, an increase of nutraceuticals has also been observed in non-pungent species under the influence of chemical MMFs [6]. However, the antioxidant capacity of the methanolic extracts of *Capsicum annum* var Revolution was not yet determined. Therefore, the objective of this investigation was to study the influence of an abiotic MMF on the nutraceuticals levels and antioxidant capacity of *Capsicum annum* var. Revolution peppers.

II. METHODOLOGY

A. Implementation of chili production under greenhouse conditions .

The pepper crop was established in a greenhouse of 108 m^2, located in the Amazcala campus of the Universidad Autónoma de Querétaro, between 20° 31'and 20° 58' latitude and between 100° 09' and 100° 24' altitude to 1850m above sea level.

B. Treatment application.

The treatment consists of a daily irrigation decreased to half (Table 1). As experimental control chile pepper plants with normal irrigation was studied.

TABLE I. AMOUNT OF WATER FOR IRRIGATION

Stage	Irrigation[a]				
	Time at 100% (min)	Time at 50% (min)	Number	Total at 100% (ml)	Total at 50% (ml)
Vegetative	2	1	3	600	300
Flowering	2	1	5	1000	500
Fructification	2	1	6	1200	600

[a]All treatments were carried out by triplicate

C. Fruit extracts of chili in post-harvest stage

Three months after transplantation in greenhouse, the fruits were harvested. Peppers began to freeze with liquid nitrogen and ground with dry ice and it was stored at -80 °C until further use. The solvent extraction process is carried out by maceration using methanol as a solvent in a ratio of 1:10 fresh matter and methanol respectively. The concentration of the methanol extract was performed in a Heidolph rotary evaporator at a temperature of 40°C in order to prevent degradation of the compounds.

D. Total phenolic compounds

Total phenolics were determined by the Folin Ciocalteu method [7]. The dissolution of the extracts used for the tests was as follows: 10 mg of the extract was weighed and diluted

with 1 ml of reagent grade methanol. The calibration curve was prepared from a gallic acid standard solution (0.1mg / ml), a volume of 0 to 160 µl were taken at intervals of 20 µl and distilled water was added to reach a volume of 500 µl. Briefly, 40 µl of the sample was put in vials and after 460 µl of distilled water was added and oxidized with 250 µl of Folin-Ciocalteu reagent (1N), after 5 min 1.25 ml of Na_2CO_3 (20%) solution was added to neutralize. Mixture was incubated for 2h without agitation. In a 96 well plate 200 µl of each sample or methanol (white) will be added, the absorbance was measured against a reference 760 nm in a Spectra Max micoplaca reader (Molecular Devices Co., Sunnyvale, USA). The concentrations are reported as milligrams of gallic acid equivalents per ml of extract.

E. Flavonoid content

Flavonoid determination was carried out by the method described by Liu et al (2002) [8] using as a standard routine. The calibration curve consisted of a routine solution at the following concentrations: 0, 2, 5, 10, 25, 50, 100, 150 and 200 µg/ml. For the assay in a 96 well plate 50 µl of each of the samples were placed, subsequently 200 µl of a solution of 2-aminodifenilborato 1% was added as control methanol was used. Absorbance was determined at 404 nm in a reader micoplaca. Versa Spectra Max (Molecular Devices Co., Sunnyvale, USA). Concentrations are reported as milligrams equivalent routine ml extract.

F. Determination of the antioxidant capacity of the methanol extracts

ABTS. This test was conducted according to the methodology described by Nenadis et al., (2004) [9]. For the standard curve Trolox solution is used at a concentration of 50,100, 200, 300, 400, 500, 600, 700 and 800 µmol. To generate the radical ABTS + a stock solution of ABTS 7mM is generated. To 5 ml of the aqueous solution, 88 µl of potassium persulfate ($K_2S_2O_8$) 140 mM was added and stored in the dark for 12 h. The solution containing the radical is measured at = 734 nm and diluted in ethanol (20 to 25 mL) until the absorbance value reaches a value less than 1.0. The samples were prepared in a 96 well plate: 20 µl of the sample was added to 230 µl of etanol, 20 µl of methanol (C1) and distilled water is added (C2) as controls, finally 230 µl of ABTS + was added to the samples. The absorbance measurement was carried out at 730 nm for a period of 0-6 min.

DPPH. The assay was performed in a 96 well plate, first 20 µl of the extracts was first added and then 200 µl of DPPH at 80% with methanol as dissolvent, for the positive control Trolox was used for all negative reagents except extracts. 520 nm absorbance was measured at different times (0, 4, 10, 30, 60, 90 and 120 min). Results were reported as % ARA (antiradical capacity).

G. Statistic analysis

Analysis of variance (ANOVA) was performed with the Statistical Software STATGRAPHICS ® Centurion XV.

III. RESULTS AND DISCUSSION

A. Total phenolic compound, flavonoids and tanins

The conditions of drought stress showed a significant increase in the amount of phenolic compounds 15.66 ± 0.74[a] GAE, and also increase the amount of flavonoids but with no significant difference were observed between control and treatment (Table II); however, a decrease in the content of tannins is observed which means that drought MMF treatment induce a modification of the secondary metabolite synthesis turning up some signaling pathways and suppressing others.

TABLE II. TOTAL PHENOLIC COMPOUNDS, FLAVONOIDS AND TANNINS PER GRAM OF DRY EXTRACT.

Treatment	Table Column Head		
	Phenolic compounds*	Flavonoids**	Tanins***
Control	13.03±0.27[b]	9.28±1.05[a]	7.34±0.50[ab]
50% drought	15.66±0.74[a]	9.53±0.26[a]	9.69±1.02[a]

* Phenol concentration in mg gallic acid equivalents (GAE) / g extract

** Concentration of flavonoids in mg equivalent of (+) - routine (RE) / g extract

*** Tannin concentration in mg equivalent of (+) - catechin (EC) / g extract

The results are the average of 3 independent experiments ± SD. The letters indicate significant difference between treatments (α>0.05).

B. Determination of antioxidant capacity in methanolic extracts

Finally, also antioxidant activity shows no significant difference between control and drought treatment. (Table III).

TABLE III. ANTIOXIDANT ACTIVITY.

Treatment	ABTS		DPPH	
	Trolox µM	%ARA	Trolox µM	%ARA
Control	292.63 ±4.00[a]	95.57 ±1.29[a]	571.76 ±0.81[a]	73.33 ±0.11[a]
50% drought	294.07 ±6.35[a]	96.04 ±2.06[a]	565.34 ±23.22[a]	71.49 ±6.05[a]

The antioxidant capacity of ABTS and DPPH is reported as mol Trolox equivalent (TE) / 10 g of extract and percentage inhibition (% anti radical activity)

The results are the average of 3 independent experiments ± SD. The letters indicate significant difference between treatments (α>0.05).

The bioactivity of plant extracts is determinated by the diversity of their secondary metabolites. The antioxidant capacity is not only related to the amount of phenolic compounds but also depends on the structure that they present [10]. All of the foregoing indicates that although no significant difference in antioxidant capacity of the pepper extracts treated with an abiotic MMF were found, the highest amount of phenolic compounds and tannins can confer other biological activities in their extracts. For example, antimicrobal activity which is reported being induced in Habanero pappers under the influence of chemical MMFs [11].

IV. CONCLUSSION

Application of water stress as abiotic Metabolism Modifying Factor in chili pepper plants (*Capsicum annuum*) var. Revolution increase the amount of bioactive compounds in their fruits and therefore can improve their nutraceutical properties.

REFERENCES

[1] FAOSTAT, 2015.

[2] K.H. Krafta, C. H. Brownb, G. P. Nabhanc, E. Luedelingd, J. J. Luna Ruize, G. C. d'Eeckenbruggef, R. J. Hijmansg and P.Geptsa, "Multiple lines of evidence for the origin of domesticated chili pepper, *Capsicum annuum,* in Mexico," PNAS. vol. 111,| no. 17, April, 2014, pp. 6165–6170.

[3] I. Torres-Pacheco, R. G. Guevara-González, L. Mejía-Teniente, A. M. Chapa Oliver, "Relación de la Inmunología Vegetal y la Producción de Alimentos," CIENCIA@UAQ, vol. 5 num.1, 2012, pp.1-7.

[4] N. Ruiz-Lau, F. Medina-Lara, Y. Minero-García, E. Zamudio-Moreno, A. Guzmán-Antonio, I. Echevarría-Machado and M. Martínez-Estévez. "Water Deficit Affects the Accumulation of Capsaicinoids in Fruits of Capsicum chinense Jacq.," HortScience, vol. 46 no. 3 march 2011, pp. 487-492.

[5] S. E. Gaikwad, R. A. Shinde, R. B. Thoke and V. T. Aparadh. "Potential of drought stress in two varieties of *Capsicum annum* grown in Maharashtra", IJRPC, vol. 3 no. 2., 2013, pp. 303-307.

[6] L. Garcia-Mier, S. Neli Jimenez-García, R. Gerardo Guevara-González, A. A. Feregrino-Pérez, L. M. Contreras-Medina and I. Torres-Pacheco, "Elicitor Mixtures Significantly Increase Bioactive Compounds, Antioxidant Activity, and Quality Parameters in Sweet Bell Pepper", Journal of chemistry, December 2015, pp. 173–181.

[7] V. Dewanto, X. Wu, K. Adom, R. Liu, "Thermal processing enhances the nutritional value of tomatoes by increasing total antioxidant activity". Journal Agricultural and Food Chemistry. vol. 50, 2002, pp. 3010-3014.

[8] M. Liu, X. Qi, C. Weber, C. Yong, J. Brown, R. Hai, 2002. "Antioxidant and antiproliferative activities of raspberries ". Journal Agricultural and Food Chemistry. vol, 50, 2002, pp. 2926-2930.

[9] N- Nenadis, L. F. Wang, M. Tsimidou, H. Y. Zhang, "Estimation of scavenging activity of phenolic compounds using the ABTS(*+) assay." J Agric Food Chem. vol, 52 no. 15, 2014, pp.4669-74.

[10] E. Bendary, R.R. Francis, H.M.G. Ali, M.I. Sarwat, S. El Hady. "Antioxidant and structure–activity relationships (SARs) of some phenolic and anilines compounds," Annals of Agricultural Sciences vol. 58 no. 2, Dec 2013; pp. 173–181.

[11] M. Vargas-Hernández, I. Torres-Pacheco, B. Álvarez-Mayorga, A. Cruz-Hernández, L. García-Mier, S. N. Jiménez-García, R. V. Ocampo-Velázquez, A. A. Feregrino-Perez and R. G. Guevara-Gonzalez. "Influence of Hydrogen Peroxide Foliar Applications on in vitro Antimicrobial Activity in Capsicum chinense Jacq.," Plant Biosystems, 2016, "in press".

Path Tracking Simulation for a Two-Degree-of-Freedom Pneumatic Manipulator Robot

Sergio-Daniel Sánchez-Solar*, Jesús-Carlos Pedraza-Ortega†, Efrén Gorrostieta-Hurtado‡ and Juan-Manuel Ramos-Arreguín§

*Universidad Autónoma de Querétaro, Facultad de Informática; e-mail: ssanchez37@alumnos.uaq.mx
†Universidad Autónoma de Querétaro, Facultad de Ingeniería; e-mail: caryoko@yahoo.com
‡Universidad Autónoma de Querétaro, Facultad de Ingeniería; e-mail: efrengorrostieta@gmail.com
§Corresponding Author: Universidad Autónoma de Querétaro, Facultad de Ingeniería; e-mail: jramos@mecamex.net

***Abstract*—Nowadays, Robotics is a broad field of research, mainly when it comes to pneumatic robots due to its high nonlinearity. Most works have been developed using electric or hydraulic actuators, there are few works that use pneumatic actuators, this is the principal reason to develop a tool that permits to simulate the behaviour of the manipulator before the physical implementation, it permits to the user to have an idea about the response of the manipulator. In this paper a simulation software for a Two-Degree-of-Freedom Pneumatic Manipulator Robot is presented, using OpenGL libraries for developing the simulator and C++ to calculate the interpolation among the points that are given as input. Matlab is used to calculate the direct and inverse kinematics to find the angles and positions that the manipulator must reach and to obtain the response of the system after the control is applied. Matlab also process the control that is applied to the system to be capable of reaching the points that were established as set-points.**

***Keywords*—Pneumatic Manipulator, Path Tracking, OpenGL Simulation, PID Controller.**

I. Introduction

Pneumatic Actuator Systems have a lot of properties such as, cheapness and cleanness in comparison to hydraulic actuators. Pneumatic actuators present more durability and they are lighter than others. This set of features has made pneumatic actuators very attractive for different applications, mainly in robotics [1].

In the other hand, pneumatic actuators present high non-linearities that make them hard to control, these non-linearities are related to compressibility of the air, the time delay provoked by the slow propagation of the air pressure waves, and the associated large friction forces [2]. Some researches present a simplified termo-mechanical model for pneumatic actuators, so it is necessary to obtain the dynamical model of the manipulator [3], and the dynamic behaviour of a pneumatic manipulator [4].

To track trajectories, is necessary to solve two main problems, trajectory planning and trajectory control [5]. It is very important to select an appropriate method that describes the trajectory that the manipulator has to follow in order to obtain a curve that fits to the original path, that is the reason for using some interpolation techniques that approximate the trajectory to the original curve.

In this paper a simulator of a Two-Degree-of-Freedom Manipulator Robot is presented, it is using a polynomial interpolation technique known as Splines that permits to obtain intermediate points from a few points given to generate a curve that the system will follow. The equations to obtain the direct and inverse kinematics, useful to obtain the points of the final position and the angles of the links, are also presented. The control that is applied to the system was developed in [6]. The morphology of the manipulator robot is similar to the used in [7] but a rotational degree is added using a pneumatic motor.

II. Kinematic Equations

It is necessary to know the kinematic equations that describe the system, they are presented in the following subsections. The system that is being controlled is shown on Fig. 1.

A. Inverse Kinematics

When the points that the manipulator must reach are given, it is necessary to get the angles that the links have to take to be able to go to those points.

Equation (4) is used to obtain the rotation angle in relation to z axis. Equations (5) and (6) represents the angles θ_2 and θ_3 in relation to the xy plane. In equation (2) and (3), α and β are auxiliary angles that permit to obtain the angle θ_2. Using Pythagoras theorem, the helper line L_a is calculated.

$$L_a = \sqrt{L_2^2 + L_3^2} \tag{1}$$

$$\alpha = sin^{-1}(\frac{h}{L_a}) \tag{2}$$

$$\beta = cos^{-1}(\frac{L_2}{L_a}) \tag{3}$$

$$\theta_1 = tan^{-1}(\frac{y_p}{x_p}) \tag{4}$$

$$\theta_2 = \alpha + \beta \tag{5}$$

$$\theta_3 = \theta_2 - \frac{\pi}{2} \tag{6}$$

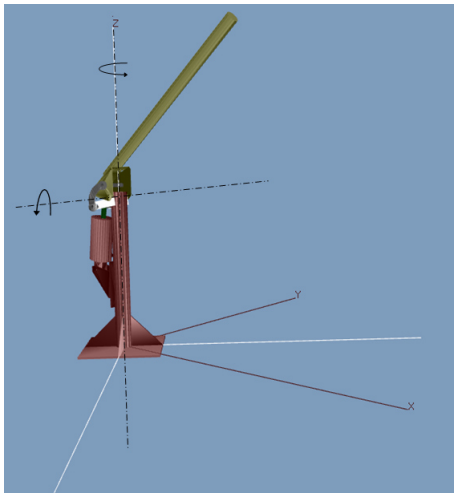

Fig. 1. Pneumatic Manipulator

B. Direct Kinematics

Direct kinematic equations (8-10) are used to obtain the Workspace of the manipulator, this means the area that can be reached by the robot.

$$\theta_2 = \theta_3 + \frac{\pi}{2} \tag{7}$$

$$x_p = (L_2 cos\theta_2 + L_3 cos\theta_3)cos\theta_1 \tag{8}$$

$$y_p = (L_2 cos\theta_2 + L_3 cos\theta_3)sin\theta_1 \tag{9}$$

$$z_p = L_1 + L_2 sin\theta_2 + L_3 sin\theta_3 \tag{10}$$

III. Workspace

Using the direct kinematic equations and specifying the movement limitations of the pneumatic manipulator (Table I), it is possible to obtain the Workspace of the system that is shown on Fig. 2.

TABLE I
Actuator Restrictions

Actuator	Minimum Value	Maximum Value
Motor	$0°$	$270°$
Cylinder	$-72°$	$86°$

The next algorithm is used to obtain the Workspace of the Manipulator:

Algorithm 1 receives the length of each link of manipulator and angles θ_1, and θ_3 (Lines 2 and 3) as inputs and an index i (Line 1) that indicates the number of data that is being obtained as output for each coordinate x_p, y_p and z_p (Lines 5, 6 and 7).

Algorithm 1 Algorithm to obtain the Workspace

Require: $i, \theta_1, \theta_3, L_1, L_2, L_3$
Ensure: x_p, y_p, x_p
1: $i = 1$
2: **for** $\theta_1 = Motor_{min} : Motor_{max}$ **do**
3: **for** $\theta_3 = Cylinder_{min} : Cylinder_{max}$ **do**
4: $\theta_2 = \theta_3 + \frac{\pi}{2}$
5: $x_p(i) = (L_2 cos\theta_2 + L_3 cos\theta_3)cos\theta_1$
6: $y_p(i) = (L_2 cos\theta_2 + L_3 cos\theta_3)sin\theta_1$
7: $z_p(i) = L_1 + L_2 sin\theta_2 + L_3 sin\theta_3$
8: $i = i + 1$
9: **end for**
10: **end for**

On each iteration the angle θ_2 is calculated such as in Line 4 considering that the angle that is composed by L_2 and L_3 is a right angle, this means that they both have the reason shown in direct kinematics.

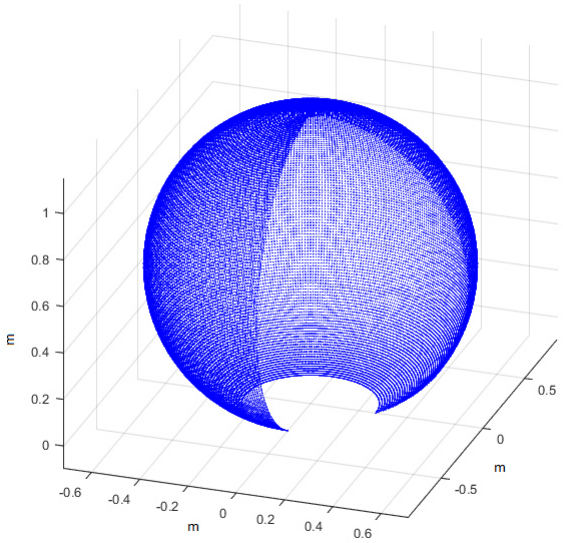

Fig. 2. Workspace of 2DOF Manipulator

IV. Path Tracking

In this section a Splines algorithm to interpolate the points that the Robot must reach is implemented. Cubic Splines are being used due to their smoothness in comparison to other interpolation techniques, such as Newton or Lagrange [8]. Splines is a method used to fit a series of unique cubic polynomials between each of the data points and let the curve obtained be continuous and appear smooth [9].

Given $n + 1$ data:

x	x_0	x_1	...	x_n
y	y_0	y_1	...	y_n

A cubic spline that interpolates these points, is a function $S(x)$ defined as follow:

$$s(x) = \begin{cases} s_0(x) & if \quad x \in [x_0, x_1] \\ s_1(x) & if \quad x \in [x_1, x_2] \\ \vdots & \\ s_{n-1}(x) & if \quad x \in [x_{n-1}, x_n] \end{cases} \tag{11}$$

where s_i is a third degree polynomial defined by:

$$s_i(x) = a_i(x - x_i)^3 + b_i(x - x_i)^2 + c_i(x - x_i) + d_i \tag{12}$$

for $i = 1, 2, 3, ..., n-1$. The first and second derivatives of these n-1 equations are fundamental to this process, and they are

$$s_i' = 3a_i(x - x_i)^2 + 2b_i(x - x_i + c_i) \tag{13}$$

$$s_i'' = 6a_i(x - x_i) + 2b_i \tag{14}$$

for $i = 1, 2, ..., n-1$.

For the development of this work, the points given were:

x	-0.1	0.1	0.2	0.4
y	-0.1	0.1	0.5	-0.2
z	1.13853	1.13853	0.871101	0.977196

And the resultant curve of the splines interpolation is shown on Fig. 3.

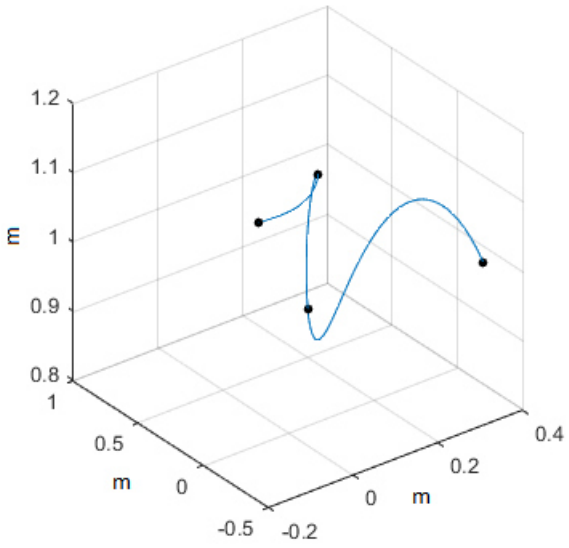

Fig. 3. Result of Cubic Splines Interpolation

V. Termo-mechanical Model

In [10] the following simplified termo-mechanical model is presented (15-24):
For the interval $0 \leq X \leq L$:

$$\dot{X} = \frac{d}{dt}X \tag{15}$$

$$D\dot{X} = \frac{d^2}{dt^2}X \tag{16}$$

For the interval $0 \leq X \leq L_{alp}$:

$$\dot{P}_{a1} = g_{21}(X)(\dot{m}_{a1} - \dot{m}_{c1} - 9.176 \times 10^{-10} P_{a1} DX) \times 10^8 \tag{17}$$

$$\dot{P}_{c1} = g_{31}(X)(\dot{m}_{c1} - 3.608 \times 10^{-8} P_{c1} DX) \times 10^6 \tag{18}$$

For the interval $L_{alp} < X \leq L$:

$$\dot{P}_{a1} = g_{22}(X)(\dot{m}_{a1} - 3.7 \times 10^{-8} P_{a1} DX) \times 10^{11} \tag{19}$$

$$\dot{P}_{c1} = g_{32}(X)(\dot{m}_{c1} - 3.7 \times 10^{-8} P_{c1} DX) \times 10^{11} \tag{20}$$

For the interval $0 \leq X \leq (L - L_{alv})$:

$$\dot{P}_{c2} = g_{41}(X)(\dot{m}_{c2} + 3.469 \times 10^{-8} P_{c2} DX) \times 10^{11} \tag{21}$$

$$\dot{P}_{a2} = g_{51}(X)(\dot{m}_{a2} + 3.469 \times 10^{-8} P_{a2} DX) \times 10^{11} \tag{22}$$

For the interval $(L - L_{alv}) < X \leq L$:

$$\dot{P}_{c2} = g_{42}(X)(\dot{m}_{c2} + 3.352 \times 10^{-8} X_4 X_6) \times 10^{13} \tag{23}$$

$$\dot{P}_{a2} = g_{52}(X)(9.983 \times 10^3 (\dot{m}_{a2} - \dot{m}_{c2}) + 1.168 \times 10^{-5} X_5 X_6) \times 10^4 \tag{24}$$

VI. Control of the Pneumatic Manipulator

Fig. 4 shows the mechanical-pneumatic system used to generate the movement of the manipulator.

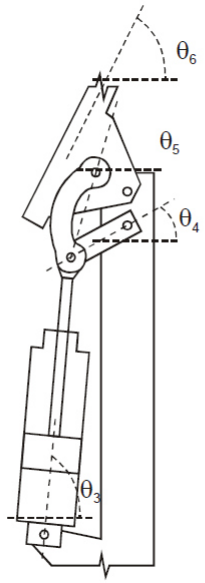

Fig. 4. Mechanical-Pneumatic System for the Pneumatic Manipulator

The displacement of the rod is what must be controlled, because it produces the output angle θ_6 of the impulse mechanism and it affects directly the movement of the final link of the manipulator.
The control that is implemented in this system is a PID control developed in [6] . The inputs of the Termo-mechanical model are the free effective area of the air flow and are shown in (25).

$$u = [A_1, A_2, A_3] \tag{25}$$

Where:
$A_1 \rightarrow$ The effective area the air flow in the base of the cylinder.
$A_2 \rightarrow$ The effective area the air flow in the rod.
$A_3 \rightarrow$ The effective area for air flow return.

The diagram of control that represents the system is shown in Fig. 5, where (e) is the error vector entering the PID controller algorithm that gives the opening percentage vector (u), that enter the pneumatic actuator system and generate the displacement of the rod (X), and this gives the enough force to generate the movement of the manipulator and to obtain the output of the plant (θ).

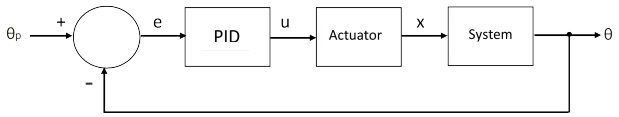

Fig. 5. Control of the angle θ of the pneumatic manipulator

Equation (26) and (27) give as result the values of (25) and they shows the control equation of each valve and the error vector.

$$e = [e_p, e_i, e_d] \tag{26}$$

$$A_j = K_p e_p + K_i e_i + K_d e_d \tag{27}$$

In (27) $j = 1, 2, 3$ indicates the valve to be controlled. K_p, K_i and K_d are the proportional, integral and derivative constants, shown in Table II. e_p, e_i and e_d are the proportional, integral and derivative errors that can be obtained from (28-30).

$$e_p = \theta_p - \theta \tag{28}$$

$$e_i = \sum_i e(T_i) \tag{29}$$

$$e_d = e(T_i) - e(T_{i-1}) \tag{30}$$

TABLE II
CONTROL VALUES USED IN PID CONTROLLER

Valve	K_p	K_i	K_d
A_1	4.00	0.0	100.0
A_2	-4.00	0.0	-100.0
A_3	0.45	0.0	0.0

VII. RESULTS

Using the graphic interface developed in OpenGL and C++ [11], it is necessary to add the trajectories obtained from the interpolation algorithm and kinematic equations, because of the computational cost of these operations, they are processed in Matlab because it has a better performance working with matrix operations. The result of the previous operations is saved in a text file and loaded into the simulator program. Resultant movement in degrees of the pneumatic motor is displayed in Fig. 6. The movement described for the second link of the manipulator in degrees is shown in Fig. 7.

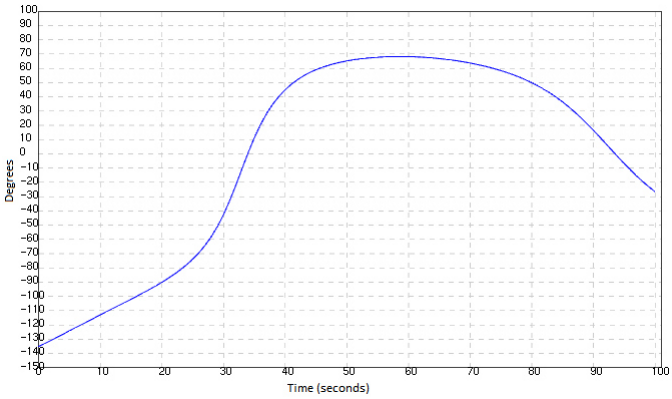

Fig. 6. Movement of the motor according to interpolation

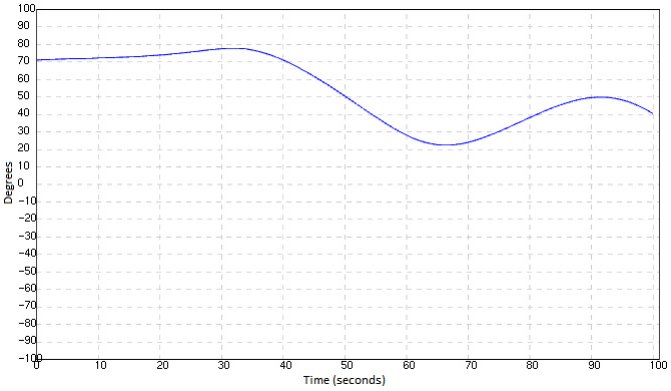

Fig. 7. Movement of the second link of the manipulator according to interpolation

After obtaining these graphics, the next step is to implement the control algorithm developed in [6] to obtain the real behaviour of the pneumatic cylinder considering the simplified

termo-mechanical model and PID controller. The result is presented in Fig. 8. In this case, the behaviour of the pneumatic motor is the same than in Fig. 6 due to its termo-mechanical model and dynamics have not been already obtained.

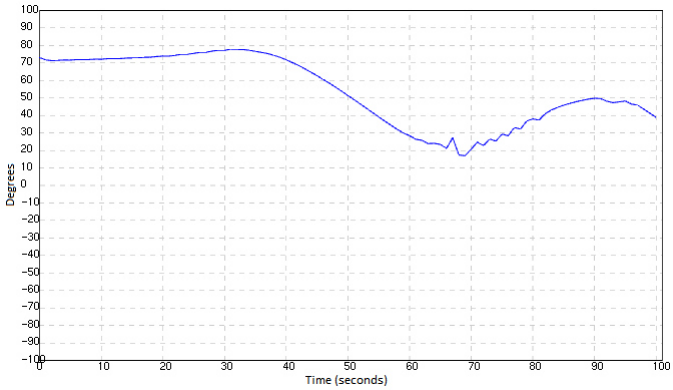

Fig. 8. Movement of the second link of the manipulator considering termo-mechanical model and applying PID control

Fig. 9 shows an interpolated trajectory of 4 points with 50 intermediate points generated between the first point and the last point. It is observed that after applying the controller, the response obtained approaches the reference trajectory but when the displacement of the rod moves out of the cylinder, it does not achieve it, and when it moves into the cylinder, it presents oscillations that are undesired.

In Fig. 10 the number of intermediate points is increased to 100 points and it is observed that when controller is applied the rod reaches the set point, but when the displacement changes its direction there are overshoots of up to 30 percent of the desired value and they remain during the rest of the movement, and this can affect the manipulator due to the limitations of the system, for example, the maximum displacement of the rod.

On the other hand, in Fig. 11 the number of intermediate points of the interpolation is increased to 500, and the response of the system after controller is applied is smoother and is more in line with the set-point given as reference. This behaviour is more convenient to the system because it does not present overshoots or oscillations that would not be acceptable to a specific application and could damage the system or even the operator.

In Fig. 12 an image that shows the simulator developed in OpenGL and C++ is presented, the coordinates x_p, y_p and z_p of the final effector are displayed, and the angles of each link. In the simulator the trajectory generated is shown, this permits to the user to supervise that the trajectory that is being followed corresponds to the established one. It is controlled by keys from the keyboard that allows to rotate the manipulator and the axis, and to execute the animation of the path tracking.

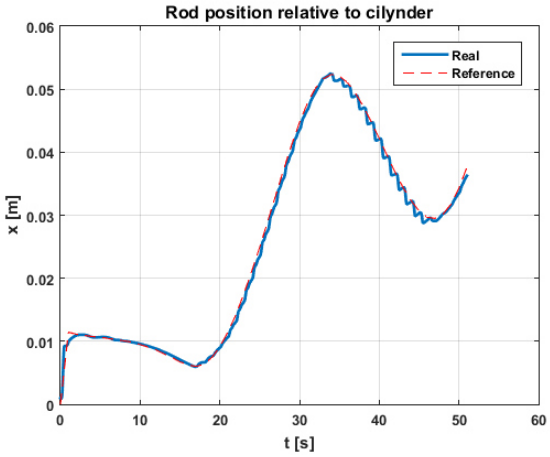

Fig. 9. Rod position of the manipulator following a 50-point trajectory generated

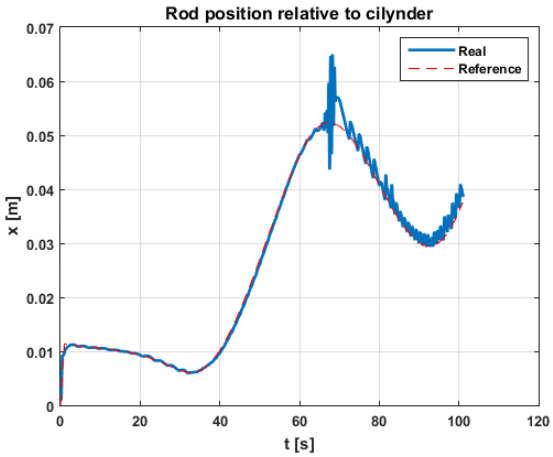

Fig. 10. Rod position of the manipulator following 100-point trajectory generated

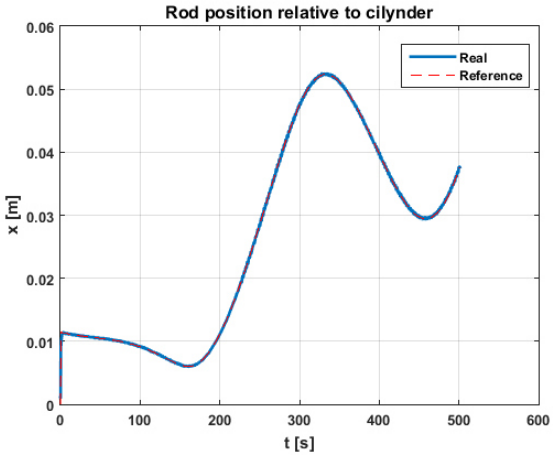

Fig. 11. Rod position of the manipulator following a 500-point trajectory generated

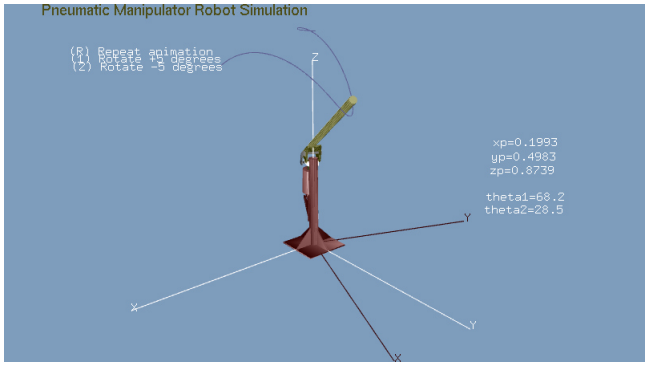

Fig. 12. Simulator Developed using OpenGL and C++

VIII. Conclusion

After applying different amounts of intermediate points resulting from the interpolation it is concluded that the higher number of points, the controller is able to bring closer the output to the set-point given which makes the system more stable and this allows to implement the path to the physical robot without damaging it. In other words, the simulator developed is a helpful tool that presents the possibility of probing the behaviour of a Pneumatic Manipulator Robot before being implemented.

This work has presented four different trajectories: a trajectory that just follows the path of the points that resulted from the interpolation, and three more trajectories where the control developed in previous works is implemented and the responses of each one of them are monitored through the graphics generated in C++ and OpenGL.

As future work, this simulator will be extended to Three-Degrees-of-Freedom which will permit to reach more points in the space. The mathematical model of the pneumatic motor will be obtained too. This will permit to obtain a better simulation that considers the dynamics of the whole system and termo-mechanical model of each actuator.

References

[1] R. R. M. Richter, C. V. Zamberlan, A. C. Valdiero, and L. A. Rasia, "Trajectory Tracking Control of a Pneumatic Actuator Special," vol. 1, no. 6, pp. 371–375, 2014.

[2] X. Wang and G. Peng, "Modeling and control for pneumatic manipulator based on dynamic neural network," in *Systems, Man and Cybernetics, 2003. IEEE International Conference on*, vol. 3, pp. 2231–2236, IEEE, 2003.

[3] J. M. Ramos, E. Gorrostieta, J. E. Vargas, and J. C. Pedraza, "New Polynomial Model of Pneumatic Cylinder Model," *Revista Internacional Información Tecnológica*, vol. 17, no. 3, 2006.

[4] J. M. Ramos-Arreguin, E. Gorrostieta-Hurtado, J. C. Pedraza-Ortega, R. J. Romero-Troncoso, M. A. Aceves, and S. Canchola, "Dynamic Behavior of a Pneumatic Manipulator with Two Degrees of Freedom," in *Robot Manipulators Trends and Development*, InTech, 2010.

[5] S. Y. Qiu, P. Yi, R. B. Yuan, H. Yang, S. Hui, and R. P. Xue, "Trajectory control for cartesian pneumatic manipulator using the terminal sliding mode control method," in *Applied Mechanics and Materials*, vol. 444, pp. 1354–1359, Trans Tech Publ, 2014.

[6] J. M. Ramos Arreguin, "Control de un Actuador Neumático," pp. 33–43, Centro de Ingeniera y Desarrollo Industrial (CIDESI), 2008.

[7] F. F. Kiyama Miramontes, "Modelado de un robot manipulador flexible," pp. 9–32, Centro de Ingeniera y Desarrollo Industrial (CIDESI), 2005.

[8] S. V. Vaseghi, *Advanced digital signal processing and noise reduction*. John Wiley & Sons, 2008.

[9] C. H. Reinsch, "Smoothing by spline functions," *Numerische mathematik*, vol. 10, no. 3, pp. 177–183, 1967.

[10] J. Ramos, E. Gorrostieta, E. Vargas, J. Pedraza, *et al.*, "Pneumatic cylinder control for a flexible manipulator robot,"

[11] M. Gamino, J. C. Pedraza, J. M. Ramos, and E. Gorrostieta, "Matlab-c++ interface for a flexible arm manipulator simulation using multi-language techniques," in *Artificial Intelligence, 2006. MICAI'06. Fifth Mexican International Conference on*, pp. 369–378, IEEE, 2006.

Convective Index on Water Vapor Imagery applied to Severe Storms

Case of study Hurricanes: Odile (15th September, 2014) and Patricia (23th October, 2015)

Meza-Ruiz Marilu
Centro de Investigaciones del Agua de Querétaro CIAQ
Universidad Autónoma de Querétaro UAQ
Querétaro, México
mr.marilu@yahoo.com.mx

Gutierrez-López Alfonso
Centro de Investigaciones del Agua de Querétaro CIAQ
Universidad Autónoma de Querétaro UAQ
Querétaro, México

***Abstract*— The classification of "severe storm" is an arbitrary classification and depends on the location and the damage they can make in populated cities. There are a lot of satellite images available for tracking and forecasting extreme hydrological storms. However there are no appropriated early warning methods proved for regional locations in Mexico. Not only for tracking and forecasting but also identifying convective patterns in order to improve weather prediction and have precise estimations of storm development. The aim of these work is develop a new technique that employ satellite imagery -based on water vapor images (WV) captured by geo-stationary satellites GOES- for analyzing extreme hydro-meteorological events comparison with records of sounding weather stations located in ground for validation proposes. The second aim is identify convective patrons and consequently use this information to improve the early warning system. The image from GOES provide an important information about the meso and local scale of hydro-meteorological events, which impact local weather generating severe rainfall, flash floods, and floods. This kind of tools can be available in real time for tracking severe storm in places where there is no available sounding data.**

Keywords—water vapor imagery; convective index; severe storm; GOES; sounding

I. INTRODUCTION

A severe storm is considered in United States if it presents any of these features: significant hail (≥ 2 in diameter) and significant wind (gusts ≥ 33.44 m/s) according with the scientific work [1, 2, 3, and 4] the observation of any tornado, automatically the storm is considered as severe storm. In contrast [4] identify that the term "severe" is an arbitrary classification and it can be given a storm which meets or exceeds some threshold or criteria and can vary around the word. For this classification rain fall rate is not considered as a specification for cataloged a severe storm in United States.

In Mexico the variation in topographic, orographic, climatic and atmospheric features determinate the storms and make it totally different compared with the storms presented in United States. The importance of determinate severity and convective index in storms relay on the understanding of atmospherics' dynamic and how water vapor (WV) can increase or reduce the develop of a severe storm, [5] conclude that "The role of convection in enhancing cyclogenesis ... remains unsolved". WV could be the answer that gives key information about convective patrons.

The Geostationary Operational Environmental Satellite, GOES-13, orbit the Earth at an approximate height of 35 thousand kilometers above the equator, at this height the speed of the satellite is equal to the angular velocity of the Earth. The satellite give a turn of 360° in 24 hours, this characteristic allow us to have a constant monitoring of the same area, in this case all Mexican territory is monitored all day in a frequency of 15 minutes.

In this work the use of WV images provided from GOES-13 and sounding information -including convective, stable and unstable atmospheric index- from the cities where two cases of study are exanimate in order to classify these convective and severity index. Finally a threshold of classification of severity and convective index are proposed in order to apply for some homogenous region hit by hurricanes in Mexican Region.

II. METODOLOGY

Wardah [6] detailed the origins of this type of storms, especially form tropical systems like hurricane. Convective systems produce the greatest rainfall rates when the environment above the ground and under the top cloud this air mass began to get cooler and began to expand. Kalinga [7] introduce the rain and no-rain discrimination in their study improving the estimates from infrared imagery, the same methodology can be applied in WV image.

A. Image Treatment

The first step involves a geo-referential treatment of the images, in order to read the brightness values from top clouds for each pixel. An image processing techniques was applied using an own computational tools; First of all, to standardize the geographical positioning and resolutions (with pixels having an approximate coverage of 2.4 × 2.4 km) and then perform a reading of WV images (representing the brightness of different concentration of WV in the atmosphere at each point, expressed as a value or gray scale which fluctuates

between 113 to 255). Once we have the location of every sounding station we can extract the bright value for each point and a complete matrix of 9×9 pixels see Fig.1. In order to get the active pixels or the convective pixels, we apply the methodology given by [8].

For a matrix of 9×9 the mean, maximum and minimum value of the 49 pixels were estimated. For the active and non-active pixel a discrimination were made resting the Pixel (i, j) to the mean. We have the lowest and the higher pixel values. Pixel with positive number were taken in count as active pixel and the rest were no take in count, the index of unitability takes in count the difference between the mayor and lowest value, once we have the index from the active pixels compared with the hole matrix the number is multiplication with the difference of values.

Fig. 1. Programm developed in CIAQ. Extract the bright value from the infrared image from GOES (left) and visualize the bright value in each pixel (right). Image from 10th September of 2013 at 00h15 UTC.

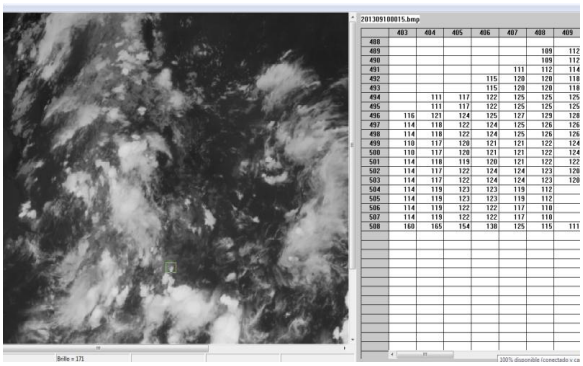

B. Sounding information

The Mexican National Meteorological Service (SMN) has 15 meteorological sounding stations in all Mexican territory (Table and Fig. 2) with at least one measure at day -except the station located in Mexico City witch is the only one with 2 records; at 00Z and 12Z (day in the format DD and hour HH in the Zulu time or UTM)-. This information are present in text blog format, when it pass to Excel format is possible to get convective, stable and unstable index whit the help of a macros programmed by the author. University of Wyoming available on internet (http://weather.uwyo.edu/upperair/sounding.html) has access to few Mexican stations which have at least two measurements at day in some cases three measurements (DD00Z, DD12Z and DD18Z). As the information given by the SMN the information from Wyoming University is passed to Excel format and with the same macros y get the stable and unstable index.

TABLE I. SOUNDING STATIONS IN MEXICO

Num.	Code	Station Name	North Latitude	West Longitude	Height
1	76805	Acapulco, Gro.	16.83	-99.93	3.10
2	76595	Cancún, Q. Roo	21.02	-86.85	10.00
3	76225	Chihuahua, Chih.	28.63	-106.08	1433.50
4	76679	México, D.F.	19.40	-99.18	2302.00
5	76256	Empalme, Son	27.95	-110.766	12.00
6	76612	Guadalajara, Jal.	20.66	-103.38	1551.10
7	76723	Isla Socorro, Col.	18.72	-110.95	35.00
8	76405	La Paz, B.C.S.	24.16	-110.30	18.50
9	76654	Manzanillo, Col.	19.05	-104.31	3.00
10	76458	Mazatlán, Sin.	23.20	-106.42	4.00
11	76644	Mérida, Yuc.	20.98	-89.65	9.00
12	76394	Monterrey, N.l.	25.86	-100.23	448.00
13	76692	Veracruz, Ver.	19.15	-96.12	16.40
14	76743	Villahermosa, Tab.	17.98	-92.93	6.50
15	76526	Zacatecas, Zac.	22.75	-102.51	2265.00

Fig. 2. Location of sounding stations in Mexico

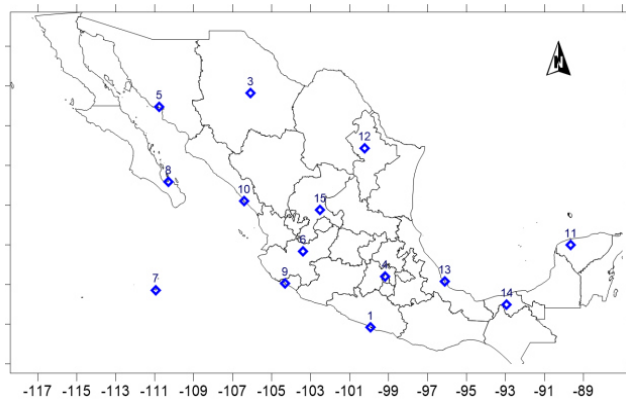

The following atmospheric index is studied; the main variable to use is environmental and dew point temperature [°C] at given height corresponding to a specific atmospheric pressure [hPa]:

- Lift Index (LI). - This index corresponds to a difference of environmental temperature at 500 hPa and the humid temperature, dew point (Tdp) of an air mass lifted at 500 hPa. The more unstable the atmosphere the lower or negative values of LI.

$$LI=T500-Tdp500 \qquad (1)$$

- Total Index (TT). - Can be estimated using Tdp at 850 hPa and temperature to 500 hPa. The warmer Tdp at 850 hPa and lower the environmental temperature at 500 hPa, the higher values of TT and the increase of an unstable atmosphere is presented.

$$TT= (T850+Tdp850) – (2×T500) \qquad (2)$$

- K Index (KI).- This index identify convective environments and give a probability of severe rainfall and can be determinate as:

$$KI= (T850 – T500) + Tdp850 - (T700 – Tdp700) \qquad (3)$$

Is important to mention that this index cannot be used to determinate the severity of the convective storm, variables at 850 hPa are used in order to determinate this index and is not applicable in mountain region where the atmospheric pressure is lower.

- Severe Weather Advisory Trend (SWEAT). - is based on a storm model from [8] and is given for specific atmospheric features from United States.

$$SWEAT = 12 \times Tdp + 20 \times (TT - 49) + 2 \times WV850 + WV500 + 125 \times (S+0.2) \quad (4)$$

Where WV850 is the wind speed at 850 hPa, in knots, WD850 is the wind direction at 850 hPa in degrees and

$$S = \sin (WD500 - WD850) \quad (5)$$

For equation (4) there are few considerations:

  - If TT <20 then 20 × (TT – 49) =0.
  - If WD 850 are between 130° and 250° or WD500 are between 210° and 310° then Eq. (5) = 0 and usually 125 × (S+0.2) =0
  - If WV 500 < WV850 then Eq. (5) =0.
  - If WV850 or WV500 < 7.167 m/s then Eq. (5) =0.

- Potential of humid temperature Index (PI). - This index is based on the difference in humid air at different height well known as gradient temperature difference as the increasing of height.

$$PI = Tdp500\text{-}Tdp850 \quad (6)$$

These five indexes qualify the atmospheric stability as stable and unstable. Give us an idea of the features of the atmosphere, is important to focus that in Mexico there is no investigations and results that show the classification of these index for every location or topographic features as United States.

III. Results

The two study cases were chosen based on the atmospheric features –very special condition for each one- and the data available.

A. *Hurricane Odile 15th september 2013*

Odile made landfall on the southern of the Baja California peninsula as a large category 3 hurricane (on the Saffir-Simpson Hurricane Wind Scale). It was the first major hurricane to strike this region in 25 years and is tied with Hurricane Olivia of 1967 as the strongest land falling hurricane in Baja California in the historical record. Odile was responsible for 11 direct deaths and over 12 billion pesos (~1 billion USD) of insured losses [9].

The maximum sustained winds were estimated to have decreased to 56.58 m/s at 0600 UTC 14 September. Data from the aircraft also indicated an expansion of the wind field, with the tropical-storm-force wind radii nearly doubling in size over the 36 h that Odile had been a hurricane. Odile's inner eyewall eroded further after the plane departed and nearly dissipated after 0000 UTC 15 September, while the outer eyewall began to contract slightly.

The hurricane further accelerated while Odile's cloud pattern remained well organized, with a symmetric central dense overcast and a roughly 18 km wide eye. Odile made landfall with 56.59 m/s winds (category 3 on the Saffir-Simpson Hurricane Wind Scale) on the southern tip of the Baja California peninsula at 0445 UTC 15 September, just to the east of Cabo San Lucas [9].

1) *Sounding Index for Hurricane Odile*

In Fig. 2 are illustrated the three sounding stations with sounding data available for the corresponding days: Station La Paz code 76405 only has available data from 1412Z (day in the format DD and hour HH in the Zulu time or UTM). For station located in Mazatlán code 76458 has since the day 13th to 16th and finally the station located in Guadalajara code 76612 has only the 1400Z, 1412Z and 1500Z. The following graphics describes the stable and unstable index for each station during the period of 13th to 16th September 2013.

Fig. 3. Location of sounding stations avilable for Hurricane Odile

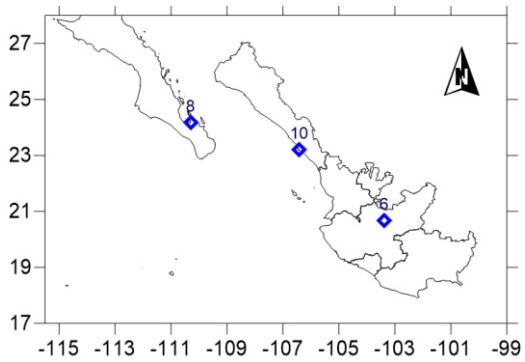

When the atmospheric conditions are not favorable, some balloons get lost and some sounding are not available, is the case of La Paz station witch only have available this two sounding. The information given can help us to see the variation compared with other stations at the same time.

TABLE II. Index from 76405 La Paz station

76405	1312Z	1412Z
LI	-16.4	5.0
TT	20.6	23.4
IK	31.5	27.9
SWEAT	194.2	148.0
PI	-3.5	-19.3

According to the classification for the index the atmospheric conditions at 1312Z LI indicates warning for tornado, TT index is classify as convective activity non-significant, IK index estimate a rainfall probability of 60-80% in contrast the most used convective index is SWEAT, in this case is no probability of severe weather, and the PI indicate a few probability of convection.

For the second day, 24 hours later, the LI indicates a stable atmosphere (positive number), TT index revel convective activity non-significant, IK and SWEAT keeps the estimate a rainfall probability of 60-80% and no probability of severe weather, finally the PI indicate a few probability of convection.

In La Paz, there are no gauges from ground automated meteorological station; the nearest station is Sierra la Laguna B.C.S. The station recordered 90.4 mm of accumulated rain during the period from 140920142050 UTC to 150920140720 UTC, when the station stops transmitting data.

- 76458 Mazatlán station

Fig. 4. Index from 76458 Mazatlán station

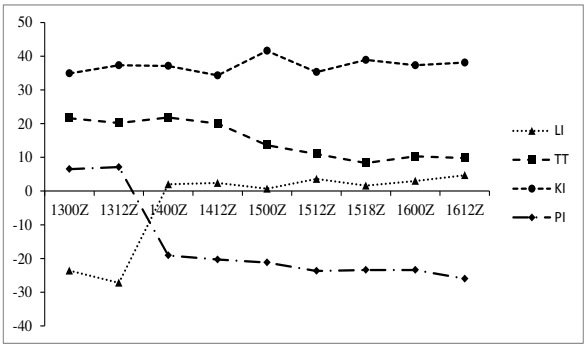

TABLE III. INDEX FROM 76458 MAZATLÁN STATION

76458	1300Z	1312Z	1400Z	1412Z	1500Z	1512Z	1518Z	1600Z	1612Z
LI	-23.6	-27.2	2	2.4	0.7	3.6	1.6	3	4.7
TT	21.6	20.2	21.8	20	13.6	11	8.3	10.3	9.8
KI	34.9	37.3	37.1	34.3	41.6	35.3	38.9	37.3	38.1
SWEAT	173.0	197.0	174.4	226.8	314.1	264.7	278.8	247.4	251.4
PI	6.5	7.1	-19.1	-20.3	-21.2	-23.7	-23.4	-23.4	-26

In this case the Mazatlán station shows a negative LI numbers for the 13th September meaning instability and the warning for tornado formation.

For TT index all the time were stable, numbers below the 22 are considered as convective non-significant.

For KI the numbers between 31 and 36 mean storm probability of 60 to 80% and numbers between 36 and 40 mean a storm probability of 80 to 90 %.

For SWEAT index, numbers below 200 means stable atmosphere conditions, numbers between 200 and 300 mean 4% probability of storms, numbers between 300 and 400 mean 26% probability of storms.

The nearest gauge station recordered an accumulated rain of 9.65 mm the 14092014 from 00 to 12 UTC, the 15092014 from 00 to 12 UTC 7.84, from 12 to 2350 UTC 13.2 mm and 16092014 from 00 to 12 UTC 6.6 mm.

- 76612 Guadalajara station

Fig. 5. Index from 76612 Guadalajara station

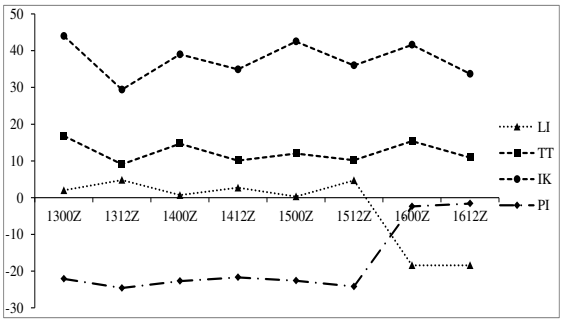

TABLE IV. INDEX FROM 76612 GUADALAJARA STATION

76612	1300Z	1312Z	1400Z	1412Z	1500Z	1512Z	1600Z	1612Z
LI	2.0	4.8	0.7	2.7	0.3	4.7	-18.4	-18.4
TT	16.8	9.1	14.7	10.1	12	10.2	15.4	10.9
IK	44	29.4	39	34.9	42.5	36.0	41.6	33.7
SWEAT	300.4	217.7	317.2	223.9	305.6	191.2	221.4	185.5
PI	-22.1	-24.6	-22.7	-21.7	-22.6	-24.2	-2.4	-1.6

LI index indicate an stable atmosphere for numbers mayor than 3, and posibles storms from nombers between -3 and 3, for numbers less than -3 respresents a severe storm.

The TT index are below 44, corresponding a classification of non-significant convective activity. IK index indicate a probability of storm between 60 to 80 %. For numbers higher than 40 indicates a 100 % of storms.

The nearest station La Primavera recordered a rainfall accumulation of 4.8 mm, the 1400Z an 1 mm of rain accumulated and finally the 1300Z there is an accumulated rain of 16.4 mm in 1600Z.

2) *Convective Index for WP image from Hurricane Odile*

The mean of 3 and 4 images were taken in order to have a homogenous lecture from the WV images e.g. if the lecture from sounding were taken at 00Z the images 15 minutes before and after were analizyed, images 2345Z for the day before, the 0000Z and 0015Z image were taken in order to have a homogenous reading of the atmosphere.

The program used (RedCiaq) use a treshold of 109 brightness value, below these treshold is no activity recordable. This is the case of the station 76405 corresponding to station located in La Paz, where the treshold were recorder, corresponding a no apreciable values of WV.

TABLE V. INDEX CORRESPONDING TO THE PIXELS LOCATED IN THE SOUNDING STATIONS FROM WV IMAGES

Station	1300Z	1312Z	1400Z	1412Z	1500Z	1512Z	1518Z	1600Z	1612Z
76405	ND[a]	1.19	ND	1.36	ND	ND	ND	ND	ND
76612	9.7	8.2	6.5	5	11.7	0.7	1.7	1.7	0.9
76458	9.8	8.4	7.1	5	11.8	0.7	1.7	1.7	0.9

[a] ND no datum available, pixel lecture below the threshold

The convective index from the station 76612 and 76458 present a similar record, in each case the movement in the pixel were similar. We can observe an intensification of the storm at 1500Z date were the hurricane was making landfall in Cabo San Lucas. After 12 hours the index decrees dramatically, special when the storm moves north and began to decay in the sounding stations located in Guadalajara and Mazatlán.

B. Hurricane Patricia 23th octuber 2015

Patricia was a category 5 hurricane (on the Saffir-Simpson Hurricane Wind Scale). Its maximum sustained winds are estimated to have reached a peak intensity of 95.172 m/s near 1200 UTC on October 23rd while centered about 130 nautical miles southwest of Manzanillo, Mexico.

Patricia earn some record as; the strongest hurricane on record in the eastern North Pacific, -surpassing Hurricane Linda in 1997, and is also stronger than any Atlantic basin hurricane on record-, is important to remark that also for the most intense eastern North Pacific hurricanes are particularly uncertain prior to 1988. Records for the most extreme Atlantic hurricanes are considered reliable beginning in the early 1970s. Patricia also have the record of the analyzed minimum central pressure of 872 represents the lowest tropical cyclone pressure on record in the western Hemisphere and the second lowest globally (behind only the 870 hPa pressure for 1979's Typhoon Tip) [10].

One of the mayor features that Patricia shows a quick develop (less than 24 hours) some catalogued as explosive deepening from October 22 to 23. Over the 24-hour period ending at 0600 UTC on October 23rd, the pressure is estimated to have fallen 100 hPa and the wind to have increased from 38.583 m/s to 92.6 m/s. The 1-day intensification of 54.0167 m/s exceeds a 48.872 m/s increase for Hurricane Wilma in 2005 while over the western Caribbean Sea [10].

Patricia weakened substantially before making landfall along a sparsely populated part of the coast of southwestern Mexico as category 4 hurricanes, with an estimated landfall intensity of 66.878 m/s and an estimated landfall pressure of 932 hPa. This makes Patricia the strongest hurricane on record to make landfall in Mexico, eclipsing the October 1959 Manzanillo hurricane (recently reassessed to have made landfall at category 4 intensity), and Hurricane Madeline in 1976. It should be noted, however, that the reliable record for extreme land falling Mexican hurricanes extends back only to 1988 [10].

3) Sounding Index for Hurricane Patricia

In these case of study as the reports information says that hurricane Patricia have a quick development in less than 24 hours son just 1 day data was available. In Fig. 6 are illustrated the six sounding stations with sounding data available for the corresponding days: Station Acapulco code 76805 only has available data from 2212Z and 2218Z, Station located in Manzanillo code 76654 has 2212Z, 2218Z and 2300Z, Station Guadalajara code 76612 has only the 2212Z, Mazatlán station code 76458 has 2212Z and 2218Z and finally Zacatecas station code 76526 has 2300Z.

Fig. 6. Location of sounding stations avilable for Hurricane Patricia

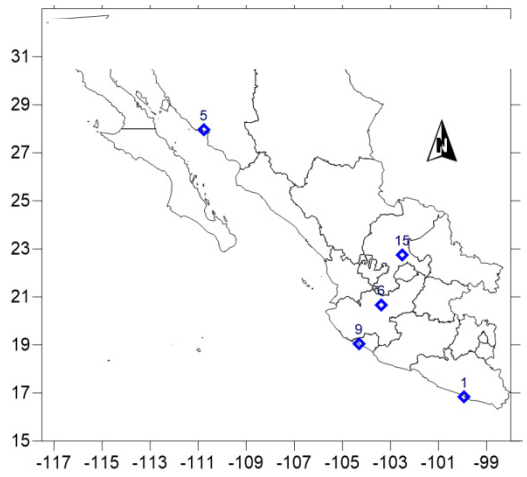

- 76805 Acapulco station

Fig. 7. Index from 76805 Acapulco station

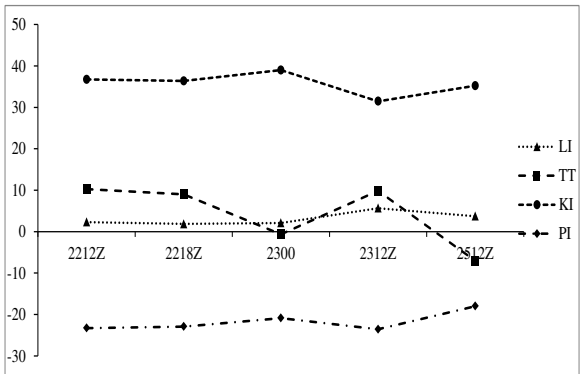

TABLE VI. INDEX FROM 76805 ACAPULCO STATION

7805	2212Z	2218Z	2300Z	2312Z	2512Z
LI	2.3	1.8	2.1	5.7	3.7
TT	10.3	9.0	-0.7	9.9	-7.1
KI	36.7	36.4	39.0	31.5	35.2
SWEAT	247.1	242.9	255.0	206.4	240.5
PI	-23.3	-22.9	-20.9	-23.6	-18.0

LI numbers from 0 to 3 indicate the possibilities of lightly storms and numbers > 3 indicates stability. TT indicates convective activity non-significant. For KI the numbers between 31 and 36 mean storm probability of 60 to 80% and numbers between 36 and 40 mean a storm probability of 80 to 90 %. For SWEAT index we have only the 4 % of severe storms. PI indicates a probability of convection.

In this case Patricia has no records of intense storms and the gauges on ground do not register any heavy rainfall from 2212Z to 2512Z. In this case the mayor of the unstable atmosphere was negative meaning that the atmosphere was stable until the high of 500 hPa.

- 76654 Manzanillo station

Fig. 8. Index from 76654 Mazanillo station

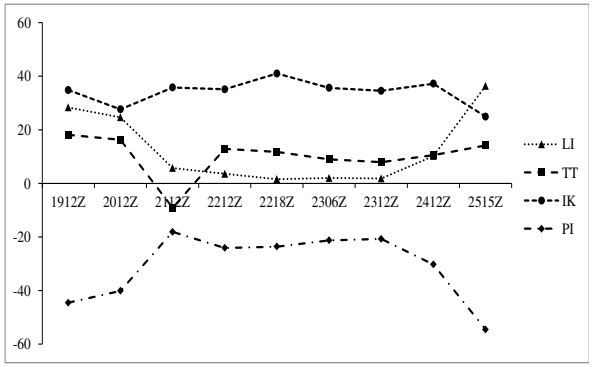

TABLE VII. INDEX FROM 76654 MANZANILLO STATION

76654	1912Z	2012Z	2112Z	2212Z	2218Z	2306Z	2312Z	2412Z	2
LI	28.4	24.7	5.7	3.6	1.5	2.0	1.9	10.2	
TT	18.1	16.3	-9.1	12.9	11.7	9.0	7.9	10.5	
IK	34.8	27.7	35.8	35.1	41.0	35.7	34.5	37.2	
SWEAT	158.8	183.0	242.6	225.4	271.2	280.5	305.1	257.2	1
PI	-44.6	-40.1	-18.1	-24.1	-23.6	-21.3	-20.7	-30.3	-54.5

LI numbers from 0 to 3 indicate the possibilities of lightly storms and numbers > 3 indicates stability. TT indicates convective activity non-significant. For KI the numbers between 31 and 36 mean storm probability of 60 to 80% and numbers between 36 and 40 mean a storm probability of 80 to 90 %. For SWEAT index we have only the 4 % of severe storms. PI indicates a probability of convection.

- 76458 Mazatlán station

Fig. 9. Index from 76458 Mazatlán station

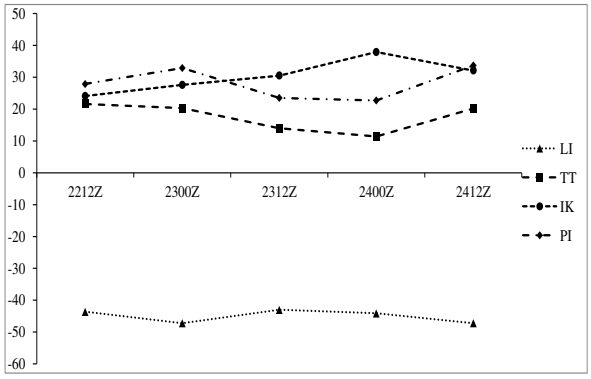

TABLE VIII. INDEX FROM 76458 MAZATLÁN STATION

76458	2212Z	2300Z	2312Z	2400Z	2412Z
LI	-43.6	-47.2	-43.0	-44.1	-47.2
TT	21.6	20.3	14.0	11.4	20.2
IK	24.1	27.6	30.5	37.9	32.1
SWEAT	173.4	142.2	215.4	233.9	172.3
PI	27.9	32.9	23.5	22.7	33.7

LI numbers indicate the possibilities of tornado. TT indicates convective activity non-significant. For KI the numbers between 21 and 25 mean storm probability of 20 to 40% and numbers between 26 and 30 mean a storm probability of 60 to 80 %. For SWEAT index we have only the 4 % of severe storms. PI indicates stability.

- 76612 Guadalajara station

Fig. 10. Index from 76612 Guadalajara station

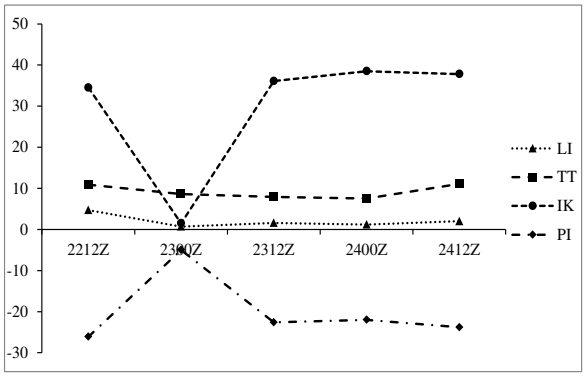

TABLE IX. INDEX FROM 76612 GUADALAJARA STATION

76612	2212Z	2300Z	2312Z	2400Z	2412Z
LI	4.7	0.7	1.6	1.2	2
TT	10.9	8.6	7.9	7.5	11.1
IK	34.5	1.5	36.1	38.5	37.8
SWEAT	201.0	13.6	242.2	262.2	228.4
PI	-26.1	-5	-22.6	-22	-23.8

LI numbers from 0 to 3 indicate the possibilities of lightly storms and numbers > 3 indicates stability. TT indicates convective activity non-significant. For KI the numbers between 31 and 36 mean storm probability of 60 to 80% and numbers between 36 and 40 mean a storm probability of 80 to 90 %. For SWEAT index we have only the 4 % of severe storms. PI indicates a probability of convection.

- 76526 Zacatecas station

TABLE X. INDEX FROM 76526 ZACACTECAS STATION

76526	2312Z	2400Z	2412Z
LI	1.6	0.8	1.6
TT	9.4	8.2	7.8
IK	2.5	4	2.8
SWEAT	18.8	50.8	32.3
PI	-6.3	-4.9	-5.5

LI numbers from 0 to 3 indicate the possibilities of lightly storms. TT indicates convective activity non-significant. For KI the numbers indicate 0% of storms. For SWEAT index we have no possibility of storms. PI indicates a probability of convection. Is important to mention that Zacatecas is located at higher altitude compared with the others soundings station, and the lecture for 850 hPa is not possible to get as [10] the mountains regions has to be treated different.

In the case of the altitude near the ground corresponding to an atmosphere pressure of 850 hPa were no available for these reason, the attitude of 775 hPa were taken as equivalent. There is no classification for these kinds of regions in Mexico. As a result the indexes of unstable atmosphere were no possible to get completed.

4) Convective Index for WP image from Hurricane Patricia

The mean of 3 and 4 images were taken in order to have a homogenous lecture from the WV images e.g. if the lecture from sounding were taken at 00Z the images 15 minutes before and after were analizyed, images 2345Z for the day before, the 0000Z and 0015Z image were taken in order to have a homogenous reading of the atmosphere.

TABLE XI. INDEX CORRESPONDING TO THE PIXELS LOCATED IN THE SOUNDING STATIONS FROM WV IMAGES

Station	2212Z	2300Z	2312Z	2400Z
76805	7.1	3.2	8.7	7.8
76654	9.6	5.0	6.4	5.6
76458	0.3	9.6	11.2	8.7
76612	6.8	2.7	4.7	6.9
76526	1.9	6.8	1.4	5.0

The mayor convective index were from the station 76458 corresponding to Mazatlán the 23th at 12Z the same as 76805 corresponding to Acapulco

IV. REMARKS

Since space technology can be accessible for countries which has not develop their own meteorological satellites is a relevant tool for those who observe and prognosticate the weather in a wide time-space resolution. The image from GOES provide an important information about the meso and local scale of hydro-meteorological events, which impact local weather generating severe rainfall, flash floods, and floods. This kind of tools can be available in real time for tracking severe storm in places where there is no available sounding data. More investigation is required, taking account a relationship between the category of a hurricane and the different index providing from sounding and pixels information. In Mexico the atmospheric features developed by hurricanes with lower categories considerably have higher impacts on ground.

The catalogue of the entire indexes from sounding and the lecture made by pixels of WV image for each hurricane and compared with the damage made and the rainfall rates recordered on ground is important.

Is necessary to catalogue, give a threshold to the WV images in six different levels; three mayor levels and three lower levels of water vapor pressure, and once we can catalogued we can stablish new grades for convective index on WV image.

There is an important field of opportunity to develop new and innovated techniques and technology based on satellite data. In further investigations imply the addition of climatic regions more specifically convective index. Is necessary a study of principal components for each index in different location, including pixel patrons of storms in all Mexican territory and homogeneous region.

ACKNOWLEDGMENT

We would like to thank to all the collaborators from RedCIAQ whom provide data base information. Special thanks to SMN (Servicio Meteorológico Nacional) for the information provided, imagery Water Vapor images corresponding to 2014 and 2015 and sounding stations data base for the same years. To *NOAA-NASA GOES Project* for sharing data and information.

REFERENCES

[1] S. T. Bryan, R.L. Thompson, J. Grams and C.Broyles. "Convective modes for significant severe thunderstorms in the contigouos United States. Part 1. Storm Classification and climatology", wheather and forecasting , vol. 27, pp. 1114-1134, March 2012.

[2] P. Santurrette and C. G. Georgievpheric. "Wheather analysis and forecasting. Applying satellite water vapor imagery and potential vorticity analysis".Elsevier academic press. 2005.

[3] D. M. Schultz and C. a. Doswell, "Analyzing and Forecasting Rocky Mountain Lee Cyclogenesis Often Associated with Strong Winds," *Weather Forecast.*, vol. 15, no. 2, pp. 152–173, 2000.

[4] R. J. Trapp and M. L. Weisman, "Low-Level Mesovortices within Squall Lines and Bow Echoes. Part II: Their Genesis and Implications," *Mon. Weather Rev.*, vol. 131, no. 11, pp. 2804–2823, 2003.

[5] C. A. Doswell and L. F. Bosart, "Extratropical Synoptic-Scale Processes and Severe Convection," *Meteorol. Monogr.*, vol. 28, no. 50, pp. 27–70, 2001.

[6] T. Wardah, S. H. Abu Bakar, A. Bardossy, and M. Maznorizan, "Use of geostationary meteorological satellite images in convective rain estimation for flash-flood forecasting," *J. Hydrol.*, vol. 356, no. 3–4, pp. 283–298, 2008.

[7] O. A. Kalinga and T. Y. Gan, "Estimation of rainfall from infrared-microwave satellite data for basin-scale hydrologic modelling," *Hydrol. Process.*, vol. 24, no. 15, pp. 2068–2086, 2010.

[8] M. R. Meza and J.A.R. Carvajal, "Metodology of geoperspective from GOES imagery," tecnique note. unpublished.

[9] K. A. Browning, J. C. Frankhauser, J. P. Chalon, P. J. Eccles, R. G. Strauch, F. H. Merrem, D. J. Musil, E. L. May, and W. R. Sand, "Structure of an evolving hailstorm part V: Synthesis and implications for hail growth and hail suppression," *Monthly Weather Review*, vol. 104, no. 5. pp. 603–610, 1976.

[10] T. S. Hanna and J. P. Cangialosi, "National Hurricane Center Tropical Cyclone Report," no. October, pp. 22–28, 2014.

[11] "Tropical Cyclone Report for 2015 ' s Hurricane Patricia released," no. October, p. 1, 2015.

[12] D. M. Schultz, P. N. Schumacher, and C. a. Doswell, "The Intricacies of Instabilities," *Mon. Weather Rev.*, vol. 128, no. 12, pp. 4143–4148, 2000.

Experimental and theoretical study of $Cd_{1-x}Zn_xS$

L. F. Morelos Medina[1], R. Nava Mendoza[3], R. Velázquez Castillo [4], A. Cuan Hernández[2]

[1 2 3 4] Dirección de Investigación y Posgrado, Facultad de Ingeniería, Universidad Autónoma de Querétaro, Cerro de las Campanas S/N. Col. Niños Héroes, C.P. 76010, Santiago de Querétaro, Querétaro, México.
[1]lmorelos10@alumnos.uaq.mx, [2]angelescuan24@yahoo.com.mx, [3]rufino@uaq.mx, [4]rodrigo.velazquez@uaq.mx

***Abstract*— A series of systematic models for $Cd_{1-x}Zn_xS$ photocatalyst are being calculated for x = 0.25, which also were synthesized and characterized by X-Ray diffraction and UV-Vis technique. The proposed models are the bulk for the CdS and $Cd_{1-x}Zn_xS$ and also different substitution of the Cd by Zn to represent the catalyst surfaces. The surface representation has been considered as an important issue, i.e., metal or sulfur atoms in the surface). The stability and the electronic properties for each proposed model were calculated using the Vienna Ab initio Simulation Package (VASP) by employing the density functional theory (DFT) and Perdew-Burke-Ernzerhof (GGA-PBE). The proposed models for the catalysts were compared among them.**

***Keywords*— Photocatalyst, theoretical study, VASP**

I. Introduction

The use of solar energy as an alternative to hydrogen production via photochemical reactions is of great importance for a clean and renewable energy source. The searching of a semiconductor material with high photocatalytic activity under visible light irradiation is one of the actual topics to be discussed. (Kudo et al, 2009; Osterloh, 2008; Navarro, 2009; Navarro et al, 2009; Gust D et al, 2009; Navarro et al., 2009). The challenge is that using sunlight design material can act as a photocatalyst and to replace those that respond only to ultraviolet light, since UV light is only a small part of the solar radiation (Navarro et al., 2009; D Gust et al, 2009; Navarro et al, 2009). The metal sulfide photocatalysts generally have a narrow band gap and they have a good respond under visible light irradiation (Li, 2010). CdS is one of the most attractive photocatalysts because the value of the band gap is about 2.4 eV which is suitable to reduce effectively the protons, H^+ (Wang et al, 2010; Subrahmanyam et al., 1996; Janet and Viswanath, 2006; Jing and Guo, 2007). However, CdS is prone to corrode in photocatalytic reactions and it's known that this material (CdS) is oxidized by photogenerated holes (Meissner, Memming and Kastening, 1988; Girginer, 2009; Upadhyay and Sahu, 2009).

There are some strategies to reduce the photocorrosion and increase the efficiency of the photocatalyst consisting of CdS. Regarding this matter, different methods have been reported in literature to modify the properties and photoactivity of CdS, such as, control of particle size, the addition of co-catalysts or addition of various elements for solid solutions (Shangguan and Yashida, 2002). Among them a combination of different semiconductor bandgap to form solid solutions resulting in the way of controlling the potential of the band conduction by changes in its composition. In this sense, it is possible to replace or substitute Zn by Cd atoms in small quantities. In this way a continuous series of solid solutions ($Cd_{1-x}Zn_xS$) are formed (Li, Jiang and Guo, 2010).

From the literature Reported based on the photoactivity of a solid solution $Cd_{1-x}Zn_xS$ has showed the importance of structural features, like the crystalline phase, crystal size and the geometric surface area, modify, not only, the band structure, but also the mobility of the charges. Even, there are both experimental and theoretical studies for this photocatalysts, the complexity of the involved phenomena in the complete process related with the holes formation and electrons recombination involved in the mechanism is not entirely clear yet. In that sense, the studies proposed here, will be oriented to gain insight in the fundamental knowledge about the phenomenon involved by studying the band distribution as well as, the electronic distribution as an important performance as a catalyst, overall for the water molecule activation in the H_2 production.

II. Methodology

A. Experimental procedure

1) Synthesis

CdS and $Cd_{1-x}Zn_xS$ samples (where x = 25 is Zn concentration were prepared from its precursors by coprecipitation of CdS and ZnS from aqueous solutions of $Zn(CH_3COO)_2•2H_2O$ (Sigma-Aldrich, analytical grade) and $Cd(CH_3COO)_2•2H_2O$ (Sigma-Aldrich, analytical grade) at room temperature using 3.4g of $Na_2S•9H2O$ (analytical grade) as precipitating agent.

2) Characterization methods

The synthetized materials were characterized by UV-vis DR spectra in the 200-800 nm range at room temperature using an Ocean Optics Inc. spectrometer (Mini-DT2) provided with a diffuse reflectance accessory. Also X-ray diffraction (XRD) technique was used to identify the preferential crystallographic grown and also it was used to calculate the particle sizes. The XRD patterns were obtained on a broker model D8 ADVANCE X-ray diffractometer with Cu Kα radiation (λ = 1.5418 Å) operated at 30 kV and 15 mA. The analysis conditions comprised a scanning angle from 0.3 to 10º (lowangle) and from 10 to 90 º (wide-angle) at a speed of 2º per min with a 2 s step count. Volume-averaged crystallite sizes were determined by applying the Debye-Scherrer equation. The molar composition of $Cd_{1-x}Zn_xS$ solid solution was obtained from the lattice parameter shifts, calculated from the angular position of the (001) reflections, according to Vegard's law.

B. *Theoretical procedure*

All calculations for the prosed models were performed by using the special code Vienna Ab-initio Simulation Package, known as VASP (Kumar, 2007; Mau AWH, 1984). For the description of electron, plane wave functions are used with a projector augmented plane wave potential used within the formalism of the density functional theory (DFT). The description of the exchange and electron correlation is treated by generalized gradient approximation with Perdew-Burke-Ernzerhof (GGA-PBE) (AWH Mau, 1984) with an energy cutoff of 520 eV and 6 6 6 k-points, for the case of CdS structure and for the $Cd_{1-x}Zn_xS$ the energy cutoff was 480 with 6 6 6 k-points.

1) Proposed models

As a reference bulk of the CdS crystal was calculated and parameterized. In Figure 1, the model for the CdS bulk is showed.

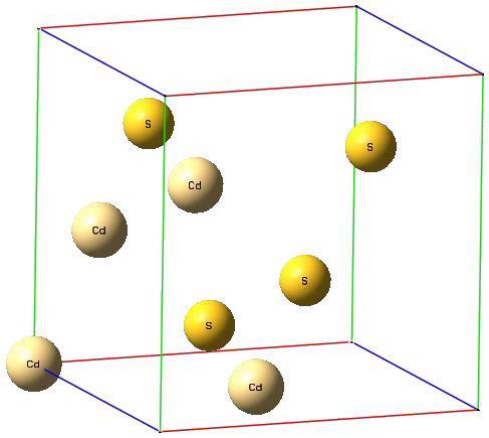

Figure 1. Schematic representation of the Cds bulk.

For the modeling of the solid solution, $Cd_{1-x}Zn_xS$, in which it has been considered x = 0.25, as it is shown in the Figure 2. This rate was chosen close to the literature reported by S. A. Macias-Sanchez et al. 2013, because it is the rate that better performance showed for the water activation molecule. In this work the rate was modify concerning with the literature, due to this rate is more convenient for the quantum chemical calculation. So, the CdS catalyst surface was constructed given a free space of the 10 Å of vacuum. Then, taking the CdS surface as a reference, the $Cd_{1-x}Zn_xS$ solid solution were constructed replacing one Cd atom by one Zn atom. The supercell size has 4 slides. The constructed surface models are shown in the Figure 6 and 7 respectively.

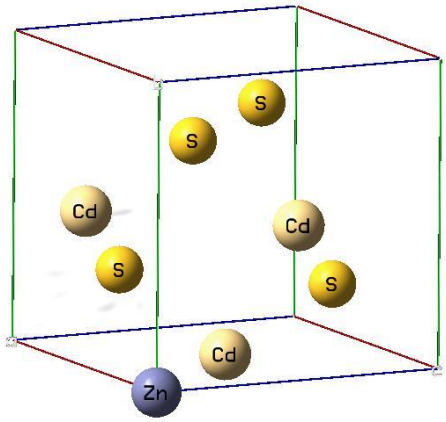

Figure 2. Schematic representation of the $Cd_{0.75}Zn_{0.25}S$ bulk.

III. RESULTS AND DISCUSSION

A. *X-ray diffraction*

The XRD data of the $Cd_{0.75}Zn_{0.25}S$ samples confirmed structure was preserved after incorporation of the metal sulfides by precipitation. All the $Cd_{0.75}Zn_{0.25}S$ samples showed X-ray diffraction profiles with (100), (001), (101) and (110) diffraction peaks (Figure 3). The low relative intensities of the higher-order diffraction peaks originate from two sources, as explained by Schüth et al. First, a high ratio of wall thickness versus pore size produces lower relative intensities for higher-order diffractions. Second, these relative intensities are also influenced by the roughness of the pore walls.

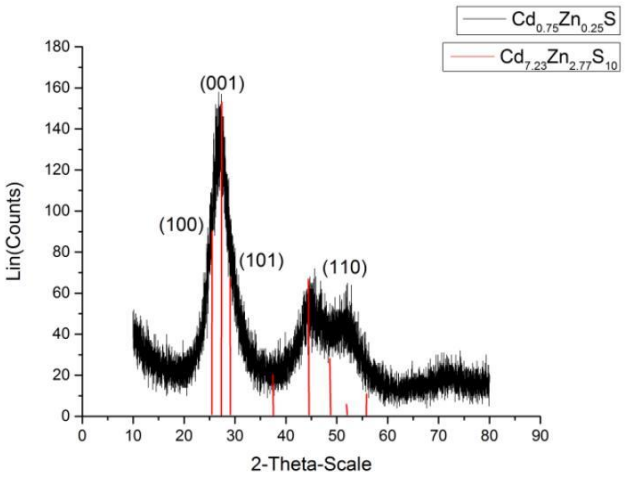

Figure 3. XRD patterns of the $Cd_{0.75}Zn_{0.25}S$ photocatalysts

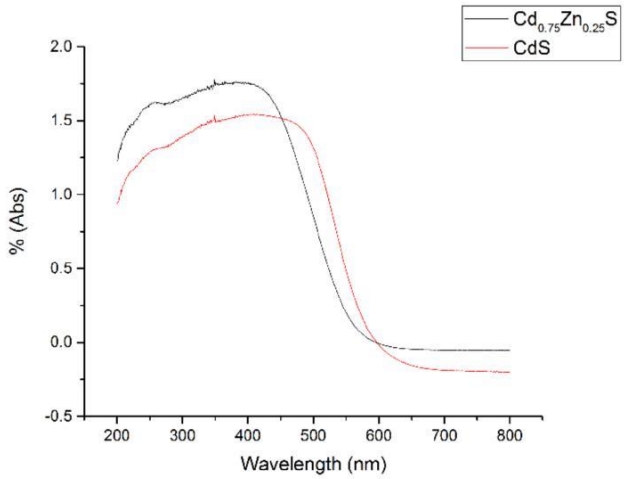

Figure 4. DRS UV-vis spectra of the CdS, and $Cd_{0.75}Zn_{0.25}S$ solid solutions.

B. UV-vis diffuse reflectance spectroscopy (DRS)

The coordination environment of Cd^{2+} and Zn^{2+} ions in calcined samples was studied by UV-vis diffuse reflectance spectroscopy. The absorption edges of $Cd_{0.75}Zn_{0.25}S$ photocatalysts gradually shift from 3.4 eV to 3.6 eV as the Zn concentration increases, as observed in Figure 4. ZnS has only one absorption edge located about 397 nm, while the CdS presents an absorption edge around 460 nm indicating some kind of electronic interaction between CdS nanoparticles resulting in a Cd-S bonding. The absorption edge of the solid solution gradually changed as the amount of cadmium increased and was distributed between the two phases of CdS and ZnS. This phenomenon can be attributed to the transition band of the solid solution of $Cd_{1-x}Zn_xS$. The band gap sizes for $Cd_{1-x}Zn_xS$ catalysts, calculated from the onset of the absorbance edge spectra. The band gap (BG) size of $Cd_{1-x}Zn_xS$ photocatalysts is a function of the Zn composition. The transitions from low to high absorption for the $Cd_{1-x}Zn_xS$ samples are not sharp as in the pure CdS and ZnS; this is indicative of a spread in cluster size. The $Cd_{1-x}Zn_xS$ samples show blue shifts in their absorption edges when the Cd concentration decreases (Zn concentration increases). With the increasing value of x, the position of the valence band of $Cd_{1-x}Zn_xS$ hardly changes, while the conduction band is more negative, leading to a marked blue shift in the band of the $Cd_{1-x}Zn_xS$ solid solution.

*C. **CdS***

1) Calibration of the system

The first task was for the model of CdS energy cutoff, k-points and the optimum geometry for CdS which is shown in the Table 1. The optimized values obtained for the CdS were of 520eV for the Ecutoff. Once the Ecutoff, we proceeded to get k points that best represent the structure, the optimum level in 6 6 6. Once Ecutoff and k-points is obtained, we proceed relax the system, obtaining a lattice constant of 5.94 Å.

Label	Ecutoff	k-points	a/Å
(CdS)	320 eV	2 2 2	5.90
(CdS)	420 eV	4 4 4	5.92
(CdS)	520 eV	6 6 6	5.94
(CdS)	620 eV	8 8 8	5.96
(CdS)	720 eV	10 10 10	5.98

Table 1. With a cutoff 520 eV and k-points 6 6 6, was varied the lattice parameter of 5.94Å being the optimum.

2) Plane selection

During optimization of the structure, we find that some groups (CdS) have more than one structure showing almost the same minimum energy. However, we have calculated the delta power to determine the structure having the lowest energy configuration, showed in the Figure 5 which corresponds to 001 plane orientation of growing according to the X-ray experimental diffraction.

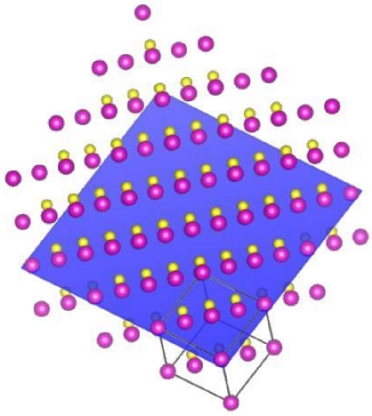

Figure 5. Supercell 3x3x3 preferential (001) to create surface, obtained with the VESTA program.

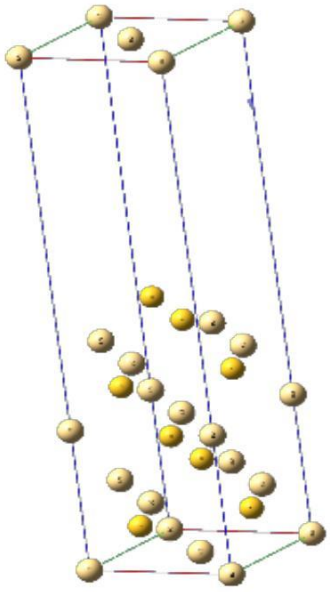

Figure 6. CdS crystal surface representation, orientation (001). The model was obtained with Gaussian09 program.

D. $Cd_{0.75}Zn_{0.25}S$

1) *Calibration of the system*

As second task was obtained for model $Cd_{0.75}Zn_{0.25}S$ to obtain the cutoff energy, the k-points and the optimum geometry. In Table 4, the optimization process is shown, ~~for~~ obtaining an Ecutoff of 480eV. And the k-points that best represent the structure, have a value of 6 6 6. Once cutoff and k-points were obtained, we proceed to relax the system, obtaining a lattice constant of 5.87 Å, see Table 2.

Label	Ecutoff	k-points	a/Å
($Cd_{0.75}Zn_{0.25}S$)	280 eV	2 2 2	5.83
($Cd_{0.75}Zn_{0.25}S$)	380 eV	4 4 4	5.85
($Cd_{0.75}Zn_{0.25}S$)	**480 eV**	**6 6 6**	**5.87**
($Cd_{0.75}Zn_{0.25}S$)	580 eV	8 8 8	5.89
($Cd_{0.75}Zn_{0.25}S$)	680 eV	10 10 10	5.91

Table 2. With a cutoff 480 eV and k-points 6 6 6, was varied the lattice parameter of 5.87Å being the optimum.

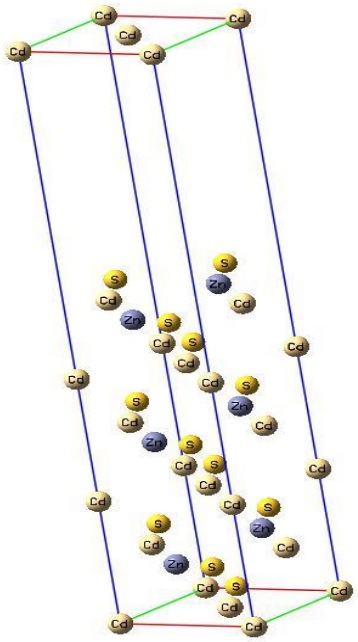

Figure 7. Growth preferential surface (001). The model was obtained with Gaussian09 program.

E. *Comparison between CdS and $Cd_{0.75}Zn_{0.25}S$*

Then with the constructed models mentioned before the electronic properties were calculated and analyzed. The Total Density of States (TDOS) is shown in the Figure 8.

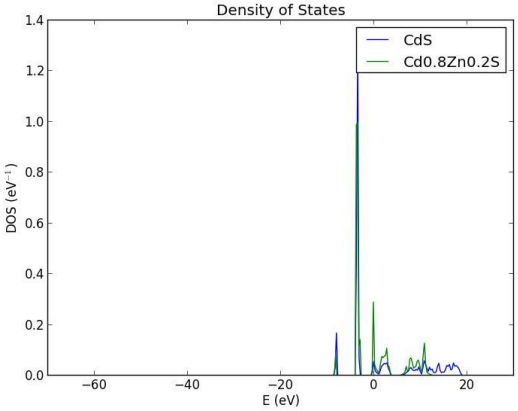

Figure 8. Total density of states for CdS and $Cd_{0.75}Zn_{0.25}S$.

From the calculated TDOS for CdS and $Cd_{0.75}Zn_{0.25}S$ can be observed that are a little modified by the Zn presence, which can be better appreciate in the partial DOS, as it can see in the Figure 7. In the Figure 9 it is shown the density of states to $Cd_{0.75}Zn_{0.25}S$ (a, b) and CdS (c, d). Other repartition in the energy band structures in which the bandgap is affected by the substitution of Zn, vide Figure 10 and 11. From the band structures calculated a diminution of the band gap value from 2.02 eV to 1.05 eV is obtained by the Zn presence in the lattice. Although, the obtained values are smaller than the experimental report 2.4 eV to 1.4 ev (S. A. Macías-Sánchez et. al) due to the well-known limitation of DFT (Stampfl C, Van de Walle CG. Phys Rev B 1999;59: 5521e35.), in this study, we focus on the relative change of the band gap after doping, and expect the band gap error hardly affect the comparative analysis.

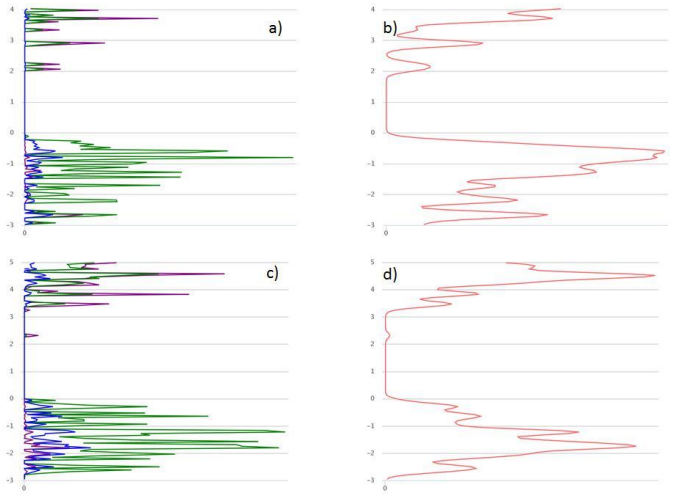

Figure 9. Calculated total and partial DOS for $Cd_{0.75}Zn_{0.25}S$ (a,b) and CdS (c,d)

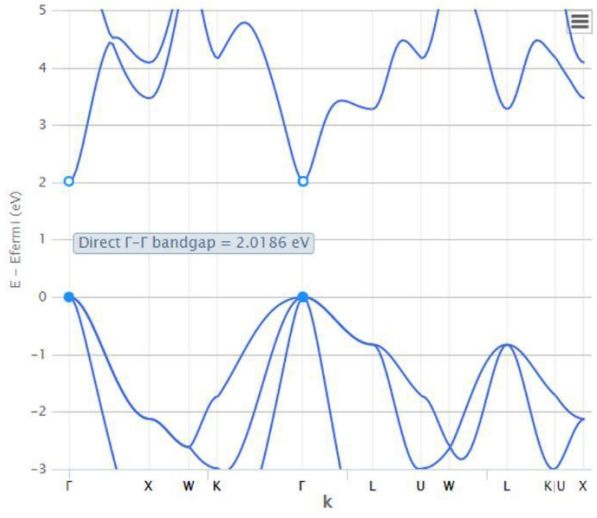

Figure 10. Calculated energy band structures for CdS.

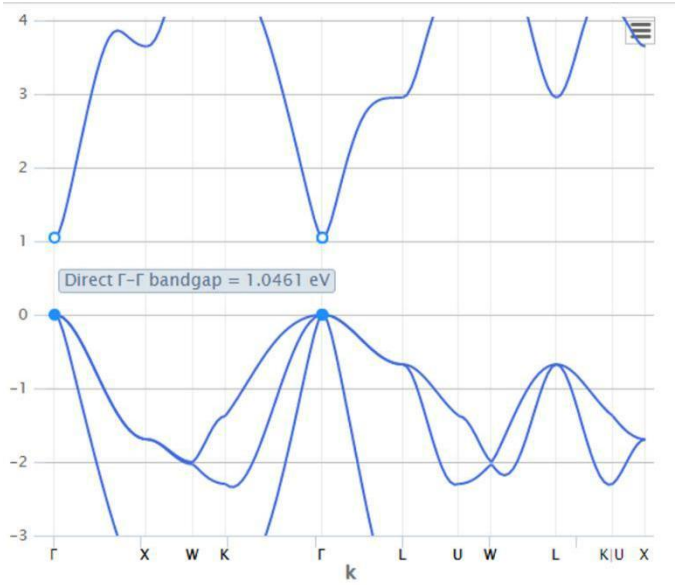

Figure 11. Calculated energy band structures for $Cd_{0.75}Zn_{0.25}S$.

IV. Conclusions

A crystals CdS and $Cd_{0.75}Zn_{0.25}S$ solid solution were synthesized experimentally obtaining cubic growing, which was corroborated by X-Ray diffraction. The experimental UV-Vis shows electronic changes in the $Cd_{0.75}Zn_{0.25}S$ with respect to CdS by the Zn presence. The experimental bandgap obtained for CdS and for $Cd_{0.75}Zn_{0.25}S$ solid solution were 5.579nm and 5.523nm, respectively. The electronic changes by the Zn presence in the $Cd_{0.75}Zn_{0.25}S$ crystal was corroborated using quantum chemical calculations based on density functional theory, which showed differences in the partial DOS distribution and also in the energy band structure. The theoretical results show a decrement in the band gap by Zn presence in the lattice, while the direct band still continuous for the solid solution.

Acknowledgment

We gratefully acknowledge the support provided by the Laboratory for Supercomputing and Visualization in Parallel Cluster YOLTLA from the UAM-Iztapalapa by the infrastructure and management of account to send all calculations of this research.

References

Girginer B, Galli G, Chiellini E. Preparation of stable CdS nanoparticles in aqueous medium and their hydrogen generation efficiencies in photolysis of water. Int J Hydrogen Energy 2009;34:1176e84.

Gust D, Moore TA, Moore AL. Solar fuels via artificial photosynthesis. Acc Chem Res 2009;42:1890e8.

Hagfeldt A, Graetzel M. Light-induced redox reactions in nanocrystalline systems. Chem Rev 1995;95:49e68.

Hirai T,Nanda M, Komasawa I. Dithiol-mediated incorporation of CdS nanoparticles from reversemicellar systeminto Zndoped SBA-15mesoporous silica and their photocatalytic properties. J Colloid Interface Sci 2003; 268:394e9.

Janet CM, Viswanath RP. Large scale synthesis of CdS nanorods and its utilization in photo-catalytic H2 production. Nanotechnology 2006;17:5271e7.

Jing DW, Guo LJ. A novel method for the preparation of a highly stable and active CdS photocatalyst with a special surface nanostructure. J Phys Chem B 2006;110:11139e45.

Jing DW, Guo LJ. Efficient hydrogen production by a composite CdS/mesoporous zirconiumtitaniumphosphate photocatalyst under visible light. J Phys Chem C 2007;111:13437e41.

Kudo A, Miseki Y. Heterogeneous photocatalyst materials for water splitting. Chem Soc Rev 2009;38:253e78.

Kumar P. Inclusion chemistry in periodic mesoporous hosts: growth of quantum-confined materials and gas separation membranes. Ph.D. dissertation. University of Cincinnati; 2007.

Li M, Jiang J, Guo L. Synthesis, characterization, and photoelectrochemical study of $Cd_{1-x}Zn_xS$ solid solution thin films deposited by spray pyrolysis for water splitting. Int J Hydrogen Energy 2010;35:7036e42.

Linsebigler AL, Lu GQ, Yates JT. Photocatalysis on TiO2 surfaces: principles, mechanisms, and selected results. Chem Rev 1995;95:735e58.

Lunawat PS, Kumar R, Gupta MN. Structure sensitivity of nano-structured CdS/SBA-15 containing Au and Pt cocatalysts for the photocatalytic splitting of water. Catal Lett 2008; 121:226e33.

Matsumura M, Furukawa S, Saho Y, Tsubomura H. Cadmium sulfide photocatalyzed hydrogen production from aqueous solutions of sulfite: effect of crystal structure and preparation method of the catalyst. J Phys Chem 1985;89:1327e9.

Mau AWH, Huang CB, Kakuta N, Bard AJ, Campion A, Fox MA, et al. Hydrogen photoproduction by Nafion/cadmium sulfide/platinum films in water/sulfide ion solutions. J Am Chem Soc 1984;106:6537e42.

Meissner D, Memming R, Kastening B. Photoelectrochemistry of cadmium sulfide. 1. Reanalysis of photocorrosion and flatband potential. J Phys Chem 1988;92:3476e83.

Navarro RM, del Valle F, Villoria JA, Fierro JLG. Chap. 4. In: Serrano B, De Lasa H, editors. Advances in chemical engineering-progress in photocatalytic reaction engineering, vol. 36. Elsevier Science Publishers; 2009. p. 111e43.

Navarro RM. Hydrogen production from renewable sources: biomass and photocatalytic opportunities. Energy Environ Sci 2009;2:35e54.

Navarro Yerga RM,A´ lvarez-Galva´n MC, del Valle F, Villoria de la Mano JA, Fierro JLG. Water splitting on semiconductor catalysts under visible light irradiation. Chem Sus Chem 2009;2:471e85.

Osterloh FE. Inorganic materials as catalysts for photochemical splitting of water. Chem Mat 2008;20:35e54.

Sahu N, Upadhyay SN, Sinha ASK. Kinetics of reduction of water to hydrogen by visible light on alumina supported PteCdS photocatalysts. Int J Hydrogen Energy 2009;34:130e7.

Shangguan W, Yashida A. Photocatalytic hydrogen evolution from water on nanocomposites incorporating cadmium sulfide into the Interlayer. J Phys Chem B 2002;106:12227e30.

Subrahmanyam M, Supriya VT, Reddy PR. Photocatalytic H2 production with CdS-based catalysts from a sulphide/sulphite substrate: an effort to develop MgO-supported catalysts. Int J Hydrogen Energy 1996;21:99e106.

Wang L, Wang W, Shang M, Yin W, Sun S, Zhang L. Enhanced photocatalytic hydrogen evolution under visible light over Cd1_xZnxS solid solution with cubic zinc blend phase. Int J Hydrogen Energy 2010;35:19e25.

Wang Y, Herron N. Optical properties of cadmium sulfide and lead(II) sulfide clusters encapsulated in zeolites. J Phys Chem 1987;91:257e60.

Descriptor creation and optimization for open air scenarios

Andras Takacs, Aurelio Dominguez-Gonzalez, Manuel Toledano-Ayala,
Alberto Pastrana-Palma, Jesus Carlos Pedraza-Ortega and Edgar A. Rivas-Araiza
Facultad de Ingeniería
Universidad Autónoma de Querétaro
Santiago de Querétaro
Cerro de las Campanas s/n
Las Campanas, 76010 Mexico
Email: andras.takacs.m@gmail.com

***Abstract*—The modern outdoor self-localizing computer vision applications require more robust and invariant descriptors and go beyond repeatability. The descriptors need to be invariant to light condition, and transformation changes likewise have to have classification power. This paper investigates a genetic algorithm based, a new self-adjusting framework with the aid of machine learning algorithms to create and optimize extendible modular descriptors for specific outdoor environments. The framework optimizes a descriptor creation from roots. It controls the image preparation and machine learning parameters and also optimizes the descriptor size through managing the active member modules and values. We compared the descriptor with the most used state-of-the-art descriptors—on speed, accuracy and invariance to light condition, image resolution changes, scale, affine transformation and rotation—and the results show that it has the best classification results.**

I. Introduction

The merging technology of self driving cars, outdoor mobile AR (Augmented Reality) applications and robotics have a growing need for accurate self localization and visual odometry, effective SLAM (Simultaneous Localization And Mapping), place recognition, object classification, obstacle detection, tracking algorithms among others. The expectations towards the descriptors are higher and higher. The more specialized tasks are not settle any more with only the tracking ability but demands more robust and highly specialized descriptors for these tasks. To achieve this the current general purpose state of the art descriptors performing poorly.

The problem is twofold: first to create a robust and invariant descriptor to light and environmental changes; second to reduce its size without loosing its descriptive power. Our aim is to show that the modular structure and optimization framework gives the opportunity to create condensed scene specialized descriptors with high robustness for classification operations. Our framework is a self adjusting optimizer creating scenery dependent descriptors, where it operates with high efficiency. The base concept is to create lightweight modular descriptors with simple, computationally cheap elements that specialized to the corresponding environment after training them with machine learning techniques using EDD [1] as a base. The framework would pick the necessary modules and values for the scenery during the optimization period and concatenate the resulted modules to a descriptor. A further goal is to create a scene detector function and let the system decide the composition of the descriptor with the objective to reduce the computed and later stored data.

This paper presents a flexible extendible framework that can optimize a feature descriptor in terms of invariance, size and segmentation power using genetic algorithm and Random Forest training method. The algorithm automatically creates descriptor based on the the training database characteristics. The first part of the article will unfold the details following the steps of the framework. The second part presents the results and discussion.

II. Related Work

There are many works on detectors and descriptors and their optimization to light changing environments [2] [3] [4] [5] [6] or size [7] [8] [9]. Each of these work concentrate using a fixed chain of calculations to obtain a fix sized descriptor or a reduced size of an existing one. Different approach for creation and optimization is to break into element the descriptor creation pipeline and concatenate them after optimization using learning approaches [10] [11] [4]. There is more control over the parameters and results of the descriptor. There are different areas in computer vision where Genetic Algorithm (GA) is used. In object recognition [12] [13] where the GA serves as a query function for large image datasets. GA applied also to select [14] or to create and optimize [15] [4] a descriptor for a specific job or environment. GA was also used for optimization methods in combination with Machine Learning Algorithm [16] to optimize descriptors with medical images where machine learning techniques used as a prediction model. But these works use already existing descriptor calculations methods.

III. Genetic Algorithm

The Genetic Algorithm is an effective stochastic algorithm taking as an example of the natural selection and genetics. The base of our design is Goldberg's [17] Simple Genetic Algorithm (SGA) (Algorith 1). The algorithm creates and

keep a population of fixed number of individuals (genomes) and modifies their composition based on probability, genetic operation—Selection, Crossover and Mutation—and evaluation function. The algorithm runs until reaches the termination criteria—creates the last set generation or the optimum score reaches a specific threshold—.

Algorithm 1 Simple Genetic Algorithm pseudocode

```
procedure GENETIC ALGORITHM
    Initialize Population with randomly generated genomes
    repeat
        Evaluation with the Objective Function to Accuracy and Invariance evaluation
        Select individuals for mating
        Mate individuals to produce offspring
        Mutate offspring
        Insert offspring into population
    until reached the termination criteria
end procedure
```

IV. Descriptor Calculation

In this section we present the scheme that creates multiple scene dedicated descriptor. Each element of the algorithm has responsibility for the size reduction and descriptor invariance: The module bank for storing of the building blocks that hold the image processing functions for the descriptor; the activation function for the dimensionality reduction which also delivers information about the relation between the structure of the descriptor and the scene characteristics; the objective function the training period which shapes the descriptor depending of the characteristics of the database.

A. Preprocessing stage

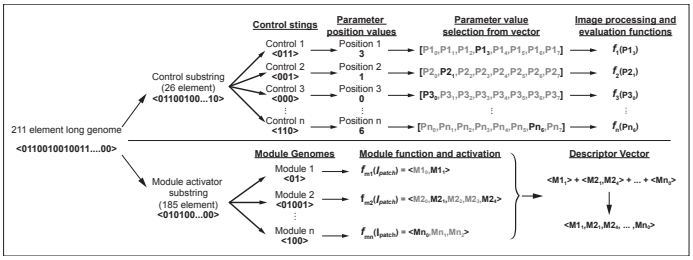

Fig. 1. Modular Descriptor Extraction Process

The binary chromosome known from genetic algorithm typically represent a solution for an optimization problem. In our case this binary string serves two purposes: the first part serves as a control panel being in charge of the image processing and evaluation function parameters, each bit of the string is responsible to activate or deactivate a value in a certain module. During this stage the algorithm—based on the current genome—sets the image processing and evaluation parameters, and assembles the modular descriptor (Figure 1). The first 26 bits of the genome specifies 10 different parameters corresponding to an image processing or evaluation stage. The parameters cover the most important stages of the optimization: Color spaces, Patch Radius, Gaussian Filter Kernel size, Gaussian Sigma, Random Forest Depth, Random Forest Size, Random Forest Best Split, Canny kernel size, Canny Threshold and Pixel Gradient Calculator.

B. Module bank and activation

The second part of the genome a 185 element long binary substring is subdivided into modules. These sub-strings are the binary representation of the modules. They have equal length as the number of values are produced by the corresponding module, and the binary value specifies that the corresponding value is active (=1) or inactive (=0). If a module has only inactive elements the algorithm flushes from the descriptor module list. This organization gives the flexibility to extend the module list infinitely. The Module Bank contains the following elements: Normalized Position; Mean and Standard Deviation of each color channels; 2^{nd}, 3^{rd}, 4^{th}, 5^{th} Order Central Moments; Hu Moments; Gevers [18] color invariant l andf c features; Geusebroek [19] color invariant C and H features; Distance Transform; Eigen values; Gradient Angles.

C. Datasets

We used two sets of images from three databases with different characteristics during the evaluation to evaluate the descriptors adaptabilities in a specific environment and in changed conditions. The Brighton images were specially chosen for the Segmentation evaluation and during the Rotation, Affine Transformation, Resize and Blur Invariance test. The Oxford dataset [20] (Figure 2 (a)-(c)) images were used for the JPEG compression, Illumination and Light condition change evaluation. The TILDE dataset [6] (Figure 2 (d)) images served for the Light condition change evaluation.

Fig. 2. Invariance evaluation images for: **(a)** light change, **(b)** JPEG compression, **(c)** Light condition change 1, **(d)** Light condition change 2

D. Objective function

To evaluate the genome we split the objective function into two function: the segmentation and the invariance optimization. The segmentation evaluation extracts the descriptors for each keypoints, train the data with Random Forest learning

algorithm, and then test the learned model. From the test results we generated confusion matrices to compare the precision of each descriptor. This formed the base to calculate the *overall recognition rate*—the average of all correctly classified patches on the test set—and the *average recognition rate* —the average per class recognition rate on the test images—. The speed probe measured two different properties. The *average descriptor extraction time* shows the time of the descriptor retrieval from the whole image with an equal amount of key-points. The *average segmentation time* demonstrates the duration of the forest evaluation and image segmentation.

During the invariance evaluation we compare a set of two identical images test the descriptor rotation, affine transform, blur and resize invariance. To compare the impact of the deformation, we kept one of the pair as ground truth and transformed the other. During the rotation, resize and affine transformation (Figure 3) assessments the same transformation matrix converts the keypoints and image pixels to place the reference points to the correct spot.

Both function returns an objective scores which later is converted in each cycle to fitness score. The results of each evaluation operation can be weighted in order to strengthen a specific feature or invariance.

Fig. 3. Affine transformation cases in invariance evaluation: **(a)-(j)** Case 1-10

For the evaluation, we used an Intel®Core™i7-4790 CPU with 3.60GHz. The large lighting condition variations—that often happen in real-world scenarios—can be modelled by a diagonal mapping.

V. Results

The genetic algorithm after 150 generations resulted an optimized descriptor with good segmentation power and similar invariance to rotation, blur, size and affine changes as the most used state-of-the-art descriptors.

We contrasted the Modular Descriptor with the state-of-the-art descriptors' performance with the same Random Forest Training parameters. Table I shows the accuracy evaluation results. Each table reports the *overall recognition rate* in the first column and the *average recognition rate* of each class in the rest of the table. The invariance results plotted on separate graphs with the average match rate on the y axes and the transformation cases on the x axes (Figure 4 and 5).

After the genetic optimization to a specific scene, the modular descriptor developed a higher class recognition power, and became more invariant to transformation changes. The modular descriptor's *overall recognition rate* is the best among the contrasted descriptors and gave the best performance—except in the "Doors and Windows" class—in the *average recognition rate*. The modular descriptor also reached a significant improvement in the transformation invariance compared to EDD, and shown a midrange invariance towards affine, blur and size changes, but it kept highly variant towards rotation. Also performed weakly in the light condition changes.

TABLE I
AVERAGE TRUE POSITIVES AT THE BRIGHTON SCENE.(%)

		Average true positive by class			
Descriptor	All	Else	Doors & Windows	Roof	Wall
SIFT	73.45	78.53	67.23	69.07	71.80
Opponent SIFT	72.45	77.66	66.76	79.15	69.54
SURF	56.18	57.58	55.94	13.96	58.34
Opponent SURF	57.63	65.16	52.30	34.72	57.84
EDD	67.42	63.89	58.17	59.77	61.92
Modular Descriptor	73.70	91.86	55.03	72.13	73.84

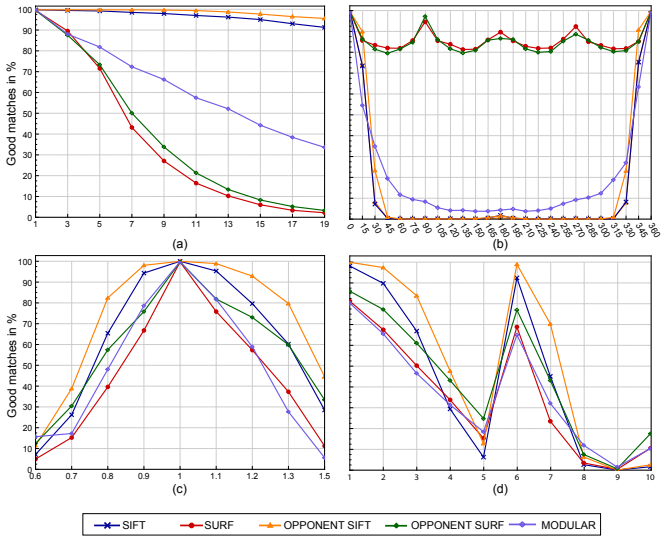

Fig. 4. Transformation Invariance results: **(a)** Gaussian blur (kernel size), **(b)** Image rotation (angle), **(c)** Image resize (size), **(d)** Affine transformation (cases)

VI. Discussion

As the results show the framework has good potential to optimize a list of candidates of a module bank, and image processing parameters into a descriptor with high recognition rate and invariance features. The algorithm also has the potential not only optimize the size of an existing descriptor [4], but refine the image processing parameters and steps. Interesting to see that after three different genetic optimization with 200 generation each, the XYZ was the most effective color space for our purposes with 100 trees in the Random Forest training period which is identical to Brieman's [21] original training

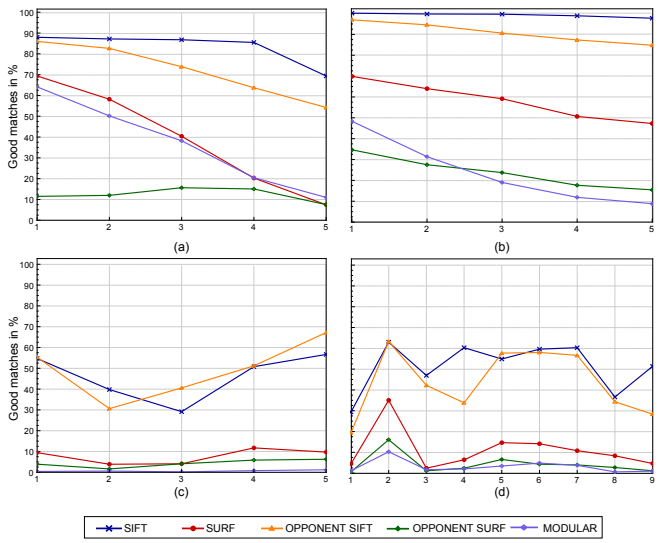

Fig. 5. Photometric Analysis results: **(a)** JPEG compression (cases), **(b)** Light change (cases), **(c)** Light condition change (Notre Dame), **(d)** Light condition change 2 (Mexico)

parameter. Also there is a substantial change comparing the patch with to EDD [1]. Meantime they use 9×9 pixel size patch, in our case for the optimum size is 21×21. This implies more information but also more computation time.

VII. Conclusion

In this paper a new, environment dedicated modular descriptor creator and optimizer algorithm were studied with respect to setup parameters, segmentation accuracy, and invariance. The results show that although the mainstream descriptors have reliable performance in feature detection and invariance, a modular descriptor which is dedicated to a specific environment and optimized in size and image preparation can have similar accuracy and invariance. This projects a new path to investigate a trained modular descriptor which can adjust characteristics of the retrieved information according to the training environment. Based on the results we are planning develop a new, two cycle recognition function where the first class best recognized class results would be removed for the second cycle. Also new modules would be developed for to enhance the invariance to light condition changes.

Acknowledgments

I would like to thank the Consejo Nacional de Ciencia y Tecnología through the project number 340519 without whom this paper could not have been completed. Also, I would like to thank the Universidad Autnóma de Quértaro for its facilities and support.

References

[1] A. Takacs, E. A. Rivas-Araiza, and J. C. Pedraza-Ortega, "Scene dedicated feature descriptor with random forest training for better augmented reality registration," *Research in Computing Science*, vol. 102, pp. 51–61, 2015.

[2] F. Tang, S. H. Lim, N. Chang, and H. Tao, "A novel feature descriptor invariant to complex brightness changes," in *Computer Vision and Pattern Recognition, 2009. CVPR 2009. IEEE Conference on*, June 2009, pp. 2631–2638.

[3] Z. Wang, B. Fan, and F. Wu, "Local intensity order pattern for feature description," in *Computer Vision (ICCV), 2011 IEEE International Conference on*, Nov 2011, pp. 603–610.

[4] H. Lategahn, J. Beck, B. Kitt, and C. Stiller, "How to learn an illumination robust image feature for place recognition," in *Intelligent Vehicles Symposium (IV), 2013 IEEE*, June 2013, pp. 285–291.

[5] C. McManus, B. Upcroft, and P. Newmann, "Scene signatures : localised and point-less features for localisation," in *Robotics: Science and Systems X*, University of California, Berkeley, CA, July 2014.

[6] Y. Verdie, K. Moo Yi, P. Fua, and V. Lepetit, "Tilde: A temporally invariant learned detector," *ArXiv e-prints*, #nov# 2014.

[7] Y. Ke and R. Sukthankar, "Pca-sift: a more distinctive representation for local image descriptors," in *Computer Vision and Pattern Recognition, 2004. CVPR 2004. Proceedings of the 2004 IEEE Computer Society Conference on*, vol. 2, 2004, pp. II–506–II–513 Vol.2.

[8] R. Gonzalez Valenzuela, W. Robson Schwartz, and H. Pedrini, "Dimensionality reduction through pca over sift and surf descriptors," in *Cybernetic Intelligent Systems (CIS), 2012 IEEE 11th International Conference on*, Aug 2012, pp. 58–63.

[9] T. Trzcinski and V. Lepetit, "Efficient discriminative projections for compact binary descriptors," in *Computer Vision ECCV 2012*, ser. Lecture Notes in Computer Science, A. Fitzgibbon, S. Lazebnik, P. Perona, Y. Sato, and C. Schmid, Eds. Springer Berlin Heidelberg, 2012, vol. 7572, pp. 228–242.

[10] S. Winder, G. Hua, and M. Brown, "Picking the best daisy," in *Computer Vision and Pattern Recognition, 2009. CVPR 2009. IEEE Conference on*, June 2009, pp. 178–185.

[11] M. Brown, G. Hua, and S. Winder, "Discriminative learning of local image descriptors," *Pattern Analysis and Machine Intelligence, IEEE Transactions on*, vol. 33, no. 1, pp. 43–57, Jan 2011.

[12] M. Sarfraz, M. ul Hassan, and M. Iqbal, "Object recognition using fourier descriptors and genetic algorithm," in *Soft Computing and Pattern Recognition, 2009. SOCPAR '09. International Conference of*, Dec 2009, pp. 318–323.

[13] M. Behnam and H. Pourghassem, "Feature descriptor optimization in medical image retrieval based on genetic algorithm," in *Biomedical Engineering (ICBME), 2013 20th Iranian Conference on*, Dec 2013, pp. 280–285.

[14] L. Trujillo, G. Olague, F. F. de Vega, and E. Lutton, "Selecting local region descriptors with a genetic algorithm for real-world place recognition," *Applications of Evolutionary Computing*, vol. 4974, pp. 325 – 334, 2008.

[15] L. Trujillo, P. Legrand, G. Olague, and C. Pérez, "Optimization of the hölder image descriptor using a genetic algorithm," in *Proceedings of the 12th Annual Conference on Genetic and Evolutionary Computation*, ser. GECCO '10, 2010, pp. 1147–1154.

[16] A. S. Reddy, S. Kumar, and R. Garg, "Hybrid-genetic algorithm based descriptor optimization and {QSAR} models for predicting the biological activity of tipranavir analogs for {HIV} protease inhibition," *Journal of Molecular Graphics and Modelling*, vol. 28, no. 8, pp. 852 – 862, 2010.

[17] D. E. Goldberg, *Genetic Algorithms in Search, Optimization and Machine Learning*, 1st ed., ser. Artificial Intelligence. Boston, MA, USA: Addison-Wesley Longman Publishing Co., Inc., 1989.

[18] T. Gevers and A. W. Smeulders, "Color-based object recognition," *Pattern Recognition*, vol. 32, no. 3, pp. 453 – 464, 1999.

[19] J.-M. Geusebroek, R. Van den Boomgaard, A. Smeulders, and H. Geerts, "Color invariance," *Pattern Analysis and Machine Intelligence, IEEE Transactions on*, vol. 23, no. 12, pp. 1338–1350, Dec 2001.

[20] K. Mikolajczyk and C. Schmid, "A performance evaluation of local descriptors," *Pattern Analysis and Machine Intelligence, IEEE Transactions on*, vol. 27, no. 10, pp. 1615–1630, 2005.

[21] L. Breiman, "Random forests," *Mach. Learn.*, vol. 45, no. 1, pp. 5–32, #oct# 2001.

Thermo-solar collector with photovoltaic backup and heating control system for high demand periods of hot water

H. Aguirre-Becerra[#1], G. Mota-Valtierra[#2], F. García-Trejo[#3], G. Soto-Zarazúa[*4]

 # Universidad Autónoma de Querétaro, Facultad de Ingeniería.
Cerro de las Campanas s/n Col. Las Campanas, CP. 76010. Querétaro, México.
[1] humberto.aguirreb@uaq.mx[2], georgina.mota@uaq.mx[3], fernando.garcia@uaq.mx
** C.A. de Sistemas Embebidos y Aplicaciones. Universidad Autónoma de Querétaro. Facultad de Ingeniería.*
Cerro de las campanas s/n. Col. Las Campanas, CP. 76010. Querétaro, México.
[4] genaro.soto@uaq.mx

Abstract – This research presents the design and implementation of a new proposal of a photovoltaic-thermal system that uses an electrical resistance for heating water inside the collector of the thermo-solar module. The dimension of system components was oriented to achieve hot water for a family of four members using a 150 l solar collector. The device not only uses a temperature sensor and a microcontroller for starting and closing the heating device but also can be programmed to use the heating resistance only when the user requires hot water, saving electrical energy and diminishing the amount of photovoltaic panels to be installed. High demand schedules for hot water can be defined through a user interface based on a capacitive touchscreen. The mechanism was installed and proved in the Bioengineering Laboratory of Campus Amazcala of the UAQ.

Keywords – solar water collector, photovoltaic system design, capacitive touchscreen

I. INTRODUCTION

A photovoltaic–thermal (PVT) module is a combination of a photovoltaic (PV) panel and a thermal collector for co-generation of heat and electricity [1]. Solar water collectors, due to its simple and compact structure, offers a promising approach for solar water heating in diverse climates; however, the combination of these systems with a PV solar arrangement has not been completely reported [1] or in most cases, they have been analyzed separately [2]. In addition, solar water collectors are liable to be shaded by nearby buildings [3] or deal with days with low solar energy [4], [5]. Most research studies focus in the use of photovoltaic systems for internal water pump in order to maintain a forced circulation of water inside the collector as in [1], [4] ,[6], [7], and generation of electricity and hot water for general household demand as in [8], [9], [10], [11], [12].

Reference [5] shows an auxiliary electrical heating system that can be intelligently controlled by a the temperature sensor in the storage water tank, and reference [4] shows an analysis that supports that solar water heating with a heat pump has a better cost-benefit ratio than that of the electrical resistance. However, this research explains a new system that not only uses a temperature sensor for starting and closing the heating device but also can be programmed to use the heating resistance only when the user requires hot water, saving electrical energy and diminishing the amount of photovoltaic panels to be installed.

II. METHODOLOGY

A. Overall description

Fig. 1 shows the general concept diagram of thermos-solar collector with photovoltaic backup and heating control system for high demand periods of hot water and the components that comprise it. The solar heater tank has an electrical resistance for water heating. The solar electricity generation array consists of an electrical load controller that receives energy from the PV and supply energy stored in the solar battery when needed. A temperature sensor is installed inside the collector for measuring water temperature. The user can select and ON/OFF schedule as considered to be of high demand trough a user interface (GUI) based one in a capacitive touchscreen. The operating principle of the system is based on ensuring the availability of hot water only at times when the user considers them to be of high demand. Activation of the heating part will be done only if necessary. If hot water is available at the scheduled time, the heating part will not be activated. In order to accomplish this task, a temperature sensor will be located inside the collector.

The following situation is proposed as an example. A family of four (parents and two children of school age) where parents work in the morning and children go to school, all at 8:00 am take a shower daily either at night or in the morning. Members who shower at night deplete supply of hot water for members who shower in the morning because cold water fills collector and overnight no solar radiation is received. This is where the control system solves the problem, since previously the user can establish 7:00 am as a “high demand period for hot water”, at 6:00 the controller will measure the temperature inside the collector and if no hot water is available, the heating element will be activated, if hot water is available the heating element will not be activated. The system will also have a manual activation button (on screen) for unexpected situations.

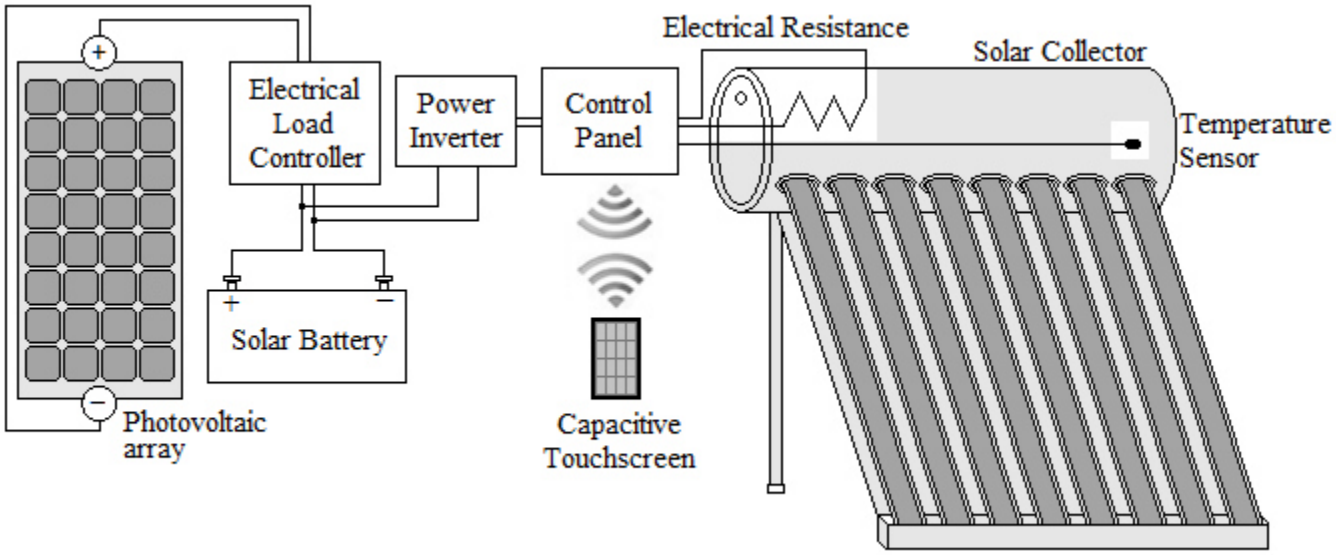

Fig.1. general concept diagram of the photovoltaic-thermal system

The system solves the following issues:

• The users can ensure hot water at any time of day by setting several "high demand periods for hot water" depending on their daily activities, regardless solar radiation intensity (night or cloudy).
• The problem of continuous discharge of solar battery overnight is solved, as activation of the system is only during the high demand hours.
• The system will not activate if hot water is already available.
• The system is completely solar based, since controller and actuators can work through the photovoltaic part.

B. User Interface

The GUI will consist of a capacitive touchscreen model ULCD - 43PCT PICASO 4.3 " 4D SYSTEMS (Fig. 2.). For saving the high demand times the display contains uSD memory in the back.

Fig. 3 shows the proposed GUI of the photovoltaic – thermal system. The main screen (Fig. 3.a) displays the "select schedule" button, the "manual activation" button (ON / OFF) and the "See schedules" button. When the user touch the "select schedule" button, Fig. 3.b appears for selecting the day of the week, then Fig. 3.c appears for hour designation. When touching the "See schedules" button, all hours of high demand programmed by the user will appear as in Fig 3.d.

The capacitive touchscreen will be in an accessible place for the user; for example, in a night table (Fig. 4). The GUI will communicate wirelessly with actuators. Actuators (electrical heating system) which will be found next to the solar heater on the roof of the house.

Fig. 2. Capacitive touchscreen model ULCD - 43PCT PICASO 4.3 " 4D SYSTEMS

C. Energy analysis and photovoltaic design

The next analysis will show the amount of energy needed to increase the temperature of water inside a solar collector with capacity of 150 l (0.150 m^3) that is commonly used for a family of four members. The solar collector has a 700 W electrical resistance backup for water heating. Starting from the assumption that water at 20 °C fills the system and water at 42 °C is considered as hot for a shower [13], the difference of temperature (ΔT) is 22 °C. It will be assumed that the collector is filled at night and that batteries would be charged during day. Equation (1) is used for determining the amount of energy (Q) needed to increase the temperature of water inside the collector, where m is the mass of liquid, C is the specific heat of the liquid and ΔT is the difference of temperature

$$Q = mC\Delta T \quad (1)$$

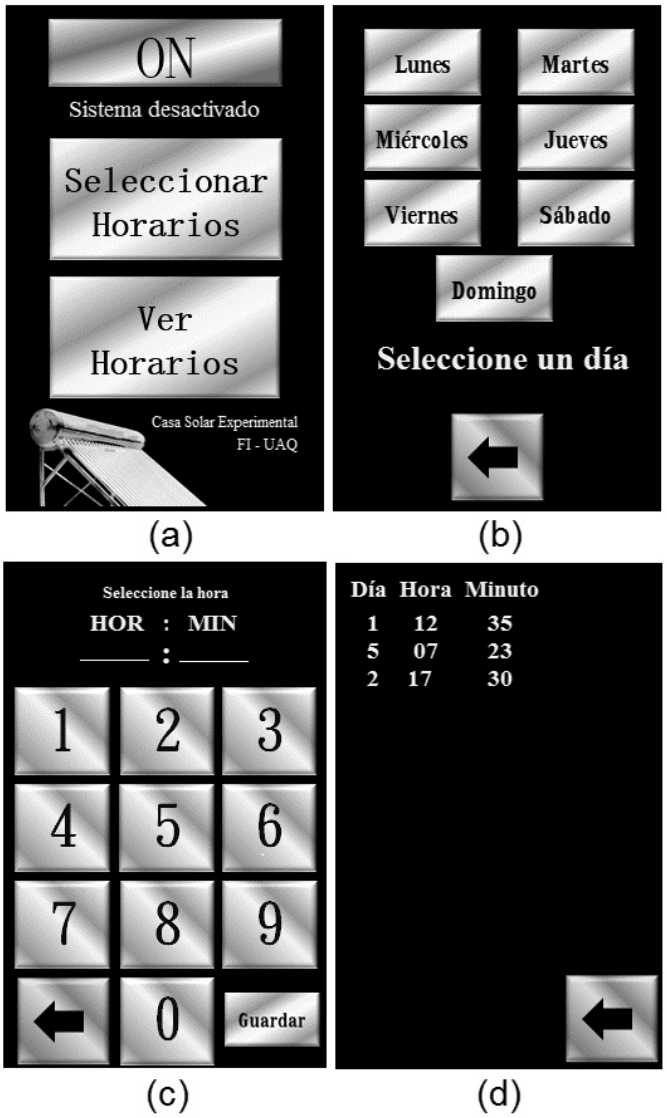

Fig. 3 Proposed GUI of the photovoltaic-thermal system.

Fig. 4. Capacitive touchscreen in a night table, close to the final user.

Since the specific heat of water is 4.186 J g^{-1} °C^{-1} and according with (1) the energy needed to accomplish a ΔT of 22°C is 13,813,800 J. This is the amount of energy that theoretically, the batteries would need to supply to the electrical heating system.

Querétaro city receives a daily amount of 5.9 kWhm^{-2} [14], this information is also used as 5.9 peak sun hours in order to make an easy estimation of PV needed in a solar electrical installation. Using PVs of 150 W, each PV would have a daily production of 885 Wh equivalent of 3,186,000 J, but with an efficiency of 75% the energy produced per panel would be 2,389,500 J or 663 Wh. The total amount of PVs of 150 W needed to accomplish 13,813,800 J (energy needed for the heating system) is 5.78 panels leading to install 6 panels, having a daily production of 3,982.5 Wh.

For the design of the PV electric system, the dimensioning of the battery backup is one of the most important calculus; if the battery backup is oversized, it has the risk of not been completely charged, if the battery backup is small, it has the risk of not delivering enough energy to keep the system working [15]. The information needed for the battery backup dimensioning is the daily energy use, days of system autonomy, battery discharge limit and environmental temperature (if lower than 25°C) [15]. Using a 600 W inverter model PSWGT-300 with 24 VCD input, and considering that the daily energy produced by the system is 3982.5 Wh, 1.5 day backup is required (5,973.75 Wh) with a battery discharge profundity limit of 80% (7,467.15 Wh), and a inverter efficiency of 90% (8,296.83 Wh) the minimum Ampere-hour capacity is 345.7 Ah. Using CALE solar batteries of 12 VCD and 115 Ah, Fig. 5 shows a proposed connection of six batteries that supplies 345 Ah and 24 VCD to the inverter.

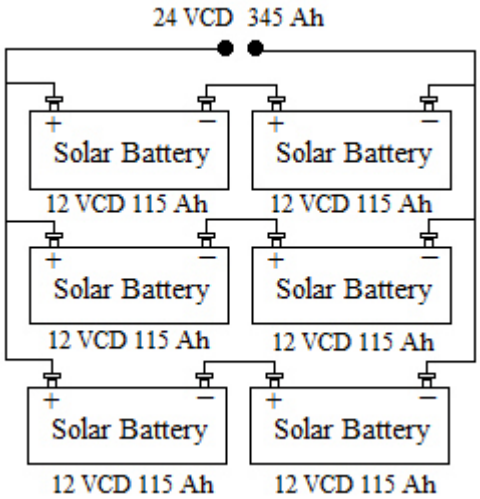

Fig. 5. Battery backup for heating system.

III. RESULTS

TEST 1

In test 1 (Fig. 6) the behavior of the tank temperature of solar heater during four consecutive days without any type of control and without hot water demand is shown in order to have a reference point in the following two tests. Because there is no demand for hot water, the temperature inside the collector behaves stably, with a minimum temperature of 21.1 ° C reported in the day of the first test and a maximum temperature of 90.9 ° C reported in the third day of the test. It is noteworthy that the first day does not reach a high temperature because it was the first day the collector tank received water.

TEST 2

In test 2 (Fig. 7) the temperature behavior of the solar heater tank during four consecutive days without any control type and high demand for hot water is shown in order to know the temperature decrease in the tank due to overnight filling with cold water. For this behavior, the solar heater was drained (simulating high demand) at 18:00 h and was filled with cold water at 5:50 h. It can be seen that water inside the collector is heated only with solar radiation received during day. The minimum temperature recorded during the test was 15.9 ° C which corresponds to the filling of the third day, and the maximum temperature recorded was 61 ° C which corresponds to the fourth day of trial. It is noteworthy that due to drainage of the heater during the afternoon and filled with cold water in the morning, it could not get a similar record as test one.

TEST 3

In test 3 (Fig. 8) the behavior of the solar heater temperature tank during four consecutive days with the control system and high demand for hot water was determined. Electrical resistance was activated during one hour at 6:00 h, by establishing 7:00 as a high demand hour. The temperature behavior was similar to test 2, with a minimum temperature of 15.8 ° C which corresponds to the second day of filling and maximum of 76.2 ° C which corresponds to the third day. It is noteworthy that the electrical resistance accomplishes no considerably effect for increasing water temperature during its activation; achieving an average temperature increase of 6.28 ° C during activation. However, it is noteworthy that due to the energy injected by the heating resistance, higher temperatures are achieved throughout the day compared with test 2.

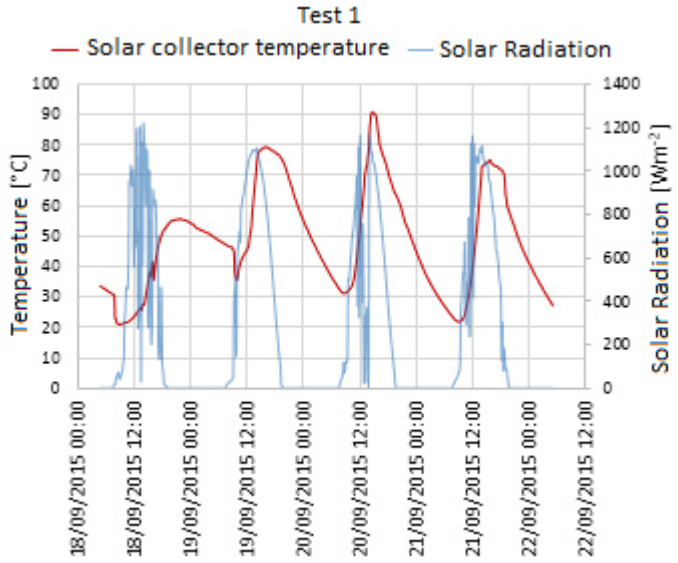

Fig 6. Temperature behavior inside the solar collector tank and received solar radiation during test one.

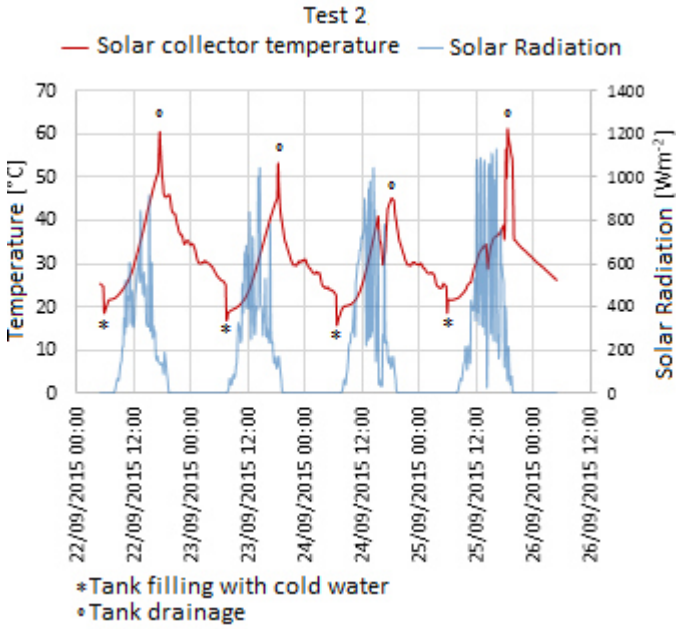

Fig 7. Temperature behavior inside the solar collector tank and received solar radiation during test two.

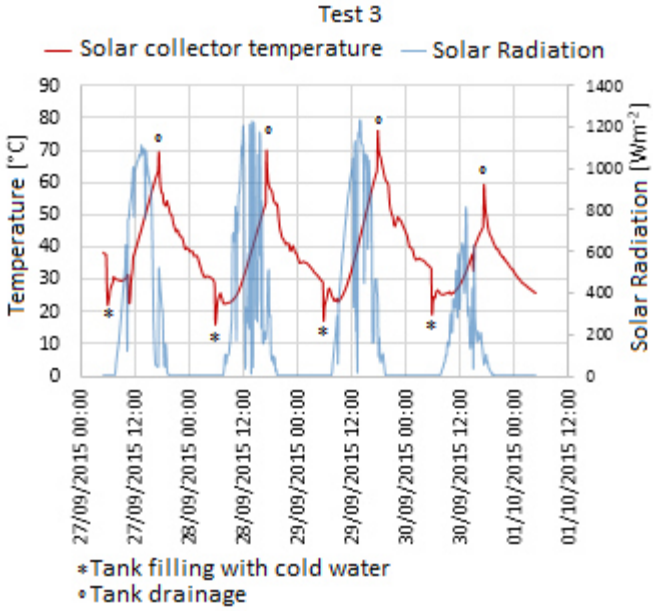

Fig 8. Temperature behavior inside the solar collector tank and received solar radiation during test three.

IV. CONCLUSION

Energy injected by the heating resistance has no significant effect on water temperature inside the tank, accomplishing an average increment of 6.28 °C of 150 l of water. However, it is noteworthy that due to the energy injected by the heating resistance during one hour, higher temperatures are achieved throughout the day.

V. DISCUSSION

This work presents the analysis of using an electrical resistance for back up of a thermal solar collector. Results suggest that this type of backup is not suitable for an immediate increment of temperature inside the collector, it only helps to achieve higher temperatures along the day; and when no solar radiation is received, temperature increases slowly when the resistance is activated. Besides, using electricity generated by solar photovoltaic, considerably increases the total cost of the system since a high amount of energy is required for water heating. Using solar electricity generation is not recommendable for this type of applications, even with a temperature control system and activation in high demand schedules. The system control for activation of heating elements would be suitable for gas heaters that can achieve faster increment of temperature.

Most researches note that energy efficiency of solar collectors with photovoltaics is suitable and can be used to improve system performance; nevertheless, in most applications, photovoltaics generated energy is used to force convection [1], [4], [6], [7] or pump water inside the collector [16], not for heating directly the water inside the collector.

ACKNOWLEDGMENT

I express my gratitude to the Research and Postgrad Direction of the Engineering Faculty (DIPFI) of the UAQ for financing this project through the “Experimental Solar House” research call. We thank our colleges of UAQ who provided insight and expertise that greatly assisted the research.

REFERENCES

[1] Ziapour, B.M., V. Palideh, and A. Mohammadnia, *Study of an improved integrated collector-storage solar water heater combined with the photovoltaic cells.* Energy Conversion and Management, 2014. **86**(0): p. 587-594.

[2] Carnevale, E., L. Lombardi, and L. Zanchi, *Life Cycle Assessment of solar energy systems: Comparison of photovoltaic and water thermal heater at domestic scale.* Energy, 2014. **77**(0): p. 434-446.

[3] Li, D. and S. Liao, *An integrated approach to evaluate the performance of solar water heater in the urban environment.* Energy and Buildings, 2014. **69**(0): p. 562-571.

[4] Reis, R.V.M., et al., *Comparative Study between a Heat Pump and an Electrical Resistance as Energy Support for a Solar Water Heater.* Advanced Materials Research, 2014. **1016**(Mechanical and Aerospace Engineering V): p. 748-752.

[5] Zhang, X.J., C. Peng, and P. Liu, *Research on High-Rise Building Integrated Automatic Tracking Solar Water Heater.* Advanced Materials Research, 2014. **935**(Green Technologies and Sustainable Development in Construction): p. 12-17.

[6] Garg, H.P. and R.K. Agarwal, *Some aspects of a PV/T collector/forced circulation flat plate solar water heater with solar cells.* Energy Conversion and Management, 1995. **36**(2): p. 87-99.

[7] Ji, J., et al., *Experimental comparison of two PV direct-coupled solar water heating systems with the traditional system.* Applied Energy, 2014. **136**(0): p. 110-118.

[8] Herrando, M., C.N. Markides, and K. Hellgardt, *A UK-based assessment of hybrid PV and solar-thermal systems for domestic heating and power: System performance.* Applied Energy, 2014. **122**(0): p. 288-309.

[9] Dubey, S. and A.A.O. Tay, *The Theoretical Modelling and Optimization of a 10 KWP Photovoltaic Thermal System for a Student Hostel in Singapore.* International Journal of Green Energy, 2013. **11**(3).

[10] Dupeyrat, P., C. Ménézo, and S. Fortuin, *Study of the thermal and electrical performances of PVT solar hot water system.* Energy and Buildings, 2014. **68, Part C**(0): p. 751-755.

[11] Ji, J., et al., *Experimental investigation of tri-functional photovoltaic/thermal solar collector.* Energy Conversion and Management, 2014. **88**(0): p. 650-656.

[12] Wei, H., J. Liu, and B. Yang, *Cost-benefit comparison between Domestic Solar Water Heater (DSHW) and Building Integrated Photovoltaic (BIPV) systems for households in urban China.* Applied Energy, 2014. **126**(0): p. 47-55.

[13] Mexicana, B.D.d.l.M.T. *El baño*. 2009.

[14] S., R.A., E.C. R., and J.B. A, *Actualizacion de los Mapas de Irradiacion Global solar en la Republica Mexicana*, 1999, Southwest Technology Development Institute, NMSU.

[15] Harper, G.E., *El ABC de las instalaciones eléctricas en sistemas eólicos y fotovoltaicos*2011

[16] A.K. Pandey, V.V. Tyagi, Jeyraj A/L Selvaraj, N.A. Rahim, S.K. Tyagi, Recent advances in solar photovoltaic systems for emerging trends and advanced applications, Renewable and Sustainable Energy Reviews, Volume 53, January 2016, Pages 859-884, ISSN 1364-0321, http://dx.doi.org/10.1016/j.rser.2015.09.043.

Energy reduction in microalgae oil production through alternative methods of harvesting, cell disruption and extraction

Juan Manuel Vera Morales, Marieke Vanthoor-Koopmans, Juan Fernando García Trejo
Dirección de Investigación y Posgrado, Facultad de Ingeniería
Universidad Autónoma de Querétaro
Querétaro, México
juan.m.vera@gmail.com

Claudia Gutiérrez Antonio
Facultad de Química
Universidad Autónoma de Querétaro
Querétaro, México

***Abstract*—Microalgae have the potential to become a sustainable source of vegetable oil, due to its production efficiency and lipid content. The current production process includes three stages: biomass dewatering by centrifugation, mechanical cell wall disruption and Soxhlet oil extraction. However, these processes are not energetically sustainable, and current research is focused on proposing different mechanisms to reduce the use of energy in the microalgae oil production. There are several proposed alternatives to each step This study is focused on the evaluation of some of these alternative methods; flocculation for dewatering, pulsed electric fields for cell disruption, and microwaving for oil extraction. A quantification of energy required for traditional centrifugation, mechanical beating and Soxhlet extraction showed a total energy consumption of 61.03 kW h/kg dry weight. Using flocculation by pH change, pulsed electric fields and microwave extraction, a total of 16.61 kW h/kg dry weight energy was required. Overall, the results suggest that these alternative processes are viable to obtain microalgae oil with less energy than the traditional methods. Moreover, the proposed alternative methods can be integrated in a continuous process that can improve the energy consumption in the future**

Keywords—microalgae; oil; flocculation; pulsed electric fields; microwaving;

I. INTRODUCTION

Vegetable oil is a viscous liquid constituted by triglyceride molecules and produced by photosynthetic organisms. Industrially, vegetable oil is extracted from oleaginous plant seeds such as soybean, palm or sunflower. Historically, vegetable oil has been mainly used in food preparation, but recently, it has been employed for other purposes such as paints and resins additive, chemical precursor for other substances or for biofuel production, mainly biodiesel [1].

In the last decade, non-food oil consumption has increased due to growing new industries requiring it in industrial processes and a global interest on alternative fuels. Also, changes on traditional diets and growing world population have increased the oil demand for human consumption, as can be seen in Figure 1 [2]. However. cultivation of traditional oil producer plants is limited due to the need for large fertile land extensions along with water and nutrient required for consumption, thus, the future of vegetable oil production is considered an important issue for the whole world [3].

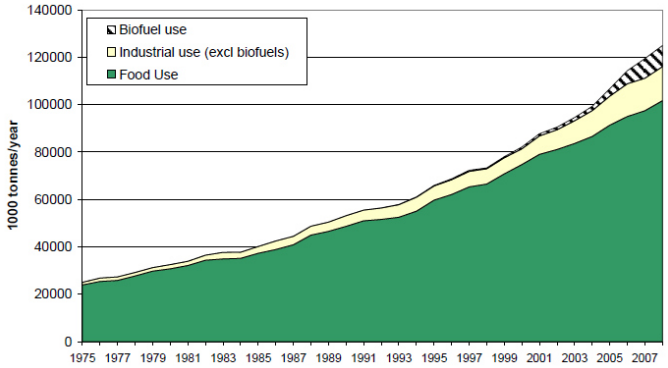

Fig. 1. Global consumption of vegetable oils by major applications [2].

Microalgae have potential as usable biomass for renewable energy production. Specifically, some species of microalgae can produce high amounts of lipids [4]. Microalgae are unicellular photosynthetic microorganisms that live in aquatic systems. Microalgae does not need soil to grow and can use multiple nutrient sources, such as wastewater or marine water. These microorganisms also produce other valuable compounds such as proteins, carbohydrates and pigments [5].

Currently, microalgae are produced to obtain specific compounds, but there is an important interest on high lipid production species. However, several obstacles limit its massive production. One of the most important problems is that microalgae oil production has high energy requirements [6]. Water-suspended microalgae cells are very diluted in the medium, and constitutes only between 0.02-0.5% of the total culture volume [7], and its cell properties, such as small size (between 5 and 20 μm) and electric charge, maintain the culture in a homogeneous and very stable suspension [8]. Microalgae cells also have a strong and flexible cell wall

which is not easily permeated, and the oil is usually found as globules adhered to internal membranes, making the extraction a difficult process [9].

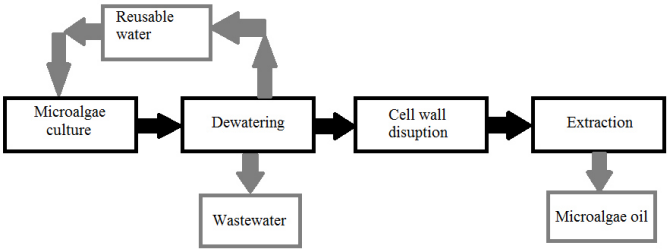

Fig. 2. Ideal process for microalgae oil production.

The typical oil extraction processes currently used have been adapted from other industries, like waste water treatment or standard oleaginous seed oil extraction. Once a microalgae culture has been produced, oil obtainment typically follows a three-stage process: biomass dewatering or harvesting, which consists on separate the microalgae biomass from the water medium -with an ideal possibility of recovering said water – and obtain a high concentrated slurry; cell wall disruption to easily access the intracellular oil; and oil extraction from the rest of intracellular content, causing the less possible damage to the rest of the biomass in order to obtain other compounds of interest. A diagram of the ideal process can be seen in Figure 2, including the alternate discard or recover water step

Standard dewatering process uses centrifuges to precipitate biomass by density difference [10]. Filters are then used to collect biomass forcing water to pass through a membrane, retaining microalgae biomass [11]. Centrifugation and filtration are efficient processes; however, both consumes high amounts of energy [12].

Flocculation consists on the formation of bigger cell aggregates that are easy to collect using cheap and simple filters or by simple draining of the excess water. Flocculation is an interesting alternative to centrifugal dewatering. Flocculation can be promoted by different methods, such as the addition of different compounds – both chemical and biological –, induction of changes in pH value, or application of electromagnetic currents [13]. In terms of energy consumption, flocculation is currently the most promising process, and, depending of the elected flocculation process, it is possible to reuse the filtered medium [14]. However, this operation normally requires extra equipment to allow the medium to flocculate, since it is acknowledged that flocculation efficiency requires steady conditions. Also, the addition of certain chemical flocculants can turn the medium unsuitable for reuse and create contamination problems with waste water [15].

Once the microalgae biomass has been collected, the cell wall must be broken in order to obtain the intracellular oil. Currently, the cell wall rupture is achieved using mechanical methods like press extrusion and mechanical bead-beating [16]. However, due to the plasticity of the cell wall, these processes are poorly effective and consume lots of energy which is mainly lost as heat [17].

An alternative to this process is electroporation, the induction of an electrical imbalance in the cell wall charges, thus reducing its impermeability. Once the cell wall is permeable, solvents can easily extract the intracellular compounds [18]. Though electroporation can be achieved by direct application of an electric shock, this can damage some compounds; so an alternative is the electroporation using high frequency pulsed electric fields (PEF) [19]. These pulses are generated through external electrodes, which create an electromagnetic field strong enough to electroporate the cell wall [20].

Soxhlet and Blight-Dyer extraction methods are extensively used to extract vegetable oil form biomass; these methods use non polar solvents such as hexane, chloroform and methanol, due to the polar affinity with oil molecules [21]. Both methods require intensive extraction times at high temperatures, which accounts for considerable amounts of energy to maintain the adequate conditions of temperature and pressure [22].

Microwave-assisted extraction consist in generation of local heating points caused by microwaves inside and outside of the cell. These heating points vaporizes small amounts of liquid, and the vapor either drags the non-polar molecules to the solvent liquid phase or creates enough internal pressure to project intracellular content to the outside of the cell [23]. This method can achieve similar oil yields compared to Soxhlet extraction, and, though it is a high energy consumption process, the time required to extract the oil are significantly shorter than Soxhlet extraction, this compensates the high energy input and can result in a reduced overall consumption [24].

This work focuses on the comparison between energy consumption required to obtain microalgae oil on a laboratory scale using the conventional processes (centrifugation, mechanical cell wall disruption, and Soxhlet extraction) in comparison with the proposed approach that includes flocculation by pH change, electroporation by PEF and solvent extraction using microwaves. The proposed methods are also performed under conditions similar to a continuous process in order to observe if the integration of these alternatives is viable under non steady conditions.

II. METHODOLOGY

A. Microalgae Culture

The scope of the work considered that, for an oil production process, microalgae culture in optimal conditions and ready to be harvested is available. A *Chlorella vulgaris* culture with a concentration of 2.7 g/L microalgae dry weight was provided by Universidad Autónoma de Querétaro, Campus Amazcala.

The culture medium was prepared with tap water and 0.1% of a commercial foliar fertilizer (Bayfolan Forte©, Total N 11.4%, phosphorus as P_2O_5 8%, potassium as K_2O 6%). *Chlorella vulgaris* was grown in an Algaemist® photobioreactor, incubated at 31°C and illuminated using cool-white LED lamps 24 h/day and continuously aerated by CO_2 for 10 days. The microalgae concentration was calculated after measuring the optical density of the culture at 750 nm and comparing the result with a previously elaborated optical density versus dry weight curve.

All the energy consumption from every equipment used in the study was measured based on the energy input it required, the full time elapsed in the process, and the total biomass processed for every step, and all results were converted to kW h/kg dry microalgae weigh (dmw) for an adequate comparison.

B. Dewatering processes

For the dewatering step using centrifugation, six samples of 10 ml of the culture were put each one in 12 ml glass tubes and centrifuged in an Eltek laboratory centrifuge TC A series at 3000 rpm for 15 minutes; the supernatant was discarded and the microalgae precipitate was collected, dried and weighted.

For the proposed flocculation process, six samples of 50 ml of the culture were collected in 100 ml beakers each one, all samples were mixed with potassium hydroxide solution, 0.1 M, to achieve a pH value of 10; immediately after that, the samples were stirred for 2 minutes in a Thermo-Scientific model SP-131015 magnetic stirrer at 120 rpm in order to flocculate the microalgae cells in a non steady state, simulating the conditions in a photobioreactor. After the 2 minutes, each sample was passed through a 20 µm Whatman filter paper, previously weighted. The filter paper was dried in an oven at 70 °C for 24 hours, and weighted again to obtain the total harvested microalgae weight.

C. Cell disruption processes

For the mechanical cell disruption method, six samples of 5 g of dried microalgae were passed through an model A-11 IKA beating mill at 20000 rpm for 1 minute, in order to measure the energy required by mechanical disruption. A beating mill was selected due to no availability of a bead-beating equipment.

For the alternative to mechanical cell disruption, electroporation using PEF was chosen A PEF chamber was constructed based on previous report from [20] as shown in Figure 3. Copper electrodes were used due to the highly conductivity of the metal. The chamber capacity was measured at 15 ml. The PEF unit was designed to work under continuous flow conditions; however, for the purposes of the present study, batch conditions were used.

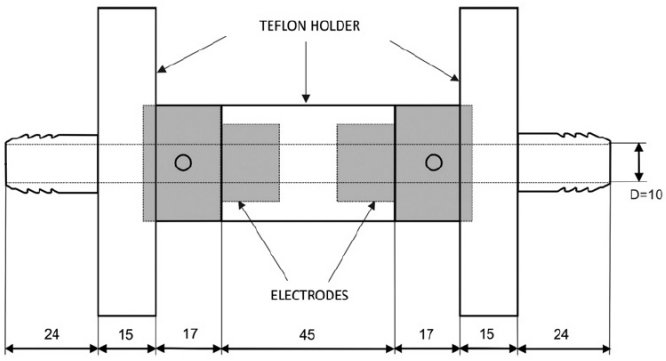

Fig. 3. PEF chamber for continuous cell electroporation, as described by [20].

Due to the fact that PEF treatment requires a liquid medium, six samples of 9 g of dried microalgae were weighted and mixed with 10 ml of a hexane-acetone 1:1 solution. Each sample was put under the same PEF conditions (4 kV/cm, 5 Hz) for one minute, After this time, all the samples were collected for extraction.

D. Oil extraction process

For the Soxhlet solvent extraction, the mechanical milled samples were put in a 1.6 µm filter paper capsule and extracted using a Soxhlet extraction chamber with a hexane-acetone 1:1 solution in a 125 ml flask. The Soxhlet equipment was heated in a Thermo-Scientific model SP-131325 hot plate for four hours at 60 °C and the extraction chamber was cooled using a PolyScience model MX7RL water pump cooler recirculator at 10°C.

Microwave extraction was performed on PEF treated samples. For this, 16 ml of the hexane-acetone solution were added to each sample to complete a total of 25 ml. All samples were microwaved under the same conditions (700 W, 2.45 GHz, 100°C, for 10 minutes) in an Anton Paar model Multiwave PRO extraction equipment.

After extraction, all samples were collected and the solvents were evaporated in a water bath at 55°C to collect the oil extracted

III. RESULTS

A. Dewatering process

Centrifuged samples were collected after the process, then dried and weighted, and a total efficiency of 97% was obtained based on the original culture concentration. The capacity of the centrifuge equipment was 60 ml; with an input of 100 W and a total harvesting yield of 0.157 g of dry microalgae cells after 5 minutes, the total energy consumption for the centrifuge equipment was calculated as 19.7 kW h/kg dmw.

Flocculation showed a lower final efficiency, an average of 78% of microalgae biomass was retained in the filters after the stirring time. However, considering the total time of the process (2 min), and a lower input (20 W) for the agitation, the energy consumption from this stage was

calculated in 4.11 kW h/kg dmw. Also, the flocculation was conducted under non-steady conditions, similar of those from a photobioreactor; which means the flocculation can occur directly in the culture, and this energy consumption can be even lower.

Another interesting result of the flocculation using alkaline pH is that, once neutered, the filtered medium is viable to grow new microalgae cultures. And, due to the remanent microalgae cells, it can regrow immediately after the dewatering process.

Both dewatering processes studied here are highly dependent on microalgae concentration in the culture. For an optimal energy consumption, higher microalgae cell concentrations are useful. However, a higher amount of microalgae slurry in the filters can increase the time required for the final biomass harvesting, or for the whole process to be complete.

B. Cell disruption process

The beating mill equipment had an input of 160 W. Considering the conditions mentioned in the previous section, a total energy of 5.33 kW h/kg dmw consumption was measured. The beating mill had a maximum capacity of 7.33 g of dried microalgae. Considering this, the optimal energy consumption using this instrument can vary. The amount used in this study was the recommended for the instrument according to the instruction book.

The beating mill used here has a higher capacity, but it also translates in higher energy consumption. Optimal conditions for the beating mill are unknown, and the energy consumption could be lower under better operational conditions.

The PEF equipment energy consumption for the 9 g samples was calculated as 2.6 kW h/kg dmw. The conditions were those used by [20]; however, optimal conditions are still being studied, and it can be possible to lower the energy required for electroporation using PEF treatments. Also, [20] proposes the possibility of microalgae oil spontaneously floating away of the cell, thus, the extraction step could be simplified or even skipped using PEF. The viability of the spontaneous release is, however, still under research and not enough evidence of it is available.

The PEF chamber used in this study can also be incorporated in a continuous flow, which could allow an integration with the flocculation system. Though for the adaptation of the process the energy required for microalgae-solvent mixture slurry should be considered.

C. Oil extraction process

For the Soxhlet extraction, at the required temperatures (72°C), the hot plate had an input of 30 W, and the water cooler pump had an input of 20 W; for the total time required for extraction, and the weight of the microalgae sample, the energy consumption was calculated as 36 kW h/kg dmw.

Soxhlet extraction can be improved adding a higher amount of microalgae in the chamber; however, the capacity of the extraction chamber was measured as approximately 7 g of microalgae, so the conditions used here seem to be near the optimum. Also, the total time was chosen based on previous reports. However, particular conditions for the Soxhlet equipment and microalgae species must be measured in order to optimize the time and temperature required for the extraction

Microwave had an input of 600 W, higher than the hot plate used for Soxhlet extraction. However, all samples required one single treatment; thus, the total capacity was higher and also the time was smaller. Microwave extraction also does not requires a condensator unit or a water pump chiller, which reduces the energy consumption and the amount of equipment required. For the conditions cited in the previous section, a total consumption of 10 kW h/kg dmw was calculated.

D. Overall results

After all processes were completed and energy requirements were measured, the results for the standard process and the alternative methods tested in this study were analyzed.

A comparative graph for energy consumptions is shown in Figure 4. As it can be seen, less energy was used in the proposed alternative methods approach, 61.03 against 16.71 kW h/kg dmw. The maximum energy saving was in the harvesting step, using flocculation by pH change and simple filtration instead of centrifugation. Though PEF treatment energy consumption was near half of the mill, both of them are not significant for the total amount of the whole process. Effectivity of both processes could be measured for a better election of a cell disruption method. Microwave extraction is not only a low-energy process, but a fast one, which is convenient for a bigger scale production, and the nature of the process makes the use of a cooler unit not indispensable.

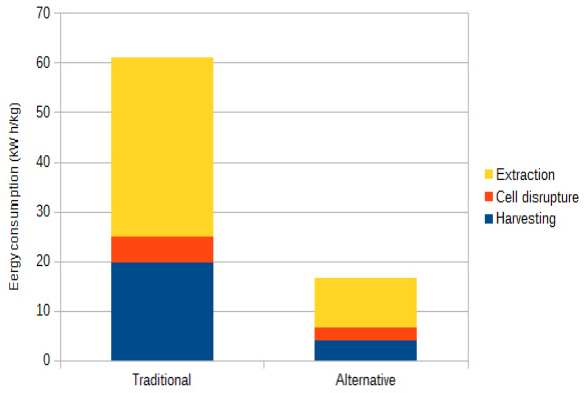

Fig. 4. A comparison between energy consumption from the two studied methods.

IV. CONCLUSIONS

This work showed alternative processes for microalgae harvesting, cell disruption and oil extraction can consume lower amounts of energy. These processes are also capable of being mounted in a continuous system. Flocculation can produce a reusable medium, and the KOH used for pH change can be neutralized and it is assimilable as a nutrient for future cultures. Though energy consumption is highly reduced, none of these alternative methods is still optimized, and a lower energy consumption is possible. Though both flocculation and PEF electroporation are methods easily adaptable to a continuous process, the microwave extraction is still applied in batch conditions, and a continuous adaptation must be proposed and tested.

ACKNOWLEDGMENT

This research was supported by Universidad Autónoma de Querétaro through the FOFI grants. Authors acknowledgment to Consejo Nacional de Ciencia y Tecnología (CONACYT) for the financial support; also, Centro de Estudios Académicos sobre Contaminación Ambiental (CEACA-UAQ) and Campus UAQ-Amazcala collaborate in the project.

REFERENCES

[1] N. Pragya, K. K. Pandey, and P. K. Sahoo, "A review on harvesting, oil extraction and biofuels production technologies from microalgae," *Renew. Sustain. Energy Rev.*, vol. 24, pp. 159–171, 2013.

[2] F. Rosillo-Calle, L. Pelkmans, and A. Walter, "A Global Overview of Vegetable Oils, with Reference to Biodiesel," *IEA Bioenergy Task 40*, no. June, pp. 1–89, 2009.

[3] R. Halim, M. K. Danquah, and P. A. Webley, "Extraction of oil from microalgae for biodiesel production: A review," *Biotechnol. Adv.*, vol. 30, no. 3, pp. 709–732, 2012.

[4] S. K. Ratha and R. Prasanna, "Bioprospecting microalgae as potential sources of 'Green Energy'—challenges and perspectives (Review)," *Appl. Biochem. Microbiol.*, vol. 48, no. 2, pp. 109–125, 2012.

[5] M. Vanthoor-Koopmans, R. H. Wijffels, M. J. Barbosa, and M. H. M. Eppink, "Biorefinery of microalgae for food and fuel," *Boresour. Technol.,* vol. 135, pp. 142-149, 2013.

[6] P. Collet, L. Lardon, A. Hélias, S. Bricout, I. Lombaert-Valot, B. Perrier, O. Lépine, J. P. Steyer, and O. Bernard, "Biodiesel from microalgae - Life cycle assessment and recommendations for potential improvements," *Renew. Energy*, vol. 71, pp. 525–533, 2014.

[7] J. Iqbal and C. Theegala, "Optimizing a continuous flow lipid extraction system (CFLES) used for extracting microalgal lipids," *GCB Bioenergy*, vol. 5, no. 3, pp. 327–337, 2013.

[8] R. Halim, R. Harun, M. K. Danquah, and P. A. Webley, "Microalgal cell disruption for biofuel development," *Appl. Energy*, vol. 91, no. 1, pp. 116–121, 2012.

[9] E. Günerken, E. D'Hondt, M. H. M. Eppink, L. Garcia-Gonzalez, K. Elst, and R. H. Wijffels, "Cell disruption for microalgae biorefineries," *Biotechnol. Adv.*, vol. 33, no. 2, pp. 243–260, 2015.

[10] N. Uduman, Y. Qi, M. K. Danquah, G. M. Forde, and A. Hoadley, "Dewatering of microalgal cultures: A major bottleneck to algae-based fuels," *J. Renew. Sustain. Energy*, vol. 2, no. 1, 2010.

[11] S. D. Rios, E. Clavero, J. Salvadó, X. Farriol, and C. Torras, "Dynamic Microfiltration in microalgae harvesting for biodiesel Production," *Ind. Eng. Chem. Res.*, vol. 50, no. 4, pp. 2455–2460, 2011.

[12] M. K. Weschler, W. J. Barr, W. F. Harper, and A. E. Landis, "Process energy comparison for the production and harvesting of algal biomass as a biofuel feedstock," *Bioresour. Technol.*, vol. 153, pp. 108–115, 2014.

[13] D. Vandamme, I. Foubert, and K. Muylaert, "Flocculation as a low-cost method for harvesting microalgae for bulk biomass production," *Trends Biotechnol.*, vol. 31, no. 4, pp. 233–239, 2013.

[14] A. K. Lee, D. M. Lewis, and P. J. Ashman, "Energy requirements and economic analysis of a full-scale microbial flocculation system for microalgal harvesting," *Chem. Eng. Res. Des.*, vol. 88, no. 8, pp. 988–996, 2010.

[15] M. R. Granados, F. G. Acién, C. Gómez, J. M. Fernández-Sevilla, and E. Molina Grima, "Evaluation of flocculants for the recovery of freshwater microalgae," *Bioresour. Technol.*, vol. 118, pp. 102–110, 2012.

[16] V. Montalescot, T. Rinaldi, R. Touchard, S. Jubeau, M. Frappart, P. Jaouen, P. Bourseau, and L. Marchal, "Optimization of bead milling parameters for the cell disruption of microalgae: Process modeling and application to Porphyridium cruentum and Nannochloropsis oculata," *Bioresour. Technol.*, vol. 196, pp. 339–346, 2015.

[17] J. Doucha and K. Lívanský, "Influence of processing parameters on disintegration of Chlorella cells in various types of homogenizers," *Appl. Microbiol. Biotechnol.*, vol. 81, no. 3, pp. 431–440, 2008.

[18] A. K. Lee, D. M. Lewis, and P. J. Ashman, "Harvesting of marine microalgae by electroflocculation: The energetics, plant design, and economics," *Appl. Energy*, vol. 108, pp. 45–53, 2013.

[19] M. Goettel, C. Eing, C. Gusbeth, R. Straessner, and W. Frey, "Pulsed electric field assisted extraction of intracellular valuables from microalgae," *Algal Res.*, vol. 2, no. 4, pp. 401–408, 2013.

[20] K. Flisar, S. H. Meglic, J. Morelj, J. Golob, and D. Miklavcic, "Testing a prototype pulse generator for a continuous flow system and its use for E. coli inactivation and microalgae lipid extraction," *Bioelectrochemistry*, vol. 100, pp. 44–51, 2014.

[21] H. Kanda and P. Li, "Simple extraction method of green crude from natural blue-green microalgae by dimethyl ether," *Fuel*, vol. 90, no. 3, pp. 1264–1266, 2011.

[22] Y. Peralta-Ruiz, A. D. González-Delgado, and V. Kafarov, "Evaluation of alternatives for microalgae oil extraction based on exergy analysis," *Appl. Energy*, vol. 101, pp. 226–236, 2013.

[23] C. L. Teo and A. Idris. "Ehancing the various solven extraction method via microwave irradiation for extraction of lipids from marine microalgae in biodiesel production," *Bioresour. Technol.,* vol. 171, pp. 477-481, 2014.

[24] F. Amarni and H. Kadi, "Kinetics study of microwave-assisted solvent extraction of oil from olive cake using hexane. Comparison with the conventional extraction," *Innov. Food Sci. Emerg. Technol.*, vol. 11, no. 2, pp. 322–327, 2010.

Effectiveness of gabions dams on sediment retention

A case study

Leandro Velázquez-Luna[1], Eusebio Jr. Ventura-Ramos[2], Isabel R. Cabrera-Baeza[3] and Rosa C. Reséndiz-Mendoza[4]
School of Engineering
University of Querétaro
Querétaro, México
leandro.luna@uaq.mx

***Abstract*— Illegal deforestation, changes in land uses and climate change have resulted in increased runoff and surface erosion from the higher parts of watersheds, impacting directly to the lower parts of the basins where human settlements are common. Such is the case of Angangueo in the state of Michoacán, México, where in 2010 an unusual weather event caused substantial damage to infrastructure, and unfortunately human deaths. Against disasters, the government has carried out actions such as implementing infrastructure to alleviate flooding and mudslides. Gabions weirs were used to control erosion and flow for being considered environmentally friendly than most of the constructed impermeable weirs. This study was carried out to evaluate the effectiveness of gabion dams in sediments retention in the El Ventilador watershed in East of Michoacán. Eight gabions dams and five masonry dams two years old were studied. A number of samples from trapped sediments were collected. The results indicated that the gabion dams detain less gravel than masonry dams, opposite case whit sand, and concerning fine sediments there were no significant differences between them. Gabion dams located upstream were more effective at trapping gravel and fine sediments, opposite case whit sand. In masonry dams, the same relationship only among which are close was found. Regarding the efficiency of barriers, there were not identified relationships since the building volume and contribution area is different in each one of them. Hence, if the objective is the retention of fine sediments any two types of dams may work, and it is recommended to place them upstream for greater effectiveness.**

***Keywords*— Weir; Sediments retention; Gabions.**

I. Introduction

Mismanagement of watersheds in Mexico have brought disruption, and its consequences have been severe, as in the case of the watershed 'EL VENTILADOR' in the town of Angangueo in the state of Michoacán, where in 2010 an unusual weather event caused substantial damage to infrastructure, and unfortunately human deaths. Implementing soil and water conservation practices have proven to be a suitable option in mitigating these effects.

Gabions weirs are porous hydraulic structures, which have been successfully used in watershed management to control erosion and flow. The gabions weirs are structures with minimal adverse impact on the water environment and is considered to be more environmentally friendly than most of the constructed impermeable weirs [3]. These structures are semi-permanent rock barriers, which are built in the longitudinal section of the channel, reducing retention upstream flow velocity, retain the sediments and promotes water infiltration into the soil [2]. They are elastic structures, can easily adapt to a site as hydraulic or geometric conditions that may be present in a natural channel [4]. However, their efficiency and effectiveness on sediments retention regarding their location was not determined well, because biophysical characteristics of the basin determine their behavior.

Few studies have focused on determining efficiency and effectiveness of gabion dams in sediments retention, most have focused to investigate the flow over gabions and their influence on the energy loss and flow velocity [4], [1]. Therefore, the main objective of this work was to determine the efficiency and effectiveness of gabion weirs in sediment retention with respect to masonry dams and so generate useful and precise information to the government and private institutions the benefits of implementing such structures, data that can be used in planning and decisions in the management and monitoring of watersheds.

II. Materials and Methods

A. Study Area and Site Selection

The watershed "El Ventilador" has an area of 362 ha and is located northeast of the township Angangueo, in Michoacán State, Mexico, between the extreme coordinates: 2,171,553 North, 2,174,046 South, 366,083 West and 368,636 East. (Fig. 1). Has a range topography elevations from 2740 to 3400 m., is located into the Balsas River Hydrological Region (RH18) and particularly in Cutzamala River Basin and sub-basin of the Rio Chiquito. The soils are volcanic medium texture, predominantly ochric Andosol (To) (290.26 has, 80.2%), followed by Litosol (I) (42.8 ha, 11.8%), and humic Andosol (Th) (28.93 ha, 8%). As regards to the vegetation of the watershed, most of it is oyamel forest, (Abies religiosa) with 47.93% of the total surface, followed by oak forest (Quercus sp.) with 11.36%. The area

occupied by agriculture is only 17%. The other types of vegetation areas occupy less than 8% of the surface thereof.

Eight gabions dams and five masonry dams were chosen, they were built with broken and angular rocks in 2011 as part of the cooperation project number SGIH-GDTT-UAQ-11/03/RF/CC between the Universidad Autónoma de Querétaro (UAQ) and Comisión Nacional del Agua (CONAGUA), their characteristics is showed in Table 1 and their locations in Fig. 2

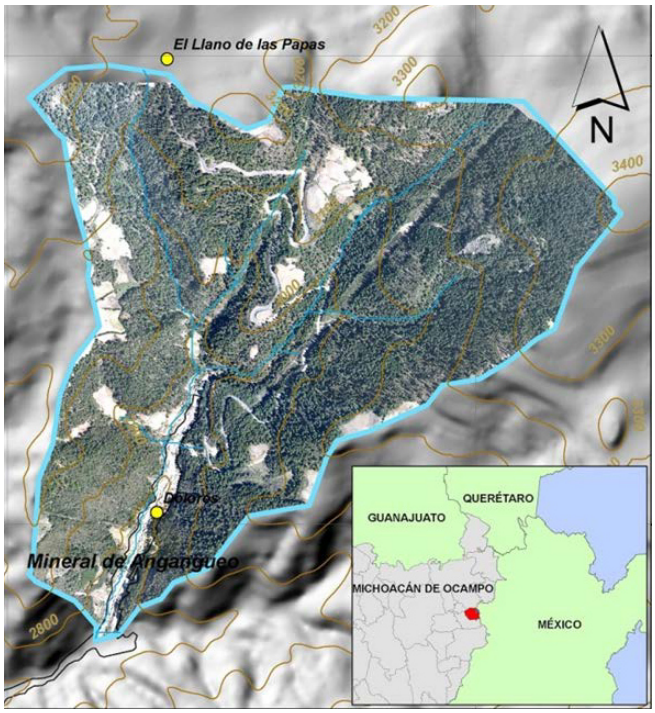

Fig. 1. Location of the watershed El Ventilador

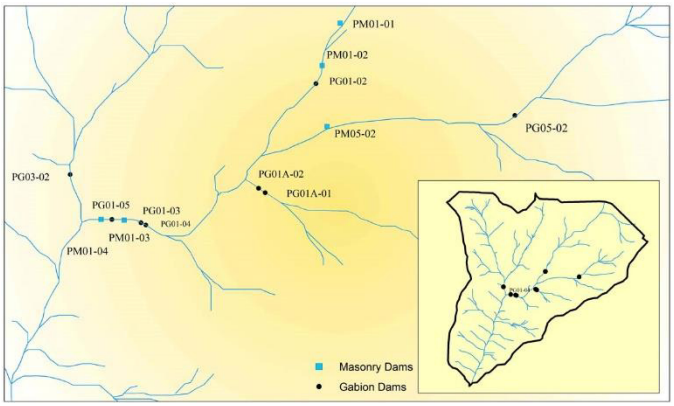

Fig. 2. Location of gabions dams in EL VENTILADOR watersh

B. *Sampling*

In order to determine the kinds of sediments retained in each dam, soil samples were taken upstream, at sediment deposit site. Samples were taken to the laboratory where dried at 105 ° C for 24 hours and sieved with a set of meshes (3/4, 3/8, 4, 10, 35, 60, 120). Sediment classification was performed, according to the granulometry and the American Geophysical Union [5]

C. *Retention capacity and reteined sediments*

The capacity of sediment retention dam was estimated based on their effective height, the length of reservoir, the width and slope of the upstream section of the river bed, values that were taken in the field (Fig.3).

TABLE I. GENERAL CHARACTERISTICS OF GABION DAMS EXAMINED

Dam name	Stream	Length of reservoir basin (m)	Effective height of the dam (m)	Original retention capacity (m^3)	Building volume (m^3)	Coordinates	
						X (m)	*Y (m)*
PG01-02	1	1.6	2.0	4.4	42.0	367337	2172945
PG01-03	1	2.5	3.0	61.4	62.5	366971	2172641
PG01-04	1	2.7	3.0	37.5	69.5	366960	2172645
PG01-05	1	3.0	3.5	99.5	127.0	366898	2172653
PG1A-01	1A	4.5	2.5	39.4	58.5	367228	2172710
PG1A-02	1A	3.9	2.5	25.2	48.0	367213	2172720
PG03-02	3	3.0	2.0	52.5	49.5	366808	2172749
PG05-02	5	6.5	2.5	21.2	39.5	367765	2172876
PM01-01	1	17.6	3.0	422.76	69.9	367389	2173075
PM01-02	1	12.3	2.0	167.53	59.5	367350	2172984
PM01-03	1	12.6	2.1	151.31	27.8	366924	2172651
PM01-04	1	7.1	1.7	101.32	35.7	366875	2172653
PM05-02	5	15.3	2.4	439.17	66.3	367361	2172852

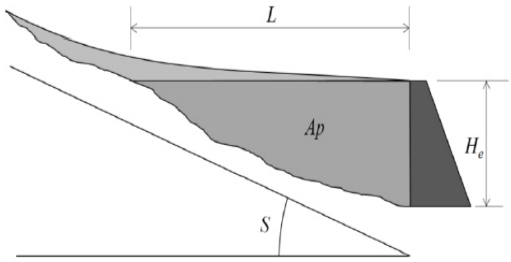

Fig. 3. Longitudinal profile of the accumulation of sediments in control structures

where:

L = Length of reservoir (m)

H_e = Effective height of the wall (m)

S = Upstream slope (%).

Profile area was obtained by the following equation:

$$A_p = \frac{L * H_e}{2} \quad (1)$$

where:

A_p = Profile area (m^2)

L = Length of the reservoir (m)

H_e = Effective height of the wall (m)

The average width of the vessel (T) is calculated by at least three transverse measurements (Fig. 4) and the following equation was used to obtain the volume or sediment retention capacity. The effect of the slope forming sediments upstream practice increases the retention volume estimated at a 1: 1.5.

$$V_s = T * A_p * 1.5 \quad (2)$$

where:

T = Average width (m)

A_p = Profile area (m^2)

V_s = Sediment volume (m^3)

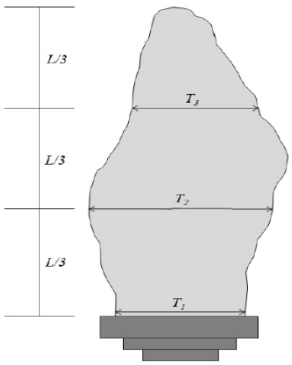

Fig. 4. Upper view of reservoir

III. RESULTS AND DISCUSSION

A. *Trapped sediment*

The grain size distribution of the sediments deposited behind the dams depends on the type of the sediments transported and the performance of the barriers in trapping the sediments [3]. In a masonry dam, water cannot pass through the dam quickly, so most sediments are trapped. In gabion dams, most of the trapped sediments may be higher in size. Nevertheless, the results show the opposite, the percent of gravel retained in gabion dams was lower than masonry dams.

For dams, gabions, half of these did not retain more than 40% of the gravel, and the other half did not hold more than 45%. In the case of masonry dams, half of them held up to 60% of the gravel and the other half retained in a range not exceeding 70% (Fig. 5). These differences are attributed to the gravels are detained in voids of the body of the dam, in spaces without letting them through.

The percentage of sand trapped behind the gabion dams is more than that for the masonry dams (Fig. 6), this confirms the good performance of gabion dams, regarding retention of sand, mainly of the dams located in the mainstream downstream (Fig. 8).

Regarding fine sediments trapped, clay and silt, no significant differences were found between gabion and masonry dams. In both cases, the percentages were low, even if, the masonry dams presented greater variation between them (Fig. 7). It is concluded that if the main propose is to retain fine sediments can build solid or porous dams.

Holistically, it recommended to implement gabion dams downstream sections where besides saving is possible to retain sand and fine sediments and collocate more economical structures upstream to trapping gravel. Such structures can be porous, nevertheless, should be sought to reduce the pore size.

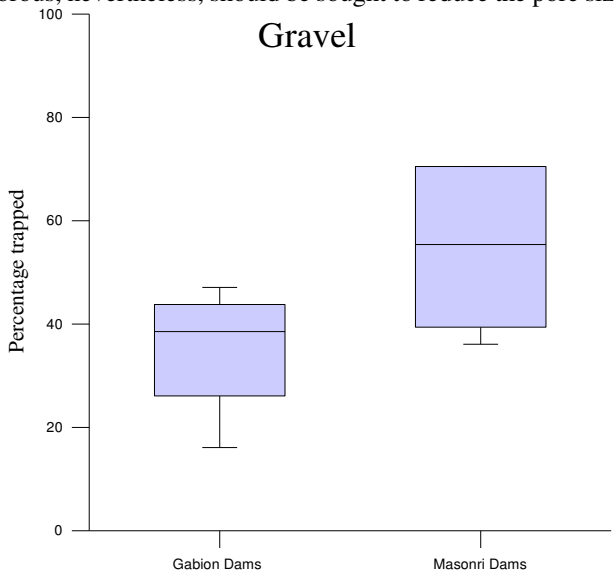

Fig. 5. Percentage of gravel trapped by studied dams in EL VENTILADOR watershed

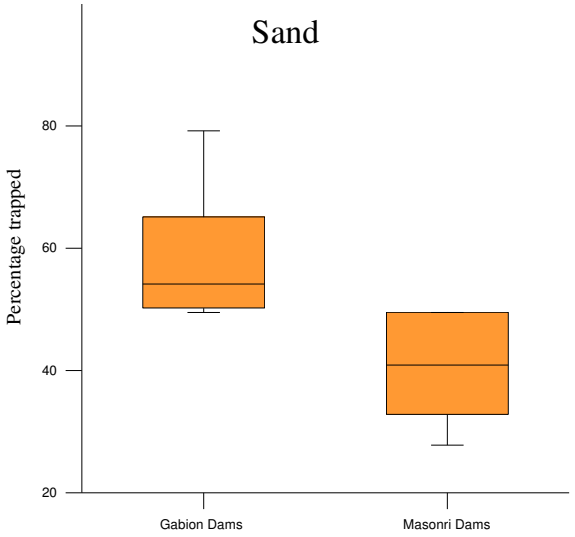

Fig. 6. Percentage of sand trapped by studied dams in EL VENTILADOR watershed

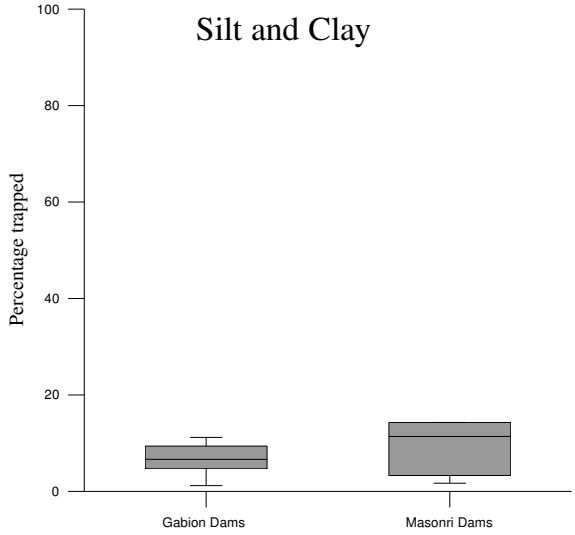

Fig. 7. Percentage of fine sediments trapped by studied dams in EL VENTILADOR watershed

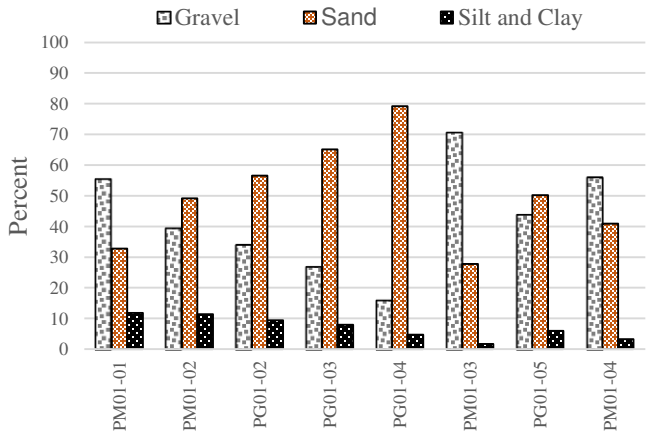

Fig. 8. Percentage of particles trapped by dams located in stream 1

As relates to gabion dams located at tributary streams, they present similar behavior to each other, trapped mostly larger diameter particles.

In addition to the particle size distribution trapped by structures, the volume retained by them 2 years after implementation was also analyzed and compared. The results showed in Table 2. Their efficiency was calculated compared the building volume whit respect to volume of retained sediment.

It was not possible to find a trend because each has different dam catchment areas and conditions of topography, however is clear that solid dams retain higher sediments volumes compared to porous dams.

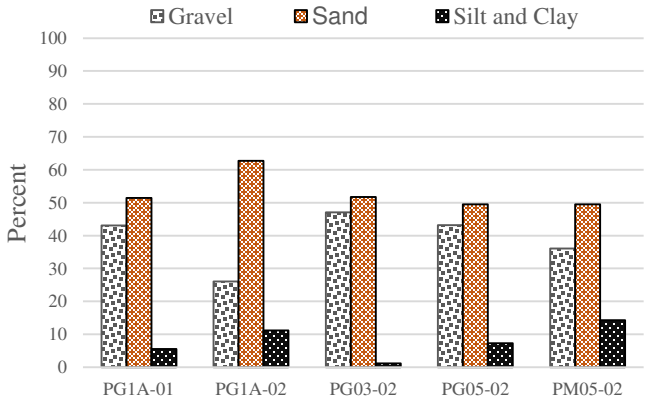

Fig. 9. Percentage of particles trapped by masonry dams in stream 1

TABLE II. EFFICIENCY RESPECT TO BUILDING VOLUME

Dam name	Volume of retained sediment (m^3)	Efficiency with respect to building volume (%)	Current capacity (%)
PG01-02	2.0	11.2	54.5
PG01-03	3.0	27.9	95.1
PG01-04	3.0	17.5	92.0
PG01-05	3.5	34.4	96.5
PG1A-01	2.5	89.4	93.7
PG1A-02	2.5	57.9	90.1
PG03-02	2.0	22.7	96.2
PG05-02	2.5	80.2	88.2
PM01-01	260.0	372.0	39.0
PM01-02	90.2	151.6	46.0
PM01-03	106.6	383.5	30.0
PM01-04	59.3	166.1	41.0
PM05-02	207.6	313.1	53.0

IV. Conclusions

The gabion dams represents a viable solution to retain sediment particles, product from water erosion and thus avoid disasters and accumulated in the lower parts of watersheds and its effect may increase if placed downstream sections.

The solid dams can retain practically all sediments except a percentage of fine sediments, however the cost of these is very high.

Gabion dams can be used to measure the effect of land use changes and by itself decreasing sediment yield in catchments.

Data obtained can be used to calibrate hydrological models for assessment and planning in the watershed restoration.

It is necessary to sample soil on the hillside of the watershed to verify the origin and the particle size of the sediments.

Acknowledgment

The authors of this work want to thanks Alondra Xareny Vega Ortiz and Alejandra Hernández González for helping with the analysis of soil samples.

References

[1] C. Chinnarasri, S. Donjadee, and Israngkura."Hydraulic characteristics of gabion-stepped weirs." J. Hydraul. Eng., 134 ed, vol. 8, pp. 1147-1152., 2008

[2] S. Grimaldi, P. Vezza, I. Angeluccetti, V. Coviello, and Kô, A. M. Koussoubé. "Designing and building gabion check dams." Engineering Geology for Society and Territory, 107 ed. Vol. 3, pp. 529-533. 2015

[3] H. I. Mohamed. "Flow over gabion weir." J. Irrig. Drain., 136 ed. Vol 1, pp. 573-577. 2010

[4] S. Pagliara, and M. Palermo. "Rock grade control structures and stepped gabion weirs: Scour analysis and flow features." Acta Geophys., 61 ed. Vol. 1, pp. 126-150. 2013

[5] American Geophysical Union, Report of the subcommittee on sediment terminology, 6th ed., vol. 28, 1947.

Flow-Mechanical Coupled Model of Soil's Consolidation

Consolidation Coupled Model

Galaviz-González, R.; Horta, J.; Rojas, E.; Pérez-Rea, M. L.
División de Investigación y Posgrado, F.I.
Universidad Autónoma de Querétaro
Santiago de Querétaro, México.
galaviz.gonzalez.r@gmail.com, horta@uaq.mx, erg@uaq.mx, perea@uaq.mx

Robles-Sotelo, J.
División de Ingenierías, C.U.C.E.I.
Universidad de Guadalajara
Guadalajara, México
jaime.robles.sotelo@gmail.com

***Abstract*— Consolidation of soils is a geotechnical problem, product of stress transfer process. This begins with the applied stress by the foundation, and is transmitted to the water phase in the soil, causing a reduction in water pore pressure and ends with a rearrangement of the solid particles, producing a soil volume decrease. Therefore, the consolidation is considered a coupled problem. This has led to the simulation of the consolidation through developed coupled models. Each model has been proposed through different theories, which consistent results were obtained. However, some models do not have a mathematical foundation that helps the understanding of thereof. This paper presents the formulation of a coupled model (flow-mechanical) of soil consolidation, formulated from transient flow, momentum balance, and movement equations. We proceeded establishing an inner product between vector functions taking into account the virtual work principle, associated to the principle variational of the minimum potential energy. The algorithm of coupled model delivers results quick and easy, due to its flexibility and allows infinite combinations. In addition, considers that there may be water flow, as a contribution or extraction, resulting in changes in pore water pressure, thus also on the horizontal and vertical displacements. Through the results obtained, an appropriate behavior of the phenomenon of consolidation is observed. Even, show consistent results with those reported by other researchers and those obtained in the laboratory.**

Keywords—coupled model; consolidation; saturated soil.

I. INTRODUCTION

Exist many geotechnical problems related to saturated soils, one of the most common is a foundation slab placed on the surface of a saturated clay thickness. This produces a volume decrease of the stratum, due to the load applied by the slab, thus reducing the drainage and the pressure produced by the water contained in the pores of soil. This process it is called "soil's consolidation".

Researchers have developed mathematical models under different approaches or theories, this in order to simulate the phenomenon of consolidation. These models, reported consistent results with those obtained in field and laboratory, however, all these models have advantages and disadvantages. These latter can be improved involving the theories mentioned in the previous paragraph.

This has motivated the formulation and development of a flow-mechanical coupled model of soil's consolidation, formulated considering the "Momentum Balance Laws", equations of "transient flow" (flow) and "Movement" (mechanical) in which the Terzaghi's "effective stress" is introduced. We proceeded establishing an inner product between vector functions taking into account the "Virtual Work Principle", associated to the "Variational Principle of the Minimum Potential Energy". In addition, the Finite Element Method (FEM) in combination with Galerkin's method that includes a pass of time in which the evolution of displacements and pore water pressure are determined as approximate solution.

II. THEORETICAL FOUNDATION

A. *Antecedents*

Due to variations in weather conditions by seasonal changes, soils are subjected to cyclic wetting and drying processes. If the soil is expansive, this will experiment contractions and expansions when decrease or increase its water content, respectively [1,2].

In addition to natural causes, situations that directly affect buildings and dwellings, it is to place a foundation on the soil surface and the change in pore pressure during construction. By covering the surface of an expansive soil, this undergoes volume changes in response to the applied load and is produced by variations in negative pore pressure (soil suction) [2]. These volume changes arise due to the water content in the soil; if the water content is low, it will result in an increase in volume with increasing water content, and this phenomenon is called "soil swelling." Moreover, when the water content is high, the load on the ground causes the water content decreases causing it to migrate down and consequently reducing the volume of soil, this phenomenon is called "soil consolidation" [1]. The variation which occurs in saturated soil consolidation

is determined by the rate at which fluid pressure may be expelled from the ground. Thus, the deformation process (mechanical strength) and the flow of water pressure (hydraulic behavior) in soils is "coupled (mechanical-flow)" [3].

In the literature there are coupled consolidation models that have been developed taking into account various considerations in order to provide results or simulations more approximate.

B. Coupled models of soil's consolidation

Some of these coupled models simulate the soil consolidation in saturated condition [1,3,4,5,6]. Most of the above models take into account the assumptions: a) the soil is saturated, b) fluid phase is incompressible, c) the solid phase is incompressible, but the arrangement is compressible, d) Darcy's law governs the behavior of the flow through the soil [1,3,4]. Besides the above, Bentler [3] used the theory of small deformations. The principle of virtual work was used by Manzolillo et al. [4] and the law of conservation of mass was considered in the models proposed by Manzolillo et al. [4] and Di-Rado et al. [5]. The latter researchers employed the saturated effective stress of soils and the application of the Galerkin's method of solution of weighted residuals [5]. Furthermore, Krishnamoorthy [6] considered the nonlinear behavior of the soil and used the hyperbolic relationship of Duncan and Chang (1970).

Previous models have shown consistent and adequate results, however, try improve existing solutions has always motivated the development of research. Therefore, this paper presents the design and development of a coupled model of soil consolidation by the basic principles of continuum mechanics and saturated soil mechanics, in which much of the theories considered by existent coupled models were combined.

The procedure for determining coupling equations consisted of the implementation of the "virtual work principle" [7], which states "The work done by the internal forces in a system is equal to the work done by the external forces acting on the same" [1]. This principle associates "Variational Principle of the Minimum Potential Energy" [8]. We proceeded in this study in an analogous fashion, establishing an inner product through vector functions.

III. FORMULATION OF COUPLED MODEL

A. Fonomonological case of Soil's solids

During movement or mechanical interactions between the body parts and their environment are described by three kinds of forces: 1) contact forces between separate parts of a body; 2) contact forces exerted on the border of a body by its environment; 3) body forces exerted at points within the body by the environment [7].

Cauchy assumes the existence of a density of surface forces $\underline{s}(\underline{n},\underline{x},t)$ defined by each vector $\underline{n}$ and everything $(\underline{x},t)$ in the path T of movement. Thus, the basic axioms connecting the "Motion" and "Force" are the "Momentum Balance Laws".

$$\int_{\partial P_t} \underline{s}(\underline{n})dA + \int_{P_t} \underline{b}dV = \int_{P_t} \ddot{\underline{\chi}}\,\underline{\rho}dV \tag{1}$$

where: $\int_{\partial P_t} \underline{s}(\underline{n})dA$ total contact forces, $\int_{P_t} \underline{b}dV$ forces at points within the body exerted by the environment, $\int_{P_t} \ddot{\underline{\chi}}\,\underline{\rho}dV$ inertial body forces.

Introducing the "Piola-Kirchhoff's Stress Tensor" in (1), which gives the force measured per unit area in the configuration of "reference". Thus, the field equation (2) was obtained.

$$Div\ \underset{\sim}{S} + \underline{b}_o = \ddot{\underline{\chi}}\,\underline{\rho}_o \tag{2}$$

Whereas $\underline{b}_o = \underline{0}$ and $\ddot{\underline{\chi}} = \underline{0}$, since the flow and settlement processes are slow. In addition, to proceed with the inner product between the vector functions and expressed in index notation $\underline{S} = \sigma_{ij,j}$. Finally, deriving in *j,* clearing $\varphi\sigma_{ij,j}$ and replacing in (2):

$$\int_V \left(\varphi_i \sigma_{ij}\right)_{,j} dV - \int_V \varphi_{i,j}\sigma_{ij}dV = 0 \tag{3}$$

Applying the "divergence theorem" [7] in the first term of (3) and replace the "Terzaghi's effective stress" which involves the components of the stress of the solid and liquid phase, (3) takes the form:

$$\int_V \varphi_{i,j}\,\overline{\sigma}_{ij}dV + \int_V \varphi_{i,j}\,p_w\delta_{ij}dV = \int_\Gamma \varphi_i\sigma_{ij}n_j dA \tag{4}$$

After engaging the field equations of elastostatics $\overline{\sigma}_{ij} = \overline{D}\varepsilon_{ij}$ which is analogous to the "Law of Hook" and according to the Cauchy's hypothesis of the stresses existence $\sigma_{ij}n_j = \underset{\sim}{S}\,\underline{n} = \underline{t}$.

$$\int_V \varepsilon_{ij}^{\varphi} \cdot \overline{D}_{ijkl}\varepsilon_{kl}^{u}dV + \int_V \varphi_{i,j}\,p_w\delta_{ij}dV = \int_\Gamma \varphi_i \underline{t}_i dA \tag{5}$$

Applying, the approximation from Galerkin's method for the linear triangular finite element, the "Virtual Work Theorem" [7]. Replacing the variations for fields φ and ε . In addition, an isotropic unitary tensor $\langle m\rangle^T = \langle 1 \quad 1 \quad 0\rangle$ that link the degrees of freedom of the displacements and pore pressure.

$$\begin{gathered}\int_V \left[B_\varphi\right]^T\left[\overline{D}\right]\left[B_u\right]dV\{U\} + ... \\ ... + \int_V \left[B_\varphi\right]^T\langle 1 \quad 1 \quad 0\rangle^T\left[N_p\right]dV\{p\} = ... \\ ... = \int_\Gamma \left[N_\varphi\right]^T\{\underline{t}_i\}dA\end{gathered} \tag{6}$$

Equation (6) can be stated as:

$$[K]\{U\}+[K_v]^T\{p\}=\{F\} \tag{7}$$

where: $[K]$ soil stiffness matrix, $[K_v]^T$ coupled matrix transpose, $\{U\}$ nodal displacements vector, $\{p\}$ nodal water pore pressure, $\{F\}$ external forces vector.

B. Fenomonological case of Soil's flow

Starting from the "Transient Flow" equation:

$$div\underline{v}-\dot{\varepsilon}=0 \tag{8}$$

Proceeding analogously to the case of solid and after applying the inner product with an arbitrary function, a job is generated. Expressing index notation we have. Finally, deriving in *i,* clearing $(\vartheta v_i)_{,i}$ and replacing in (8):

$$\int_V(\vartheta\underline{v}_i)_{,i}dV-\int\vartheta_{,i}v_i dV-\int_V\vartheta\dot{\varepsilon}_{ii}dV=0 \tag{9}$$

Applying the "divergence theorem" [7] in the first term of (9) and replace the "Darcy's Law" $v_i=k_{ij}(\gamma_w h_i)_{,j}/\gamma_w$, and the piezometric level $h=p_w/\gamma_w+z$ but, regardless of the reference level z , takes the form:

$$\int_V\vartheta_{,i}\frac{k_{ij}}{\gamma_w}\{p_w\}_{,j}dV+\int_V\vartheta\dot{\varepsilon}_{ii}dV=\int_\Gamma\vartheta\underline{q}_i dA \tag{10}$$

Applying, the approximation from Galerkin's method for the linear triangular finite element, the "Virtual Work Theorem" [7]. Replacing the variations for fields φ and ε . In addition, an isotropic unitary tensor $\langle m\rangle$, we take:

$$\begin{gathered}\frac{1}{\gamma_w}\int_V[B_\theta]^T[k][B_p]dV\{p\}+...\\ ...+\int_V\{\delta\theta\}^T[N_\theta]^T\langle 1\quad 1\quad 0\rangle^T[B_v]\left\{\dot{U}\right\}dV=...\\ ...=\int_\Gamma[N_\theta]^T\{\underline{q}_i\}dA\end{gathered} \tag{11}$$

Equation (11) can be stated as:

$$[K_v]\left\{\dot{U}\right\}+\frac{1}{\gamma_w}[K_h]\{p\}=\{Q\} \tag{12}$$

where: $[K_v]$ coupled matrix, $[K_h]$ drained matrix, , $\{p\}$ nodal water pore pressure, $\{Q\}$ external/internal flow vector, $\left\{\dot{U}\right\}$ velocity vector of nodal displacements.

Finally, (7) and (12) are the equations resulting from the coupled model (flow-mechanical) consolidation of soils and can be expressed in matrix form:

$$\begin{bmatrix}0&0\\K_v&0\end{bmatrix}\begin{Bmatrix}\dot{U}\\\dot{p}\end{Bmatrix}+\begin{bmatrix}K&K_v^T\\0&\frac{1}{\gamma_w}K_h\end{bmatrix}\begin{Bmatrix}U\\p\end{Bmatrix}=\begin{Bmatrix}F\\Q\end{Bmatrix} \tag{13}$$

To establish the dynamic process, it means, the process of evolution of displacements and pore pressures over time, the "mean value theorem" was considered. Thus, the evolution of the vectors take the form:

$$\begin{gathered}\{F\}=\{F_a\}+\theta\{\{F_b\}-\{F_a\}\}\\ \{Q\}=\{Q_a\}+\theta\{\{Q_b\}-\{Q_a\}\}\\ \{p\}=(1-\theta)\{p_b\}+\theta\{p_a\}\\ \{U\}=(1-\theta)\{U_b\}+\theta\{U_a\}\\ \left\{\dot{U}\right\}=\{U_b\}-\{U_a\}/\Delta t\end{gathered} \tag{14}$$

where: $\{F_a\}$, $\{Q_a\}$, $\{p_a\}$ and $\{U_a\}$ are the initial vectors, $\{F_b\}$, $\{Q_b\}$, $\{p_b\}$ and $\{U_b\}$ are the vectors after an interval of time, θ is the value of Galerkin's parameter which helps the FEM to obtain a numerical solution of evolution over time, and Δt is the adequate pass of time to avoid numerical oscillations, we can obtain it by the relationship:

$$\begin{gathered}\Delta t\le\frac{\alpha}{1-\theta}\\ \alpha_{\min}=\frac{2A}{9C_v}\end{gathered} \tag{15}$$

where: A area of the linear triangular finite element, C_v is the coefficient of consolidation for the soil.

Finally, substituting (14) and (15) in (7) and (12), we obtain the equations (16) and (17) governing the dynamic process of soil's consolidation coupled model:

$$\begin{gathered}\{p_b\}=[\overline{K}_b]^{-1}[\overline{K}_a]\{p_a\}+[\overline{K}_b]^{-1}[\overline{K}_c]\{U_a\}+...\\ ...+[\overline{K}_b]^{-1}\{Q_a\}+[\overline{K}_b]^{-1}\theta\{\Delta Q\}-...\\ ...-[\overline{K}_b]^{-1}[\overline{K}_c][K]^{-1}\{F_a\}-[\overline{K}_b]^{-1}[\overline{K}_c][K]^{-1}\theta\{\Delta F\}\end{gathered} \tag{16}$$

$$\{U_b\}=\frac{1}{\theta}[K]^{-1}\{F_a\}+[K]^{-1}\{\Delta F\}-[K]^{-1}[K_v]^T\{p_b\}-... \tag{17}$$

$$\ldots - \left(\frac{1-\theta}{\theta}\right)\{U_a\} - \left(\frac{1-\theta}{\theta}\right)[K]^{-1}[K_v]^T\{p_a\}$$

Subsequently, in order to evaluate the ability of coupled model, a program was developed in APDL language for Ansys environment [9].

IV. Description of the Procedure

In the first stage is necessary to indicate the domain dimensions of the soil, such as the length (L), layer thickness (H), and the height of the linear triangular finite element (h_{FE}). It also requires introducing the soil properties, it means, the Elastic Modulus (E), Poisson's ratio (ν) and the value of the permeability (k_x) and (k_y). Subsequently, we must establish whether there are displacement restrictions on the borders (bottom and side). With this, the soil domain including the meshing of FE are shown. From the above, the basic matrices needed for the mechanical model shown in (6) are obtained. Such matrices are: the elastic matrix [D], shape function matrix [N] and $[N]^T$, shape function derivatives matrix [B] and $[B]^T$, the overall stiffness matrix [K], reduce stiffness matrix $[K_D]$, without restrictions, and conversely reduce stiffness matrix $[K_D]^{-1}$.

In addition, specify whether there are permeable boundaries in the domain, it means, borders in which the value of pore pressure is zero. So, if there are permeable borders, the vector of node drained $\{K_p\}$ is generated.

To end the first stage, the basic matrices of the flow model shown in (11) are generated, such as: the permeability matrix [k], shape function derivatives matrix [B] y $[B]^T$, the overall flow matrix $[K_h]$, including the vector $\{K_p\}$, and the reduce flow matrix $[K_{hD}]$, without vector $\{K_p\}$. Furthermore, the total coupled matrix $[K_v]$ including restrictions, reduce coupled matrix $[K_{hD}]$, excluding restrictions, and reduce coupled matrix transpose $[K_{hD}]^T$ shown in (6) and (11) are generated. Fig. 1 shows the flow chart of the first stage process.

The second stage involves the action of the forces applied on surface {F} in the Mechanical Model. These forces can be considered as constant or that evolve over time. Therefore, it must specify if there are or not the application of surface forces. If any, it is necessary to indicate the analysis time (t) and the passage of time (Δt) required to perform the dynamic process which will take place in fourth stage.

Subsequently, it is necessary to indicate if the application of superficial forces are constant or vary with time. If it be the case where the forces are constant, only the magnitudes of the forces are introduced as negative values (-F), since this indicates the direction of forces is applied down. Terminating this process, the external forces vector {F} is generated.

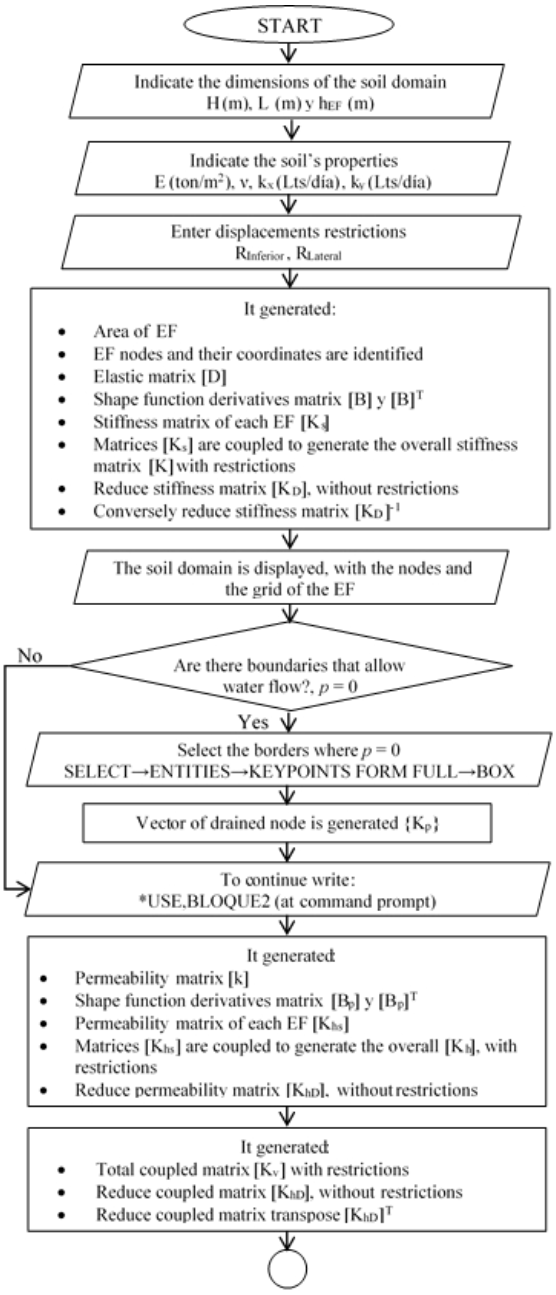

Fig. 1. Flow chart of first stage process (dimensions, properties and restrictions of the domain).

Moreover, if the forces vary with time, the sequence in which the forces evolve must be specified. Subsequently, the values of the forces ($-F_i$) and time (t_i) in which increases or decreases each one, should be indicated. Finishing the second stage, the external forces vector {F} for each passage of time (Δt) and their respective differences $\{F_a\text{-}F_b\}=\{\Delta F\}$ are generated. Fig. 2 shows the flow chart of second stage process (external forces).

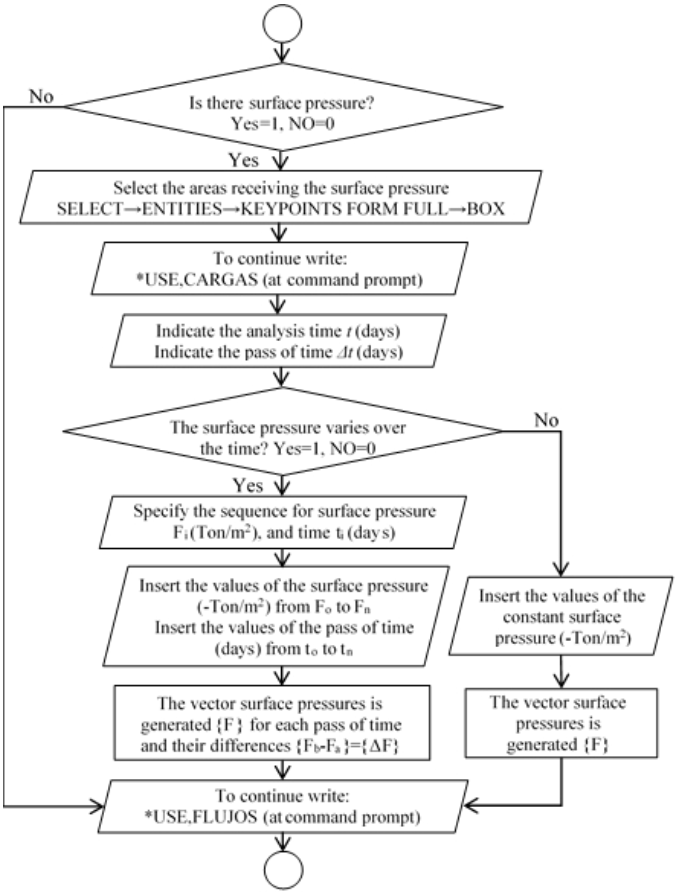

Fig. 2. Flow chart of second stage process (external forces on surface).

The third stage is related to the internal/external flow {Q} that can act in the domain. This flow may be considered as internal/external due to the water flow which it occurs within/outside the domain, this is produced by the application of the forces on surface, and this flow is considered as a positive. On the other hand, the model is able to take into account that there may be internal flow due to the contribution of water leaking pipes that are within the domain. Furthermore, it is also considered that there may be flow (positive or negative) in the upper border. The flow will be positive when considering a percentage loss by evapotranspiration. By contrast, the negative flow will be produced by precipitation or water leaking hosepipe outside the domain. Thus, any contribution of water is considered as negative flow.

Therefore, in the flow model it is necessary to indicate whether there is water flow and what kind is (internal or external). If the flow is external, it should be specified the areas of the surface where this flow is presented. On the other hand, if the flow is internal, a part of flow is automatically recognized as positive, because is produced by the surface forces application, and also it may consider water flow by punctual leaking pipes (maximum 3).

Subsequently, if there are flow, it required indicate whether the internal/external flow varies over time. Thus, if the flow does not evolve over time, only the value of the constant flow is introduced, either positive or negative. Completing this stage, the flow vector {Q} is constructed. Conversely, if the flow evolves over time, the sequence in which the flow evolve must be specified. Subsequently, the values of the flow ($-q_i$) and time (t_i) in which increases or decreases each one, must be introduced. Finishing the third stage, the flow vector {Q} for each passage of time and their respective differences $\{Q_a\text{-}Q_b\}=\{\Delta Q\}$ are generated. Fig. 3 shows the flow chart of third process (acting internal/external flow).

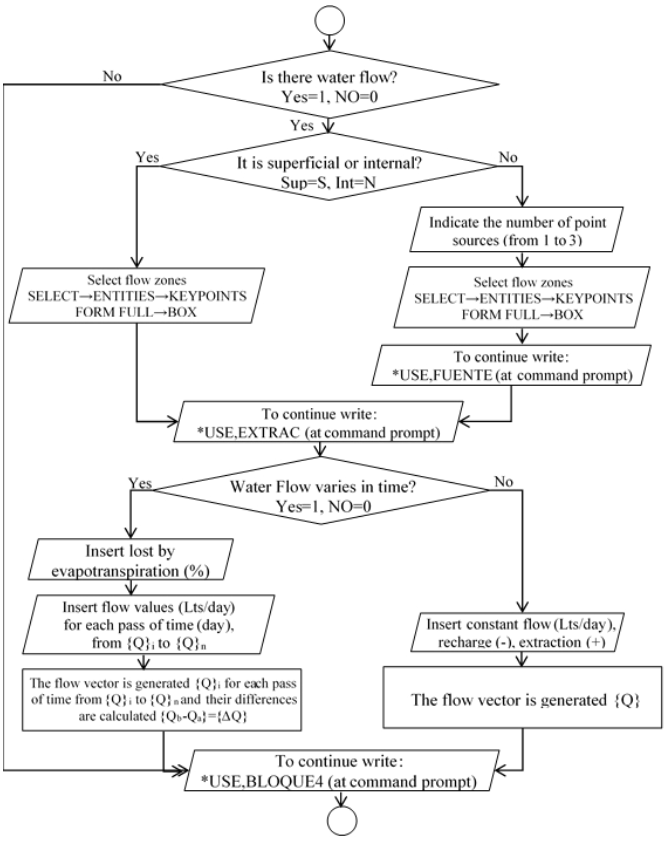

Fig. 3. Flow chart of third stage process (acting internal/external flow).

The fourth stage involves the dynamic process, it means, the evolution process of pore water pressures {p} and displacements {U}, which are governed by equations (16) and (17), respectively.

In the initial part of the dynamic process, it requires the determination of the constant matrices [K*], [K_a] [K_b] [K_c] and the vector {f} that appear in (17). These elements depend on the basic matrices of Coupled Model shown (16) and (17), where:

$$\begin{aligned}
\left[\overline{K}_a\right] &= \left[\left(\left(1/\Delta t\right)\left(1-\theta/\theta\right)+\left(1/\Delta t\right)\right)\left[K_v\right]\right] \\
\left[\overline{K}_b\right] &= \left[\theta\left[K_h\right]-\left(1/\Delta t\right)\left[K^*\right]\right] \\
\left[K^*\right] &= \left[K_v\right]\left[K\right]^{-1}\left[K_v\right]^T \\
\left[\overline{K}_c\right] &= \left(1/\theta\Delta t\right)\left[K_v\right] \\
\left\{f\right\} &= -\left[\overline{K}_c\right]\left[K\right]^{-1}\left\{F_a\right\}+\theta\left[\overline{K}_c\right]\left[K\right]^{-1}\left\{\Delta F\right\}+\left\{\left\{Q_a\right\}+\theta\left\{\Delta Q\right\}\right\}
\end{aligned} \tag{18}$$

Thus, the dynamic process starts with the vectors of the pore water pressure and displacement equal to zero. This means that for an initial time $\{p_a\}=\{0\}$ and $\{U_a\}=\{0\}$, with these (16) and (17) reduce to:

$$\{p_b\}=\left[\overline{K}_b\right]^{-1}\{f\} \tag{19}$$

$$\{U_b\}=(1/\theta)[K]^{-1}\{F\}-[K]^{-1}[K_v]^T\{p_b\} \tag{20}$$

Subsequently, using (19) and (20) the first vectors $\{p_b\}$ and $\{U_b\}$ are obtained. Thus, for the first passage of time, it means, the first iteration, the above vectors $\{p_b\}$ and $\{U_b\}$ are become $\{p_a\}$ and $\{U_a\}$. Then, using (16) and (17) we obtain new vectors $\{p_b\}$ and $\{u_b\}$. The above process is repeated until the analysis time (t) is completed or if the i-th vectors of displacement and pore pressure are equal, that is, $\{p_b\}=\{p_a\}$ and $\{U_b\}=\{U_a\}$. Once arrived the previous point, the dynamic process ends and we get the analysis solution.

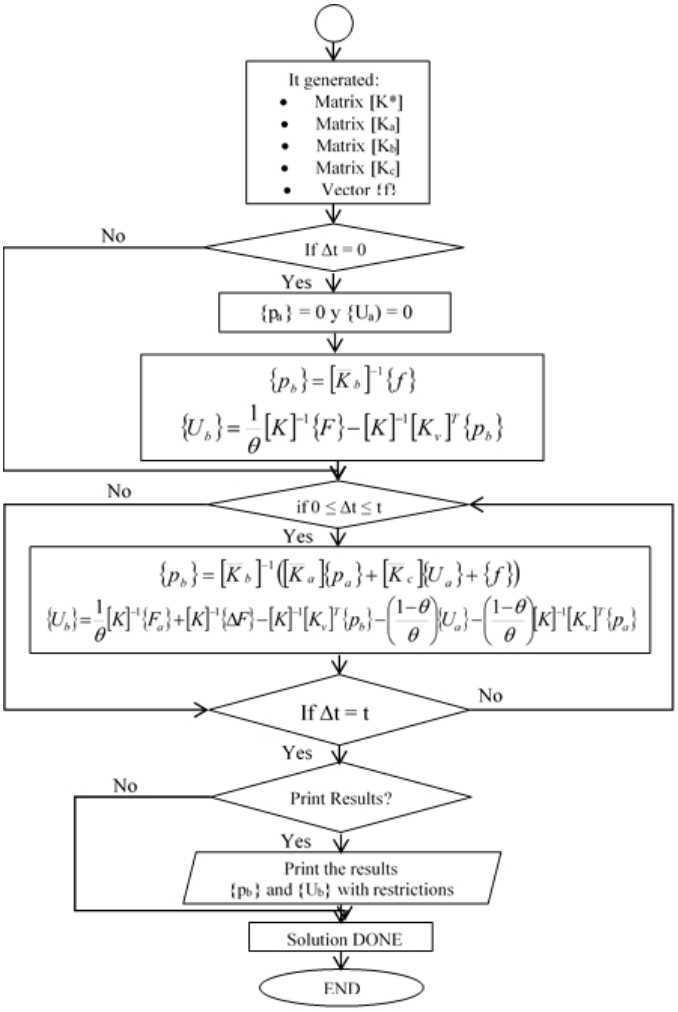

Fig. 4. Flowchart of the dynamic process of saturated consolidation coupled model of soils.

Finally, we can print the results for each passage of time (t). These results are graphs that show the distribution of displacements in the direction Ux and Uy, including restrictions are obtained. Also, the pressure distribution of pore water nodal p are determined. In addition, the distribution and evolution of superficial soil profile formed with the vertical displacements called settlements is displayed. We can also obtain a vertical profile of the evolution of pore water pressure. All above results show a typical and consistent behavior of the saturated consolidation process. Fig. 4 shows the flowchart of the dynamic process of saturated consolidation coupled model of soils.

V. Numerical Results

To validate the saturated consolidation coupled model, it was necessary to make a mechanical test to reproduce the phenomenon of saturated consolidation. For such a case, a rectangular slab foundation of L = 5.0m, and infinity wide (plane strain state) that transfers a uniform force F = 4.0 Ton/m^2 (40 kPa) on a thickness of clay soil of H = 3.0 m was analyzed.

The displacements Ux and Uy are restricted in both lateral boundary and the lower boundary of the soil. Furthermore, the clay layer is placed above a layer of sand, which allows flow water at the lower boundary of the stratum of clay, indicating that the pore pressure is zero at this boundary. Also, the lateral borders do not allow water flow. For simplicity, the mesh spacing of 0.25 m (height of the linear triangular finite element) because it already has the adequate passage of time for that FE. Fig. 5 shows the soil stratum in study.

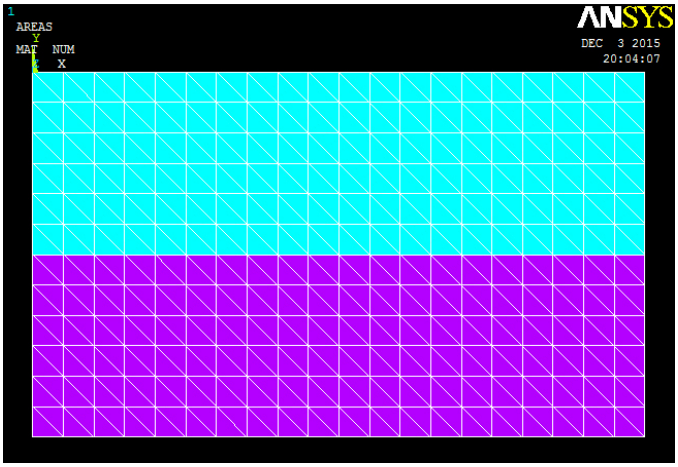

Fig. 5. Soil stratum in study including finite element mesh.

During the implementation of the algorithm we proceeded to perform various mechanical tests in order to calibrate the model. This was done by changing the significant variables, such as: a) the saturated coefficient of permeability, b) the lateral restrictions, c) the elastic modulus, d) the passage of time, and e) the parameter θ. Thus, after calibration it was determined that the analysis time was t = 900 days and the passage time Δt = 10 days.

The soil properties required for mechanical analysis are shown in Table 1, these values do not necessarily represent an actual soil, and however, the values are suitable for a saturated clayey soil.

TABLE 1. PROPERTIES OF CLAYEY SOIL STRATUM FOR CONSOLIDATION ANALYSIS.

Soil Properties	Symbol	Magnitude
Elastic Modulus	E	20000 kPa
Poisson's ratio	ν	0.35
Coefficient of permeability (x direction)	k_x	0.000117 m/day
Coefficient of permeability (y direction)	k_y	0.000117 m/day

As a result of the analysis can be seen that various figures showing soil behavior are obtained. Fig. 6 shows the distribution of pore pressure in a passage of time, corresponding to 50 days. As is near of the initial time is expected that the value of pore pressure at the surface is very close to the value of force applied -40 kPa (-4 Ton/m^2, the negative sign comes from the direction of force application), however, this value is not close because it has passed 50 days. On the other hand, the pore pressure in the lower boundary is zero, as was seen in the initial condition. In addition, we see that the behavior is consistent with the results obtained by other authors and laboratory assays.

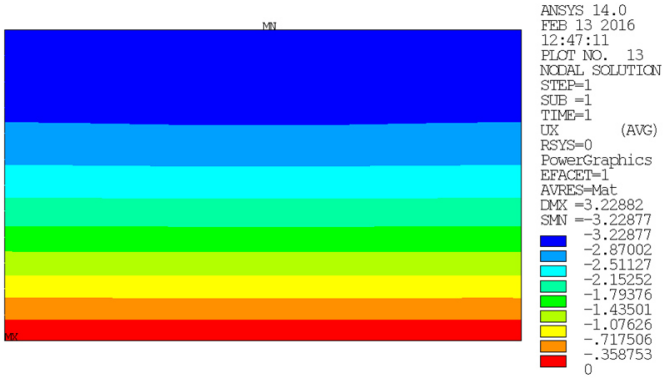

Fig. 6. Pore water pressure distribution at 50 days.

The analysis also shows that the pore water pressure dissipates (tending to zero) as time passes and continue the forces applied on the surface. This can be seen through Table 2, this shows the distribution of pore water pressure on 50, 450, and 900 days. Fig. 6 shows the distribution of pore pressure at 50 days, the diagram is the same at 450 and 900 days, but with different values of the pore water pressure.

TABLE 2. PORE WATER PRESSURE DISTRIBUTION.

Pore water pressure distribution Ton/m^2 (x 10 kPa)			
Color Scale	*50 days*	*450 days*	*900 days*
	-3.229	$-0.463x^{-4}$	$-0.197x^{-9}$
	-2.870	$-0.412x^{-4}$	$-0.175x^{-9}$
	-2.511	$-0.360x^{-4}$	$-0.153x^{-9}$
	-2.153	$-0.309x^{-4}$	$-0.131x^{-9}$
	-1.794	$-0.257x^{-4}$	$-0.109x^{-9}$
	-1.435	$-0.206x^{-4}$	$-0.875x^{-10}$
	-1.076	$-0.154x^{-4}$	$-0.656x^{-10}$
	-0.718	$-0.103x^{-4}$	$-0.437x^{-10}$
	-0.359	$-0.515x^{-5}$	$-0.219x^{-10}$

In order to demonstrate the above, the model provides a graph that shows the evolution of pore water pressure through vertical profiles, which can be selected at any point along the length of the domain under study. Thus, Fig. 7 shows the profiles of pore water pressure for each passage of time and observes that these tend to decrease down to values close to zero, that is, the pore water pressure dissipates over time. This pressure starts equal to the applied forces and reach null values. This is due to the application of the forces on surface.

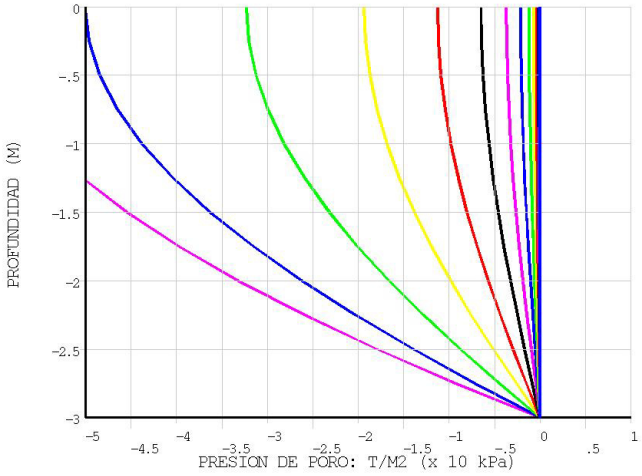

Fig. 7. Evolution of the vertical profiles of pore water pressure.

Another important aspect that requires observation of the phenomenon of consolidation, is the variation of the vertical displacements. These diminish by the applied load as time goes on. Thus, Fig. 8 shows the vertical displacements in the passage of time at 50 days. Through this figure it can be seen that displacements are about -0.0168 m in the superficial edge, while near the bottom border are near zero. Here, the negative sign indicates the direction in which evolve the displacements. The behavior of the evolution of vertical displacement is consistent with those obtained in the laboratory and the field. This is evidenced noting Fig. 8 and Table 3.

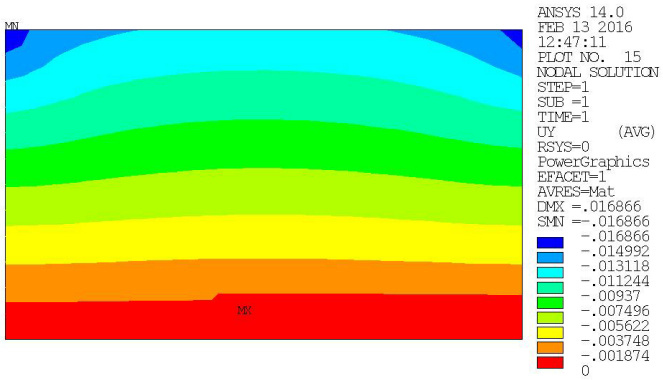

Fig. 8. Distribution of the vertical displacements U_y.

In addition, the diagrams of distribution and evolution of the displacements are equal, only change the values of these as time goes on. Therefore, Fig. 8 shows such distribution, and Table 3 shows the values of the displacements at 50, 450, and 900 days. Furthermore, through Table 3, the maximum displacement observed on surface, is reached at 450 days. In turn, these displacements represent the final values that were

caused by the forces transmitted by the slap foundation. To verify this assertion, the model also provides a figure that shows the evolution of the profile of surface displacements at each passage of time. Thus, the profile of the final displacements of soil due to the applied load is obtained (see Fig. 9).

TABLE 3. DISTRIBUTION OF VERTICAL DISPLACEMENTS U_Y.

Vertical displacements U_y m			
Color Scale	*50 days*	*450 days*	*900 days*
	-0.0169	-0.0189	-0.0189
	-0.0149	-0.0168	-0.0168
	-0.0131	-0.0147	-0.0147
	-0.0112	-0.0126	-0.0126
	-0.0094	-0.0105	-0.0105
	-0.0075	-0.0084	-0.0084
	-0.0056	-0.0063	-0.0063
	-0.0037	-0.0042	-0.0042
	-0.0018	-0.0021	-0.0021

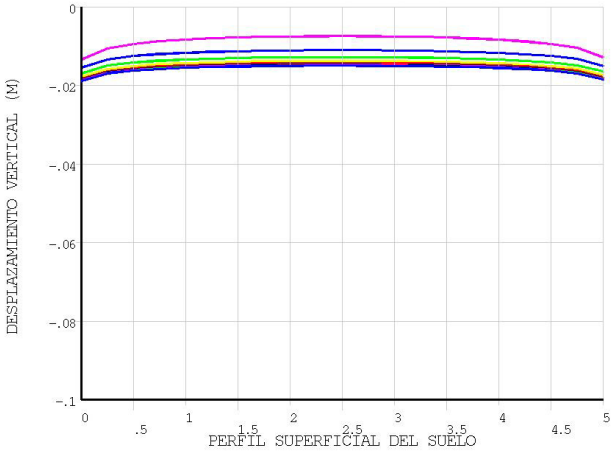

Fig. 9. Superficial profile of soil.

Another case of interest is when an isolated foundation on a saturated clay soil is placed as shown in Fig. 10. For the next exercise the same domain with L=5.0 m was used, but only one isolated footing is placed to the center and transfers a distributed load of -40 kPa (-4 Ton/m^2) over 2.5 m. With this, it is observed that the free parts of the upper border allow water flow (1.25 m on each side of the foundation) it means that the pore pressure is zero. Also, the lower boundary also allows water flow. The displacements are restricted in the lateral and lower boundaries (see Fig. 10). Table 4 shows the properties of the soil, the passage of time and the time required for dynamic analysis.

TABLE 4. DATA REQUIRED FOR THE DYNAMIC ANALYSIS.

Data for dynamic analysis	Symbol	Magnitude
Elastic Modulus	E	20000 kPa
Poisson's ratio	ν	0.35
Coefficient of permeability (x direction)	k_x	0.00117 m/day
Coefficient of permeability (y direction)	k_y	0.00117 m/day
Passage of time	Δt	30 days
Time analysis	t	900 days

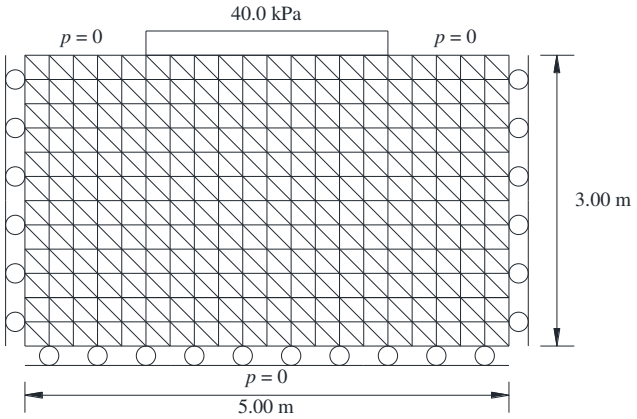

Fig. 10. Soil's domain in study with isolated footing applied to the center.

After the analysis is complete, we note that pore pressure for a time step of 30 days is very close to the value of the pressure applied by forces on the surface. Thus, Fig. 11 shows the distribution of pore pressure for time steps of 30 days, but the diagram of the distribution is the same for 450 and 870 days, only change the values of pore water pressures as are shown in Table 5. Furthermore, Table 5 shows again that pore water pressure dissipates, it means, tending to null values.

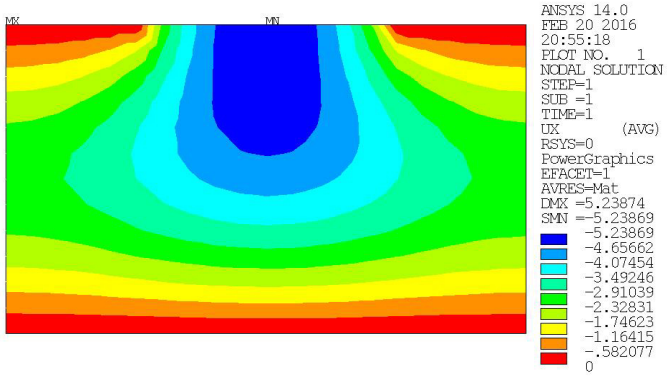

Fig. 11. Distribution of pore water pressure for isolated footing at 30 days.

TABLE 5. DISTRIBUTION OF PORE WATER PRESSURE FOR ISOLATED FOOTING.

Pore water pressure distribution Ton/m^2 (x 10 kPa)			
Color Scale	*30 days*	*450 days*	*870 days*
	-5.238	-0.441	-0.023
	-4.656	-0.392	-0.021
	-4.074	-0.343	-0.018
	-3.492	-0.294	-0.016
	-2.910	-0.245	-0.013
	-2.328	-0.196	-0.010
	-1.746	-0.147	-0.008
	-1.164	-0.098	-0.005
	-0.582	-0.049	-0.003

Another result of analysis obtained by using the coupled model, are the vertical profiles of the pore water pressure. Fig. 12 shows a vertical profile of pore pressure at a distance of 1.25 m, this is in the domain zone that is uncharged, and allows water flow. Thus, it can be seen that the pore pressure is zero at

the surface and the lower border, while within the domain undergoes variations.

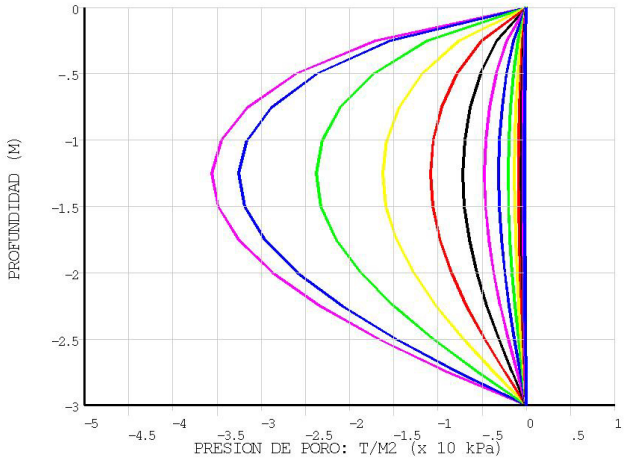

Fig. 12. Evolution of the vertical profiles of pore water pressure at 1.25 m.

Moreover, the figure 13 shows the vertical profile of the pore water pressure at 2.50 m (center line of the domain). We can see that the values, start very close to the value of the applied force on surface, and as the depth increases, the value decreases. In both figures, the values of pore water pressures tend to be zero.

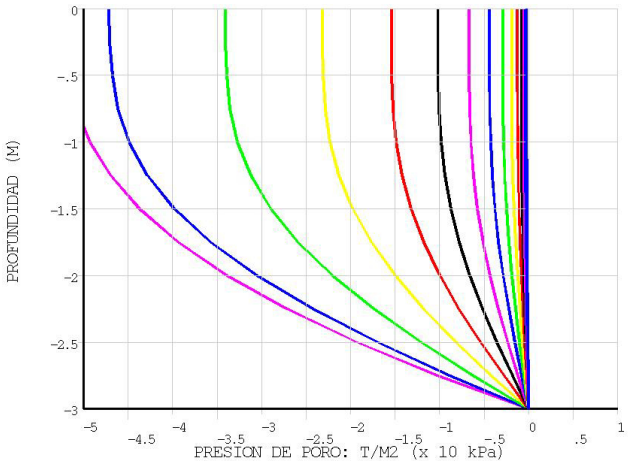

Fig. 13. Evolution of the vertical profiles of pore water pressure at 2.50 m.

As for measuring the displacements, the model provides diagrams of distribution of horizontal Ux and vertical Uy displacement. Thus, Fig. 14 shows the distribution of horizontal displacement and Fig. 15 the vertical displacements. Additionally, Table 6 and Table 7 show the distribution of displacement Ux and Uy for each time step (30, 450, and 870 days).

Through Fig. 14 and Table 6, a characteristic phenomenon of symmetrical problems due to loads applied at center is observed. So, from the center line to the left, we have offset values with a negative sign. This is due to the direction in which they occur, given a coordinate system in which the y-axis corresponds to the center line. Moreover, the values of the displacements are positive, from the center line to the right.

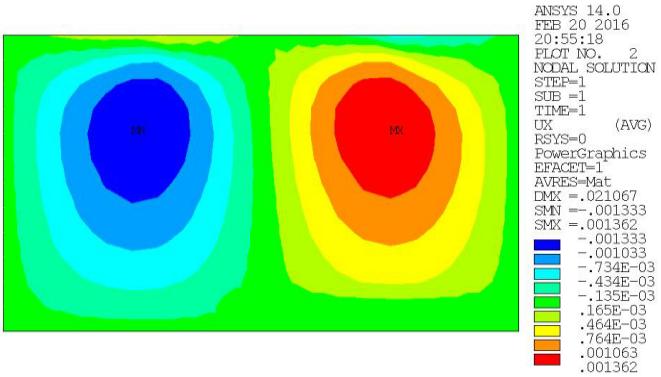

Fig. 14. Distribution of the horizontal displacements U_x for isolated footing.

TABLE 6. DISTRIBUTION OF UX DISPLACEMENTS FOR ISOLATED FOOTING.

Uy displacements distribution (m)			
Color Scale	*30 days*	*450 days*	*870 days*
	$-1.33x10^{-3}$	$-1.52x10^{-3}$	$-1.51x10^{-3}$
	$-1.03x10^{-4}$	$-1.18x10^{-4}$	$-1.17x10^{-4}$
	$-7.34x10^{-4}$	$-8.35x10^{-4}$	$-8.26x10^{-4}$
	$-4.34x10^{-4}$	$-4.91x10^{-4}$	$-4.86x10^{-4}$
	$-1.35x10^{-4}$	$-1.48x10^{-4}$	$-1.46x10^{-4}$
	$1.65x10^{-4}$	$1.96x10^{-4}$	$1.95x10^{-4}$
	$4.64x10^{-4}$	$5.40x10^{-4}$	$5.35x10^{-4}$
	$7.64x10^{-4}$	$8.83x10^{-4}$	$8.75x10^{-4}$
	$1.06x10^{-4}$	$1.23x10^{-4}$	$1.22x10^{-4}$

Observing Fig. 15 and Table 7, the evolution of the vertical displacement U_y, is appreciated. Furthermore, through this figure it can be seen that displacements are about -0.0069 m in the superficial edge, while near the bottom border are near zero. Here, the negative sign indicates the direction in which evolve the displacements. Vertical displacements are produced by the load applied on the surface and the center of the length of the domain. It is notable that these values also have a symmetrical behavior. They are also appropriate and consistent with the results reported by other researchers.

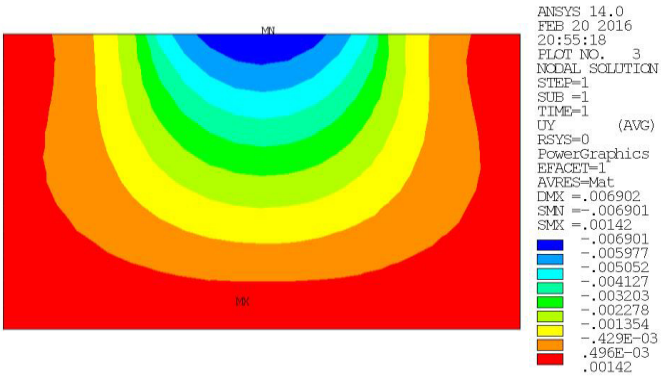

Fig. 15. Distribution of the vertical displacements U_y for isolated footing.

Fig. 16 shows the surface profile of vertical displacements. Again, we can see that these are negative (decrease of volume) and the maximum value (-0.0130 m) occurs in the middle of the domain, it means, in the part that is subjected to surface forces. Furthermore, in areas uncharged positive offsets values

are presented. This shows us that these areas suffer an increase in volume or bulging.

TABLE 7. DISTRIBUTION OF U_Y DISPLACEMENTS FOR ISOLATED FOOTING.

Uy displacements distribution (m)			
Color Scale	*30 days*	*450 days*	*870 days*
	$-6.90x10^{-3}$	$-1.30x10^{-2}$	$-1.30x10^{-2}$
	$-5.97x10^{-3}$	$-1.16x10^{-2}$	$-1.16x10^{-2}$
	$-5.05x10^{-3}$	$-1.10x10^{-2}$	$-1.10x10^{-2}$
	$-4.13x10^{-3}$	$-8.68x10^{-3}$	$-8.68x10^{-3}$
	$-3.20x10^{-3}$	$-7.23x10^{-3}$	$-7.23x10^{-3}$
	$-2.28x10^{-3}$	$-5.79x10^{-3}$	$-5.79x10^{-3}$
	$-1.35x10^{-3}$	$-4.34x10^{-3}$	$-4.34x10^{-3}$
	$-4.29x10^{-4}$	$-2.89x10^{-3}$	$-2.89x10^{-3}$
	$-4.96x10^{-4}$	$-1.45x10^{-3}$	$-1.45x10^{-3}$

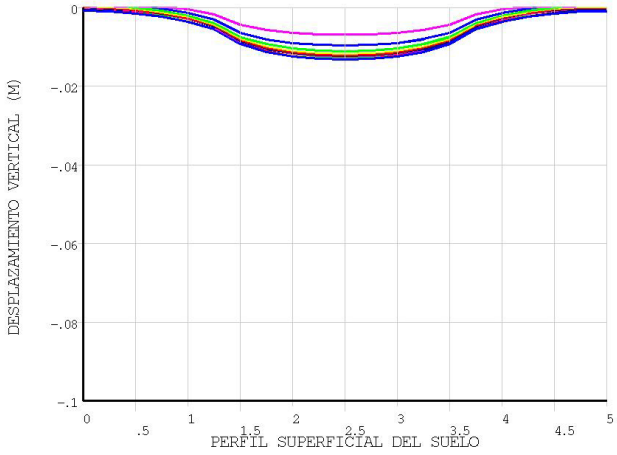

Fig. 16. Superficial profile of soil for isolated footing.

VI. CONCLUSIONS

The algorithm of coupled model delivers results quickly and easily, with just introducing basic soil parameters. This, due to the model is flexible because it allows infinite combinations, which helps us to reproduce any condition that is present in field or laboratory. In addition, another important aspect that helps reproduce any problems is that it considers that there may be water flow, as a contribution or extraction, resulting in changes in pore water pressure, thus also on the horizontal and vertical displacements. Through the results obtained, an appropriate behavior of the phenomenon of consolidation is observed. Even, show consistent results with those reported by other researchers and those obtained in the laboratory.

ACKNOWLEDGMENT

The authors would like to thank Consejo Nacional de Ciencia y Tecnología (CONACyT) and the Universidad Autónoma de Querétaro for their support and founding the project "Metodología para el diseño de cimentaciones en suelo expansivo por el método de interacción suelo-estructura utilizando el principio de esfuerzos efectivos (FoVin13-T-021)" in which the authors are working.

REFERENCES

[1] R. Magaña, and M. P. Romo, "Modelo numérico para estudiar el movimiento de agua en suelos no saturados", Instituto de Ingeniería, Universidad Nacional Autónoma de México, 1980, pp. 1-23.

[2] T. T. Wong, D. G. Fredlund, D. G. and J. Krahn, "A numerical study of coupled consolidation in unsaturated soils", Canadian Geotechnical Journal, vol. 35, 1998, pp. 926-937.

[3] D. J. Bentler, "Coupled consolidation, Finite element analysis of deep excavations, 1998, pp. 83-102.

[4] J. E. Manzolillo, H. A. Di-Rado, and A. M. Awruch, "Simulación numérica del comportamiento de suelos saturados bajo cargas de fundaciones", Comunicaciones Científicas y Tecnológicas, Universidad Nacional del Nordeste, 2000.

[5] H. A. Di-Rado, P. A. Beneyto, J. L. Mroginski, J. E. Manzolillo, and A. M. Awruch, "Análisis tridimensional de la consolidación de suelos saturados utilizando el MEF", Mecánica Computacional, vol. 23, 2004, pp. 607-617.

[6] M. S. Krishnamoorthy, "Consolidation analysis using finite element method", The 12th International Conference of International Association for Computer Methods and Advances in Geomechanics (IACMAG), 2008, pp. 1157-1161.

[7] M. E. Gurtin, "An introduction to continuum mechanics", Mathematics in Sciences and Engineering, Academic Press Elsevier, 2003.

[8] M. Santander, "Intruducción al calculo variacional", Departamento de Física, Universidad de Valladolid, 2003.

[9] ANSYS Inc., Software, ver. 1, Canonsburgh PA, USA, 2014.

Synthesis of Pd-Ni nanocatalysts for methanol oxidation reaction in alkaline medium

R. Gutierrez, J. Ledesma-García*
División de Investigación y Posgrado, Facultad de Ingeniería.
Universidad Autónoma de Querétaro.
Querétaro, México.
*Corresponding e-mail address: janet.ledesma@uaq.com.mx

J. Maya-Cornejo
Centro de Investigación y Desarrollo Tecnológico en Electroquímica.
Querétaro, México.

***Abstract*—This work presents the comparison of three different synthesis methods of bimetallic electrocatalyst based on Pd-Ni supported on Vulcan XC-72 carbon and their application toward methanol oxidation in alkaline medium. The electrocatalytic properties of Pd-Ni based materials were tested by cyclic voltamperometry in the presence of 0.1M methanol, and compared with the electrochemical response of commercial Pd.**

Keywords—Palladium catalyst, Palladium-Nickel catalyst Alkaline medium, Methanol Oxidation reaction.

I. INTRODUCTION

Nowadays the study of new sources of clean energy is critical to reducing contaminants produced by daily human activities, among which is the use of machinery using combustion for power generation, these emit pollutants to the environment, fuel cells in this area can generate electricity based on a chemical reaction between hydrogen of a fuel and oxygen in which energy, water and heat are obtained as reaction product. A fundamental part of any fuel cell is the catalyst, which is responsible for carrying out the reaction in which electrical energy is obtained, which is why is searched the creation of efficient catalysts for different fuels and different applications.

Direct alcohol fuel cells (DAFC) which used methanol, ethanol, and butane as fuel have attracted the attention of researchers because it possess a number of advantages such as a liquid fuel, quick refueling, low cost of methanol and the compact cell design making it suitable for various potential applications including stationary and portable applications. Continue with the importance of these fuel cells, the methanol oxidation reaction has taken a serious relevance in these days for his application in Direct Methanol Fuel Cells (DMFC) [1-2], which have shown a high efficiency.

The methanol releases six protons and electrons per molecule during its oxidation, this is a high energy density (6100 W h kg-1), one of the reasons than makes the methanol a suitable fuel for fuel cells [3]. DMFC works at low and intermediate temperatures (up to 150ºC) and are fed with a dilute aqueous solution of methanol in water.

To use some fuel cell as portable application one of the most important consideration is the compact design. To have a compact size and small weight this cells have to work at low temperature, and DMFC are the most viable fuel cell technology to work under this conditions [4].

Platinum-based electrocatalysts have been study for many years, getting great electrocatalytic activities, but the high cost of this materials are the principal problem for their use [5].

Additionally, the platinum-based electrocatalysts present another problems like the poisoning by intermediary products in the reaction, like the CO in an acid medium [6]. In this way some investigations have founded that palladium-based materials are the most promising in the oxidation of different alcohols like the ethanol [7] and the methanol [8] even improving the electrocatalytic activity that the platinum present. Different groups [9-10] have proved that the palladium-based electrocatalysts resist the poisoning effect by CO and consequently show high efficiency in DMFC.

While the palladium present better performance instead the platinum, in many occasions the catalytic activity of these materials are insufficient for future applications. The deactivation of these materials still appears as result of the poisoning and production costs are still high. One way to solve this problem is by combining the palladium with another materials to create a bimetallic catalysts [11] Such as V, Cr, Fe and Co [12-13] whit the purpose to develop a cheap catalyst which could improve the catalytic activity synergizing the properties between the catalyst and the different material [14].

Nickel is another possible candidate for this position to increase the catalytic activity, showing in many studies better activity by alloying with palladium than the palladium alone [15-16], because this alloy not only offering more active sites also changes the electronic structure of the palladium, which facilitate the removal of poisoning intermediates on Pd [17].

Ni and Pd belong to the same group in the periodic table, the interactions (mixing) between Ni 3d84s2 electrons and Pd 4d105s0 electrons are very likely involved in intermetallic Ni-Pd bonding. Such effect on the catalysis by nanometer-sized Ni-Pd clusters is certainly interesting.

A good synthesis method to prepare mono dispersed metal particles is the polyol process, this method used a dyol or polyalcohol, in this case etilengycol for the reduction of the metallic salts, and it serves as reducing agent and solvent at the same time [18].

This method is very used because help with the shape and the size of the nanoparticle. Is very common that this method use polyvinylpyrrolidone (PVP) to stabilize the nanoparticles, preventing the oxidation and the agglomeration.

In this work preliminary results about the synthesis and electrochemical characterization of Pd-Ni/C bimetallic nanocatalysts are presented. The polyol method, already reported by Maya-Cornejo and coworkers [19], was modified in the addition of ascorbic acid for one synthesis and the addition of PVP in other synthesis order to improve and to optimize the method. The prepared materials based on Pd-Ni were tested toward methanol oxidation by cyclic voltammetry in acid media and compared to commercial Pd/C material.

II. Experimental

A. *Preparation of the catalyst*

For the synthesis of the bimetallic electrocatalysts all used reagents were analytical grade and used without further purification. Potassium tetrachloropalladate (K_2PdCl_4) (99.9%, Aldrich) and nickel sulfate ($NiSO_4$) (99.9%, Aldrich) were used as precursor salts.

For the first synthesis (PdNi/C-1), in 10 ml of ethylene glycol as reducing agent was added 100 mgr. of PVP and bring it to 80°C. pH was adjusted to 1 with 300 µl of 0.5M sulfuric acid . After that, 60 mgr. of $NiSO_4$ was added. As surfactant agent 683 mgr. of acid ascorbic and 250 mgr. of sodium bromide (NaBr) were added and put in constant agitation for two hours. After that 28 mgr. of K_2PdCl_4 was added and finally 57 mgr. of Vulcan XC-72 carbon as support were incorporated to the mixture and stirring for 30 minutes.

For the second synthesis (PdNi/C-2) we follow the same steps with the exception of the ascorbic acid, instead to add directly, the ascorbic acid was diluted in 3 ml of water separately, to see after if this step change the size and the morphology of the nanoparticles.

And finally in the third synthesis (PdNi/C-3), 10 ml of ethylene glycol was placed in a flask, then separately the PVP mixed with the ascorbic acid were added to the ethylene glycol. After that the sodium bromide was added, and the pH value is adjusted to 1. $NiSO_4$ was incorporated to the solution and remained under constant agitation. Finally K_2PdCl_4 and the Vulcan carbon are added. The three different synthesis were at the same concentrations only we change the order of some steps. For comparison purposes, commercial Pd supported on Carbon as tested. In the figure 1 we can see the different synthesis method with his different modification

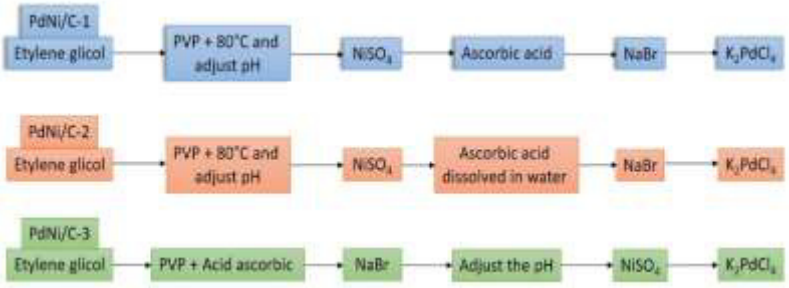

Fig. 1. This scheme shows the different synthesis method of nanocatalyst.

B. *Electrochemical characterization*

For the electrochemical characterization a potentiostat with an array of 3 electrodes-glass cell was used. A glassy carbon with a diameter of 5 mm and an Hg/HgO, NaOH (1M) were employed as working and reference electrodes respectively. The catalytic ink was prepared with 1 mg of catalyst, 75 µl of isopropyl alcohol and 7 µl of Nafion and mixed in an ultrasonic bath. The voltamperometry tests were performed in 0.3 M KOH solution, subjected to a several cycles in a rate to -1.0 to 1.1 V with a scanning rate of 50 mV/s. then the oxidations were performed in a 0.3 M KOH solution an in the presence of 0.1 M methanol with a scanning rate of 20 mV/s. The current density was normalized with the working electrode geometric area.

III. Results and Discussion

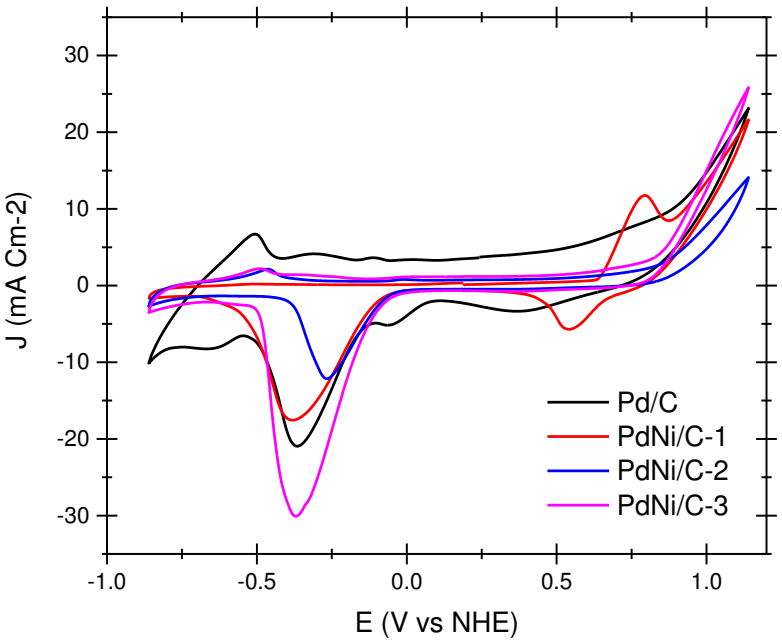

Fig. 2. Voltamperometric profiles of the PdNi electrocatalysts in 0.3M KOH solution at a scan rate of 50 mV s^{-1}.

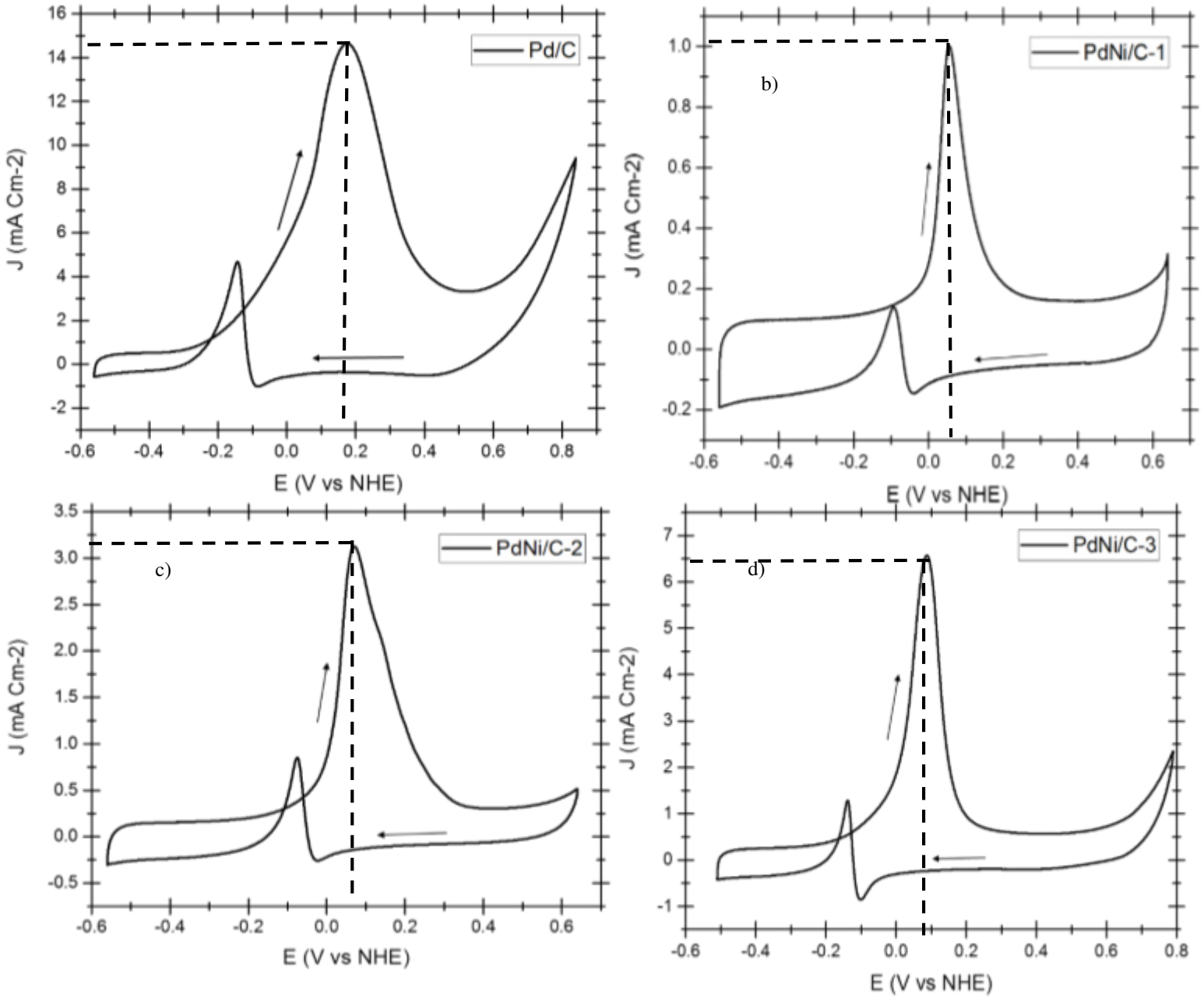

Fig. 3 Electrocatalytic response of a) Pd/C, b) Pd-Ni/C-1, c) Pd-Ni/C-2, d) Pd-Ni/C-3 for the oxidation of 0.1M methanol at 20 mV s^{-1} scan rate

Figure 2 compares the voltamperometric profiles of the PdNi-based materials prepared by three different methods. Pd commercial material is also included. As can be seen, the absorption/ desorption of hydrogen appearing between -1.0 to -0.5 V. This Figures shows from 0.1 to 0.25 V the cathodic peaks associated to the typical reduction process of Pd oxides formed during the forward-going potential scan.

Synthesis	E (V vs NHE)	J (mA cm^{-2})
PdNi/C-1	0.055	1.008
PdNi/C-2	0.079	3.125
PdNi/C-3	0.087	6.571
Pd/C commercial	0.175	14.648

Table 1. Comparison of oxidation potential and current density values of methanol oxidation on PdNi-based material synthesized by different methods.

This peak confirmed the presence of palladium. Nickel also can be confirmed with the oxidation peak of $Ni(OH)_2$ to NiOOH in the anodic sweep in the interval of 0.75 to 1.5 V, and the reduction of NiOOH to $Ni(OH)_2$ in the range of 0.5 to 0.75 V, but this peak only appear in the material prepared by the PdNi/C-1 synthetic route. This doesn't mean that in the PdNi/-2 and PdNi/C-2 samples we don't have nickel in the bimetallic nanoparticles, these maybe occurs because we have a high probability to have core-shell structures with nickel in the core covered with palladium.

Figure 3. Presents the cyclic voltammograms of PdNi/C synthesized by different methods in the presence of 0.1 M methanol in 0.3 M KOH. The values which they are marked with a dotted line correspond to the values of potentials and current densities for the maximum peak of oxidation, this values are in table 1.

Is clearly to see that the Pd/C present a better kinetic advantage current density than the other materials, but in this case the tree synthesized materials present a lowest positive potential, that's means that this materials require lowest energy to start the oxidation of the methanol. Independently of Pd/C, the PdNi/C-3 present the best values for the current density being two time higher than the PdNi/C-2 and six times higher than PdNi-/C-1. We can see that the addition of nickel modifies the properties of the catalysts, this may be due to a modification in the structure of the catalysts.

IV. Conclusion

Three different PdNi/C nanocatalyst were synthesized by a modified polyol method and used as electrocatalyst for methanol oxidation. With cyclic voltammetry we obtain the profiles of the nanocatalyst and the electrocatalytic activity oxidizing methanol. The three PdNi/C nanocatalyst shows that need lowest values of energy to oxidize methanol than the Pd/C catalyst, this is attributed to the addition of the nickel that change the electronic structure of palladium.

It can also see than the synthesis method offer a good alternative to prepare bimetallic catalyst systems which is applicable over a wide range of metals.

V. References

[1] B.D McNicola, D.A.J Randb, K.R Williamsc, "Direct methanol–air fuel cells for road transportation," J. Power Sources, Vol. 83, pp.15–31, October 1999.

[2] E. Antolini, J.R.C. Salgado, E.R. Gonzalez, "Carbon supported Pt75M25 (M = Co, Ni) alloys as anode and cathode electrocatalysts for direct methanol fuel cells," J. Electroanal Chemistry, Vol.580, pp. 145–154, June 2005.

[3] A. S. Aricò, S. Srinivasan, V. Antonucci "DMFCs: From Fundamental Aspects to Technology Development" Fuel Cells, vol. 1, pages 133–161, July, 2001

[4] Y. Shimazaki, Y. Kobayashi, S. Yamada, T. Mika, M. Konno "Preparation and characterization of aqueous colloids of Pt–Ru nanoparticles" J. Colloid. Vol. 292, pp 122-126, 2005.

[5] T.R. Ralph, M.P. Hogarth, "Catalysis for Low Temperature Fuel Cells", Platinum Metal Rev, 2002,46, pp. 3-14.

[6] R. Dillon, S. Srinivasan, A.S. Arico, V. Antonucci, "International activities in DMFC R&D: status of technologies and potential applications," J. Power Sources, Vol. 127, pp. 112–126, March 2004.

[7] S.Y. Shen, T.S. Zhao, J.B. Xu, Y.S. Li, "Synthesis of PdNi catalysts for the oxidation of ethanol in alkaline direct ethanol fuel cells," J. Power Sources, Vol. 195, pp.1001–1006, 2010.

[8] Yanchun Zhao, Xiulin Yang, Jianniao Tian, Fengyang Wang, Lu Zhan, "Methanol electro-oxidation on Ni@Pd core-shell nanoparticles supported on multi-walled carbon nanotubes in alkaline media," Int j hydrogen energ., Vol. 35, pp. 3249–3257, 2010.

[9] Ha S, Larsen R, Zhu Y, Masel RI. "Direct formic acid fuel cells with 600 mAcm2 at 0.4 V and 22" C. Fuel Cells, vol. 4, pp.337–43, 2004.

[10] Ha S, Larsen R, Masel RI. "Performance characterization of Pd/C nanocatalyst for direct formic acid fuel cells". J Power Sources, vol. 144, pp 28–34, 2005.

[11] S.Y. Shen, T.S. Zhao, J.B. Xu, Y.S. Li, "Synthesis of PdNi catalysts for the oxidation of ethanol in alkaline direct ethanol fuel cells" J Power Sources, vol. 164, pp. 527–531, February 2007.

[12] Yange Suo, Lin Zhuang Prof., Juntao Lu, "First-Principles Considerations in the Design of Pd-Alloy Catalysts for Oxygen Reduction" Angew. Chem, vol. 46, pp. 2862–2864, April 2007.

[13] Y.-X. Wang, P.B. Balbuena, "Design of Oxygen Reduction Bimetallic Catalysts: Ab-Initio-Derived Thermodynamic Guidelines" J. Phys. Chem. B, vol. 109, pp.18902–18906, September 2005.

[14] Wang J, Li Y, Sun X, "Challenges and opportunities of nanostructured materials for aprotic rechargeable lithium–air batteries" Nano Energy, vol. 2, pp. 443–467, 2013.

[15] K. Lee, O. Savadogo, A. Ishihara, S. Mitsushima, N. Kamiya, K. Ota, "Methanol-Tolerant Oxygen Reduction Electrocatalysts Based on Pd-3D Transition Metal Alloys for Direct Methanol Fuel Cells" J. Electrochem. Soc. Vol. 153 , A20-A24, 2006.

[16] Z.L. Liu, X.H. Zhang, L. Hong, "Physical and electrochemical characterizations of nanostructured Pd/C and PdNi/C catalysts for methanol oxidation"

[17] Chen L, Guo H, Fujita T, Hirata A, Zhang W, Inoue A, "Nanoporous PdNi bimetallic catalyst with enhanced electrocatalytic performances for electro-oxidation and oxygen reduction reactions" AdvFunct Mater, vol. 21, pp. 4364–4370, November 2011.

[18] S. Sun, "Recent Advances in Chemical Synthesis, Self-Assembly, and Applications of FePt Nanoparticles" Adv.Mater, vol. 18 pp. 393–403, February 2016.

[19] J. Maya-Cornejo, E. Ortiz-Ortega, "Copper–palladium core–shell as an anode in a multi-fuel membraneless nanofluidic fuel cell: toward a new era of small energy conversion devices" Chem. Commun, vol. 51 pp.2536, December 2014.

Review on the visual impact of traffic signs on the drivers

*Jesús Esteban Gulliver Santiesteban
Estudiante de la Maestría en Ingeniería de Vías Terrestres, Transporte y Logística
Facultad de Ingeniería Universidad Autónoma de Querétaro
Querétaro, Querétaro
Jesban_15@hotmail.com

Saúl Antonio Obregón Biosca
Docente-Investigador
Facultad de Ingeniería Universidad Autónoma de Querétaro
Querétaro, Querétaro
Saul.obregon@uaq.mx

Abstract*— The present work aims to carry out a discussion of articles and methodologies employed by researchers in which intervenes the conductor and his perception towards road signs, this is a broad subject which traffic engineers have given the importance that it deserves because the human factor is the most important, since without it, it is not possible that there are roads users. As a conclusion we can say that by employing the methodology of eye movement recording system, help us to determine the principal objects where eye fixations are focused and so it is easier to know which signs are or not perceived by drivers and their reasons.

Keywords—oculars movements, drivers, traffic signs.

I. INTRODUCTION

Currently performed works that deal with the driver and visual attention to different devices of control of traffic that are located in the road infrastructure, the present research focuses on traffic signs which have to provide the user of the land routes, notably to the automobile driver, information about via which pass and thus help to adjust your behavior as needed [1].

Information provided by traffic signals to the driver is perceived visually, that is why traffic engineers believe necessary to study the driver from the point of view of the psychology of traffic (behavior), Therefore the human factor is of great importance for this research [2]. A research on the cognitive characteristics of traffic signs, noticed that they give information to the user of the road infrastructure and its main objective is to warn, regulate and guide them with the help of symbols, words, or both [3].

Another aspect important in this type of research is the location of signs on the road infrastructure, since this will depend on that they are perceived in a better way to perform the necessary maneuvers and reach the destination safely, when driving on an urban or rural roads we can find a wealth of information which we have to process in an efficient manner, but usually much stays on the road and in some cases do not have a proper locateon and that's not possible attend [4]. [5] others have observed that when the driver is experienced traffic accidents may be caused by a bad placement of signage rather than by bad driving. So the experience of the driver is essential in this type of study.

It is important to evaluate the signals of traffic and its impact on the driver, since one of the major problems that exist when going through an urban or rural, and are a cause of road accidents is the lack of attention to them. In [6] they noted that to identify road signs in an efficient way in space and time suitable helps the driver to reach your destination and thus ensure the stability of its passengers.

II. LITERATURE REVIEW

This paragraph describes the evolution of the methodologies employed in reported investigations, which involves devices of control of traffic and the perception that drivers have on the visual aspect to these objects, the studies involved where the eye fixations while driving started in the Decade of the 60's, [7] they are the principal investigators who conducted this type of study.

It can make the study of areas where the driver located his gaze to travel along a road or fixed his eyes on some object of interest (signs of traffic, mirrors, etc.), It helps to know the attention that motorists have to such thanks to eye movement control device [8]. Sometimes through a roads we can find signals that are not perceived easily and therefore not can be addressed since they need more bindings to be understood, so they need more time to react are cause for an improper manoeuvre and attentive with the safety of the driver and its surroundings.

TABLE I shows a list of studies in real environment carried out in chronological order, where involved automobile drivers, fixings and looks to certain objects. The characteristics presented contains information about the objectives of the same materials and main conclusions this in order to help future researchers and serve as a tool to update according to studies that currently exist:

TABLE I. Description schematic chronologically from studies in real environment objectives, materials used, and main conclusions.

Título	Authors(year)	Objective	Materials used	Main Conclusions
Strategies of visual search by novice and experienced drivers.	[9].	Meet the visual exploration with the experience of drivers.	Registration system of eye movement using a TV.	Inexperienced drivers, setting his eyes in mediated minor areas that earned confidence while driving.
Eye movements while driving cars around curves.	[10].	Determine if the pattern of eye movement on curves is influenced by the experience of the driver.	Eye movement registration system NAC eye-mark-recorder, III	Of eye fixations were distributed on both sides of the curve, as well as in other areas of the roads.
Differences in eye movements and mental workload between experienced and inexperienced motor-vehicle drivers.	[11].	Consider whether the duration of fixations eye while driving are related to the experience of the driver.	Eye movement registration system NAC eye-mark-recorder, V.	The duration of fixation may be indicative of the State of mind of the driver
Aspects of driving behaviour in learner and inexperienced drivers.	[12].	See how developed the visual search in relation to the experiendia the ride.	Video camera (not record brand and model).	The driver tends to be from 2 to 3 bindings per second.
Maintaining lane position whit peripheral vision during in-vehicle tasks	[13].	To determine how it affects eye fixations within an atentacional task and its relationship to the experience of the driver.	Two camcorders Panasonic WV-CD2	Inexperienced drivers need foveal vision at the start of the journey and forms move improve your peripheral vision.
Effects of experience and proccesing demands on visual information acquisition in drivers.	[14].	Study of visual exploration strategies for different traffic situations.	Eye movement registration system NAC eye-mark VII.	It is suggested an experiment where you select Visual strategies according to the complexity of the road.

Driving experience and time-sharing during in-car tasks in roads of different width	[15].	Whether experienced drivers have low variability in weather observing a task unrelated to driving, compared to the inexperienced.	Video camera (not record brand and model).	The time provided by inexperienced drivers to traffic conditions is greater with respect to the experienced.
Atencion a señales de velocidad y de orientacion mediante movimientos oculares	[2].	The description of the patterns of visual inspection of different signs of circulation. The description of the patterns of visual inspection of different signs of circulation.	Eye movement registration system	Orientation signs are looks more frequently than the speed.

III. USED METHODOLOGIES

In investigations of real environment (field studies) that same complexity of road infrastructure is which makes it difficult to control the high number of factors that can affect dice results and, consequently, to interpret these unequivocally.

To determine visual attention which the driver has to traffic signals it has worked with some methodologies which then develop both have been used by researchers to help there is a better traffic psychology.

There are three methodologies to determine the driver attention to traffic signals in field studies, listed below:

- Detention of vehicle and test of memory through a survey.
- Take measurements of the behavior of the driver.
- It is the recognition of eye movement during driving.

Vehicle detention questionnaires

This is one of the methodologies used to detect attention that automobile drivers have different traffic signs in which stops the driver of the vehicle and is a test, in order to know the ability to uptake of the motorist. Enquiries carried out in the test are structured in the following way according to [16] [17]:

What was the latest sign of traffic that has passed?

Remember if the latest sign of traffic that has passed was a general warning? (only if you did not answer the first question).

Are you professional driver? (i.e., truck driver).

With frequency driving along this road?

Year in which obtained his driver's license?

Average of miles driving per year?

Has he been interviewed before this research?

Driver behavior

Measures which are taken into account in this methodology are maximum speed limits and what is the behavior of drivers have faced such signs. Researchers should take some recommendations which are shown in [18]:

- Roads with speed of 80 km/hr or above it.
- The study must be in traffic, with free flow rate conditions.
- It uses a radar gun and a car that does not call the attention of drivers and put them on warned.

Recognition of eye movements

One of the ways in which recognition of movements can be eye is through the recording of the movement of the eye, which offers information about possible and visual search patterns to use instruments of automated registration [7], the figure 1 and 2, are devices used currently and in the past respectively:

Figure 1. Current eye movement recording systems.[7]

Figure 2. Ancient eye movement recording systems.[7]

Eye movement analysis has been used in a manner more common in recent years as a system that benefits research having to do with the visual aspect, the main reasons why it helps the technique of recording of eye movements to visual information are those parts of the environment of the roads that can be observed in detail, so the peripheral vision is of great importance [10].

For the study of visual search required sophisticated systems and powerful tools which are able to achieve a good data-processing, since the eye tends to move quickly and very subtle [7].

Coinciding with [7] these systems have the disadvantage of providing information on eye fixation, but not on the further processing of the information. On the other hand, the role played by the peripheral vision on the recording is not clear. Another drawback is that only a small number of participants can be recorded.

IV. DRIVER

Factors involved in traffic or circulation, are the person, the vehicle and route. In Spain, [19] is considered the person as a protagonist of the movement, and their behavior depends definitely on its safety and can serve as driver, pedestrian, or guardian of the vehicle, so we us is of interest driver object of study.

The driver is the most important element in road circulation. In this sense, [20] refers to the movement of vehicles depend only of them, and the quality of the circulation is the result of its ability to adapt the movement of your vehicle to road and traffic characteristics.

The [19] refers to the usual driver as the person who has the permission or driving license required, which will be registered in the register of drivers and offenders, has been designated by the owner of the vehicle, prior knowledge, by being one which as usual leads such a vehicle.

V. EXPERIENCE DRIVER

The experience of the driver is definitive when it comes to perceive signs that are located on the road infrastructure, interest is understanding and reaction to the road signs by drivers to understand the Act of the latter and thus possibly reduce the accident rate which can lead to unfortunate consequences. Relating thereto [2] infer that its main function is the transmit the driver situation pathway on which transit and on this basis, can make a better decision that does not affect their well-being, therefore is of utmost importance to assess their efficacy and effectiveness. In addition, identification of the signs and their proper interpretation help in the enforcement of traffic regulations, and in the same sense of security, so in [6], it is concluded that the correct identification of signals in place and the right time is important to ensure reaching your destination safely.

Drivers with a more specific experience they gain a greater visual attention to objects that are in your environment with respect to the inexperienced, because that new drivers last longer, looking at objects and become familiar with them, this is to be able to acquire experience on the driving and their environment [15], in the [2] this research was performed in Madrid was determined that drivers tend to pay more attention to guidance signals in comparison with the maximum speed. Another investigation [5] came to the conclusion that traffic signs are seen most frequently on the right track, since the left side is taken as not suitable to place traffic signs, since the experience of the driver it tends to look on the opposite side. To realize this behavior, Figure 3 shows the proof of this:

Figure 3. Illustration of the lack of attention to the signs on the left side.

VI. VERTICAL SIGNALS AND ITS INFLUENCIA WITH THE DRIVER

Currently performed studies that directly relate the traffic signs and driver perception towards them, through systems that determine the movement of the eye. [21] mentioned that drivers always capture traffic information for your eyes when they are driving on the road and this has an impact on road safety. [22] reported that in metropolitan areas is where you can more easily find examples of sites from the road where within a few minutes of driving time there are dozens of traffic signals, in addition to other sources of information and distractions.

In some cases the lack of visibility of road signs is by different factors that affect the driver in an important way to perform their function in an efficient manner. In this sense [23] discussed the visual impairment is caused by the presence of other vehicles, whether they are ahead, adjacent and even those traveling in the opposite direction which block the line of sight between the driver of the vehicle and any sign placed on the road.

It is important to assess the impact of signs at the conductor, since one of the major problems that exist when going through an urban or rural, and are a cause of road accidents is the lack of attention to them. The above stands in [6], exposing that to identify traffic signs in an efficient way in space and time suitable helps the driver to reach your destination and thus ensure the stability of its passengers.

VII. CONCLUSIONS

It is important to know the work carried out in this line of research, sometimes when driving by a road we can find signals that are not perceived easily and therefore not can be addressed since they need more bindings to be understood, so they need more time to react are cause for an improper manoeuvre and attentive with the safety of the driver and its surroundings.

Eye movement recording system can help us to know the points in which the eye fixations tend to observe traffic signs and whether they are or not perceived by drivers and their reasons. These systems have been updated thanks to the technology that exists today..

The lines of future research are proposed from the exposed methods are: i) the analysis of the visual impact of drivers on the restrictive, preventive and informative signs, and ii) as well as other control devices.

ACKNOWLEDGMENT

The authors wish to thank the National Council of science and technology (CONACYT) and the Universidad Autónoma de Querétaro for their support and support to this article.

REFERENCES

[1] Fisher, James (1992) Testing de effect of road traffic signs´informational value on driver behavior. Human Factors, 2(34), pp. 231-237.

[2] Conchillo-Jiménez, Ángela, Pérez-Moreno, Elisa y Recarte-Goldaracena, Miguel (2010) Atención a señales de velocidad y de orientación mediante movimientos oculares. Psicothema, 4(22), pp. 720-724.

[3] Chan Alan H. y W.Y; Annie (2007) Cognitive Design Features on Traffic Signs. Engineering Letters, 1 (14), pp. 13-18.

[4] Hughes, P. K; Cole, B.L. (1986) What attracts attention when driving? Ergonomics, 29, pp. 377-391.

[5] Borowsky, Avinoam, Shinar, David y Parmet Yisrael (2008) The relation between driving experience and recognition of road signs relative to their locations. Human Factors, 2(50), pp. 173-182.

[6] Sathiya, S; Balasubramanian, M. y Palanivel, S. (2014) Pattern Recognition Based Detection Recognition of Traffic Sign Using SVM. International Journal of Engineering and Technology, 2 (6), pp. 1147-1157.

[7] Castro, Candida (2009) Human Factors of Visual and Cognitive Performance in Driving. Human Factors, pp. 1-30.

[8] Tejero-Gimeno, Pilar, Pastor-Cerezuela, Gemma y Crespo, Antonio (2004) Exploración visual y movimientos oculares en conductores con distinta experiencia. Anales de Psicología, 1(20), pp. 127-145.

[9] Mourant, R. y Rockwell, T. (1972). Strategies of visualsearch by novice and experienced drivers. Human Factors,14 (4), 325-335.

[10] Cohen, A. S. y Studach, H.(1977) Eye Movements while driving cars around curves. Perseptual and motor skills, 3(44), pp. 683-689.

[11] Unema, P. y Rötting, M. (1990). Differences in eye movements and mental workload between experienced and inexperienced motor-vehicle drivers. En D. Brogan (Ed.), Visual search. London: Taylor & Francis.

[12] Velde Harnsenhorst, J. J. y Lourens, P. F. (1991). Aspects of driving behaviour in learner and inexperienced drivers. En A. G. Gale, I. D. Brown, C. M. Haslegrave,I. Moorhead , S. P. Taylor (Eds.), Vision in vehicles– III (pp. 63-70). Amsterdam: Elsevier.

[13] Summala, H., Nieminen, T. y Punto, M. (1996). Maintaining lane position with peripheral vision during invehicle tasks. Human Factors, 38(3), 442-451.

[14] Crundall, D. E. y Underwood, G. (1998). Effects of experience and processing demands on visual information acquisition in drivers. Ergonomics, 41(4), 448-458.

[15] Wikman, A. S; Nieminen, T; y Summala, H.(1998) Driving experience and time-sharing during in-car task of roads of different width . Ergonomics, 3(41), pp. 358-372.

[16] Johansson, G., and Rumar, K. (1966). Drivers and road signs: A preliminary investigation of the capacity of car drivers to get information from road signs. Ergonomics, 9, 57-62.

[17] Johansson, G., and Backlund, F. (1970). Drivers and road signs. Ergonomics, 13, 749-759.

[18] Lajunen, T., Hakkarainen, P., y Summala, H. (1996). The ergonomics of road signs: Explicit and embedded speed limits. Ergonomics, 39, 1069-1083.

[19] DGT (2011), Normas y señales reguladoras de la circulación, elaborado por el área de formación y comportamiento de los conductores. Edición 2011.

[20] Kraemer, Carlos, Pardillo, J; María, Rocci, Sandro, Romana, Manuel, G; Sanchez, Victor y Val, Miguel. (2004) Ingeniería de Carreteras, Ed. Mc Graw Hill Cap. 25 Vol I pp. 363-384.

[21] You, X.W., Zhang, E.J., Zhang, Q.X., (2008). Modern road traffic engineering. Tsinghua university press, Beijing Jiao tong university press. Beijing, pp. 185.(In Chinese).

[22] Zhi, Xu, Hongzhi, Guan, Hai, Yan. (2011). Incorporating Saliency Map into Prediction of Drivers' Eye Fixations on Traffic Signs. Beijing Transportation Engineering. Pp. 1627-1639.

[23] Pietrucha, M. T., Donnell, E. T., Lertworwanawich, P., and Elefteriadou, L. 2006. Effects of Traffic Characteristics and Mounting Location on the Visibility of On-Premise Commercial Signs. Journal of Transportation Engineering. Pp. 862-871.

Motion Control Platform based on All Programmable SoC Technology

Miguel-Angel Martínez-Prado,
Universidad Autónoma de Querétaro, Facultad de Ingeniería, Ingeniería en Automatización, Querétaro, México,
miguel.prado@uaq.mx

Juvenal Rodríguez-Reséndiz
Universidad Autónoma de Querétaro, Facultad de Ingeniería, Ingeniería en Automatización. Querétaro, México.
juvenal@uaq.edu.mx

Gerardo-Israel Pérez-Soto,
Universidad Autónoma de Querétaro, Facultad de Ingeniería, Ingeniería en Automatización, Querétaro, México,

Roberto-Augusto Gómez-Loenzo,
Universidad Autónoma de Querétaro, Facultad de Ingeniería, Ingeniería en Automatización, Querétaro, México,
rob@uaq.mx

Diana-Carolina Toledo-Pérez
Universidad Autónoma de Querétaro, Facultad de Ingeniería, Ingeniería en Automatización. Querétaro, México.

***Abstract*— The performance evaluation of control algorithms demands a short implementation time. In particular, those related with motion control, require of a well-structured platform to measure the performance of the controlled system. The novelty of this research work lies on the implementation of a mixed hardware/software platform based on the all programmable system on a chip (SoC) technology, for the rapid implementation of several control algorithms for motion control applications. Experimental tests have been carried out in order to probe the functionality of the proposed architecture; which demonstrate that the combination of an ARM processor system and the reconfigurable logic provide flexibility and high-speed capabilities for motion control.**

Keywords—motion-control;VHDL; FPGA; Zynq-7000

I. INTRODUCTION

The use of reconfigurable logic is not novel in the state of the art of motion control. One of the first works in this filed describes the implementation on an FPGA (field programmable gate array) of a quadrature counter for position control of a servo motor [1]. Another research work deals with the implementation of space vector PWM (pulse width modulation) control for an inverter [2]; the authors also describes a digital mixed architecture composed by a DSP (digital signal controller) and an FPGA.

From nineteenth decade, different approaches in the digital motion control have been surged. Those one which are focused into achieve lower logic consumption with a higher bandwidth [3–6]. And the other hand, those which combine several technologies in order to control plants whose dynamics is no linear or to implement complex control strategies [7–9].

A few years ago, Xilinx which is one of the most popular silicon devices manufacturer, has released a new family [10] of FPGAs which includes a dual core ARM Cortex-A9 processor system into the same chip.

The idea of a motion controller platform based on the ARM processor and an FPGA is not new. For instance, in [11] it is described the implementation of a motion control system using both technologies. However, processor and logic array are independent devices.

In [12], authors present the design and implementation of an underwater robot. The electronic design is based on the all programmable SoC technology. Given that control strategies and the algorithms are implemented by software, authors conclude that this platform reduces considerably the development time. And at the same time that improves flexibility and it provides high degree of modularity.

Another case of study is presented in [13]. In this research work, the implementation of a motor controller on an all programmable SoC device is described. The authors remarks that this new technology permits to implement high complexity algorithm by software while high speed signal processing is implemented on the reconfigurable logic at the same silicon device. Above it is traduced in a lower cost, since such devices replaces a host PC, DSP and standalone FPGA.

This paper describes the architecture design of a platform for rapid implementation of control algorithms for motion control applications and its implementation on an all programmable SoC Zynq-7000 device. The advantage of this platform despite its flexibility is the cost saving and availability of its components. The crossover frequency method is

implemented by software in order to tuning a PD (proportional-derivative) controller and a step-response test validates the functionality of this new architecture.

II. METHODOLOGY

The proposed architecture is thought to control a DC motor

with an incremental encoder as feedback device. It includes the embedded system (Digilent Zybo) and an amplifier in current mode (Texas IC LMD18245) as is illustrated in figure 1.

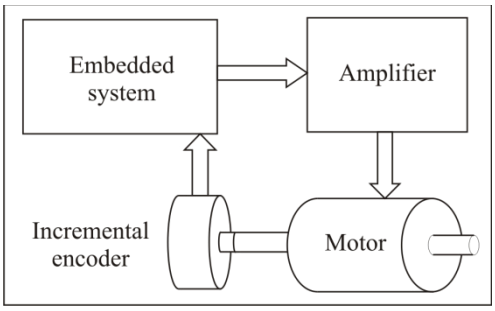

Figure 1. Platform architecture.

As have been mentioned before, the embedded system is composed by two processing units: programmable software and reconfigurable hardware.

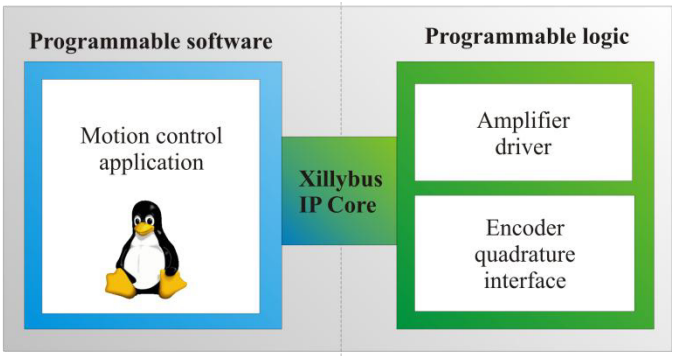

Figure 2. Embedded architecture.

Programmable software is used to implement the identification and control algorithms while the reconfigurable logic is used to describe the peripherals with the incremental encoder and amplifier. Above is illustrated in figure 2.

A. *Programmable logic*

In order to obtain a feedback signal from the incremental encoder, it is necessary to describe a quadrature interface in the programmable logic device.

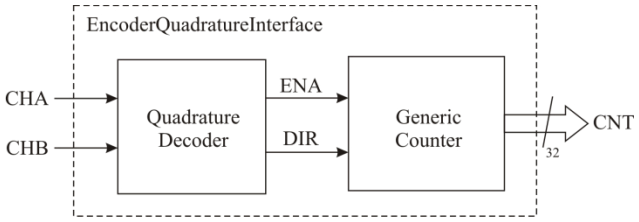

Figure 3. Encoder quadrature interface blocks diagram.

The *EncoderQuadratureInterface* instantiates a *GenericCounter* and a *QuadratureDecoder* modules as is shown in figure 3. The output of this module has 32 bits of width.

On the other hand, the output of the processing system, i.e., the control signal has 8 bits of with and it corresponds to the magnitude and direction of the desired current of the servo motor. The amplifier driver decodes the 2's complement value and separates the magnitude and direction. The magnitude bus has four bits of width while the direction has a single bit.

The interface bridge between the processing system and the programmable logic is the Xillibus IP core. This core has two manners to interchange signals: FIFO and RAM based interfaces.

B. *Programmable software*

The processing system part runs the Ubuntu operating system. The Xillibus bundle package also includes the drivers for input/output operations. Two algorithms are implemented for this research work: crossover frequency tuning method and a PD controller which has the form:

$$u(t) = K_p\left[e(t) + T_d\frac{de(t)}{dt}\right]. \qquad (1)$$

The crossover frequency tuning method lies on the frequency response control theory. It establishes that a causal system exited with a sinusoidal input always responds with another sinusoidal wave of the same frequency, but with different amplitude and phase.
By measuring these values, amplitude and phase, it is possible to determine the gain and phase of the plant for a given frequency.

The design requirements include the crossover frequency ω_c and margin phase θ_m of the system. Frequencies for most of the servo mechanisms are in the range of 50 and 600 [rad/s], while the margin phase is between 30 and 60 degrees, in order to obtain a well damped response [14].

The identification process consists of feed forward the plant H(s) with a sinusoidal wave with the form:

$$u(k) = A\sin(\omega_c kT) \qquad (2)$$

for $k = 0, 1, 2, \ldots t$; where T is the sampling time.

Thus, the system is expected to respond with a signal wave of the form:

$$\theta(k) = B\sin(\omega_c kT + \emptyset_1)\,[counts] \quad (3)$$

From (2) and (3) it is possible to determine the gain and phase of the system as follows:

$$K = \frac{B}{A}, \quad (4)$$

and the phase $\emptyset_1$ is estimated from the differential time Δt between common points of the sinusoidal waves.

$$\emptyset_1 = \omega_c \Delta t\,[rad] \quad (5)$$

Procedure design starts with the computation of the plant gain at the desired crossover frequency. In this case, the plant H(s) is composed by the servo motor and the amplifier, i.e.:

$$K = \|H(j\omega_c)\| = \left\|\frac{k_a k_t}{j\omega_c[(j\omega_c)(J_m) + k_b]}\right\| \quad (6)$$

Where k_a is the gain of the amplifier; k_t, J_m, and k_b are the torque constant, inertia and viscous friction constant of the servo motor.

Analogously, it is required also to compute the phase at the same frequency as follows:

$$\emptyset_1 = \arg[H(j\omega_c)] = -tan^{-1}\left(\frac{k_b\omega_c}{-J_m\omega_c^2}\right)[rad] \quad (7)$$

Given that the controller is implemented in a discrete form, it is necessary to include the phase delay $\emptyset_2$ introduced by the sampling process. This phase delay can be computed as:

$$\emptyset_2 = -\frac{\omega_c T}{2}\,[rad] \quad (8)$$

Once the gain and phase are obtained, it is possible to compute the phase lead $\emptyset_3$ that the controller must introduce to the system in order to satisfy the design condition as follows:

$$\theta_m = \pi + \emptyset_1 + \emptyset_2 + \emptyset_3 \quad (9)$$

Thus, the derivative time constant of the controller is written as:

$$T_d = \frac{\tan\emptyset_3}{\omega_c} \quad (10)$$

With the above result, the gain of the controller may be calculated as follows:

$$K_c = \sqrt[2]{1 + (T_d\omega_c)^2} \quad (11)$$

Finally, the constant K_p is obtained as:

$$K_p = \frac{1}{K_c K} \quad (12)$$

The second algorithm is thought to evaluate the performance of the tuning process. It implements in a discrete form the PD controller, i.e.:

$$u(k) = K_p\left\{e(k) + \frac{T_d}{T}[e(k) - e(k-1)]\right\}, \quad (13)$$

$$k = 0,1,2\ldots$$

The entire tuning and evaluation process can be summarized in the following steps:

1. Feed the system with a sinusoidal waveform and sampling the response.
2. Compute gain and phase from the obtained response.
3. Tuning the controller.
4. Evaluate the performance.

III. EXPERIMENTAL SETUP

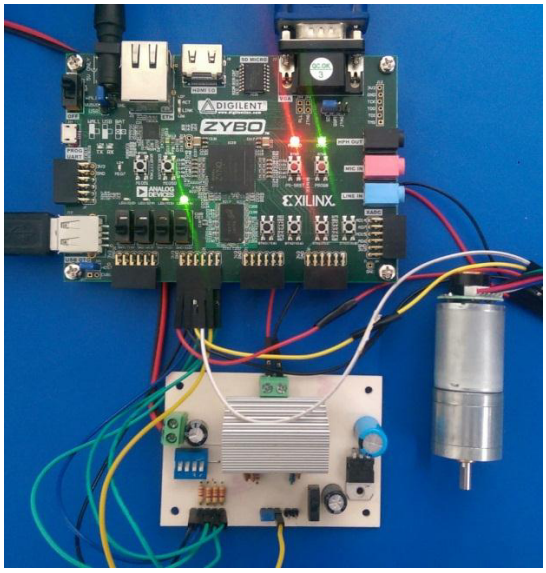

Figure 4. Experimental setup.

As it is mentioned in above paragraphs, the system is composed by an embedded system for programmable software and reconfigurable logic, the amplifier is the *LMD18245* by *Texas Instruments* and the *Pololu* servo motor 25Dx56L which has an incremental encoder of 480 pulses per revolution. Above is shown in figure 4.

IV. RESULTS

ω_c	K	$\emptyset_1$	$\emptyset_3$	K_p	T_d
50	4.160	-172.066	38.499	0.188	0.016
60	3.008	-176.953	43.672	0.240	0.016
70	2.222	-180.299	47.305	0.305	0.015
80	1.626	-186.463	53.755	0.364	0.017
90	1.346	-188.217	55.795	0.418	0.016
100	1.072	-190.329	58.194	0.492	0.016
110	0.906	-192.678	60.829	0.538	0.016
120	0.793	-194.142	62.580	0.581	0.016
130	0.693	-196.930	65.654	0.595	0.017

Identify applicable sponsor/s here. If no sponsors, delete this text box (*sponsors*).

140	0.557	-197.983	66.994	0.702	0.017
150	0.518	-200.779	70.076	0.658	0.018
160	0.437	-202.400	71.984	0.708	0.019
170	0.405	-204.726	74.596	0.656	0.021
180	0.388	-204.274	74.431	0.692	0.020
190	0.331	-208.834	79.277	0.562	0.028
200	0.295	-209.539	80.268	0.574	0.029
210	0.293	-211.656	82.672	0.435	0.037
220	0.261	-212.666	83.968	0.403	0.043

Table 1. Identification and tuning results.

Primary results are related with the identification process. Table 1 enlists the results of the identification and tuning processes. The servo motor has been tuned at frequencies in the range of 50 and 220 rad/s. For all tuning test, the margin phase $\theta_m$is set to 45°. The frequencies greater than 220 rad/s cannot be tuned properly since the phase compensation requires more than 90°.

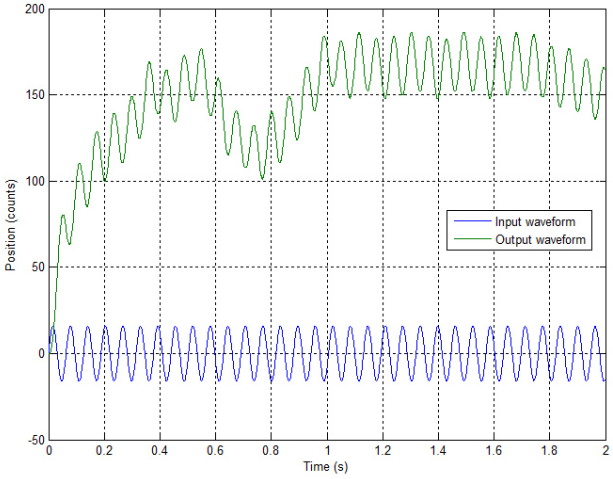

Figure 5. Input and output waveforms obtained in the identification procedure at $\omega_c = 100$ rad/s and $\theta_m = 45°$.

Figure 5 illustrates the waveforms generated and obtained in the identification process. The blue one corresponds to plant input while the green one to the motor output.

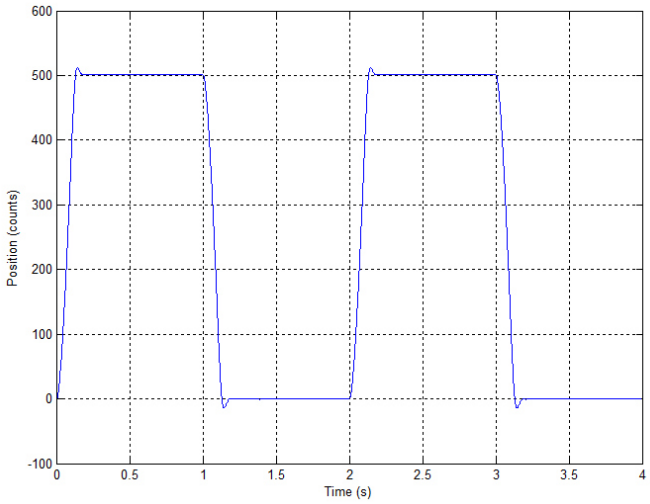

Figure 6. Step response of the controller tuned at $\omega_c = 100$ rad/s and $\theta_m = 45°$.

The next step in the experimentation corresponds to the evaluation of the performance controller. This test consists of a series of step changes in the set-point. The control period $T = 0.001s$ and the maximum step change of 500 encoder counts as it is illustrated in figure 6.

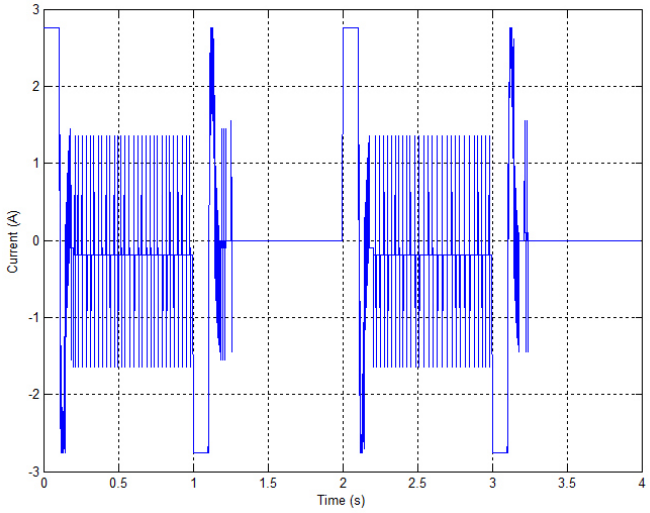

Figure 7. Controller output of the step test.

Figure 7 illustrates the output of the controller. From this figure it is possible to observe that the output has been saturated since the amplifier can drive up to 3A of maximum current. It is important to note that the controller output is very noisy; however, this can be considered quite normal since the derivative part of the controller has been computed just as a simple differentiation between two samples of the error.

V. CONCLUSIONS

It has been demonstrated in an experimental manner that the combination of an dual core of ARM-Cortex9 processor is fast

enough to achieve a sampling period of 1 kHz for identification and position control of a servo motor.

The flexibility of the system permits the implementation of several control strategies and also reduces the development time considerably. Above since the complexity of the control algorithm is implemented by software while the critical timing tasks are implemented by hardware.

It is also remarkable that the cost of this platform is quite lower than other alternatives based on the combination of DSP and FPGA. Authors conclude that the trend of the digital control is oriented to the usage of this new technology.

REFERENCES

[1] A. K. Oudjida, Y. I. EI-Haffaf, S. Tagzout, I. Hamani, B. Bouzouia, and K. Kara, "A reconfigurable counter controller for digital motion control applications," *Microelectron. J.*, vol. 28, no. 6–7, pp. 683–690, Aug. 1997.

[2] Y.-Y. Tzou and H.-J. Hsu, "FPGA realization of space-vector PWM control IC for three-phase PWM inverters," *IEEE Trans. Power Electron.*, vol. 12, no. 6, pp. 953–963, Nov. 1997.

[3] R. A. Osornio-Rios, R. de J. Romero-Troncoso, G. Herrera-Ruiz, and R. Castañeda-Miranda, "The application of reconfigurable logic to high speed CNC milling machines controllers," *Control Eng. Pract.*, vol. 16, no. 6, pp. 674–684, Jun. 2008.

[4] Y. S. Kung, R. F. Fung, and T. Y. Tai, "Realization of a Motion Control IC for Table Based on Novel FPGA Technology," *IEEE Trans. Ind. Electron.*, vol. 56, no. 1, pp. 43–53, Jan. 2009.

[5] J. U. Cho, Q. N. Le, and J. W. Jeon, "An FPGA-Based Multiple-Axis Motion Control Chip," *IEEE Trans. Ind. Electron.*, vol. 56, no. 3, pp. 856–870, Mar. 2009.

[6] M. Martinez-Prado, A. Franco-Gasca, G. Herrera-Ruiz, and O. Soto-Dorantes, "Multi-axis motion controller for robotic applications implemented on an FPGA," *Int. J. Adv. Manuf. Technol.*, vol. 67, no. 9–12, pp. 2367–2376, Dec. 2012.

[7] X. Shao and D. Sun, "Development of a New Robot Controller Architecture with FPGA-Based IC Design for Improved High-Speed Performance," *IEEE Trans. Ind. Inform.*, vol. 3, no. 4, pp. 312–321, Nov. 2007.

[8] S. Jung and S. s Kim, "Hardware Implementation of a Real-Time Neural Network Controller With a DSP and an FPGA for Nonlinear Systems," *IEEE Trans. Ind. Electron.*, vol. 54, no. 1, pp. 265–271, Feb. 2007.

[9] J. B. Huang, Z. W. Xie, H. Liu, K. Sun, Y. C. Liu, and Z. N. Jiang, "DSP/FPGA-based Controller Architecture for Flexible Joint Robot with Enhanced Impedance Performance," *J. Intell. Robot. Syst.*, vol. 53, no. 3, pp. 247–261, May 2008.

[10] "A generation ahead for smarter systems: 9 reasons why the Xilinx Zynf-700 all programmable SoC platform is the smartest solution," *Xilinx*, 2014. [Online]. Available: http://www.xilinx.com/publications/prod_mktg/zynq-7000-generation-ahead-backgrounder.pdf.

[11] L. L. W. X. C. Weihai, "Implementation of Robot Motion Controller Based on ARM and FPGA [J]," *Comput. Meas. Control*, vol. 9, no. 1, p. 20, 2007.

[12] S. Pan, S. Guo, L. Shi, Y. He, Z. Wang, and Q. Huang, "A spherical robot based on all programmable SoC and 3-D printing," in *2014 IEEE International Conference on Mechatronics and Automation (ICMA)*, 2014, pp. 150–155.

[13] H. Yun, Y. P. Lee, Y. S. Moon, and Y. Bae, "Implementation of motor controller using Zynq EPP," in *15th International Symposium on Soft Computing and Intelligent Systems (SCIS), 2014 Joint 7th International Conference on and Advanced Intelligent Systems (ISIS)*, 2014, pp. 1224–1228.

[14] J. Tal, *Motion Control by Microprocessors*, Galil MC., vol. 1. 1984.

"ALGORITHMS FOR SPATIAL DISTRIBUTION OF FIBERS AND ITS INFLUENCE ON THE MECHANICAL BEHAVIOR OF CONCRETE MATRIX COMPOSITES"

Ing. Maria Edith Vázquez Arvizu.
Facultad de Ingeniería.
Universidad Autónoma de Querétaro.
Querétaro, Qro.

Dr. Jaime Moises Horta Rangel.
Facultad de Ingeniería.
Universidad Autónoma de Querétaro.
Querétaro, Qro.

Abstract— **This paper presents a review of the methods and algorithms used to generate a matrix composite reinforced concrete and fibers, which can be made of steel, polymers or natural fibers. Proper mixing or distribution of fibers substantially affects the mechanical behavior of the composite. At present such compounds based fibers are used in floor slabs, walls, and to a lesser extent in floor systems. The outline of a proposed numerical-computational process that allows spatial generation of fibers based on APDL programming codes running on the Ansys program and is based on the spatial distribution of volumetric finite elements generated by Ansys is also shown in pre-processing phase. This procedure will be useful to propose a comprehensive solution to the stress-strain behavior of the composite.**

Keywords—composite materials, random fiber distribution, computer modeling, mechanical behavior.

I. INTRODUCTION.

The reinforced concrete structures are very effective for building because of its versatility and almost no maintenance, making it undoubtedly the most widely used building material today. Concrete has the ability to not only be reinforced with steel rods if the use of polymer fibers that help to 6% increase in compression strength, its toughness, the flexural strength and impact resistance ACI Code 544 [1].

Undoubtedly the concrete has become one of the great alternatives for infrastructure development worldwide, this is designed to withstand external loads caused by stress and strain with different characteristics, linked to the type of building design. These designs are based on rules and regulations of construction that has proved adequate for most structures. However when the reinforcement for concrete not only conventional steel rod and an additional reinforcement is used, such as fibers, necessary to consider its contribution.

There are different sources that we have designs for reinforced concrete structures with polymer fibers. In these addiction fiber it has a direct impact on the cracking process, since a significant increase is obtained in the voltage compression structure

The addition of short fibers randomly distributed throughout a cement matrix can significantly improve the fracture properties of these compounds fiber reinforced cement (FRCC). For moderate percentages of fiber used in many commercial mixtures (0.5-2% by volume), the uniaxial tensile and compressive strengths are increased only a relatively small amount, but the overall hardness, adsorption energy and crack width control features that can be dramatically improved by the introduction of these fibers [2].

In the study of concrete - fiber composite, must be a particular study in the random distribution of the fibers within the matrix specific fibers, since this distribution depends on the behavior of our element therefore is to propose a new analytical model spatial prediction of fibers that allows to study the behavior of an element and its future implementation.

II. TESTING OF COMPOSITE FIBER CONCRETE.

A. Material and concrete mixes used.

Aggregates used meet Mexican Standard NMX-C-486ONNCCE-2014, Construction Industry Mortar structurally – Masonry - use specifications and test methods, which defines the following [3]:

- Aggregates (sand): These are materials stone nature which may come from mines, banks extraction, crushing of concrete elements or as a result of an industrial process which, when mixed with hardening, allow preparation of mortars.
- Hydraulic cement. Hydraulic binder produced by pulverizing clinker and calcium sulfate in some forms.

- Mortar. Material formed by mixing one or more cementing, sand, water and optionally additives or additions finely pulverized (limestone, clay, pozzolan, granulated blast furnace slag, fly ash) has the ability to set both in the air as in water and form a hardened mass which acquires strength with time to a peak [3].

B. Mixture proportions.

The dosage will be held from the Complementary Technical Norms of the Federal District, for bikers in structural elements with a proportioning 1 cement: sand 2.5, as shown in Table 1.

Regarding the percentage of fibers to be used it is determined from the weight of the cement-sand aggregates. Polyethylene fibers were used with a length of 25 mm and 1mm thick on average [4].

TABLE I. PROPORTIONING BY VOLUME RECOMMENDED FOR MORTAR STRUCTYRAL ELEMENTS.

Proporcionamientos.					
Type of mortar.	***Parts of hydraulic cement .***	***Parts bricklaying cement.***	***Parts of hydrated lime.***	***Parts sand.***	***Nominal compressive strength f , Mpa (kg/cm2)***
I	1	---	0 a 1/4	Less than 2.25 and not more than 3 times the amount by volume of cementations.	12.5 (125)
	1	0 a 1/2	---		
II	1	---	1/4 a 1/2		7.5 (75)
	1	1/2 a 1	---		
III	1	---	1/2 a 1 1/4		4.0 (40)

[1] The volume of sand will be measured in loose condition.

The mixture is held in a conventional concrete mixer with capacity of 90 liters. Sand and water absorption homogenizers first, then the cement and water mixed reaction for a few minutes will be added. The water content is determined by fluidity test.

C. Specimens.

The specimens were prepared under Rule C1018 - 97 Standard Test Method for Flexural Toughness and First-Crack Strength of Fiber- Reinforced Concrete (using Beam With Third - Point Loading) [5].

Where established using a simple beam thickness of 1 inch or less. The test sample should have a ratio of largest span length depending on the thickness of the sample, between 16 to 1 and 30 to 1.

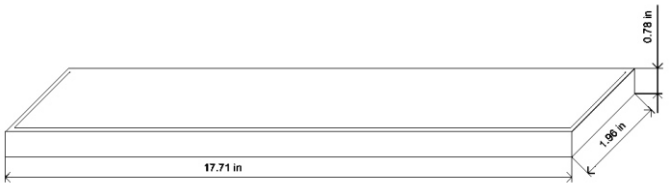

The total length of the sample shall be a minimum of 1 inch (25mm) longer than the size of the specimen. The nominal width of the sample is 2 inches (50mm) as shown in “Fig.1"

Fig. 1. Dimensions of the beam relative to the ASTM C 1018-97

D. Test specimens of mortar.

Once cast and forged beams, the pure bending resistance of concrete is determined as stable Standard C78-00 Flexural Strength of Concrete (Using Simple Beam With Third- Point Loading) using a testing machine, the procedure specimens consists of turning on one side with respect to the molding position. It focuses on the support blocks; these in turn must be centered with respect to the applied force. The load applying block is brought into contact with the specimen surface third-point between the supports. It must have full contact between the load application and the supporting blocks with the specimen surface. It must be sanded surfaces of the specimen or leather straps used if separation line contact between them and the blocks is greater than 0.039 inches. It is recommended that sanding the side surfaces of the specimens is minimal, because you can change the physical characteristics of the same and therefore affect the results. Also, you should use leather straps only when the surfaces of the specimens in contact with blocks of load application, deviate from a plane by no more than 0.196 inches [3].

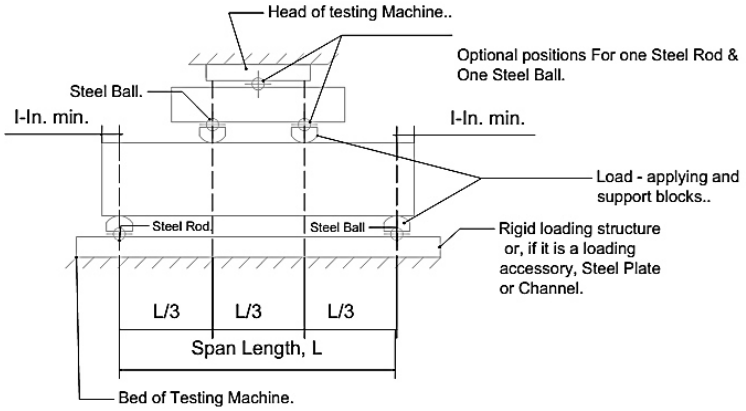

Fig. 2. Testing machine according to ASTM C 78-00

The load application should be applied at a uniform rate such that the increased effort extreme fiber does not exceed 980 kPa / min (10 kgf / cm2 per min), allowing higher speeds before 50% of the estimated load rupture. The "Fig." 2. Shows a schematic view of a testing machine for testing flexural beams [6].

III. SPECIFIC ANALYTICAL METHODS FIBER

Since the nineties, we have studied the application of different fibers in concrete, even the American Concrete Institute (ACI) has created standards for synthetic or natural and some researchers have created a series of models fibers, in order to predict the behavior of composite concrete fibers among them are:

A. Model Imam.

This model predicts the ultimate shear strength of beams of fiber-reinforced concrete without stirrups, is based on the form by Bazant and Sun (1), (2), (3) and separates the contribution of the concrete abutments and fibers in three terms [7].

$$V_u = 0.6\varphi^3\sqrt{w}\left[\sqrt{f_{cm}} + 275\frac{\sqrt{w}}{\left(\frac{a}{d}\right)^5}\right]bd \quad (1)$$

$$\varphi = 1 + \left[\frac{\left(\frac{5.08}{d_a}\right)^{1/2}}{\left(\frac{1+d}{25d_a}\right)^{1/2}}\right] \quad (2)$$

$$w = \omega = \rho(1+4F) \quad (3)$$

$$\boldsymbol{\rho = \frac{A_s}{bd}} \quad (4)$$

Finally, the contribution of the stirrups is calculated by the following formula (5) in addition to (1):

$$V_w = \left(\frac{A_{sw}}{s}\right)0.9df_{ywm} \quad (5)$$

Where: [a] = Clear shear (mm), [b] = beam width (mm), [d] = effective depth of the beam (mm) [da] = maximum size of coarse aggregate (mm), [d_f] = coefficient of efficiency. (1 for fiber hook and 0.5 for straight fibers) [f_{cm}] = compressive strength of fiber-reinforced concrete. (N / mm2), [f_{ymw}]= Effort in stirrups (mm2), [s] = Distance between the brackets (mm), [A_s] = longitudinal reinforcement area (mm2) [A_{sw}] = Area of the stirrups (mm2), [D_f] = diameter of the fiber (mm) [F] = Factor of the contribution of the fibers, [L_f] = fiber length (mm) [V_f] = volume fraction of fibers, [V_w] = shear strength provided by the stirrups (kN) [Vu] = last a theoretical shear strength (kN) [ρ] = ratio of longitudinal stress [ɯ] = ratio of longitudinal effort and the effort of the fibers, [φ] = Factor of effect size .

B. Model de C. Octavio, D. Diaz-da- Costa .

Raises two equations (6) and (7) which bypasses the weight of the fiber and calculates the external forces, according to a vector containing additional degrees of freedom due to a discontinuity in the given element, also proposes degrees of freedom they act as a transmission medium opening discontinuity regular finite element nodes [2].

$$df^e = \int_{\Omega^e/\Gamma_d^e} N_w^{eT}\bar{b}^e d\Omega^e + \int_{\Gamma_t^e} N^{eT}\bar{t}^e d\Gamma^e \quad (6)$$

$$df_w^e = \int_{\Omega^e/\Gamma_d^e} N_w^{eT}\bar{b}^e d\Omega^e + \int_{\Gamma_t^e} N_w^{eT}\bar{t}^e d\Gamma^e \quad (7)$$

Where: [Γ_d] = Discontinuity surface, [(.)^e] = Belonging to the element, [f_w] = Vector force at the regular nodes, [Ω] = body, [Nw] = enhanced shape function matrix, [T] = discontinuity constitutive matrix, [$\bar{b}$] =body forces vector, [$\bar{t}$] =natural force vector.

C. Voronoi.

It describes a general approach to modeling short fiber reinforced cement-fiber composites, using crystals Boronoi, wherein each fiber is modeled as a discrete entity, allowing direct contacts between the micromechanical fiber - matrix and performance material compound. The method is computationally efficient, since no additional degrees of freedom are required for modeling the fibers

In this method the matrix material is divided into a set of convex polygons having random geometry “Fig. 3". Voronoi constructions are used here. Each polygon is considered as a rigid particle having two degrees of freedom : translation and rotation defined at the centroid of the particles, the particles are interconnected along their edges by flexible interfaces, or sets equivalent springs, whose stiffness are determined for approximating the elastic properties of the overall series continues .

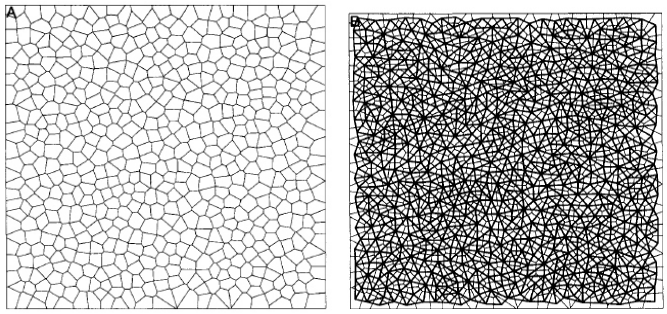

Fig. 3 Representation discrete element matrix material: (a) Voronoi polygon mesh; (B) dual lattice representation geometry - Random beam elements [8].

The system discrete element is actually a random lattice network geometry beam elements. That is, each set of two particles acts as a kind of beam element connecting the centroids of particles [9].

D. Horta Rangel.

They present a mathematical model is based on an analysis deformation of particular fiber composite (8) in a quasi-dynamic analysis, which requires an iterative loading-unloading procedure for determining the end performance of the material [10].

$$\left(\int [B]^T[D][B]dv\right) = \int_V [N]^T\{b\}dv + \{P\} \quad (8)$$

where [B] = matrix of shape function derivatives, [D] = matrix of elastic constants, [N] = shape function matrix,

[U] = displacement vector, [b] = vector of body forces, [P] = vector of punctual external loads. The first integral involves the energy deformation of the composite under loads [2].

E. Jean – LouisTaihan, Pierre Rossi, Dominic Daviau-Desnoyer.

His numerical model is based on three physical evidences:

- Concrete is a heterogeneous material in which the heterogeneities can be modelled through a random spatial distribution of mechanical properties considered as dominant in the cracking process, namely the Young's modulus and the tensile strength.
- Scale effects of concrete cracking (experimentally proved) are taken into account by the fact that the mechanical properties of the material depend on the size of the mesh elements chosen for the finite element analysis.
- Cracking is explicitly treated through the creation of random kinematic discontinuities, which provides access to quantitative information on the cracking state (number of cracks, opening and spacing). Numerically speaking, these cracks are represented by interface elements.

The criterion for the crack creation is very simple: the interface element opens when the normal tensile stress at the center of the interface element reaches a critical value (probabilized through a Weibull distribution function. This means that the rigidity of the interface element becomes equal to zero (perfect brittle behavior). As mentioned above, the value of this critical value depends on the total volume of the two volumetric elements interfaced by the considered interface element [11]. The criterion of crack creation is schematically presented in Fig. 4.

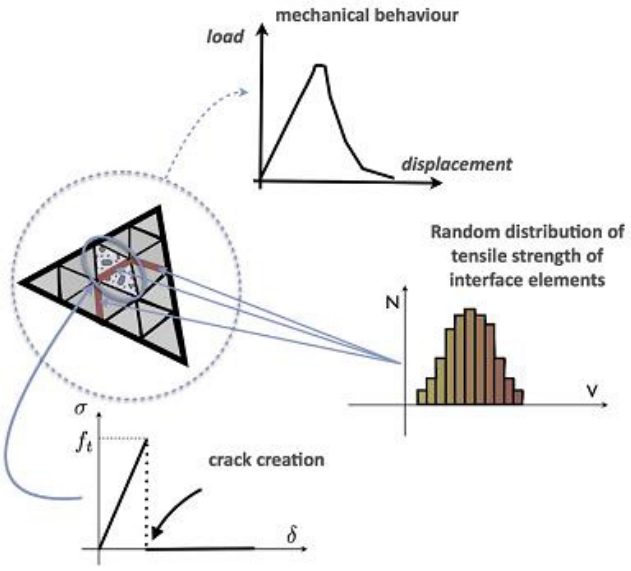

Fig. 4 Criterion of crack creation in the matrix (discrete probabilistic cracking).

IV. METHODOLOGY.

As mentioned different studies have been developed on the composite fiber - concrete, some of these studies are based on the identification of failure mechanisms that identify fractures and evolution while other procedures are based on micromechanical models. Forces the fiber-matrix interface is of great importance for the understanding of the behavior of all of the compound [10].

Taken into account the above references, it is proposed a new analytical procedure for the spatial location (Random) of fibers in a composite material, posing a volumetric model based on finite element tetrahedral type for the matrix body being studied.

Also a mesh is developed throughout the body to study using finite element tetrahedral types, taking as limit its volume with support from ANSYS program, taking very careful in thickness, and to consider a minimum of three fibers in each element thus the number of nodes and generated element is obtained

Based on the resulting discrete conformation analysis algorithm is developed, this is intended to generate the fibrous structure of the compound reticular. For mesh generation cylindrical coordinate system is placed in one of the nodes randomly and considering the fiber length, the following coordinate system is placed, obtaining two points, thereby generating the fibrous matrix. This is repeated again and again randomly selecting nodes from 1 to the total number of nodes that were generated, with support from ANSYS. At the end the actual percentage of fibers that has been generated within the element, which must not be very physically distant from the proposed initially for the composite fiber-concrete is calculated.

Finally the element created in the spatial distribution (random) fiber is analyzed. Once the element with the required percentage of fibers created another subroutine is performed in the ANSYS program analyzing the particular compound - fibers under bending loads, with the data the initial charge, last and the intervals at which the load increases are applied, enabling review efforts and displacements of the compound. The actual percentage of fibers that has been generated within the element, which must not be very far from the beginning proposed to be calculated

V. POSSIBLE OUTCOMES AND CONTRIBUTIONS.

The results obtained by the spatial convolution algorithm fiber, were employed for the analysis of structural elements reinforced polymeric fibers, allowing and builders, have a method of mechanical prediction, the model relates to the performance of the composite allow simulating the behavior of the structure, through the finite element solution for predicting stress-strain behavior of the compound.

ACKNOELEDGMENT.

To The Universidad Autonoma de Querétaro and CONACYT for their valuable guidance and support in the development of this project.

REFERENCES.

[1] J.- Juárez, «Comportamiento analítico-experimental a cortante en vigas de concreto fibroreforzado.,» *Concreto y Cemento Investigacion y desarrollo. ,* pp. 74-79, Enero-Junio 2015.

[2] C. Octavio, «Modelling the behaviour of steel fibre reinforced concrete using a discrete strong discontinuity approach.,» Journal of Material Science, Portugal, 2015.

[3] A. Instituto Mexicano del Cemento y Concreto, «NMX-C-486ONNCCE-2014,» Sección Coleccionable, Número 94, México, Df., Junio 2015.

[4] «NORMAS TÉCNICAS COMPLEMENTARIAS PARA DISEÑO Y CONSTRUCCIÓN DE ESTRUCTURAS DE MAPOSTERIA.,» *gASETA OFICIAL DEL DISTRITO FEDERAL,* p. 12, 6 OCTUBRE 2004.

[5] ASTM, «Standard Test Method for Standard Test Method for Fiber-Reinforced Concrete (Using Beam With Third-Point Loading),» *ASTM C 1018-97,* vol. 04.02, pp. 1-8, 1998.

[6] ASTM, «Standard Test Method for Flexural Strength of Concrete (Using Simple Beam with Third-Point Loading),» *ASTM C 78-00,* vol. 04.02, p. 2, 2001.

[7] B. Fariborz Majdzadeh, «Shear strength of reinforced concrete beams with a fiber concrete matrix..,» Canadian Jornal of Civil Engineering., 2006.

[8] J. B. Jr., «Fracture analyses using spring networks,» Department of Civil and Environmental Engineering, University of California, Davis, California, USA, 1997.

[9] J. B. J. a. S. Saiotot., «Discrete Modeling of Short-Fiber Reinforcement in Cementitious Composites,» *Journal,* pp. 77-85, 1997.

[10] Horta-RangelJ., «3D Computer Modeling of the catastrophic collapse of Fiber Reinforced Concrete structures,» Journal of Material Science, Querétaro,qro., 2015.

[11] D. Jean-Louis Tailhan, «Probabilistic numerical modelling of craking in steel concretes (SFRC) structures.,» journal, Montréal, Québec, Canada, 22014.

An Innovative Embedded Photoacoustic System for Nanofluids Biomedical Applications

Method based on thermal parameters of nanoscale temperature rises.

Luis D. Luna-Hernandez
Electronics and Telecommunications Engineering,
Hidalgo State Autonomous University
Cd. Universitaria, Carretera Pachuca-Tulancingo Km. 4.5,
Col. Mineral de la Reforma, CP 42076, Hidalgo,
México.e-mail: mustaine36@gmail.com

Alejandro Castañeda-Miranda
Engineering Cold technology, Apan School,
Hidalgo State Autonomous University
Calle Ejido De Chimalpa Tlalayote S/N, Col. Chimalpa,
Apan Hidalgo, C.P. 43920, México.
e-mail: alejandro_castaneda@uaeh.edu.mx

José A. Pescador-Rojas
Engineering Cold technology, Apan School,
Hidalgo State Autonomous University
Calle Ejido De Chimalpa Tlalayote S/N, Col. Chimalpa,
Apan Hidalgo, C.P. 43920, México.
e-mail: josealfredo_pescador@uaeh.edu.mx

Victor M. Castaño-Meneses
Applied Physics and Advanced Technology Center,
Mexico National Autonomous University
Boulevard Juriquilla 3001 Santiago de Querétaro
Querétaro, 76230, México.
e-mail: meneses@unam.mx

***Abstract*— In this work, an experimental tool implementation of an embedded system based develops to investigate thermal-based Photoacoustic (PA) generation as a mean of absorbing particles with nanoscale temperature rises on Photothermal (PHT) generation in Nano biomedical applications. The experimental technique consists of a medium-power laser, which develops switches by an electro-optical modulator (EOM), subsequently incident on the sample, the radiation is collected and focused focused into a microphone. In the process to detect the weak signal collected by the microphone needs to be processed to extract the useful electrical signals from the noise. The lock-in amplifier technique is one of the important methods to extract weak signal submerged in noise, which is widely used in the infrared spectra measurement field, thereby obtaining the amplitude and phase of the modulated signal, data are collected in a database by an embedded system (SE), as a means of transmission using serial communication. The data is analyzed to determine sample parameters in Ag nanoparticles (NP) of 10 to 30 nm on diameter average were obtained by chemical reduction of $AgNO_3$, the solution containing 0.025 µm silver nitrate in 250 mL of deionized water was heated to 100 C and stirred mechanically. A citrate solution of 1, 0.5, 0.25, 0.125 and 0.062 % in water was added. In addition, experimental results new applications for the analysis of sample treatment in the frequency domain are reported quantitatively studying both thermal and electronic properties biomedical nanomaterials with nanoscale temperature rises by applying modulation frequencies up to 1 GHz. We have studied Nanofluids (NF) for the purpose of establishing its electronic thermal uniformity.**

Keywords*— *Photoacoustic; Thermal expansion coefficient; Nanofluids; Nanoparticles; Silver nitrate; Nanoscale rises.

I. INTRODUCTION

Infrared radiation was discovered by William Herschel in 1781. The infrared spectrum region includes radiation with wave number comprised between 12800 and 10 cm^{-1} corresponding to wavelengths of 0.78 to 1000 µm (microns), divided into three called near-infrared regions, middle and far East. The vast majority of analytical applications have been restricted to the use of mid-infrared part comprised finds 4000 and 400 cm-1 (2.5 to 25 mm), now associating thermal changes as infrared radiation from a body, where the body heat as thermal energy absorbed or released during a temperature change is defined. Moreover, Alexander Graham Bell (1880) reported the first PA effect writing, two thin discs in many substances emitted sounds when exposed to the action of a quick interruption of sunlight. The sound production from samples results of the solar energy absorption in the infrared part of the spectrum. The PA effect is based on the generation of acoustic waves due to light absorption. The infrared absorption of a photon excites a molecule in a high vibrational state. Collisions transform vibration energy to translational energy, i.e. heat. Modulating the intensity of light causes the sample temperature is increased and periodically decays. For a gas in a closed volume this temperature variation is accompanied by a variation in pressure, which creates a sound wave that can be detected with a microphone. The PA techniques have grown in importance for the thermal characterization of semiconductor [1], metal materials [2], and organic [3] among others most recent application is in biomedical [4]. The PA has taken the lead of PHT techniques mainly because of its non-destructive nature, remote, non-contact, and allows the analysis of samples online besides its low cost due to the use of a microphone as sensor, these instruments are those which were developed for various applications, including in the natural gas industry [5], airborne hygrometry [6], source apportionment of urban light-absorbing aerosols [7], measurements of gas permeability [8], and clinical research [9]. The data acquisition and control system (DACS) has a fundamental role in a PA system. It drives the laser: tunes and stabilizes its wavelength and modulates its emitted light

[10] which requires knowledge of the ranges and modes of operation of electronic devices used in the embedded system as they are the lock-in and the using a microphone.

II. PHYSICS RFI FUNDAMENTALS

Thermal properties materials are when an absorbent body is made incident monochromatic radiation or modulated polychromatic, a change also modulated the surface temperature, as a result of the absorption of radiation and nonradioactive energy conversion occurs. The energy emitted by the body, can be observed through the emission of black body radiation from the surface and bulk (Planck radiation). Measuring variations of black body emission is possible to obtain information on the absorption spectrum, physical properties (thermal and electronic) among others. The physical basis of the detection by this technique is the law of black body radiation, which describes the total radiated emission, W, over an infinite bandwidth of a body in thermal equilibrium at a temperature T is defined by Eq. 1.

$$W = \varepsilon\sigma T^4 \ [W/cm^2] \quad (1)$$

From Eq. 1 where σ is the Stefan-Boltzmann constant (5.67 $x10^{12}$ W/cm^2K^4) and ε is the emissivity of the body. If the PHT process induces temperature changes in the material surface, ΔT(w) and this change is very small compared to the equilibrium temperature, the emittance changing, can be written and defined by Eq. 2.

$$\Delta W = 4\ \varepsilon\sigma T^4\ \Delta T(w) \quad (2)$$

From the point of view optical material is characterized by optical opacity, which is determined by the relationship between the optical absorption length $\mu_\beta = 1/a_j$ and the material thickness l. So according to the optical opacity, the solids can be divided into two groups, the first case is when optically transparent, when all the intensity of light reaching the surface thereof a small part is absorbed throughout the thickness of the specimen, but most is transported. This is expressed mathematically as μs>l. The second case is when it is optically opaque, when the intensity of light reaching the solid surface is attenuated completely long before passing through the sample.

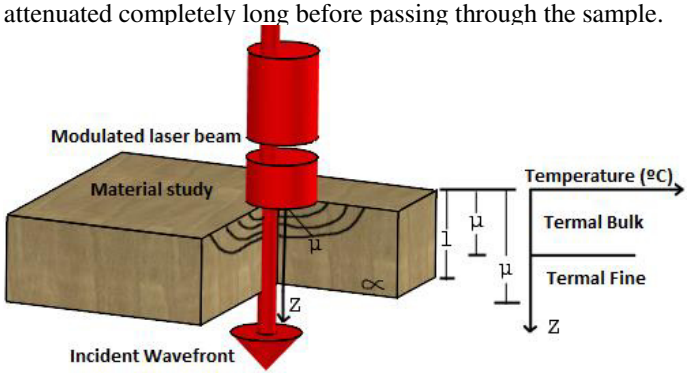

Fig. 1. Illustration thermally thick and thermally thin behavior.

It is written μs>>l. Furthermore, since the thermally solid it can be classified according to the relationship between the magnitude of the thermal diffusion length, defined as μ_s and thickness of the sample is according to Eq. 3.

$$\mu_s = \sqrt{\frac{\alpha}{\pi f}} \quad (3)$$

Thin thermally, such materials are considered to thermal diffusion length μ_s is greater than the thickness of the sample μ_s>l, as shown in Fig. 1. The thermally thick materials are characterized in that the thermal wave is attenuated within the sample μ_s<l. In this paper we consider only material thermally thick and optically opaque. For PA in recent years, extensive development both in theory and methodology PA techniques has allowed in a non-destructive developments in research methodologies solids [11] and biological materials [12]. The same group also built the first image using a spatial distribution of signal to room temperature and a wavelength using numerical methods to calibrate measurements instrument [13] but the image is not that of the components defined was ruling signal due to the absence a theory that would lead to determination of weighting functions. After the comparison of their images with the profile of dislocation density, they concluded that the radiometric signal was generated by non-radioactive and was sensitive to even low densities. Sweeps in frequency, were subsequently used for material analysis as an alternative to purely thermal techniques that had been used for some time for analyzing homogeneity nanoscale temperature [14] and thermal parameters in implanted, including damage surface [15]. Heretofore, the black body emission was associated mainly to photonic des excited states, only the thermal contribution of the network. One of the most important contributions to the understanding of the PHT phenomena was supplied using laser modulation [16] which showed that carriers generated optimally increase the emission of infrared from the surface of a body. The primary mechanism for generation of PA signal in heat conduction is generated in the sample gas into the cell. This mechanism was considered to present a model of PA signal generation, called thermal diffusion.

UNITS FOR PA PHOTOTHERMAL PARAMETERS

Parameter	*Denomination*	*Units*
K_j	Material thermal conductivity j	W/nm-K
ρ_j	Material density j	gr/nm^3
c_j	Material specific heat j	W/g-K
α_j	Material thermal diffusivity j	nm^2/seg
a_j	Material thermal diffusion coefficient j	nm^{-1}
$\mu_j = 1/a_j$	Material thermal diffusion length j	nm
σ_j	Complex thermal diffusion coefficient j	nm
l_s	Sample thickness	nm
l_b	Support thickness	nm
l_g	Gas column thickness	nm
β	Optical absorption coefficient	nm^{-1}
μ_β	Optical absorption length	nm

Another mechanism PA signal generation, the thermal expansion of the sample, that is, heating to suffer radiation absorption, the sample was periodically expands, itself functioning as a vibrating piston which gives rise to an acoustic wave in the gas. This mechanism was taken into

account for the first time to propose a model composite piston, which considered the existence of two vibratory Pistons, one formed by the adjacent gas chamber, as in the model Rosencwaing and Gersho and another formed by the surface of the sample. The mechanism of thermal expansion may be dominant at high modulation frequencies and samples of low optical absorption coefficient and depends on the average temperature of the sample. The third mechanism for generating PA signal is thermoelastic bending. This mechanism occurs when the modulated radiation absorption creates a temperature gradient in the sample perpendicular to the surface. Due to the temperature gradient, the expansion of the sample is dependent on the depth, resulting in a bending of the sample. This periodic bending causes the surface of the sample produces an acoustic signal. The latest generation mechanism PA signal is Photobarium effect, which can occur in Photochemically active samples with gas exchange between the sample and the PA gas cell. The properties of materials under the diffusion mechanism are shown in Tab. I, where the notation for describing and PA modeling signal is shown. The magneto-photo-acoustic imaging in vivo implementation [17] by contrast-enhanced.

III. THEORETICAL MODEL PA PHOTOTHERMAL

The theory of the PA cell involves open microphone cross section as shown in Fig. 2, in which the electret foil having a charge density, dielectric constant σ_0 with thickness l_m and separate metal support an air thickness s_1, there is also a voltage V due to resistive load R it is generating an electric field E, that the applied air is called E_0 where ε_R= 1,00051≈1 and ε_0=8.8541878176x10-12 F/m are used for the permittivity.

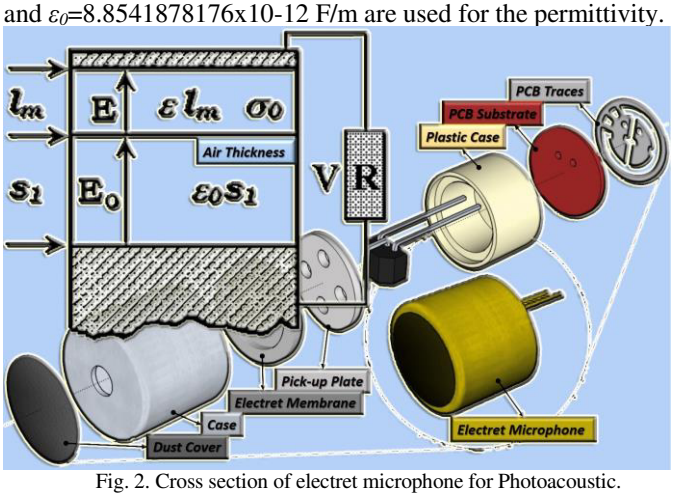

Fig. 2. Cross section of electret microphone for Photoacoustic.

If a wave hits periodically changing electrical fields and charges indicated in the dielectric plates, applying Gauss theorem at the interface of the electret and the air chamber and between the bladder and support, using Eq. 4 and Eq. 5 have.

$$\varepsilon_o E_0 = \sigma_i \tag{4}$$

$$\varepsilon \cdot \mathrm{E} - \varepsilon_o E_0 = \sigma_0 \tag{5}$$

The induced surface charge density is we can relate it to V by Ohm's Law (V = IR). Now we can write Eq. 6.

$$V = RA\frac{d\sigma_i}{dt} = RA\varepsilon\frac{d\mathrm{E}_o}{dt} \tag{6}$$

Where A represents the area of the support. Now try to find E of Fig. 1 are f (x) and F (x) electrical potentials in the electret (0 <x <lm) and the air chamber [lm <x < (lm + s1)] as a pair of capacitors connected in parallel. The fields in these regions are constant and potential are lines, the potential differences between the metal plate that covers the electret and the metal bracket can be written as Eq. (7).

$$V = -(\mathrm{E}_o s_1 + El_m) \tag{7}$$

As the mathematical behavior described Eq. 7, E can be written as Eq. (8).

$$\mathrm{E}_o = \frac{\varepsilon V + l_m\sigma_o}{l_m s_o + s_1\varepsilon} \tag{8}$$

Differentiating the equation Eq. 8 with respect to time (rate) and using the result in Eq. 6 get differential equations for V which are defined as Eq. 9 and Eq. 10.

$$RC\frac{dV}{dt} + \left(1 - \frac{RC\varepsilon}{l_m\varepsilon_o + s_1\varepsilon}\frac{ds_1}{dt}\right)V = RC\frac{l_m\sigma_o}{l_m\varepsilon_o + s_1\varepsilon}\frac{ds_1}{dt} \tag{9}$$

$$C = \frac{A\varepsilon\varepsilon_o}{l_m\varepsilon_o + s_1\varepsilon} \tag{10}$$

Where C is the capacitance microphone. Due to the diaphragm reflection by the sound we can write s1 as Eq. 11 and Eq. 12.

$$s_1 = l_b + \eta e^{j\omega t} \tag{11}$$

$$\frac{ds_1}{dt} = j\varpi\eta e^{j\varpi t} \tag{12}$$

Where $\eta e^{j\omega t}$ reflection diagram is caused by $\delta P e^{j\omega t}$ pressure. Substituting Eq. 12 in Eq. 9, the Eq. 13 is obtained.

$$RC\frac{dV}{dt} + \left(1 - \frac{j\varpi\eta RC\varepsilon}{(l_m\varepsilon_o + s_1\varepsilon)}e^{j\varpi t}\right) \tag{13}$$

If we assume that $\eta << l_b$, Eq. 9 is reduced Eq. 14.

$$\frac{dV}{dt} + \frac{V}{RC} = j\varpi\eta\left(\frac{l_m\sigma_o}{l_m\varepsilon_o + l_b\varepsilon}\right) \tag{14}$$

The solution to the differential equation represented by Eq.14 is Eq. 15.

$$V = \frac{l_m\sigma_o}{l_b\varepsilon + l_m\varepsilon_o}\frac{j\varpi\eta RC}{1 + j\varpi RC}e^{j\varpi t} \tag{15}$$

From Eq. 15, is the output voltage of the microphone when the diaphragm is subjected to harmonic fluctuations. We can identify this equation equivalent electret microphone circuit is an RC circuit in parallel with a power proportional to the rate of change of current reflection microphone. The displacement of the membrane can solve an equation of motion for a circular membrane extended, under tension T. This is the model (Kettel-Drum model) for electret microphone. The movement of the membrane compresses and expands the air from the chamber located behind the diaphragm and it reacts in the opposite direction to the movement of the membrane by changing its natural frequency and general behavior. If the wave velocity is considerably less than the speed of sound in the air, then the compression and expansion of air in the chamber is roughly the same over the entire membrane and

depends on the average displacement of this. Considering the reaction force, also as the drag force due to the sound pressure, the equation of motion of sound is written as Eq. 16.

$$M\frac{\partial^2\eta}{\partial t^2}=T\nabla^2\eta+\delta Pe^{j\varpi t}-\frac{P_gV_g}{l_b}\bar{\eta} \tag{16}$$

Where M is the mass per unit area of the membrane, P_gV_g is the density of air (sound velocity). The temperature fluctuation in the system displays gas-chamber-membrane is obtained from the solution of the diffusion equations in the same system. Assuming that a frequency modulated monochromatic radiation ω=2πf and given intensity normally incident on the sample $I_0e^{j\omega t}$, obtaining an optical absorption coefficient β and nonradioactive relaxation time in the incident wavelength τ, now you can write the set of diffusion equations system is ultimately defined by Eq. 17.

$$V_{opc}=V_o\frac{j\varpi RC}{1+j\varpi RC}\frac{\Theta_m+\Theta_s}{T_o}e^{j\varpi t} \tag{17}$$

The expression for the amplitude of the PA signal is complex but can be simplified for specific cases. These cases can be grouped according to the thermal and optical opacity of the sample. In all approaches assume that gas is thermally thick, a fairly reasonable approximation when considering gas lengths of 1 mm and a modulation frequency higher than 10 Hz. Given that a sample can behave to certain types of radiation and transparent or opaque. A sample may be characterized according to their optical and thermal properties, thus being transparent or opaque to incident radiation. The parameters described in the expression of Eq. 17 are shown in Eq.18, Eq.19 and Eq. 20.

$$V_o=\frac{l_bl_m\sigma_o}{\left(l_b\varepsilon+l_m\varepsilon_0\right)} \tag{18}$$

$$\Theta_s=\frac{I_or\left[\cosh(l_g\sigma_g)-1\right]\left\{2r-e^{-\beta l_s}\left[(r+1)e^{l_s\sigma_s}+(r-1)e^{l_s\sigma_s}\right]\right\}}{(1+j\varpi t)l_g\sigma_gk_s\sigma_s(r^2-1)\sinh(l_g\sigma_g)\left[e^{l_s\sigma_s}-e^{-l_s\sigma_s}\right]} \tag{19}$$

$$\Theta_m=\frac{\beta' I_oe^{-\beta l_s}\cosh(l_m\sigma_m)\left[\cosh(l_g\sigma_g)-1\right]}{l_g\sigma_gk_m\sigma_m\sinh(l_m\sigma_m)\sinh(l_g\sigma_g)} \tag{20}$$

IV. EXPERIMENTAL ASSEMBLY AND METHOD

This device consists of a radiation source can be monochromatic, optoacoustic modulator a PA cell and a system to record both the amplitude and phase. This experimental arrangement allows an embedded system record both the amplitude and the phase of the PA signal as a function of the modulation frequency. In the system monochromatic radiation of a laser is used, an EOM allows us to modulate signals from 0.1 Hz. To 1MHz, this is performed stably unlike a mechanical modulator (chopper) which is noisy at low and high frequencies, the acoustic-optic modulator the signal to noise ratio decreases. The beam expander and collimating lens give the possibility of obtaining a beam collimator lens and give the possibility of a Gaussian beam that would allow us to work with the theory of Rosencgwaig Gersho. Detecting the PA signal it is performed with the PA cell is designed from a sensitive microphone electrode. The signal detected by the microphone is analyzed in a lock-in amplifier tuned to the modulation frequency of the incident radiation. Modulator acquisition and data logging amplitude and phase of the signal. Finally, the data were analyzed by adjustment programs. Some classification of PA based on different system attributes whit nanoscale temperature raises is shown in Fig. 3.

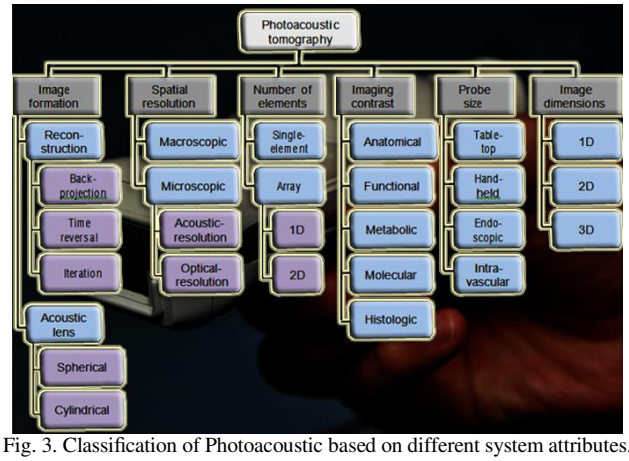

Fig. 3. Classification of Photoacoustic based on different system attributes.

This experimental setup used to calculate the time constant of the microphone, a sample of high thermal diffusivity is used. To sign thermally thin PA signal behaves in Eq. 21.

$$PA=\frac{C}{\sqrt{1+(2\pi.f\tau)^2}}\cdot\frac{1}{\sqrt{f_c}} \tag{21}$$

Where PA signal can be known that in experimental, f is frequency and τ is the time constant required to obtain the experimental data set. The regime PA signal decreases as f. The sample used to calibrate the experiment must be thermally thin, the signal must behave as thermally fine for frequencies below the cutoff frequency is f_0.

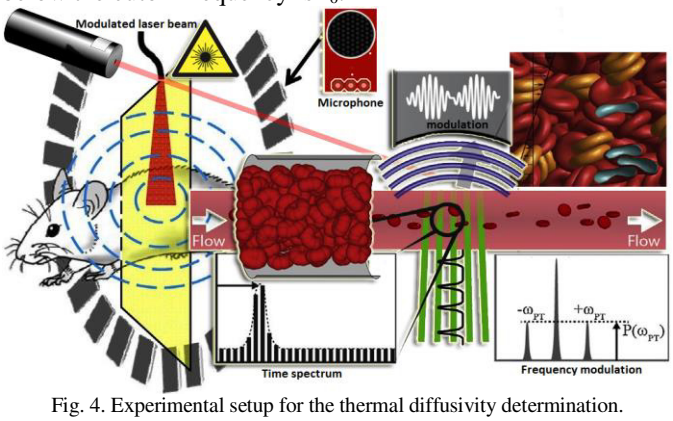

Fig. 4. Experimental setup for the thermal diffusivity determination.

In Fig. 4 the basic experimental setup is shown for thermal diffusivity measurements where the frequency of the laser pulses or time spectrum are essential to determine the modulation frequency to be determined by an absorption spectrum thermal parameters measured on the sample.

V. RESULTS

A solution containing 0.025 µm silver nitrate in 250 mL of deionized water was heated to 100 C and stirred mechanically. A citrate solution of 1, 0.5, 0.25, 0.125 and 0.062 % in water was added, typically Turkevich and Frens methods. At the first 5 minutes the colour of the solution slowly turned into greyish

yellow. Boiling then continued for 90 minutes. The Ag NP of 10 to 30 nm on diameter average were obtained by chemical reduction of $AgNO_3$. In this study as two-step process, ultrasonic agitation was used to improve dispersion in highly concentrated NF, exists the problem that the NP flocculate, since NP form agglomerates easily. Measurements were made in silver NP, with different average diameters, dispersed in water to obtain their thermal diffusivity values; each sample was stirred for 10 minutes before being placed in the quartz cell and proceeds to the measurement of thermal diffusivity. Compared with the reported value of thermal diffusivity for deionized water (α= 1.4 x 10−3 $cm^2 \cdot s^{-1}$) it is possible to see an increment. Thermal diffusivity of silver NF is increased nonlinearly up to 14% as the size of particles decreased from 30 to 10 nm, all diffusivity measurements were performed at room temperature. Samples containing noble metal NP exhibit higher thermal diffusivities than water without particles.

TABLE I. EXPERIMENTAL DATA, OBTAINED FROM PA

Average size (nm)	*α (10^{-3} $cm^2.s^{-1}$)*	*α Increment (%)*
35	***1.43 ± 0.22***	***2.1***
30	***1.53 ± 0.34***	***9.3***
25	***1.57 ± 0.35***	***12.1***
20	***1.58 ± 0.22***	***12.9***
35	***1.60 ± 0.24***	***14.3***
30	***1.62 ± 0.23***	***15.7***

For particle sizes of 30, 25, 20, 15, and 10 nm increases correspond to 9.3, 12.1, 12.9, 14.3, and 15.7% respectively. Tab. II summarizes the thermal diffusivity values obtained from the fitting of equation 21. Since the technique uses a very small volume fraction of the total sample volume, we consider our results valid, its use for determination of thermo-optical properties of nanoparticles-liquid matrix.

VI. CONCLUSIONS

Through this work, it was established that the results encourage the idea that there is a significant effect of Brownian motion (hydrodynamic) NP in the liquid and which shows the result of thermal diffusivity. Despite the controversy regarding the effect of Brownian motion in the thermal conductivity in NF, there are studies determining effect on heat conduction and theoretical work related to the study of NF and improved response to heat transport, in which Brownian motion is noted as one of the most outstanding. We believe that this process is fundamental to explain the results observed in our study. Our experimental results agree with the theoretical explanation in which it is considered that the determining factor for thermally characterize the NF is related to Brownian speed and showed results about the theoretical explanation that the determining factor for thermally characterize the NF, related to Brownian speed, as fundamental process responsible on the results.

ACKNOWLEDGMENT

The authors wish to thank Rene Preza-Cortés, Carmen Vázquez and Adrián Oskam for their technical support. The financial support of SEP in 2015 (SEP-23-005 F-PROMEP-38 Develop a Platform Computerized Axial Tomography using Radiometry Photothermal Infrared), is also, gratefully acknowledged.

REFERENCES

[1] M. Pawlak, and M. Malinski, "Noncontact measurement of the thermal diffusivity of IR semi-transparent and semiconducting n-CdMgSe mixed crystals by means of the photothermal radiometry", Infrared Physics & Technology, vol. 64, pp. 87–90, 2014.

[2] B. Arnala, C. Pereza, C. Weia, J. Xiaa, M. Lombardo, I. Pelivanov, T.J. Matula, L.D. Pozzo, and M. O'Donnell,, "Sono-photoacoustic imaging of gold nanoemulsions: Part I. Exposure thresholds", Photoacoustics, vol. 3(1), pp. 26–34, 2015.

[3] B. Arnala, C. Pereza, C. Weia, J. Xiaa, M. Lombardo, I. Pelivanov, T.J. Matula, L.D. Pozzo, and M. O'Donnell, "Sono-photoacoustic imaging of gold nanoemulsions: Part II. Real time imaging", Photoacoustics, vol. 3(1), pp. 26–34, 2015.

[4] M.Srivalleesha, K. Seungsoo, K. Andrei, P.J. Pratixa, S. Konstantin, and E. Stanislav, "Visualization of molecular composition and functionality of cancer cells using nanoparticle-augmented ultrasound-guided photoacoustics", Photoacoustics, vol. 3(1), pp. 26–34, 2015.

[5] V. Hanyecz, A. Mohácsi, S. Puskas, A. Vago, and G. Szabo, "Instrument for benzene and toluene emission measurements of glycol regenerators", Meas. Sci. Technol., vol. 24 (11), pp. 115901, 2013.

[6] D. Tatrai, Z. Bozoki, H. Smit, C. Rolf, N. Spelten, M. Krämer, A. Filges, C. Gerbig, G. Gulyas, and G. Szabo, "Dual channel photoacoustic hygrometer for airborn measurements: background, calibration, laboratory and in-flight inter-comparison tests", Atmos. Meas. Tech., vol. 8, pp. 33-42, 2015.

[7] N. Utry, T. Ajtai, A. Filep, M. Pinter, Z.s. Torok, Z. Bozoki, and G. Szabo, "Correlations between absorption Angström exponent (AAE) of wintertime ambient urban aerosol and its physical and chemical properties", Atmos. Environ., vol. 91, pp. 52–59, 2014.

[8] Z. Filus, N. Toth, G. Gulyas, T. Guba, G. Szabo, and Z. Bozoki, "Carrier gas flow arrangement based photoacoustic detection method for measuring gas permeability of polymer membranes", Polym.Test., vol. 32 (6), pp. 1099–1104, 2013.

[9] E. Tuboly, A. Szabo, G. Eros, A. Mohacsi, G. Szabo, R. Tengolics, G. Rakhely, and M. Boros, "Determination of endogenous methane formation by photoacoustic spectroscopy", J. Breath Res., vol. 7, pp. 046004, 2013.

[10] D. Tatrai, Z. Bozoki, G. Gulyas, and G. Szabo, "Embedded system based data acquisition and control system for photoacoustic spectroscopic applications", Measurement, vol. 63, pp. 259–268, 2015.

[11] M. Chen, Y. He, J. Zhu, and R. Kim, "Enhancement of photo-thermal conversion using gold nanofluids with different particle sizes", Energy Conversion and Management, vol. 112, pp. 21–30, 2016.

[12] I. Sorrell, R.J. Shipley, V. Hearnden, H.E. Colley, M.H. Thornhill, C. Murdoch, and S.D. Webb, "Combined mathematical modelling and experimentation to predict polymersome uptake by oral cancer cells", Nanomedicine: Nanotechnology, Biology, and Medicine, vol. 10, pp. 339–348, 2014.

[13] K. Andrzej, M. Jiri, B. Jean, and D. Rostislav, "Using pulsed and modulated photothermal radiometry to measure the thermal conductivity of thin films" , Thermochimica Acta, vol. 556, pp. 1–5, 2013.

[14] O. Simandoux, A. Prost, J. Gateau, and E. Bossy, "Influence of nanoscale temperature rises on photoacoustic generation: Discrimination between optical absorbers based on thermal nonlinearity at high frequency" , Photoacoustics, vol. 3(1), pp. 20–25, 2015.

[15] Z. Zhang, B. Tsai, and G. Machin, Radiometric Temperature Measurements, I. Fundamentals. USA: Academic Press, ISBN: 978-0-12-374021-2, 2009.

[16] Z.M. Zhang, B.K. Tsai, and G. Machin, Radiometric Temperature Measurements, II. Applications. USA: Academic Press, ISBN: 978-0-12-374021-2, 2009.

[17] M. Qu, M. Mehrmohammadi, R. Truby, I. Graf, K. Homan, and S. Emelianov, "Contrast-enhanced magneto-photo-acoustic imaging in vivo using dual-contrast nanoparticles" , Photoacoustics, vol. 2, pp. 55–62, 2014.

Classification and recognition system for leaf species using morphological and shape hallmarks

Vargas-Vazquez D., Vázquez Cruz M. A.
Facultad de Ingeniería
Universidad Autonoma de Queretaro
Queretaro, Mexico
damianvv@uaq.mx

Luna-Rubio R
Departamento de Mecatronica
Universidad Tecnologica de Corregidora
Corregidora, Queretaro, Mexico
ricardo.luna.rubio@gmail.com

Abstract— **Currently there are several computer programs to identify plants or flora species, but this type of software depends on human responses to be able to carry out the classification; on the other hand, there are computer tools to evaluate morphological characteristics of foliage elements, as well as commercial equipment that provides approximate measurements of leaf area. However, there are few non-commercial tools that provide complete information about the various parameters of the leaves (leaf area, length, width, perimeter, circularity, etc.). This work presents a method based on artificial neural networks and image processing in order to classify different leaves species considering the shape and parameters of the leaves, as an economical alternative to the market products.**

Keywords— Segmentation, leaf shape, neural networks, morphological characteristics.

I. INTRODUCTION

The achievement of a rational criterion for vegetable classification has been an important concern in history of botanics. It was during XVIII century that the rules for nomenclature were definitely established by the Swedish Carl Von Linneo. Any of the classification methods has the success of the sexual method by Linneo, due to the binary nomenclature, precision, clarity of the descriptions without any distinction of species, varieties, and the gathering of all the known between each genera [1].

Nowadays informatics programs available are based in the utilization of dicotomic clues in order to identify species of plants and flowers, which depend upon human answers to perform identification and classification. Some systems applying such tools are: Delta [2], and ActKey [3]. Some others offer alternatives as search by means of taxonomic ubiquity and diagnostic characters, along with an image gallery, scientific names, etc., as Hebestigma.

However there are informatic tools to evaluate morphological characters from leaves automatically, as well as commercial equipment offering measures form leaf area. Leaf area refers to the amount of surface of each leaf, which is a parameter widely used in crop ecophysiology [4]. Daughtry [5] described different direct methods to obtain the leaf area. In [6], an informatic tool was designed (LAMINA) in order to produce classic traits of shape in the leaves and area, which are normally required for correlation analysis among productivity and biomass. In [7], a method to estimate leaf area was reported by means of digital analysis using a scanner and software freely available. Also, a new methodology to obtain additional measurement parameters of the leaves was developed in [8].

Neural networks have an important field of application among the computational tools. One of the most applied techniques in order to train a neural network is the backpropagation method (BPM), based on an algorithm which is supervised by the programmer. This method requires a group of training patterns, and the respective outputs, and they are adjusted automatically by the connection weights between neurons. The correction of the weights is made by a set of rules selected by the training and, in consequence, a correlation between inputs and outputs is obtained.

The goal of this investigation was to develop a method based on artificial neural networks and image processing in order to classify different leaves species. This becomes a complex problem for computational systems because it implies to distinguish between edges, surfaces, colors, shapes, etc. In order to improve the classification, the leaf shape was choose due to the characteristic contour. This was made by means of considering the distance from the centroid as starting point.

II. MATERIALS AND METHODS

For image acquisition a conventional scanner was employed. Once the picture is taken this is cut at the size of the leaf (in order to avoid a long processing time). Image is acquired in BMP format to be managed in C++. In the first stage a total of 13 leaf species were analyzed. Some samples of these species are shown in Figure 1. A total of 50 samples from each leaf species were used. More samples were obtained from a free dataset called FLAVIA (http://flavia.sourceforge.net/), which contains 32 types of plants (52-70 images of each one).

Segmentation is an important step in image processing and analysis; it simplifies the image by splitting the image in parts remarking the regions of interest to simplify the process of identification and analysis.

Fig. 1. Samples of leaf species.

Most of the algorithms for segmentation are based in two properties: discontinuity and and similitude [9]. For image segmentation a discriminant analysis was used [10], where Otsu defines the variance among classes of an image and it allows the selection of an optimum range automatically, once the image is processed and segmented, a filter was applied in order to reduce the noise in the image [11].

A. Selection of methods and evaluation

There are several ways to solve this problem, based on mathematical models such as invariant moments of Hu [12], these represent important data which are invariant to the size and leaf rotation. In this way similar values were obtained for same species and distinctive in comparison with other species which are obtained from the next equations:

$$\phi_1 = \eta_{20} + \eta_{02} \tag{1}$$

$$\phi_2 = (\eta_{20} + \eta_{02})^2 + 4\eta^2_{11} \tag{2}$$

$$\phi_3 = (\eta_{30} - 3\eta_{12})^2 + (3\eta_{21} - \eta_{03})^2 \tag{3}$$

$$\phi_4 = (\eta_{30} + \eta_{12})^2 + (\eta_{21} + \eta_{03})^2 \tag{4}$$

$$\begin{aligned}\phi_5 = {} & (\eta_{30} - 3\eta_{12})(\eta_{30} + \eta_{12})\left[(\eta_{30} + \eta_{12})^2 - 3(\eta_{21} + \eta_{03})^2\right] \\ & + (3\eta_{21} - \eta_{03})(\eta_{21} + \eta_{03})\left[3(\eta_{30} + \eta_{12})^2 - (\eta_{21} + \eta_{03}))^2\right]\end{aligned} \tag{5}$$

$$\begin{aligned}\phi_6 = {} & (\eta_{20} - \eta_{02})\left[(\eta_{03} + \eta_{12})^2 - (\eta_{21} + \eta_{03})^2\right] \\ & + 4\eta_{11}(\eta_{30} + \eta_{12})(\eta_{21} + \eta_{03})\end{aligned} \tag{6}$$

$$\begin{aligned}\phi_7 = {} & (3\eta_{21} - \eta_{03})(\eta_{30} + \eta_{12})\left[(\eta_{30} + \eta_{12})^2 - 3(\eta_{21} - \eta_{03})^2\right] \\ & + (3\eta_{12} - \eta_{30})(\eta_{21} + \eta_{03})\left[3(\eta_{30} + \eta_{12})^2 - (\eta_{21} + \eta_{03})^2\right]\end{aligned} \tag{7}$$

Central normalized momentum is represented by n_{pq} and defined as:

$$\eta_{pq} = \frac{\mu_{pq}}{\mu^{\gamma}{}_{00}} \tag{8}$$

Where:

$$\bar{\gamma} = \frac{p+q}{2} + 1 \tag{9}$$

And the momentum of order (p+q) of a digital image f(x,y) of size M x N is defined by:

$$\mu_{pq} = \sum_{x=0}^{M-1}\sum_{y=0}^{N-1}(x - \bar{x})^p (y - \bar{y})^q f(x, y) \tag{10}$$

However, such momentums are insufficient in order to correct classification; therefore this work was also based in data acquisition of different parameters which can give additional information of leaf species such as: eccentricity, rectangularity, and length/width ratio.

Each one of these proposed parameters gives a helpful data, as the leaf excentricity, a parameter that determines the grade of deviation of a conical section (ellipse) respect to a circumference. It is important to mention that most of the leaves, or the common ones, tend to exhibit an oval shape. In the database, there are four species with oval shape, and two species closer to a rounded shape. Thus, more tools are required to distinguish among them. Due to the latter, the parameter rectangularity has been integrated to the analysis in order to give a match between a rectangle and the rectangle formed by the leaf. On the other hand, eight of the species tend to an oval shape and their rectangularity may fit in a similar range, in this case the ration among length and width will also be measured. Each one of these parameters will produce significant information in order to be closer to the correct classification of each species. However, is not possible to discard that certain percentage of the cases these values are close related between them, in such case in first instance it is necessary to check what relations are correct and in what way they can be used.

All the aforementioned values, factors and estimated ratios, by themselves do not have any sense, that is the reason why an Artificial Neural Network is proposed (fig. 2), due to its similitude with the human brain, it processes important amounts of information in seconds [13][14][15]. The ANN is proposed as a method which allows that such values can be related among them in order to give a sense for them.

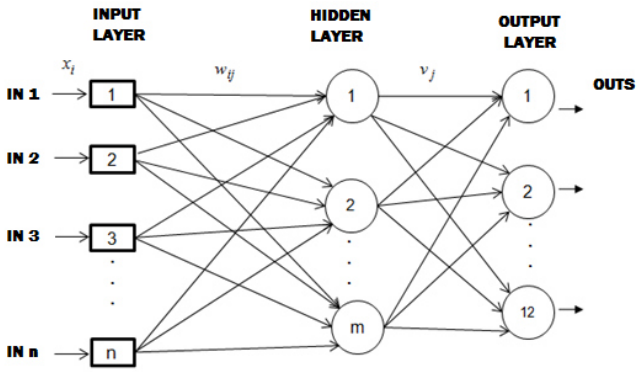

Fig. 2. Neural Network used for classification process.

B. *Signature acquisition*

The limit or edge (Ω) of any surface or object consists of a finite number (N) of an ordered sequence of λ points which define the shape of the surface or object [16].

$$\Omega = \{\lambda_i = (x_i, y_i), i = 0,..., N-1\} \tag{11}$$

The next suppositions are considered:

- Ω is closed, λ_0 is followed by λ_{n-1}
- Ω has only one width point
- Ω has no internal holes

A signature is a characteristic vector which reflects the probability of occurrence for a characteristic in a surface. In general, if *S* indicates a sign of size *N* and S_i indicates de *i-th* component of *S*, then

$$\sum_{i=0}^{M-1} S_i = 1 \tag{12}$$

where $0 \le S_i \le 1$ and $0 \le i \le M$.

The distance function (d_{ij}) between two points, λ_i and λ_j , on Ω is defined by

$$d_{ij} = d(\lambda_i, \lambda_j) = \sqrt{(x_j - x_i)^2 + (y_j - y_i)^2} \tag{13}$$

A signature is a 1D representation of a contour or edge of an image. The basic idea is to reduce the representation of a 1D function which allows the description of the original in 2D.

One way to estimate the signature is considering as reference the center of mass of the image. A binary image *g(i,j)*, allows to obtain the centroid by means of the momentum equation of first order, and the coordinates of the centroid are

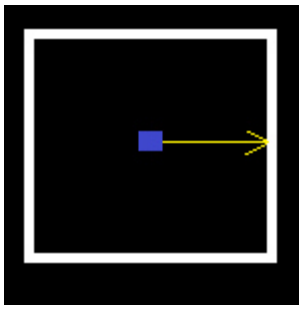

Fig. 3. Searching of the first point of the edge.

obtained (*xc* and *yc*) for the signature calculation, considering all the points in the image edge.

Now considering the centroid as reference point, equation [13] becomes this way:

$$d_{ij} = d(\lambda_i, \lambda_j) = \sqrt{(x_c - x_i)^2 + (y_c - y_j)^2} \tag{14}$$

In order to begin the search of the first point, it was considered the centroid and followed horizontally the image until the first point of the edge was found and so on the search of the next points continued (fig. 3).

Once all the distances between points are obtained, the maximum distance inside the distance vector was looked, and from this point on is where the beginning of the vector was considered (signature).

III. Results and Discussion

A. *Classification based on momentum*

For this first stage, different characteristic data were obtained based on the geometrical moments. Table 1 shows an example with geometrical moments and characteristics of some leaves of apricot specie.

Analyzing these data with the implemented tools it is possible to obtain a way to classify such species, when image is opened the software provides important data of the leaf being analyzed, such as width, leaf area, length, perimeter, and elongation factor (fig. 4).

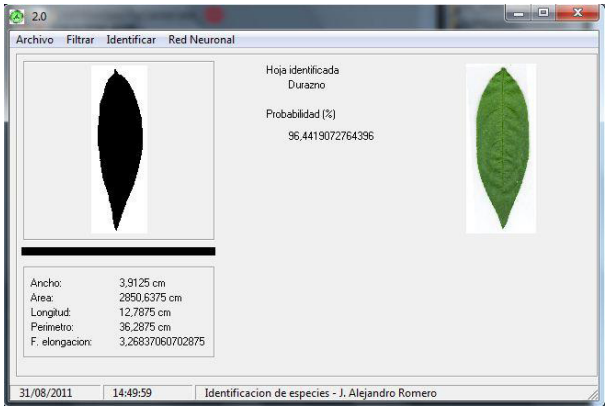

Fig. 4. Leaf classified as "Apricot" (Durazno_H1_011).

TABLE I. CORRESPONDING DATA TO APRICOT LEAVES

M2	M3	M4	Excentric.	Rectangul.	Elongat. Factor
0.592257	0.015093	0.007345	0.592257	0.395690	3.014888
0.528889	0.029417	0.015569	0.528889	0.371904	2.487323
0.689978	0.039872	0.021439	0.689978	0.340054	3.268370
0.612651	0.025605	0.011472	0.612651	0.371830	3.012383
0.686731	0.024031	0.013876	0.686731	0.357187	3.342948
0.684403	0.023121	0.012479	0.684403	0.355923	3.283439
0.681064	0.012028	0.006583	0.681064	0.340864	3.175718
0.609401	0.026957	0.014142	0.609401	0.378360	3.012500
0.587477	0.011725	0.005565	0.587477	0.400000	0.285555
0.517560	0.008335	0.003146	0.517560	0.431070	2.518731

B. *Classification based on signatures*

The applied methods in previous stage allowed to distinguish and classified some species, but in some cases the algorithm was not able to recognize the differences among them, still in such cases leaves had a distinctive form. Therefore, it was proposed to add an additional method based on the specific shape of the leaf among species (fig. 5) [17] [18]. Thus, this could allowed to distinguish between species. As a proposal for a descriptor shape signatures were applied [19] (Gonzalez and Woods, 2008). Such signatures represent or associate a shape with a unidimensional function derived from the edge points.

On figure 6 some examples of signatures for a leaf type are shown.

For this stage it was considered the longer distance as the beginning of the signature, taking into account the centroid as a reference point in order to all begin in the same point. However, it was observed that not always the longer distance matches the same point for all the images even when it was the same type of leaf. Therefore, it was necessary that such type of signature was considered as another sample during the net training.

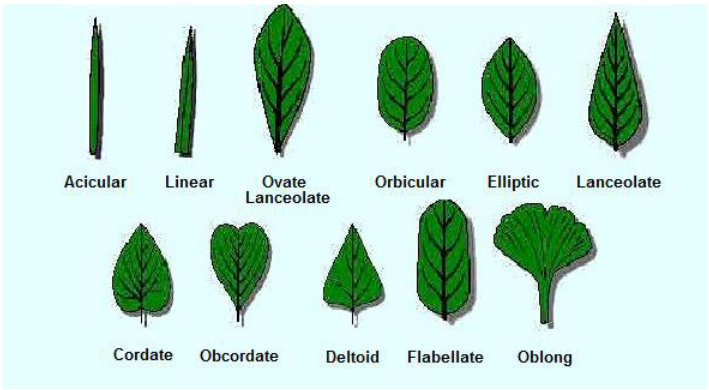

Fig. 5. Examples of typical leaf shape.

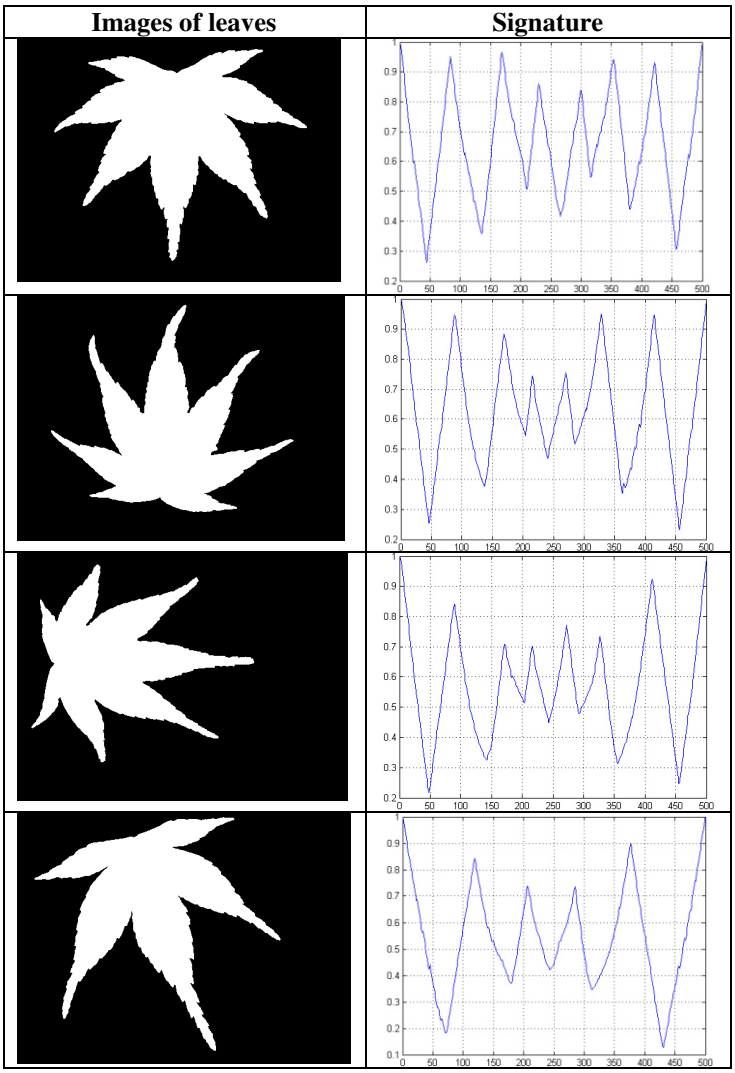

Fig. 6. Examples of signatures obtained from different viewpoint of a leaf type.

C. *Classification of leaves based on their signature*

There is a type of leaf classification based on the type of shape. For this task twelve classes were selected as it is shown in table 2. For this classification method a neural network with 12 outputs was employed (using retropropagation method). These outputs represent the types or classes of leaves according to the shape. For the net training 30 signatures were employed for each type of leaf, thus, a total of 360 signature vectors were considered, and the rest of images were used as trial vectors.

From a total of 1374 images of leaves of 12 selected categories, 189 presented authentication errors, this offers a percentage of classification of 86.2445%, being the linear species which obtained the best results with a percentage of 95.4839% (155 samples, only 7 of them had problems), as opposed to the lanceolate species who presented a percentage of 72.4638% (207 samples, with 57 errors).

TABLE II. LEAF CLASSIFICATION APPLIED IN THIS WORK

1. Linear
2. Lanceolate
3. Cordate
4. Palmately lobed
5. Orbicular
6. Obovate lanceolate
7. Elliptic oblong
8. Ovate lanceolate
9. Acicular
10. Deltoid
11. Flabellated
12. Lobed

During this work it was not found an alternative method to compare the selected parameters; in future analyses the amount of distinctive characteristics for leaves will be increased in order to tune the process and improve the classification percentage.

IV. CONCLUSIONS

The methods and techniques for image processing were implemented in order to develop a program to evaluate and classify leaf species, based on an algorithm, which could process images in grey scale obtained under controlled illumination conditions with a scanner; in this way, it is obtained data for parameters such as eccentricity, circularity, rectangularity, perimeter and length ratio, length and width ratio, and perimeter-length ration in addition with width.

Using the distinctive parameters characteristic for leaves, an observation of the interval variation in results was performed in order to obtain confident data and in combination during different processes show significant information for each species and build a complete data base. Due to variations among characteristics between species an ANN was trained with all species using the weights of the net in order to look for a unique and representative value. The weights were used in a single ANN for all species, 13 species were considered for trials and applications.

Classification according to leaf shape was performed considering the edge signature as main characteristic to classify using an ANN obtaining 86.24% of classification precision. This percentage can be increased if the number of classes is reduced (classes with similar shape characteristics).

ACKNOWLEDGMENT

This research project has been supported by the “Fondo para el fortalecimiento de la investigación” UAQ 2014 (FIN 201412) and by the scholarship “Solicitud de Apoyo a la Incorporación de Nuevos PTC” (F-PROMEP-38/Rev-03).

REFERENCES

[1] A. Arber, Herbals. Their origin and evolution. A chapter in the History of Botany 1470-1670. Cambridge University Press, New York, ISBN 0-521-33879-4, 1987.

[2] I. S. Askevold, and C. W. O’Brien, “DELTA, an invaluable computer program for generation of taxonomic monographs”, Ann. Entomol. Soc. Am. 87, pp. 1–16, 1994.

[3] C. S. Kuoh, and H. R. Song, “Interactive key to Taiwan grasses using characters of leaf anatomy”, The ActKey Approach, 50(4), pp. 261-271, 2005.

[4] E. D. Astegiano, J. C. Favaro, and C. A. Bouzo, “Estimación del área foliar en distintos cultivares de tomate (LycopersiconesculentumMill.) utilizando medidas foliares lineales”, Investigación Agraria: Producción y Protección Vegetales, v.16, pp. 249-256, 2000.

[5] C. Daughtry, “Direct measurements of canopy structure”. Rem. Sens. Rev. 5(1), pp. 45-60, 1990.

[6] M. Bylesjö, V. Segura, R. Y. Soolanayakanahally, A. M. Rae, J. Trygg, P. Gustafsson, S. Jansson, and N. R. Street, “LAMINA: a tool for rapid quantification of leaf size and shape parameters”, BMC Plant Biol. 8(1), 2008.

[7] M. E. O’Neal, D. A. Landis, and R. Isaacs, “An inexpensive, accurate method for measuring leaf area and defoliation through digital image analysis”, J. Econ. Entomol. 95(6), pp. 1190-1194, 2002.

[8] A. Femat-Díaz, D. Vargas-Vázquez, E.Huerta-Manzanilla, E. Rico-Garcia, and G. Herrera-Ruiz, “Scanner image methodology (SIM) to measure dimensions of leaves for agronomical applications”, African Journal of Biotechnology 10(10), pp. 1840-1847, 2011.

[9] T. Y. Young, and K. S. Fu, Handbook of pattern recognition and image processing, Academic Press Publishers, ISBN: 0127745602, 1986.

[10] N. A. Otsu, “Threshold selection method from gray-level histograms”, IEEE Trans. Syst. Man. Cybern. 9(1), pp. 62–66, 1979.

[11] M. A. Jaramillo, J. A. Fernandez, and E. M. Salazar, “Filtro de mediana sobre redes neuronales”, Proc. XXI Jornadas de Automática, Sevilla, Spain, 2000.

[12] M. K. Hu, “Visual pattern recognition by moment invariants”, IRE Treans. InfoTheory, volIT-8, pp. 179-187, 1962.

[13] J. A. Freeman, and D. M. Skapura, Neural Networks Algorithms, Applications, and Programming Techniques, Addison-Wesley Publishing Company, 1991.

[14] S. Haykin, “Neural Networks: A comprehensive foundation”, Second Edition, Pearson education, 2001, pp. 43-60.

[15] W. S. McCulloch, “A logical calculus of the ideas immanent in nervous activity”, Bull Math. Biophysics, 52(1-2), pp. 99-115, 1990.

[16] A. A. Y. Mustafa, “Boundary signature matching for object recognition”, VI2001 Vision Interface Annual Conference, pp. 72-79, 2001.

[17] Website: El mundo de las plantas. (1999-2015). http://www.botanical-online.com/botanica2.htm. Last accessed in February 2016.

[18] Website: Plants DB. (2011-2012) http://www.plantsdb.gr/en/kingdom-plantae/453-leaf-structure-morphology-functions. Last accessed in February 2016.

[19] R. González, and R. Woods, Digital Image Processing, Prentice Hall, 3rd Ed., 2008, pp. 808-810.

A New Self-tuning Controller Using Fourier Series Neural Network

E. Espíndola-López, R.V. Carrillo-Serrano
Universidad Autónoma de Querétaro
Facultad de Ingeniería
División de Investigación y Posgrado
Santiago de Querétaro, Qro., México
Email: eespindola19@alumnos.uaq.mx
Email: roberto.carrillo@uaq.mx

Alfonso Gómez-Espinosa
Tecnológico de Monterrey
División de Ingeniería
Santiago de Querétaro, Qro., México
Email: agomeze@itesm.mx

***Abstract*—A new iterative adaptable controller is designed based on Fourier Series Neural Network for some class of linear and nonlinear SISO systems. In this paper is used the gradient of a function that represent the system error dynamics. Here is obtained an iterative algorithm for update the coefficients of a truncated Fourier Series which is used as control law and it can represent any required control signal. The controller designed is robust to the influence of random and constant disturbances, it decreases the system variability and suppress the error caused by system nonlinearities and deterministic uncertainties.**

***Keywords*—Fourier Series Neural Network; adaptable controller; delta rule; control law as Fourier series**

I. Introduction

The Fourier series are useful tools in many disciplines due to their potentiality as universal function approximator. Additionally they reveal frequency components and particular properties of functions [1]–[3]. In automatic control area the Fourier series have had some contributions, especially as additional functions on control signal [4] for to solve nonlinearities that cause problems like torque ripples in three-phase motors [5]–[7]. The application of Fourier series on speed three-phase motors control can reduce the cogging effects, the average power excitation, vibrations and acoustic noise besides of torque ripple as it is shown in [8]. They exhibit an analysis of torque ripple using the exponential Fourier series in the torque model, from which is designed an optimal weighting of stator current harmonics in closed form.

In intelligent control area, the identification systems are studied since they have some important applications on difficult to model systems. Also the identification systems are studied because they are near of become controllers like neural networks. An identification system was developed by [9] based in a special neural network architecture called Fourier Series Neural Network (FSNN), which have neurons with complex exponential as activation functions. The FSNN have a finite number of neurons representing the harmonic components of final Fourier series. It is shown the coefficients update algorithm obtained from Delta learning rule and it is demonstrated the global stability of the FSNN learning dynamics.

A FSNN can be designed for to approximate a nonlinear, complex and unknown function like frictional phenomenon in servo systems. The friction in servo systems are difficult to model and many controllers as proportional integral derivative (PID) control cannot reach acceptable result. However, a FSNN based robust adaptive variable structure control is an efficient solution for servo systems with friction as is shown in [10].

The Fourier series representation of the reference voltage in a pulsewidth modulation (PWM) inverter can be used to control the output voltage more efficiently than others controllers. With this representation it is possible to obtain a graphical transformation between complex voltage vectors and the phase voltage in time domain. Using a modulation index it is possible to choose the reference angles or holding angles for to keep the output voltage constant before frequent variations of the source voltage as is shown in [11].

Some controllers become robust in the face of deterministic modeling uncertainties if they consider a feedback controller in frequency domain. For example, a controller with a part based in a proportional-derivative (PD) controller and other part based in a Fourier series learning controller is more efficient than a simple PD controller, when is controlled a positioning table with nonlinear uncertainties such as friction and backlash as is shown in [12].

Actually the applications of the Fourier series in control area have been carried to robotics. Quadrocopters have flight dynamics complex and modeling is difficult. Because the typical control of this robots are based in simplified models with feedback corrections compensating, significant tracking errors are presented. To solve this, it is designed a iterative learning controller based on a Fourier series decomposition of the input and output signals for periodic quadrocopter flight. The controller has one part based in a time-invariant dynamics of system to determine correction values from observed errors and it use another part for parametrize the non-causal tracking error compensation as Fourier series, with which it is reached a high-performance motion as is shown in [13].

The underwater robotic vehicles are other robots where have been used the Fourier series for to help at the controller. Using

Fourier series it is possible to build a reference signal generator for an output feedback controller solving a trajectory tracking problem. The combination of the Fourier series with output regulation problem allows to bypass the need to compute explicitly the Fourier coefficients as is shown in [14]. They show a simulation with a good performance of a nonlinear dynamic controller that solves the bottom-following problem using Fourier series expansion and pseudo-spectral methods.

One of the most important contribution of Fourier series is helping in controllers as functional approximation (FA) that they are difficult to establish an accurate dynamic model. The biggest advantage of FA is that it is possible to design robust controllers model-based like sliding-mode control without known the model of the plant. Using Fourier series as FA it is possible to found an update law for the Fourier coefficients and at the same time assure the stability of the closed loop system. In addition, the Fourier series as FA has benefits in controllers like compensation of time-varying uncertainties, not model dynamics, reduces the effect of random disturbances and the error caused by deterministic uncertainties [15]–[19].

The Fourier neural network (FNN) or FSNN take advantage of the Fourier series properties and it is possible to develop feedback controllers that decreases system variability, reduces the influence of random disturbances and suppress the error caused by system nonlinearities and deterministic uncertainties. The orthogonal complex Fourier exponentials as activation functions are a good way to define the topology of a FNN as is shown in [20]. They introduced a variable structure FNN for to deal with the tracking control of nonlinear dynamical systems and shown the good behavior of controller when is proven on a gear box and a belt-driven positioning table.

Therefore the most of controllers mentioned are model-based and depend of other controllers in the time domain e.g. PID or feedforward controllers. They use Fourier series as auxiliary of main controller and in some cases their coefficients are constant or updated based-model. In this paper our main objective is shown a new controller which has Fourier series as main controller and it not require system model moreover coefficients are updated using the dynamics error.

Actually exist few topologies of this class of neural networks and the Fourier coefficients update rules are difficult to found. However, in this paper it is designed a FSNN controller with a simple topology and it is shown a easy way to obtain the Fourier coefficients update rules. To probe the controller are used two systems, a linear system and a nonlinear system. The first is a position control of brushed DC motor which is periodically disturbed and a simple PD control can not solve it. This is the probe in a linear system. The second probe is realized in a strongly nonlinear system which also is periodically disturbed and is shown how the proposed controller can diminish the error with lesser energy than a PID control.

The following paper is planned with six sections. In section II is described the single input single output (SISO) self-tuning FSNN controller structure. In section III is talked about the FSNN architecture and topology. In section IV is presented the FSNN coefficients update algorithm. In section V are shown the simulated results. Finally, in section VI are provided the conclusions.

II. Self-tuning FSNN controller structure

The controller structure proposed for a SISO system in closed loop is shown in Fig. 1. Note that FSNN does not have the error system e_y as input, but it is used for to update the FSNN coefficients.

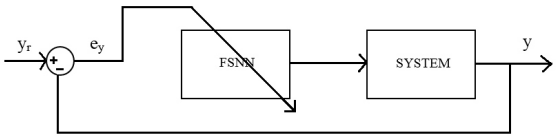

Fig. 1. Scheme of the SISO self-tuning FSNN.

In this closed loop process we have two types of error. One is the control signal error e_u measured as the difference between FSNN output u and the control signal necessary u_n for to bring the system to the reference y_r:

$$e_u(t) = u_n(t) - u(t) \tag{1}$$

and the process output error is calculated as follows:

$$e_y(t) = y_r(t) - y(t) \tag{2}$$

We need these errors (1) and (2) to obtain the update rule of FSNN coefficients. The error in (2) have to be minimized by FSNN. Note that the explicit FSNN input is the process time because it is necessary for activation functions.

III. FSNN Architecture

The Fourier series can always represent any continuous time function that satisfies the Dirichlet condition [21]. Then, the control signal necessary for eliminate the closed loop system error (2) also can be represented by Fourier series. The Fourier series neural networks imply that the Fourier coefficients are dynamics and they must to be updated until to obtain the correct ones. The topology or architecture proposed is shown in Fig. 2.

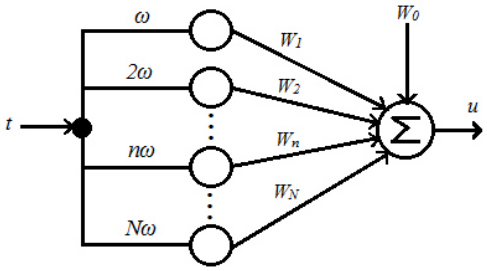

Fig. 2. FSNN Architecture.

This topology is designed for SISO linear or nonlinear systems. It is composed by three layers. The first layer is the input layer and only have one input that it is the process time. The second layer is the intermediate layer and it is composed by N neurons associated with the number of terms in a truncate Fourier series. Neurons in the intermediate layer have complex exponential as activation functions. The inputs in second layer are the products of the time t by the frequency wights. These frequency weights are fixed and equal to an integer n the frequency number, times a base frequency $\omega = \frac{2\pi}{L}$; when the inputs are scaled to a range $[0, L]$ or period L. The third layer is the output layer with one neuron, this neuron sums the weighted outputs from layer two and a bias W_n yielding the output u of the neural network [9].

The output of neural network is calculated as follows:

$$u(t) = W_0 + \sum_{n=1}^{N} W_n h_n(t) \tag{3}$$

where:

$$h(t) = e^{jn\omega t} \tag{4}$$

The FSNN is the complex form of Fourier series and the weights W_n are complex numbers in which stays the knowledge. Because the implementation of complex function (3) is difficult to implement, it is used the real form of truncated Fourier series that it is possible to obtain from (3) easily and is given by:

$$u(t) = \frac{a_0}{2} + \sum_{n=1}^{N} a_n cos(n\omega t) + b_n sin(n\omega t) \tag{5}$$

The control law (5) can represent any control signal as long as the number of terms is sufficiently large. The coefficients a_0, a_n and b_n have to be updated depending of (2).

IV. FSNN Coefficients Adaptation Algorithm

We present the adaptation algorithm of FSNN coefficients that is obtained from Delta rule, namely the gradient of a specific function that we want minimize. This rule is frequently adopted for tuning regulator parameters in the model-reference adaptive control scheme [9]. At first we defined an dynamic reference error function as:

$$s(t) = \alpha e_y(t) + \gamma \dot{e}_y(t) \tag{6}$$

Where α and γ are positive constants. Then, taking (6) is defined the function that we want minimize with the FSNN as:

$$E(t) = \frac{1}{2} \sum_{k=1}^{t} s^2(k) \tag{7}$$

The gradient of (7) is a multi-dimensional vector whose depends of partial derivatives $\frac{\partial E(t)}{\partial a_0}$, $\frac{\partial E(t)}{\partial a_n}$ and $\frac{\partial E(t)}{\partial b_n}$, namely:

$$\nabla E(t) = \begin{bmatrix} \frac{\partial E(t)}{\partial a_0} \\ \frac{\partial E(t)}{\partial a_n} \\ \frac{\partial E(t)}{\partial b_n} \end{bmatrix} \tag{8}$$

Applying the chain rule, we can obtain the partial derivatives with respect to the coefficients of the output neuron, it is define:

$$\nabla E(t) = \begin{bmatrix} \frac{\partial E(t)}{\partial a_0} \\ \frac{\partial E(t)}{\partial a_n} \\ \frac{\partial E(t)}{\partial b_n} \end{bmatrix} = \begin{bmatrix} \frac{\partial E(t)}{\partial s(t)} \frac{\partial s(t)}{\partial e_y(t)} \frac{\partial e_y(t)}{\partial e_u(t)} \frac{\partial e_u(t)}{\partial u(t)} \frac{\partial u(t)}{\partial a_0} \\ \frac{\partial E(t)}{\partial s(t)} \frac{\partial s(t)}{\partial e_y(t)} \frac{\partial e_y(t)}{\partial e_u(t)} \frac{\partial e_u(t)}{\partial u(t)} \frac{\partial u(t)}{\partial a_n} \\ \frac{\partial E(t)}{\partial s(t)} \frac{\partial s(t)}{\partial e_y(t)} \frac{\partial e_y(t)}{\partial e_u(t)} \frac{\partial e_u(t)}{\partial u(t)} \frac{\partial u(t)}{\partial b_n} \end{bmatrix} \tag{9}$$

Solving the partial derivatives we obtain:

$$\nabla E(t) = \begin{bmatrix} \frac{\partial E(t)}{\partial a_0} \\ \frac{\partial E(t)}{\partial a_n} \\ \frac{\partial E(t)}{\partial b_n} \end{bmatrix} = \begin{bmatrix} s(t)\alpha \frac{\partial e_y(t)}{\partial e_u(t)}(-1)(\frac{1}{2}) \\ s(t)\alpha \frac{\partial e_y(t)}{\partial e_u(t)}(-1) cos(n\omega t) \\ s(t)\alpha \frac{\partial e_y(t)}{\partial e_u(t)}(-1) sin(n\omega t) \end{bmatrix} \tag{10}$$

If we need to minimize the function (7) we need to go in the direction of the negative gradient $-\nabla E(t)$. Then we can define the update rules of Fourier coefficients from the result in (10) as:

$$a_0(t+1) = a_0(t) + \eta\alpha \frac{1}{2} \frac{\partial e_y(t)}{\partial e_u(t)} s(t) \tag{11}$$

$$a_n(t+1) = a_n(t) + \eta\alpha \frac{\partial e_y(t)}{\partial e_u(t)} cos(n\omega t) s(t) \tag{12}$$

$$b_n(t+1) = b_n(t) + \eta\alpha \frac{\partial e_y(t)}{\partial e_u(t)} sin(n\omega t) s(t) \tag{13}$$

The constant η is the learning coefficient and it can be experimentally determined from the observation of closed loop performance when it is selected different references. The learning coefficient is used for increase the convergence speed of the weights. The term $\frac{\partial e_y(t)}{\partial e_u(t)}$ is called "equivalent gain" of the plant and it is unknown. However, actually it is demonstrated by [22] that it is only required to know the sign of that term to ensure the convergence of the weighting coefficients because the magnitude can be incorporated in the learning coefficient η. Also the sign of that term can be easily estimated with a simple experiment on the process. The sign of $\frac{\partial e_y(t)}{\partial e_u(t)}$ is positive if for a input system of known sign the output system have the same sign, otherwise it is negative.

Then, considering the above the algorithm of adaptation is determined with the update rules of Fourier coefficients and they are calculated as follows:

$$a_0(t+1) = a_0(t) + \eta\alpha\frac{1}{2}s(t) \tag{14}$$

$$a_n(t+1) = a_n(t) + \eta\alpha cos(n\omega t)s(t) \tag{15}$$

$$b_n(t+1) = b_n(t) + \eta\alpha sin(n\omega t)s(t) \tag{16}$$

V. Simulation Results

We will test this controller in a linear system with periodic disturbances, and later in a no linear system. The first test is the position control of brushed DC motor with permanent magnet and one disturbance given by the function $f(t) = sin(4\pi t)$ at time $t = 50\ s$. The position reference is $y_r = \pi$. In Fig. 3 is shown the response of proportional-derivative (PD) control with gains $K_p = 0.3$, $K_d = 0.01$.

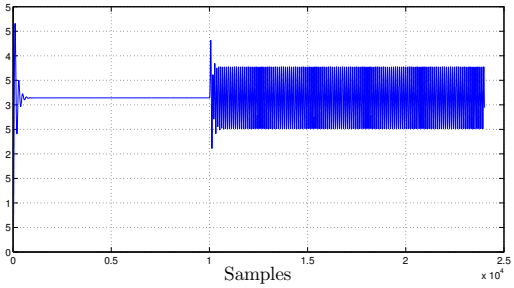

Fig. 3. PD control of position when motor is under a periodic disturbance.

The response of the propose FSNN controller is shown in Fig. 4, it can be note that the intelligent controller proposed is robust to disturbances in comparative with typical PD controller.

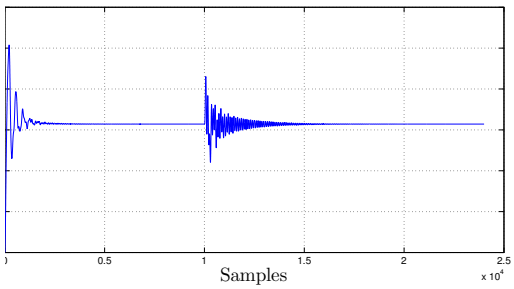

Fig. 4. Response of FSNN controller when motor is under a periodic disturbance.

The first simulation showed how the propose controller decreases the periodic disturbance in a linear system and the PD controller can not compensate it. However, the method proposed has application in control systems more complex. The next test of the controller will be in a non linear system under a periodic disturbance. It is a turbine-dome electricity generator, this system is shaped of a boiler for steam generation, which flow through a valve and it expands in a high-pressure turbine followed by others turbines of intermediate and low pressure. The electricity is generated by an alternator adjoined to the turbines. The mathematical model of this system is given by [23]:

$$\dot{x}_1 = 0.014u_1 - 0.0033x_1^{1.125}u_2 \tag{17}$$

$$\dot{x}_2 = 0.01408x_1^{1.125}u_2 - 0.064x_2 \tag{18}$$

$$y = 0.2957x_1^{1.125}u_2 + 3.456x_2 + v \tag{19}$$

Where x_1 is the pressure in the dome $[kg/m^2]$, x_2 is the pressure in the pre-heater, u_1 is the fuel flow $[tons/h]$, u_2 is the valve position $[m]$, y is the power output $[MW]$ and v is the representation of variations in the energy consumption. For this test, we will consider $v = 0$, a reference output $y_r = 100$ and a disturbance function $f(t) = sin(4\pi t - \frac{\pi}{2})$, which begin in $t = 200s$. We will compare the response of the proposed controller and a classic controller PID.

In the Fig. 5 is shown the simulation diagram of the non linear system controlled with a PID, the gains are $K_p = 3.5$, $K_d = 0.2$ and $K_i = 0.0017$. In the simulation diagram can be seen some zero order holders, which are used for simulate a discrete system taken output samples each $0.005s$. Also was connected a small system for calculate the sum of squared errors. In the scopes we will compare the system output, the fuel input and the squared errors.

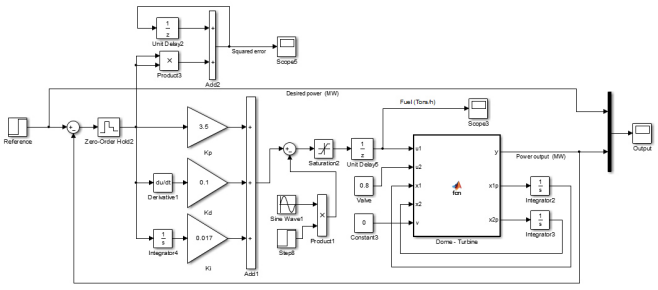

Fig. 5. Simulation diagram of non linear system controlled with PID.

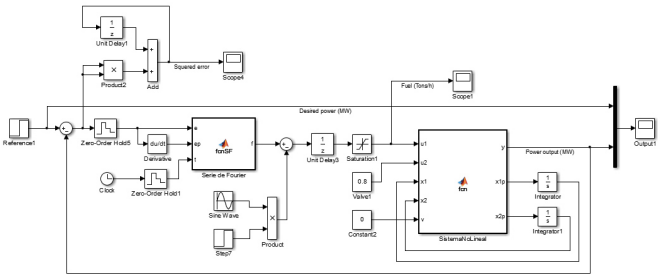

Fig. 6. Simulation diagram of non linear system controlled with FSNN.

In the Fig. 6 is shown the simulation diagram for the FSNN controller. Note that the time is an input for the FSNN, due to is used in the trigonometric functions of Fourier Series. Other input to the FSNN is the error and the error derivative, which are summed and later transformed as the function that we want to decrease.

During the first $400s$ of simulation we obtained the responses shown in Fig. 7 (PID) and Fig. 8 (FSNN). It can be seen that with PID controller the output reach the desired value faster than FSNN controller, but with an overshoot not presented in the case of the FSNN. When the disturbance is presented the PID compensate it faster than the FSNN. However, with the PID, the output carries a periodic variation with amplitude of $0.001\ MW$ and in the case of the FSNN this variation is smallest ($0.0001\ MW$) and practically indiscernible.

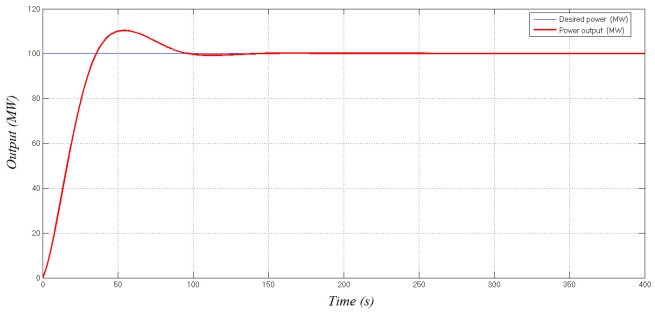

Fig. 7. System output when is controlled with PID.

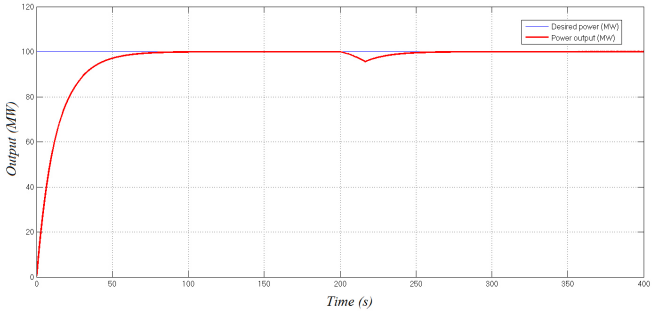

Fig. 8. System output when is controlled with FSNN.

The gains of the dynamic reference error function were $\alpha = 0.1$ and $\gamma = 9.1$. The learning coefficient used for the FSNN were chosen different for the component of the DC (η_0) and the trigonometric terms (η_{cs}) due to the requirements of system. Then, the learning coefficients were $\eta_0 = 0.5$ and $\eta_{cs} = 0.00001$. This will do that the trigonometric terms learn slower than the DC component.

The response of the system with FSNN do not have overshoot and it can be seen that error decrease gradually. When the periodical disturbance begin, the error increments, but approximately in $50\ s$ it is compensated and carried to zero again. In Fig. 9 is shown the fuel injected to the system by the PID controller. It can be seen that the PID needs a lot of energy for to compensate the disturbance when it begin at $200s$. After the peak energy fed, the fuel injected variate periodically trying to compensate the disturbance.

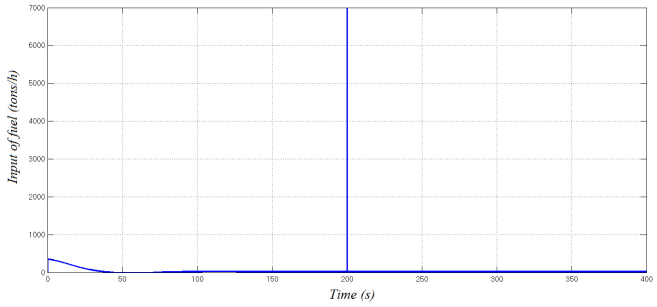

Fig. 9. System input when is controlled with PID.

In Fig. 10 is shown the output of the FSNN controller that is the fuel inserted to non linear system. It can be observe that the proposed controller do not needs a lot of energy for compensate the disturbance. With this point of view the proposed controller is a best option in comparison with the PID. In other words, the fuel required by the PID for to compensate the disturbance is not possible to apply in the real system and the PID is discarded.

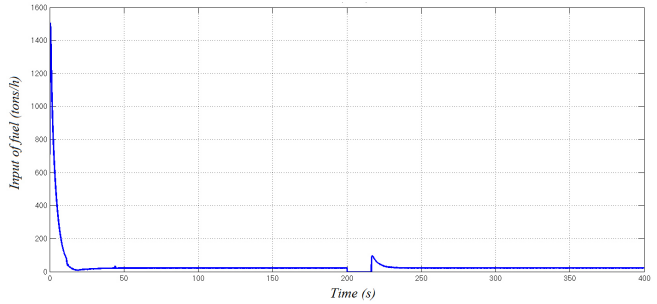

Fig. 10. System input when is controlled with FSNN.

By last we will compare the sum of squared errors. In Fig. 11 can be seen the sum of squared errors when the system is controlled by the PID. Note that error reach over 11×10^8 MW^2 during the $400s$ of simulation.

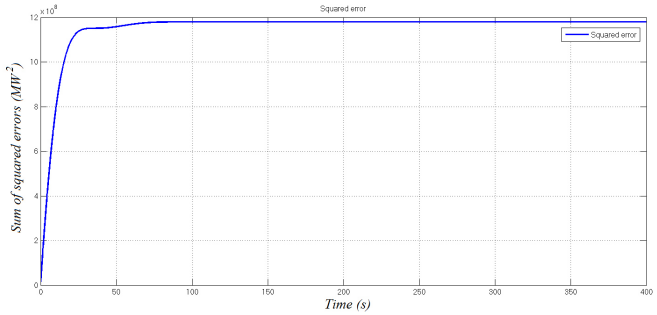

Fig. 11. Sum of squared errors in system controlled by PID.

In Fig. 12 is shown the sum of squared errors when the system is controlled by the FSNN. It is possible to observe

that this signal does not reach the $7 \times 10^8\ MW^2$ and again the response of the proposed controller is better than the PID performance. The proposed controller can dominate non linear systems and reach better performances than others like the PID controller. In spite of periodic disturbances and non linearities of a system the proposed FSNN controller can has an acceptable performance.

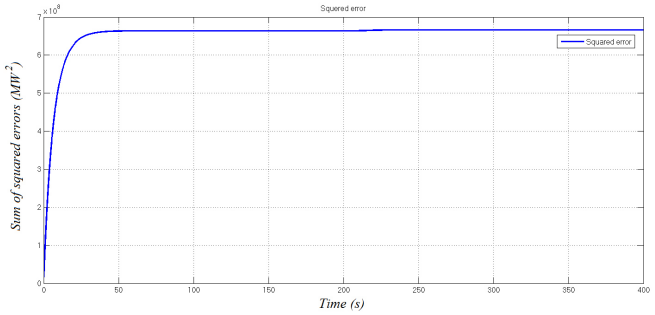

Fig. 12. Sum of squared errors in system controlled by FSNN.

VI. Conclusion

In this paper was designed a new FSNN controller robust to periodic disturbances for linear and nonlinear SISO systems. We design the update rules for Fourier coefficients from gradient of a function that represent the dynamics error. This FSNN controller used the Fourier series like control law. Whence using an appropriate adaptation algorithm any control law can be represented by this controller. Also it is possible to modify directly some harmonics that it is not necessary in control signal. Simulation results shown that this controller is a good candidate for to use in real systems. According with results, this controller can reduce the influence of random disturbances, decreases system variability, and suppress the error caused by system non linearities and deterministic uncertainties being that is a frequency adaptable controller.

References

[1] M. Dogruel and H. Hüseyin celik, "Harmonic control arrays method with a real time application to periodic position control," *IEEE transactions on control systems technology*, vol. 19, no. 3, pp. 521–530, 2011.

[2] X. Ruan and Z. Li, "Convergence characteristics of pd-type iterative learning control in discrete frequency domain," *Journal of Process Control*, vol. 24, no. 12, pp. 86–94, 2014.

[3] C.-I. Kang, S.-E. Baek, and J.-S. Shim, "A new seek servo controller for minimizing power consumption in micro hard disk drives," *Magnetics, IEEE Transactions on*, vol. 40, no. 4, pp. 3127–3129, 2004.

[4] X. Wu, S. Panda, and J. Xu, "Dc link voltage and supply-side current harmonicsminimization of three phase pwm boostrectifiers using frequency domain basedrepetitive current controllers," *Power Electronics, IEEE Transactions on*, vol. 23, no. 4, pp. 1987–1997, 2008.

[5] A. Khalil and I. Husain, "A fourier series generalized geometry-based analytical model of switched reluctance machines," *Industry Applications, IEEE Transactions on*, vol. 43, no. 3, pp. 673–684, 2007.

[6] W. Qian, S. K. Panda, and J.-X. Xu, "Torque ripple minimization in pm synchronous motors using iterative learning control," *Power Electronics, IEEE Transactions on*, vol. 19, no. 2, pp. 272–279, 2004.

[7] A. Gómez-Espinosa, V. M. Hernández-Guzmán, M. Bandala-Sánchez, H. Jiménez-Hernández, E. A. Rivas-Araiza, J. Rodríguez-Reséndiz, and G. Herrera-Ruíz, "A new adaptive self-tuning fourier coefficients algorithm for periodic torque ripple minimization in permanent magnet synchronous motors (pmsm)," *Sensors*, vol. 13, no. 3, pp. 3831–3847, 2013.

[8] J. Hung and Z. Ding, "Design of currents to reduce torque ripple in brushless permanent magnet motors," *Electric Power Applications, IEE Proceedings B*, vol. 140, no. 4, pp. 260–266, 1993.

[9] C. Zhu and F. Paul, "A fourier series neural network and its application to system identification," *Journal of dynamic systems, measurement, and control*, vol. 117, no. 3, pp. 253–261, 1995.

[10] C.-L. Hwang, "Fourier series neural network-based adaptive variable structure control for servo systems with friction," in *Control Theory and Applications, IEE Proceedings*, vol. 144. IET, 1997, pp. 559–565.

[11] D.-C. Lee and G.-M. Lee, "A novel overmodulation technique for space-vector pwm inverters," *Power Electronics, IEEE Transactions on*, vol. 13, no. 6, pp. 1144–1151, 1998.

[12] L. Cai and W. Huang, "Fourier series based learning control and application to positioning table," *Robotics and Autonomous systems*, vol. 32, no. 2, pp. 89–100, 1999.

[13] M. Hehn and R. DAndrea, "A frequency domain iterative learning algorithm for high-performance, periodic quadrocopter maneuvers," *Mechatronics*, vol. 24, no. 8, pp. 954–965, 2014.

[14] A. Adhami-Mirhosseini, M. J. Yazdanpanah, and A. P. Aguiar, "Automatic bottom-following for underwater robotic vehicles," *Automatica*, vol. 50, no. 8, pp. 2155–2162, 2014.

[15] F. Aghili, "Adaptive reshaping of excitation currents for accurate torque control of brushless motors," *Control Systems Technology, IEEE Transactions on*, vol. 16, no. 2, pp. 356–364, 2008.

[16] H.-Y. Chen and J.-W. Liang, "Adaptive sliding control with self-tuning fuzzy compensation for a piezoelectrically actuated x–y table," *IET control theory & applications*, vol. 4, no. 11, pp. 2516–2526, 2010.

[17] ——, "Model-free adaptive sensing and control for a piezoelectrically actuated system," *Sensors*, vol. 10, no. 12, pp. 10 545–10 559, 2010.

[18] C.-L. Zhang and J.-M. Li, "Adaptive iterative learning control of non-uniform trajectory tracking for strict feedback nonlinear time-varying systems," *International Journal of Automation and Computing*, vol. 11, no. 6, pp. 621–626, 2014.

[19] L. Dong and W. C. Tang, "Adaptive backstepping sliding mode control of flexible ball screw drives with time-varying parametric uncertainties and disturbances," *ISA transactions*, vol. 53, no. 1, pp. 110–116, 2014.

[20] W. Zuo and L. Cai, "A new iterative learning controller using variable structure fourier neural network," *Systems, Man, and Cybernetics, Part B: Cybernetics, IEEE Transactions on*, vol. 40, no. 2, pp. 458–468, 2010.

[21] E. W. Kamen, M. A. G. Guzmán *et al.*, *Introduction to signals and systems. Introducción a señales y sistemas*. Mexico: Continental, 1996.

[22] X. Cui and K. G. Shin, "Direct control and coordination using neural networks," *Systems, Man and Cybernetics, IEEE Transactions on*, vol. 23, no. 3, pp. 686–697, 1993.

[23] A. Aguado, A. Gómez, and A. del Pozo, "Controlador predictivo neuro-genético," *Revista iberoamericana de automática e informática industrial RIAI*, vol. 4, no. 4, pp. 94–108, 2007.

Synthesis and characterization of MgO nanoparticles supported on SBA-16 for biodiesel transesterification

Vázquez-Maya N. [#1], Nava-Mendoza R. [#1], Vanthoor-Koopmans M. [#1]

[#1] *División de Investigación y Posgrado, Facultad de Ingeniería, Universidad Autónoma de Querétaro (UAQ), Cerro de las Campanas s/n, C.P. 76000 Querétaro, Qro., México*

[1] naancyvm5@gmail.com

[2] rufino@uaq.edu

[3] mariekekoopmans81@gmail.com

Abstract*— Catalysts for biodiesel production were prepared. This process consisted on the synthesis of heterogeneous alkaline catalysts of MgO/SBA-16 with different percentage by weight (5, 7.5, 10%), for the biodiesel reaction from waste cooking oil. The methodology consisted in the Sol.Gel process for the synthesis of the support SBA-16, and the impregnation method for the particles of MgO. The catalysts were characterized by different techniques: x-ray diffraction, diffuse reflectance spectroscopy on the ultraviolet-visible range (UV-vis), nitrogen physisorption at 77 k (SBET) and thermogravimetric analysis (TGA).

Keywords: SBA-16, impregnation, catalyst

I. Introduction

Energy is very important and determinant for the development of world economy. The mainstream of energy comes from the non-renewable fossil fuels and is considered as the main factor for global warming [1]. The uncertainty in availability of the non-renewable sources and the pollution problem are considered as important causes for researchers to explore renewable sources for replacing fossil fuels [2, 3].

Biodiesel is one of these alternative resources for diesel engines. It is defined as the mono-alkyl esters of long chain fatty acids derived from vegetable oils or animal fats. The use of biodiesel is becoming more common worldwide [4]. This energy source has several benefits that promote its acceptance; for example, it is bio-renewable, nontoxic and biodegradable. Its liquid state allows its use in diesel engines currently in circulation without the need for significant changes [5-7].

The general production process of biodiesel is performed by transesterification reaction, which consists of triglyceride oil to react with methanol in the presence of a catalyst. Conventional catalysts used are alkali homogeneous catalysts such as sodium hydroxide or potassium hydroxide; and acid homogeneous catalysts, as hydrochloric acid and sulfuric acid [8]. However, this process presents some disadvantages, as it requires the use of high amounts of catalyst (which cannot be recovered), the production of different streams which might be treated (neutralization step and wash step), and the purification of glycerin to reuse it. These aspects also play important roles in the economy of the process [9].

Heterogeneous catalytic process is expected to be future biodiesel production process. This process lowers the cost and minimizes the environmental impacts due to the simpler production steps and purification processes which are normally carried out under very mild conditions. The common problem associated with the heterogeneous biodiesel production process is its low reaction rate due to poor interaction between the oil and alcohol during the reaction due to their mutual immiscibility [10, 11].

In this sense, this investigation project focuses in the catalyst preparation using heterogeneous catalysts such as MgO supported on a SBA-16 mesoporous silica. The main idea consists in prepare small particles of MgO highly dispersed inside the SBA-16 pores, and examine their influence on the catalytic efficiency of the different percentages of the catalysts.

II. Methodology

A. *Catalyst preparation*

Siliceous SBA-16 mesoporous material was synthesized according to the procedure described by Zhao et al. [12]. The Pluronic triblock copolymer (BASF, EO106–PO70–EO106, F127) was used as the structure-directing agent and tetraethylorthosilicate (TEOS, 98%, Aldrich) as a source of silica. In a typical synthesis, the triblock copolymer was dissolved in a mixture of deionized water and 2 M hydrochloric acid solution stirred for 1 h, after which the required amount of TEOS was added to the solution at 308 K and kept under stirring conditions for 24 h. The mixture was heated for 24 h. After synthesis, the obtained solid was filtered, washed, dried, and finally was calcined to remove the organic template [12].

B. *Mesoporous material SBA-16 with MgO particles impregnation.*

The incorporation of the nanoparticles of MgO on the inner surface of the pores of SBA-16 was made by the impregnation method by pore filling, using as a precursor of MgO, magnesium acetate ($Mg(CH_3COO)_2$). 5%, 7.5% and 10% by weight of MgO were incorporated into the SBA-16, using

aqueous solutions of magnesium acetate with different concentrations.

An appropriate concentration of magnesium acetate diluted in water was prepared in each of the catalysts. The catalyst was deposited inside the SBA-16 support drop wise with a syringe, stirring constantly to form a muddy solution which is stirred again. Finally it allowed to dry for 3 hours in order to evaporate gently, and achieve a deposition of solutes on the support.

C. *Characterization Methods.*

1) X-ray diffraction (XRD): X-ray diffraction (XRD) measurements of the samples in powder were carried out using the Cu Kα radiation with a wavelength of 1.54 Å in the range of 0.5°-80° on a Bruker D8 Advance diffractometer. Particle size calculation was made using the Scherrer equation.

2) N2 adsorption–desorption isotherms: The textural properties of the mesoporous matrices were determined from the nitrogen adsorption isotherms recorded at 77 K with a Quanthachrome iQ2 apparatus. The samples were previously degassed at 423 K for 24 h under a vacuum (10-4 mbar) to ensure a clean, dry surface, free of any loosely bound adsorbed species. The specific areas of the samples were calculated according to standard BET procedure using nitrogen adsorption data collected in the relative equilibrium pressure interval of $0.03 < P/P0 < 0.3$. Pore size distributions were calculated from the desorption branches of the corresponding nitrogen isotherm using the BJH method. The total pore volume (Vtotal) was estimated from the amount of nitrogen adsorbed at a relative pressure of 0.99.

3) Diffuse reflectance spectroscopy (DRS): The UV–Vis diffuse reflectance spectra of the mesoporous matrices were recorded at room temperature using an Ocean Optics Inc. spectrometer First in Photonics (Mini-DT 2) in the 200-400 nm range. The respective support of each mesoporous matrix was used as a reference.

4) Thermogravimetric analysis (TGA/DTG): Thermogravimetric analysis (TGA/DTG) data was obtained with TA Instruments Model TGA-Q500 thermobalance with a quartz furnace tube, with a constant heating rate of 10 C/min, starting the race in 25°C, employing a dynamic atmosphere of nitrogen with the flow 50 mL/min. Each experiment was conducted at constant pressure so that temperature dependence of transitions could be measured. Five milligram samples were used in platinum pans of 20 µL in each analysis, with an approximately 0.5 mm hole in the lid. TGA curves, as well as derivate thermogravimetric (DTGA) curves were used in the study.

III. Results and Discussion

A. *Physicochemical properties of SBA-16 and modified SBA-16 materials.*

Figure 3.1 shows XRD patterns of the materials 5%MgO/SBA-16, 7.5%MgO/SBA16, and 10%MgO/SBA16. As seen in this figure, all SBA-16-based samples show three well-resolved typical diffraction peaks, which are associated with a symmetry cubic (*Im 3m*) cage-structured mesoporous silica material (SBA-16) [20]: one intense reflection centered approximately at 22° in 2θ, which can be indexed as the (100), (110) and (200) *khl* reflections, respectively [20]. Thus, one might infer that the mesoporous structure of SBA16 adsorbent did not suffer modification upon MgO addition. However, it can be observed that the position of the reflection corresponding to SBA16 moves slightly to higher angles when the SBA-16 is modified superficially. This result indicated that the SBA-16 modification occurs inside of their mesoporous structure, so that the MgO is bonding on the internal surface of the SBA-16 substrate.

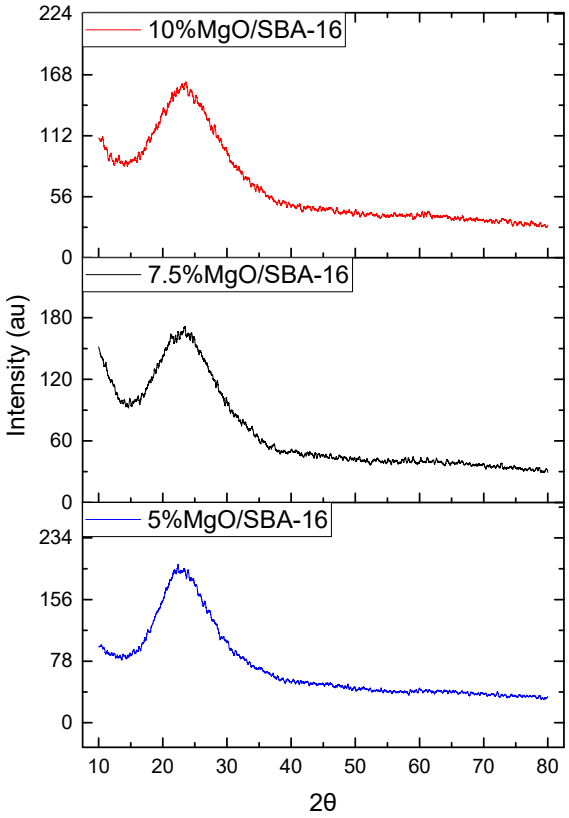

Figure 3.1. XRD patterns of 5%, 7.5% and 10% MgO/SBA-16

Figure 3.2 shows the absorption spectra of the MgO/SBA-6 catalysts (5, 7.5, 10%wt MgO). In the spectra can be observed an absorption band in the UV 200 range to 300 nm, according to literature this absorption is assigned to Mg^{2+} in the magnesium oxide (MgO) The intensity of this band increases

with increasing in wt% MgO. Therefore this result confirms the presence of MgO in the synthesized catalysts.

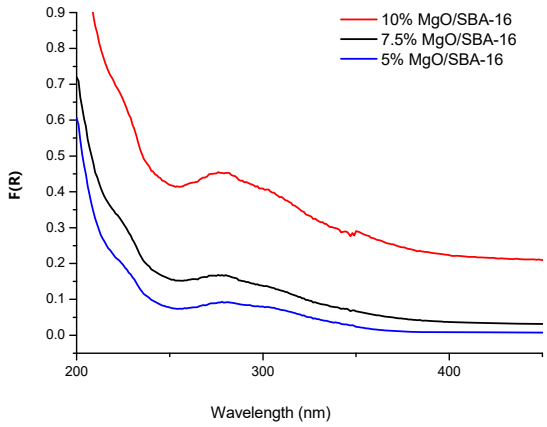

Figure 3.2 Uv-vis of 5, 7.5 and 10% MgO/SBA-16

Table 3.1 summarizes the textural properties (surface area, pore volume and average pore diameter) of silica mesoporous support our SBA-16 compared to our catalysts with different weight percentages of MgO.

It can be appreciated the pore volume and high surface area presented by the SBA-16, and the decrease of these properties as is increasing the percentage by weight of MgO, possibly caused by the filling of the MgO particles within the pores SBA-16.

TABLE 1. TEXTURAL PROPERTIES OF SBA-16 BEFORE AND AFTER OF MODIFICATION WITH MGO PARTICLES.

Textural Properties of SBA-16 before and after of modification with MgO particles.			
Sample	**Área superficial (m^2/g)**	**Volumen de poro (cm^3/g)**	**Diámetro de poro (nm)**
SBA-16	625.00	0.500	3.5
5% MgO/SBA-16	485.004	0.139	3.417
7.5% MgO/SBA-16	275.644	0.035	3.415
10% MgO/SBA-16	295.494	0.008	3.410

Figure 3.3 shows N_2 adsorption-desorption isotherms at 77 K for determine the textural properties, the isotherms of 5%, 7.5% and 10%MgO/SBA-16 having maximum concentration of MgO, exhibited irreversible type IV adsorption-desorption isotherms with a H_2 hysteresis loop in the partial pressure range from 0.4 to 0.6 p/p0, characteristic of materials with 3-6 nm pore diameter [13, 17]. These results are typical for materials with cubic pores and pore network connectivity like SBA-16 and reveals that the mesoporous nature of the material is preserved even though the grafting has occurred, as shown in the material MgO/SBA-16 with the mayor concentration of MgO. A well-defined step occurs approximately at P/P0 ≈ 0.4, which is associated with the filling of the mesopores due to capillary condensation. In the material after modification with MgO, the amount of adsorbed nitrogen increases and the inflection point of the step shifts from 0.4 to 0.41 value of relative pressure. The minimum value of adsorbed nitrogen suggests the modification in the pores with MgO, while the shift of the step to a higher value of relative pressure is indicative of mesopore sizes. The pore size distributions of the MgO/SBA-16 materials, as calculated from the adsorption branch of N2 isotherm by using the Barrett-Joyner-Halenda (BJH) model [22], are shown in both samples Fig. 3 (inlet). It should be noted that the MgO/SBA16 show a uniform, narrow pore size distributions centered at about 3.39 and 3.4 nm, respectively, confirming that the modification of the SBA-16 with maximum concentration of MgO does not damage the cubic structure of this mesoporous material.

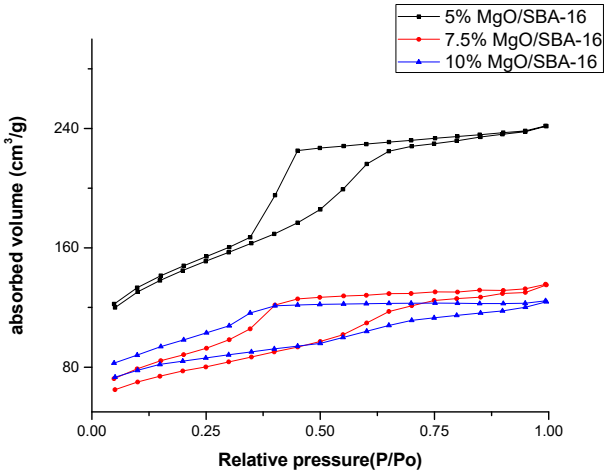

Figure 3.3 N_2 adsorption-desorption isotherms at 77 K of 5%, 7.5%, and 10% MgO/SBA-16 catalysts.

Thermogravimetric analysis (TGA) is a technique for characterizing a material (element, compound, or mixture) by measuring changes in its physicochemical properties expressed as weight change as a function of increasing temperature [17]. Therefore, the change in mass of a substance is measured as a function of increasing temperature and it is correlated to the thermal stability of a material that is directly related to the material's volatility or thermal degradation to gaseous products. The boiling point is an important property of the biodiesel and is a parameter that relates to the quality of the biodiesel, as determined by ANP [18]. Thermogravimetric analysis is a fast, easy, cheap, and very useful technique to measure the biodiesel boiling point [19, 20]. Besides, thermogravimetric analysis can confirm the occurrence of the transesterification reaction because the boiling points of the triglycerides and esters (biodiesel) are very different [20].

Figure 3.4 percentage variation shown by weight of the catalysts according to the temperature. It can be seen as increasing the percentage will by weight MgO in the catalysts, they require more temperature to decrease its total weight percent. What this indicates that the MgO deposited on our support.

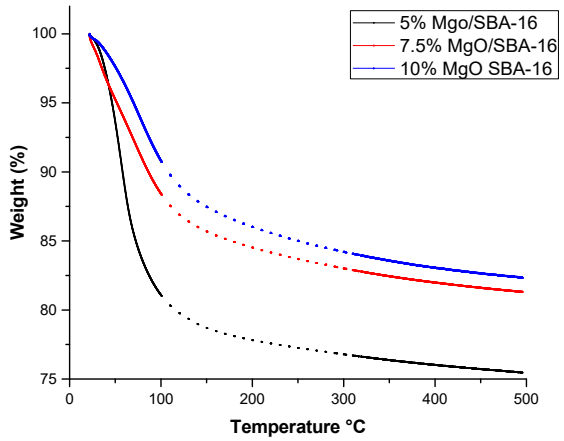

Figure 3.4 Thermogravimetric analysis of 5%, 7.5%, and 10% MgO/SBA-16 catalysts.

CONCLUSSIONS

The mesoporous silica SBA-16 were successfully synthesized by the sol-gel method. We can see in the N_2 adsorption-desorption isotherms that the deposit of the MgO nanoparticles inside the pores by the impregnation method does not destroy or modify its mesoporous cubic structure. The nanoparticles were successfully deposited on the catalyst support with the concentrations as we see in the XRD patterns, as well as in the termogravimetric analysis we can see that the support does not wear down so we have a catalyst fully resistant to be used for the biodiesel transesterification.

ACKNOWLEDGMENT

The authors express their gratitude to the following persons for the catalyst's characterization by different techniques: R. Velázquez Castillo (FI-UAQ, México); Financial support by PROMEP (Project UAQ-PTC-190) and FOFI-UAQ-2012 is gratefully acknowledged.

REFERENCES

[1] Eilhann EK, Jaegun S, Yi Haakrho. Transforming animal fats into biodiesel using charcoal and CO2. Green Chem 2012;14:1799.

[2] Harun R, Singh M, Forde GM, Danquah MK. Bioprocess engineering of microalgae to produce a variety of consumer products. Renew Sustain Energy Rev 2010;4:1037e47.

[3] Mata TM, Martins AA, Caetano NS. Microalgae for biodiesel production and other applications: a review. Renew Sustain Energy Rev 2010;14:217e32.

[4] T. Vega, L. Díaz, E. Hernandez, F. May, P. Castro, A. Castillo, G. González, L. Maldonado, "Thermogravimetric analysis as a rapid and simple method to determine the degradation degree of soy biodiesel"

[5] Agarwal AK, Rajamanoharan K. Biofuels (alcohols and biodiesel) applications as fuels for internal combustion engines. Progress in Energy and Combustion Science 2007;33(3):233–71.

[6] Singh SP, Singh D. Biodiesel production through the use of different sources and characterization of oils and their esters as the substitute of diesel: a review. Renewable and Sustainable Energy Reviews 2010;14(1):200–16. [5] Lapuerta M, Armas O, Rodrı´guez FJ. Effect of biodiesel fuels on diesel engine emissions. Progress in Energy and Combustion Science 2008;34(2): 198–223.

[7] Ahmad AL, Yasin NHM, Derek CJC, Lim JK. Microalgae as a sustainable energy source for biodiesel production: a review. Renewable and Sustainable Energy Reviews 2011;15(1):584–9

[8] Santos, I. C. M. S.; Paz, F. A. A.; Simo˜es, M. M. Q.; Neves, M. G. P. M. S.; Cavaleiro, J. A. S.; Klinowski, J.; Cavaleiro, A. M. V. Catalytic Homogeneous Oxyfunctionalization with Hydrogen Peroxide in the Presence of a Peroxotungstate. Appl. Catal., A 2008, 351, 166.

[9] De Vos, D. E.; Sels, B. F.; Jacobs, P. A. Practical Heterogeneous Catalysts for Epoxide Production. Adv. Synth. Catal. 2003, 345, 457.

[10] Hoegaerts, D.; Sels, B. F.; De Vos, D. E.; Verpoort, F.; Jacobs, P.A. Heterogeneous Tungsten-Based Catalysts for the Epoxidation of Bulky Olefins. Catal. Today 2000, 60, 209.

[11] Gao, R.; Yang, X.; Dai, W.-L.; Le, Y.; Li, H.; Fan, K. High-Activity, Single-Site Mesoporous WO_3-MCF Materials for the Catalytic Epoxidation of Cycloocta-1,5- Diene with Aqueous Hydroge Peroxide. J. Catal. 2008, 256, 259.

[12] D.Y. Zhao, J.L. Feng, Q.S. Huo, N. Melosh, G.H. Fredrickson, B.F. Chmelka, G.D. Stucky, Science 279, (1998) 548–552.

[13] C.L. Peza, L. Escamilla, R. Nava, B. Pawelec, J.L.G. Fierro, Appl. Catal. A: Gen. 375 (2010) 37-48.Goodrum J. Volatility and boiling points of biodiesel from vegetable oils and tallow. Biomass Bioenergy 2002;22:205–11.

[14] Demirbas A. Comparison of transesterification methods for production of biodiesel from vegetable oils and fats. Energy Convers Manage 2008;49:125–30.

[15] Gunstone FD. The chemistry of oils and fats: sources, composition, properties and uses. 1st ed. Boca Raton: CRC Press; 2004.

[16] Ott LS, Huber ML, Bruno TJ. Density and speed of sound measurements on five fatty acid methyl esters at 83 kPa and temperatures from (278.15 to 338.15) K. J Chem Eng Data 2008;53:2412–6.

[17] Chand P, Reddy CV, Verkade JG, Wang T, Grewell D. Thermogravimetric quantification of biodiesel produced via alkali catalyzed transesterification of soybean oil. Energy Fuels 2009;23:989–92.

[18] Chien Y-C, Lu M, Chai M, Boreo FJ. Characterization of biodiesel and biodiesel particulate matter by TG, TG_MS, and FTIR. Energy Fuels 2009;23:202–6.

[19] Focke WW, Van de Westhuizen I, Grobler AL, Nshoane KT, Reddy JK, Luyt AS. The effect of synthetic antioxidants on the oxidative stability of biodiesel. Fuel 2012;94:227–33.

[20] Souza FHN, Maia FJN, Mazzetto SE, Nascimento TL, de Andrade N. Oxidative stability of soybean biodiesel in mixture with antioxidants by thermogravimetry and Rancimat method. Chem Biochem Eng Q 2013;27:327–34.

Mobile application for monitoring and visualization of data applied to power quality systems

P C. Ramirez-Echeverria
Facultad de Ingeniería Querétaro
Universidad Autónoma de Querétaro.
San Juan del Rio, México.
pramirez@hspdigital.org

L. Morales-Velazquez
Facultad de Ingeniería Querétaro
Universidad Autónoma de Querétaro.
San Juan del Rio, México

R. de J. Romero-Troncoso
División de Ingenierías Campus Irapuato
Universidad de Guanajuato.
Salamanca, México.

R. A. Osornino-Rios.
Facultad de Ingeniería Querétaro
Universidad Autónoma de Querétaro.
San Juan del Rio, México

D. Morinigo Sotelo
Departamento de Ingeniería Eléctrica
Universidad de Valladolid
Valladolid, España

Abstract— **This paper presents the development of a mobile application for the android platform to perform sampling, Synchronization, transmission and control over a data-logger system for power quality analysis. The main function of this system is the sampling process and data storage of voltage and current values taken from the electrical assembly power grid. The power quality system transmits the data via basic Bluetooth radio frequency communication. Afterward, this data gets processed, classified, and displayed in real time.**

Keywords—*Android, Power Quality, Bluetooth, GUI*

I. INTRODUCTION

In the last century automation, telecommunications and computer industries have experienced an unprecedented growth. However the new generation of electronics is getting more sensitive to electromagnetic disturbances to the point that any disruption of the supply voltage may have destructive effects on the installed equipment, any disturbance manifested in the voltage, current, and frequency from the standard rate is treated as a power quality (PQ) problem. Power quality covers several aspects including the measuring, analysis and the improvement of the load bus voltage [1]. A lot of the phenomena related to power quality may appear and disappear arbitrarily, because of this finding electric disturbances are more complicated than a simple measurement of an electric parameter. It is necessary to monitor the grid over a long time interval to acquire a big amount of data to get a better idea of what is going on in the power grid [2]. The most typical approach for power quality analysis systems in the industry is having an on-purpose-built monitoring device that takes cares of the plotting, analysis, monitoring and graphic user interface [3]. However, this system is expensive at prices range of 9000 USD with closed software and a lack of versatility on the hardware. There are cases where the number of devices needed to perform a PQ analysis make it economically unreasonable [4]. Therefore, methods that may reduce the price of power quality analyzer (PQA) system are needed. There are several works where the use of a mobile implementation can increase the efficiency of industrial and commercial processes [5-7]. In some cases, several power quality systems get connected to a single power grid to analyze the estate and investigate if a PQ event occurring in one part of the grid can affect other components of the power grid [4]. For this reason, a way to synchronize all the data logging systems and the option to turn on and off the sampling is needed. The motivation for the approach described in this text was to allow on-site technicians to be able to use their everyday mobile phone for wireless diagnostic purposes both in terms of data acquisition as well as signal processing. The PQ system used in this work is a based-field programmable gate array (FPGA) used for data logging. This system can perform a fast and precise data acquisition of the supply voltage and current, it has the capacity to connect to a smartphone to transmit and acquire data wirelessly. In this work the feasibility of using a mobile phone application for signal processing, the monitoring, and synchronizing of a PQ data logging system is presented.

II. THEORETICAL BACKGROUND

A. Android mobile device

Thanks to the constant advances in the development of mobile phones, android technology has become more efficient each generation and the amount of sensors and other hardware have increased depending on the necessities of the consumers. Android runs on an open-source Linux Kernel [8], designed from the beginning as an advanced mobile operating system. Nowadays the majority of the people counts with a smartphone, this gives the possibility of having sensors and

data analysis systems on the palm of the hand of the majority of technicians, because of this, the possibility of doing tasks like plotting, graphic interface and data acquisition is possible to perform on a mobile platform and its open philosophy ensures an easy and growing development [9].

B. Bluetooth

Bluetooth is one of the most popular and economic wireless technology, this is because Bluetooth is robust, has low cost, low power consumption and is used worldwide [10]. The communication protocol is defined in the hardware abstraction of the Bluetooth. The pairing and data control are defined by the Bluetooth special interest group (Bluetooth SIG) [11], the packet structure of a Bluetooth transmission gets defined on logical link control and adaptation layer protocol (L2CAP), this define that the max limit of the packet for the serial transmission is 64 kilobytes and it gets recommended that the velocity of transmission do not go over 113200 if the communication gets done in an environment with a lot of physical and radio frequency interferences. Wireless communication via Bluetooth in the Android is managed by the application programming interface (API) Bluetooth, this API exist since the release version number one of Android OS, it permits applications to use the Bluetooth hardware in a mobile phone, to connect to other Bluetooth hardware, scan for other devices and establish R FCOM channels [12].

C. Power Quality Analisis

To have a basic analysis of the state of the data acquisition system indices of power quality $Vpeak$ and $Ipeak$ are acquired in the time domain like the max values in the analyzed interval, as it is shown on (1) and (2) [13].

$$Vpeak = max(V(t)) \tag{1}$$

$$Ipeak = max(I(t)) \tag{2}$$

The root mean square (RMS) are other values that are processed and it is needed to get an average of the values in the channel. Formulas are shown in (3) and (4) [14].

$$Vrms = \frac{1}{\sqrt{2}} \sqrt{\sum_{n=1}^{N} {V_n}^2} \tag{3}$$

$$Irms = \frac{1}{\sqrt{2}} \sqrt{\sum_{n=1}^{N} {I_n}^2} \tag{4}$$

III. METODOLOGY

The developed application consist of a synchronization module, a plotting module, and a data acquisition, request and classification modules and the user commands that dictate which operation must be executed. A functional diagram of the monitoring system developed is presented In Fig. 1. The Android mobile device is bonded via Bluetooth to the PQ system. Depending on the control, the instruction sent by the mobile phone the PQ system sends data requested. When the data reach the mobile phone, the ways the data is going to be used depends on the instruction given by the user, this is if the user needs to plot or to synchronize the data-logger FPGA system. Settings such as scale, color, offset, style and name of the signals on the plot are set by the user on the Plot Editor.

Fig. 1. Functional Diagram of the systems used in this paper.

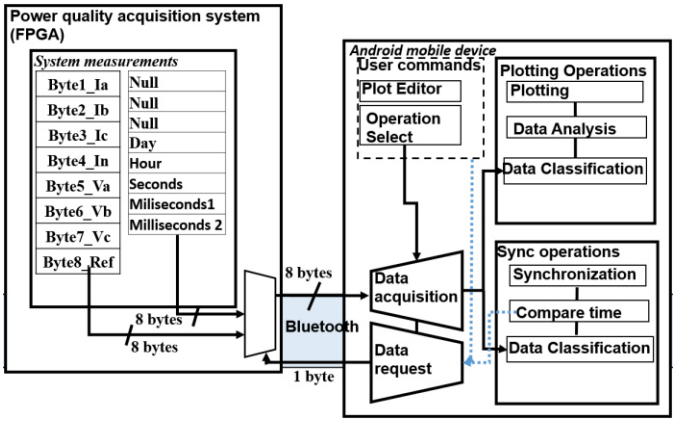

A. User commands

User commands comprehend all the configurations and operations that the user input via the user interface and the *Plot Editor*. In Fig. 3, a flow diagram showing how the *Plot Editor* manages actions is shown. *Plot Editor* is in here in order to change and set values as gains, color, offset. Etc. Actions like deciding to plot or synchronize are selected in this section by the user. This set of commands get implemented primarily by buttons with OnClickListener method events [15] for plotting, synchronization and the *Plot Editor*.

B. Data acquisition ,Data request and data classification

After the connection with the PQ system, data acquisition is administrated by Bluetooth APIs. The data sent by the power quality acquisition system is a total of 8 bytes for each one of the signals acquired from the data logger. This data gets saved on a first in, first out (FIFO) type of buffer declared on the main function like a global buffer and every class has access to a copy of this FIFO when it needs the sampling data. In Fig. 2 a diagram of the packets of the data logger and the Android platform packets transfer is presented. When the Android sends the character "Z" in binary the PQ system sends the data logged sampled values taken in the request moment. In Fig. 1 and Fig. 2, when executing the plotting the data gets separated on channels each one with 1 byte for each point of the plot being drawn. After being divided, each one of the channels gets assigned a label set on the *Plot Editor*. The application can also request for time data when a synchronization is getting requested. In Fig. 3 the data transfer of the synchronization operations is shown, in this process, the data being acquired gets divided into values of time and sent to the

sync operations until the system gets a successful synchronization.

Fig. 2. Data transfer packages between the android application and the PQ data logger.

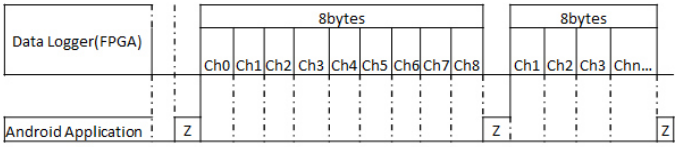

C. Sync Operations

Sync Operations is the module than the Android application uses in order to get a successful synchronization. In Fig. 3 a diagram of the packages sent is shown. In this diagram, time data is sent and received in binary coded decimal (BCD) in Fig. 3 the composition of the data packages is shown, in this packages the character "t" is used to indicate when does each of the packages ends and begins, the values represented by Y, d, h, m, s, ms1 and ms2 correspond to the values in BCD of the year, day, hour minute, second, the first part of the milliseconds value and the second part of the millisecond value. In Fig 4, the flow diagram of the algorithm used to synchronize is shown. In this figure, Hand is the coordinated universal time (UTC) of the Android phone. Hfpga, is the FPGA time, the character "a" is sent to indicate the beginning of a synchronization to the PQ system, the character "D" is used to set the PQ system time 10 second forward and, character "U" is used to set the time 10 second backwards.

Fig. 3. Data packages in the process of the synchronization.

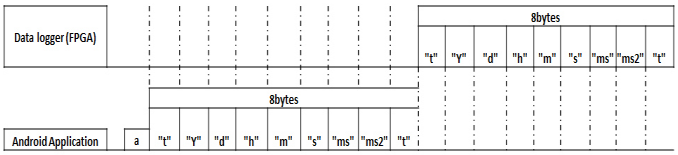

Fig. 4. Synchronization process between Android and the PQ system.

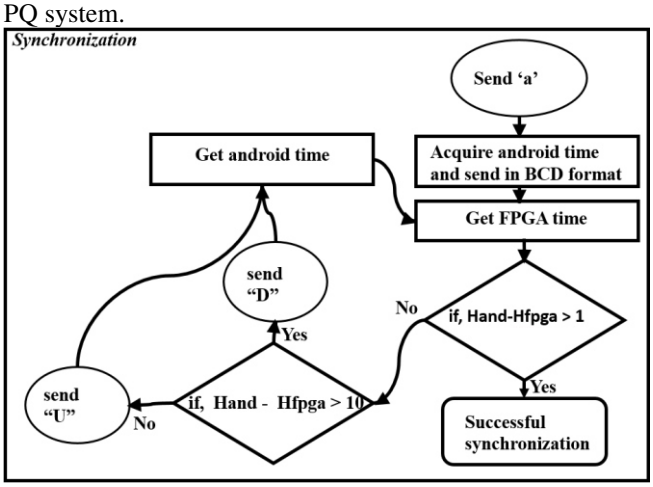

To acquire the UTC time the mobile phone needs to use the method CurrentTimeMillis of the class System [16]. This method always returns UTC time, this measurement of time can be found in the majority of mobile devices and GPS, the method CurrentTimeMillis gives the values of time in milliseconds and the user has to transform or transcribe the data depending on the necessity when an algorithm or the class SimpleDateFormat that permits the user to format and parse dates gets executed. UTC have the precision needed to perform a synchronization and is easy to use for inexperienced users in time formats because the format is almost identical to the local time format. When doing a synchronization, one pulse per second is the minimum to get an acceptable synchronization [17], and precision of the application developed in this work can reach a precision of 1 millisecond. It is worth mentioned that every smartphone has a different internal clock, however, all the Android mobile devices are coordinated or synchronized with the UTC time via internet.

E. Data analisis.

On the data analysis, the RMS and peak values of the voltage and current are obtained using (1), (2), (3) and (4) whith the class math [18], from each one of the channels, and assign a variable to get used in the plot of the signal.

F. Android Paint and Canvas

Classes Canvas [19] and Paint [20] are methods that exist since API number one and are part of the Android Open Source Project [21], this means all the Android devices are able to use these classes, in the Android OS. To draw the screen, you need a valid canvas object by extending the view class. The paint object stores far more than color. The Paint class encapsulates the style and complex color and rendering information that can be applied to a drawable.

G. Plotting

In Fig. 5, the process to plot is presented. When the stream of data gets separated, each channel is painted with Canvas and Paint. Canvas, in this case, is used to determine the view where the plot is going to be draw, Canvas also drawn each one of the points from all the channels via the method drawline [19], plotting the acquired data from the power quality acquisition sampling the values calculated of the RMS and peak, these values are shown using the method drawtext [19]. Paint is used in a dedicated thread, the plot user interface (UI) also has some commands to control when you want to start or stop plotting, the colors chosen to plot each one of the channels and their gains can be modified from the *Plot Editor*.

Fig. 5. Flow diagram for the plotting module.

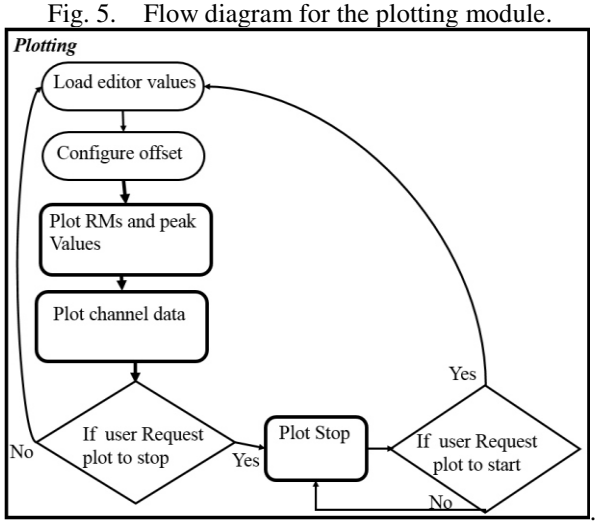

IV. RESULTS

A. Experimental setup

The data was generated on a dedicated test rig which is presented in Fig. 4, it is comprised of a .74kW induction motor with nominal speed of 3355 RPM.

Fig. 6. Induction motor on the test rig.

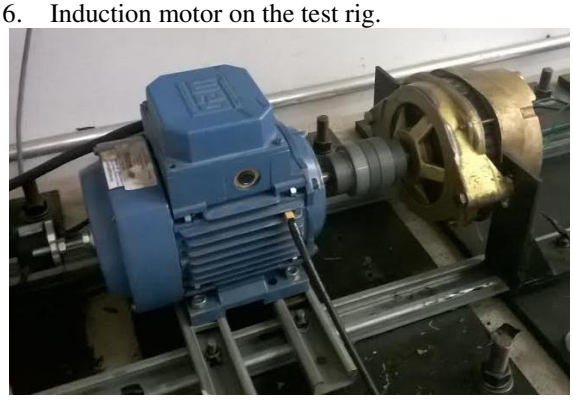

The instrumentation in Fig. 5,is comprised of 4 banana cables connected to three phase electric voltage *a*, *b* , c and neutral voltage and 4 AC Current Clamps i200 [22] to get the values of current *a, b, c* and the neutral of the three phase electric power.

Fig. 7. Instrumentation on the test rig.

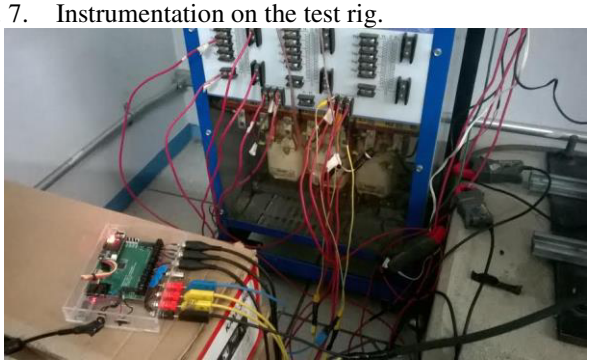

The last component of the test rig was the Power Quality data acquisition system PQ_UAQ, this system is an FPGA based system developed by the Universidad Autonoma de Queretaro (UAQ). This main function of this system is to work as a data-logger of the electric events on the motor. It uses an HC-06 Bluetooth to transmit data wirelessly to the mobile phone, and obtains the data through an ADC data acquisition system developed by UAQ. The Android smartphone used in this test was a LG-H420 with Android version 5.01. The test consisted of running the motor, Synchronizing the PQ_UAQ, turning on the data-login in the mobile phone application PQ_UAQ, plotting data from the moment the motor started running and, drawing the data being sent to the Android phone by the PQ_UAQ.

B. Results

This section shows the results of monitoring the power quality system PQ_UAQ by the application installed on a smartphone. At the moment of the test, the sine wave of each voltage on the three-phase power lines connected to the motor could be easily observed, RMS and Peak of the voltage and current during the test were displayed on the screen as shown in Fig. 8 .Each of the Voltage and Current of the three phase connection could be observed, current lag could also be observed. The way the channels displayed look, was edited on the application plot editor by the user. It's worth to mention that currently there are other kinds of android applications to monitor measurement system like fluke connect, however this kind of program doesn't have compatibility with a lot of old or recent Android versions phones and its only possible to use the limitation of only being able to use it with some specific fluke products make it a bad choice to monitor the PQ_UAQ.

Fig. 8. Plot of the monitoring Application working on a smartphone.

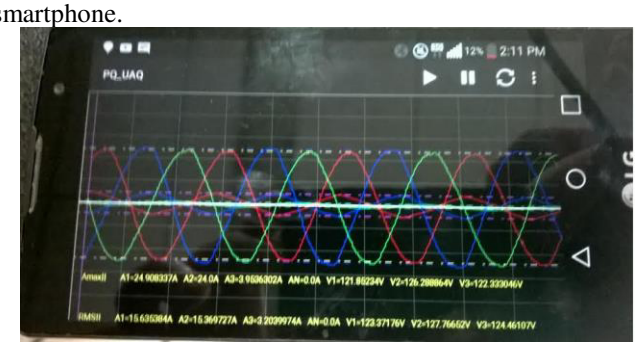

V. CONCLUSION

The use of mobile application for monitoring a power quality system enabled that anyone who wanted to monitor the system signal could see in what estate the connection was, problems such as cables disconnected were detected in the moment of the installation and synchronization of the power quality system, this implementation made power quality events easier to detect in the moment of an analysis of the data saved in the

system. Not to mention the use of a mobile application would mean that typical plotting in real time of the power quality signal could be performed without the need for extra equipment which would make the system more costly and less practical. The process of creating the application has proven that the mobile monitoring and synchronizing of a power quality system is possible and it can improve the efficiency of existing systems.

A. Autores y aflicaciones

Pablo Cesar Ramírez Echeverría, masters student of the Maestría en ciencias de la mecatrónica, in the Universidad Autónoma de Querétaro, campus San Juan del Rio.

ACKNOWLEDGMENTS

The authors of this work whishes to thanks the Universidad Autónoma de Querétaro, Campus San Juan del Río and the Universidad de Valladolid, España, for facilities granted to carry out this investigation.

This work was partially supported by CONACyT scholarship number 632286 and by projects SEP-CONACyT 222453-2013 and PROMEP 103.5/14/710401.

Partially financed by FOFIUAQ-FIN201613

REFERENCES

[1] K. Mazlumi, "Power Quality Monitoring", in Power Quality Monitoring, Analysis and Enhancement, A. zobba, Ed. ISBN: 978-953-307-330-9, In Tech, 2011.

[2] G. Găşpăresc, "Methodes of Power Quality Analysis", in Power Quality Monitoring, Analysis and Enhancement, A. zobba, Ed. ISBN: 978-953-307-330-9, In Tech, 2011.

[3] Fluke 430 Series II, Technical Data, Fluke Corporations, 2012.

[4] N. Gupta, A. Swarnkar, and K. R. Niazi, "Distribution network reconfiguration for power quality and reliability improvement using Genetic Algorithms," Int. J. Electr. Power Energy Syst., vol. 54, pp. 664–671, 2014.

[5] P. Rzeszucinski, M. Orman, C. T. Pinto, A. Tkaczyk, and M. Sulowicz, "A signal processing approach to bearing fault detection with the use of a mobile phone," pp. 310–315, 2015.

[6] T. H. Khan, R. Shrestha, K. a. Wahid, and P. Babyn, "Design of a smart-device and FPGA based wireless capsule endoscopic system," *Sensors Actuators A Phys.*, vol. 221, pp. 77–87, 2015.

[7] M. del Rosario, S. Redmond, and N. Lovell, "Tracking the Evolution of Smartphone Sensing for Monitoring Human Movement," *Sensors*, vol. 15, no. 8, pp. 18901–18933, 2015.

[8] B. Pon, T. Seppälä, and M. Kenney, "Android and the demise of operating system-based power: Firm strategy and platform control in the post-PC world," *Telecomm. Policy*, vol. 38, no. 11, pp. 979–991, 2014.

[9] R. Meier, Android Application Development, Wiley Publishing, Inc., vol. 131. 2010.

[10] R. Heydon, Bluetooth low energy : The developer's handbook. " Prentice Hall. 2012.

[11] Specification of the Bluetooth System Master Table of Contents & Compliance, vol. 0,Agere systems, Inc, Ericsson Technology Licensing, AB, IBM Corporation , Intel Corporation, Microsoft Corporation, Microsoft Corporation, Motorola, Inc, Nikia Corporation, Toshiba Corporation, 2004.

[12] L. D. Granados, "Análisis en maquinaria CNC ante variaciones de bajo voltaje y sus efectos de calidad de la energía.", PhD Tesis, Universidad Autónoma de Querétaro, San juan del rio, Querétaro, Jul 2013.

[13] H. Junfeng, S. Hao, and W. Xiaolin, "Design of Power Quality Monitor Based on Embedded Industrial Computer," *Phys. Procedia*, vol. 24, pp. 63–69, 2012.

[14] The Android Open Source Project, Bluetooth [Online]. Aviable: http://developer.android.com/intl/es/guide/topics/connectivity/bluetooth.html.

[15] The Android Open Source Project, View.OnClickListener [Online]. Aviable: http://developer.android.com/intl/es/reference/android/view/View.OnClickListener.html

[16] The Android Open Source Project, System [Online]. Aviable: http://developer.android.com/intl/es/reference/java/lang/System.html.

[17] Y. Zhang, L.T. Yang, J.Ma, "Detailed DSRC-WAVE Architecture", In Unlicensed mobile access technology, Boca Raton, Florida, Us, Taylor & Francis Group , 2009, Ch. 15. Sec. 15.5.2, pp. 311.

[18] The Android Open Source Project, Math [Online]. Aviable: http://developer.android.com/intl/es/reference/java/lang/Math.html.

[19] The Android Open Source Project, Canvas [Online]. Aviable:

http://developer.android.com/intl/es/reference/java/lang/System.html.

[20] The Android Open Source Project, Paint [Online]. Aviable: http://developer.android.com/intl/es/reference/java/lang/System.html.

[21] The Android Open Source Project, Android Open Source Project [Online]. Aviable: https://source.android.com/.

[22] FLUKE i200/i200s Ac Current Clamp, Technical Data, Fluke Corporations, 2005.

Electricity production from maize processing wastewater in a microbial electrochemical cell

Manuel Alejandro Garita Meza
Ingenierías Renovables
Universidad Tecnológica de Querétaro
Querétaro, Mexico
Alejandro_garita@hotmail.com

Bibiana Cercado, Roberto Contreras
Subdirección de Investigación
CIDETEQ S.C.
Pedro Escobedo, Mexico
bcercado@cideteq.mx

***Abstract*— Microbial fuel cells (MFCs) are devices that convert chemical energy into electrical energy via the metabolic activity of microorganisms. The MFCs can be fed with organic matter present in wastewater, thus a double benefit is obtained: pollution removal and clean energy production. Nowadays, the maize processing wastewater (MPWW) from small enterprises is discharged with no previous treatment because the wastewater volume is low. Nevertheless the organic content in MPWW could be exploited. The aim of the present work is to determine the feasibility of using real MPWW to produce electricity in a MFC. The MPWW was tested in a three-electrode electrochemical cell with no dilution as control, and with 1:2, 1:3, and 1:4 dilutions. A potential of +0.1 V/Ag/AgCl was applied to the cell for 12 days and the current production was monitored. The organics removal was followed as the chemical oxygen demand (COD) reduction. The results indicated that the MPWW contained electrochemically active microorganisms, but the 1:2 dilution was the most favorable for current production reaching 100 mA m^{-2} in 9 days. The COD removal percentage was from 7.8 % to 13.7 % for 12-14 days of the test. This work demonstrates that real MPWW can be exploited for electricity production in MFCs, and the findings provide the basis to develop this technology in Mexico.**

Keywords— ***Microbial fuel cell; electricity; wastewater; bioenergy; depollution***

I. INTRODUCTION

Microbial fuel cells (MFCs) are devices that convert the chemical energy in organic matter into electricity via the catalytic activity of microorganisms. The microorganisms capable of transferring electrons to a solid material are called electrochemically active. These microorganisms adhere onto carbon based electrodes to form bio-electrodes. As regular electrochemical cells, the MFCs are composed of an anodic chamber where the oxidation of organic matter occurs to produce CO_2, H_2O, electrons, and protons. The electrons are transferred from the anode toward the cathode via an external electrical circuit. The protons migrate from the anodic chamber toward the cathodic chamber reducing the oxygen present in the media [1]. Because the fuel in MFC is organic waste matter, a broad diversity of wastewater has been utilized as a substrate for the electrochemically active microorganisms. For instance domestic and food industry wastewater has been frequently utilized [2].

Maize industry in Mexico has a great impact. The grains are processed with a high water volume at high temperature. It is estimated that the consumption of 75 L of water to process 50 kg of maize is required. The monthly generation of maize processing wastewater (MPWW) is reported to be 1.2 x 106 m^3 [3]. The effluents of MPWW have various pollutant characteristics: pH 11, chemical oxygen demand (COD) 40 g L^{-1}, total solids 2.5%, in addition to high temperature because of the thermic-alkaline process involved. However MPWW also contains proteins (0.11%), carbohydrates (0.85%), vitamins and minerals that might be exploited [4].

The small-sized enterprises that produce MPWW in low volume do not treat the effluents; instead the effluents are discharged into soil or sewage. Thus, these type of effluents provoke environmental pollution. Nowadays this activity is not regulated in Mexico, therefore reports on the magnitude of discharges are not available.

Organic matter in food industry wastewater has been exploited in MFCs with some drawbacks. The complex and high organic content regularly prevents the optimal MFC performance [5]. Nevertheless Sevda et al. [6] has proposed diluting the high strength wastewater with sewage wastewater to improve the MFCs performance.

The MPWW is a regional problem for that reason nowadays no report exists on its use in MFCs. This work intends to demonstrate that the MPWW can be utilized as fuel or substrate in MFCs to produce electricity. This strategy will allow environmental pollution to be reduced, and to produce clean and sustainable energy such as electricity for small-sized enterprises.

The present work aimed to exploit the carbohydrate and protein content in MPWW. Dilution of real samples and their evaluation in three-electrode electrochemical cells was performed. Current production, experimental charge, identification of redox processes, and organic removal were determined for each dilution. The best conditions for energy production and COD removal were determined.

II. MATERIALS AND METODS

A. Wastewater samples

The main characteristics of the MPWW were a pH 12.05 ± 0.35, a conductivity 7.55 ± 0.07 mS/cm and a COD 2317 ± 138 mg L^{-1}. The MPWW was diluted to 1:2, 1:4, and 1:10 ratios with a phosphate buffer solution 50 mM and pH 7. Table I shows the final characteristics for each dilution.

TABLE I. CHEMICAL CHARACTERISTIC OF RAW AND DILUTED MPWW.

Parameter	Dilution			
	Raw	*1:2*	*1:4*	*1:10*
pH	11.6	6.7	6.6	6.7
Conductivity (mS cm^{-1})	6.3	6.9	10.0	11.6
Disolved solids (ppt)	3.2	4.4	5.6	5.8
COD (mg L^{-1})	2317	1158	579	232

B. Electrochemical experimental setup

A three-electrode electrochemical cell was used in the test. Carbon felt in 2 cm x 2 cm x 0.5 cm size (Carbon Lorraine, France) was used as the working electrode, platinum mesh in 2.5 x 2.5 cm (Alfa Aesar, USA) as the counter-electrode, and an Ag/AgCl, 3 M KCl as the reference electrode. All the voltage values refer to this electrode. The external connections were made with titanium wire (Alfa Aesar, USA). The electrodes were connected to a potentiostat/galvanostat to control and monitor the process (BioLogic VSP, EC-Lab software v10.23). The total and operational volume of the electrochemical cell was 120 mL and 100 mL respectively. The temperature in the cells was kept constant in a water bath at 30 °C.

C. Analytical characterization

The pH and conductivity of the MPWW were measured with a meter multiparameters (Oakton PCD 50, USA). The COD was determined in the raw and diluted MPWW with the reflux method of a COD high range kit (Hach, USA). The electrode was characterized by the voltage at the open circuit over 2 h and cyclic voltammetry in the range from +1.0 V to -1.0 V at a scan rate of 10 mV s^{-1}. The electrochemically active biofilm was developed at +0.1 V for 12 days, and the current density production was monitored by chronoamperometry. The chemical and electrochemical tests were performed at the startup and end time in all the experiments.

III. RESULTS AND DISCUSSIONS

The first test intended to determine the presence of electrochemically active microorganisms. Thereafter, the electrochemical cell performance was improved by dilutions of the organic content in the MPWW. The bioelectrochemical process was monitored by various electroanalytical techniques, and the best operational conditions were determined.

A. Presence of electrochemically active microorganisms

Current density did not increase in the first 2 days with raw MPWW in the electrochemical cell; therefore acetate (20 mM) was supplemented. After 1.5 days the current began to increase and reached up to 0.0128 mA (32 mA m^{-2}) in 6.5 days of operation. This result indicated that electrochemically active microorganisms were present in the MPWW.

The acetate has been broadly recognized as the substrate that produces the best performance in MFCs [2]. The addition of sodium acetate to raw MPWW stimulated the activity of electrochemically active microorganisms, which was a first step to prove the feasibility of using this type of wastewater for electricity generation. However the current produced was moderate because the environmental conditions were not optimal for the electron transfer and the microbial growth. Therefore the strategy of wastewater dilution with a buffer for pH adjustment was followed.

B. Open circuit potential of electrodes and bioelectrodes

The open circuit potential of bioelectrodes for the different MPWW dilutions is shown in Table II. The stabilization time (2 h) was enough to determine the open circuit values, however it was noted that these values were more stable in the electrode when the biofilm had already been developed, i.e. at the end time.

TABLE II. OPEN CIRCUIT POTENTIAL (V) OF GRAPHITE CARBON ELECTRODE IN RAW AND DILUTED MPWW.

Test	Startup time		End time	
	Initial	*Final*	*Initial*	*Final*
No diluted MPWW	-0.54	-0.64	-0.05	-0.05
1:2 dilution	-0.01	-0.01	-0.44	-0.43
1:4 dilution	0.001	0.009	-0.35	-0.36
1:10 dilution	-0.008	0.005	-0.05	-0.06

The more unstable open circuit potential measurements at the beginning of the test were due to the process of biofilm formation. This involves the adhesion of bacteria to the solid surface, the growth of colonies, and the spreading out of the colonies in horizontal and vertical direction [7].

The open circuit voltage at the end of the test was modified toward more negative values for all dilutions. Conversely, this voltage increased at the end of the test only for the raw MPWW. The more negative potential value was observed for the bioelectrode with the 1:2 dilution.

The more negative potential values indicated an accumulation of reduced species on the electrode. The reduced species might be diverse; for instance catalytic proteins involved in the proton transport chain such as NADH, molecules produced during catabolic microbial reactions (as volatile fatty acids), or even that the protons of the buffer solution. A shift in the bioanode potential toward negative values has been observed for MFCs operating in better conditions and therefore has the best performance [8].

Therefore it can be assumed that the bioelectrode from the 1:2 dilution with the more negative potential could be the most adequate to construct a MFC.

C. *Identification of oxidation processes by cyclic voltammetry*

The identification of electrode reactions was supported by cyclic voltammetry. The current density observed along the voltage scan of the bioelectrodes had a greater current at the end of the test than at the beginning of it. This comportment was repeated for all MPWW dilutions, but the opposite results were obtained with the raw MPWW. Utilizing undiluted MPWW the current density was lower at the end than at the beginning of the test (Fig. 1A).

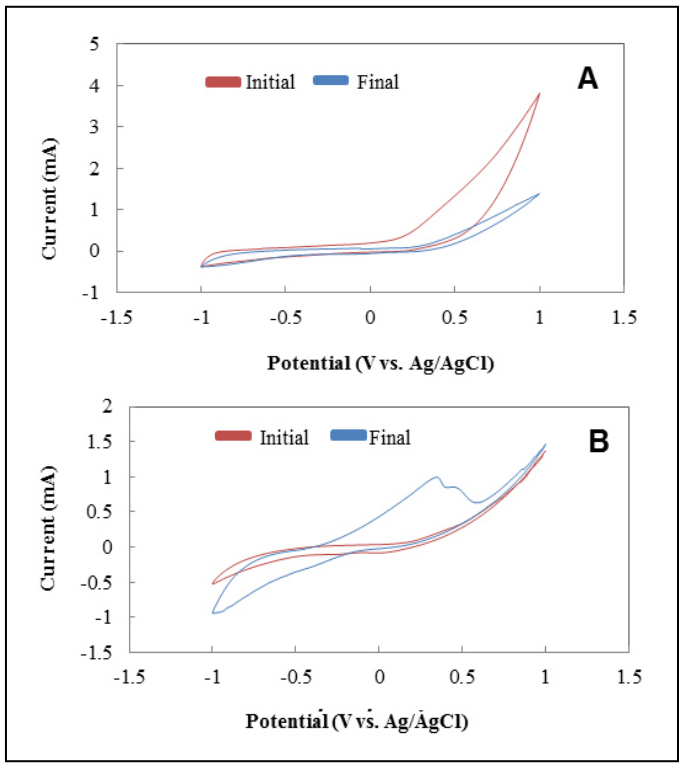

Fig. 1. Cyclic voltammetry of carbon felt in MPWW. A) Wastewater with no dilution, B) Watewater with 1:2 dilution. Test at 10 mV s^{-1} in anodic direction

The current density observed at the beginning of the test with the raw MPWW during the cyclic voltammetry was explained by the presence of easily biodegradable molecules in the medium. It can be assumed that a small amount of monomers were present at the startup time. These molecules were easily consumed by the microbial population generating a relatively high current density. Because the organic polymers such as starch required a period to be degraded into oligomers and monomers, very likely the microbial population lacked of a ready-consumption substrate at the end of the test, thus provoking a low current density. Another explanation for a final low current density could be the inability of the microorganisms growing in a basic medium to transfer electrons. This last assumption was based on the absent redox peaks in the voltamperogram, suggesting that the current density observed was mainly due to an abiotic oxidation rather than to a microbial oxidation of organic matter on the electrode.

The voltamperograms of bioanodes at the end of the test, when the biofilm was entirely formed, showed oxidation peaks with current intensity depending on the dilution ratio. The 1:2 dilution resulted in a oxidation peak of 0.95 mA (2375 mA m^{-2}) at +0.3 V (Fig. 2B); the 1:4 dilution generated a peak of 0.25 mA (625 mA m^{-2}) at -0.1 V, and finally the 1:10 dilution led to a peak of 0.30 mA (750 mA m^{-2}) at +0.3 V. Even though the voltamperograms at the initial time showed some redox signals, these signals were much lower than those observed at the end of the experiments, except for the highest dilution (1:10) where redox signals were similar at the beginning and end of the test.

The oxidation peaks in the voltamperograms of MPWW dilutions were the result of the developed electroactive biofilm along the test. The oxidation peaks were not related to the presence of reduction peaks, which indicated that the reaction was irreversible and oxidation reactions predominated over reduction reactions. The oxidation signals in voltamperograms has been explained by the direct contact of the electrode with catalytic proteins in the microbial membranes, these proteins commonly are attributed to cytochrome C complexes [9]. Therefore the intensity of the oxidation peak could be proportional to the quantity of the adhered microorganisms, but also could be proportional to the compounds accumulated in the biofilm-electrode interface that continue to be oxidized.

Overall, the 1:2 dilution seemed to be the most adequate to form bioelectrodes as indicated by the highest oxidation peak; moreover this result agrees with the more negative open circuit potential registered for the bioanode with the same dilution.

D. *Current density production by chronoamperometry*

The chronoamperograms for the raw MPWW and the dilutions are shown in the Fig. 2. The undiluted MPWW produced the lowest current density (1.7 μA), followed by the highest dilution 1:10 (6.1 μA), the 1:4 dilution (10 μA), and finally the 1:2 dilution, which reached up to 40 μA (100 mA m^{-2}).

The experimental charge followed the same pattern for the raw and diluted MPWW being the highest experimental charge 22.5 C for the 1:2 dilution and the lowest 1.8 C for the 1:10 dilution. The rate of increase in current density was also affected by the dilutions. The more diluted sample attained the maximum current peak faster than the other samples (Fig. 2).

The differences in the startup time, experimental charge, and maximum current density were the result of a synergic effect of the available substrate, microbial population density, and mass transfer phenomena. A fast current production can be associated to a faster biofilm formation, which is conditioned by a nutritional stress; thus the more diluted sample resulted in the faster current production.

On the other hand, a high organics concentration provokes a divergent flux of electrons by biotransformations that are not associated with the electron transfer toward the electrode.

Complex and concentrated substrates promote the growth of suspended cells, which compete with the attached cells for nutrients, as well as deviate the electrons toward redox reactions in the liquid phase rather than electrochemical reactions in the liquid-solid interphase [5].

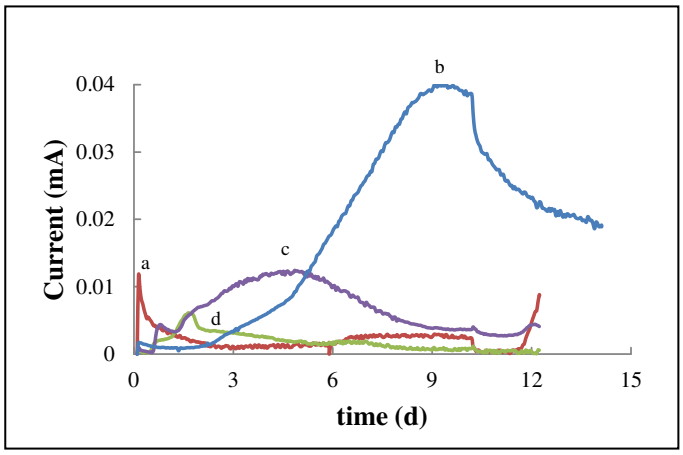

Fig. 2. Cronoamperometry of carbon felt in MPWW. a) Wastewater with no dilution, and diluted wastewater in b) 1:2 dilution, c) 1:4 dilution, d) 1:10 dilution.

The maximum current density is attained when an equilibrium between the substrate concentration and the biofilm thickness occurs. It has been assumed that the biofilm thickness is proportional to the amount of electrochemically active bacteria on the electrode, and thus to the current generation [10]. However a larger microbial density could hinder the substrate diffusion to the inner layer of the biofilm, so reducing the electron transfer originated by the oxidation of substrates [10].

The equilibrium mentioned above, among the substrate concentration and the biofilm thickness, seemed to be reached with the 1:2 dilution, and was in agreement with the open circuit potential and the oxidation signals by cyclic voltammetry.

E. Organic matter removal

The organics removal was quite low for the raw and the diluted solutions of MPWW. The COD reduction was from 2317 mg L^{-1} to 2135 mg L^{-1} with the raw wastewater, which corresponded to 7.8%. Similarly, the COD concentration with the highest dilution 1:10 reduced from 232 mg L^{-1} up to 200 mg L^{-1}, i. e. a 13.7% percentage removal.

Regularly the COD removal depends on the initial COD concentration. In that sense, the lowest percentage removal was observed for the less diluted sample. This performance is explained by the catalytic capabilities of microorganisms to mineralize the organic matter into CO_2, as well by the hindered mass transport phenomena in a more concentrate medium.

Even though the microbial population is able to transform the organic compounds in the medium, the extremely high concentration of these compounds resulted in a small inoculum to substrate ratio. The microorganisms were then not capable of transforming the organic matter at a high rate enough to reduce the COD concentration in an acceptable percentage value.

In a practical point of view, the highest dilution 1:10 led to a COD concentration similar to those of domestic wastewater that can be treated easily with common biological methods [11], nevertheless the interest in the present work is to exploit the MPWW in its actual physical-chemical characteristics. Alternatively, a strategy to dilute the input liquid current to a microbial fuel cell is recirculation of its own effluent, or diluting the input current with other process discharges.

In Central America and in Mexico the use of maize grains is broadly extended. The MPWW from small-sized enterprises is regularly ejected to sewage or to bare soils. Moreover this type of practice occurs in rural areas where electrical supply might be scarce. The bioelectrochemical systems such as the microbial fuel cells could contribute to exploit the MPWW to produce electricity in rural areas. In the present work the proof-of concept for a MPWW based microbial fuel cell has been validated. The improvement of the current density production was achieved by dilution of raw MPWW with a buffer solution. Although there exist some engineering strategies to overcome the dilution step, for instance with recycling or dilution with domestic wastewater, more investigation is necessary to optimize this bioelectrochemical process.

IV. Conclusions

Microbial fuel cells are of increasing interest because they allow the exploitation of wastewater to produce clean energy. This work demonstrated that maize processing wastewater contains electrochemically active microorganisms. However, the high concentration of the complex compounds hindered a high performance. The current production was improved by dilutions of the raw wastewater with a buffer solution. The optimal dilution was determined as 1:2 ratio; which resulted in 100 mA m^{-2}. That dilution ratio also allowed the maximum experimental charge 22.5 C, and the maximum oxidation peak determined by cyclic voltammetry as 2,375 mA m^{-2}.

Acknowledgment

This research was financially supported by the SEP-CONACYT project 177441, and the research is related to the SENER-CONACYT projects 246052 and 247006. MAGM thanks CONCYTEQ for the scholarship from Nuevos Talentos Científicos y Tecnológicos program. The authors thank Eric A. Huston from Peace Corps for proofreading the manuscript.

References

[1] B. E. Logan, B. Hamelers, R. A. Rozendal, U. Schrorder, J. Keller, S. Freguia, et al., "Microbial fuel cells: Methodology and technology," Environmental Science & Technology, vol. 40, pp. 5181-5192, Sep 2006.

[2] D. Pant, G. Van Bogaert, L. Diels, and K. Vanbroekhoven, "A review of the substrates used in microbial fuel cells (MFCs) for sustainable energy

production," Bioresource Technology, vol. 101, pp. 1533-1543, Mar 2010.

[3] A. Salmeron-Alcocer, N. Rodriguez-Mendoza, V. Pineda-Santiago, E. Cristiani-Urbina, C. Juarez-Ramirez, N. Ruiz-Ordaz, et al., "Aerobic treatment of maize-processing wastewater (nejayote) in a single-stream multi-stage bioreactor," Journal of Environmental Engineering and Science, vol. 2, pp. 401-406, Sep 2003.

[4] C. Valderrama-Bravo, E. Gutierrez-Cortez, M. Contreras-Padilla, I. Rojas-Molina, J. C. Mosquera, A. Rojas-Molina, et al., "Constant pressure filtration of lime water (nejayote) used to cook kernels in maize processing," Journal of Food Engineering, vol. 110, pp. 478-486, Jun 2012.

[5] A. ElMekawy, S. Srikanth, K. Vanbroekhoven, H. De Wever, and D. Pant, "Bioelectro-catalytic valorization of dark fermentation effluents by acetate oxidizing bacteria in bioelectrochemical system (BES)," Journal of Power Sources, vol. 262, pp. 183-191, Sep 15 2014.

[6] S. Sevda, X. Dominguez-Benetton, K. Vanbroekhoven, H. De Wever, T. R. Sreekrishnan, and D. Pant, "High strength wastewater treatment accompanied by power generation using air cathode microbial fuel cell," Applied Energy, vol. 105, pp. 194-206, May 2013.

[7] K. Hori and S. Matsumoto, "Bacterial adhesion: From mechanism to control," Biochemical Engineering Journal, vol. 48, pp. 424-434, Feb 15 2010.

[8] B. Cercado-Quezada, M. L. Delia, and A. Bergel, "Testing various food-industry wastes for electricity production in microbial fuel cell," Bioresource Technology, vol. 101, pp. 2748-2754, Apr 2010.

[9] Y. Yang, M. Xu, J. Guo, and G. Sun, "Bacterial extracellular electron transfer in bioelectrochemical systems," Process Biochemistry, vol. 47, pp. 1707-1714, Dec 2012.

[10] C. Picioreanu, I. M. Head, K. P. Katuri, M. C. M. van Loosdrecht, and K. Scott, "A computational model for biofilm-based microbial fuel cells," Water Research, vol. 41, pp. 2921-2940, Jul 2007.G. Eason, B. Noble, and I. N. Sneddon, “On certain integrals of Lipschitz-Hankel type involving products of Bessel functions,” Phil. Trans. Roy. Soc. London, vol. A247, pp. 529–551, April 1955.

[11] G. Tchobanoglous, F. L. Burton. Wastewater engineering. Treatment, Disposal, Reuse. 3rd ed., Singapore:McGraw Hill, , 1991, pp.47-11.

TRIP GENERATION MODELS

Estimation of trip generated in Querétaro Metropolitan Area as a case study

Martín Ossiel Bailón Mejía *(Author)*
Estudiante de la Maestría en Ingeniería de Vías Terrestres, Transporte y Logística
Facultad de Ingeniería, Universidad Autónoma de Querétaro
Querétaro, México
E-mail: martin34_32@hotmail.com

Saúl Antonio Obregón Biosca *(Author)*
Profesor-Investigador, División de Estudios de Posgrado
Facultad de Ingeniería, Universidad Autónoma de Querétaro
Querétaro, México
E-mail: saul.obregon@uaq.mx

Abstract: *The urban and interurban transportation takes an essential role in the economic and social organization of the cities. Most of the problems in a lot of cities are generated by the population interaction, this interaction is translated into people movements and merchandises within a transportation system, which is possible modelling statistically. From this, modelling trips becomes a necessity to become possible the reproduction or, even, predict the transportation demand.*

Models will be designed to estimate the trip generation and attraction in the Queretaro metropolitan area (ZMQ, in its Spanish acronym) using Multiple Linear Regression (MLR), in order to show the model have a low dependence between the observations.

Keywords— Trip Generation, Transportation Models, Urban Transportation, Planning Transport

I. INTRODUCTION

Urban and inter-urban transport play an essential role in economic and social organization of cities and the population centers around the world. Most of the urban problems in many cities are related to the exchange processes that are generated by the interaction of the population [1]. This exchanges, leads to a need for movement of people and goods in a transportation system that is not very efficient or does not meet the demands of the population; even if such claims have unfavorable characteristics as the schedules concentration of travel, roads heavily congested given regular and random system conditions, so it is necessary to develop some analysis methodologies to evaluate and in some cases anticipate the problems causes this interaction.

From this, it is necessary to create a model that reproduces in the best possible way the interaction of the study area. Planning transport requires, as a first stage, to generate trips between the areas under study. The classic model implies to correlate the data zone in order to predict the attracted or generated trips. Multiple linear regression (MLR) models has been created from explanatory variables of the Queretaro Metropolitan Area, these models are compared each other by analyzing their hypothesis, observations and the required adjustments. Then, the obtained model is analyzed, showing the correlation between the observations.

II. REVIEW OF THE LITERATURE

As a result from the activities that are commonly developed in the society, it has been constituted diverse complex systems in which many activities take place. In the case of the transportation system, to assure the development of the economic activities, it becomes a necessity to create an efficient transportation system of goods and people. Then, the transportation planning becomes important, being necessary to create, in a logical manner, the conditions observed in the context [2].

In transportation planning, the classic model is based in the quantification of trips generated by the people, and the trips attracted into an area to do an activity.

A. Transport Planning

According to the four stages planning model the first stage is the trip generation so, considering that the model focuses on travel, is vital to collect proper information [3], the same processing and interpretation, so that errors in the model by statistical processing of data and, as mentioned, is represented in the best way reality system are minimized.

The objective of trip generation is to estimate the number of trips originated in each zone within the study area, which it is usually correlated to the socioeconomic characteristics of the resident population in that zone [4].

That is why transport planning becomes a necessity. To planning transport is usual to use a travel-based model, which, as its name implies, the important unit of analysis is the journey. The classic model of four stages, that is accepted as a valid tool for transportation planning is generally employed [5]. This procedure, first developed in the early 50s, used aggregated data from subdivisions of the territory (area traffic analysis) to estimate travel with the current network. The steps or stages that make up the four standard process steps are Generation Travel, Travel Distribution, Modal Selection and Assignment of travel (both transit and automatic) [6]. Allocation Land Use should be the first step in the process (thus creating a five-stage model), but usually is omitted because it is generated in isolation since the beginning of the process.

B. Trip Generation

The purpose of the trip generation is usually correlated with the socioeconomic characteristics of the population of each area, then, it is premised that the trip generation is equal to the sum of travel based home more non home-based [6]. That is, traveling can be classified into trips leave home, travel to return home, and not based at home. From the perspective of transport demand, the most important feature of the users is their SES.

Therefore, planning is necessary in transport systems directing it towards certain specific objectives for each area of study so that planning achieves clearly adapt to changes that are required for developing society. Priority then becomes the improved modeling of the transport system, trying to recreate the model is logically the conditions seen in the context [7].

C. Fundamentals of trip generation

The objective of the trip generation stage is to obtain appropriate identification and quantification of the trips to and from the different zones in which the study area is divided [8].

The number of trips generated are frequently very difficult to determine and estimate directly. Some information characterizing the zones can explain the trip generation more precisely than directly estimating the trips; this information is known as explanatory variables. The information regarding land-use, the socioeconomic characteristics in the zones within the study area and the characteristics of the transportation system are usually regarded as explanatory variables [9].

The trip generation models are made up of functional relationships between the trips generated and the explanatory variables, so that the trip demand in a given future scenario can be accurately estimated by knowing the explanatory variables in that scenario.

Trip generation can be divided into:

a) Estimation of the number of trips from each zone (productions).

b) Estimation of the number of trips into each zone (attractions).

The total number of productions must be equal to the total number of attractions in the study area, although this is not necessary the case in each particular zone. This is due to the fact that the home-based trips (HB) are always produced by the zone in which the home is and attracted by another zone (or the same), no matter what way the trip is; on the contrary, non-home-based trips (NHB) are always produced by the origin zone and attracted by the destination zone [10].

Therefore, the productions are higher than attractions in residential areas and attractions are higher than the trip productions in industrial, educational or commercial zones.

D. Variables explaining the trips generation.

The main factors affecting the trip generation involves income, vehicle ownership, type of household (housing) and family size. In addition to factors such as land use, residential density and accessibility are also considered for modeling at the zonal level. The attraction travel is influenced by factors such as the covered space available for industrial, commercial and other services. A zonal level, occupation and accessibility are also used [11]. Modeling trip generation, as well as personal travel, travel load are also of interest, especially in the development of regional load models, so their contribution to congestion becomes significant [12].

III. METHODOLOGY

An O-D survey allows to obtain updated information on the number and the location of the principal points of attraction and generation of trips, predicting the user behavior and the needs of displacement of the people. The optimal sample size usually is linked to its cost, and, therefore, it's necessary to decide which variables are the most important to pick up, so its cost don't exceed the available budget [13].

Consequently, the determination of the sample size and the optimal sampling schemes is impossible in the practice, due to the data will be used as an entrance to different models, many of them complementary and for different analysis.

The sample that was used for the O-D survey in the metropolitan area of Queretaro was stratified, that is, the population was divided in strata so that in each one there was all the homogeneous elements for variables in study. For division into strata, it was used the Basic Geostatistical Area (AGEB, in its Spanish acronym), which is the basic territorial statistical unit of the National Institute of Geography and Informatics of Mexico, it was used and proved to be an total of 658 census tract. The application of the questionnaires was conducted between November 2010 and February 2011 and from March to June 2012 (in both cases were not interviewed during holiday periods). The variables included in the questionnaire were: generation and attraction points of travel, travel time, motive and means of travel, time distribution, socio-economic status of individuals, and overall mobility features in the study area.

The sample was determined from the totality of households counted in the ZMQ as recommended by SEDESOL (S. F.), Ibeas et al. (2007), Bruton (1985) and Ortúzar and Willumsen (2008). It proceeded to survey a total of 3,730 households with a total of 248,626 households in the ZMQ since the population according to the results of the National Census of Housing 2010 is 1,097,025 inhabitants it was decided to interview the 1.5% of households, which is higher than the recommended 1% minimum, providing any type of error and the lack of response or committed by interviewers and country people. The questionnaire to all household members aged seven and asking for all the journeys made yesterday with a time duration of more than five minute trip was applied. All the homes were visited from Tuesday through Saturday, only if the previous day was not a holiday or had not a natural phenomenon that modify travel patterns.

Descriptive statistics was used to determine the socioeconomic characteristics of the users of each means of transport, the time spent on their trips, number of trips, motives, In order to determine the trips generated, we use the MLR to fit the most important variables obtained by the survey, and the trips generated in every AGEB.

IV. RESULTS AND DISCUSSION

To predict trips, is used the multiple regression model, that model relates variables that describe the population or economic activity of each zone and the variables that characterize land use. If this model is applied, variables are required to conform well to the statistical theory that the variables are independent of each other and continuous, in addition to the results of the surveys fit a normal distribution [14]. However, it is likely that in practice not comply because there is correlation between variables but its distribution is not always normal.

A review of the multiple linear regression model is that it treats the explained variable (trip) as a continuous variable, when in fact it is a discrete variable. The specification of a linear model for count data (such as trip) produces partial, inefficient and inconsistent results of its parameters [15]. Also another review arises from the assumption of normality of the error term, which could lead to negative values of the explained variable (trip), which is impossible in the technical implementation cannot exist as "negative trip".

After analyzing several multiple regression models, the model with the best correlation between variables in ZMQ is shown in the table 1.

TABLE I. VARIANCE ANALISIS

VARIABLE	DF	Adj SS	Adj MS	F-Value	P-Value
REGRESSION	3	18556	6185.3	8.93	0
POBLACIÓN	1	15330	15330.4	22.13	0
USO SUELO	1	314	314.4	0.45	0.501
INGRESO	1	1090	1089.9	1.57	0.21
Error		654	453021	692.7	
Lack-of-Fit	96	187057	1948.5	4.09	0
Pure Error	558	265964	476.6		
TOTAL		657	471577		

TABLE II. MODEL SUMMARY

S	Variance	Variance (adjusted)	Variance (predicted)
26.3191	3.93%	3.49%	2.33%

TABLE III. TABLE OF COEFFICIENTS

Term	Coef	SE Coef	T-Value	P-Value	VIF
Constant	4.7	11.8	0.39	0.694	
POBLACIÓN	3.279	0.697	4.7	0	1.07
USO SUELO	-1.31	1.94	-0.67	0.501	1.53
INGRESO	1.35	1.08	1.25	0.21	1.52

In the case of the ZMQ the linear regression model did not have a good fit by a single model so, it is necessary to determine what kind of statistical model presented a better fit for that metropolitan area considering the spatial variables instead. [16] Therefore, the data will be analyzed statistically with linear regression model, and then a model that best fit the data distribution so that the error when estimating travel is minimized is searched.

It is helpful to compare the value p (P value) with significance level (also called alpha or α). A significance level of 0.05 works correctly, since an α of 0.05 means that the probability of concluding that the model fits the data when you really do is just 5%. In short, if a variable has a p value less than α can be concluded that the model fits the data [17]. Given that, it's possible to say that the Multiple Regression Model applied to the ZMQ shows a small relation and a low significance level.

Then it is possible to propose another models that consider spatial correlation, with reference to previous models that do not considering spatial correlation. The modeling process is primarily focused on including the variables related to road network intensity that have already proven to be relevant in the study area, so it's necessary to create a matrix contacts through the creation of Thiessen Polygons, that incorporate the areal neighbors into the spatial model.

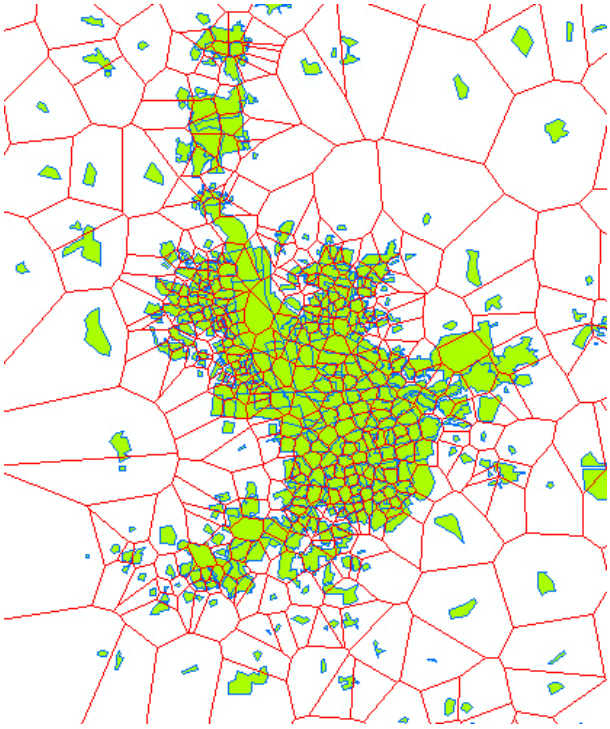

Fig. 1. Thiessen Polygons of ZMQ used to create the matrix contacts

The importance of analyzing these spatial dependence models is that they allow to create a model of variables, such as the behavior of an area, showing how these variables are influenced by the characteristics of its neighbors. Then, this is an important research line, that can be used to adequate the prediction of trips in the study area.

V. CONCLUSIONS

A regression model shows lack of fit when it fails to adequately describe the relationship between the experimental factors and the response variable. A lack of adjustment may occur if significant model terms are not included, such as

interactions or quadratic terms. It may also occur if, at the time we adjust the model, numerous waste with very large values are produced.

The program which models were made was Minitab. This program shows the unadjusted test when the data contains replicas (multiple observations x identical values). The replicas represent a "pure error" because the random variation can cause differences between the values observed response.

These model can be modified by adding, deleting terms or changing data input, that is, the unusual observations could have characteristics as extreme values or atypical values in relation to the regression line in the trip model. In some cases, there are trips values equals to cero, which means that the area cannot produce trips because that area is an industrial zone that only attract home or non-home based trips.

To determine how much effect does the unusual observation, it is possible to adjust the model with and without the unusual observation and comparing the coefficients, p values, the values of variance and other model parameters. If the model changes significantly when these unusual observation is deleted, first, can you determine if the observation corresponds to an error of measurement or data entry, once discarded this option is used to examine the model to determine if an important term or variable that can best fit the model, or if you specified the model incorrectly omitted.

ACKNOWLEDGMENT

This work was made possible thanks to Dr. Saúl Obregón Biosca and a financing from CONACYT, and the program FOMIX that allows the realization of Origin-Destiny surveys.

REFERENCES

[1] RODRIGUE Jean-Paul, COMTOIS Claude, SLACK Brian. (2013) “The Geography of Transport Systems”. Routledge. 3rd Edition. 416 pp.

[2] COVITUR, (1987), Manual de Operación del Sistema de Planeación del Transporte Urbano, UTPS. México.

[3] ORTÚZAR, Juan De Dios, WILLMUNSEN, Luis. (2001) “Modelling Transport”. John Wiley & Sons. Chichester, United Kingdom

[4] ORTÚZAR, Juan De Dios. (1998) Modelos de Demanda de Transporte. Eds. Universidad Católica de Chile, 247 pp.

[5] STOPHER Peter; MCDONALD, Kathie. (1983) “Trip generation by cross-classification: An alternative methodology”. Transportation Research Record, 944 (1983), Washington, United States 84–91.

[6] MOLINERO, Molinero Ángel y SÁNCHEZ Arellano, Luís Ignacio (1996) “Transporte Público: Planeación, Diseño, Operación y Administración.” Quinta del Agua Ediciones. Primera edición. México

[7] COVITUR, (1987), Manual de Operación del Sistema de Planeación del Transporte Urbano, UTPS. México.

[8] ALDANA, Claudia Marcela (2006), "Modelación de la generación y atracción de viajes en el valle de Aburrá" Facultad Nacional de Minas, Universidad Nacional de Colombia Sede Medellín, Colombia.

[9] AMAVI Alexandre, ROMERO Juan, DOMINGUEZ Alberto, IBEAS Angel. (2004) “Advanced Trip Generation/Attraction Models” Procedia - Social and Behavioral Sciences, 160: 430-439 pp. Santander, España.

[10] ORTÚZAR, Juan de Dios y ROMÁN, Concepción (2003) "El problema de modelación desde una perspectiva desagregada: el caso del transporte". EURE, vol. 88, nº 29, p. 149-171.

[11] STOPHER Peter; MCDONALD, Kathie. (1983) “Trip generation by cross-classification: An alternative methodology”. Transportation Research Record, 944 (1983), Washington, United States 84–91.

[12] KULPA, Tomasz (2014) “Freight truck trip generation modelling at regional level” EWGT2013 – 16th Meeting of the EURO Working Group on Transportation. Porto, Portugal.

[13] IBEAS, Ángel, GONZÁLEZ, Felipe, DELL OLIO, Luigi y MOURA, José (2007) Manual de encuestas de movilidad (preferencias reveladas). España: Escuela Técnica Superior de Ingenieros de Caminos, Canales y Puertos de Santander. 159 p.

[14] MIRALLES-GUASCH, Carme (2012) Las encuestas de movilidad y los referentes ambientales de los transportes. EURE, vol. 38, nº 115, p. 33-45.

[15] LONG, Scott John. (1997). “Regression Models For Categorical and Limited Dependent Variables” Thousand Oaks, Sage Publications. California, United States.

[16] OBREGÓN Biosca, Saúl Antonio y BETANZO, Quezada Eduardo (2015) “La Estadística en los estudios de movilidad urbana en la Zona Metropolitana de Querétaro”. En: “Estadística y ciencia: investigación cuantitativa en diversas disciplinas”, BOWATER Rusell y Gómez D. (Ed.) Fontamara: México (en prensa).

[17] WALPOLE, Ronald E; MYERS, Raymond H; MYERS, Sharon L. (1999) “Probabilidad y Estadística para Ingeniería y Ciencias”. Pearson Educación, pp. 739

UNIVERSIDAD AUTÓNOMA DE QUERÉTARO